# NATIONAL ADVISORY COMMITTEE FOR AERONAUTICS
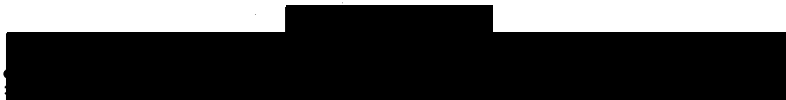
## NACA CONFERENCE ON HIGH-SPEED AERODYNAMICS

### A COMPILATION OF THE PAPERS PRESENTED

Ames Aeronautical Laboratory
Moffett Field, Calif.

215- 130
CLASS. CHANGED TO UNCLASS.
BY AUTHORITY OF NASA CLASS.
CHANGE NOTICE / 5/ 7/
EFFECTIVE _____

MARCH 18, 19, and 20, 1958

13364

NACA CONFERENCE ON

HIGH-SPEED AERODYNAMICS

A Compilation of the Papers Presented

Ames Aeronautical Laboratory
Moffett Field, Calif.

March 18, 19, and 20, 1958

# TABLE OF CONTENTS

Session Chairman:   Robert R. Gilruth

Session Chairman:  Charles J. Donlan

# INTRODUCTION

This document contains reproductions of technical papers presented by staff members of the NACA Laboratories at the NACA Conference on High-Speed Aerodynamics held at the Ames Aeronautical Laboratory of the NACA, March 18, 19, and 20, 1958. The primary purpose of the conference was to convey to the military services and their contractors the results of recent research and to provide those attending with an opportunity to discuss the results.

The papers in this document were prepared for presentation at the conference and are considered to be complementary to, rather than substitutes for, the Committee's more complete and formal reports.

A list of the conferees is included.

CONFIDENTIAL

LIST OF CONFEREES


The following were registered at the NACA Conference on High-Speed Aerodynamics, Ames Aeronautical Laboratory, Moffett Field, Calif., March 18, 19, and 20, 1958:


ABBOTT, Ira H.                         NACA Headquarters
ADAMS, Dr. Mack C.                     Avco Research Laboratory
ALFORD, Joseph S.                      NACA Subcommittee on Internal Flow
ALLEN, H. Julian                       NACA - Ames Laboratory
ALTMAN, John                           North American Aviation, Inc.
AMES, Milton B.                        NACA Headquarters
ANDERSON, Lewis A.                     NACA - Ames Laboratory
ANDERSON, Roger A.                     NACA - Langley Laboratory
ANDREWS, Harold                        Bureau of Aeronautics
ANTONATOS, Philip P.                   Wright Air Development Command
APPOLD, Col. Norman C.                 Air Research and Development Command
AULT, Comdr. Frank W.                  Bureau of Ordnance
AYDELOTTE, John H.                     Boeing Airplane Co.

BAALS, Donald D.                       NACA - Langley Laboratory
BAILEY, Frederick J., Jr.              NACA - Langley Laboratory
BANNER, Richard D.                     NACA High-Speed Flight Station
BARLOW, Capt. John W. B., USAF         Atomic Energy Commission
BARNES, William H.                     Wright Air Development Center
BARTFIELD, James E.                    North American Aviation, Inc.
BASSETT, Preston R.                    NACA Committee on Aircraft, Missile,
                                          and Spacecraft Aerodynamics
BATDORF, Samuel B.                     Lockheed Aircraft Corp.
BATES, G. P.                           NACA Headquarters
BECKELMAN, Bernard F.                  NACA Subcommittee on Internal Flow
BECKER, John V.                        NACA - Langley Laboratory
BEELER, D. E.                          NACA High-Speed Flight Station
BELSLEY, Steven E.                     NACA - Ames Laboratory
BENNETT, Dwight H.                     Convair
BERKOW, Lt. Col. Joseph J.             Air Force Flight Test Center
BERNSTEIN, Harry                       Radioplane Co.
BERTRAM, Mitchel H.                    NACA - Langley Laboratory
BIRD, John D.                          NACA - Langley Laboratory
BISHOP, Bruce A.                       Bendix Aviation Corp.
BLACK, Samuel                          Goodyear Aircraft Corp.
BLAIS, Robert A.                       Gilfillan Bros., Inc.
BLEVISS, Dr. Zegmund O.                Douglas Aircraft Co., Inc.
BLOM, Trygve                           Wright Air Development Center

CONFIDENTIAL

BODE, Dr. H. W. — NACA Special Committee on Space Technology

BOGDONOFF, Prof. Seymour M. — Gas Dynamics Laboratory, Princeton Univ.

BOHLING, Raymond F. — Bureau of Aeronautics
BOND, Aleck C. — NACA - Langley Laboratory
BONNEY, E. Arthur — NACA Subcommittee on Aerodynamic Stability and Control

BOSWELL, Maj. Harry R., USAF — Air University
BOYD, John W. — NACA - Ames Laboratory
BOWMAN, Richard G. — Republic Aviation Corp.
BOYKIN, James A., Jr. — Air Research and Development Command
BRASLOW, Albert L. — NACA - Langley Laboratory
BREUHAUS, W. O. — NACA Subcommittee on Aerodynamic Stability and Control

BRINDLE, Clayton C. — David Taylor Model Basin
BRINICH, Paul — NACA - Lewis Laboratory
BRODSKY, Dr. Robert F. — Convair
BROOKS, William A., Jr. — NACA - Langley Laboratory
BROWN, Clinton E. — NACA - Langley Laboratory
BROWN, Harvey H. — NACA Headquarters
BROWN, Sherwood H. — Northrop Aircraft Corp.
BROWNE, Thomas P. — Douglas Aircraft Co., Inc.
BULLOCH, James E. — Bendix Aviation Corp.
BURBANK, Paige B. — NACA - Langley Laboratory
BURGESS, Edward G., Jr. — Ford Instrument Co.
BURNER, Edwin F. — Bureau of Aeronautics
BUTT, Charles S., Jr. — Bureau of Aeronautics
BUTTERWORTH, Wesley T. — North American Aviation, Inc.
BUXTON, Elliott R. — North American Aviation, Inc.

CALDERBANK, Col. John B. — Wright Air Development Center
CAMPBELL, Dr. George S. — Hughes Aircraft Co.
CAMPBELL, Gordon W. — North American Aviation, Inc.
CARLSON, John W. — Wright Air Development Center
CELNIKER, Leo — Lockheed Aircraft Corp.
CHAMBERLIN, Robert B. — General Electric Co.
CHAPMAN, Charles E. — Convair
CHAPMAN, Dr. Dean R. — NACA - Ames Laboratory
CHARTERS, Dr. A. C. — NACA - Ames Laboratory
CHAUVIN, Leo T. — NACA - Langley Laboratory
CLARK, Carl C. — Naval Air Development Center
CLARK, Edward E. — Glenn L. Martin Co.
CLARK, John R. — NACA Subcommittee on High-Speed Aerodynamics

CLOUSING, Lawrence A. — NACA - Ames Laboratory

x

COHEN, Clarence B.       Ramo-Wooldridge Corp.
COHEN, Stanley R.       Republic Aviation Corp.
COHN, Benedict       Boeing Airplane Co.
COLES, Donald E.       California Institute of Technology
COLLIER, Maj. Robert E., USAF       U. S. Air Force Academy
COOK, William H.       Boeing Airplane Co.
CORNOG, Robert A.       Ramo-Wooldridge Corp.
COUGHLIN, Kenneth J.       Glenn L. Martin Co.
CRAMER, Raymond H.       Applied Physics Laboratory - J.H.U.
CRANE, Robert M.       NACA - Ames Laboratory
CRONVICH, Lester L.       Applied Physics Laboratory - J.H.U.
CROUCH, Capt. Jack G., USAF       Air Force Institute of Technology
CROWDER, Jack R.       Bureau of Aeronautics
CULVER, Irven H.       Lockheed Aircraft Corp.
CZARNECKI, K. R.       NACA - Langley Laboratory

DANIEL, Dr. John H.       Dept. of Defense
DaROS, Charles J.       Douglas Aircraft Co., Inc.
DAUM, F.       Wright Air Development Center
DAVIDSON, Edward Y., III       Air Technical Intelligence Center
DAVIS, Maj. Ernest J., Jr., USAF       Air Research and Development Command
DAVIS, Maj. Howard S., USAF       Air Research and Development Command
DAVIS, Wallace F.       NACA - Ames Laboratory
DAWSON, John R.       NACA - Langley Laboratory
DECREVEL, Roland       Bell Aircraft Corp.
DEEP, Raymond A.       Redstone Arsenal
DeFRANCE, Dr. Smith J.       NACA - Ames Laboratory
DEMORET, Robert B.       Glenn L. Martin Co.
DEMUTH, Orin J.       Aerojet-General Corp.
DIEHL, Capt. Walter S., USN (Ret.)       NACA Committee on Aircraft, Missile, and Spacecraft Aerodynamics
DONALDSON, Coleman duP.       Aeronautical Research Assoc. of Princeton
DONELY, Philip       NACA - Langley Laboratory
DONLAN, Charles J.       NACA - Langley Laboratory
DOOLEY, Donald A.       Aeronutronic Systems, Inc.
DOUGHERTY, Floyd G.       NACA Subcommittee on Fuels
DRAKE, Hubert M.       NACA High-Speed Flight Station
DRAKE, James F.       Marquardt Aircraft Co.
DRAKE, John A.       NACA Subcommittee on Internal Flow
DRYDEN, Dr. Hugh L.       NACA Headquarters
DRYER, Murray       NACA - Lewis Laboratory
DUGGER, Gordon L.       Applied Physics Laboratory - J.H.U.

EBELKE, Maj. William H., USAF       Air Research and Development Command
ECKHARDT, Homer D.       Radio Corp. of America

EDWARDS, Dr. Richard H. — Hughes Aircraft Co.
EGGERS, Dr. Alfred J., Jr. — NACA - Ames Laboratory
EKLOF, Theodore H. — AF Tactical Air Command Headquarters
ELLIS, Frampton E., Jr. — Bureau of Aeronautics
ELLIS, Macon C., Jr. — NACA - Langley Laboratory
EMMONS, Paul C. — NACA Subcommittee on Aerodynamic
  Stability and Control

ENTZ, Phillip H. — Boeing Airplane Co.
EPSTEIN, Albert D. — NACA Subcommittee on Loads
ERICKSON, Albert L. — NACA - Ames Laboratory
ERICKSON, Myles D. — NACA - Ames Laboratory
ETESSAM, Alexander H. — General Electric Co.
EVANS, A. J. — NACA Headquarters
EVERETT, Maj. Phillip E., USAF — Air Research and Development Command

FAGET, Maxime A. — NACA - Langley Laboratory
FARRIOR, Col. William O., USAF — Air Technical Intelligence Center
FEDZIUK, Henry A. — NACA - Langley Laboratory
FEHLNER, Leo F. — Applied Physics Laboratory - J.H.U.
FISHER, Robert E. — Marquardt Aircraft Co.
FLANAGAN, L. E. — Chance Vought Aircraft, Inc.
FLYNN, Warren A. — Tempco Aircraft Corp.
FORBRAGD, Maj. Maurice H., USAF — Air Research and Development Command
FOULDS, Bert A. — Douglas Aircraft Co., Inc.
FOX, Jerome L. — Lockheed Aircraft Corp.
FOX, Dr. Robert H. — Univ. of California Radiation Lab.
FRICK, Charles W., Jr. — Convair
FRIEND, Carl F. — Lockheed Aircraft Corp.
FURLONG, G. Chester — Arnold Engineering Devel. Center
FURUMOTO, Nobuo — Naval Air Missile Test Center

GARNER, William G. — Redstone Arsenal
GARRARD, Wilfred C. J. — Lockheed Aircraft Corp.
GAYNOR, Frank A. — NACA Subcommittee on Automatic
  Stabilization and Control

GIBBONS, H. B. — Chance Vought Aircraft, Inc.
GILLIGAN, Frank — Bureau of Aeronautics
GILRUTH, Robert R. — NACA - Langley Laboratory
GOETT, Harry J. — NACA - Ames Laboratory
GOLD, Archie — Radio Corp. of America
GOODRICH, Maj. J. W., USAF — Wright Air Development Center
GORANSON, R. Fabian — NACA Headquarters
GRADY, Walter T. — Wright Air Development Center
GRAFF, George S. — McDonnell Aircraft Corp.
GRAHAM, Ernest W. — Douglas Aircraft Co., Inc.
GRAY, Edward Z. — NACA Subcommittee on Loads

| | |
|---|---|
| GREENE, Larry P. | NACA Subcommittee on High-Speed Aerodynamics |
| GRIFFITH, Wayland C. | Lockheed Aircraft Corp. |
| GRIZZELL, J. O., Jr. | Wright Air Development Center |
| GROGAN, George C., Jr. | Convair |
| GUDERLEY, Dr. Karl G. | Wright Air Development Center |
| GUNKEL, Robert J. | Douglas Aircraft Co., Inc. |
| | |
| HAAS, Sidney G. F., Jr. | Convair |
| HABER, Bernard D. | North American Aviation, Inc. |
| HALE, Roy E., Jr. | NACA Subcommittee on Loads |
| HALL, Charles F. | NACA - Ames Laboratory |
| HALL, Russell S. | NACA Subcommittee on Engine Performance and Operation |
| HALLETT, Raymond | Douglas Aircraft Co., Inc. |
| HALLOWELL, Frederick C., Jr. | Naval Air Development Center |
| HAMILTON, William T. | NACA Subcommittee on Aerodynamic Stability and Control |
| HANAWALT, Arnold | Bell Aircraft Corp. |
| HANSEN, C. Frederick | NACA - Ames Laboratory |
| HARGIS, C. L. | Air Research and Development Command |
| HARKNESS, John L. | Defense Research Laboratory - Univ. of Texas |
| HARSHMAN, Jack D. | Boeing Airplane Co. |
| HARTLIEB, Dr. Robert J. | Hughes Aircraft Co. |
| HARPER, Charles W. | NACA - Ames Laboratory |
| HARTMAN, Edwin P. | NACA - Western Coordination Office |
| HASERT, Chester N. | Air Force Scientific Advisory Board of Chief of Staff |
| HAUGEN, Maj. Gen. Victor R., USAF | Air Research and Development Command |
| HAVENSTEIN, Comdr. P. L. | Bureau of Aeronautics |
| HAWKINS, S. D. | Wright Air Development Center |
| HAYDEN, Capt. William C., USAF | Air Force Ballistic Missile Div. |
| HEASLET, Dr. Max. A. | NACA - Ames Laboratory |
| HEAD, Prof. Richard M. | U. S. Naval Postgraduate School |
| HEAD, Robert R. | Redstone Arsenal |
| HEALD, Ervin R. | Douglas Aircraft Co., Inc. |
| HEATON, Col. Donald H., USAF | Air Force Research and Development |
| HEDRICK, Ira G. | Grumman Aircraft Engineering Corp. |
| HEGE, Jeremiah C. | Applied Physics Laboratory - J.H.U. |
| HEILIG, Louis F. | Northrop Aircraft Corp. |
| HEIMS, Steve P. | NACA - Ames Laboratory |
| HELDENFELS, Richard R. | NACA - Langley Laboratory |
| HEPPE, Ralph R. | Lockheed Aircraft Corp. |
| HERMACH, Charles. A. | NACA - Ames Laboratory |

HERMANN, Robert A. — Air Force Missile Development Center
HIGGINS, Prof. George J. — Naval Postgraduate School
HILDEBRAND, Robert B. — Boeing Airplane Co.
HLEDIK, John — Naval Ordnance Laboratory
HOEKSTRA, Harold D. — NACA Committee on Aircraft, Missile, and Spacecraft Aerodynamics

HOFF, Dr. Nicholas J. — NACA Committee on Aircraft, Missile, and Spacecraft Construction

HOFFMAN, S. K. — NACA Special Committee on Space Technology

HOHENNER, Dr. Werner W. — Westinghouse Electric Corp.
HOLLEMAN, Euclid C. — NACA High-Speed Flight Station
HOLLENBERG, Harold O. — Bureau of Aeronautics
HOLM, Col. Florian H., USAF — Air Research and Development Command
HOLTBY, Kenneth F. — Boeing Airplane Co.
HOOD, Manley J. — NACA - Ames Laboratory
HUBBARD, Samuel H. — Bureau of Aeronautics
HUGLIN, Col. H. P., USAF — Wright Air Development Center
HUNTSBERGER, Ralph F., Jr. — NACA - Ames Laboratory
HYATT, Abraham — NACA Committee on Aircraft, Missile, and Spacecraft Aerodynamics


IMSTER, Harry F. — McDonnell Aircraft Corp.
ISENBERG, Joel S. — Bell Aircraft Corp.

JACK, Col. Jean — Wright Air Development Center
JACKSON, Roy P. — NACA Subcommittee on High-Speed Aerodynamics

JAGIELLO, Leonard T. — Naval Ordnance Test Station
JANSEN, George R. — Douglas Aircraft Co., Inc.
JARMOLOW, Kenneth — Glenn L. Martin Co.
JOHNSON, Clarence L. — NACA Committee on Aircraft, Missile, and Spacecraft Aerodynamics

JOHNSON, Henry C. — Glenn L. Martin Co.
JOHNSON, Dr. Kent R. — Massachusetts Institute of Technology
JONES, Donald L. — Sperry Gyroscope Co.
JONES, Maj. Kenneth L., USAF — Armed Forces Special Weapons Project
JONES, Robert T. — NACA - Ames Laboratory

KAATTARI, George E. — NACA - Ames Laboratory
KAHR, Prof. Charles H., Jr. — Naval Postgraduate School
KAMM, Robert — Arnold Engineering Development Center
KAPLAN, Dr. Carl — Air Research and Development Command
KARPOV, Boris G. — Ballistic Research Laboratories
KARTVELI, Dr. A. — NACA Committee on Aircraft, Missile, and Spacecraft Aerodynamics

KATKOV, Robert B.     NACA Subcommittee on Aerodynamic Stability and Control
KATZEN, Elliott D.     NACA - Ames Laboratory
KATZOFF, Dr. S.     NACA - Langley Laboratory
KAUFMAN, Harold     Naval Air Development Center
KEARNS, Thomas F.     Bureau of Aeronautics
KEATOR, Col. Randall D., USAF     NACA Committee on Aircraft, Missile, and Spacecraft Aerodynamics

KELLY, Howard R.     Naval Ordnance Test Station
KELSO, Lt. Col. William R., USAF     Office Asst. Secy. of Air Force
KLANN, John L.     NACA - Lewis Laboratory
KLEPINGER, R. H.     Wright Air Development Center
KNACKSTEDT, Dr. W.     Wright Air Development Center
KOCH, Charles J.     NACA Subcommittee on High-Speed Aerodynamics

KOHLER, Prof. Henry L.     Naval Postgraduate School
KORF, Robert S.     NACA Subcommittee on Engine Performance and Operations

KOTCHER, Ezra     Wright Air Development Center
KRICKENBERGER, Lt. Comdr. Custer, USN     Armed Forces Special Weapons Project

KRUG, Edwin H.     Lear, Inc.
KUEHN, Donald M.     NACA - Ames Laboratory
KUGEL, Howard E.     NACA Subcommittee on Loads
KULLAS, Albert J.     NACA Subcommittee on Loads
KURRLE, Christian     AF Deputy Chief of Staff Headquarters

LAMAR, Dr. Edward S., USN     Bureau of Ordnance
LAMAR, William E.     Air Research and Development Command
LAMPROS, Alexander F.     Naval Air Missile Test Center
LECAT, Robert J.     Fairchild Guided Missiles Div.
LEE, John G.     NACA Subcommittee on High-Speed Aerodynamics

LELAND, Paul M.     Rosemount Aeronautical Laboratories - Univ. of Minnesota

LENZ, Ralph C.     Wright Air Development Center
LEW, Dr. Henry G.     General Electric Co.
LEWIS, Lt. Col. William E., USAF     Air Research and Development Command
LI, Dr. Ta Chung Heng     Convair
LIEPMAN, Prof. Hans P.     Aeronautical Engineering Laboratories - Univ. of Michigan

LINDELL, Lt. Col. Keith G., USAF     AF Deputy Chief of Staff Headquarters
LINDEN, J. E.     Bureau of Aeronautics
LINSLEY, Edward L.     Redstone Arsenal
LIVINGSTON, Floyd R.     Minneapolis-Honeywell Regulator Co.
LOBB, Dr. R. Kenneth     Naval Ordnance Laboratory

LOEB, Alfred A. — Picatinny Arsenal
LONG, Joseph E. — NACA Subcommittee on Aerodynamic Stability and Control

LONGFELDER, Harlowe J. — NACA Subcommittee on High-Speed Aerodynamics

LORENZO, Michael — AF Development Planning Headquarters
LOVE, Eugene S. — NACA - Langley Laboratory
LOVELACE, Dr. W. Randolph, II — NACA Special Committee on Space Technology

LOVELL, P. M. — NACA Headquarters
LU, Hoshen R. — Republic Aviation Corp.
LUNDELL, John H. — NACA - Ames Laboratory
LUSKIN, Harold T. — Douglas Aircraft Co., Inc.

MADDOX, Arthur R. — Douglas Aircraft Co., Inc.
MAGGIN, Bernard — NACA Headquarters
MAGNUS, Dr. Richard J. — Aerophysics Development Corp.
MALTHAN, Leonard V. — Douglas Aircraft Co., Inc.
MANGINELLO, E. J. — NACA - Lewis Laboratory
MARCINEK, Jack J. — Convair
MARCKS, Carl A. — Bureau of Aeronautics
MARSCHNER, Lt. Col. B. M., USAF — NACA Subcommittee on Fluid Mechanics
MARTINA, Albert P. — Computation and Ext. Ballistics Lab. - Dahlgren

MATTING, Fred W. — NACA - Ames Laboratory
McCAULEY, Comdr. Charles N., USN — Naval Aviation Ordnance Test Station
McCAULEY, William D. — North American Aviation, Inc.
McCULLOUGH, Capt. Chester E., USAF — Air Research and Development Command
McDONALD, Dr. John C. — NACA Committee on Aircraft, Missile, and Spacecraft Construction

McLELLAN, Charles H. — NACA - Langley Laboratory
MEAD, Merrill H. — NACA - Ames Laboratory
MELKUS, Harald A. — Air Force Missile Development Center
MELROSE, George B. — Bell Aircraft Corp.
MICHAELS, L. E. — Wright Air Development Center
MIGOTSKY, Dr. E. — Avco Manufacturing Corp.
MILLIKAN, Dr. Clark B. — NACA Committee on Aircraft, Missile, and Spacecraft Aerodynamics

MITCHAM, Grady L. — Naval Ordnance Experimental Unit
MOLELLA, Roslo J. — Naval Air Materiel Center
MONTANY, Eugene R. — United Aircraft Corp.
MOOK, Conrad P. — Army Ordnance
MOORE, Franklin K. — Cornell Aeronautical Laboratory
MORDFIN, Leonard — National Bureau of Standards
MOREHOUSE, Lt. Col. Gilbert G., USAF — U. S. Air Force Academy

MORRIS, O. G. — NACA - Langley Laboratory

MOSES, Jason J.                         Ryan Aeronautical Co.
MOUL, Martin T.                         NACA - Langley Laboratory
MURRAY, Maj. Arthur, USAF               Air Research and Development Command
MYERS, Boyd C., II                      NACA Headquarters
MULHOLLAND, Donald R.                   NACA - Western Coordination Office

NAY, Col. Paul F., USAF                 Air Research and Development Command
NEICE, Stanford E.                      NACA - Ames Laboratory
NEILL, Howard W.                        Naval Ordnance Laboratory
NEITZEL, Robert E.                      General Electric Co.
NETTLES, J. Cary                        NACA - Lewis Laboratory
NEWBY, Clinton T.                       NACA Subcommittee on Loads
NEWTON, Floyd C., Jr.                   Douglas Aircraft Co., Inc.
NICHTENHAUSER, Alfred                   Grumman Aircraft Engineering Corp.
NIELSEN, Dr. Jack N.                    NACA - Ames Laboratory
NORELL, Robert G.                       Convair
NULL, Dr. Fay E.                        Air Proving Ground Command

OBERY, Leonard J.                       NACA - Lewis Laboratory
O'CONNOR, Lt. Arthur D., USAF           Air Force Special Weapons Center
O'KEEFE, Charles J.                     Republic Aviation Corp.
O'LAUGHLIN, Burton D.                   Lockheed Aircraft Corp.
O'MALLEY, James A., Jr.                 Bell Aircraft Corp.
ORAZIO, F. D.                           Wright Air Development Center
OSWALD, Dr. William B.                  Douglas Aircraft Co., Inc.
OVERMAN, W. R.                          Air Research and Development Command

PAKE, Frank A.                          Goodyear Aircraft Corp.
PALMER, Carl B.                         NACA Headquarters
PAPPAS, C. C.                           NACA - Ames Laboratory
PARSONS, John F.                        NACA - Ames Laboratory
PATTILLO,                               Air Research and Development Command
   Lt. Col. L. G., Jr., USAF
PEARSON, E. O.                          NACA Headquarters
PEARSON, J. B.                          North American Aviation, Inc.
PECK, Robert F.                         General Electric Co.
PENN, Maj. William W., Jr., USAF        Air Research and Development Command
PERKINS, Prof. Courtland D.             Princeton University
PERKINS, Frank M.                       Convair
PERRY, Charles S., Jr.                  Applied Physics Laboratory - J.H.U.
PERSH, Jerome                           Bureau of Ordnance
PFENNINGER, W.                          Northrop Aircraft Corp.
PIETRANGELI, Gene J.                    Applied Physics Laboratory - J.H.U.
PLATOU, Anders S.                       Ballistic Research Laboratories
PRUITT, Dow C.                          Link Aviation, Inc.
PUSIN, Herman                           NACA Committee on Aircraft, Missile,
                                           and Spacecraft Construction

RADCLIFFE, Maj. John B., Jr., USAF  Atomic Energy Commission
RADCLIFFE, William F.  NACA Subcommittee on High-Speed
    Aerodynamics

RADEY, Kendrick  North American Aviation, Inc.
RAINEY, Robert W.  NACA - Langley Laboratory
RALSTON, Capt. Frank M., USN  Dept. of Defense
RASMUSSEN, R. R.  Wright Air Development Center
RAY, George D.  NACA Committee on Aircraft, Missile,
    and Spacecraft Construction

REESE, David E., Jr.  NACA - Ames Laboratory
REED, James F.  Sandia Corp.
REID, Frank A.  Chrysler Corp.
REINHARDT, William J.  Reaction Motors, Inc.
RELLER, John O., Jr.  NACA - Ames Laboratory
REYNOLDS, L.  Wright Air Development Center
RICLES, R. E.  Avco Manufacturing Corp.
RIDDELL, Dr. Frederick R.  Avco Manufacturing Corp.
RILEY, John B.  Bureau of Aeronautics
RISCHEL, Robert L.  Aerojet-General Corp.
RISLEY, R. S.  Air Research and Development Command
RITCHIE, Dr. Donald J.  AF Development Planning Headquarters
RIZOS, James G.  Wright Air Development Center
ROBERTS, Dr. Leonard  NACA - Langley Laboratory
ROBINSON, Robert F.  NACA Subcommittee on High-Speed
    Aerodynamics

ROBINSON, Russell G.  NACA - Ames Laboratory
ROBINSON, William C.  Dept. of Defense
RODGERS, Col. Thomas A., USA  Dept. of the Army
ROGERS, Milton  Air Research and Development Command
ROPER, Capt. Kenneth H., USAF  Air Force Institute of Technology
ROSE, Leonard  North American Aviation, Inc.
ROSS, Don H.  Massachusetts Institute of Technology
ROSTKOWSKI, Capt. F. J., USAF  Air Research and Development Command

SANDERSON, Herbert C.  Glenn L. Martin Co.
SAVAGE, Charles A.  Convair
SAVET, Dr. Paul H.  American Bosch Arma Corp.
SCHAAF, Samuel A.  Univ. of California
SCHAIRER, George S.  NACA Committee on Aircraft, Missile,
    and Spacecraft Aerodynamics

SCHERRER, Richard  NACA - Ames Laboratory
SCHEUING, Richard A.  Grumman Aircraft Engineering Corp.
SCHNEIDER, William C.  Bureau of Aeronautics
SCHULDENFREI, Marvin  Bureau of Aeronautics
SEA, Austin L.  Air Research and Development Command
SEABERG, Ernest C.  Radio Corp. of America

| | |
|---|---|
| SEATON, Charles H. | Convair |
| SEIDMAN, Oscar | NACA Subcommittee on High-Speed Aerodynamics |
| SEIFF, Alvin | NACA - Ames Laboratory |
| SELNA, James | Radioplane Co. |
| SEN, William J. | Air Research and Development Command |
| SHAPIRO, Norman M. | Redstone Arsenal |
| SHEEHAN, William F. | Sperry Gyroscope Co. |
| SIBILA, A. I. | Chance Vought Aircraft, Inc. |
| SILVERSTEIN, Abe | NACA - Lewis Laboratory |
| SIVELLS, James C. | Arnold Engineering Development Center |
| SKAVDAHL, Howard | RAND Corp. |
| SLIVKA, William R. | NACA Committee on Aircraft, Missile, and Spacecraft Propulsion |
| SMELT, Ronald | NACA Subcommittee on High-Speed Aerodynamics |
| SMITH, C. B. | Pratt & Whitney Aircraft Div. |
| SNOW, Edward C. | White Sands Proving Ground |
| SNYDER, George | NACA Committee on Aircraft, Missile, and Spacecraft Construction |
| SOLLENBERGER, Comdr. Robert L. | Naval Air Test Center |
| SOULÉ, Hartley A. | NACA - Langley Laboratory |
| SPIEGEL, Joseph M. | Southern Calif. Coop. Wind Tunnel |
| SPIELBERG, Irvin N. | Ramo-Wooldridge Corp. |
| STALDER, Jackson R. | NACA - Ames Laboratory |
| STAUFFER, Warren A. | NACA Subcommittee on Loads |
| STEINMETZ, Harold F. | McDonnell Aircraft Corp. |
| STEVENS, Victor I., Jr. | NACA - Ames Laboratory |
| STEVENSON, C. H. | NACA Committee on Aircraft, Missile, and Spacecraft Construction |
| STEWART, Elwood C. | NACA - Ames Laboratory |
| STITT, Leonard E. | NACA - Lewis Laboratory |
| STONE, David G. | NACA - Langley Laboratory |
| STONE, Howard N. | Raytheon Manufacturing Co. |
| STONEY, William E., Jr. | NACA - Langley Laboratory |
| STRATHY, Col. Charlton G., USAF | Air Research and Development Command |
| SUMMERS, Lyle J. | Glenn L. Martin Co. |
| SUTHERLAND, Rodney D. | Convair |
| SUTOR, Alois T. | North American Aviation, Inc. |
| SUTTON, James F. | Lockheed Aircraft Corp. |
| SUTTON, Richard C. | Westinghouse Electric Corp. |
| SWIHART, John M. | NACA - Langley Laboratory |
| SYVERTSON, Clarence A. | NACA - Ames Laboratory |
| TANGREN, Robert F. | Aerojet-General Corp. |
| TAPSCOTT, Lt. Col. Wilbur A., USAF | Air Defense Command |

| | |
|---|---|
| TAYLOR, Harlan D. | United Aircraft Corp. |
| TEPLITZ, Jerome | NACA Subcommittee on Aerodynamic Stability and Control |
| THOMPSON, Floyd L. | NACA - Langley Laboratory |
| THOMPSON, Lt. Wendell J. | Bureau of Aeronautics |
| TILLINGHAST, Norwood W. | Ryan Aeronautical Co. |
| TIMMONS, Kenneth P. | Link Aviation, Inc. |
| TINLING, Bruce E. | NACA - Ames Laboratory |
| TINNAN, Lt. Leonard M., USAF | Air Research and Development Command |
| TITUS, Paul V. | North American Aviation, Inc. |
| TOLL, Thomas A. | NACA - Langley Laboratory |
| TOWNSEND, Capt. Robert L., USN | NACA Committee on Aircraft, Missile, and Spacecraft Aerodynamics |
| TRENT, Warren C. | Chance Vought Aircraft, Inc. |
| TRILLING, Prof. Leon | Massachusetts Institute of Technology |
| TUCKER, Maurice | Lockheed Aircraft Corp. |
| TUSCH, Carl W. | Air Research and Development Command |
| TYNDALL, James W. | White Sands Proving Ground |
| UNDERWOOD, William J. | NACA Liaison Officer, Wright-Patterson AFB |
| VAGLIO-LAURIN, Dr. Roberto | Polytechnic Institute of Brooklyn |
| VAN EVERY, Kermit E. | Douglas Aircraft Co., Inc. |
| VAN METER, James T. | Minneapolis-Honeywell Regulator Co. |
| VINCENTI, Prof. Walter G. | Stanford University |
| VOGELEY, A. W. | NACA - Langley Laboratory |
| VOLLUZ, Ray J. | General Motors Corp. |
| VON DOENHOFF, Albert E. | NACA - Langley Laboratory |
| WAALAND, Irving T. | Grumman Aircraft Engineering Corp. |
| WALL, John K. | Douglas Aircraft Co., Inc. |
| WALLACE, Richard E. | Boeing Airplane Co. |
| WALTER, Capt. William C., USAF | Air Research and Development Command |
| WARD, Edward J. | Wright Air Development Center |
| WARREN, Dr. Walter R. | General Electric Co. |
| WASICKO, R. J. | Wright Air Development Center |
| WASSERMAN, Saul | Picatinny Arsenal |
| WEBB, Henry G. | North American Aviation, Inc. |
| WEISMAN, Yale | NACA Subcommittee on Loads |
| WESESKY, John L. | Air Force Flight Test Center |
| WESTERBACK, Ivar S. | Sperry Gyroscope Co. |
| WESTKAEMPER, John C. | Defense Research Laboratory - Univ. of Texas |
| WHITMIRE, Maj. Warren T., USAF | AF Tactical Air Command Headquarters |
| WHITMORE, Dr. William F. | Bureau of Ordnance |

WHITTEN, James B.               NACA - Langley Laboratory
WILBUR, Stafford W.             NACA Headquarters
WILLIAMS, Edgar P.              RAND Corp.
WILLIAMS, Dr. Thomas W.         NACA Subcommittee on Internal Flow
WILLIAMS, Walter C., Jr.        NACA High-Speed Flight Station
WILSON, Homer B., Jr.           Redstone Arsenal
WIMBROW, William R.             Arnold Engineering Development Center
WINOVICH, Warren                NACA - Ames Laboratory
WISNIEWSKI, Richard J.          NACA - Lewis Laboratory
WONG, Thomas J.                 NACA - Ames Laboratory
WOOD, Donald H.                 NACA - Ames Laboratory
WOOD, Robert M.                 Douglas Aircraft Co., Inc.
WOODLING, C. H.                 NACA - Langley Laboratory
WRAY, Maj. Gen. Stanley T., USAF    Wright Air Development Center
WYSZPOLSKI, Eugene F.           Bureau of Aeronautics

ZABINSKY, Joseph M.             Bell Aircraft Corp.

STUDY OF MOTION AND HEATING FOR ENTRY

INTO PLANETARY ATMOSPHERES

By Dean R. Chapman

Ames Aeronautical Laboratory

INTRODUCTION

One of the many challenging problems associated with space flight is the so-called reentry problem. Intense aerodynamic heating of the structure and possibly severe decelerations of human occupants may occur when orbiting vehicles enter either the atmosphere of the earth or the atmosphere of another planet.

Previous analytical studies of the entry problem have been made with more specific vehicles than those in the present study. By limiting consideration to specific vehicles it is possible to disregard various combinations of the forces which appear in the overall problem. For example, in a study of ballistic vehicles, Allen and Eggers (ref. 1) have shown that very good results can be achieved even though the gravity forces and the centrifugal forces are disregarded. Also, in the case of glide vehicles operating at hypersonic Mach numbers or orbital velocities, it is possible to disregard the vertical component of drag force and the vertical acceleration but not possible to disregard the gravity or centrifugal forces. The early studies of Sänger (ref. 2) have been made on this basis. For the case of a satellite entering an atmosphere through the process of a naturally decaying orbit, however, a realistic solution is not obtained if either the gravity force or the centrifugal force or the vertical component of drag force is disregarded. Full consideration is given herein to these various forces by means of a mathematical transformation which reduces the problem to a form simple enough to handle these various forces without undue complication. In fact, all of the results of this paper are based on the discovery of a mathematical transformation which reduces the relatively complicated pair of motion equations to a single ordinary differential equation that is amenable to solution. This paper is concerned with the problem of entering planetary atmospheres and provides a generalization and extension of previous analytical studies of the entry problem to a wider class of vehicles and to different types of entry than have previously been studied with analytical methods. A more complete report of this study is given in reference 3.

# SYMBOLS

The notation employed is illustrated in figure 1, wherein the flight path is illustrated for a vehicle entering the atmosphere of a planet.

r      distance from center of planet

mg      force of gravity acting upon vehicle towards center of planet

L      lift force, normal to flight path

D      drag force, parallel to flight path

$\varphi$      flight-path angle relative to local horizontal direction, or entry angle

u      component of velocity in local horizontal direction

$\bar{u}$      dimensionless independent variable; $\bar{u} = 1.0$ when velocity is equal to local circular orbital velocity, and $\bar{u} = \sqrt{2}$ when velocity is equal to escape velocity

Z      dependent variable proportional to density of undisturbed atmosphere ahead of vehicle

$\beta$      exponential decay parameter $\left( \dfrac{\rho}{\rho_0} = e^{-\beta y} \right)$

y      altitude

A      reference area for drag $\left( D = C_D \, \dfrac{1}{2} \rho V^2 A \right)$

V      resultant velocity, $u/\cos\varphi$

S      wetted area

$\bar{Q}$      factor for total heat absorbed

$\bar{q}$      factor for heating rate

Q      total heat absorbed

$\left( \dfrac{dQ}{dt} \right)_{MAX}$      maximum heating rate

## ANALYSIS

The basic principle of the method is that, when the horizontal component of velocity is taken as the independent variable and the function $Z$ (proportional to density) is taken as the dependent variable, the complete pair of motion equations can be transformed into a single, second-order, ordinary differential equation:

| Vertical acceleration | Vertical drag force | Gravity minus Centrifugal force | Lift |
|---|---|---|---|

$$\bar{u}\frac{d^2 Z}{d\bar{u}^2} - \left(\frac{dZ}{d\bar{u}} - \frac{Z}{\bar{u}}\right) = \frac{1 - \bar{u}^2}{\bar{u}Z} - \frac{L}{D}\sqrt{\beta r} \tag{1}$$

In completing this transformation, two terms in the complete equations which are small compared with the others are disregarded (ref. 3). For the present analyses an explanation of the physical significance of the various terms appearing in this differential equation is sufficient. In equation (1) it can be seen that the first term on the left-hand side represents the transformed vertical acceleration and the second term represents the vertical component of drag force. The first term on the right-hand side of equation (1) represents the gravity force minus the centrifugal force and the last term represents the vertical component of lift force.

Inasmuch as this differential equation is of second order, two initial conditions suffice for determining a solution. For these conditions the value of the function $Z$ at some initial velocity $\bar{u}_i$ and the value of the derivative $Z'$ at the same initial velocity are selected: $\bar{u} = \bar{u}_i$; $Z(\bar{u}_i) = 0$; $Z'(\bar{u}_i) = \sqrt{\beta r}\,\varphi_i$. It is noted that the initial value $Z'(\bar{u}_i)$ is proportional to the initial angle of descent $\varphi_i$ (negative for descent). The dimensionless parameter $\sqrt{\beta r}$ is essentially constant for any planet and is approximately 30 for the planet Earth. The following example illustrates the initial conditions for the decay of a satellite orbit: $\bar{u}_i = 1$; $Z(1) = 0$; $Z'(1) = 0$. In this case the dimensionless initial velocity is 1.0. The initial angle of descent is negligible, as is the initial density compared with the density at conditions near peak heating or maximum deceleration. Consequently, the initial conditions are simply those indicated.

In order to obtain a better understanding of this differential equation, assume that all of the terms on the right-hand side of equation (1) were neglected - that is, the gravity force, the centrifugal force, and the lift force. Then, the remaining terms on the left-hand side of this equation form a linear differential equation, the solution of which yields exactly the solution of Allen and Eggers for ballistic entry (ref. 1). This should not be surprising inasmuch as they disregarded the forces represented by the terms on the right-hand side of this equation. On the other hand, assume that the terms on the left-hand side of the equation were disregarded - that is, the vertical acceleration and the vertical component of drag force - then, the solution to the remaining terms on the right side is a simple algebraic solution for the Z-function which is exactly the same as the solution for equilibrium gliding flight of hypersonic vehicles originally advanced by Sänger (ref. 2). In the present paper, however, none of the terms in this equation are disregarded, so that all of the subsequent results are numerical solutions based upon equation (1) as given.

## DISCUSSION

Some examples that illustrate the types of results which can be obtained from the method are now considered. In figure 2, a plot is shown of the maximum deceleration together with the miss distance in range due to a $0.5^{\circ}$ error in the initial angle of entry $\varphi_i$ for nonlifting vehicles. It is seen that, if a nonlifting vehicle were intended to enter at an angle of $2^{\circ}$ initially but inadvertently entered at either $1.5^{\circ}$ or $2.5^{\circ}$, the change in impact point would be roughly 100 miles. Therefore, as would be expected, the larger the initial entry angle, the smaller is this error in entry range for a given error in initial entry angle. As can be seen in figure 2, however, arbitrarily large initial entry angles cannot be employed if the device is to carry a human occupant. At an initial entry angle of approximately $3^{\circ}$, the approximate limit of human tolerance to accelerative stress is reached. At lower angles, such as $0^{\circ} < -\varphi_i < 1^{\circ}$ the maximum deceleration is seen to be a little over 8g. This certainly would not be comfortable but is well within the limit of human tolerance. In this figure and subsequently in figure 7, where the approximate human limit to deceleration stress is indicated, it is to be understood that this limit corresponds to transverse orientation of the acceleration loads (that is, with the stresses either in the back-to-chest or chest-to-back orientation). This limit takes into account the approximate duration of the acceleration stress in a manner that is believed to be conservative. It is regarded as only an approximate limit.

As would be expected, the maximum rate of heating also increases with an increase in the initial angle of descent, as indicated in figure 3, where the curve for $\bar{q}_{MAX}$ is seen to be quite similar to the curve for maximum deceleration already discussed in figure 2. The larger the initial angle of descent, the lower is the altitude at which the intense heating takes place and, hence, the higher are the density, the deceleration, and the maximum rate of heating. As is shown in figure 3, however, the total heat absorbed follows an opposite trend to the maximum heating rate. What happens, of course, is that, although the maximum heating rate is increased, the time duration over which the intense heating occurs is very much reduced for the larger initial angles of entry. The net effect is a reduction in the total heat absorbed with increasing entry angle. For example, the heat absorbed at an initial entry angle of $0°$ is twice that absorbed at an initial entry angle of $3°$.

There is a simple and general equation developed by Allen (ref. 1) in his studies on ballistic entry, which helps to understand the qualitative variations of total heat absorbed, as presented in figure 3 and, also, as presented in figures 5, 6, 9, 11, and 12 wherein curves of total heat absorbed are included. The equation for total heat absorbed is

$$\Delta Q = \frac{C_F'}{2C_D} \frac{S}{A} \Delta\left(\frac{mV^2}{2}\right) \tag{2}$$

This equation was developed in the study of ballistic-type entry but actually is general and can be applied to an arbitrary entry path. The equation states that the total heat absorbed for a given change in kinetic energy $\Delta\left(\frac{1}{2} mV^2\right)$ is proportional to the ratio of the wetted area $S$ to the reference area $A$ and, also, is proportional to the ratio of the effective skin-friction coefficient $C_F'$ to the drag coefficient $C_D$.

It is the known qualitative variation of skin-friction coefficient with Reynolds number which explains the qualitative variation of total heat absorbed in figure 3. As the initial angle of descent is increased, the reduction in kinetic energy does not change but heating takes place at lower altitudes, where the densities and Reynolds numbers are higher and, hence, where the skin-friction coefficients are smaller. Thus, equation (2) shows that, in this case or in any other case where heating occurs at lower altitudes for a given loss in kinetic energy, the total heat absorbed is less than if heating occurs at high altitudes.

The entry of lifting vehicles starting with a negligible initial angle of descent $(\varphi_i \simeq 0)$, as would be the case for the orbital decay

of a satellite, is now considered. Figure 4 represents a plot of the Reynolds number per foot at the conditions of maximum heating as a function of the parameter $W/C_D A$ where $W$ is the vehicle weight in Earth pounds. It is seen from the equation in the figure that the Reynolds number is proportional to the Z-function. The point of practical interest, however, is that for typical values of the loading parameter $W/C_D A$, say, in the range between 10 and 100 pounds per square foot, the Reynolds number at peak heating is only of the order of $10^3$ to $10^4$ per foot. These values are low enough to expect extensive runs of laminar flow. For this reason, the calculations of heat transfer in equation (2) and for figures 4 to 6 and 8 to 12 are based upon the assumption of laminar flow. As may be noted in figure 4, the relative values of Reynolds number for the planets Venus, Mars, and Jupiter are not greatly different from those of Earth. Consequently, for entry into the atmospheres of these planets the Reynolds numbers at conditions near maximum heating are sufficiently small to expect much laminar flow on many types of vehicles.

In figure 5, some curves are presented that illustrate the effect of lift-drag ratio on the maximum heating rate experienced during entry from a decaying satellite orbit. The equation for maximum heating rate, shown in the upper right side of this figure, is seen to consist of a series of factors. The group of factors within the braces represents the influence of the particular planet - that is, the coefficient of viscosity $\mu$, the gravitational acceleration $g$, the planet radius $r$, and the exponential decay parameter $\beta$ of the atmosphere. The group of factors under the radical represents the influence of the physical characteristics of the vehicle -- that is, the mass, shape, and dimensions. The factor $\bar{q}$ is related to the Z-function and, as indicated, depends only upon the lift-drag ratio of the vehicle. If the drag coefficient were maintained constant and the lift-drag ratio were increased, such as might be conceived if reaction lift were employed rather than aerodynamic lift, then the maximum heating rate during entry would continually decrease as the lift-drag ratio is increased, as indicated by the dashed curve in figure 5. For aerodynamic lift, however, the drag coefficient and the lift-drag ratio are always coupled in the sense that the lift-drag ratio cannot be indefinitely increased without eventually decreasing drag coefficient. As the formula given in figure 5 indicates, a decrease in the drag coefficient would correspond to an increase in the maximum rate of heating. This coupling between $C_D$ and $L/D$ is different for each family of aerodynamic shapes, three families of which are illustrated in figure 5. The solid curves represent the quantity $\bar{q}/\sqrt{C_D}$. The family of half-cones and the family of half-paraboloids are maintained with the flat surface in the flight direction; the lift-drag ratio is changed by changing the fineness ratio. For the family of flat plates, however, the lift-drag ratio is changed by changing the angle of attack. In all cases, the forces are computed by use of the

Newtonian theory. It is seen that the net effect of the coupling between drag coefficient and lift-drag ratio is such that about the best that can be expected by the use of aerodynamic lift is that the peak rate of heating can be reduced roughly 50 percent for lift-drag ratios in the neighborhood of 0.5 to 1.0. Inasmuch as the dashed curve is closely proportional to $1/\sqrt{L/D}$ (ref. 3), it follows from the equation given in figure 5 that the maximum heating rate would be nearly proportional to $1/\sqrt{C_L}$ and, hence, would be a minimum for vehicles entering at $C_{L_{MAX}}$. Thus, for practical purposes, the maximum heating rate may be minimized by entering in this manner.

In figure 6, a plot similar to that presented in figure 5, in which radiation is disregarded, is shown only for the total laminar heat absorbed. In this case the structure of the corresponding equation for Q also is composed of a series of factors; the group within braces again represents the influence of the planetary atmosphere, the group under the radical represents the influence of the physical characteristics of the vehicle, and the factor $\overline{Q}$ is related to the Z-function and, as indicated, depends only upon the lift-drag ratio. The interesting point in this figure is that for a given drag coefficient the variation in total heat absorbed with lift-drag ratio is just opposite that observed for maximum rate of heating. The explanation for this may be understood by reference to equation (2). As the lift-drag ratio is increased, the overall loss in kinetic energy does not change but the heating takes place at higher altitudes where the friction coefficients are larger and, hence, the total heat absorbed must also be larger. In figure 6 the coupling between drag coefficient and lift-drag ratio is seen to result in an optimum at negative lift-drag ratios in the vicinity of approximately -0.5. The minimum value of total heat absorbed, however, is not greatly different from the value for nonlifting vehicles. When it is considered that the use of negative lift-drag ratios, at least for entry into the Earth's atmosphere, results in large deceleration, it may be concluded that the practical optimum for minimizing total heat absorbed will be achieved by essentially nonlifting vehicles. A large penalty in total heat absorbed by the use of a lifting vehicle is evident from figure 6. Also shown in this figure is a point representing an optimum skip starting from circular orbital velocity. This optimum skip occurs at a lift-drag ratio of about 0.7 $\left(\text{which corresponds to } C_{L_{MAX}}\right)$ and is seen to result in much less total heat absorbed than for the case of smoothly gliding entry. The difference amounts to about a factor of 3. The reason for this may again be seen from equation (2). As compared with a gliding vehicle, a skip vehicle penetrates deeper into the atmosphere where the density is lower and the friction coefficients are lower and, hence, much less heating occurs for a given loss in kinetic energy.

A comparison of the decelerations and aerodynamic convective heating problems for several neighboring planets is now considered. A plot is presented in figure 7 of the maximum deceleration in Earth g units as a function of the vehicle lift-drag ratio for the planets Mars, Venus, Earth, and Jupiter. These curves correspond to entry from satellite velocity starting with $\varphi_i = 0$. The pronounced effect of lift-drag ratio in reducing the maximum deceleration is evident from this figure. For example, a lift-drag ratio of the order of a few tenths reduces the maximum deceleration for Earth from about 8 to 2 or 3. Inasmuch as the circular orbital velocity for Mars is only 12,000 feet per second as compared with roughly 25,000 feet per second for Earth and Venus and 140,000 feet per second for Jupiter, the relative positions of the various curves in figure 7 are to be expected. The decelerations for entry into Mars are sufficiently low that even vehicles with negative lift can be employed without exceeding the approximate limit of human tolerance to deceleration. These limits indicated in figure 7 are different for the different planets, inasmuch as the duration of the deceleration is different for each planet. For example, the duration of entry into Mars is much less than into Jupiter and, therefore, the maximum deceleration tolerable is greater (fig. 7). Entry into Jupiter would impose many problems not imposed by entry into Venus or Mars, inasmuch as the gravitational acceleration even for a vehicle at rest would be at least 2.7g and the velocity necessary to escape from Jupiter is 200,000 feet per second. These factors impose very severe problems indeed and, hence, Jupiter cannot be given practical consideration but is included in figure 7 and in other figures merely for purposes of comparison.

For the same type of entry as was considered in figure 7, the corresponding maximum-temperature parameter experienced during entry for radiation equilibrium is shown as a function of the lift-drag ratio for these planets in figure 8. The quantity $\epsilon$ represents the surface emissivity and would be 1.0 for a black body. In order to understand the numbers on the ordinate, assume that the radius $l$ of the stagnation point is 10 feet and that the parameter $W/C_DA$ has a value of 10 pounds per square foot. Consequently, the denominator $\left(W/C_DAl\right)^{1/8}$ would be 1.0 and, hence, for a black body the numbers indicated on the ordinate scale would represent nearly the maximum surface temperature in $^{\circ}R$. For Mars the maximum surface temperatures are not really severe (as low as 1,300$^{\circ}$ R) when compared with those of the other planets. For Earth and Venus the maximum surface temperature can be as low as roughly 2,000$^{\circ}$ R, which is within the limitations of current metals. For Jupiter, however, the temperatures are of the order of at least 5,000$^{\circ}$ R and would impose a much more severe problem for any radiation-cooled device. As can be seen from the curves in figure 5, the minimum surface temperature occurs in the region of lift-drag ratio between about 0.5 and 1.0.

Curves for total laminar heat absorbed during entry from satellite velocity are shown in figure 9 for the same planets. As would be expected from their relative orbital velocities, the planets in this figure bear the same relative position to each other as in figure 8. The ordinate in this figure represents the total heat absorbed per unit area at a stagnation point of radius of curvature $l$. The units are as indicated in figure 9. In this figure the minimum heat absorbed occurs at negative lift-drag ratios, as would be expected from the discussion of figure 6.

A different type of entry - namely, atmosphere braking - is now considered. In order to land on any of the planets, it is assumed, first, that the velocity must be reduced from some value near escape velocity $(\bar{u} = \sqrt{2})$ to a value near satellite velocity $(\bar{u} = 1)$. If this reduction in velocity is attempted by means of chemical rockets, it would be very inefficient in terms of weight. If it is attempted by means of a low-thrust space engine, it would be inefficient in terms of time. Consequently, there is interest in the process of making successive passes through the atmosphere in order to decrease the velocity from roughly escape velocity to satellite velocity. This type of entry is illustrated schematically in figure 10. The solid line represents a pass through the atmosphere which slows the vehicle down and reduces the apogee of the orbit in preparation for another entry to reduce further the velocity and apogee, etc., until circular velocity is obtained. The ordinate in this figure is the same as that in figure 8. The abscissa is the maximum acceleration experienced during the braking process. A number of other parameters could have been plotted as the abscissa. For example, the altitude of closest approach to the planet's surface could be employed inasmuch as the closer the vehicle passes to the surface, the greater the maximum deceleration experienced during this pass. Of course, if the vehicle passes too close to the surface, then in a single pass the velocity would be reduced sufficiently to cause an impact with the surface in the first pass. This type of entry is indicated by the long-dash lines in figure 10. From this figure it is seen, for example, that, in order to limit the maximum temperatures to the order of 2,500° R, about the greatest number of g units that can be experienced during a single pass is only a few tenths. As it turns out, this is sufficient to complete the reduction from escape velocity to circular satellite velocity in roughly six or seven passes. If the vehicle experiences greater decelerations, as would be the case by making the pass closer to the planet's surface, it is seen that the maximum deceleration is steadily increased up to a certain point where it discontinuously increases to a value corresponding to the completion of entry in the first pass. In the case of Earth, for example, the curve in figure 10 shows that, when the maximum deceleration is somewhat less than 4g, the single pass will slow the vehicle down sufficiently to complete the entry in the first pass. This means that circular orbital velocity is obtained before leaving the atmosphere. At this point (represented by a small vertical

bar in fig. 10) the maximum value of the deceleration suddenly increases to about 7.2g as the vehicle completes the entry, but the temperature does not increase inasmuch as the maximum temperature already has been experienced before the vehicle has been reduced from escape velocity to satellite velocity. About the largest deceleration that can be experienced in the process of atmosphere braking on Mars is somewhat less than 1 g. For Jupiter, as would be expected, much more deceleration can be experienced without completing the entry in the first pass, but the temperatures also become very large.

The heat absorbed during a single pass through the atmosphere is presented in figure 11. The ordinate is the same as that in figure 9. Again, the same relative position of the different planets is noted. In figure 11, however, it is seen that, once a sufficient deceleration is experienced to slow down a vehicle to circular orbital velocity, a further increase not only discontinuously increases the maximum deceleration but also discontinuously increases the heat absorbed. This of course is because of the additional heat which must be absorbed in reducing the velocity from satellite velocity to zero. Up to the point beyond which a single pass to impact occurs, the heat absorbed in the single pass of atmosphere braking increases because of the greater loss in kinetic energy. Where only a single pass occurs (long-dash curves in fig. 11), the total change in kinetic energy is the same. As may be seen for Mars, the greater the maximum deceleration, the lower is the total heat absorbed. The reason for this can again be seen from equation (2). As the vehicle passes closer to the planet's surface and experiences increased deceleration upon entry, heating occurs at lower and lower altitudes where the friction coefficients also are lower and, hence, the total heat absorbed is lower. It is seen in figure 11 that, if the heat absorbed in a single pass is kept within the same limitations as for the heat absorbed during the entire reentry from satellite velocity to impact (about 3,000 for Earth), the maximum deceleration which can be experienced during the braking process is about 1.5g. As it turns out this is sufficient to complete the reduction from escape velocity to satellite velocity in two passes. In such a procedure, of course, the heat absorbed in the first pass could be radiated away before the satellite returns to begin the second pass.

The curves in figure 12 illustrate the effect of lift-drag ratio on the heat absorbed during a single pass through the atmosphere. In this figure, the abscissa is now the dimensionless velocity $\bar{u}_{ex}$ at the exit of the braking process, that is, at the exit of the single pass. The pass in all cases starts with an initial velocity representing escape velocity. A given value of $\bar{u}_{ex}$ represents a given loss in kinetic energy per unit mass; hence, for a given change in kinetic energy during a single pass, the heat absorbed is reduced as the lift-drag ratio is increased. This is just opposite the trend observed in figure 6, where
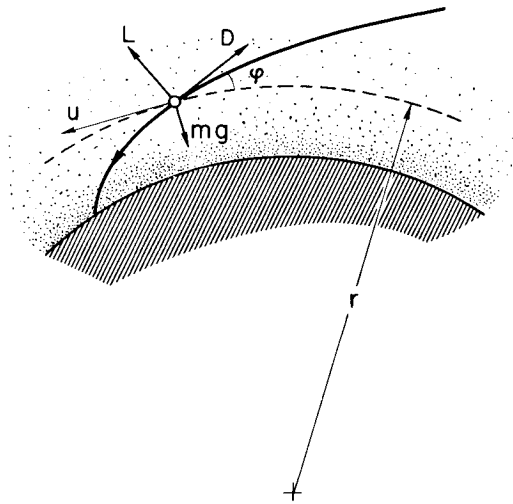
it was noticed that the greater the lift-drag ratio the greater is the total heat absorbed during entry from satellite velocity. The explanation is as follows: in order to reduce the velocity by a given amount in a single pass, a lifting vehicle must penetrate deeper into the atmosphere than a nonlifting vehicle. This means that, for a given change in kinetic energy, the greater the lift the lower is the altitude at which heating occurs; hence, the lower the friction coefficient the less is the heating (eq. (2)). Although it is desirable, insofar as heat absorbed is concerned, to use a vehicle with lift in the process of atmosphere braking, once the velocity is reduced to circular satellite velocity it is desirable to use a nonlifting vehicle or even a vehicle with negative lift.

## REFERENCES

1. Allen, H. Julian, and Eggers, A. J., Jr.: A Study of the Motion and Aerodynamic Heating of Missiles Entering the Earth's Atmosphere at High Supersonic Speeds. NACA TN 4047, 1957. (Supersedes NACA RM A53D28.)

2. Sänger, Eugen: Raketen-Flugtechnik. R. Oldenbourg (Berlin), 1933.

3. Chapman, Dean R.: An Approximate Analytical Method for Studying Entry Into Planetary Atmospheres. NACA TN 4276, 1958.

NOTATION



TRANSFORMATION

$$\bar{u} \equiv \frac{u}{\sqrt{gr}}$$

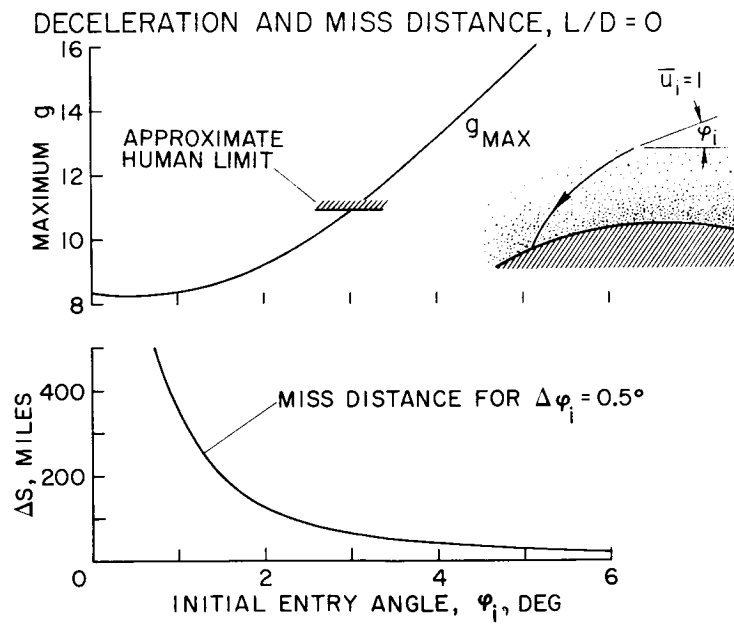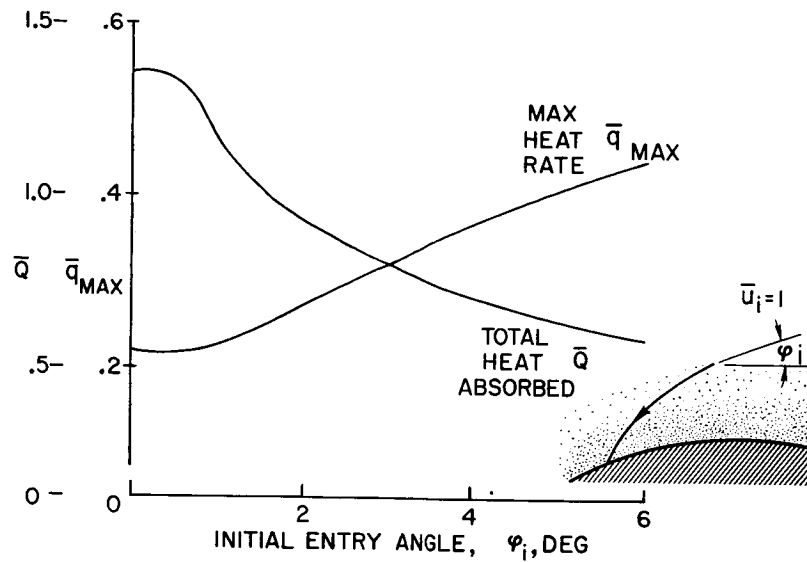$$Z(\bar{u}) \equiv \left[\frac{\sqrt{r/\beta}}{2(m/C_D A)}\right]\bar{u}\rho$$

Figure 1

DECELERATION AND MISS DISTANCE, L/D = 0



Figure 2

ENTRY HEATING FOR LAMINAR FLOW, L/D=0



Figure 3

REYNOLDS NO. AT MAX HEATING ($\overline{u}_i=1, \varphi_i=0$)
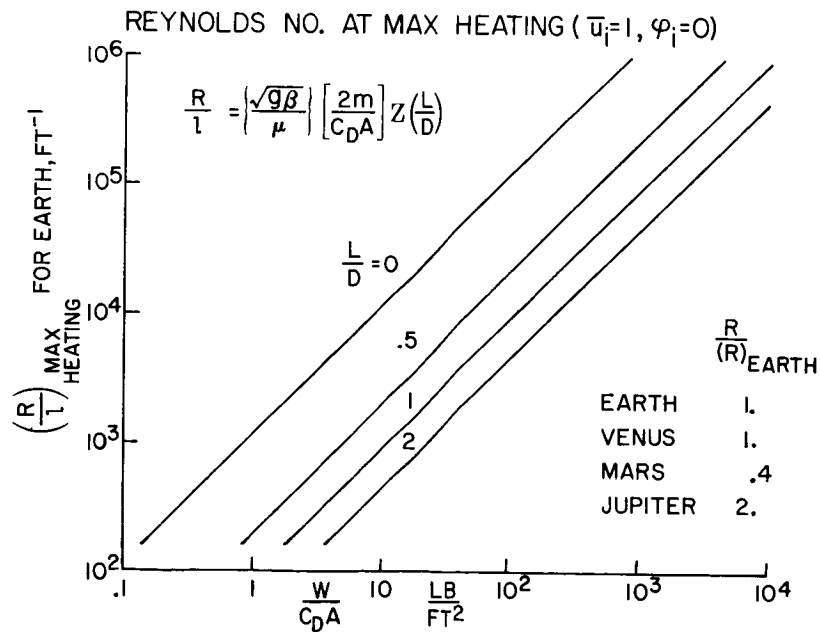


Figure 4

## EFFECT OF L/D ON LAMINAR HEATING RATE, $\bar{u}_i=1$  $\varphi_i=0$

$$\left(\frac{dQ}{dt}\right)_{MAX} \sim \left\{\mu^{\frac{1}{2}} g^{\frac{3}{2}} r^{\frac{5}{4}} \beta^{\frac{1}{4}}\right\} \sqrt{\frac{m}{C_D A l}} \, \bar{q}\left(\frac{L}{D}\right)$$
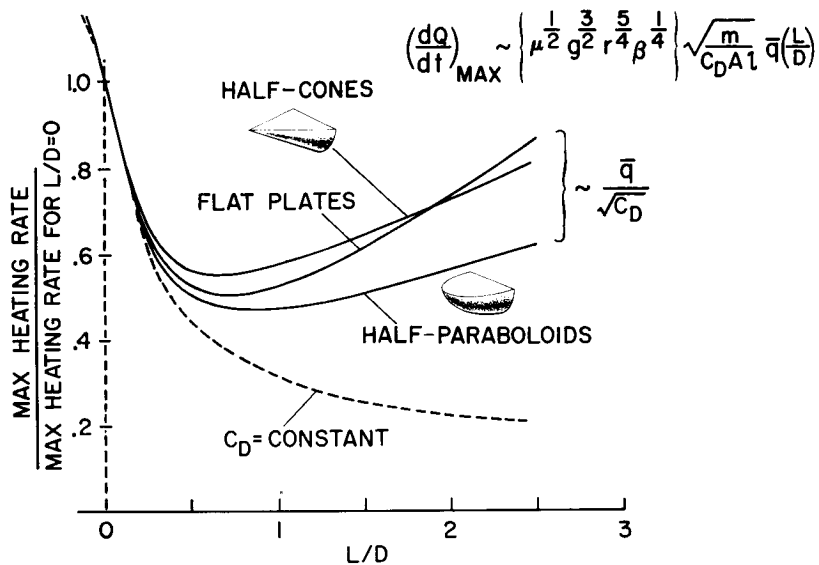
Figure 5

## EFFECT OF L/D ON TOTAL HEAT ABSORBED, (LAMINAR)

$$Q \sim \left\{\frac{\mu^{\frac{1}{2}} g r^{\frac{5}{4}}}{\beta^{\frac{1}{4}}}\right\} \sqrt{\frac{m}{C_D A l}} \, \bar{Q}\left(\frac{L}{D}\right)$$

Figure 6

MAX DECELERATION FOR ORBITAL DECAY, $\left(\overline{u}_i = 1, \varphi_i = 0\right)$

APPROXIMATE
HUMAN LIMIT

JUPITER

MARS

EARTH
VENUS

Figure 7

MAXIMUM SURFACE TEMPERATURE
ORBITAL DECAY

JUPITER

$\dfrac{T_{W_s} \epsilon^{\frac{1}{4}}}{\left(\dfrac{W}{C_D A l}\right)^{\frac{1}{8}}}$

$\dfrac{°R}{\left(\dfrac{LB}{FT^3}\right)^{\frac{1}{8}}}$

EARTH

VENUS

MARS

L/D
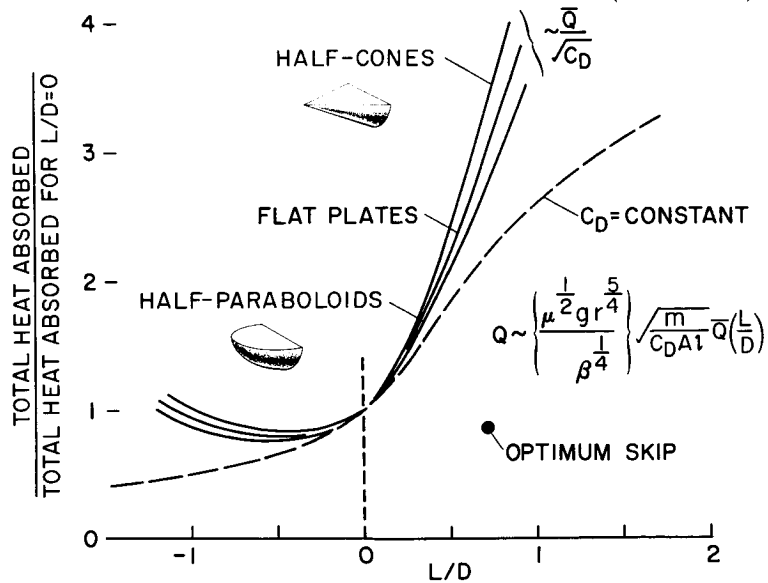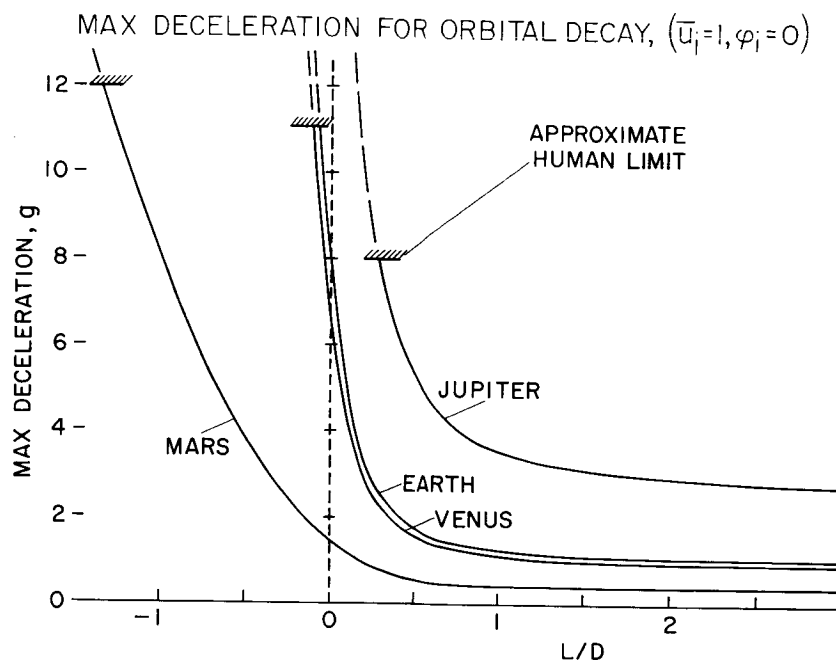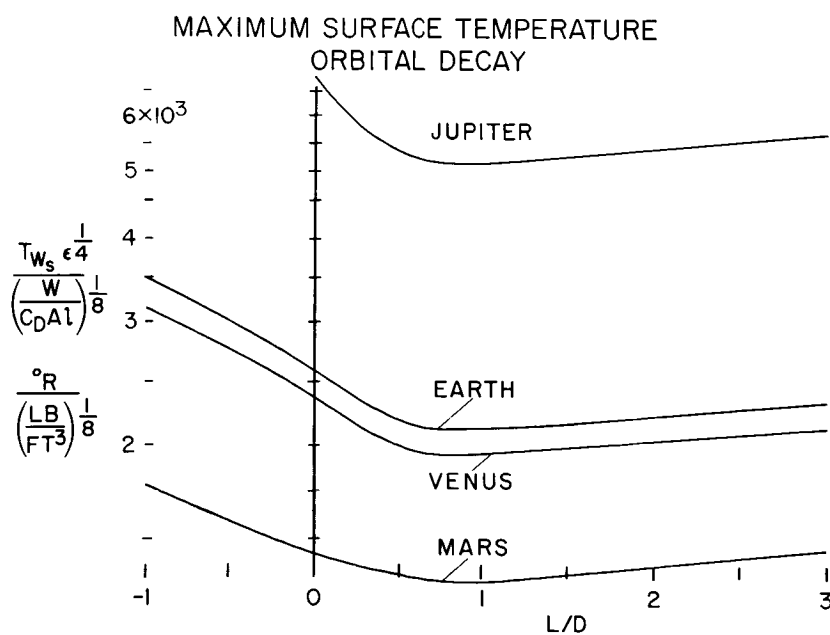
Figure 8

TOTAL LAMINAR HEAT ABSORBED FOR ORBITAL DECAY
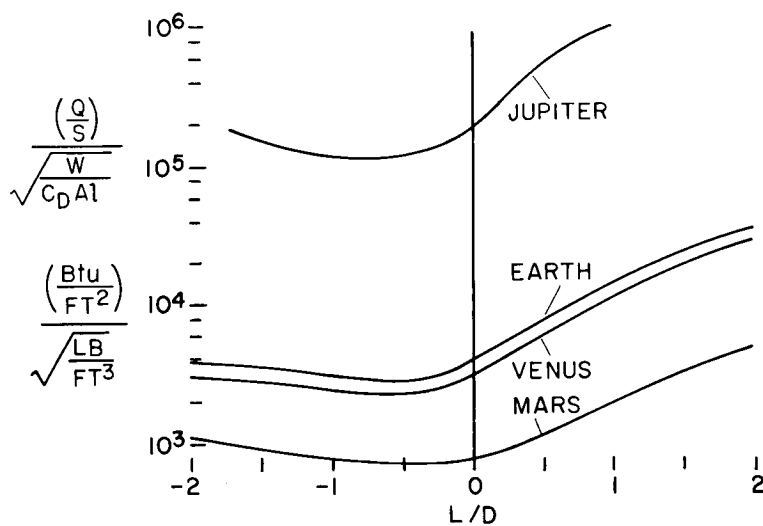


Figure 9
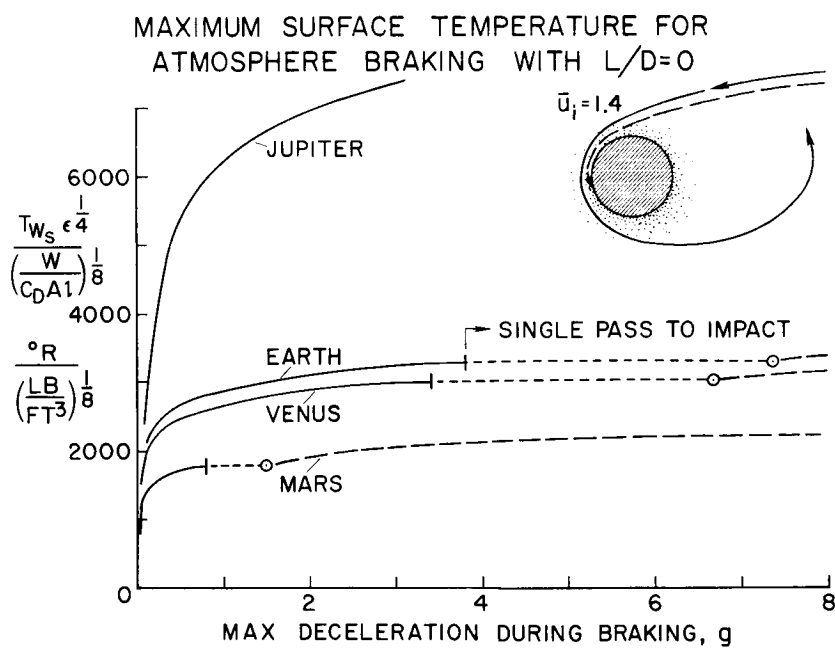
MAXIMUM SURFACE TEMPERATURE FOR
ATMOSPHERE BRAKING WITH L/D=0



Figure 10

## LAMINAR HEAT ABSORBED IN SINGLE PASS FOR ATMOSPHERE BRAKING WITH L/D=0, $\bar{u}_i$=1.4



$$\frac{\left(\frac{Q}{S}\right)}{\sqrt{\frac{W}{C_D A_1}}}$$

$$\frac{\left(\frac{Btu}{FT^2}\right)}{\sqrt{\frac{LB}{FT^3}}}$$

MAX DECELERATION DURING BRAKING, g
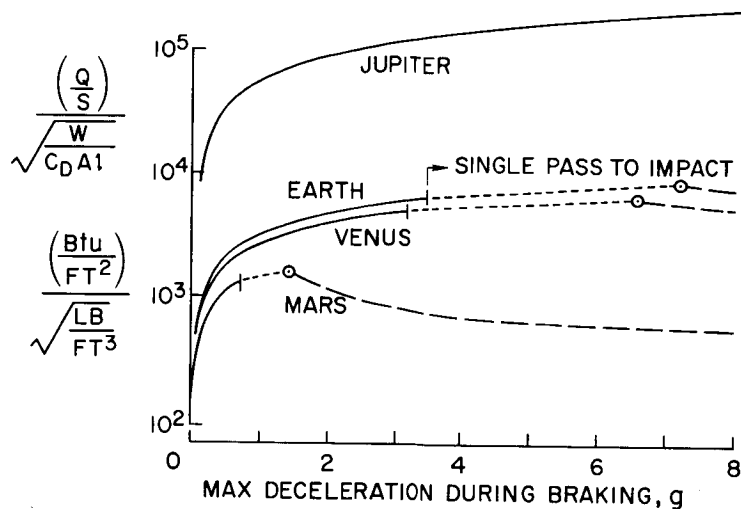
Figure 11

## EFFECT OF L/D ON LAMINAR HEAT ABSORBED IN SINGLE PASS FOR ATMOSPHERE BRAKING



DIMENSIONLESS TOTAL HEAT ABSORBED DURING BRAKING, $\bar{Q}$

DIMENSIONLESS VELOCITY AT EXIT OF BRAKING, $\bar{u}_{ex}$

Figure 12

PRELIMINARY STUDIES OF MANNED SATELLITES

WINGLESS CONFIGURATION:   NONLIFTING

By Maxime A. Faget, Benjamine J. Garland,
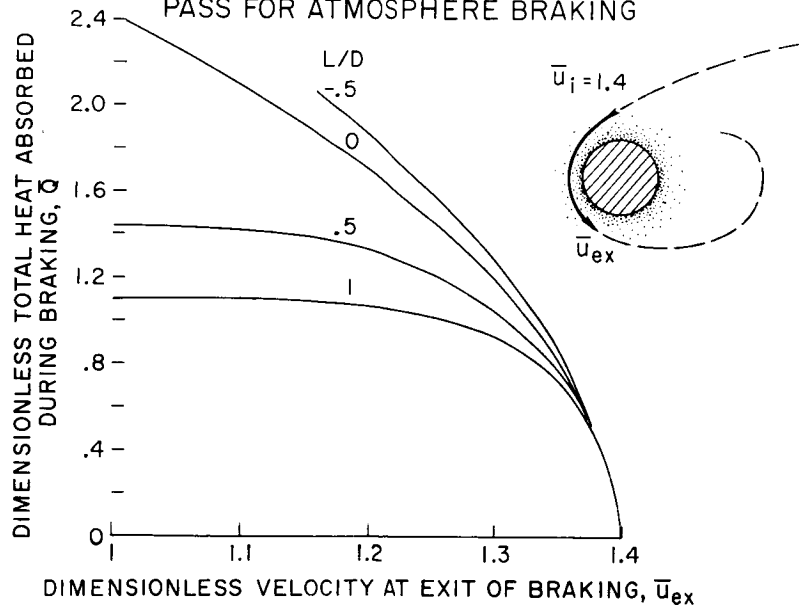and James J. Buglia

Langley Aeronautical Laboratory

INTRODUCTION

This paper is concerned with the simple nonlifting satellite vehicle which follows a ballistic path in reentering the atmosphere. An attractive feature of such a vehicle is that the research and production experiences of the ballistic-missile programs are applicable to its design and construction.

The ballistic reentry vehicle also has certain attractive operational aspects which should be mentioned. Since it follows a ballistic path there is a minimum requirement for autopilot, guidance, or control equipment. This condition not only results in a weight saving but also eliminates the hazard of malfunction. In order to return to the earth from orbit, the ballistic reentry vehicle must properly perform only one maneuver. This maneuver is the initiation of reentry by firing the retrograde rocket. Once this maneuver is completed (and from a safety standpoint alone it need not be done with a great deal of precision), the vehicle will enter the earth's atmosphere. The success of the reentry is then dependent only upon the inherent stability and structural integrity of the vehicle. These are things of a passive nature and may be thoroughly checked out prior to the first man-carrying flight. Against these advantages the disadvantage of large area landing by parachute with no corrective control during the reentry must be considered.

In a previous paper, Dean R. Chapman has shown that the minimum severity of the deceleration encountered during a ballistic reentry is related to the fundamental nature of the planet. Thus it can be considered a fortunate circumstance that man can tolerate this deceleration with sufficient engineering margin.

- SYMBOLS

L             lift

D             drag

W            weight

$C_D$          drag coefficient

A             cross-sectional area (frontal)

$C_{N_\alpha}$        normal-force coefficient slope per radian

$C_{L_\alpha}$        lift coefficient slope per radian

$C_{m_\alpha}$        pitching-moment coefficient slope per radian

I             moment of inertia (general)

m            mass

P             period

$a_n$          normal acceleration

$a_X$          acceleration (longitudinal)

$R_d$          Reynolds number based on diameter

$T_j$          thrust of jet

M            Mach number

$C_m$          pitching-moment coefficient

$C_N$          normal-force coefficient

d             diameter

y             distance

For aerodynamic coefficients, the frontal area is the reference area and the diameter is the reference length.

## DISCUSSION

Figure 1 shows man's approximate tolerance to "g" loads for several positions in which he may be supported. The information shown was obtained from reference 1. It should be noted that the tolerance to acceleration varies for different individuals and that figure 1 does not give a complete picture of the problem. It does, however, neatly establish an approximate basis for consideration of the acceleration loads to be described.

The deceleration history of a typical reentry is presented in figure 2. For this case the reentry angle is -0.8° and results in a maximum deceleration of 8.5g. It should be noted that the buildup in deceleration is very gradual and that the overall severity is well within human tolerances. In fact, larger reentry angles resulting in a more severe deceleration history should be tolerable.

The acceleration loads which may be encountered during launching are presented in figure 3. The acceleration history shown was calculated by using elements of a present-day ballistic-missile propulsion system as a basis. The severity of this acceleration history is approximately the same as the deceleration history in figure 2 and is well within the human tolerance limit.

The one maneuver which the ballistic reentry vehicle must perform is the retrograde maneuver. This maneuver consists of deflecting the orbit by the proper application of an impulse provided by the retrorocket.

The performance required from the retrorocket to initiate reentry from a circular orbit of 800,000 feet altitude is shown in figure 4. This figure shows the flight-path angle that would be obtained at the 350,000-foot level when the retrorocket "kicks" the satellite with various velocity changes. It can be seen that use of a rearward impulse is much more effective than a downward one. The downward one has some merit, however, in that it would cause reentry to occur much sooner after the impulse was applied. With a rearward impulse the satellite would travel approximately halfway around the earth before reentering the atmosphere; with a downward impulse the satellite would travel only about one-fourth of the way around before reentry.

There are some particular advantages to be gained if reentry is made from an elliptical orbit. Figure 5 is a schematic drawing of an elliptical orbit and will help illustrate this. The elliptical orbit has a perigee point where it passes close to the earth's surface and an apogee point which is 180° away and is the point of highest altitude. Inasmuch as the satellite is closest to the earth at the perigee, the perigee forms a bucket as far as determining the landing point is concerned. Since the landing

point naturally tends to be in vicinity of perigee, the accuracy of the reentry maneuver is improved when the landing point is purposely made in the vicinity of the perigee.

Inspection of figure 5 suggests an interesting possibility. If the satellite is given a moderate rate of spin about its longitudinal axis at last-stage burnout, it can be attitude-stabilized in space and will be traveling exactly backward at the apogee in the correct attitude for firing the retrorockets. Also at the perigee it will be in the correct nose-first attitude for entry. The required spin rates are well within the tolerance of a supine or prone pilot. This technique of spin stabilization might simplify considerably the guidance and control equipment necessary for attitude stabilization.

Figure 6 shows the required performance of the retrorocket when used in initiating reentry from the apogee of an elliptical orbit. It can be seen that increasing the height of the apogee decreases the amount of impulse required to produce a given reentry path angle.

During the last several years the National Advisory Committee for Aeronautics has been intensively studying the important aerodynamic aspects of ballistic-missile reentry bodies. Much of this work is directly applicable to the problem at hand. Thus, fairly well established information is available to help in the choice of the configuration for the ballistic reentry vehicle. Table I summarizes some aerodynamic characteristics for four different types of nose shapes.

The nose shapes shown in table I are compared on a basis of equal weight and diameter. A weight of 2,000 pounds was chosen as being reasonable for the ballistic reentry satellite. A diameter of 7 feet was chosen as being adequate for the occupant supported in the prone or supine position. The aerodynamic characteristics shown in the table are those associated with the forebodies (shown by the solid lines). The afterbodies are arbitrary shapes. Four different nose shapes are shown. They are a hemisphere, a heavily blunted $15^\circ$ cone, a $53^\circ$ cone, and a nearly flat nose consisting of a spherical segment. The position of the neutral point and an arbitrary center-of-gravity location are indicated for each of these noses.

Values of $W/C_D A$, total heating load, and maximum heating rate are also listed for these noses. The heating was computed for reentry starting at 350,000 feet with a path angle of $-0.8^\circ$. Computations were based upon the methods shown in references 2 and 3 and the experimental data presented by William E. Stoney in a subsequent paper. It should be noted that the heating is dependent upon both the shape and the $W/C_D A$. The peak heating rates are of an order of magnitude less than those

experienced by ballistic missiles. The other aerodynamic derivatives shown are of interest when the motion of the body during reentry is considered.

The heating shown is based on the assumption that laminar flow exists over the entire face of the nose. This assumption at least seems to be justified for the nearly flat nose and is illustrated in figure 7. Figure 7 shows the variation of Reynolds number based on nose diameter with Mach number for several possible reentry paths in which the initial path angle is varied from -0.5° to -2.5°. Also shown are two flights of rocket powered models (refs. 4 and 5) in which laminar flow was measured over the entire flat nose of the model. Although these flights do not indicate the maximum Reynolds number which could be obtained with laminar flow, they do show that laminar flow does exist at Reynolds numbers greater than those which would be expected during the reentry.

Based upon the foregoing statements, a specific configuration was chosen in order to bring into focus some of the more detailed reentry problems. This configuration is shown in figure 8. This space capsule is conceived of as traveling in two directions. During launching it would provide a fairly low-drag nose for the boosting system, but during reentry it would have the desired heat shield in the front. This reversal in attitude also simplifies the support system for the occupant, since the same couch is properly alined for both the acceleration and deceleration phases of the flight. The heat shield chosen is the one with the lowest heating of the four shapes studied.

During reentry the attitude control system will be used to aline the vehicle with the flight path. Although this alinement should usually be accomplished with sufficient precision, one can expect that either through error or malfunction the capsule will occasionally enter the atmosphere with an attitude error. It is assumed that if no corrective control is applied, the capsule will develop a pitching and yawing oscillation.

In a subsequent paper, John D. Bird will show that the limit envelope of this oscillation is not affected by the degree of static stability and is independent of dynamic stability down to the point of maximum deceleration. From this framework it is easy to study the violence of the residual oscillation at maximum g. Figure 9 shows the period and normal acceleration that would be encountered during an oscillating reentry. The equations shown for $P$ and $a_n$ were developed by simply substituting $q = \dfrac{a_x W}{C_D A}$ into the standard expression for these quantities.

Inspection of the resulting equation shows that the length of the period is directly proportional to the square root of $C_D/C_{m_\alpha}$. Thus to

decrease the severity of the oscillation, the period may be lengthened by choosing a shape having a high value of $C_D/C_{m_\alpha}$. Similarly, the severity of the oscillation may be decreased by reducing the resulting normal acceleration for a given angle of attack. Here it is desired to have a large ratio of $C_D$ to $C_{N_\alpha}$. It can be seen that from both these considerations the nearly flat nose is very favorable. It is estimated that this configuration would have a period of roughly 1 second at maximum deceleration and that, with an initial attitude error of $10^\circ$ at the start of reentry, the maximum normal acceleration would be approximately 0.1g.

The particular configuration shown may have negative damping and, as John D. Bird will show, this situation will result in a buildup in the oscillation amplitude after the point of maximum deceleration is passed. This amplitude will approximately equal the initial attitude error of reentry when sonic velocity is reached. In order to determine the limit that the oscillation might build up to in the subsonic region, some tests (unpublished) were carried out in the Langley 20-foot free-spinning tunnel. These tests showed that the configuration oscillated at an amplitude of approximately $45^\circ$. The use of a small drogue chute about one-half the diameter of the capsule reduced the amplitude of the oscillation to about $20^\circ$. An extendable flared skirt originating at the maximum diameter essentially eliminated any oscillatory motion. However, such a device may be unduly complicated to be practical. An alternate configuration, the $53^\circ$ cone shape, was tested and proved to have very little oscillatory motion.

It appears very likely that, after initial flights of the ballistic reentry type of satellite, the need to reduce the size of landing area which must be kept under surveillance may result in the desire to improve the landing-point accuracy. For this reason several simple means of producing small amounts of lift have been investigated. Figure 10 illustrates three such schemes.

The use of the attitude jets provide a simple method since they would already be in existence. Because of a low value of $C_{m_\alpha}$, a high moment arm, and a high negative $C_{L_\alpha}$, these jets appear to be fairly effective in producing lift. With this arrangement an $L/D$ of 0.1 could be produced during the entire reentry deceleration with an expenditure of approximately 80 pounds of $H_2O_2$. A drag flap is shown to be very effective by some tests carried out in the Langley 11-inch hypersonic tunnel and presented by John A. Penland in a subsequent paper. A trimmed $L/D$ of 0.2 may be obtained with a flap area 4.5 percent of the frontal area. Similarly, a small center-of-gravity shift is also very effective in producing lift.

Figure 11 illustrates the effect of a small amount of lift during reentry. It is seen that with a lift-drag ratio of 0.2 the maximum deceleration is roughly half of that with no lift. This value will also stretch the range by 280 miles. Similarly, the landing point may be deflected to the side by the use of lift. A 90° bank angle, for instance, will provide a lateral displacement of roughly 60 miles with a lift-drag ratio of 0.1.

These possibilities of variations in range or lateral displacement of the landing point may be looked upon in two ways. As previously stated it may be considered as a useful method of correcting errors in the ballistic path.

However it should be pointed out that this condition should also be considered as an indication that, in the case where a pure ballistic reentry trajectory is desired, the ballistic path will be highly sensitive to small aerodynamic misalinements and center-of-gravity displacements. The employment of a slow rate of spin to produce an averaging effect may prove to be a necessity in order to avoid this difficulty. The use of a shape which is incapable of producing lift such as the sphere would also avoid this difficulty.

## CONCLUSION

In conclusion it appears that, as far as reentry and recovery is concerned, the state of the art is sufficiently advanced so that it is possible to proceed confidently with a manned satellite project based upon the ballistic reentry type of vehicle.
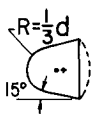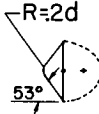
CONFIDENTIAL

# REFERENCES

1. Beckman, E. L., Zeigler, J. E., Duane, T. D., and Hunter, H. N.: Some Observations on Human Tolerance to Accelerative Stress. Phase II. Preliminary Studies on Primate Subjected to Maximum Simple Accelerative Loads. Jour. Aviation Medicine, vol. 24, no. 5, Oct. 1953, pp. 377-392.

2. Fay, J. A., and Riddell, F. R.: Theory of Stagnation Point Heat Transfer in Dissociated Air. Jour. Aero. Sci., vol. 25, no. 2, Feb. 1958, pp. 73-85, 121.

3. Lees, Lester: Laminar Heat Transfer Over Blunt-Nosed Bodies at Hypersonic Flight Speeds. Jet Propulsion, vol. 26, no. 4, Apr. 1956, pp. 259-269.

4. Stoney, William E., Jr., and Swanson, Andrew G.: Heat Transfer Measured on a Flat-Face Cylinder in Free Flight at Mach Numbers up to 13.9. NACA RM L57E13, 1957.

5. Bland, William M., Jr., Swanson, Andrew G., and Kolenkiewicz, Ronald: Free-Flight Aerodynamic-Heating Data at Mach Numbers up to 10.9 on a Flat-Faced Cylinder. NACA RM L57K29, 1958.

CONFIDENTIAL

TABLE I

COMPARISON OF NOSE SHAPES
WEIGHT, 2,000 LB;   DIAMETER, 7 FT

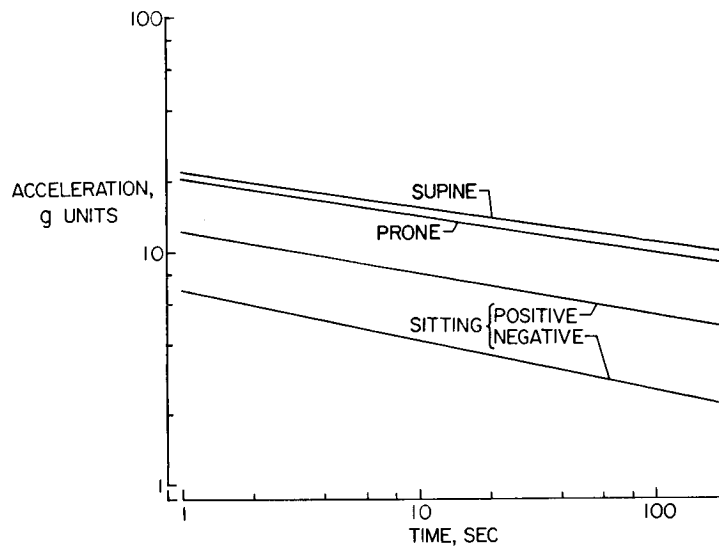| NOSE SHAPE |  | $R=\frac{1}{3}d$  15° | $R=2d$  53° | $R=1.5d$  |
|---|---|---|---|---|
| $W/c_DA$ | 57 | 104 | 37 | 33 |
| TOTAL HEAT INPUT, BTU | 338,000 | 414,000 | 293,000 | 256,000 |
| MAXIMUM HEATING RATE AT STAG POINT BTU/(SQ FT) (SEC) | 125 | 215 | 166 | 64.5 |
| $c_{N_\alpha}$ | .92 | .97 | .69 | .24 |
| $c_{L_\alpha}$ | 0 | .47 | -.71 | -1.32 |
| $c_{m_\alpha}$ | -.16 | -.09 | -.22 | -.13 |

APPROXIMATE HUMAN TOLERANCE TO ACCELERATION



Figure 1
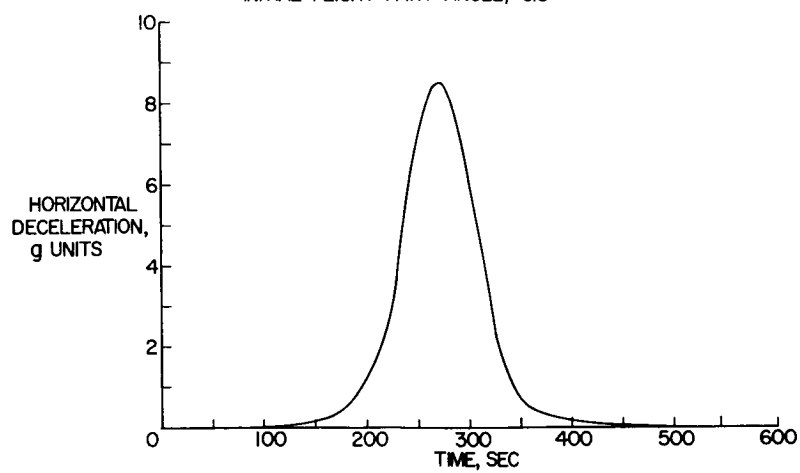
TYPICAL REENTRY DECELERATION
HISTORY STARTING AT 350,000 FT;
INITIAL FLIGHT-PATH ANGLE, -0.8°
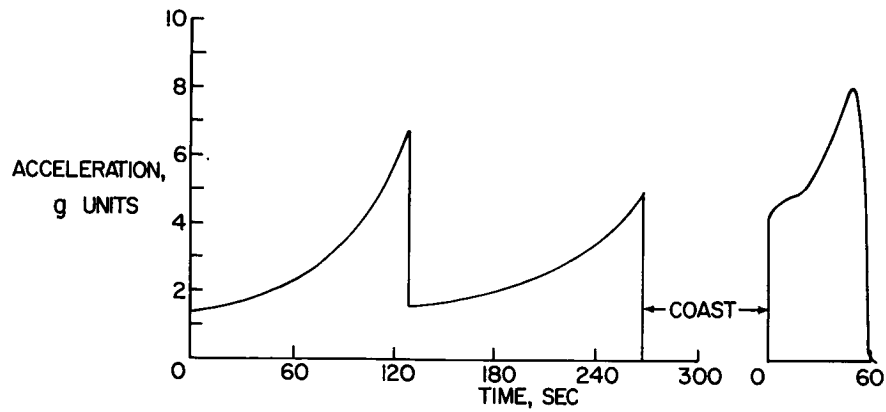


Figure 2

ACCELERATION HISTORY DURING LAUNCHING



Figure 3

DESCENT MANEUVER FROM CIRCULAR ORBIT AT 800,000 FT



Figure 4

## SCHEMATIC OF DESCENT MANEUVER

PERIGEE

ORBIT DEFLECTED BY
RETRO ROCKET

NORMAL
ORBIT

RE-ENTRY AND DESCENT
IN VICINITY OF PERIGEE

APOGEE

RETRO ROCKET REDUCES VELOCITY
IN VICINITY OF APOGEE

Figure 5

DESCENT MANEUVER FROM ELLIPTICAL ORBITS WITH PERIGEE
AT 800,000 FT

REARWARD IMPULSE APPLIED AT APOGEE

APOGEE AT
6,000,000 FT

APOGEE AT
3,000,000 FT

RE-ENTRY
ANGLE AT
350,000
FT, DEG

CIRCULAR ORBIT
AT 800,000 FT

VELOCITY DECREMENT, FPS
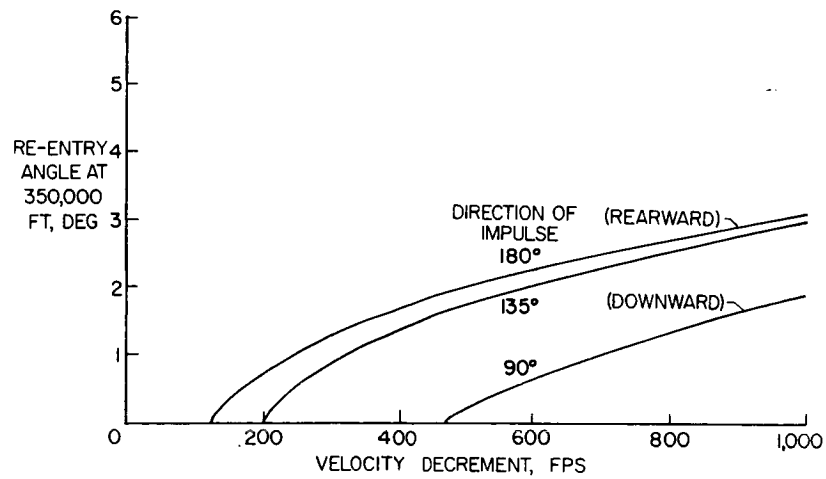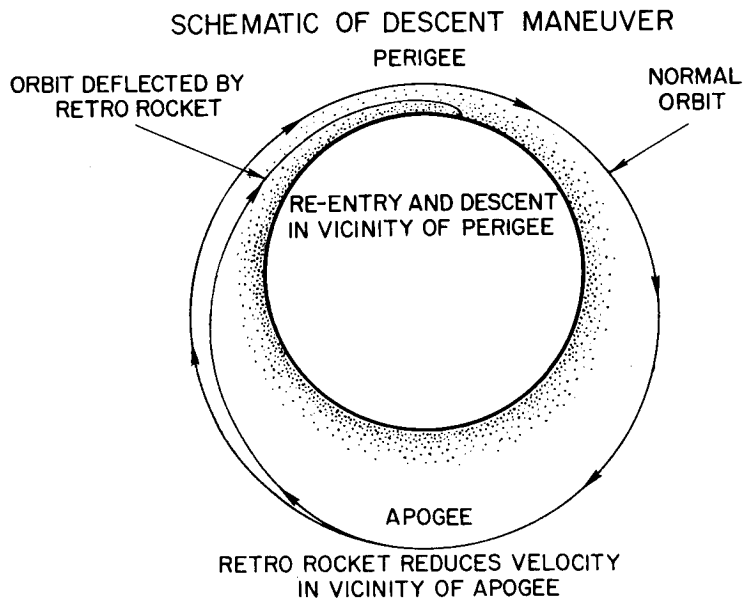
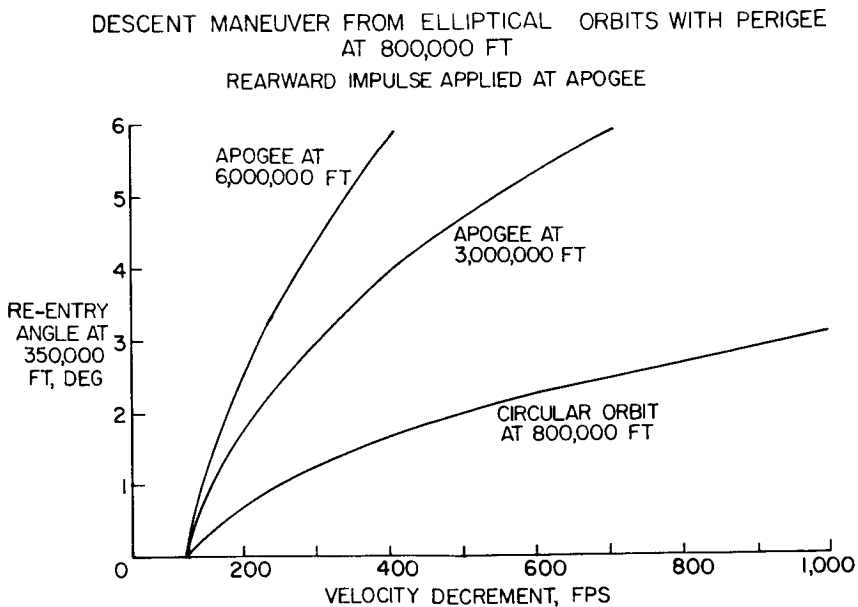Figure 6

## REYNOLDS NUMBER HISTORY DURING REENTRY

$$\frac{W}{C_D A} = 33$$
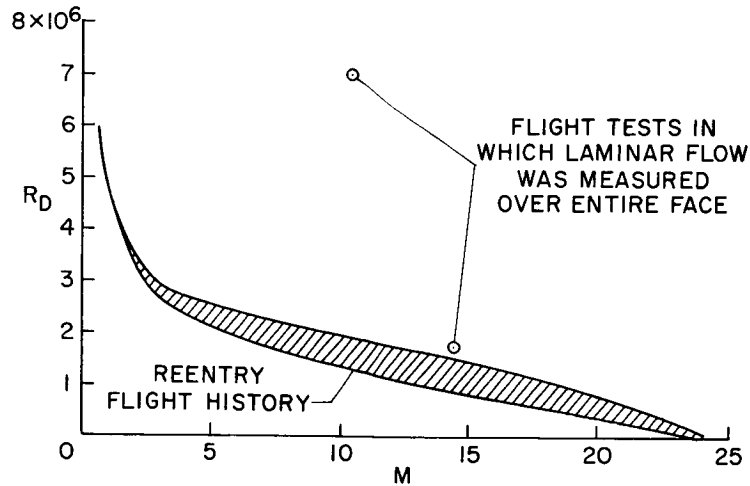


Figure 7

## CONFIGURATION STUDIED
### LENGTH, 11 FT; DIAMETER, 7 FT; WEIGHT, 2,000 LB



FLIGHT DIRECTION DURING LAUNCHING

FLIGHT DIRECTION DURING REENTRY
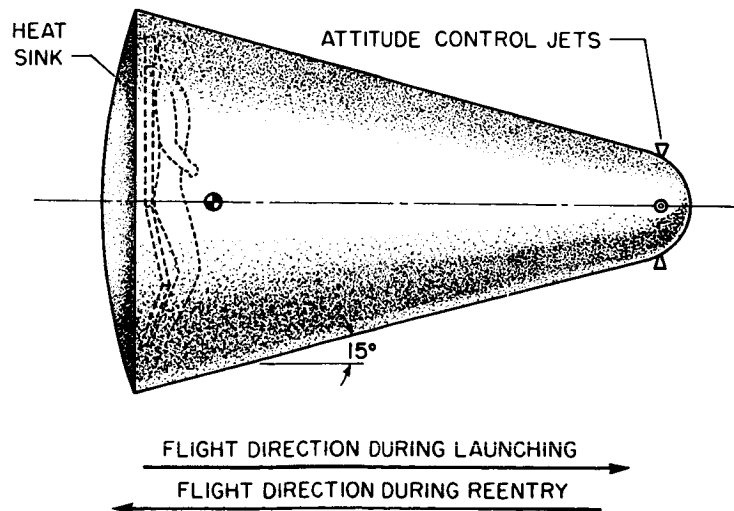
Figure 8

## NORMAL ACCELERATION AND PERIOD
## DURING OSCILLATORY REENTRY
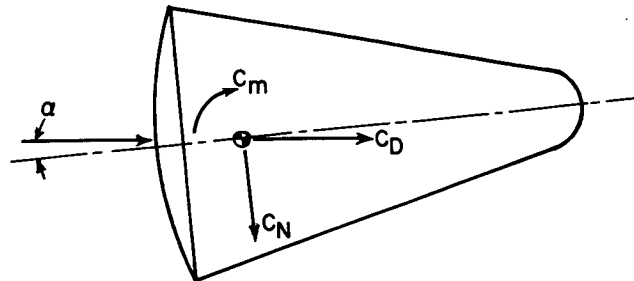
$$P \approx 2\pi \sqrt{\frac{I\, c_D}{m\, a_X\, c_{m_\alpha}}}$$

$$a_n = \frac{a_X\, \alpha\, c_{N_\alpha}}{c_D}$$

Figure 9

## METHODS FOR PRODUCING LIFT
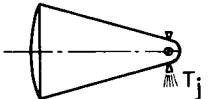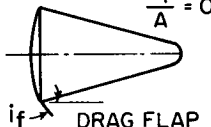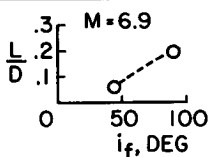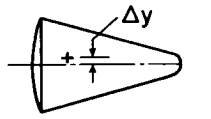
| CONTROL METHOD | PERFORMANCE |
|---|---|
| REACTION JET | $L = 12\, T_j$ |
| $\frac{S_f}{A} = 0.045$ — DRAG FLAP | $M = 6.9$; $\frac{L}{D}$ vs $i_f$, DEG |
| $\Delta y$ — C.G. SHIFT | $\frac{L}{D} = 10.1 \frac{\Delta y}{d}$ |

Figure 10

EFFECT OF LIFT DURING REENTRY
HISTORY STARTING AT 350,000 FT;
INITIAL FLIGHT-PATH ANGLE, -0.8°

| $\frac{L}{D}$ | CHANGE IN RANGE NAUT. MILES |
|---|---|
| 0.05 | 45 |
| .10 | 100 |
| .15 | 195 |
| .20 | 280 |

HORIZONTAL DECELERATION, g UNITS

TIME, SEC

Figure 11

3

# PRELIMINARY STUDIES OF MANNED SATELLITES

## WINGLESS CONFIGURATIONS: LIFTING BODY

By Thomas J. Wong, Charles A. Hermach, John O. Reller, Jr.,
and Bruce E. Tinling

Ames Aeronautical Laboratory

## INTRODUCTION

An exploratory study has been made of a manned satellite in which the man is considered to be an active part of the system during orbiting and reentry flight. The maximum horizontal deceleration on a fixed-geometry nonlifting vehicle is of the order of 8g. In order to take this kind of loading, the man may have to be so securely supported that he is essentially immobilized. On the other hand, a lifting vehicle with a lift-drag ratio of 0.5 experiences a maximum deceleration of about 2g. This is within the tolerable limit for a man in a sitting position and is sufficiently low to permit him to have active control over reentry. Because of the effectiveness of low lift-drag ratios in reducing decelerations and the effectiveness of high drag in reducing total heat convection (ref. 1), the 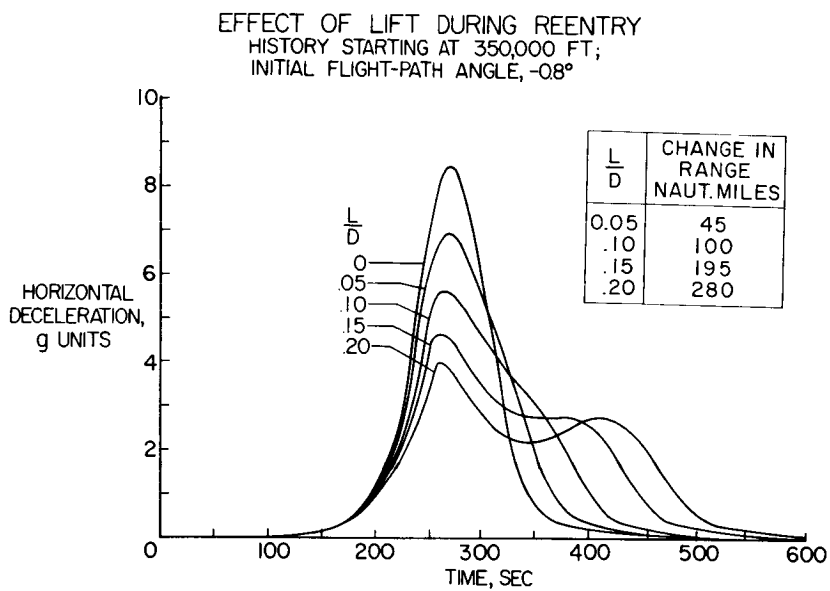possibility of using a modified ballistic-missile shape as a lifting element was considered. Another attractive virtue of high-drag shapes is that they are known to have aerodynamic characteristics which are relatively insensitive to changes in Mach number and Reynolds number at high supersonic speeds in the continuum-flow regime. Therefore, high-drag shapes can be investigated in existing test equipment, and the aerodynamic characteristics obtained are representative of those to be expected at the hypervelocities of reentry.

Now consider how lift might be developed on a ballistic-missile shape such as that shown in figure 1. A symmetrical high-drag shape of the type shown at the top left of the figure has a small lift-curve slope so that increasing angle of attack is a relatively ineffective method for developing lift. On the other hand, lift can be effectively developed on a high-drag shape simply by removing the upper portion of the body. On the resulting shape, the pressures which previously developed only high drag now develop high lift as well.

A configuration based on this concept is shown at the bottom of figure 1. A cone with a semiapex angle of $30^\circ$ was selected as a basic

shape for this configuration. A blunter cone would, of course, have a smaller amount of heat convected to it during reentry. However, a blunter configuration would have less satisfactory stability character- istics and would experience higher decelerations during reentry than the configuration chosen. The body was made slightly deeper than a half-cone to provide more usable depth for a given length, the corners and nose were rounded to reduce local heat-transfer rates, and trailing- edge flaps were provided for longitudinal and lateral control. Drag can be increased by flaring all controls simultaneously, which provides a method for varying the longitudinal glide range. The aspect ratio of the controls was kept low (0.6) to minimize the effects of shock-wave— boundary-layer interaction and Mach number on control effectiveness.

## AERODYNAMIC CHARACTERISTICS

### Theoretical Calculations

The aerodynamic characteristics of this configuration were calcu- lated by using Newtonian impact theory for the nose, conical surface, and controls and two-dimensional shock-expansion theory for the upper surface; the pressure coefficient on the base was assumed to be 0.7 of the vacuum pressure coefficient. Calculations were made for Mach numbers of 3 to 6 and ∞. The calculations indicated that the configuration would be stable and controllable at supersonic speeds.

### Experiment

A series of wind-tunnel tests was conducted to verify these calcula- tions and to determine the static stability and control characteristics of the configuration at subsonic and low supersonic speeds. A representa- tive portion of the results is shown herein. All force and moment coeffi- cients are referred to the fuselage plan area $(S = 0.9L^2)$, pitching-moment coefficients are referred to body length, and yawing- and rolling-moment coefficients are referred to body diameter.

### Performance

The calculated and experimental values of trim lift coefficient and lift-drag ratios are shown in figure 2. At $M = 3$ and above, the con- figuration self-trims (i.e., with controls undeflected) at an angle of attack of about $10^\circ$ as shown. Also at $M = 3$ and above, theory and experiment are in good agreement. At these speeds, little variation with Mach number is observed, and the calculated values at $M = \infty$ are very close to the values obtained at $M = 3$ to 6.

The configuration should therefore glide at a constant lift coefficient and a constant lift-drag ratio of about 0.5 throughout most of the reentry speed range. Experimental data for this configuration were obtained up to a Mach number of 6. Tests at Mach numbers from 3 to 12.2 of a similar configuration having a small wing also showed very little change in aerodynamic characteristics at Mach numbers greater than 4. At lower Mach numbers, the configuration is not self-trimming at lift coefficients below the maximum. At these Mach numbers, the configuration was trimmed with the lower controls deflected. The maximum control deflection used was about $45^\circ$ at $M = 0.25$.

## Stability Characteristics

The static stability characteristics are presented in figure 3. Values for longitudinal stability $C_{m_\alpha}$, directional stability $C_{n_\beta}$, and dihedral effect $C_{l_\beta}$ are plotted as functions of Mach number. The results indicate that the configuration is stable about all three axes and at all test Mach numbers. Again at $M = 3$ and above, theory and experiment are in good agreement, little variation with Mach number is noted, and all measured values are close to the estimated values for $M = \infty$. Preliminary calculations were made for the Dutch roll oscillation using the vehicle weight and trajectory to be discussed subsequently. Assuming zero rotary and cross derivatives, it is indicated that the oscillation is stable (although lightly damped) and has periods varying from about 5 seconds at a velocity of 25,000 feet per second to a minimum of 1.6 seconds at 5,500 feet per second.

## Control Characteristics

High-speed control characteristics are given in figure 4. Incremental changes in forces and moments with changes in control deflection are given. Moments due to aileron deflection are shown on the left and forces and moments due to elevator deflection are shown on the right. The control loads, in general, are fairly well estimated by the Newtonian impact theory. Thus, the effects of Mach number and shock-wave—boundary-layer interaction are apparently negligible. The ailerons produce yawing moments having the same sign as the rolling moments. This is desirable for the proposed two-control operation of the vehicle. Preliminary calculations indicate that these controls should have adequate effectiveness when the dynamic pressure increases to about 7 pounds per square foot. As mentioned previously, drag can be increased by flaring all controls simultaneously. It is shown that the upper controls deflected $60^\circ$ and the lower controls deflected about $35^\circ$ have lift and pitching-moment increments which are approximately equal and of opposite sign.

With controls in this position the trim lift coefficient remains
about the same; however, L/D is reduced from about 0.5 to about 0.44.
This reduction in L/D represents about 10 percent reduction in longi-
tudinal glide range or, for the trajectory to be considered in the fol-
lowing section, a variation of about 700 miles in longitudinal location
of the landing point. The results of this investigation indicate that
a vehicle of this shape can be made stable and controllable throughout
the reentry speed range.

## TRAJECTORY

In order to calculate the trajectory, a total reentry weight of
4,000 pounds and a body length of $6\frac{2}{3}$ feet were assumed for the vehicle.

The vehicle was assumed to be in a circular orbit at an altitude of
100 statute miles, and it was assumed that sufficient reverse thrust
was used to bring the vehicle down to an altitude at which aerodynamic
drag becomes significant (in this case, about 70 miles). From this
altitude the vehicle follows an equilibrium glide path calculated by
the method of Eggers, Allen, and Neice (ref. 2).

The variations of altitude and flight velocity with reentry range
are shown in figure 5. The total reentry range is about 20,000 miles.
It is apparent that the flight velocity remains close to satellite speed
over 80 percent of the range and that the glide phase amounts to about
1/3 of the total range. The total time of descent is 76 minutes. The
amount of reverse thrust employed $\left(T_r = 4\frac{1}{4} \text{ pounds}\right)$ was fixed by the

requirement that the angle of descent and velocity at the end of reverse
thrust match up with the corresponding quantities at the beginning of
the equilibrium glide trajectory. Thus, the transition to the glide
phase is accomplished without introducing an oscillatory or skipping
motion.

## HEATING AND STRUCTURE

The convective heating experienced by the vehicle during reentry is
shown in figure 6. Heating rate q at various parts of the body is
plotted as a function of reentry range. The indicated heating rates are
for the case of a cool wall immersed in continuum flow and include the
effects of dissociation calculated by the method of Eggers, Hansen, and
Cunningham (ref. 3). Stagnation-point heating rates calculated by this
method compare well with measured values obtained by Rose and Stark
(ref. 4). Laminar flow was assumed in calculating the heating rates

since the flight Reynolds numbers based on maximum diameter were less than $10^6$ throughout the critical heating range. It can be seen that the majority of the heating occurs in the last half of the glide phase, with the peak stagnation-region heating rate of about 71 Btu per square foot per second occurring at an altitude of about 40 miles and a velocity of 23,000 feet per second. Average heating rates at the bottom and top surfaces are about 1/4 and 1/20 of the stagnation-region value, respectively. The total amount of heat convected to this configuration is of the order of $10^6$ Btu for the entire period of descent. These heat loads determine the heat-shield requirements for the configuration. One attractive heat shield may consist of a heat-sink material covered by an external layer of ceramic insulation. The use of insulation appears attractive inasmuch as it permits higher surface temperatures with a resultant increase in the portion of the total heat that can be radiated to the atmosphere. The weight of heat-sink material required is thereby reduced. The effectiveness of this approach in relation to other possible approaches will be discussed in a subsequent paper by William A. Brooks, Jr., Roger A. Anderson, and Robert T. Swann.

For the preliminary study made, a conservative unit weight of 7 pounds per square foot of surface area was used. The resultant weight breakdown for the vehicle is presented in figure 7 along with a sketch of the vehicle. It can be seen that the heat-shield weight is about 1/4 of the total weight of the vehicle. A possible arrangement for the pilot and internal equipment are shown. Also shown are the aerodynamic and reaction controls at the rear. In this structural concept, the pilot and the equipment are contained in a pressurized capsule and the external heat shield is thermally isolated from the capsule.

## CONCLUDING REMARKS

As a result of this investigation it appears that a high-lift high-drag configuration of the type discussed has attractive possibilities for the reentry of a satellite vehicle. Decelerations are low enough to permit the pilot to perform useful functions during the reentry period. The configuration appears to be stable and controllable down to subsonic speeds and is sufficiently maneuverable to allow a lateral deviation of about ±230 miles and a longitudinal variation of about 700 miles in the choice of a landing point. Moreover, it appears that this type of configuration may have an acceptably low structural weight.

# REFERENCES

1. Allen, H. Julian, and Eggers, A. J., Jr.: A Study of the Motion and Aerodynamic Heating of Missiles Entering the Earth's Atmosphere at High Supersonic Speeds. NACA TN 4047, 1957. (Supersedes NACA RM A53D28.)

2. Eggers, Alfred J., Jr., Allen, H. Julian, and Neice, Stanford E.: A Comparative Analysis of the Performance of Long-Range Hypervelocity Vehicles. NACA TN 4046, 1957. (Supersedes NACA RM A54L10.)

3. Eggers, A. J., Jr., Hansen, C. Frederick, and Cunningham, Bernard E.: Stagnation-Point Heat Transfer to Blunt Shapes in Hypersonic Flight, Including Effects of Yaw. NACA TN 4229, 1958.

4. Rose, P. H., and Stark, W. I.: Stagnation Point Heat Transfer Measurements in Dissociated Air. Jour. Aero. Sci., vol. 25, no. 2, Feb. 1958, pp. 86-97.

EVOLUTION OF CONFIGURATION



HIGH DRAG

HIGH DRAG
HIGH LIFT

CONFIGURATION STUDIED
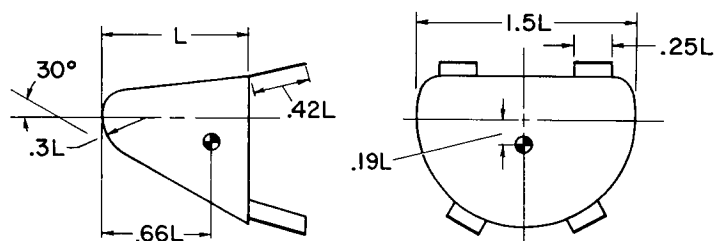


Figure 1

TRIMMED AERODYNAMIC CHARACTERISTICS
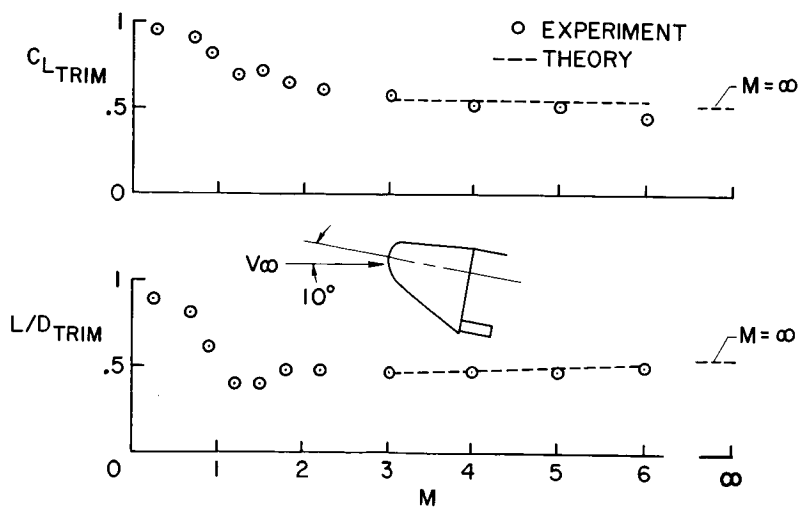


Figure 2

STATIC STABILITY

△ ○ □ EXPERIMENT
— — — THEORY

$C_{n_\beta}$ , PER DEG
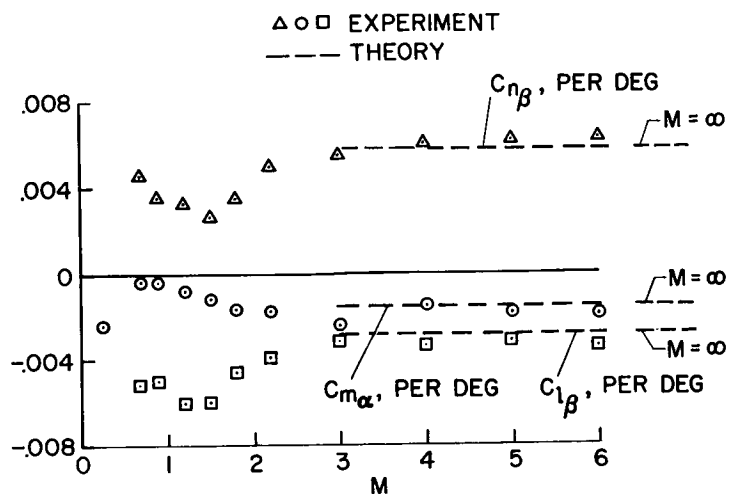


Figure 3

CONTROL CHARACTERISTICS

○ EXPERIMENT M=3
□ EXPERIMENT M=4
— — IMPACT THEORY
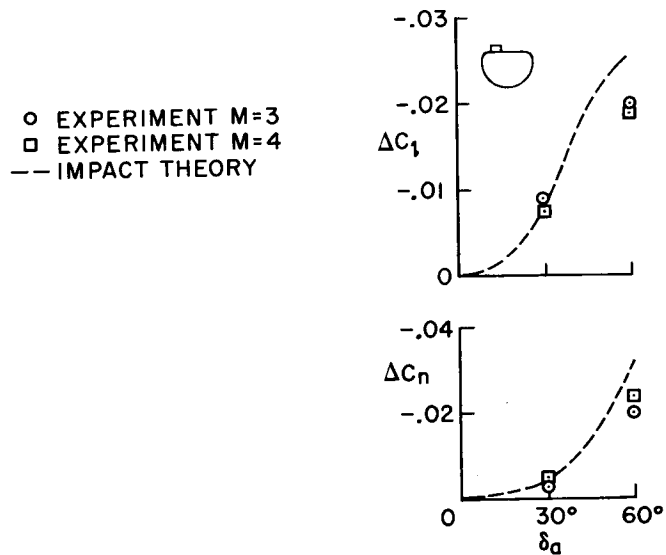


Figure 4(a)

CONTROL CHARACTERISTICS
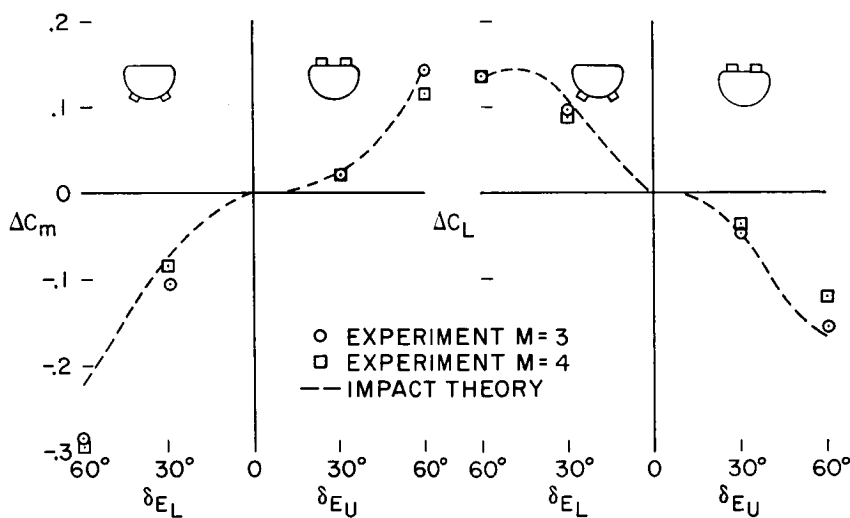


Figure 4(b)

ALTITUDE AND VELOCITY DURING RE-ENTRY
W = 4,000 LB    L = 6.67 FT
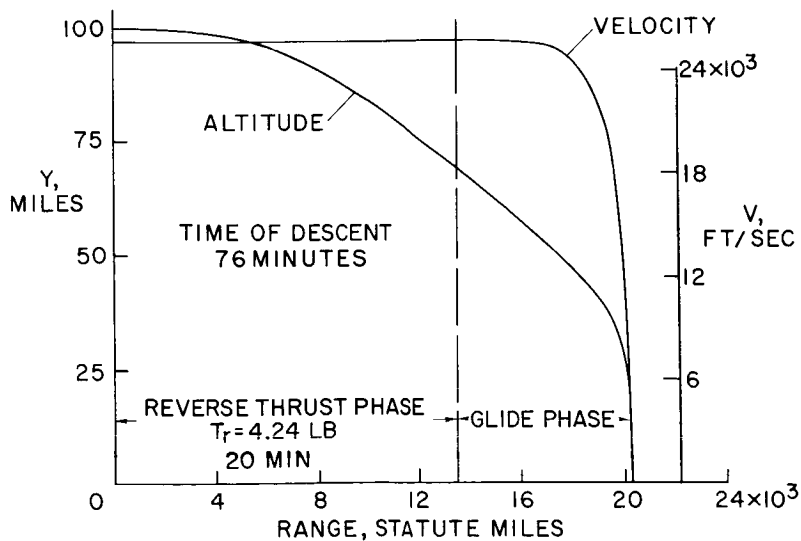


Figure 5

## CONVECTIVE HEATING DURING RE-ENTRY

TOTAL HEAT LOAD ≅ 10⁶ Btu

REVERSE THRUST PHASE — GLIDE PHASE

STAGNATION REGION

$q, \dfrac{Btu}{FT^2 SEC}$

BOTTOM SURFACE

TOP SURFACE

RANGE, STATUTE MILES

Figure 6

## STUDY VEHICLE

6'8"

10'

6'10"

A. CAPSULE                                3100 LB
   1. Capsule Structure              500
   2. Pilot and Equipment            880
   3. Flight and Guidance Instruments 850
   4. Control and Recovery Equipment  650
   5. Research Instrumentation        220
B. EXTERNAL STRUCTURE                     1100 LB
            TOTAL WEIGHT IN ORBIT      4200 LB

Figure 7

# PRELIMINARY STUDIES OF MANNED SATELLITES

## WINGED CONFIGURATIONS

### By John V. Becker

### Langley Aeronautical Laboratory

## PROBLEMS OF WINGED CONFIGURATIONS

Previous studies of hypersonic gliders have been concerned mainly with those having a high lift-drag ratio (L/D). (Symbols used herein are defined in the appendix.) In figure 1 it is seen that designs of this type have undesirably long glide ranges for a typical reentry condition. (This type of high L/D glider is shown in fig. 2.) Obviously, operation at a lower lift-drag ratio would be preferable for satellite reentry since long range within the atmosphere 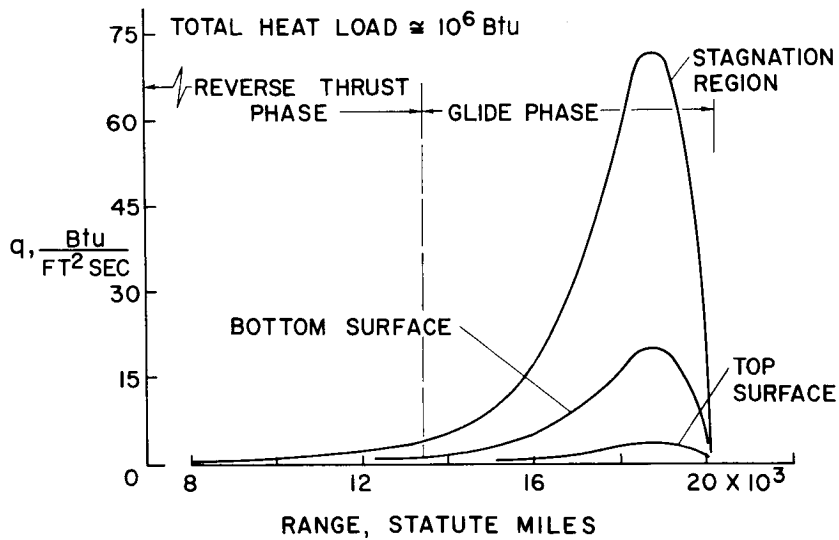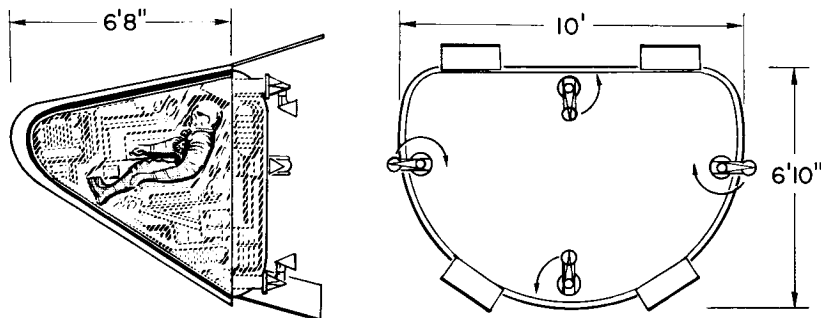is of little significance. With this low lift-drag-ratio mode of operation, the high-convective-heat load characteristic of the glider with high lift-drag ratio can also be avoided. A method of achieving low lift-drag ratios, which is particularly favorable from the heating viewpoint, is to operate at high angles of attack, extending upward to maximum lift. Because the requirements for high lift-drag ratio configurations (such as slender fuselage proportions, small leading-edge radius, and thin wings) are not necessary, configurations like that shown in the lower sketch of figure 2 can be considered. A range of the design lift-drag ratio from about 0.7 near maximum lift coefficient to perhaps 2 at an angle of attack of 25° would permit the reentry range to be varied by some 10,000 miles. This range would provide a large margin for correcting errors made in the initiation of the reentry. In a subsequent paper by Hubert M. Drake, Donald R. Bellman, and Joseph A. Walker, the large lateral range capability, which is also inherent in this type of winged vehicle, is discussed.

The deceleration rates for the maximum-lift-coefficient $\left(C_{L,MAX}\right)$ type of reentry are very low, a fraction of 1 g; thus, at no part of the reentry would the pilot's ability be limited by high deceleration rates as it would be in the high-drag reentry vehicles.

Another mode of reentry for a winged vehicle is illustrated in figure 1. The reentry is made without lift (or with only small lift)

until low supersonic speeds are reached, at which point a transition is made to the normal glide attitude. In addition to permitting a normal landing, the wing serves to produce a relatively low $W/C_DA$ with the associated low heating rate. As has been brought out in the previous papers, the use of low lift with high drag will reduce the peak deceleration rate to a more acceptable level than that of the nonlifting reentry. A brief review of the problems and potentialities of these low-lift-drag-ratio modes of operation will be presented.

## HEATING PROBLEMS CONSIDERED

The structure is assumed to be of the type in which nearly all the imposed heat is disposed of by radiation rather than by absorption into the structure. (Previous studies have shown that the absorption type of structure tends to be excessively heavy for winged gliders.) The primary design factor for the radiation structure is the peak heating rate, which determines the peak or design value of the skin temperature. The extent to which the use of high lift can alleviate the heating environment will be considered first. In figure 3, machine-calculated trajectories are shown for the optimum-lift case $\left( \approx C_{L,MAX} \right)$, the optimum-drag case $\left( \approx C_{D,MAX} \right)$, and an intermediate case for high drag and low lift. Of interest is the condition for peak heating which occurs in all cases near $V = 22{,}000$ ft/sec. Since the velocity is essentially fixed, the peak stagnation heating rate depends mainly on the atmospheric density and radius of the body nose. For the present, only the density or environmental factor is considered; that is, the parameter $q_{MAX}r^{1/2}$ will be investigated as a function of the factors $W/S$, $C_L$, and $C_D$ which control the trajectory. The corresponding parameter $q_{MAX}x^{1/2}$, for the lower surface of the wing, will also be evaluated for comparison purposes. Figure 4 presents these heating parameters plotted against wing loading (or disk loading for the bodies). These parameters increase as $(W/S)^{1/2}$. Comparison of the two upper curves for the spherical nose shape indicates the extent to which the use of $C_{L,MAX}$ has alleviated the heating problem; the optimum-lift case has about one-half of the heating parameter of the optimum-high-drag case, a result which agrees with that obtained by Dean R. Chapman. The flat-faced shapes, such as the airplane at $\alpha = 90^O$, have the benefit of a more favorable nose shape which reduces their stagnation-heating parameter to about the same level as that of the spherical nose in the lifting case. The surface-heating parameter is considerably lower than the stagnation-heating parameter because of the lower pressures on the surface.

These comparisons (illustrated in fig. 4) show the beneficial effect of lift on the heating environment. An additional favorable nose shape factor effect is present in the lifting case. That is, a spherical nose faired into a flat wing surface at a high angle of attack will have a lower stagnation heating rate than the isolated spherical nose shape operating at the same altitude. This shape effect will reduce the heating-rate parameter to a level below that of the lifting case of figure 4 which includes only the environmental effect. This shape factor is not known accurately for the angle-of-attack range and for the wing plan forms of greatest interest in this problem.

The leading edge is of greater practical importance than the nose of the configuration because of its much larger area. The basic heating rate for the leading edge will be less than that of the nose by a factor of about 0.7 in transforming to quasi two-dimensional flow. Some further beneficial effect can be achieved by sweep. Obviously, however, the effective sweep angle $\Lambda_{EFF}$ at high angles of attack is less than the plan-form geometric sweep angle $\Lambda_0$ according to the relation $\sin \Lambda_{EFF} = \sin \Lambda_0 \cos \alpha$. An estimate of the leading-edge maximum-heating-rate parameter in which all the above modifying effects were included indicates values of about the same level as the surface heating-rate parameter of figure 4. Further heat-transfer research on wings with blunt swept leading edges at high angles of attack and high Mach number is needed.

In figure 5 the peak heating rate is calculated from the parameters of figure 4 for typical dimensions of lifting and nonlifting vehicles. The long-dashed line (fig. 5) applies to the surface at a distance of 0.5 foot from the leading edge of an assumed sharp-edged wing. A leading-edge radius of the order of 0.5 foot is estimated to produce about the same heating rate as the surface at $x = 0.5$ foot. (In practice a somewhat smaller radius should be possible if internal radiation from the leading edge to the upper surface of the wing occurs. Heat conduction through the structure will also tend to reduce the skin temperature at the stagnation point.) It is interesting to note that the average rate for the lower surface of the wing in the high-drag zero-lift reentry is slightly lower than the lower surface lifting case. Thus, the same basic wing structure would be adequate for either type of reentry. The horizontal short-dashed line (fig. 5) represents the rate at which heat can be radiated from a blackened surface at 2,000° F. This rate represents a nominal upper limit for pertinent metallic structures. Evidently, wing loadings of 30 pounds per square foot or less are required for radiation structures for this application. When the winged vehicle is compared with a capsule of 2.5-foot radius, it is clear that the capsule will generally require the heat-sink approach, since the disk loading will usually be 50 pounds per

square foot or higher. An exception to this requirement can be achieved
by use of a parachute or similar drag device capable of reducing the
capsule disk loading to 10 pounds per square foot or less. (It should
be noted that the drag capsule has a comparatively low total heat load
as has been pointed out in the previous papers. Thus, it is not depend-
ent on the use of a radiation structure for low weight to the same extent
as the lifting case.)

An important heating problem for winged vehicles arises during the
initial dip into the atmosphere and the subsequent pull-up to the desired
glide path. Reentry will occur at an angle ranging upward to perhaps
as high as $-3^\circ$, depending on the shape of the orbit, the retrograde
action utilized, and the type of vehicle. The typical path shown in fig-
ure 6 is for a $\gamma = -1^\circ$ reentry at $C_L = 1$ that is followed by the
indicated pushover into either glide path. A peak in the skin tempera-
ture will occur at the bottom of the dip (see fig. 6); this peak temper-
ature cannot be allowed to exceed the peak design temperature that is
reached later in the glide at $V \approx 22,000$ ft/sec. By using machine
calculated trajectories for the atmosphere (ARDC model 1956), $T_1$ has
been evaluated for the range of reentry angles shown in figure 7. Evi-
dently, angles as high as $-1^\circ$ are feasible for a design temperature of
$2,000^\circ$ F. Thus, the radiation structure, contrary to what is sometimes
believed, is not restricted to the gradually decaying orbit type of
approach to the glide path. The results of figure 7 can be extended to
other wing loadings or $C_L$ values from the relation $T_1 \propto \left(\frac{W}{S} C_L\right)^{1/8}$

## EXPERIMENTAL LIFT RESULTS

Exploratory experiments at $M = 7$ and $10$ for several winged con-
figurations at high angles of attack have recently been completed. The
static stability, control, and trim results are discussed in a subsequent
paper by Robert W. Rainey. Additional data for both lifting and non-
lifting configurations are included in a subsequent paper by Jim A.
Penland and William D. Armstrong. These papers conclude that statically
stable trimmed configurations for high angle-of-attack operation can be
achieved. However, additional data are required at angles of attack
above $30^\circ$ (the limit of most of the tests to date) and at higher Mach
numbers.

One of the objects of this experimental program was to determine
the maximum lift capability of these vehicles, since this factor is
important in the heating problem. Figure 8 summarizes the available
experimental data at $M = 6.9$ for delta wings of various plan form and
cross section. The lift is referenced to the theoretical two-dimensional
value for a flat plate and is plotted against angle of attack. An

extrapolation from $30^\circ$, the limit of the tests, to $45^\circ$ is involved as is shown by the long-dashed lines. Examine first the sharp-edged wings of increasing sweep and note that in all cases the flow is detached from the leading edge at the high angles of attack and significant losses in lift occur as the sweep is increased. A thick wing with a sweep of $70^\circ$ and a large leading-edge radius (indicated by short-dashed lines), which is representative of an all-wing satellite vehicle, is compared here with the sharp thin wing. A loss in lift of about 10 percent is noted for the thick wing. A wing-body combination, which had a large leading-edge radius and blunt fuselage (configuration 3-B in the subsequent paper by Jim A. Penland and William D. Armstrong), is compared with the $75^\circ$ sharp wing, and a loss of some 5 percent is noted. These results can be interpreted to indicate that a configuration with a $70^\circ$ swept wing and a large leading-edge radius would have a lift coefficient $C_L$ of about 0.8, the value assumed in the previous heating evaluations.

In the extrapolation of these results to the much higher speed (but still continuum flow) regime where heating is critical, no large deterioration of the lift from the values indicated in figure 8 are anticipated. For example, the Newtonian maximum lift is 0.77, and the shock-expansion value at shock detachment is of the order of 1.0 at $M \approx 22$.

## CONFIGURATIONS CONSIDERED

Consider first a possible configuration for the high-drag type of reentry winged vehicle. The aerodynamic and structural supporting studies of this type of vehicle are in a less advanced state than those for the hypersonic glider but, nevertheless, a few generalizations can be made. A significant feature of the high-drag reentry vehicle is that the wing plan form is not subject to any obvious restrictions. Furthermore, since all components are completely shielded by the wing during reentry, they can be shaped to produce an optimum configuration for low-speed approach and landing. (The boost phase would probably present the most serious structural problem for these components which are shielded during reentry and might impose some additional shape restrictions that are not considered here.) A design which capitalizes on the potentialities of the drag-type reentry is shown in figure 9. The circular section on the lower surface of the wing is intended to promote static stability in the reentry attitude. The wing tips fold outward to effect the transition to normal gliding flight and to provide static stability at subsonic speeds. A lift-drag ratio of the order of 10, a turning radius of less than 1,000 feet, and a landing speed as low as 75 knots should be possible with this type of configuration.

A minimum winged vehicle capable of reentry from orbit is represented in figure 10. This design is intended primarily for the high-lift hypersonic-glide type of reentry, but it would also be capable structurally of the high-drag reentry. The leading edge and the lower surface are designed to radiate all the imposed heat load with a maximum design temperature of 2,000° F. A discussion of the structural concepts applicable to this type of vehicle is given in a subsequent paper by William A. Brooks, Jr., Roger A. Anderson, and Robert T. Swann. The fuselage is a pressure capsule essentially independent of the wing structure. Some upward tilt of the nose of the wing is required for trim at high angles of attack. The flaps extend rearward for low-speed stability. With an estimated low-speed lift-drag ratio of about 4, this vehicle could be landed under favorable conditions but, obviously, it would be less satisfactory in this respect than the previous design. Aerodynamically, the design might be improved by using less sweep, extending the flaps outward instead of rearward, and by using a smaller leading-edge radius. The use of a smaller leading-edge radius would, of course, require substitution of a material that would withstand higher temperatures or the use of a coolant in the leading edge. The use of a small jet engine would greatly simplify the landing operation.

The weight estimate for this minimum manned winged satellite vehicle is noted. A payload of 1,400 pounds is assumed (a payload that is 200 pounds more than that considered necessary in the drag capsule vehicle discussed by Maxime A. Faget). The structural and systems weights are estimated to be 1,660 pounds on the basis of the analysis of William A. Brooks, Jr., Roger A. Anderson, and Robert T. Swann for their unprotected thick-wing case. The gross weight of 3,060 pounds is only about 1,000 pounds higher than that of the minimum drag vehicle. Thus, it may be concluded that the minimum winged satellite vehicle is not prohibitively heavier than the drag type. The weight is sufficiently low to permit launching by booster systems similar to that for the drag vehicle described in a previous paper by Maxime A. Faget, Benjamine J. Garland, and James J. Buglia.

APPENDIX

SYMBOLS

| | |
|---|---|
| $f_1, f_2$ | functions |
| $a_t$ | tangential acceleration |
| $\alpha$ | angle of attack |
| V | velocity |
| L | lift |
| D | drag |
| W | weight |
| S | surface area |
| $C_L$ | lift coefficient |
| $C_D$ | drag coefficient |
| q | convective heat-transfer rate |
| $\rho$ | density |
| x | distance |
| r | radius |
| T | temperature |
| $\gamma$ | reentry angle |
| $\Lambda$ | sweep angle |
| A | cross-sectional area |
| M | Mach number |
| $\epsilon$ | emissivity |

Subscripts:

| | |
|---|---|
| O | zero angle of attack |

| 1 | initial |
| --- | --- |
| SAT | satellite |
| MAX | maximum |
| EFF | effective |
| DESIGN | design |

RE-ENTRY RANGE AND PEAK DECELERATIONS
$V_I = V_{SAT} - 100$ FPS



Figure 1

GLIDER CONFIGURATION

HIGH L/D

SATELLITE
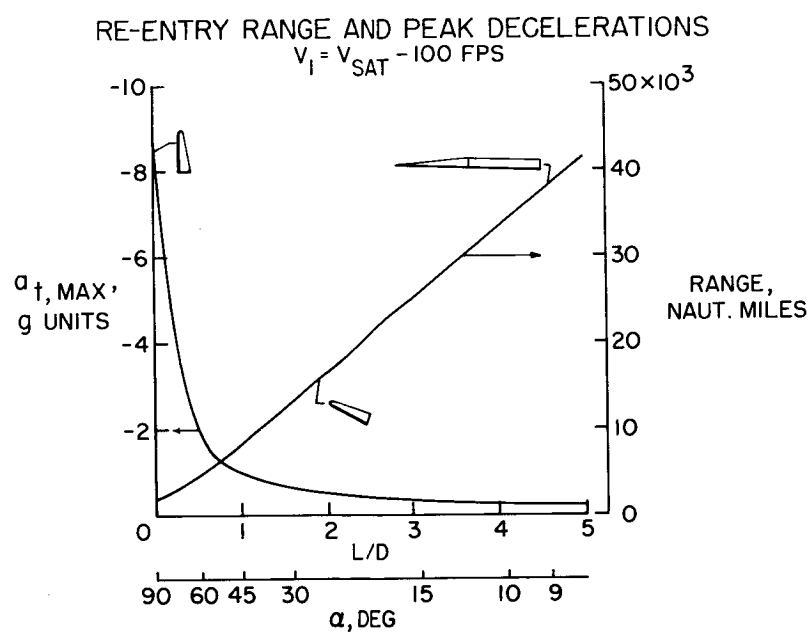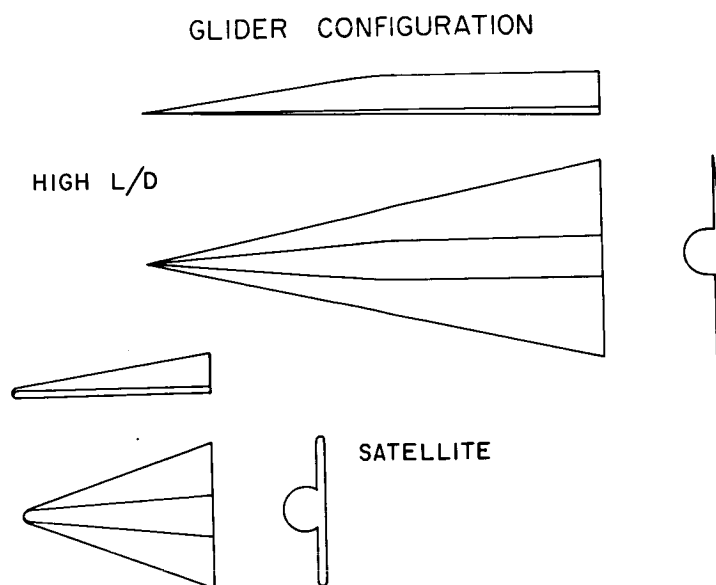


Figure 2

COMPARISON OF CONDITIONS FOR PEAK HEATING RATE
W/S = 20 LB/SQ FT



$$\text{NOSE: } q_{MAX} \propto \rho^{\frac{1}{2}} r^{-\frac{1}{2}} \qquad q_{MAX} r^{\frac{1}{2}} = f_1\left(W/S, C_L, C_D\right)$$

$$\text{SURFACE: } q_{MAX} x^{\frac{1}{2}} = f_2\left(W/S, C_L, C_D\right)$$

Figure 3

MAXIMUM-HEAT-RATE PARAMETERS



Figure 4

COMPARISON OF MAXIMUM HEAT RATES



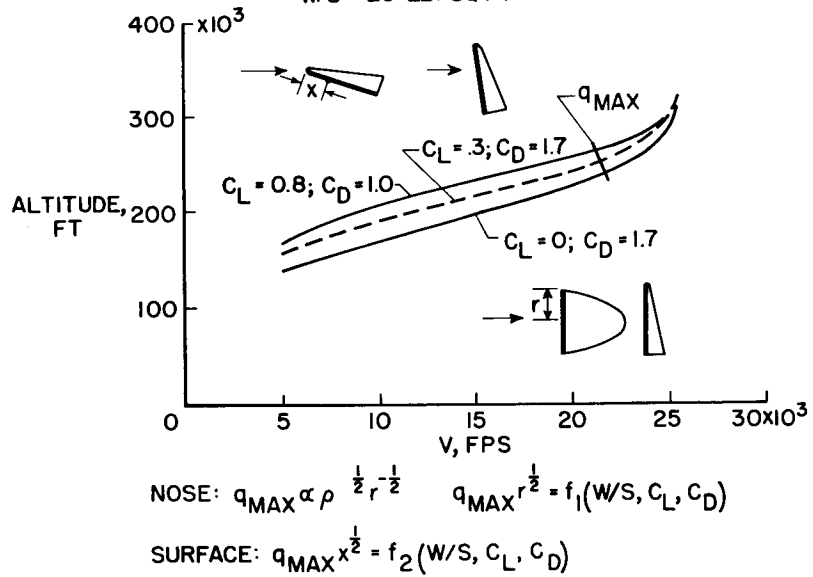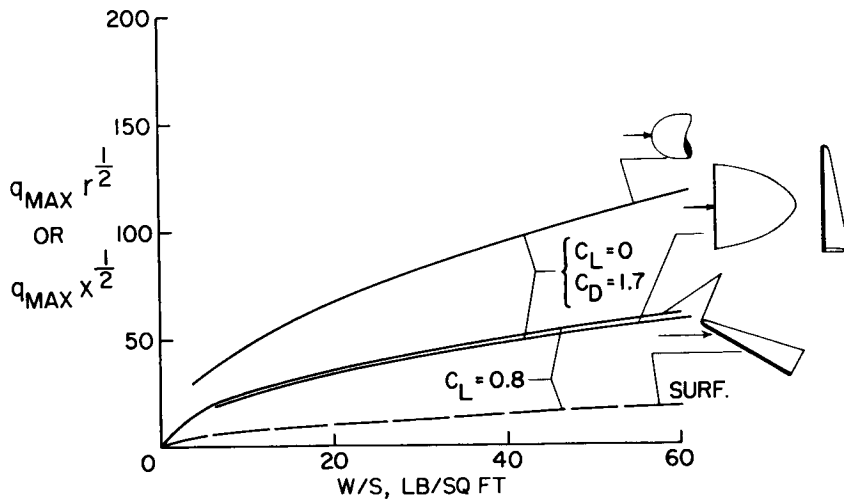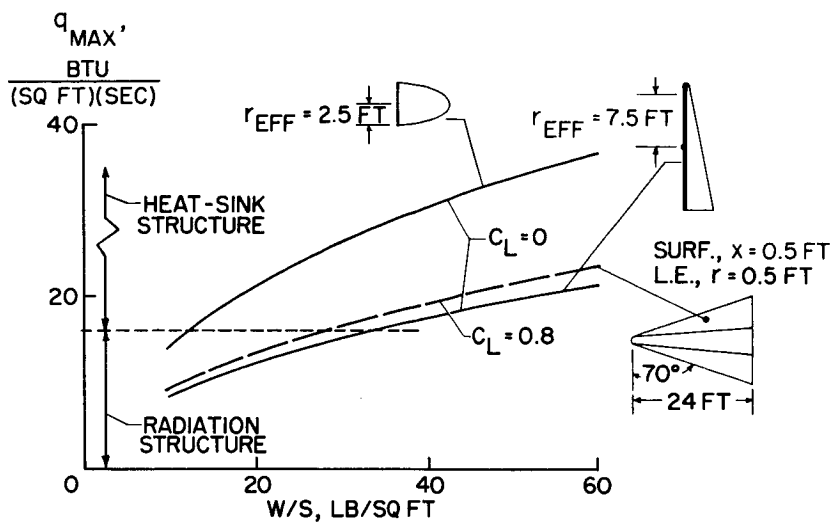Figure 5

TRANSITION FROM REENTRY TO GLIDE PATHS
$V_{350,000\ FT} = 25,900\ FPS; W/S = 20\ LB/SQ\ FT$



Figure 6

MAXIMUM TEMPERATURE IN REENTRY PULL-UP
W/S = 20 LB/SQ FT; $\epsilon$ = 0.9; $C_L$ = 1



Figure 7

LIFT CAPABILITY OF DELTA-WING CONFIGURATIONS
M = 6.9



Figure 8

HIGH-DRAG RE-ENTRY CONFIGURATION



27'

22'

Figure 9

HIGH-LIFT-GLIDE RE-ENTRY CONFIGURATION



25.5'

75°

12'

4'

PAYLOAD   1400 LB
STRUCTURE AND SYSTEMS   1660
3060 LB
W/S, 16 LB/SQ FT

Figure 10

# PRELIMINARY AERODYNAMIC DATA PERTINENT TO MANNED

## SATELLITE REENTRY CONFIGURATIONS

By Jim A. Penland and William O. Armstrong

Langley Aeronautical Laboratory
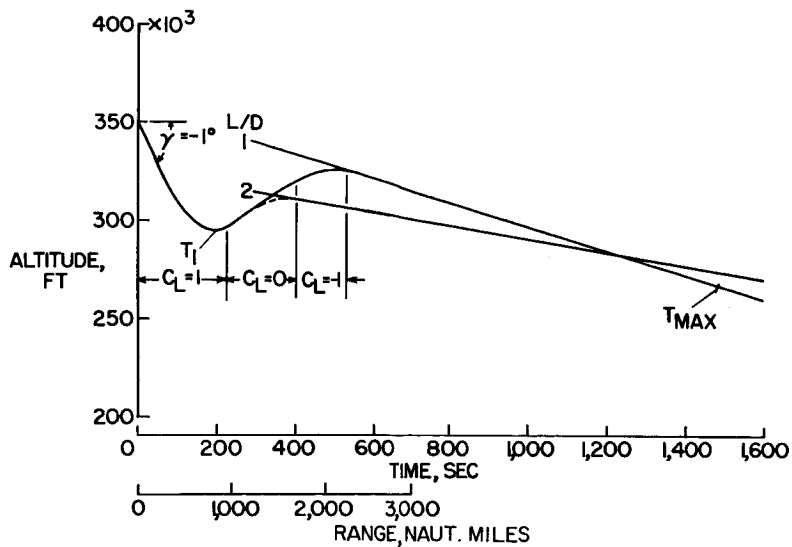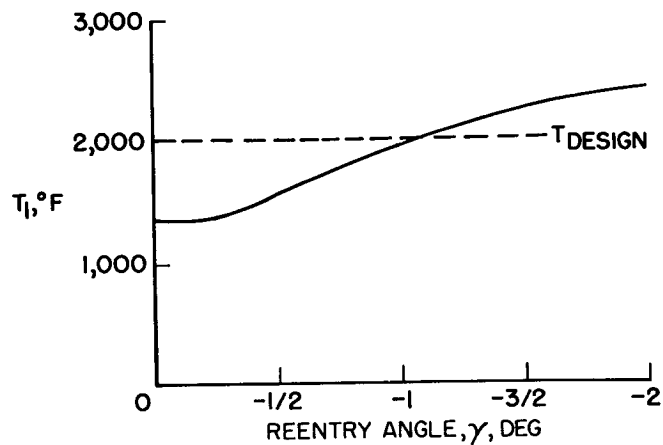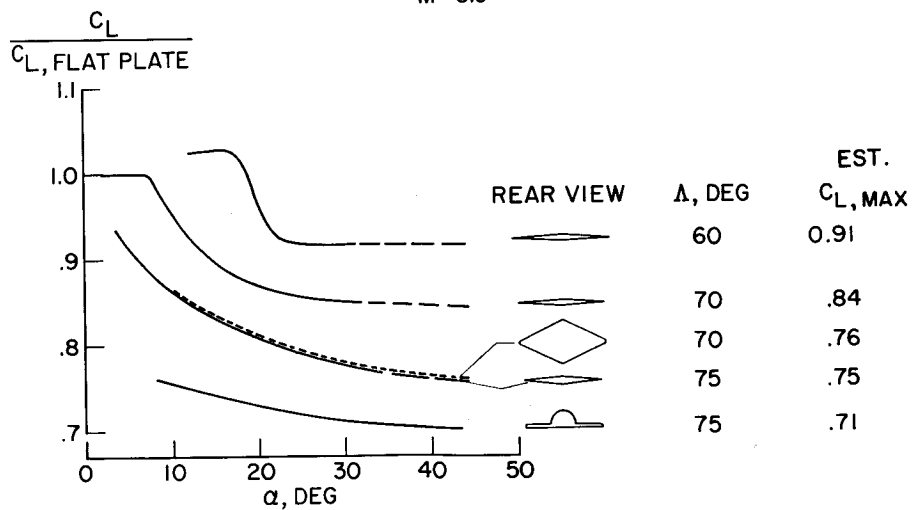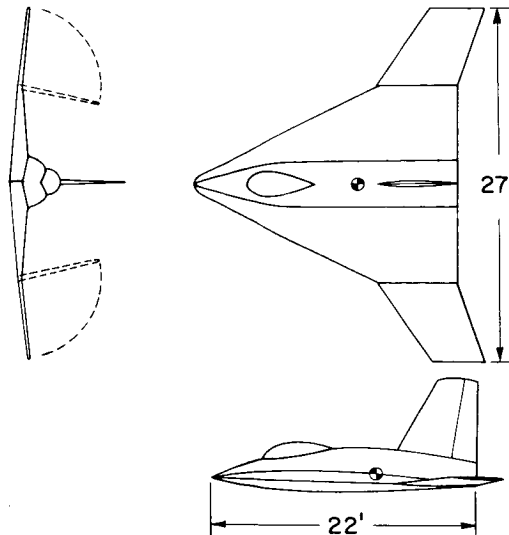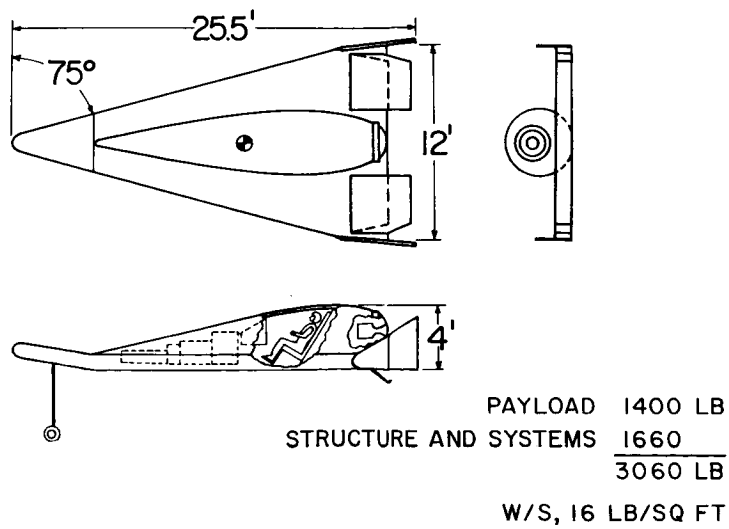
## SUMMARY

Some recent experimental data, together with calculations made by the modified Newtonian and shock-expansion theories, are presented for a variety of aerodynamic shapes considered for use as manned reentry vehicles. These vehicles were grouped in three basic categories: non-lifting bodies, lifting bodies, and airplane-like vehicles. The results indicate that from aerodynamic considerations, all of these configuration types are suitable for consideration as manned reentry vehicles.

5

## INTRODUCTION

The aerodynamic characteristics of satellite reentry vehicles at hypersonic speeds are essential for adequate prediction of their reentry characteristics. The purpose of the present paper is to present some basic data of this type obtained in the Langley 11-inch hypersonic tunnel at $M = 6.9$ in air. The data concern three types of configurations:

(1) Axisymmetrical nonlifting bodies that would follow purely ballistic reentry paths.

(2) Bodies equipped with flaps capable of being trimmed to produce finite lift. These are referred to as lifting bodies.

(3) Highly swept airplane-like configurations.

Comparisons of the experimental results with theoretical predictions are included.

## SYMBOLS

| | |
|---|---|
| $A$ | frontal area |
| $\bar{c}$ | mean aerodynamic chord |
| $C_D$ | drag coefficient, based on wing area or maximum body cross section |
| $\left(C_D\right)_{\alpha=0^\circ}$ | drag coefficient at zero angle of attack |
| $C_L$ | lift coefficient, based on wing area or maximum body cross section |
| $\left(C_L\right)_{TRIM}$ | lift coefficient at $C_m = 0$ |
| $C_m$ | pitching-moment coefficient, based on mean aerodynamic chord or body length |
| $C_p$ | pressure coefficient |
| $C_{p,MAX}$ | maximum pressure coefficient |
| $d$ | diameter |
| $i_f$ | elevator incidence angle |
| $i_N$ | nose incidence angle |
| $l$ | body length |
| $L/D$ | lift-drag ratio |
| $\left(L/D\right)_{TRIM}$ | lift-drag ratio at $C_m = 0$ |
| $M$ | Mach number |
| $R$ | Reynolds number based on mean aerodynamic chord or maximum body diameter |
| $r$ | radius |
| $S_f$ | unshielded area of flaps |

$S_{REF}$        reference area

W        weight

$x_{cp}$        center of pressure, percent body length

α        angle of attack

δ        flow-deflection angle

θ        cone semiapex angle

## CONFIGURATIONS

Sketches of the test configurations are shown in figure 1. The configurations include seven nonlifting bodies, two lifting bodies, and two airplane-like configurations.

## RESULTS AND DISCUSSION

### Nonlifting Bodies

For nonlifting reentry vehicles, the aerodynamic characteristic of main interest is the drag coefficient, since $W/C_D A$ is the predominant variable in determining range and heating. Figure 2 compares the measured drag at $M = 6.9$ of a series of cones and cone-cylinders of various apex angles at zero angle of attack with predictions made by shock-expansion theory and by modified Newtonian theory; that is, the local pressure coefficient is given by $C_p = C_{p,MAX} \sin^2 \delta$ where δ is the flow-deflection angle (refs. 1 and 2). Calculations by shock-expansion and modified Newtonian theory were made for only the cones, with no allowance for skin friction. Additional experimental data are given in reference 3 for cones and cone-cylinders in which the afterbodies were 4 diameters long.

Figure 2 shows good agreement between the predictions by shock-expansion theory and experimental data up to a semiapex angle near shock detachment ($56.7^\circ$ for $M = 6.9$). Modified Newtonian theory shows rather poorer agreement with experiment and tends to underpredict drag for the less blunt cone shapes and to overpredict drag for the more blunt shapes. It may also be seen from this figure that the increase in experimental $\left(C_D\right)_{\alpha=0}$ with increasing apex angle beyond shock detachment is relatively

small. This variation in $\left(C_D\right)_{\alpha=0}$ follows a linear path beyond shock detachment, with the value for a circular disk normal to the stream ($\theta = 90^\circ$) falling between the values calculated by assuming stagnation pressure and static pressure behind the normal shock.

The drag coefficients and center-of-pressure location for a representative group of nonlifting reentry shapes over a wide Mach number range are shown in figure 3. All data shown in this figure other than that at $M = 6.9$ were obtained from references 4 to 8. The drag coefficient (lower half of figure) predicted by modified Newtonian theory remains relatively constant with Mach number above a Mach number of about 4. This prediction is fairly well verified by experimental data taken on the cylinder and sphere, which were tested up to Mach numbers of about 7 and 10, respectively. The measured data indicate that there is little change in drag with Mach number in the hypersonic speed range from 7 to 10 and it appears reasonable to assume that in continuum flow these data are representative of the entire hypersonic speed range.

The upper half of figure 3 shows that modified Newtonian theory fairly accurately predicts the center-of-pressure location for those bodies shown. It appears that these bodies can be made statically stable in the hypersonic speed range with practical center-of-gravity locations.

## Lifting Bodies

The second group considered in this paper consists of high-drag configurations which can utilize some lift to decrease reentry decelerations and provide limited range control.

The accuracy with which predictions may be made on simple bodies over a wide angle-of-attack range is of fundamental interest when consideration is given the aerodynamics of high-drag lifting configurations. Figure 4 compares the experimental drag coefficient of a series of cones of various apex angles at $M = 6.9$ and at angles of attack up to $130^\circ$ with calculations made by the modified Newtonian theory. It is seen that the modified Newtonian theory gives an excellent representation of the trends of the drag coefficient for cones with angles of attack from $0^\circ$ to $130^\circ$.

Figure 5 shows the details of configuration 2-A, a drag-type reentry vehicle with flaps for trimming the vehicle at some positive angle of attack, to obtain lift for trajectory-path control. This configuration consists of a frustum of a $15^\circ$ half-angle cone with a spherical nose.

The untrimmed experimental and modified Newtonian longitudinal characteristics of this configuration are shown in figure 6. The configuration

is statically stable about a moment reference center at 50 percent of the body length. Theory and experiment are in excellent agreement for pitching moment. The lift-curve slope is positive and the lift coefficient is also predicted fairly well by theory through the angle-of-attack range. The predictions of $C_D$ and $L/D$ are much less accurate than are the predictions of $C_L$ and $C_m$, as is to be expected, since theory underpredicts drag for this configuration.

The experimental trim characteristics of this configuration at $M = 6.9$ are shown in figure 7. The flaps used for trim have an effective area equal to 8.84 percent of the body base area. The configuration is statically stable for all conditions of the tests. With flap deflections of $-20°$ and $-40°$, the vehicle was trimmed at angles of attack of $4°$ and $10°$, respectively. There is a noticeable reduction in $L/D$ due to increasing trim drag with increasing trim effectiveness.

Figure 8 is a detailed sketch of configuration 2-B, which represents a more blunt reentry vehicle. This model consists of a reverse frustum of a $15°$ half-angle cone with spherical bases. The vehicle is trimmed with a drag-type flap, located on the circumferential edge of the front surface, which has an area 4.5 percent of the base reference area. Figure 9 presents the untrimmed (flap removed) longitudinal stability characteristics of this reentry vehicle through an angle-of-attack range from $0°$ to $90°$. This figure gives an indication of the general aerodynamic characteristics of a very blunt reentry body over a wide angle-of-attack range and compares the results of experimental data with that obtained by modified Newtonian theory.

The trends of $C_L$, $C_D$, and $L/D$ are predicted reasonably well by the modified Newtonian theory; however, pitching-moment coefficient is not very accurately predicted. It can be seen from the pitching-moment data that this body is statically stable up to an angle of attack of $45°$. The lift-curve slope for this vehicle is negative and maximum $L/D$ is about 0.5 at an angle of attack of $-40°$. Configuration 2-B has approximately the same volume as configuration 2-A (shown in fig. 5), but as a result of the increase in body bluntness, configuration 2-B has approximately three times the drag of configuration 2-A.

The experimental trim characteristics of model 2-B with the flaps on are shown in figure 10. The pitching moment and lift-drag ratio are presented for various flap angles through an angle-of-attack range from $0°$ to $45°$. This vehicle is statically stable throughout the range of angles of attack of the tests and was trimmed at angles of attack up to $23°$ with flap deflections up to $140°$. The moment reference for these tests was 29 percent of the body length from the nose. The lift-drag ratio for this vehicle is negative for positive angles of attack, and

shows little change due to trim. Because of the negative lift-curve slope, this configuration would have to be flown at negative angles of attack to generate positive lift.


## Airplane-Like Configurations

The final category of manned reentry vehicles considered in this investigation is the airplane-like configuration, or glider, utilizing both high lift and high drag to control reentry decelerations. This vehicle can be operated at a higher $L/D$ than the other two basic reentry categories discussed. This higher $L/D$ permits the glider to exercise greater control over range and position, and therefore more latitude is allowed in landing-site selection and touchdown. Figure 11 shows the all-wing configuration 3-A. This delta-plan-form configuration is trimmed longitudinally by a combination of nose and flap deflections. As indicated in this figure the nose can be deflected upward to an angle of $20^\circ$ and the flaps can be deflected from $20^\circ$ to $-20^\circ$. Directional control can be maintained by lateral deflection of leading-edge side plates located at the rear of the model.

Figure 12 presents the untrimmed longitudinal-stability characteristics of this vehicle at a Mach number of 6.9. The experimental values of $C_m$, $C_L$, $C_D$, and $L/D$ are compared with values obtained by shock-expansion theory over the angle-of-attack range. The two-dimensional theory used here would be expected to overestimate the lift and drag at high angles of attack because of leading-edge-flow-detachment effects. However, the theory does predict fairly accurately the pitching-moment coefficient throughout the range of angles of attack. This configuration is statically stable with the center of gravity located at 42 percent mean aerodynamic chord and has a maximum untrimmed $L/D$ of about 2.

The trim capabilities of configuration 3-A are presented in figure 13 for various nose and flap deflections. Plotted in this figure are $\left(C_L\right)_{TRIM}$, $\left(L/D\right)_{TRIM}$, and flap incidence for trim against angle of attack for nose settings of $0^\circ$, $10^\circ$, and $20^\circ$. The data cover a trim angle-of-attack range up to $30^\circ$. If the experimental data are extrapolated, it appears that with various combinations of nose and flap settings this vehicle can probably be trimmed at angles of attack approaching $50^\circ$. Maximum $\left(L/D\right)_{TRIM}$ is about 1.7 at $\alpha = 10^\circ$ and decreases to values less than 1.0 at the higher angles of attack.

Figure 14 shows details of configuration 3-B, which consists of a flat delta-wing model with a spherical nose, a large uniform leading-edge radius, and a cone-shaped body mounted on the upper surface.

The untrimmed longitudinal characteristics of this configuration at $M = 6.9$ are shown in figure 15. This model appears to have a region of low static stability at small angles of attack but shows increasing stability with increasing angle of attack. The maximum L/D is about 2.9 and occurs at an angle of attack of $10^\circ$.

## CONCLUDING REMARKS

Results are presented of an aerodynamic investigation at Mach number 6.9 of several configurations of interest for satellite reentry in the nonlifting-body, lifting-body, and winged categories. Preliminary analysis of these data indicates that trimmed, statically-stable arrangements are attainable for practical designs in each category.

REFERENCES

1. Grimminger, G., Williams, E. P., and Young, G. B. W.:  Lift on Inclined Bodies of Revolution in Hypersonic Flow.  Jour. Aero. Sci., vol. 17, no. 11, Nov. 1950, pp. 675-690.

2. Penland, J. A.:  Aerodynamic Characteristics of a Circular Cylinder at Mach Number 6.86 and Angles of Attack up to 90°.  NACA TN 3861, 1957.  (Supersedes NACA RM L54A14.)

3. Cooper, Ralph D., and Robinson, Raymond A.:  An Investigation of the Aerodynamic Characteristics of a Series of Cone-Cylinder Configurations at a Mach Number of 6.86.  NACA RM L51J09, 1951.

4. Potter, J. Leith, Murphree, William D., and Shapiro, Norman, M.:  Normal Force and Center of Pressure on Right Circular Cylinders.  Jour. Aero. Sci. (Readers' Forum), vol. 22, no. 3, Mar. 1955, pp. 214-215.

5. Long, J. E.:  Supersonic Drag Coefficients of Circular Cylinders up to Mach Number 8.  NAVORD Rep. 4382, U. S. Naval Ord. Lab. (White Oak, Md.), Oct. 26, 1956.

6. Charters, A. C., and Thomas R. N.:  The Aerodynamic Performance of Small Spheres From Subsonic to High Supersonic Velocities.  Jour. Aero. Sci., vol. 12, no. 4, Oct. 1945, pp. 468-476.

7. Hodges, A. J.:  The Drag Coefficient of Very High Velocity Spheres.  Jour. Aero. Sci., vol. 24, no. 10, Oct. 1957, pp. 755-758.

8. Seiff, Alvin, Sommer, Simon C., and Canning, Thomas N.:  Some Experiments at High Supersonic Speeds on the Aerodynamic and Boundary-Layer Transition Characteristics of High-Drag Bodies of Revolution. NACA RM A56I05, 1956.

CONFIGURATIONS TESTED
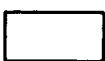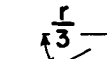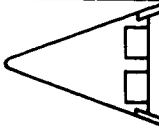


Figure 1

VARIATION OF CONE DRAG WITH SEMIAPEX ANGLE
M = 6.9; α = 0°
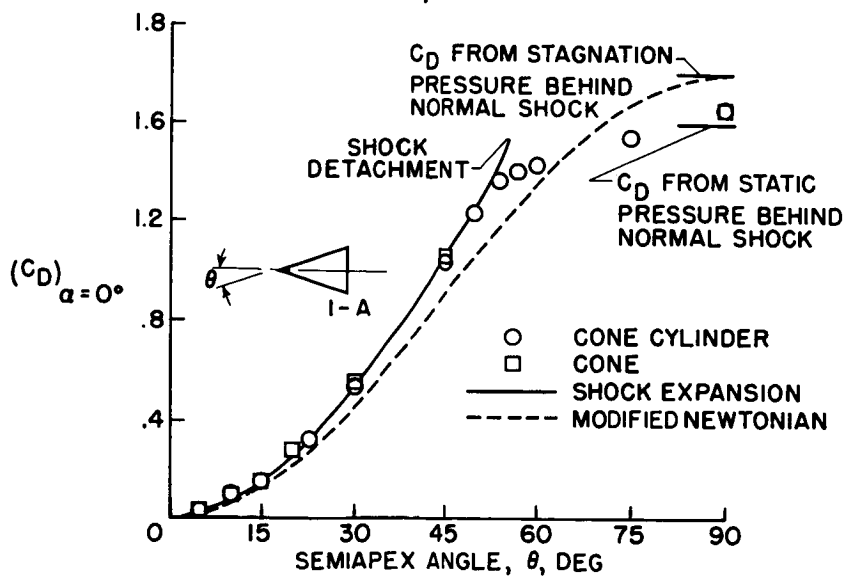


Figure 2

EFFECT OF MACH NUMBER ON DRAG AND CENTER OF PRESSURE
OF NONLIFTING REENTRY BODIES
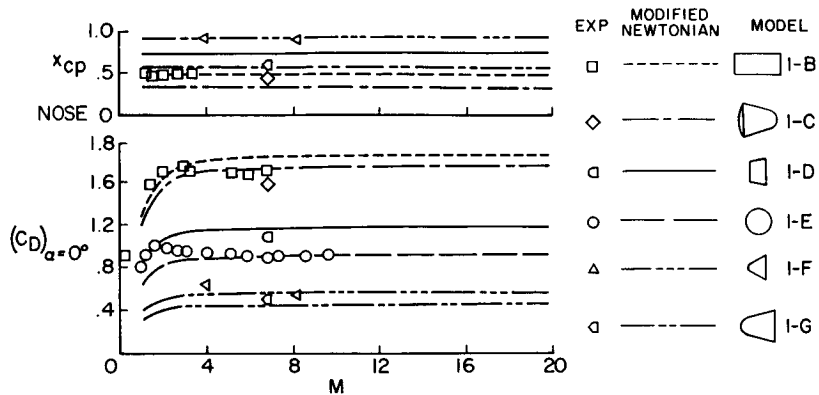


Figure 3

DRAG COEFFICIENTS OF A SERIES OF CONES OVER A WIDE RANGE OF α
M = 6.9
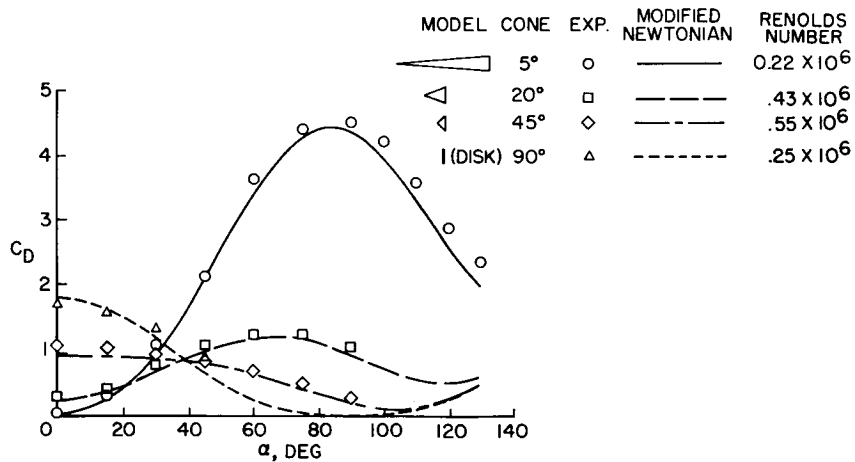


Figure 4

DETAILS OF CONFIGURATION 2-A

$S_f = 8.84\% \ S_{REF}$
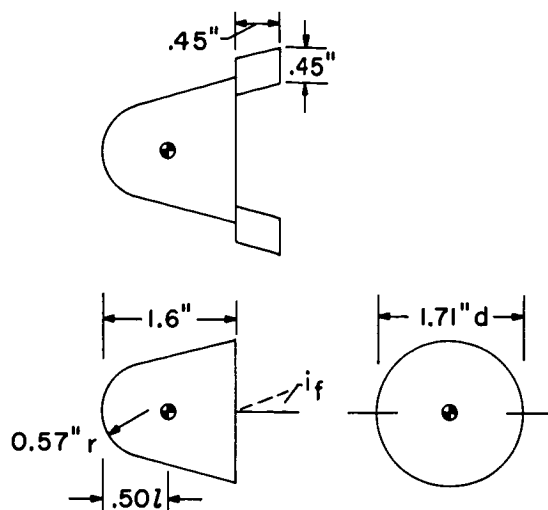


Figure 5

LONGITUDINAL CHARACTERISTICS OF CONFIGURATION 2-A

$M = 6.9; \ R = 0.17 \times 10^6$
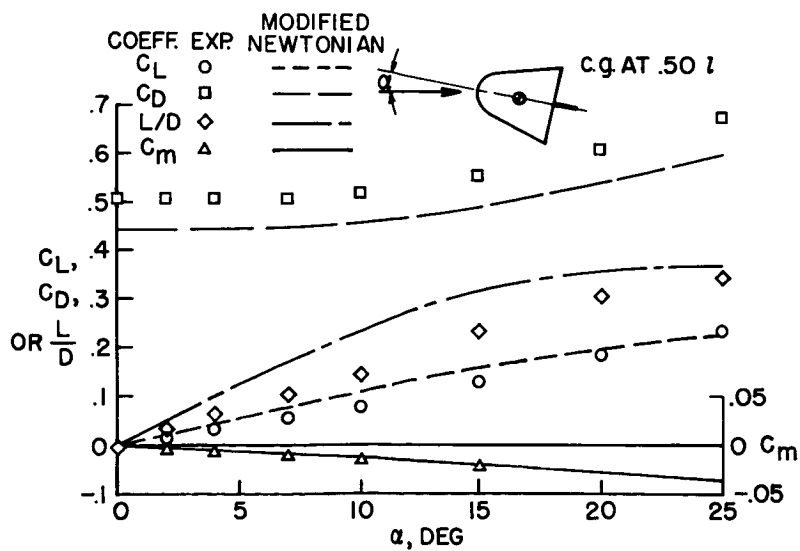


Figure 6

EXPERIMENTAL TRIM CHARACTERISTICS OF CONFIGURATION

$M = 6.9; R = 0.17 \times 10^6$
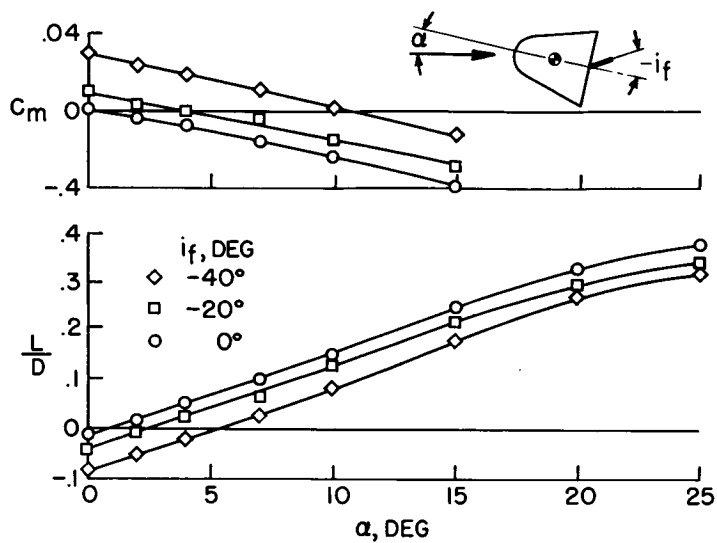


Figure 7

DETAILS OF CONFIGURATION 2-B

$S_f = 4.5\% \ S_{REF}$
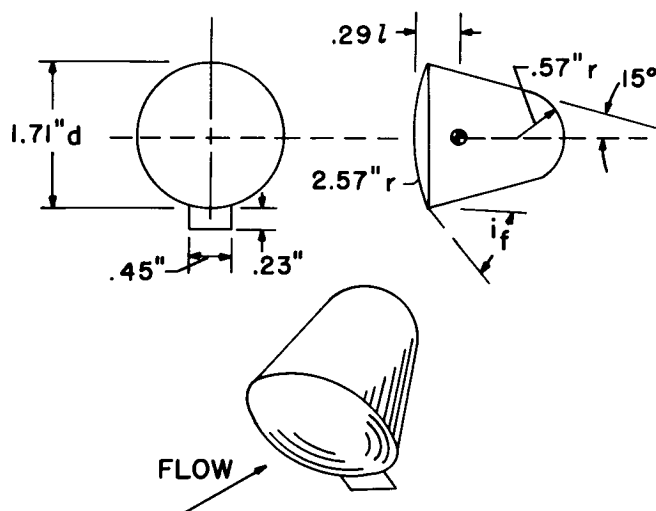


Figure 8

LONGITIDUAL STABILITY CHARACTERISTICS
OF CONFIGURATION 2-B
M = 6.9; R = 0.25 X 10⁶
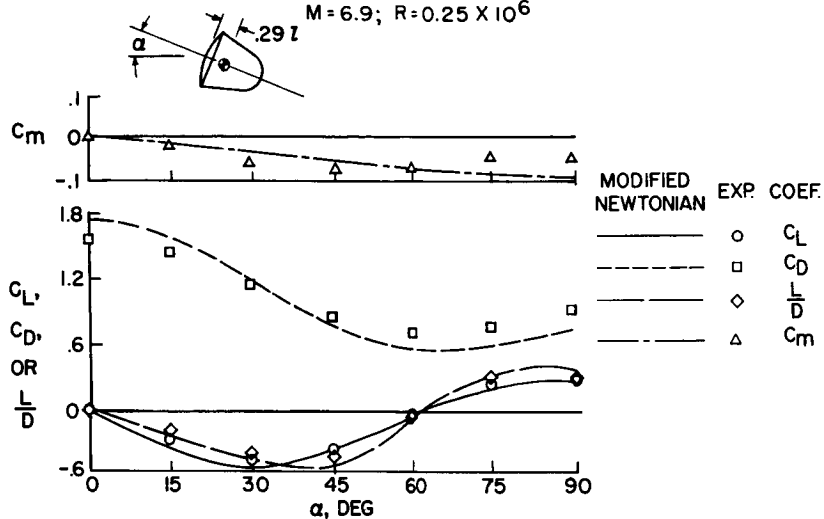


Figure 9

EXPERIMENTAL TRIM CHARACTERISTICS
OF CONFIGURATION 2-B
M = 6.9; $S_f$ = 4.5% $S_{REF}$
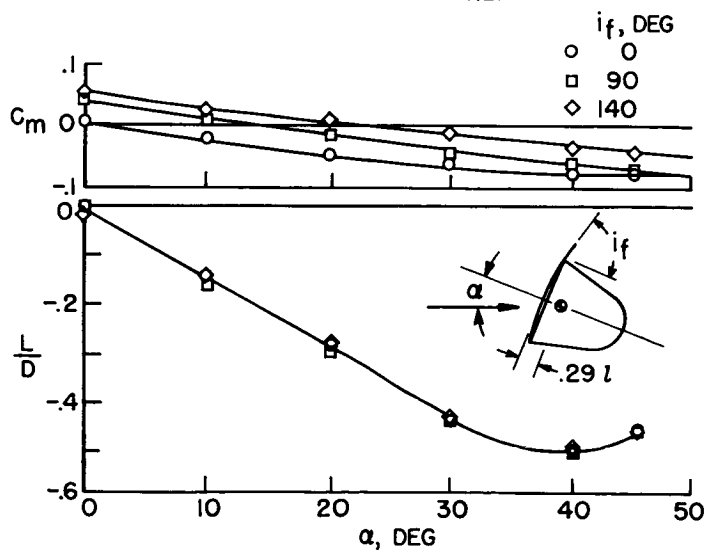


Figure 10

DETAILS OF CONFIGURATION 3-A
c.g. AT 0.42 $\bar{c}$
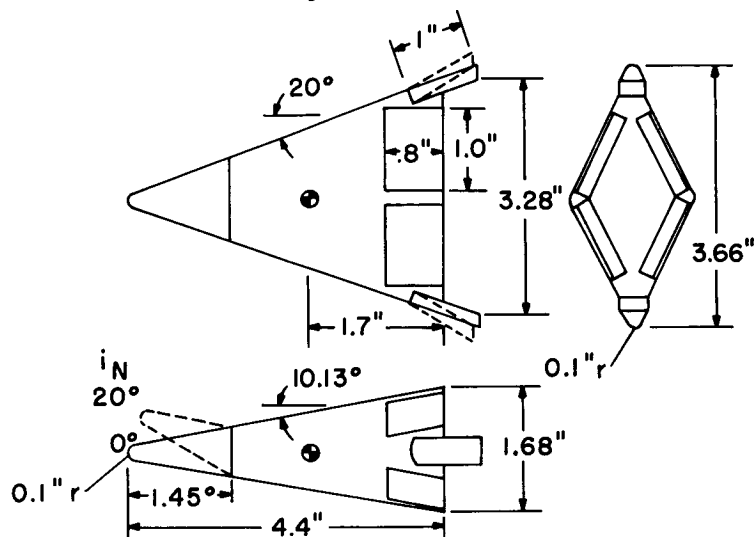


Figure 11

UNTRIMMED LONGITUDINAL
STABILITY CHARACTERISTICS OF CONFIGURATION 3-A
M= 6.9; c.g. AT 0.42 $\bar{c}$; R = 0.45 X 10$^6$



Figure 12

## TRIM CAPABILITY OF CONFIGURATION 3-A
### M = 6.9; R = 0.45 X 10⁶



Figure 13

## DETAILS OF CONFIGURATION 3-B



c.g. AT 0.37 c̄

Figure 14

LONGITUDINAL CHARACTERISTICS OF CONFIGURATION 3-B
$M = 6.9; R = 0.25 \times 10^6$
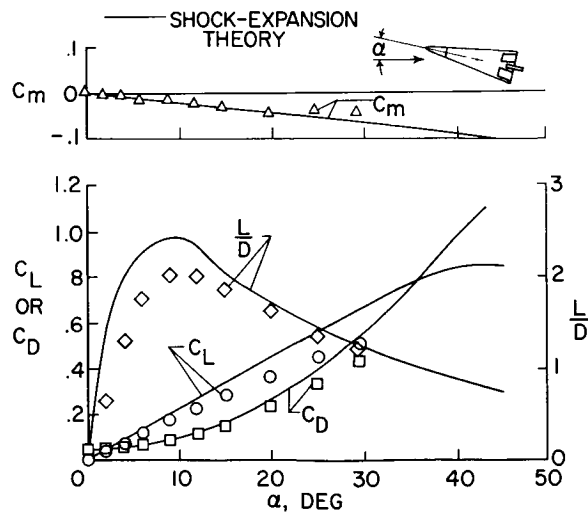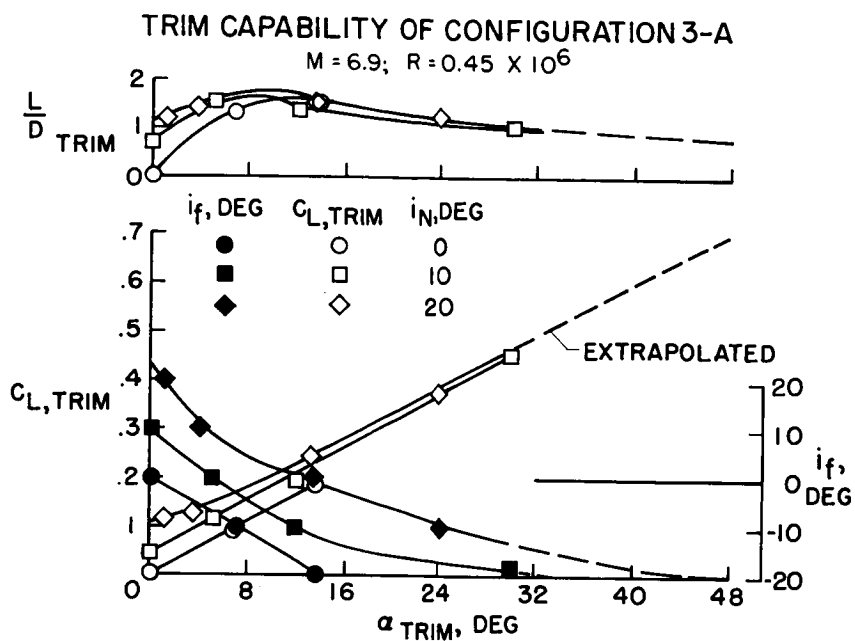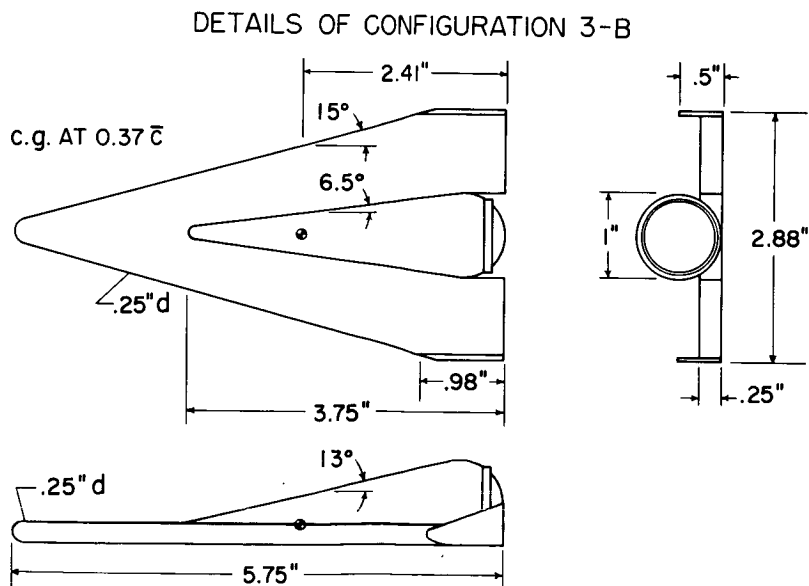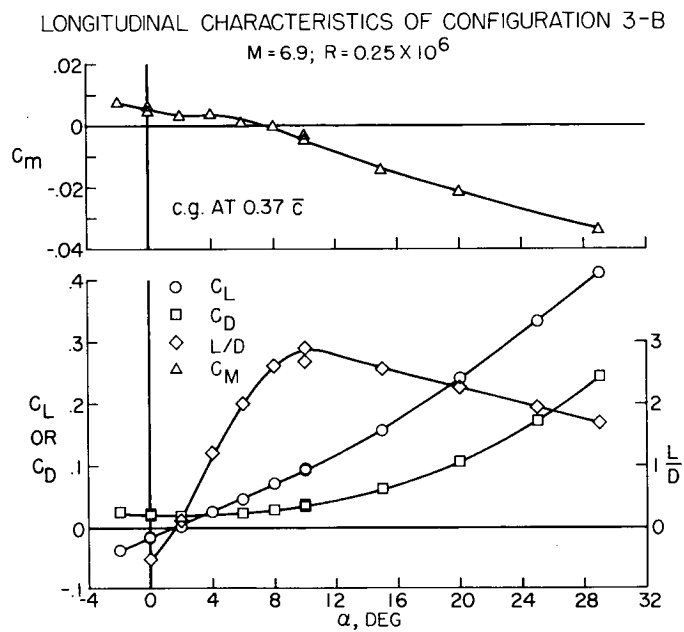
Figure 15

## STRUCTURAL DESIGN CONSIDERATIONS FOR BOOST-GLIDE

## AND ORBITAL REENTRY VEHICLES

By William A. Brooks, Jr., Roger A. Anderson,
and Robert T. Swann

Langley Aeronautical Laboratory

## INTRODUCTION

The preceding papers have discussed the aerodynamics and heating
of several vehicles designed for atmospheric reentry from satellite
orbits. Because of large heating inputs, some fundamental questions
about the structure of these vehicles are also raised. Although there
are many factors which influence structural design, only a brief exam-
ination of the relationship between heating input and structural weight
is discussed here. For this purpose the heating inputs associated with
the four vehicles shown in figure 1 are employed.

## SYMBOLS

Be        beryllium

$M_i$        bending moment per inch (intensity)

q        heating rate

$T_e$        equilibrium temperature

$\epsilon$        emissivity

Subscript:

MAX        maximum

## DISCUSSION

The first vehicle shown in figure 1 (vehicle A) is a high-drag zero-lift reentry body; the second (vehicle B) is a reentry body which develops a small amount of lift; the third (vehicle C) is a reentry glider which utilizes a large amount of lift; and the fourth (vehicle D) is a boost glider with a high lift-drag ratio. The heating histories for all three of the reentry vehicles were calculated for a small entrance angle to the earth's atmosphere. The heating for the boost glider is associated with a boost to 18,000 feet per second at an altitude of 180,000 feet and a glide to earth over a 5,000-mile range. Individual histories show significant differences in time duration of heating and in maximum heating rate as well as in total heat input which is given by the area under each curve.

The vehicles which develop the highest lift-drag ratios, vehicles C and D, have the longest duration of heating and the highest total heat input. Total heat input varies from about 6,000 $Btu/ft^2$ in the case of the zero-lift body to over 20,000 $Btu/ft^2$ for the boost glider. It should be noted that the heating history for the ballistic reentry capsule (vehicle A) has a peak rate of heating about an order of magnitude less than for comparably shaped ballistic missiles which reenter at steeper angles, whereas the duration of heating is about an order of magnitude greater.

The curves shown in figure 1 are applicable to particular areas on each vehicle. For vehicle A the heating history applies to the stagnation region but is very close to the average over the entire face. For vehicle B a large variation in heating rate is encountered along the under surface. The curve shown gives the average rate along the center meridian of the under surface. In the present analysis this average rate is taken as indicative of the heating problem for the vehicle. For both of the gliders (vehicles C and D), the heating history applies to a point one foot rearward of the leading edge on the lower surface of the wing and is taken as indicative of the structural problem for the wing. In the present paper, the heating of the leading edges of the gliders is not considered, inasmuch as the appropriate structural treatment for this region depends heavily on the degree of leading-edge bluntness.

The heat inputs are next considered from the standpoint of the structural design problems that they present. A very important design consideration is the level of temperature that may be encountered. An indication of potential structural temperature is provided by the scale at the right in figure 1. These are the surface temperatures at which a balance is achieved between the convective heat input and the radiation

output from a surface having an emissivity of 0.8. If 2,000° F is taken as the maximum temperature at which present structural metals can be used with some reliability, it is apparent that the maximum equilibrium temperatures for important areas of these vehicles are equal to or greater than present structural-material operating limits. Basic structural approaches for handling this situation are shown in figure 2.

The first approach is that of an unprotected structure represented by a sandwich skin of high-temperature material. Structural temperature in this case is controlled only by the heat capacity available in the skin and the ability of the structure to radiate the incoming heat. This approach can be used in those areas of the vehicles where structural weight is not greatly increased by operation at high temperatures.

The remaining approaches are basically methods to either block or absorb a portion of the convective heat input in order to limit the rise in structural temperature. The simplest method is to supply a thicker structural skin (approach 2) in order to obtain the required capacity to absorb heat. Alternatively, heat capacity of the structure can be raised by the incorporation of materials of higher specific heat, such as beryllium, or by the addition of a coolant, such as water. This type of approach is ideally suited to the vehicle with a high peak heating rate but with a small total heat input.

A third approach makes use of an external heat shield or insulation to retard the flow of heat to the structure and, hence, increase the proportion of heat which is radiated. The heat which passes through the insulation must be absorbed by the structure or by a cooling system which is indicated here (fig. 2) by some piping. With this approach, some of the problems in the design of the primary structure are transferred to the heat shield which must withstand the effects of a high-temperature boundary layer. This approach is considered for vehicles B, C, and D.

The fourth approach, which is known as ablation, makes use of an external layer of material which absorbs heat as it is consumed during the heating period. Application of this technique may be feasible for the high-drag bodies which have higher rates of heat input.

The weight associated with the use of an unprotected structure for the wings of the glide vehicles is considered first. Figure 3 shows how the weight of the wing primary structure is affected by design temperatures. Two types of structures are considered: One is a thick wing with sandwich cover skins and may be suitable for a reentry glider with blunt leading edges. The other is a thin wing of full-depth honeycomb construction which may be suitable for a boost glider of higher aerodynamic efficiency. The weights were computed by using a value of bending moment of 5,000 in-lb/in., which is conservative for the

maneuver loads but which provides a needed margin for carrying thermally induced bending moments in a hot structure. Structural materials appropriate for the temperature range were used. These materials are in current use for engine construction. Haynes alloy No. 25 is a cobalt-base alloy and René 41 is a nickel-base alloy superior to Inconel X. For the thin wing, the wing depth was allowed to vary between 2 and 4 inches in order to obtain the least weight at any given temperature. In the design temperature range for these vehicles, which is 1,600° F and higher, it is seen that the weight begins to rise sharply because of rapid deterioration in the strength of available materials.

In the case of the thick wing, a constant weight with increasing temperature is obtained up to 1,900° F. This result simply reflects the fact that for a thick, lightly loaded wing the weight is determined by minimum sheet gages rather than by loads. It was assumed that a minimum gage of at least 0.010 inch is desirable for the construction of sandwich panels which are to be subjected to a hypersonic airstream.

It is of interest now to compare these basic structure weights with the weight required to provide adequate insulation to a wing of a glide vehicle. Figure 4 gives the combined weight of insulation and coolant required to maintain the wing structure at specified temperatures. These weights were computed by using the particular boost-glider heating history which has a maximum equilibrium temperature of 1,900° F. The lower curve shows the weight when a highly efficient insulating material is used in combination with a cooling system. The cooling system is assumed to be capable of absorbing 1,000 Btu/lb of cooling-system weight. This analysis indicates that insulation and cooling weights of between 2 and $2\frac{1}{2}$ lb/ft$^2$ of wetted wing area are required to maintain structural temperatures at values significantly below the maximum equilibrium value of 1,900° F. In an alternate calculation, the cooling system was replaced by beryllium in order to augment the heat capacity of the structure, and from the resulting upper curve it is seen that larger weights are obtained. Although the weight difference between the two curves may not be considered large, it was found that the optimum-weight combination of insulation and beryllium gives rise to insulation thicknesses that may be unacceptable, particularly at low structural temperatures. At 500° F the insulation thickness associated with the upper curve approaches 5 inches, as compared with about $1\frac{1}{2}$ inches for the lower curve. However, at allowable structural temperatures of 1,000° F and higher, this difference in insulation thickness is not so large, and the nonmechanical system begins to compare favorably with a mechanical cooling system.

If the heat-protection weights and the weight of the primary structure for corresponding design temperatures are now added together, the

total weights shown in figure 5 are obtained. Inasmuch as primary
structure weight increases and heat-protection weight decreases with
increasing design temperature, a nearly uniform trend in combined struc-
ture and heat-protection weight prevails. It is seen that minimum
weight is achieved by keeping the structure at a low temperature with
insulation and a cooling system. However, if the structural tempera-
ture is allowed to rise to 1,300° F, both an insulated structure with a
cooling system and an insulated structure augmented by a beryllium heat
sink provide essentially equal weights.

The weights for the insulated wing may be compared with the weight
of an unprotected thin wing shown by the solid-curve segment on the
right in figure 5. This curve is a portion of the weight curve for thin
wings shown in figure 3 and spans the range of probable design tempera-
tures for the particular heating history being examined. The lower end
of the curve is at 1,750° F, which is the estimated temperature of the
lower surface of the wing when heat is transferred by radiation to the
cooler upper surface. The upper end of the curve is at 1,900° F, which
is the maximum possible structural temperature for this heating history.
It is obvious that at these temperature levels, small changes in the
design temperature for the structure produces large changes in the weight
of unprotected wings, and for this reason, on a weight basis, there is
not a clear-cut choice between protected and unprotected wings. It is
evident, however, that by considering both of these approaches, the
weight of the wing of a boost glider is bracketed between 3 and 4 $lb/ft^2$
of wetted area, or 6 to 8 $lb/ft^2$ of plan-form area. On the other hand,
for a small lightly loaded reentry glider which could use a thick wing,
it does not appear that an insulated structure will provide a weight
saving unless structural design temperatures exceed 2,000° F.

A corresponding weight analysis has been made for fuselages where
cooling of the contents was assumed to be a design necessity. This
analysis shows that it is desirable, from weight considerations, to
externally insulate the fuselage structure for a vehicle such as a
boost glider which may have large pressurized areas; however, for a
reentry glider with only a small lightly pressurized cabin, an unpro-
tected structure with internal insulation appears to lead to the least
weight.

High-drag reentry vehicles which are subjected to higher peak rates
of heating and, hence, must have protection in some form for a successful
design are considered next. Figure 6 gives the heat input that must be
absorbed in order to keep structural temperatures in the range under
2,000° F. The left-hand end of each of these curves gives the total
amount of heat that must be absorbed for only a minor temperature rise
in the structure. These values may be assumed to represent the heat
input to an ablation shield. The amount of heat that must be absorbed

by a metallic heat sink which is permitted to rise in temperature is given by the solid curves, while the dashed curves give the heat capacity required in an ideal cooling system. The difference in required heat capacity between the heat-sink and cooling-system curves for each vehicle arises because radiation cooling is more significant for the cooling system.

This difference is explained with the use of figure 7. Here the heating-rate histories for the two high-drag vehicles A and B are shown. The operation of an ideal cooling system can be defined in the following manner: The cooling system is not operated during the initial heating period; therefore, the structure, having very little thermal inertia, rapidly reaches some desired temperature limit as shown by the dashed line. At this time the cooling system is put into operation, and a constant structural temperature is maintained until the heating rate reaches the peak value and drops back to the material limit line. The total heat absorbed by the coolant is equal to the cross-hatched area above the dashed line, and the area beneath the dashed line represents heat that is radiated by the hot structure. On the other hand, a metallic heat sink designed for the same temperature limit has a much slower temperature response, shown by the lower solid curves, and does not reach peak temperature until near the end of the heating cycle. The bounded areas above the curves represent the heat which must be absorbed, whereas the areas below the curves represent the heat radiated by the hot structure. It is apparent that with heat-sink designs, a smaller proportion of the heating input can be radiated and more must be absorbed by the metal. The difference between the amount of heat that can be radiated by a heat-sink structure and a structure with a cooling system is seen to be fairly significant for the heat input for vehicle B but of much less importance for vehicle A. This fact is also reflected by the differences between the curves of figure 6. From the standpoint of practical operation, it may be expected that the heat absorbed by actual cooling systems will lie between the extremes represented by the ideal cooling system and by the simple metallic heat sink.

The weight associated with these two methods of absorbing heat is shown in figure 8 for the high-drag zero-lift vehicle. The weight of a heat sink obviously depends on the specific heat of the material and the temperature rise permitted. Beryllium was chosen for the material because of its high specific heat, and a temperature rise less than its melting point, which is about 2,300° F, was utilized. For the cooling system a constant cooling efficiency of 1,000 Btu/lb, which, for example, can be achieved by boiling water, was assumed. The weight of actual systems of this efficiency will lie in the hatched band between the curves, with the weight of the ideal system given by the lower edge of the band. From this comparison it is seen that a temperature rise of 1,600° F in a beryllium heat sink leads to the same weight as does the mechanical cooling system. It is believed that a temperature rise of

this magnitude can be permitted in a beryllium shield backed by a load-carrying structure. The required beryllium weight is about 6 lb/ft$^2$.

The weight of an ablation heat shield may be estimated from the coolant curve if it is assumed that an effective heat of ablation of 1,000 Btu/lb can be realized under these low-heating-rate conditions. On this basis, the least weight of such a shield would also be 6 lb/ft$^2$. This weight represents the weight of material actually consumed and makes no allowance for an additional thickness required to prevent heat from flowing into the structure during the heating period. Relatively little is known about the ablation of materials under heating rates of less than 75 Btu/ft$^2$-sec, but it is obvious that acquisition of a suitable ablating material will provide an attractive alternate to a metal heat shield.

Analyses similar to these have been carried out for the semiballistic reentry vehicle (vehicle B), and the results are shown in figure 9. Because a larger total heating input is involved for this vehicle, several methods for absorbing heat were investigated. In addition to results for the cooling system and the beryllium heat sink, results are shown for a beryllium-oxide heat sink, a beryllium heat sink insulated with ROKIDE "Z", and a beryllium heat sink insulated with a very low conductivity, lightweight ceramic. A beryllium-oxide heat sink offers no weight advantage over a beryllium heat sink for an equal temperature rise, but it does offer a possibility for operation at higher temperatures. At these higher temperatures, radiation of heat becomes very significant, and a beryllium-oxide heat sink operating at a very high temperature can provide a weight saving over a beryllium heat sink operating at a lower temperature. A more promising method for achieving higher surface temperatures and, hence, more benefit from radiation is to insulate the heat sink externally. With a presently available insulating material, ROKIDE "Z", which can be applied by flame spraying, a weight advantage is obtained over an uninsulated beryllium shield for equal temperature rise in the beryllium. Substantially larger reductions in weight are possible with insulating materials of lower conductivity and density, as shown by the lower curve. The properties used in this calculation correspond to those of commercially available ceramic refractories. Because of the large temperature gradients which exist in the insulating ceramic, it may be premature to assume that the weights given by the curve can be achieved in a practical design at the present time. However, the potential benefits of current research effort in this direction are clearly indicated.

If the cooling-system curve is used as a guide to the weight of an ablating shield, it is apparent that such a shield will have to absorb heat with an efficiency substantially greater than 1,000 Btu/lb in order to obtain savings in weight over the other systems indicated.

## CONCLUDING REMARKS

It has been shown that for glide vehicles which utilize large amounts of lift (vehicles C and D), large total heat inputs are encountered, but the maximum rates of heating are low enough that, for the temperatures generated, available engine materials are satisfactory. It appears, therefore, that the major part of the heat can be radiated, and structural unit weights may be obtained which are comparable to low-aspect-ratio winged aircraft of contemporary design.

For a semiballistic vehicle (vehicle B) which develops a small amount of lift, the problems of higher temperatures and large total heat input are present. The consequence is that with the present state of the art, estimated structural weight per unit of heated area is somewhat larger than that for a high-lift reentry vehicle (vehicle C); however, total surface area should be less than that for a winged vehicle, and this factor is of equal importance in determining total structural weight. At the extreme is the case of the zero-lift high-drag vehicle (vehicle A) which encounters high heat rates for a relatively short period of time, with the total heat input being at a minimum. For this case, a light-weight structure can be obtained with a relatively simple heat-sink design, and a considerable amount of engineering experience has been accumulated for this purpose.

HEATING–RATE HISTORIES FOR TYPICAL VEHICLES
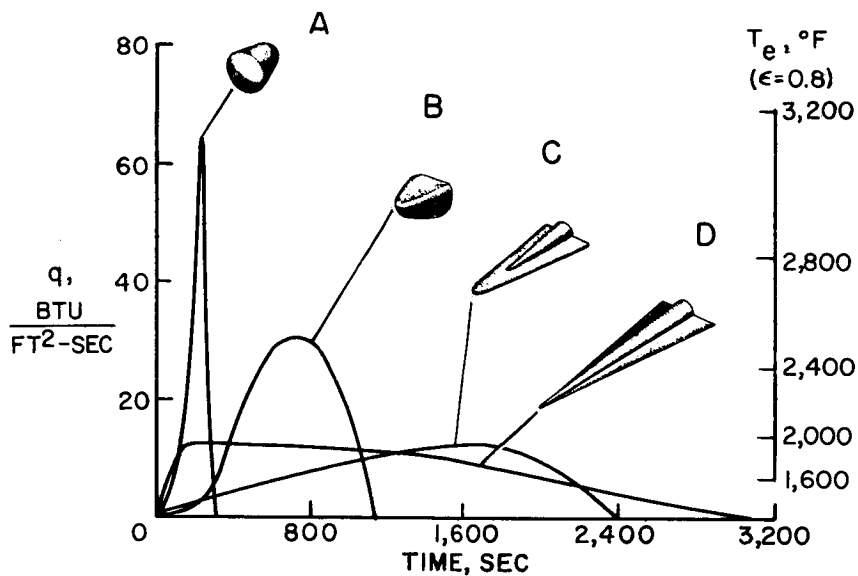
Figure 1

STRUCTURAL APPROACHES
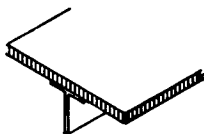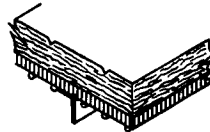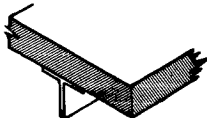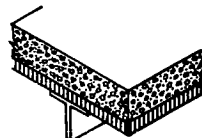
Figure 2

WING WEIGHT FOR GLIDE VEHICLES

UNPROTECTED STRUCTURE; $M_i = 5,000$ IN-LB/IN.
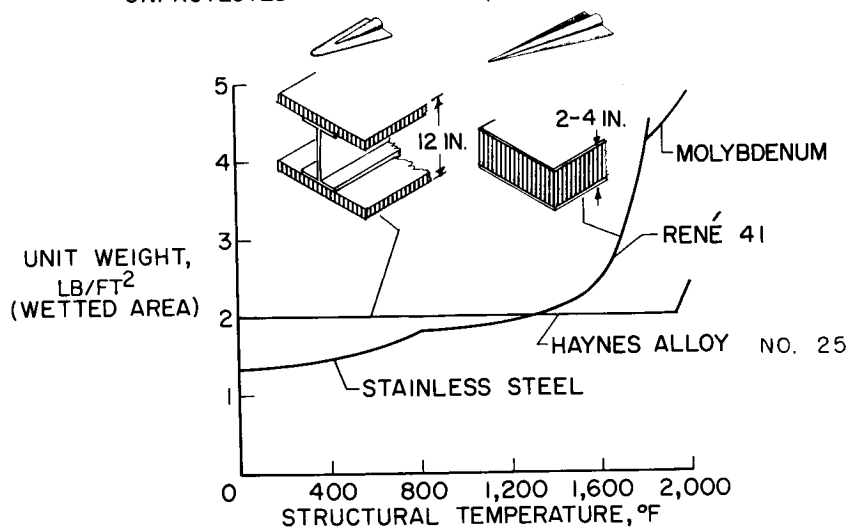


Figure 3

HEAT-PROTECTION WEIGHT FOR GLIDER WITH
HIGH LIFT-DRAG RATIO
$T_{e,MAX} = 1,900 °F$
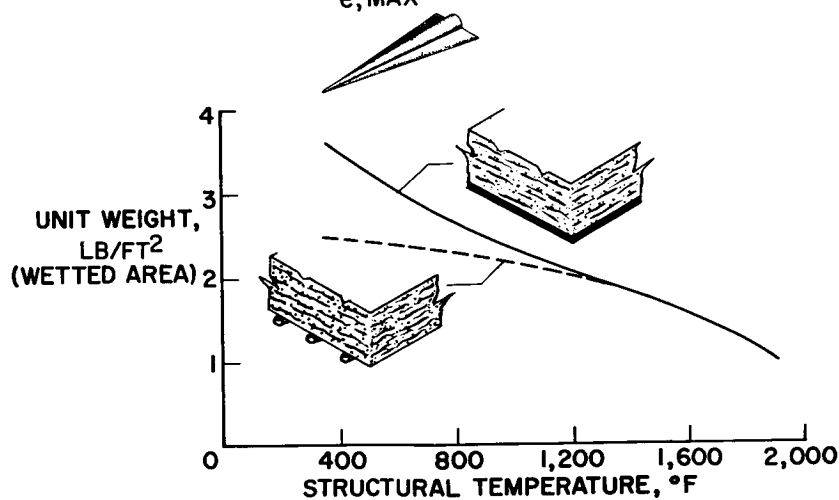


Figure 4

WEIGHT COMPARISON FOR UNPROTECTED AND HEAT-
PROTECTED WING STRUCTURE

$T_{e, MAX} = 1,900°$ F
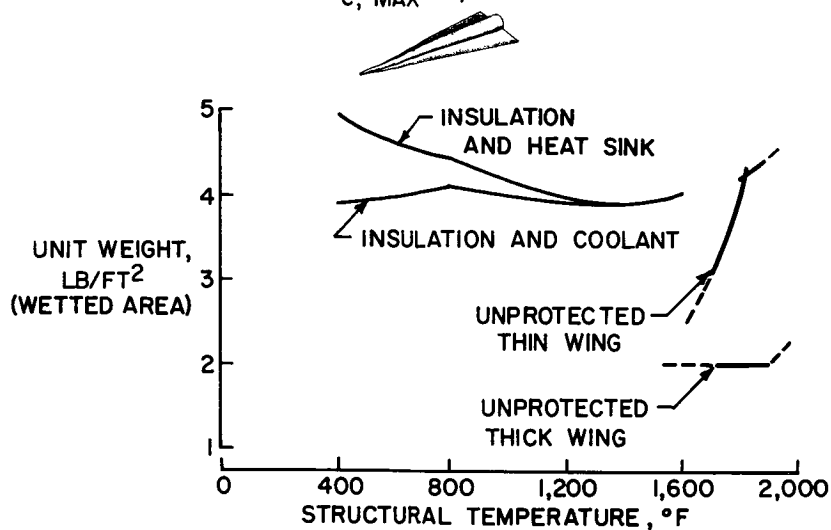


Figure 5

REQUIRED HEAT CAPACITY FOR DRAG VEHICLES
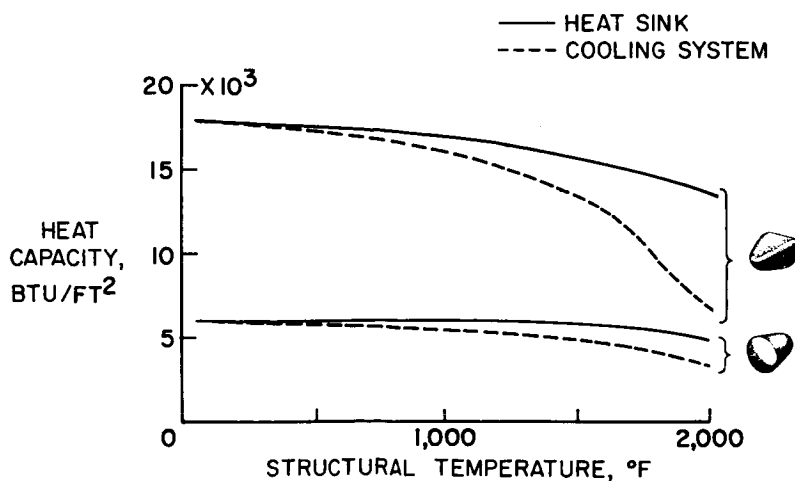


Figure 6

## CHARACTERISTICS OF HEAT-PROTECTION SYSTEMS
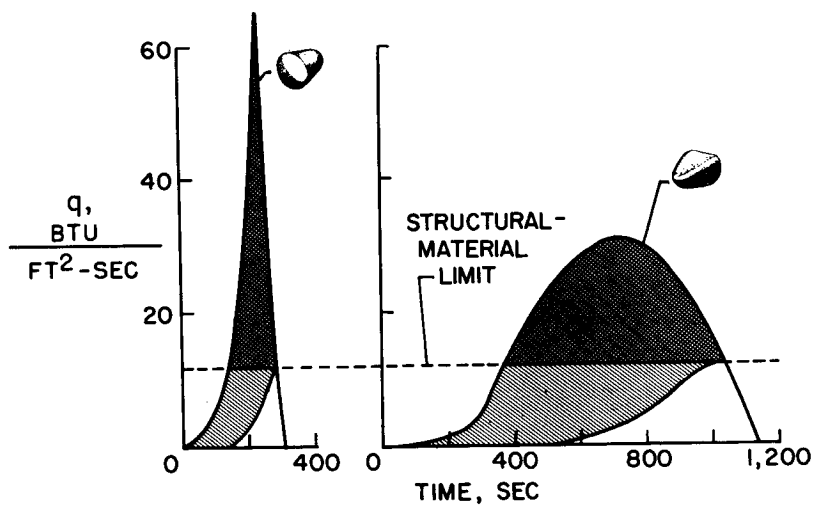


Figure 7

## UNIT HEAT-SINK AND COOLING-SYSTEM WEIGHTS FOR HIGH-DRAG VEHICLE
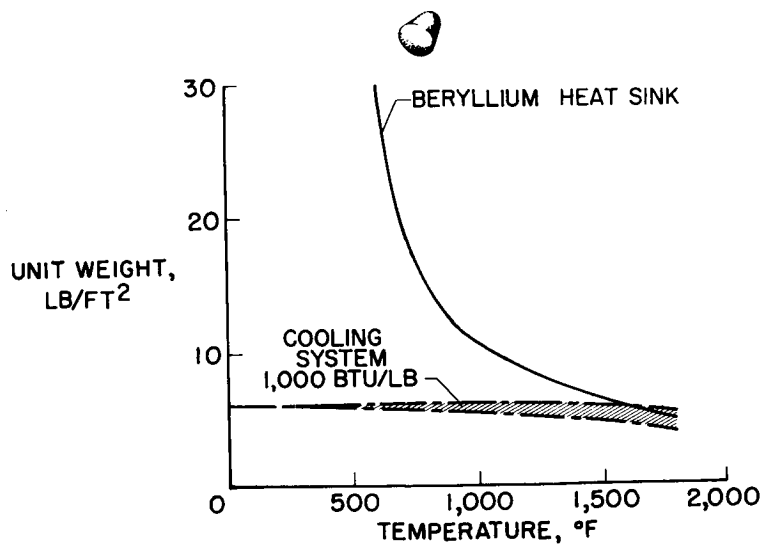


Figure 8

UNIT HEAT-SINK AND COOLING-SYSTEM WEIGHTS
FOR DRAG VEHICLE
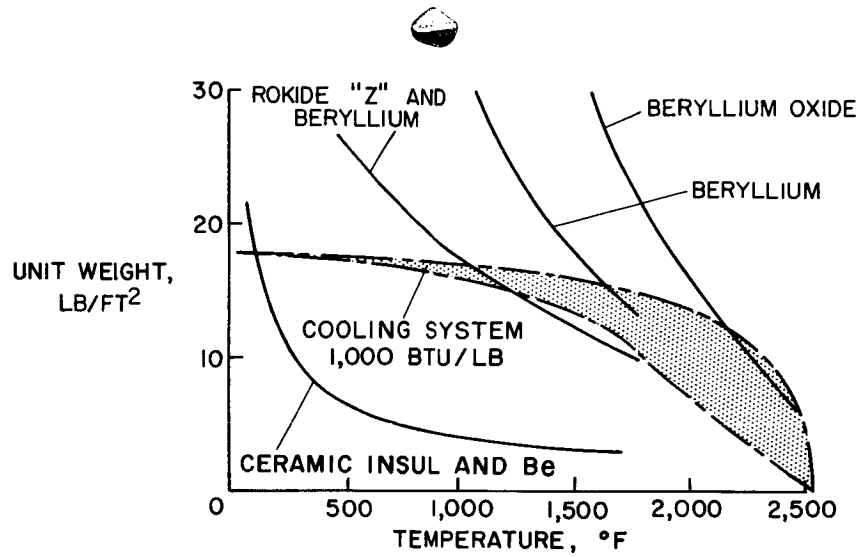


Figure 9

OPERATIONAL PROBLEMS OF MANNED ORBITAL VEHICLES

By Hubert M. Drake, Donald R. Bellman,
and Joseph A. Walker

NACA High-Speed Flight Station

INTRODUCTION

Manned vehicles of orbital performance potential introduce many
operational problems as a result of their extreme performance and the
relative inflexibility of their operations.  The present paper attempts
to discuss some of the major problems and to indicate their possible
effects on flight research operations.

The vehicles being considered for possible use as manned satellites
fall in the three general categories that were discussed by the previous
speakers and are shown in figure 1.  Briefly, the first vehicle is the
ballistic type, characterized by the use of drag alone for entry decel-
eration and for reducing the heat load.  The second category, the semi-
ballistic vehicle, employs lift to reduce the peak decelerations and to
provide some degree of aerodynamic flight-path control.  The final cate-
gory consists of what might be called winged vehicles, that is, vehicles
capable of aerodynamically efficient flight.  It should be pointed out
that this category may also be considered of the semiballistic type
because it can obtain lift-drag ratios as low as zero by operating at
high angles of attack.  In general, only the ballistic and winged types
will be discussed in detail, inasmuch as the capabilities of the
semiballistic type fall between these extremes.  The general problem
areas of escape, piloting, orbit selection, entry, flight termination,
range requirements, and flight-test program are discussed briefly.

Although both vertical rocket-boost take-off and air-launch might
be considered for orbital flight, the major operational problems for the
two types of launch differ only during the initial phases.  Since the
vertical take-off presents the more stringent problems, it is the type
considered herein.

ESCAPE AND SURVIVAL

The presence of the human in the orbital vehicle requires that mal-
functions be either nondestructive or such that an escape system can

provide survival. The provision of a means of escape from all reason-able emergency conditions requires an escape system with all the characteristics of the final vehicle. It therefore appears that the final stage should be designed to serve as the major element of the escape system. A primary goal should be the design of the final stage and the tailoring of the entire flight operation to provide the greatest possible survival potential for this stage. A positive means of pilot separation from the final-stage survival vehicle, such as a high-performance ejection seat, is also required.

The presence of propellants, the take-off operation, stage separation and ignition, and high dynamic pressure combine to make the launch operation (fig. 2) the most critical escape region. Significant survival regions are indicated by the lettered areas on the launch trajectory of figure 2 and are further described in table I. Only two areas, A and C, are discussed in any detail.

Escape at lift-off, region A, is difficult in that the use of the ejection seat would require its reorientation, and the normal final-stage powerplant possesses insufficient acceleration to permit satisfactorily rapid separation from a malfunctioning first stage. A possible escape technique consists of providing high-thrust, jettisonable, solid rocket units attached to the final stage. Rockets sufficient to place the final stage at an altitude of 1,000 feet and a speed of 300 knots within 3 to 4 seconds will probably be adequate for escape from all take-off accidents that do not involve an actual detonation. This end condition permits airplane final stages to be airborne and allows sufficient time for an attempted engine start. Should the engine fail to start, a gliding landing is made, if possible, or the ejection seat may be used. Ballistic or semiballistic vehicles can make a normal parachute landing. These auxiliary rockets and any necessary stabilizing surfaces should be retained to the altitude at which a normal separation and recovery can be made. An example of such a system has been investigated, and it was found that carrying the system to an altitude of about 20,000 feet reduces the first-stage burnout velocity by only about 40 feet per second.

Another critical area for escape and survival is that indicated as region C in figure 2 and table I, where escape by use of final stage may subject the man to excessive decelerations or the vehicle to excessive heating. The extent of this region is greatly influenced by such design and operational factors as the type of vehicle, firing of final-stage power, launch trajectory, lift-drag ratio, and lift or drag loading.

With the ballistic vehicle in this region there is a danger that the man will be subjected to excessive decelerations in case of booster malfunction as shown in figure 3. The solid line indicates the decelerations encountered in the event of a malfunction during the normal gravity-turn launch of a vehicle similar to that discussed in a previous paper by

Maxime A. Faget. The decelerations in this case reach values of about 22g. It might be well to point out that the final satellite vehicle would also have a peak deceleration near 22g at malfunction speeds near 2,000 feet per second if it were separated from the boosters at this point. The lower decelerations shown result from retaining the final boost stage with the vehicle to increase its sectional density during the coast to high altitude following malfunction. Separation of the final vehicle at the peak of the coasting period results in the low decelerations shown. Possible means of reducing the decelerations at high speed of course include the use of lift (the semiballistic vehicle), provision of thrust to reduce flight-path angle, and variable drag geometry. Another possibility is the use of a launching trajectory which has been modified in such a manner that the vehicle will, in case of booster failure, always enter the atmosphere at a sufficiently flat angle to keep the accelerations to a tolerable level. A first approximation to such a trajectory has been calculated and the resulting decelerations are shown as the line labeled "safety" trajectory. In this case the peak decelerations have been reduced by one-half, the peak value being about 11g.

Figure 4 shows that the safety trajectory is considerably flatter than the optimum launching path; thus, the boosters are subjected to higher aerodynamic and control loads and to increased heating. These factors may result in a further performance penalty above that incurred by the use of the nonoptimum trajectory. This performance penalty would have to be judged against the costs of other means of insuring survival in this region. It might be mentioned that figure 4 does not show the entire launch operation for the safety trajectory. The conditions at burnout yield an elliptical orbit having an apogee at 150 miles; an additional speed increment must be applied at this point to obtain a circular orbit.

A similar condition exists for the winged vehicle in region C. In this case there is a possibility, following booster failure, that the vehicle will be forced to perform a skipping entry under conditions that will expose it to excessive heating. A similar trajectory modification may be made to avoid this region. Here, again, possible use of final-stage thrust can greatly alleviate the problem. The investigation of safety trajectories has been a neglected field of research which must be explored for manned satellite vehicles.

It is difficult to envision a reason for evacuating the vehicle in orbit; however, a malfunction in orbit may make the entry operation hazardous. Examples of such malfunctions are the failure or explosion of auxiliary power units, or fuel tanks, and the failure of stabilization systems. Adequate reliability, isolation, and duplication of such critical systems are the best safety and survival provisions. The prevention

of such accidents should be a primary design goal. In some designs if adequate reliability cannot be attained it may even be desirable to incorporate a special escape capsule of the drag-entry type for orbital or entry escape.

It might be well to emphasize a point that has been inferred throughout the foregoing; that is, that the final stage should be designed with the most reliable powerplant and auxiliary power system possible. The final-stage powerplant can, by reliable stop and restart capabilities, greatly alleviate many otherwise dangerous emergencies.

## PILOTING

Consider now the piloting of a satellite vehicle, particularly during the launching phase. Although complete automatic stabilization and control is feasible, it would be desirable to take advantage of the abilities of the pilot to simplify the system and thus increase the reliability and safety of the operation. An exploratory simulator investigation has been made to determine the accuracy with which a pilot could fly a three-stage vehicle to a desired orbit. The guidance used consisted of a presentation of error between programed and actual pitch angle and indications of altitude, rate of climb, velocity, and angle of attack. Figure 5 shows some of the results of this investigation. The plot on the left side of the figure indicates the accuracy in angle and velocity required to obtain an orbit having a perigee above 75 miles and indicates the manner in which an error in angle can be compensated by an increase in velocity. The plot on the right side of the figure shows the piloting accuracy for various conditions. The basic condition, using a rate-of-climb instrument of 25 ft/sec indication for guidance, gave a piloting accuracy of $\pm 0.1°$. Using sensitive or insensitive altimeters increased the errors as shown. Reducing the damping augmentation to zero caused the vehicle to become difficult to control with sufficient accuracy to consistently approach the desired orbital conditions. It appears that the damping system must be of extreme reliability. Although not shown, loss of the static stabilization system, resulting in an extreme value of aerodynamic instability during the first 200,000 feet of the trajectory, had little effect on the pilots' ability to establish a satisfactory orbit.

The effect of inaccuracy or malfunction of the pitch programing presentation was also investigated. With normally operating presentation the pilot could attain the desired orbital altitude to an accuracy of $\pm 2,000$ feet. The malfunctions simulated included inaccurate computations, and complete failure, as early as 20 seconds after lift-off. It was found that the pilot was able to place the vehicle at the desired orbital conditions to an accuracy of $\pm 8,000$ feet using the altitude and speed indicators and several checkpoints during the climb. The early loss of

guidance, or automatic control, would probably be sufficient reason to abort the flight; however, if failure occurred at a later stage in the launch it might well be safer to proceed under pilot control and attempt to establish the orbit.

Although the simulation used was by no means optimum or even desirable, the results indicate that pilot guidance of a launching vehicle with adequate accuracy was feasible. It appears that proper design of presentation and use of the pilot may considerably reduce the complexity of the vehicle and increase its overall reliability, particularly in case of malfunctions.

## ORBIT SELECTION, ENTRY, AND LANDING

The orbital factors of primary importance in manned operations are altitude and inclination. The altitude of the orbit will be determined primarily by the desired lifetime, at least for the purposes presently being implemented, and will probably be between 100 and 300 miles.

The inclination of the orbit may determine, or be determined by, the factors of use, survival, and operational ease. With regard to use, military satellites will require, and geophysical satellites will probably desire, orbits as steep as 90°. Satellite research vehicles have less stringent requirements; whereas, permanent, high-altitude, space terminals will undoubtedly have equatorial orbits, inasmuch as this orbit has the greatest stability and passes over the same points on the earth on each rotation, thus considerably simplifying the supply and rendezvous problems.

The vehicle survival potential of an orbit is primarily associated with the problems of entry, landing, and rescue following landing and is therefore discussed in that aspect. Considering first the ballistic vehicle, malfunction during the launching operation could possibly cause the vehicle to land anywhere around the world, approximately on the first orbital path. In actuality, malfunctions over 90 percent of the boost period would cause impact in the first 6,000 miles and use of the retrorockets could, in any case, limit this distance to about 12,000 miles. Intentional landings from later orbits, in general, can occur anywhere between the extreme latitudes obtained by the orbit. The only azimuth control, in this case, is the crude one of choice of orbit on which to enter. To offset this lack of azimuth control, and thus minimize the area to search for rescue, the equatorial orbit is an obvious choice if the mission permits.

The passenger does, of course, have complete freedom of choice in range, since he is able to fire his recovery rockets at any point in his

orbit and thus land wherever he desires. It was pointed out in a previous paper by Maxime A. Faget that the prediction of the impact point is least sensitive to errors if the retrorockets are fired at the apogee of an elliptical orbit. The determination of the apogee point by the pilot will be relatively easy by use of a radio altimeter and clock. If everything progresses satisfactorily, a rather unlikely event, the point of landing can be predicted before launch within a circle perhaps 60 miles in diameter. In the more probable case in which the flight and recovery are not executed with the desired precision, the area to be searched may be much greater. Consideration of the launch malfunction problem mentioned before indicates a possible maximum area of 12,000 miles by 100 miles for landing. The difficulties of search and rescue in an area this large composed of open sea or jungle cannot be overemphasized. This problem may give the ballistic vehicle an inherently lower survival potential than the other two types.

The winged vehicle places fewer requirements on the inclination of the orbit because the pilot is able to modify the entry path and approach and land at preselected area which may be considerably off the orbital path. In an emergency this would require that only about six or seven emergency landing areas be available on the first orbital path. Figure 6 shows the lateral deviation available to the semiballistic or winged vehicles as a function of lift-drag ratio for entry from a 100-mile orbit. Even the lower lift-drag ratios result in making available a large area for landing. In addition, a curve is shown for the case where aerodynamic heating requires the initial entry to be made at a lift-drag ratio of unity down to a velocity of 16,000 ft/sec, and a lift-drag ratio of 4 is available for the remaining distance. An indication of what this means to the pilot is given in figure 7 which depicts this region superimposed on a map. The large elliptical region indicates the area which, if intersected by the orbital track, will permit a landing anywhere within the smaller elliptical area. The orbits from which a possible landing could be made for these orbital conditions are indicated. In this case a landing could be made from any of the first four orbits and then from the tenth through the eighteenth. This gives the pilot greatly increased flexibility of operation. An interesting point indicated here is that only slightly greater maneuverability would be required to enable landing in the continental United States from an equatorial orbit. Such maneuverability can also be attained by use of thrust in space. However, the amount of maneuverability shown in this figure would require a mass ratio of about 2.5 at a specific impulse of 250.

Consideration of the actual landing maneuver indicates a high probability of a water landing for the ballistic vehicle and a possibility of a similar landing for the other types. The vehicles should be designed, therefore, with water landing capability. The landing can be made by conventional landing gear or parachute with the winged vehicle or by parachute with the ballistic vehicle.

The factor of operational ease is indicated only briefly. It is thought that the maximum operational ease will probably be attained with a winged-type vehicle launched and recovered within the continental limits of United States. The ballistic vehicle in an equatorial orbit has the operational problems of shipboard or island launch of extremely large vehicles, search and rescue of a large area roughly 22 percent jungle and 78 percent water, and the problems of establishing the sea-borne range. The problems of shipboard or island launch and seaborne range are of course associated with the equatorial orbit and would also be true of the winged vehicle in such an orbit.

RANGE REQUIREMENTS

Undoubtedly, manned operations will require exact position and trajectory data, monitor and command data link, communications, long-range GCA, and homing in certain parts of the orbit. The coverage desired of these facilities is again affected by the type of vehicle, while the number of installations is determined by this desired coverage and by the limits of line-of-sight radio propagation. This effectively limits any one installation to a radius of about 850 miles for an orbit altitude of 100 miles. This distance can be increased by about 1,200 miles for UHF communications by employing a repeater station in an aircraft at high altitude.

The range requirements of the ballistic and winged vehicles differ considerably, with the ballistic vehicle substituting complexity of ground installations for vehicle complexity. The minimum coverage required for a ballistic vehicle is shown in figure 8. This vehicle requires complete coverage, as shown, for a distance of about one-half that around the world for location and rescue in case of launch malfunction. An additional station at 180° from the launch site is desirable for orbit verification and for aiding in entry initiation. The darker region shown in the Pacific Ocean is the primary launch and data-taking region while the other areas are, as indicated, only for location and communication. At the other extreme the coverage required for the winged vehicle in a nonequatorial orbit is shown in figure 9. This coverage consists of the first 3,000 miles after take-off, the intermediate stations shown, and the last 2,000 miles before landing. The first region is used to monitor the take-off and initial portion of the orbit to make an initial determination of the orbit and check the pilot's instrument indications. The intermediate points are selected for orbit verification, to insure communication with the pilot at least once per revolution, and to assist the pilot in initiation of entry. The final coverage is in the nature of long-range GCA for the final approach. The vehicle itself must, of course, incorporate the required communications, beacons, telemeters, and homing equipment.

It would probably be desirable during the launch operation, and the first orbits, to have the maximum communications coverage possible. The stations shown for the ballistic vehicle of course provide complete coverage for the first 12,000 miles, leaving about a 40-minute gap; whereas, those for the winged configuration leave gaps of as much as 20 minutes in which communications are lacking. As mentioned previously, this coverage can be improved easily and quickly by use of airborne repeaters. The pilots have a natural desire for continuous worldwide communications; however, it appears improbable that such coverage can be achieved with earthbound stations. A promising solution in this case is the provision of communication satellites in the "stationary" (22,000-mile altitude) orbit. The ability to establish such facilities may well precede the capability of establishing manned satellites.

## FLIGHT TESTING

One final matter that should be mentioned in any discussion of manned satellite operations is the flight-test program. Any flight-test program should utilize the usual procedure of a rational buildup of performance on successive flights in order to explore, with reasonable safety, successively higher performance ranges. This procedure would have the desirable effect of providing the longest period possible for the improvement and demonstration of booster reliability. The provision of boosters of sufficient reliability is, of course, one of the greatest obstacles to the accomplishment of manned orbital flight.

## CONCLUDING REMARKS

Although this cursory survey has not indicated any insurmountable operational problems to manned orbital flight regardless of configuration type, the problems of the various satellite configurations do materially affect operations and must be considered early in the design. Safety and survival requirements must be taken into consideration in manned operations and may force considerable deviation from optimum procedures. Although the presence of man in the vehicle requires increased emphasis on reliability and safety, proper use of his abilities can considerably simplify design and increase reliability.

TABLE  I

## LAUNCH   ESCAPE   REGIONS

| | APPROXIMATE   CONDITIONS | | | PROBLEM | ESCAPE  PROVISIONS |
|---|---|---|---|---|---|
| | H, MI | V, FT/SEC | q, LB/SQ FT | | |
| A | 0 TO 4 | 0 TO 1,000 | 0 TO 600 | ESCAPE  FROM LAUNCH  AREA | 1. BOOSTED  FINAL STAGE<br>2. EJECTION  SEAT |
| B | 4 TO 20 | 1,000 TO 5,000 | 300 TO ≈1,500 | AS FOR NORMAL OPERATION | 1. FINAL  STAGE |
| C | 20 TO 90 | 5,000 TO 24,000 | 300 TO ≈ 0 | POSSIBILITY  OF EXCESSIVE g OR HEATING  ON ENTRY | 1. PROPER  TRAJECTORY<br>2. FINAL  STAGE (POWER ON, IF POSSIBLE) |
| D | >90 | 24,000 TO ORB. | | AS FOR ENTRY FROM  ORBIT | 1. FINAL  STAGE |

## EXAMPLES OF MANNED ORBITAL VEHICLES
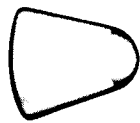


| BALLISTIC | SEMI-BALLISTIC | WINGED |
|-----------|----------------|--------|
| $L/D \approx 0$ | $0-1$ | $0-5$ |
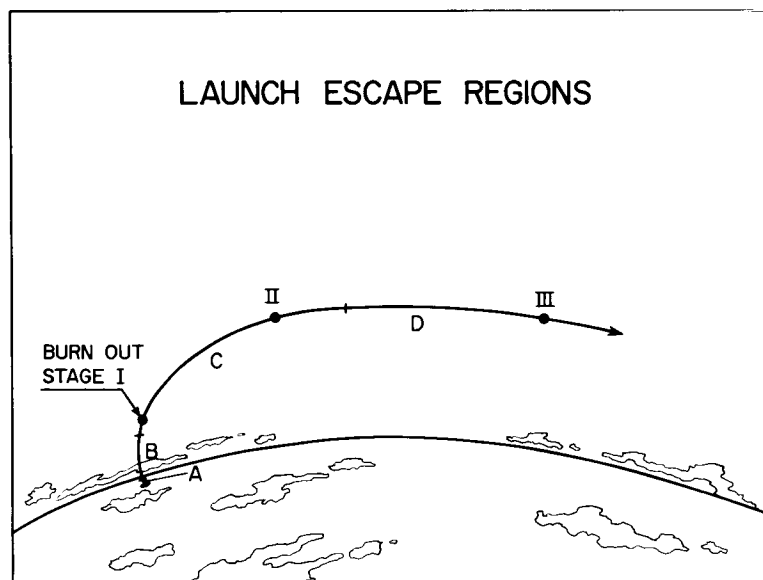
Figure 1



Figure 2

# DECELERATIONS FROM ABORTED LAUNCH

## BALLISTIC VEHICLE, 150 MILE ORBIT
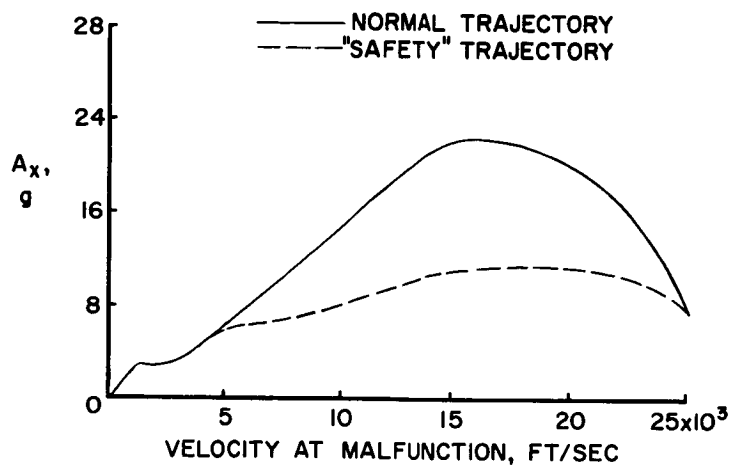
Figure 3

# BALLISTIC VEHICLE LAUNCH TRAJECTORIES

## ORBIT ALTITUDE, 150 MILES
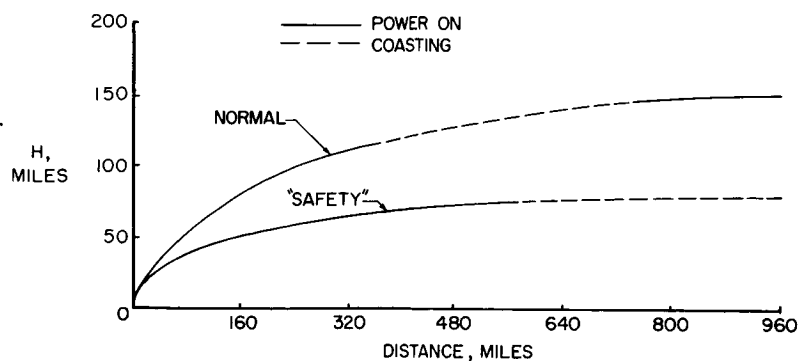
Figure 4

# PILOTING ANGULAR ACCURACY AT BURNOUT
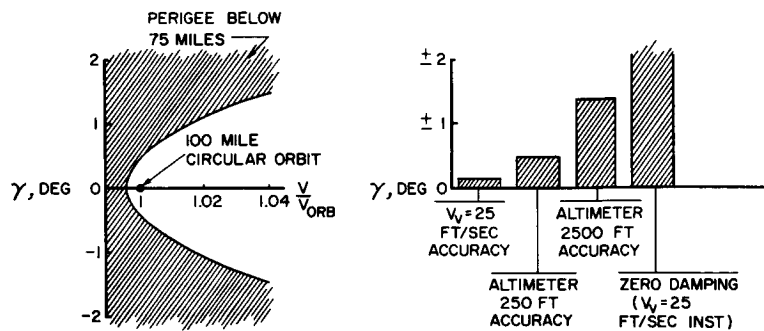


Figure 5

# MANEUVERABILITY DURING ENTRY



Figure 6

# LANDING ORBITS



ORBIT  4,18   3,17   2,16   1,15   14   13   12   11   10

INCLINATION 35°, PERIOD 90 MINUTES

$\frac{L}{D} = 1, V > 16,000$ FPS
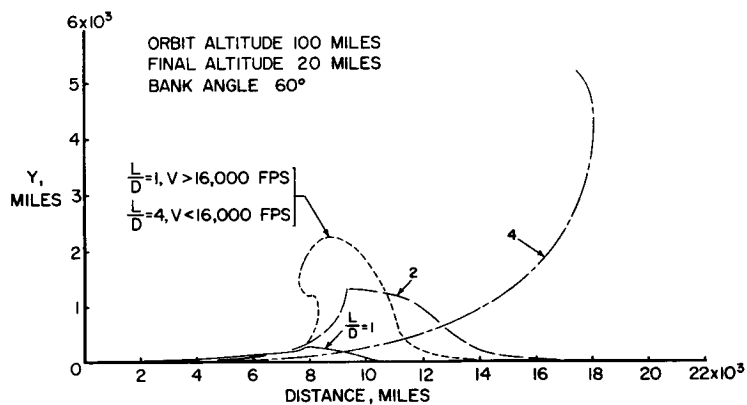
$\frac{L}{D} = 4, V < 16,000$ FPS
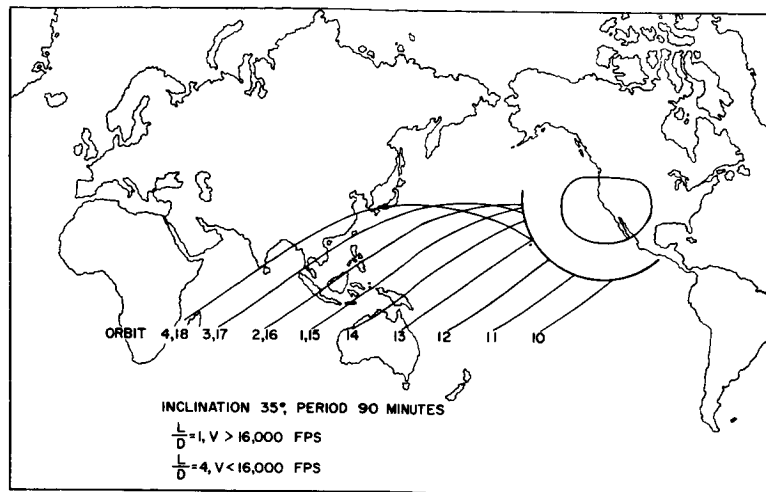
Figure 7

# RANGE REQUIREMENTS
# BALLISTIC VEHICLE



ACQUISITION, TRAJECTORY, COMMUNICATION, DATA MONITOR, COMMAND LINK, VISUAL BEACON.

ACQUISITION, COMMUNICATION, VISUAL BEACON.
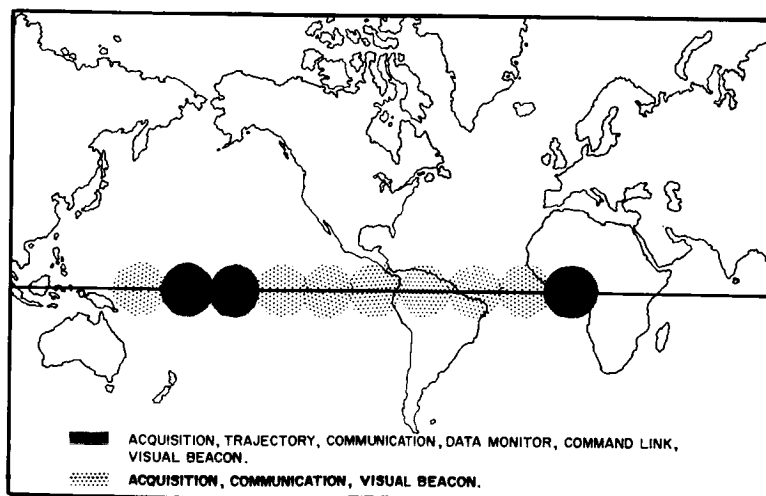
Figure 8

## RANGE REQUIREMENTS
## WINGED VEHICLE

ACQUISITION, TRAJECTORY, COMMUNICATION, DATA MONITOR, COMMAND LINK, HOMING
TRAJECTORY, COMMUNICATION, DATA MONITOR, COMMAND LINK
ACQUISITION, TRAJECTORY, COMMUNICATION, VISUAL BEACON
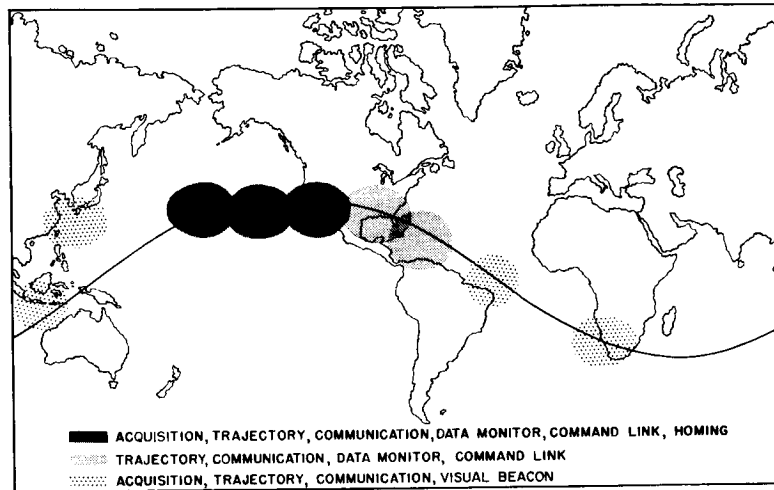
Figure 9

# STABILITY OF BALLISTIC REENTRY BODIES

By John D. Bird
Langley Aeronautical Laboratory

and David E. Reese
Ames Aeronautical Laboratory

## SUMMARY

Various features of the stability of ballistic reentry shapes are discussed, including those considerations pertinent to ballistic-missile and manned-satellite reentry capsules. Calculations and aerodynamic data are used to indicate the problems involved. It is concluded that, with proper allowance for desirable geometrical features, the attainment of satisfactory stability of reentry bodies having subsonic terminal velocities is not too difficult but, in efforts to minimize weight in solution of the heating problem, undesirable features may be introduced which will cause marginal stability characteristics. The attainment of satisfactory stability of reentry bodies having supersonic terminal velocities appears to offer fewer problems.

## INTRODUCTION

The analysis of Allen (ref. 1) indicated the essential features of the problem of reentry stability in terms of Bessel functions. In this work and the related work of others, the powerful constraining effect on the motion of the rapid increase of dynamic pressure was shown in addition to the destabilizing influence of the drag force. The criterion of stability was expressed by Allen in reference 1 in terms of a now well-known damping factor which includes the drag, lift, and pitch-damping coefficients. This solution is good for the range of Mach numbers where the stability derivatives are essentially constant as assumed in the analysis and only undergoes some modification near and below the transonic region where the aerodynamic characteristics change radically and the motion has slowed to the point where the influence of gravity becomes significant. In this work it was shown that satisfactory directional stability was the factor of primary concern down to an altitude in the vicinity of 100,000 feet for the densities of missiles generally under consideration and that the

damping derivatives, that is, the drag, lift-curve slope, and the damping in pitch, made themselves felt primarily below that altitude.

The purpose of the present investigation is, first, to discuss some aerodynamic characteristics of blunt reentry shapes and to give some indication of the significance of these characteristics as related to the dynamics of ballistic-missile reentry bodies, second, to discuss the dynamics of a manned lightweight reentry capsule and, third, to mention a few points in connection with work on slender, high-terminal-velocity bodies for ballistic missiles.

## SYMBOLS

$C_D$      drag coefficient

$C_{L_\alpha}$      lift-coefficient derivative with respect to angle of attack, per radian

$C_{m_q} + C_{m_{\dot\alpha}}$      pitch-damping derivative based on $\dfrac{l}{2V}$

$l$      characteristic length, generally maximum diameter

$\sigma$      radius of gyration

$M$      Mach number

$\alpha$      angle of attack

$\alpha_E$      angle of attack on reentry to atmosphere

$W$      weight of reentry body

$A$      reference area, generally maximum cross-sectional area

$C_{N_\alpha}$      normal-force derivative with respect to angle of attack, per radian

$I_Y$      moment of inertia

$\gamma$      flight-path angle, positive up

$C_{m_\alpha}$      pitching-moment-coefficient derivative with respect to angle of attack, nondimensionalized by reference area and length, per radian

$V$      forward velocity

R          Reynolds number

f          frequency

$q_{max}$      maximum dynamic pressure

t          time

## DISCUSSION

Examples of the pitch damping obtained for blunt shapes at various Mach numbers are shown in figures 1 and 2. The data shown in these figures in the subsonic Mach number range were obtained in the Ames 12-foot pressure tunnel by Donald A. Buell, whereas those in the supersonic Mach number range were obtained in the Ames 8- by 7-foot Unitary Plan wind tunnel by Benjamin H. Beam. Figure 1 shows results obtained on a very shallow reentry shape. It can be seen that unstable pitch damping is obtained in the supersonic region for this shape with a moderately sized afterbody. This would result in an undesirable dynamic behavior of this configuration unless there is an appreciable modification of the pitch damping in the lower or higher supersonic Mach number range.

One of the most interesting points in connection with these data is the influence of afterbody shape. At the supersonic Mach numbers increasing the size of the afterbody was beneficial (made the pitch damping more negative), whereas at both subsonic and supersonic speeds reducing the size of the afterbody was beneficial. This beneficial effect of afterbody-size reduction at subsonic speeds is better shown by the data of figure 2 which are for a parabolic configuration. For this configuration, reduction of afterbody size produced a pronounced effect at subsonic speeds but had essentially no effect at the supersonic speeds. Also, the pitch damping for this configuration was stable in the supersonic region as contrasted with the results for the more shallow configuration of figure 1.

A factor that has been given some attention in connection with damping measurement is that of the influence of a small angle of attack that may arise from unsymmetrical distortion of the body. In the case of the blunt shallow reentry shapes this effect has been found to be quite significant at a Mach number of 2.5. (See fig. 3.) Small angles of attack are sufficient to cause marked changes in the pitch damping. In the case of the configuration with a moderate afterbody the damping is changed from an unstable value to a stable one by a change of $2^{\circ}$ in angle of attack. Damping of the configuration with a small afterbody,

however, becomes unstable at $2°$ angle of attack. These results show a decided nonlinear damping behavior which dictates the study of pitch damping to amplitudes commensurate with those to be tolerated in the particular application in order to obtain a reasonable perspective. The results shown in figure 3 indicate the strong probability of limit cycle operation for the model with the moderate-sized afterbody.

The effect of a change in pitch damping on reentry body motion is shown in figure 4. Calculations are shown in this figure for optimum-range intercontinental-ballistic-missile (ICBM) reentry conditions for which the aerodynamic derivatives used are given in table I. These calculations were made by use of an IBM type 704 electronic data processing machine. The complete nonlinear equations of motion were employed. In one case in figure 4 the aerodynamic characteristics correspond generally to those of the shallow body with moderately sized afterbody, and in the other case the aerodynamic characteristics correspond generally to those of the shallow body with a small afterbody. It can readily be seen that an increase of damping is beneficial. The calculation diverges to considerably greater amplitude prior to a Mach number of 1 for negative pitch damping than for zero pitch damping. When the stable subsonic pitch damping comes into play, the motion of the body with small afterbody subsides. The calculation with negative pitch damping was not carried completely to the ground. It should be remembered that limit cycle performance will very probably prevent bodies similar to the shallow model with moderately sized afterbody from exceeding a certain relatively small amplitude. In general, considerable divergence can be tolerated prior to a Mach number of 1.0 if good subsonic damping is present and care is taken not to have too great an angle of attack at reentry. Pitch damping as great as -0.3 would give an almost linear decay of the pitching motion to zero amplitude at about an altitude of 40,000 feet. Artificial pitch damping as great as -3.0 would cause the motion to subside by the time an altitude of 100,000 feet is reached.

One possibility for improving the stability characteristics of subsonic reentry bodies in the transonic region that has been given some thought involves the use of a spool-like form as shown in figures 5 and 6. These data were obtained in the Langley transonic blowdown tunnel and Mach 3 jet by Lewis R. Fisher and William Letko, respectively. The theory behind the use of this configuration is that the flare at the end of the body will be extremely effective in the near transonic region and, hence, will contribute to the pitch damping in large measure at low speeds but will not greatly affect the aerodynamic characteristics nor will the flare encounter great heating loads at the higher speeds, because of its location, if it is made sufficiently small. Some beneficial effect should be obtained for this arrangement at the extremely high reentry altitudes because of the improvements in directional stability at the large angles of attack that may be encountered without precise orientation by automatic means. It can be seen that a surprisingly large value

of directional stability is obtained with this arrangement in comparison with that obtained with the simple flared model at the left in figure 5. Results at a Mach number of 3.0 on somewhat different models indicate that spool models do not experience as great an increase of stability over simple flared models for supersonic speeds as was the case for transonic speeds (fig. 6). The damping in pitch of a spool model can be seen from the data of figure 7. These data were obtained in the Langley high-speed 7- by 10-foot tunnel by Herman S. Fletcher. The simple flared model shows unstable damping at the higher subsonic speeds, whereas the spool model shows a powerful damping influence. It is quite likely that an optimum spool shape would have less flare than the models for which data are shown because these models have more directional stability than is required.

The unstable pitch damping shown for the simple flared model as the transonic region is approached has been obtained for other shapes in greater or lesser degree and has caused some concern. However, a considerable degree of unstable damping may be tolerated in the transonic region for subsonic-terminal-velocity bodies which make rapid transit of the transonic region if the subsonic pitch damping is stable. This unfavorable pitch damping effect can be seen from the calculations shown in figure 8, the conditions for which are given in table I. It can be seen in figure 8 that a reversal in sign of the pitch damping in the transonic region does not impose an intolerable burden because not too great an amplitude is reached before the transonic region is passed. The result may be entirely different, of course, for a reentry body having a transonic terminal velocity; this body would be exposed to any transonic peculiarity for a much longer period of time.

Recently there has been a general belief that a high-drag bluff body would make an adequate minimum reentry body for a man-carrying satellite (ref. 2). In such an application a low angle of reentry would be employed in order to minimize the acceleration on the occupant. An example of the motion of a vehicle on reentry to the atmosphere is shown in figure 9. Aerodynamic data for the reentry capsule shown in this figure were used for the present calculation. The various mass and aerodynamic quantities used in the calculation are given in table I. The equations for these calculations included the effect of the earth's curvature and were integrated by use of an IBM type 704 electronic data processing machine. The sketch in figure 9 shows the general character of this reentry. A maximum deceleration of 9.9g is encountered at an altitude of 145,000 feet. Also shown in this figure is a plot of the amplitude envelope of the oscillation during reentry for an assumed error in alinement with the flight path of $1^0$ at reentry. The first few cycles of the oscillation are shown as a dashed line in the right-hand side of this plot. The amplitude of oscillation at Mach number 1 is much the same as that at reentry. Thereafter, an increase in

divergence occurs in spite of the stable subsonic pitch damping. The damping factor is unstable in this region as well as for the remainder of the reentry because of the negative lift-curve slope. An increase of pitch damping in the subsonic region to -0.20 effected by adding a tail assembly or flare produces a more stable behavior. The frequency history of the capsule during reentry is presented in figure 10. It is evident from the figure that the frequency and dynamic pressure are not excessive. The maximum frequency is about 1.0 cycle per second which occurs at an altitude of 145,000 feet. The maximum normal acceleration, which is extremely low because of the small normal lift-curve slope and small error in alinement of the satellite on reentry, is about 0.12g and occurs at an altitude of about 125,000 feet. These results indicate this to be a reasonable form of reentry vehicle from the stability point of view.

An example of the negative lift-curve slopes of several forms of blunt reentry bodies which contribute to the low-altitude divergence shown for the satellite is given in figure 11. These data were obtained in the Langley transonic blowdown tunnel by Lewis R. Fisher and Joseph R. DiCamillo. In this figure the lift-curve and pitching-moment-curve slopes are shown for several blunt shapes at a Mach number of 1.0. It can be seen that the very blunt forms have destabilizing negative lift-curve slopes and that there is a pronounced Reynolds number effect for one of the intermediate shapes. The negative lift-curve slopes for the blunt rounded-corner forms shown in figure 11 become somewhat smaller as the supersonic region is entered and the aerodynamics approaches the Newtonian consideration more closely. Instability from this particular source may be well in evidence in the terminal phase of flight for bodies with relatively low pitch damping.

Recently, it has become apparent that, for ballistic missiles, terminal velocities to a Mach number of 2.0 or higher are not unreasonable with present methods and materials. As a result, increased emphasis has been given to long slender shapes having low rather than high drag coefficients. An examination of the Allen damping factor (ref. 1)

$$C_D - C_{L_\alpha} + \frac{1}{2}\left(C_{m_q} + C_{m_{\dot{\alpha}}}\right)\left(\frac{1}{\sigma}\right)^2$$

indicates that this trend is favorable inasmuch as the destabilizing drag quantity is reduced considerably when long slender shapes are used. In addition, the sometimes troublesome transonic region is avoided completely, and the possibility of destabilizing negative lift-curve slopes is eliminated because the lift-curve slope of slender, more pointed bodies is positive.

One approach to the design of ballistic missiles having high terminal velocities might be to utilize slender arrangements in the form of artillery shells that have no stabilizing surfaces to protect from heating. Such an arrangement would generally have some degree of instability if packaged more or less uniformly which would have to be counteracted by sufficient spin or by other means to provide stabilization. An examination of the spin stability criterion indicates that the required spin rates are likely to be excessive for so complicated a device as a reentry warhead or a man-carrying satellite. Also, the higher gyroscopic stiffness introduced tends to maintain large amplitudes of yaw well into the region of high heating. Such behavior may be advantageous for applications in which appreciable loss of heat by radiative cooling is obtained; in this case a body could be toasted more or less evenly on all sides.

Because of the difficulties of spin stabilization one of the most promising considerations in conjunction with the design of adequate stability and damping into slender reentry bodies having high terminal velocities involves the use of flares. It has been shown by rocket-propelled-model tests conducted at the Langley Pilotless Aircraft Research Station at Wallops Island, Va., that heating loads obtained on the flared portion of blunt bodies are not unreasonable. The location of the flare at the end of the body is advantageous from the standpoint of damping because lifting elements generally contribute to pitch damping in proportion to the squares of their lever arms and lift is not generated by expanding portions of the body in front of the center of gravity which tend to cancel the contributions to stability of the rearward portions.

Work by Becker and Korycinski (ref. 3) has shown a tendency for slender flared bodies to develop large regions of separated flow in front of the flare for low Reynolds numbers at Mach numbers near 7.0. The net effect of this phenomenon is to reduce the efficiency of the flare in contributing to directional stability. This reduction in efficiency necessitates a greater area of flare than might be anticipated otherwise.

A measure of the pitch damping of two of these rocket-propelled models from a program conducted by John C. McFall, Jr., together with data from tests of a flared rounded-nose model at Thompson Aeroballistics Laboratory, is given in figure 12. These data are referenced to frontal body diameter and area rather than to base diameter and area. Adequate pitch damping is shown for all of the models in the supersonic region, but definite unstable values exist for the flared and the blunt cylinder models in the subsonic region. Similar results have been obtained at subsonic Mach numbers for a flared blunt model in wind-tunnel tests at the Langley Laboratory. Rocket-propelled-model tests on simple 10° cone models have indicated good damping at Mach numbers of approximately 6.0.

In one rocket-propelled-model flight, a $10^\circ$ amplitude wandering motion of a flared model was obtained in the transonic region. Figure 13 shows the time history in this particular flight of the flared model compared with a time history for a more stable configuration. At least one wind-tunnel measurement has indicated that this flared configuration has unstable damping in the subsonic region. It is quite possible, of course, that the sharp corner is an undesirable feature of the flared configuration with regard to damping.

<div align="center">CONCLUDING REMARKS</div>

With proper allowance for desirable geometrical features, the attainment of satisfactory stability of reentry bodies with subsonic terminal velocities is not too difficult but in efforts to minimize weight in solution of the heating problem undesirable features, such as, extremely flat noses, short skirts, and bulging afterbodies, may be incorporated into the system. Use of these features will require a much more precise determination of stability because they may produce marginal characteristics. The attainment of satisfactory stability of reentry bodies with supersonic terminal velocities appears to offer fewer problems but a number of good measurements of pitch damping are needed for low drag shapes.

<div align="center">REFERENCES</div>

1. Allen, H. Julian:  Motion of a Ballistic Missile Angularly Misalined With the Flight Path Upon Entering the Atmosphere and Its Effect Upon Aerodynamic Heating, Aerodynamic Loads, and Miss Distance. NACA TN 4048, 1957.

2. Faget, Maxime A., Garland, Benjamine J., and Buglia, James J.:  Preliminary Studies of Manned Satellites - Wingless Configuration: Nonlifting.  (Prospective NACA paper.)

3. Becker, John V., and Korycinski, Peter F.:  Heat Transfer and Pressure Distribution at a Mach Number of 6.8 on Bodies With Conical Flares and Extensive Flow Separation.  NACA RM L56F22, 1956.

## TABLE I

CONDITIONS FOR MOTION CALCULATIONS

| | $\frac{W}{C_D A}$, LB/SQFT | $C_D$ | $C_{m_\alpha}$ | $C_{N_\alpha}$ | $C_{m_q} + C_{m_{\dot\alpha}}$ | SPIN, RPM | $I_Y$, SLUG-FT$^2$ | $\gamma$, DEG |
|---|---|---|---|---|---|---|---|---|
| AFTERBODY SHAPE | 113 | 1.05 M>1<br>.70 M<1<br>1.05 M>1<br>.90 M<1 | -.2 | .89 | .2 M>1<br>-.1 M<1<br>0 M>1<br>-.2 M<1 | 0 | 230 | -22½ |
| TRANSONIC DAMPING | 108 | 1.11 | -.36 | .89 | VARIES | 0 | 230 | -22½ |
| SATELLITE REENTRY | 29 | 1.55 M>1<br>.90 M<1 | -.2 | .28 | 0.04 M>1<br>-.08 M<1 | 0 | 340 | -3 |

EFFECT OF BODY SHAPE ON PITCH DAMPING
α = 0°
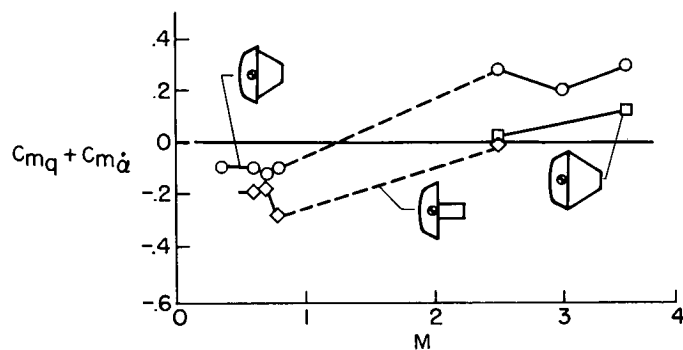


Figure 1

EFFECT OF BODY SHAPE ON PITCH DAMPING
α = 0°
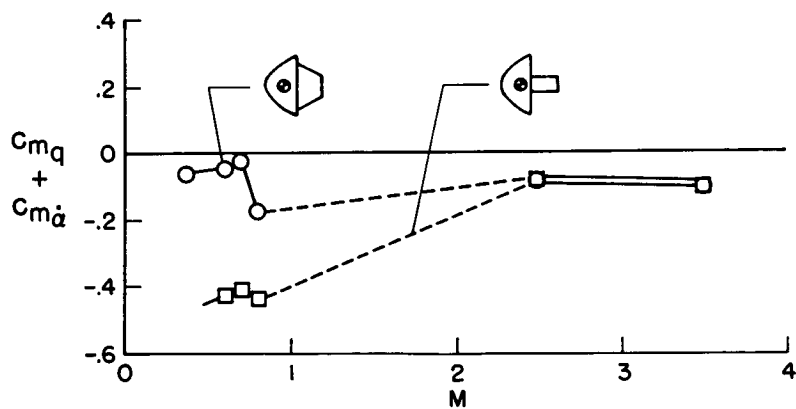


Figure 2

EFFECT OF ANGLE OF ATTACK ON PITCH DAMPING
M=2.5

$c_{m_q} + c_{m_{\dot{\alpha}}}$

$\alpha$, deg
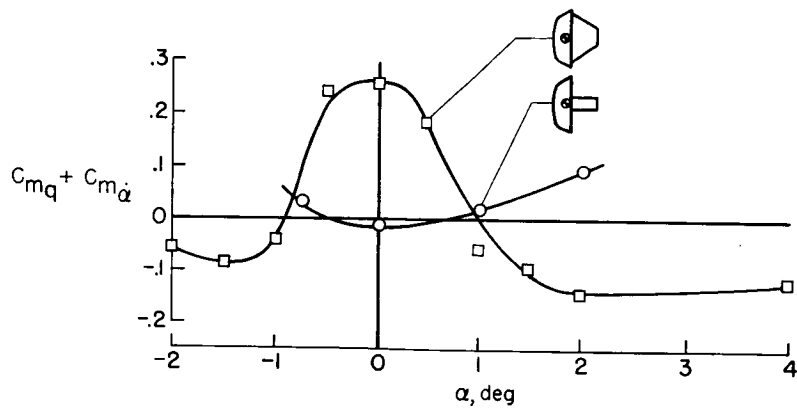
Figure 3

EFFECT OF PITCH DAMPING ON AMPLITUDE ENVELOPE
W/$C_D$A = 108 LB/SQ FT

$\left(\dfrac{\alpha}{\alpha_E}\right)_{ENVEL}$

M = .8 1.0    3    10  15    20          21.6

ALTITUDE, FT
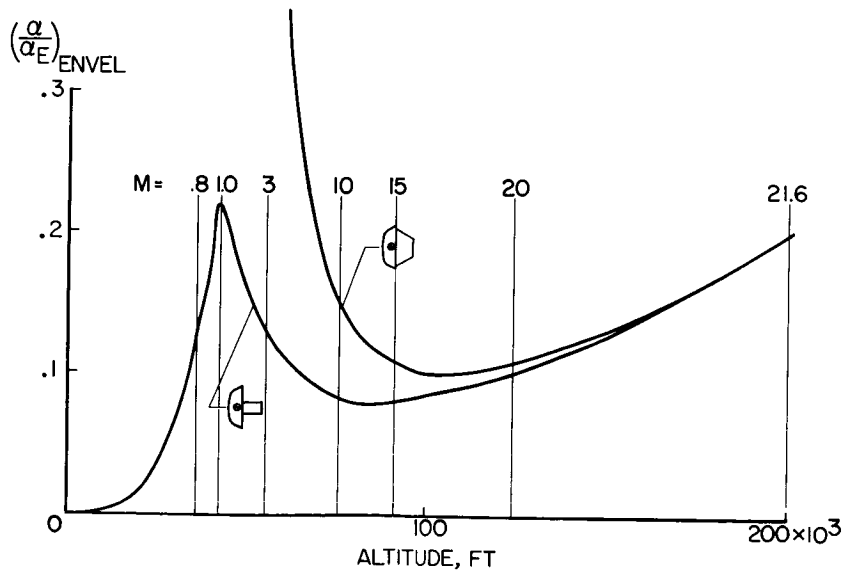
Figure 4

CONFIDENTIAL

EFFECT OF CONTRACTION NEAR CENTER OF BODY
$M = 1; R = 5.6 \times 10^6$
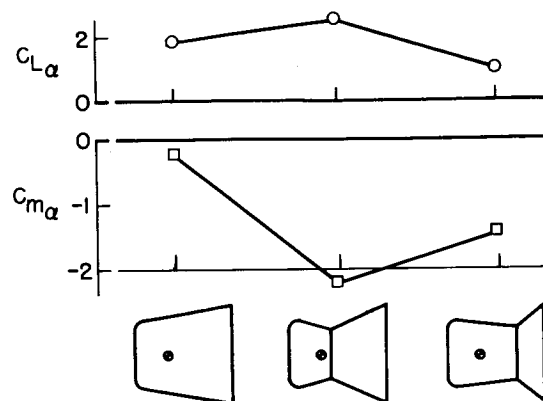


Figure 5

EFFECT OF CONTRACTION NEAR CENTER OF BODY
$M = 3; R = 6 \times 10^6$
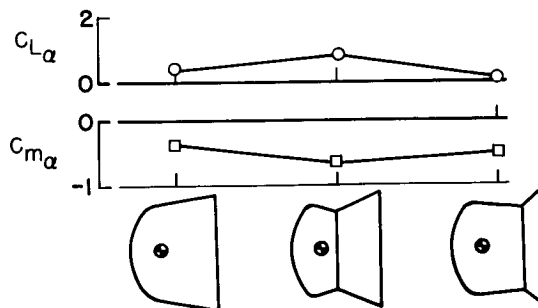


Figure 6

CONFIDENTIAL

EFFECT OF CONTRACTION NEAR CENTER OF
BODY ON PITCH DAMPING
$R \approx .65 \times 10^6$
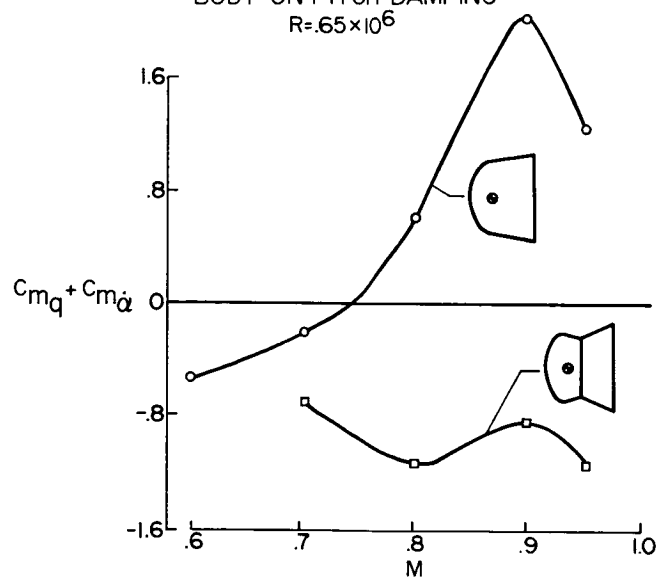


Figure 7

EFFECT OF UNFAVORABLE DAMPING IN TRANSONIC REGION
$$\frac{W}{C_D A} = 108 \text{ LB/SQ FT}$$



Figure 8

MOTION OF BALLISTIC REENTRY CAPSULE
$\gamma = -3°$ AT 400,000 FT; $\alpha_E = 1°$
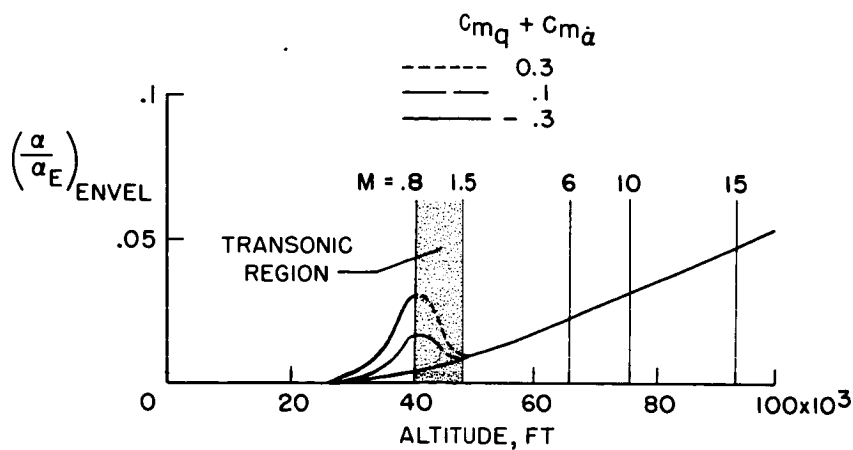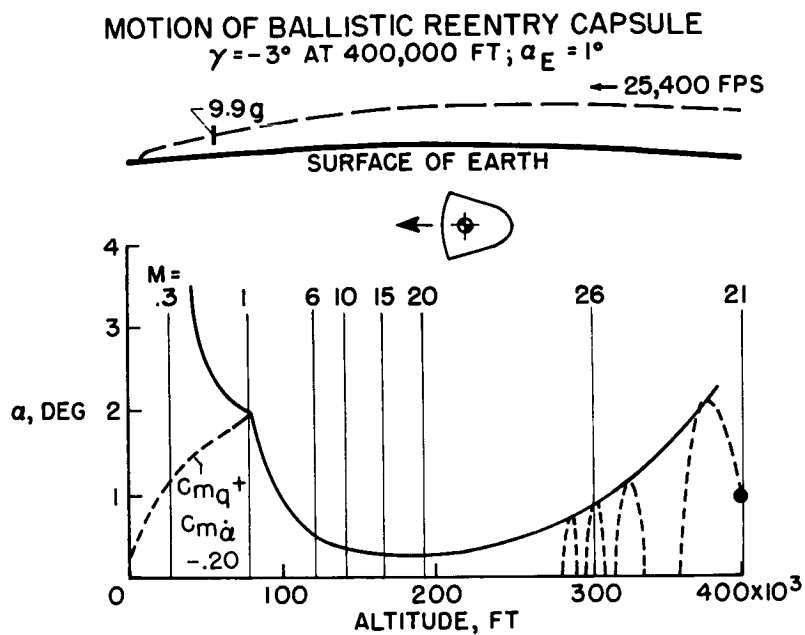


Figure 9

MOTION OF BALLISTIC REENTRY CAPSULE
$\gamma = -3°$ AT 400,000 FT; $\alpha_E = 1°$



Figure 10

## EFFECT OF SHAPE ON $C_{L_\alpha}$ AND $C_{m_\alpha}$
### $M \approx 1.0$
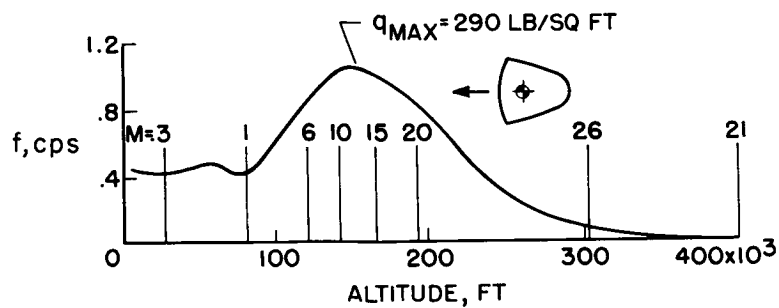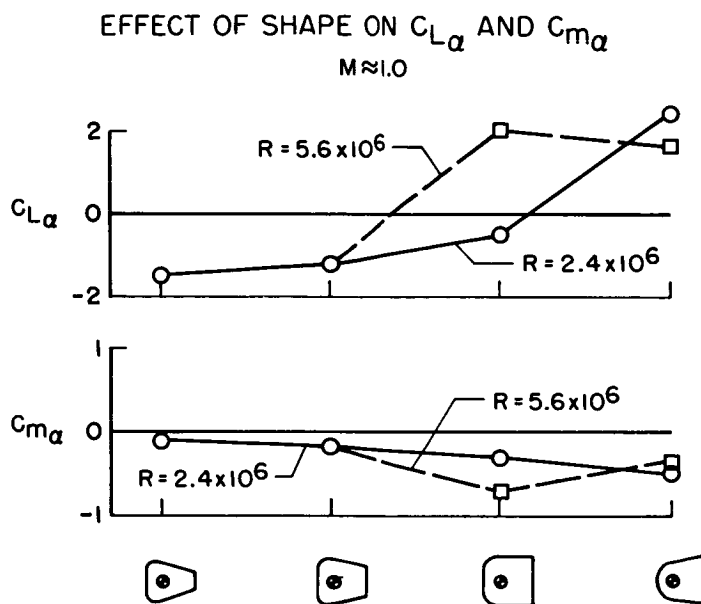


Figure 11

## PITCH DAMPING OF HIGHER FINENESS RATIO MODELS
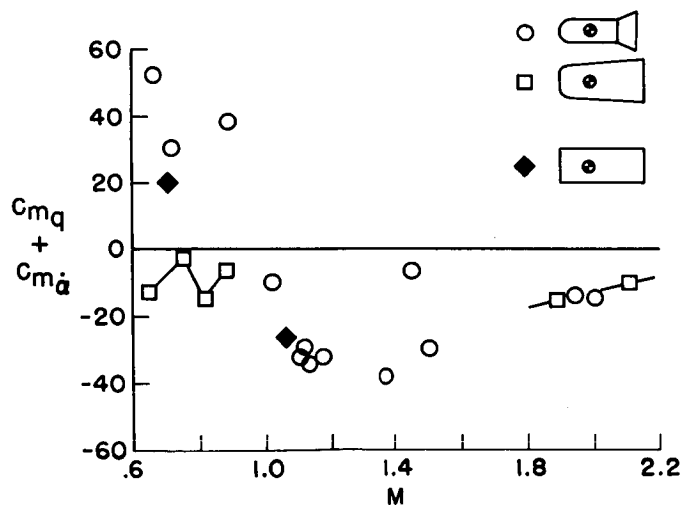


Figure 12

MOTION OF ROCKET-PROPELLED MODELS
M = 1.4
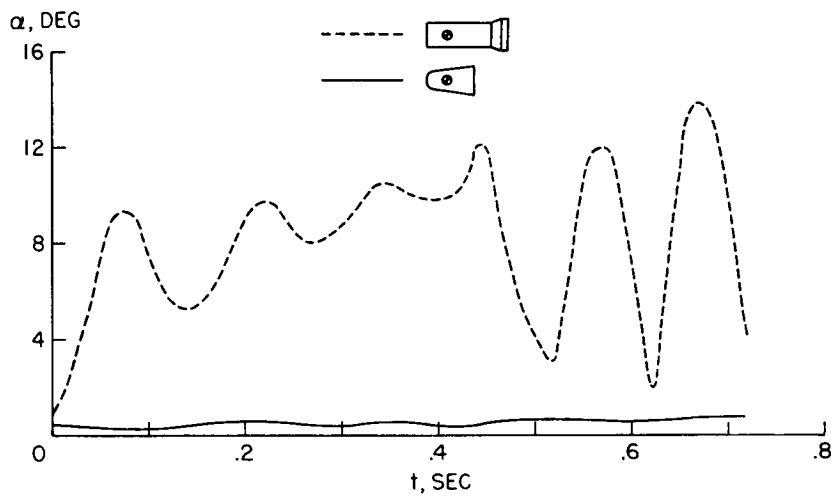


Figure 13

# AERODYNAMIC PERFORMANCE OF HYPERSONIC GLIDERS

By C. A. Syvertson
Ames Aeronautical Laboratory

and Charles H. McLellan
Langley Aeronautical Laboratory

## INTRODUCTION

There are three major considerations which influence the design of a hypersonic glider. First, there is aerodynamic heating; second, aerodynamic performance; and third, stability and control. The heating and structure problems were discussed in a previous paper by William A. Brooks, Jr., Roger A. Anderson, and Robert T. Swann. Aerodynamic performance will be discussed in this paper; and stability and control are discussed in reference 1. Since aerodynamic heating is one of the most important factors at hypersonic speeds, the attainment of high aerodynamic performance is not always desirable since it can prolong flight times at conditions of high heating rates. This situation exists particularly at speeds in the neighborhood of 20,000 feet per second. At somewhat lower speeds as might be required for ranges of the order of 5,000 nautical miles, however, aerodynamic performance or lift-drag ratio has its usual importance in determining range (ref. 2). Since there seems to be little problem in obtaining low lift-drag ratios at hypersonic speeds, the discussion in this paper will be confined to the achievement of high lift-drag ratios and to the discussion of some recently obtained results. Some previous work on this subject may be found in references 3 to 5.

## RESULTS AND DISCUSSION

In figure 1(a), maximum lift-drag ratios $\left(\frac{L}{D}\right)_{MAX}$ are presented for three simple glider configurations as a function of equivalent Mach number $M_{EQ}$. All three configurations had the same arrow-plan-form wing with $77.4°$ of leading-edge sweep and an aspect ratio of 1.4. Three different fuselage locations were tested. In one case the fuselage was a half-cone mounted entirely beneath the wing in a flat-top arrangement. This model is shown in figure 1(a). With this flat-top arrangment, the wing experiences favorable lift interference from the pressure field of

the fuselage (refs. 3, 5 to 8). In the second case, the fuselage was symmetrically disposed relative to the wing. In this case, the body had a smaller diameter to keep the volume the same as that for the flat-top model. In the third case, the fuselage was a half-cone located entirely above the wing in a flat-bottom arrangement. According to impact theory, this arrangement should be the most efficient at hypersonic speeds. (See refs. 9 to 11.)

All of the results have been corrected to flight conditions with an assumed transition Reynolds number of $3 \times 10^6$ and with base drag included. The base-pressure coefficient was assumed to be $-\frac{1}{M^2}$. The methods employed to correct the skin friction are given in references 12 to 15.

At Mach numbers from 3 to 6, the results were obtained by standard test techniques and are shown by the open symbols. At these speeds, the results support previous findings that the use of favorable lift interference can significantly improve aircraft performance.

At Mach numbers greater than 6 the results were obtained by application of the hypersonic similarity rule and are shown by the solid symbols. This rule is thoroughly treated in references 16 to 18, and in the present tests it was employed as follows: A second set of models were constructed with thickness-to-chord and span-to-chord ratios doubled relative to the original models. These models were also tested at Mach numbers from 3 to 6 and with the aid of relations given by the similarity rule; the data were transformed to give results applicable to the original models at twice the actual test Mach number. Since these data were obtained in this manner, the abscissa of figure 1(a) is labeled equivalent Mach number.

The two sets of results overlap at a Mach number of 6 and show good agreement, and the differences between corresponding points is 2 percent or less. These results show that the differences between the three fuselage arrangements decrease with increasing Mach number and are of the order of a few percent at a Mach number of 12.

Similar trends are shown in figure 1(b) for uncorrected wind-tunnel test results. For Mach numbers M of 6.9 and 9.6, the results were obtained from tests in air at a Reynolds number R of $0.69 \times 10^6$. Those for a Mach number of 13 were obtained from tests in helium at a Reynolds number of $3.1 \times 10^6$. This much higher test Reynolds number accounts for the lift-drag ratios being higher at this Mach number. The upper part of figure 1(b) is for a model with a modified-arrow-plan-form wing and a minimum-drag body of revolution (ref. 19). In this case, a symmetric

model with the same volume distribution was also tested at a Mach number of 6.9. The configuration shown in the bottom part of figure 1(b) had an arrow wing and a conical fuselage of slightly different cone angle than the configuration shown in figure 1(a). The trends shown in figure 1(b) are essentially the same as those shown in figure 1(a). In this case, however, the symmetric model was slightly more efficient than the flat-top model at a Mach number of 6.9. In addition, the differences at the higher Mach numbers are even less than those shown in figure 1(a). In fact, no difference was measured at the higher Mach numbers. The conclusion here is clear. At the higher Mach numbers, the effect of fuselage arrangement is small and the choice for a particular glider will depend on factors other than performance.

None of the models discussed thus far were, of course, directionally stable. One scheme suggested for achieving directional stability is to use deflected wing tips (ref. 3). Some indication of the performance penalty this scheme involves is shown in the bar graph in figure 2. These results are for the models shown in the upper part of figure 1(b) and are at a Mach number of 6.9. In all cases the tips were deflected 45°. The results indicate that deflection of the wing tips always produces a penalty, but for either a flat-top or flat-bottom model the penalty is smaller if the tips are bent downward. For the symmetric model there is no difference.

With these results in mind, the performance of gliders which are stable both longitudinally and directionally will be considered. Since fuselage location has a small effect, first, a flat-top design is considered and then a flat-bottom design is considered. The aerodynamics of both configurations has been studied in some detail, but only a summary of the results will be discussed herein.

The flat-top glider is shown in figure 3(a). The dimensions shown are those estimated for a full-scale vehicle which could, if so desired, be man carrying. The fuselage is formed from a minimum-drag body of revolution. The weight was estimated to be about 22,000 pounds exclusive of fuel with the center of gravity at 76 percent of the root chord.

The wing is of essentially arrow plan form with the tips expanded to provide for controls. The leading-edge sweep is 77.4°; the aspect ratio, approximately 1; and the wing loading is 20 pounds per square foot. The wing and fuselage are blunted because of aerodynamic heating. To provide directional stability, the wing tips have a droop of 45° about a line toed in 3° with respect to the plane of symmetry. To supplement directional stability at Mach numbers less than 6, a retractable ventral fin is provided. Longitudinal and lateral control are obtained from plane trailing-edge flaps at the wing tips. Directional control

at low Mach numbers is provided by a conventional rudder on the ventral fin and at high Mach numbers, by body flaps which can also function as dive brakes.

For this glider, a scale model and a hypersonically similar model with thickness-to-chord and span-to-chord ratios doubled were tested in air at Mach numbers from 3 to 6 in the manner described previously. In addition, the scale model was tested in helium at a Mach number of 12 and the similar model was tested at a Mach number of 9 in order to provide data for a Mach number of 18.

The performance results are summarized in figure 3(b) where trim lift-drag ratios are shown for equivalent flight Mach numbers from 3 to 18. At Mach numbers less than 6, the symbols are flagged to indicate that the ventral fin was extended. Although these results were obtained from four test techniques, the overall variation of lift-drag ratio appears to be consistent. The decrease in lift-drag ratio at lower Mach numbers is associated with the increased contribution of base drag. The decrease at higher Mach numbers is associated in part with the relative increase in skin friction and in part with the increased drag due to lift. In general, the results indicate that lift-drag ratios between about 5 and 6 are obtainable with the flat-top glider.

The flat-bottom glider is shown in figure 4(a). Again the dimensions are those estimated for a full-scale man-carrying vehicle. The weight was also about 22,000 pounds and the center of gravity was estimated to be at 42 percent of the mean aerodynamic chord which was the center of pressure at low subsonic speeds and which was used in reference 20.

The wing has a triangular plan form with $78.2^\circ$ of leading-edge sweep. The nose and leading edge are blunted as indicated. In order to provide a positive trimming moment and thus reduce trim-drag penalties, the forward section of the glider has been cambered upward $6^\circ$. Directional stability is provided by fins located at the wing tips. These fins are toed in $6.8^\circ$ to improve their effectiveness. Longitudinal and lateral control are provided by trailing-edge flaps and directional control is provided by rudders on the tip fins.

The aerodynamic performance at flight conditions for this glider is shown in figure 4(b). The curves shown were obtained theoretically, allowing the altitude and Reynolds number to vary as required to maintain the wing loading. The base-pressure coefficient was assumed to be $-\frac{1}{M^2}$. For the upper set of curves, laminar boundary layer was assumed and the glider was untrimmed and had no directional surfaces. The difference between the dashed and solid curves indicates the magnitude of

boundary-layer displacement effects (refs. 15 and 21) on maximum lift-drag ratio for flight conditions. It is observed that in this case the effect on $\left(\dfrac{L}{D}\right)_{MAX}$ is small. The effects of the boundary-layer displacements are discussed in references 15 and 21. The assumption of a laminar boundary layer is undoubtedly optimistic and for the three lower curves a local transition Reynolds number $R_{l,t}$ of $3 \times 10^6$ was assumed. The middle curves are for the glider without directional surfaces and show the effect of trim. A very small trim penalty results when a cambered nose is used; in fact, the two curves are so nearly coincident that they appear as a single heavy line. Experimentally, no loss in $\left(\dfrac{L}{D}\right)_{MAX}$ was detectable when the nose camber was incorporated. For the bottom curve, the configuration is trimmed and the directional surfaces are included. Achieving directional stability results in a decrement in lift-drag ratio of about 0.5. The tip fins used, however, have not been optimalized from the standpoint of lift-drag ratio.

Experimental results corrected to flight conditions are shown for comparison; the flagged symbols correspond to the lower curve. In general, the agreement is good and provides considerable confidence in the theoretical estimates. Essentially, the same methods have been used in calculating the boundary layer as were used in references 15 and 21 where excellent agreement was found in predicting model skin friction in the tunnel. For the trimmed and directionally stable glider, the lift-drag ratios varied between about 5 and 6. These values are essentially the same as those for the flat-top glider and, in fact, the trends in lift-drag ratio with Mach number are also very similar.


CONCLUDING REMARKS


These results have shown something of the aerodynamic performance obtainable with hypersonic gliders. From the lift-drag ratios obtained in these studies, estimates have been made of the range capabilities of the gliders. The results were essentially the same for both flat-top and flat-bottom configurations. With an initial glide velocity of 12,000 feet per second, the range was estimated to be about 2,200 nautical miles. For an initial velocity of 18,000 feet per second, it was 5,700 nautical miles.

CONFIDENTIAL

# REFERENCES

1. Rainey, Robert W.: Static Stability and Control of Hypersonic Gliders. (Prospective NACA paper.)

2. Eggers, Alfred J., Jr., Allen, H. Julian, and Neice, Stanford E.: A Comparative Analysis of the Performance of Long-Range Hypervelocity Vehicles. NACA TN 4046, 1957. (Supersedes NACA RM A54L10.)

3. Eggers, A. J., Jr., and Syvertson, Clarence A.: Aircraft Configurations Developing High Lift-Drag Ratios at High Supersonic Speeds. NACA RM A55L05, 1956.

4. McLellan, Charles H., and Dunning, Robert W.: Factors Affecting the Maximum Lift-Drag Ratio at High Supersonic Speeds. NACA RM L55L20a, 1956.

5. Syvertson, Clarence A., Wong, Thomas J., and Gloria, Hermilo R.: Additional Experiments With Flat-Top Wing-Body Combinations at High Supersonic Speeds. NACA RM A56I11, 1957.

6. Ferri, Antonio, Clarke, Joseph H., and Casaccio, Anthony: Drag Reduction in Lifting Systems by Advantageous Use of Interference. PIBAL Rep. 272 (Contract AF 18(600)-694), May 1955.

7. Rossow, Vernon J.: A Theoretical Study of the Lifting Efficiency at Supersonic Speeds of Wings Utilizing Indirect Lift Induced by Vertical Surfaces. NACA RM A55L08, 1956.

8. Migotsky, Eugene, and Adams, Gaynor J.: Some Properties of Wing and Half-Body Arrangements at Supersonic Speeds. NACA RM A57E15, 1957.

9. Sänger, Eugen: Raketen-Flugtechnik. R. Oldenbourg (Berlin), 1933, pp. 112, 120-121.

10. Sänger, E., and Bredt, I.: A Rocket Drive for Long Range Bombers. Translation CGD-32, Tech. Information Branch, Bur. Aero., Navy Dept., Aug. 1944, pp. 58-64.

11. Resnikoff, Meyer M.: Optimum Lifting Bodies at High Supersonic Airspeeds. NACA RM A54B15, 1954.

12. Rubesin, M. W., and Johnson, H. A.: A Critical Review of Skin-Friction and Heat-Transfer Solutions of the Laminar Boundary Layer of a Flat Plate. Trans. A.S.M.E., vol. 71, no. 4, May 1949, pp. 383-388.

13. Sommer, Simon C., and Short, Barbara J.:  Free-Flight Measurements of Turbulent-Boundary-Layer Skin Friction in the Presence of Severe Aerodynamic Heating at Mach Numbers From 2.8 to 7.0.  NACA TN 3391, 1955.

14. Lees, Lester, and Probstein, Ronald F.:  Hypersonic Viscous Flow Over a Flat Plate.  Rep. No. 195, Princeton Univ., Aero. Eng. Lab., Apr. 20, 1952.

15. Bertram, Mitchel H.:  Boundary-Layer Displacement Effects in Air at Mach Numbers of 6.8 and 9.6.  NACA TN 4133, 1958.

16. Tsien, Hsue-Shen:  Similarity Laws of Hypersonic Flows.  Jour. Math. and Phys., vol. XXV, no. 3, Oct. 1946, pp. 247-251.

17. Hayes, Wallace D.:  On Hypersonic Similitude.  Quarterly Appl. Math., vol. V, no. 1, Apr. 1947, pp. 105-106.

18. Hamaker, Frank M., Neice, Stanford E., and Wong, Thomas J.:  The Similarity Law for Hypersonic Flow and Requirements for Dynamic Similarity of Related Bodies in Free Flight.  NACA Rep. 1147, 1953. (Supersedes NACA TN 2443 by Hamaker, Neice, and Eggers and NACA TN 2631 by Hamaker and Wong.)

19. Eggers, A. J., Jr., Resnikoff, Meyer M., and Dennis, David H.:  Bodies of Revolution Having Minimum Drag at High Supersonic Airspeeds. NACA Rep. 1306, 1957.  (Supersedes NACA TN 3666.)

20. Moul, Martin T., and Paulson, John W.:  Dynamic Behavior of High-Performance Aircraft.  (Prospective NACA paper.)

21. Bertram, Mitchell H., and Henderson, Arthur, Jr.:  The Effects of Boundary-Layer Displacement and Leading-Edge Blunting on the Pressure Distribution, Skin Friction, and Heat Transfer of Bodies at Hypersonic Speeds.  (Prospective NACA paper.)

FLIGHT $\left(\dfrac{L}{D}\right)_{MAX}$ OBTAINED WITH HYPERSONIC SIMILARITY RULE
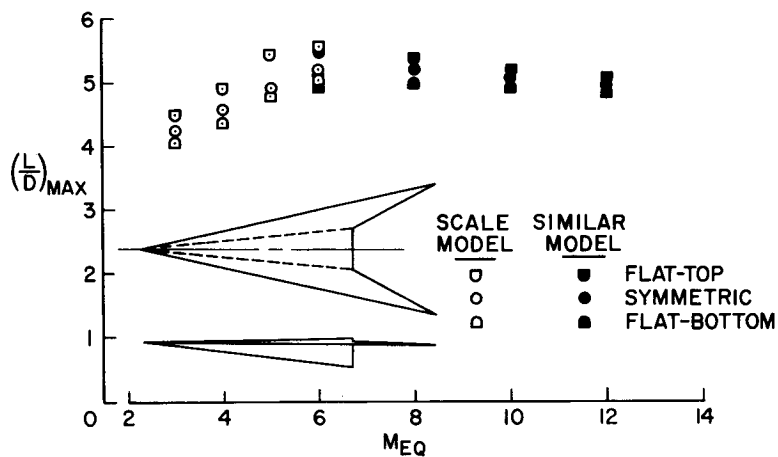


Figure 1(a)

$\left(\dfrac{L}{D}\right)_{MAX}$ OBTAINED IN AIR AND HELIUM AT HIGH MACH NUMBERS
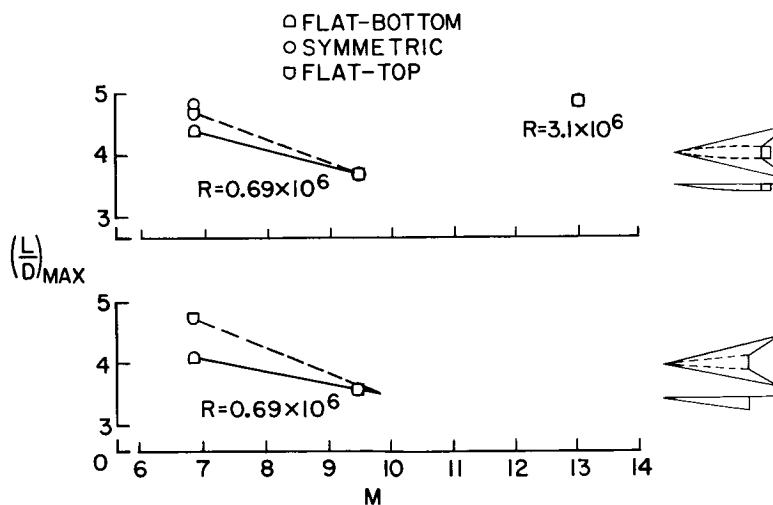


Figure 1(b)

EFFECT OF BODY-WING ORIENTATION AND WING-TIP DROOP
M = 6.9;  R = .69×10$^6$
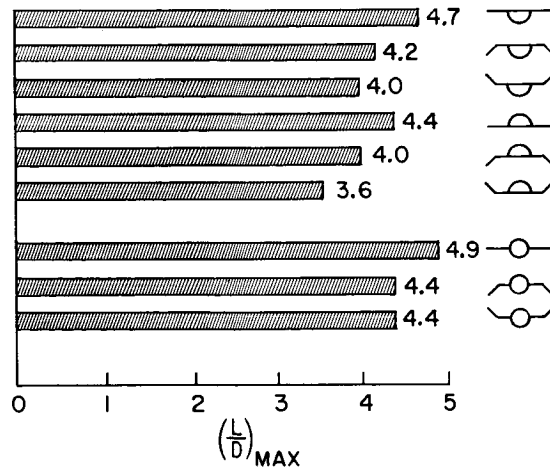


$$\left(\frac{L}{D}\right)_{MAX}$$

Figure 2

FLAT-TOP GLIDER
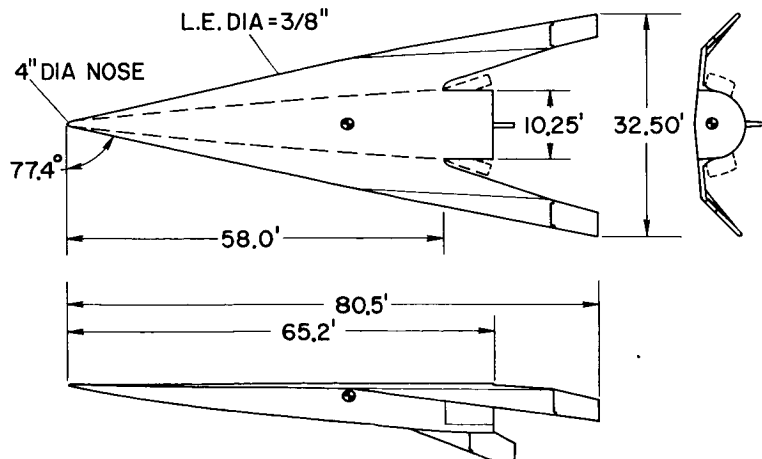


Figure 3(a)

FLIGHT $\left(\dfrac{L}{D}\right)_{MAX}$ FOR FLAT-TOP GLIDER
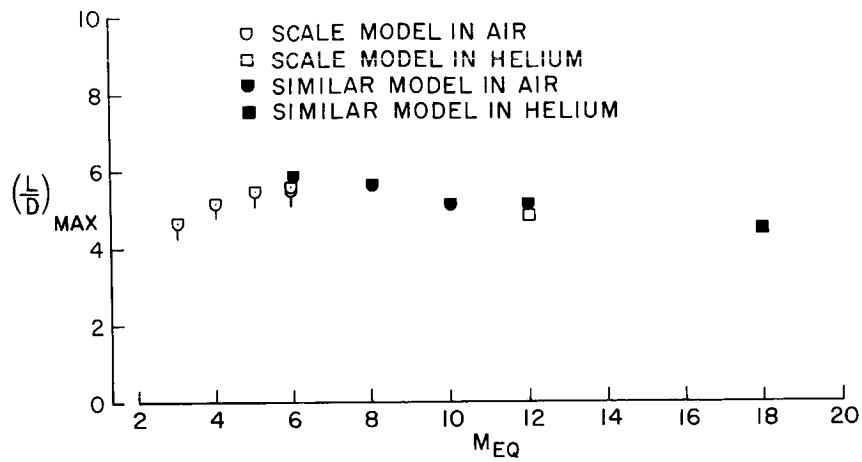


Figure 3(b)

FLAT—BOTTOM GLIDER
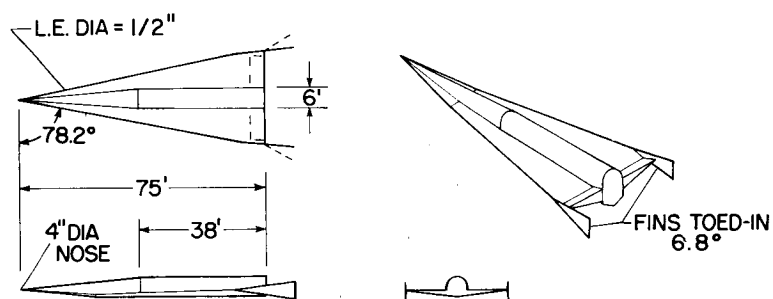


Figure 4(a)

FLIGHT $\left(\frac{L}{D}\right)_{MAX}$ FOR FLAT-BOTTOM GLIDER

B. L. DISPL. EFFECTS
———— WITH
———— WITHOUT
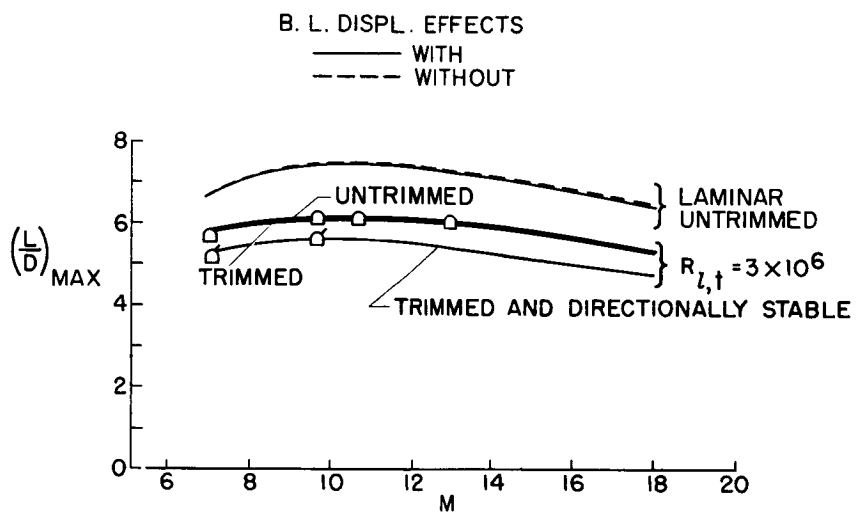


Figure 4(b)

# STATIC STABILITY AND CONTROL OF HYPERSONIC GLIDERS

By Robert W. Rainey

Langley Aeronautical Laboratory

## SUMMARY

A study has been made of the static stability and control problems associated with several hypersonic boost gliders. It appears that, in general, it is possible to obtain the desired trim features. The flat-top configuration was found to be essentially self trimming, whereas for the flat-bottom configuration negative camber provided an effective means to trim. Furthermore, at the low angles of attack, directional stability and control were adequate for the complete configurations investigated; however, there is a need for further study of directional stability in the high angle-of-attack range and of lateral stability at all angles of attack.

## INTRODUCTION

The aerodynamic characteristics of two categories of winged hypersonic boost gliders have been studied. One of these includes moderate range vehicles which operate in the sensible atmosphere at relatively high lift-drag ratios; the other includes vehicles which might be used for manned reentry and do not require high lift-drag ratios. Some lift-drag characteristics of the high lift-drag-ratio vehicles are discussed in reference 1. Some aspects of the static stability and control will be presented herein.

## SYMBOLS

$b$      wing span

$C_D$      drag coefficient, $\dfrac{\text{Drag}}{q_\infty S_W}$

$C_L$      lift coefficient, $\dfrac{\text{Lift}}{q_\infty S_W}$

$C_l$        rolling-moment coefficient, $\dfrac{\text{Rolling moment}}{q_\infty S_W b}$

$C_m$       pitching-moment coefficient, $\dfrac{\text{Pitching moment}}{q_\infty S_W \bar{c}}$

$C_n$       yawing-moment coefficient, $\dfrac{\text{Yawing moment}}{q_\infty S_W b}$

$c$         chord

$\bar{c}$         mean aerodynamic chord

$i$         incidence angle, deg

$L/D$      lift-drag ratio,   $C_L/C_D$

$M$        Mach number

$q$         dynamic pressure

$S$         plan-form area

$\alpha$         angle of attack, deg

$\beta$         angle of sideslip, deg

$\delta$         control deflection angle, deg

Subscripts:

EQ      equivalent

e         elevator

f         flap

N        nose

R        wing root

r         rudder

w          wing (with tips undrooped for flat-top configuration)

∞          free stream

## DISCUSSION

Since a substantial portion of the flight of gliders will be at, or near, trim conditions, it is instructive to consider the approximate range of interest in trim characteristics. (See table I.) In table I, the high-lift-drag-ratio type of glider is envisioned as being the type that operates in the atmosphere at values of trimmed $L/D$ of the order of 5 to obtain ranges of the order of 5,000 nautical miles. The low-lift-drag-ratio type of glider is applicable to global missions or possibly orbital reentry missions. Trimmed angles of attack greater than $45^{\circ}$, as indicated in table I, would undoubtedly be necessary to obtain values of trimmed $L/D$ of the order of one-half for the winged vehicles considered.

### High-Lift-Drag-Ratio Type of Gliders

Firstly, a flat-top configuration will be considered (fig. 1). Longitudinal and lateral control is obtained by use of wing-tip flaps. Directional control at subsonic and supersonic speeds is obtained by use of the rudder on the ventral fin. At hypersonic speeds $(M > 6)$, body flaps provide the directional control and may serve as speed brakes at all speeds. Studies of the static stability and control characteristics have been made by Thomas J. Wong of the Ames 10- by 14-Inch Supersonic Wind Tunnel Branch.

The longitudinal stability and control characteristics at trim for this flat-top configuration are presented in figure 2. The open symbols are for results obtained by use of scale models at the Mach numbers indicated. The flagged symbols indicate that the ventral fin was extended. Solid symbols designate results obtained with hypersonically similar models at the equivalent free-stream Mach number as obtained from the hypersonic similarity law. (See ref. 1.) At supersonic speeds, the variation in pitching moment with lift coefficient was reasonably linear and $C_{m_{C_L}}$ was essentially invariant with Mach number. The usual destabilizing shift at subsonic speeds is about 0.05 and the glider is neutrally stable. At subsonic speeds in the high-lift range, however, a pitch-up tendency was found. Elevator deflection required for trim is shown on the lower part of figure 2. The deflections required are small; thus the glider is essentially self-trimming.

Directional stability is shown in figure 3 as a function of equivalent Mach number for two angles of attack, $3^\circ$ and $7^\circ$. It is clear that the glider maintains directional stability throughout the ranges of Mach number and angle of attack shown, although at lower Mach numbers this stability is achieved with the aid of the ventral fin. At Mach numbers around 3, there is some loss in stability with increasing angle of attack.

Lateral stability is shown in figure 4. Here it is observed that $C_{l_\beta}$ is sometimes positive; that is, the effective dihedral is negative, particularly at the higher Mach numbers and lower angles of attack. Some roll instability is, therefore, indicated. Automatic roll stabilization for the glider has been studied, but the situation is complicated by the fact that the roll controls are located on the drooped wing tips. Thus, aileron deflection produces yawing as well as rolling moments. A satisfactory roll-stabilization scheme was found only after both the ailerons and body-flap controls were employed in combination.

Secondly, a flat-bottom configuration is considered (fig. 5) which has negative camber to provide trim, trailing-edge flaps for longitudinal and lateral control, and rudders on the toed-in wing-tip fins for directional control.

Calculations of the longitudinal stability characteristics of the basic body-wing combination without negative camber have been made at free-stream Mach numbers from 6.9 to 18. The configuration is shown in figure 6 along with the flow fields assumed in the theoretical analysis. It was assumed that the half-cone and cylinder of the body operated in the local flow of the upper wing surface throughout the ranges of $\alpha$ and M. The interference region is shown shaded and bounded by the inviscid shock wave generated by the nose cone and the average expansion from the cone-cylinder juncture. Constant pressure was assumed in the region between the two average expansions as well as between the wing leading edge and nose-cone shock waves. Two-dimensional analysis was applied to the lower wing surface. Finally, through the use of experimental results, the induced effects and effects of leading-edge shock detachment were included. This was accomplished by first plotting the ratio of measured $C_L$ to calculated $C_L$ (using two-dimensional shock-expansion theory) as a function of the hypersonic similarity parameter $M_\alpha$ (where $M_\alpha = M$ times $\alpha$ in radians) for the wings of reference 2. This ratio of measured $C_L$ to calculated $C_L$ was plotted for each wing, and each curve was designated as having a specific value of $M_\epsilon$ (where $M_\epsilon = M$ times $\epsilon$ in radians, and $\epsilon$ is the wing half-apex angle). Then, by use of the hypersonic similarity relations, $M_\alpha$ and $M_\epsilon$, the appropriate $C_L$ ratios were obtained and multiplied times the calculated values for

$C_L$ of the vehicle at the four Mach numbers and various angles of attack. Application of this $C_L$ ratio was also made to the pitching moments.

In figure 7 it is indicated that the calculations predicted $C_m$ very well and overestimated $C_L$ somewhat. The Mach number effects upon $C_m$ are small and $C_L$ is reduced somewhat as the Mach number is increased. It is also noted that in the desired range of trim $C_L$ (around 0.08), there is a sizeable pitching moment to be trimmed out.

The use of several devices considered for trim and control are shown in figure 8. The trailing-edge flaps may be considered for longitudinal and lateral control; in this instance some means must be provided for directional stability and control. The three wing-tip-mounted controls may be considered for longitudinal, lateral, and directional stability and control.

In figures 9 and 10 are presented the characteristics of the configuration with these controls at deflection angles of $0^\circ$ and $-20^\circ$ at $M = 6.9$. These results demonstrate the inability of these controls to produce trim in the desired lift-coefficient range of about 0.08. The highest values of trim $C_L$ were obtained with the trailing-edge flap, and this was only about 0.045.

Obviously a better method for trim is required, and the use of negative camber appears adequate as shown in figure 11. The measured and calculated results of the same configuration untrimmed and trimmed by the use of negative camber are presented. By this means a trim lift coefficient of about 0.09 and a trim angle of attack of about $9^\circ$ were obtained and may be accurately predicted. A loss in stability was realized by trimming; however, the configuration is longitudinally stable at trim. Similar results were obtained at $M = 9.6$.

In figure 12 are presented the measured and predicted $C_{n_\beta}$ characteristics of the configuration without and with two types of tip controls. For these predictions, the assumptions for the flow field were similar to those for the longitudinal calculations. It is seen that the configuration without controls is directionally unstable. The directional stability parameter $C_{n_\beta}$ with either control is about the same at $M = 6.9$ and essentially invariant with Mach number. The predictions of $C_{n_\beta}$ are conservative. Additional results at $M = 6.9$ indicated that the use of negative camber had little effect upon $C_{n_\beta}$. Also, the control effectiveness parameter $C_{n_{\delta_r}}$ appeared to be adequate and was predicted with reasonable accuracy by using conical-flow theory for the tip cones and oblique-shock relations for the tip fins at $M = 6.9$. Some additional results of

wind-tunnel tests at $M = 6.9$ indicate that $C_{n_\beta}$ increases with $\alpha$ in the $\alpha$ range from $0^\circ$ to $16^\circ$ and that the configuration had positive dihedral effect at $\alpha$ greater than $5^\circ$.

## Low-Lift-Drag-Ratio Type of Gliders

Consider now the low-lift-drag-ratio type of vehicles which may operate in the atmosphere or might also be considered as orbital reentry vehicles. As indicated in table I, it appears desirable for these vehicles to trim at angles of attack from $20^\circ$ to $45^\circ$, or greater, at lift coefficients of from about 0.3 to 0.8.

In figure 13 are presented two configurations which are of the low-lift-drag-ratio type. For the vehicle on the left, trim is accomplished by the use of trailing-edge flaps; the combined use of deflected nose and flaps accomplishes trim for the vehicle on the right. In both instances, the flaps in the upper and lower surfaces deflect in the same direction. Cavities (shown as darkened regions on the rear of the vehicles) provide a means to deflect the flaps within the vehicles. Both vehicles were directionally stable at $\alpha = 0^\circ$ (no results for $\alpha > 0^\circ$). Directional control was accomplished by deflecting the rearward portion of the leading edges (shown by dashed lines in the plan views in fig. 13).

The experimental results in figure 14 indicate for this vehicle a trim capability at $C_L$ of about 0.2 at an angle of attack of about $15^\circ$ with the flaps deflected $-20^\circ$. For the other vehicle (fig. 15), a trim $C_L$ of about 0.45 and a trim $\alpha$ of about $30^\circ$ was obtained with $i_N = 20^\circ$ and $\delta_f = -10^\circ$. Extrapolation of additional measured results (with $i_N = 20^\circ$ and $\delta_f = -20^\circ$) show a trim capability at a $C_L$ greater than 0.7 and an $\alpha$ in excess of $45^\circ$. For both vehicles, optimization of the combination of nose and flaps would undoubtedly increase the attainable trim $C_L$ and $\alpha$.

## CONCLUDING REMARKS

It appears that, in general, it is possible to obtain the desired trim features. The flat-top configuration was found to be self-trimming, whereas for the flat-bottom configuration negative camber provided an effective means to trim. Furthermore, at the low angles of attack, directional stability and control are adequate for the complete configurations investigated; however, there is a need for further study of directional stability in the high angle-of-attack range and of lateral stability at all angles of attack.

REFERENCES

1. Syvertson, C. A., and McLellan, Charles H.: Aerodynamic Performance of Hypersonic Gliders. (Prospective NACA paper.)

2. Bertram, Mitchel H., and McCauley, William D.: An Investigation of the Aerodynamic Characteristics of Thin Delta Wings With a Symmetrical Double-Wedge Section at a Mach Number of 6.9. NACA RM L55B14, 1955.

TABLE I

DESIRED CHARACTERISTICS AT TRIM

| PARAMETER | TYPE OF BOOST GLIDER | |
|---|---|---|
| | HIGH $\frac{L}{D}$ | LOW $\frac{L}{D}$ |
| $\frac{L}{D}$ | 4 TO 6 | .5 TO 2 |
| $\alpha$, DEG | 6 TO 9 | 20 TO 45 |
| $c_L$ | 0.06 TO 0.09 | $\approx$ 0.3 TO 0.8 |
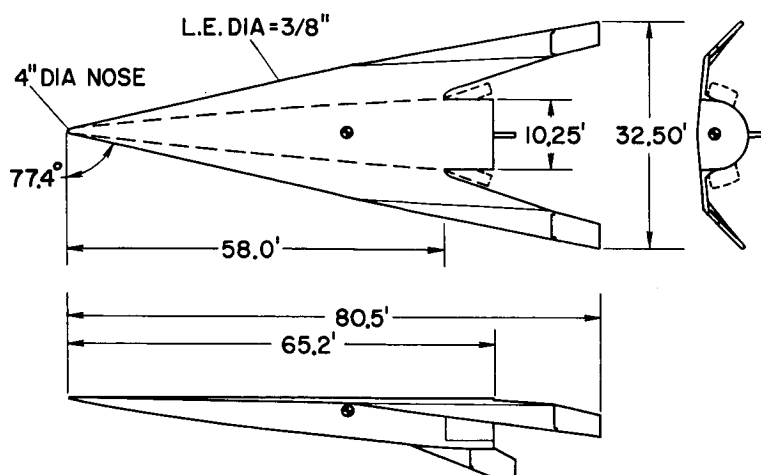
## FLAT-TOP GLIDER

L.E. DIA = 3/8"

4" DIA NOSE

77.4°

58.0'

10.25'

32.50'

80.5'

65.2'

Figure 1

## LONGITUDINAL STABILITY AND CONTROL

C G AT 0.76 $c_R$

$\left(\dfrac{dC_m}{dC_L}\right)_{TRIM}$

-.10

-.05

0

$\delta_{e_{TRIM}}$

4°

0

-4°

0   2   4   6   8   10   12   14   16

$M_{EQ}$

Figure 2

## DIRECTIONAL STABILITY



Figure 3

## LATERAL STABILITY
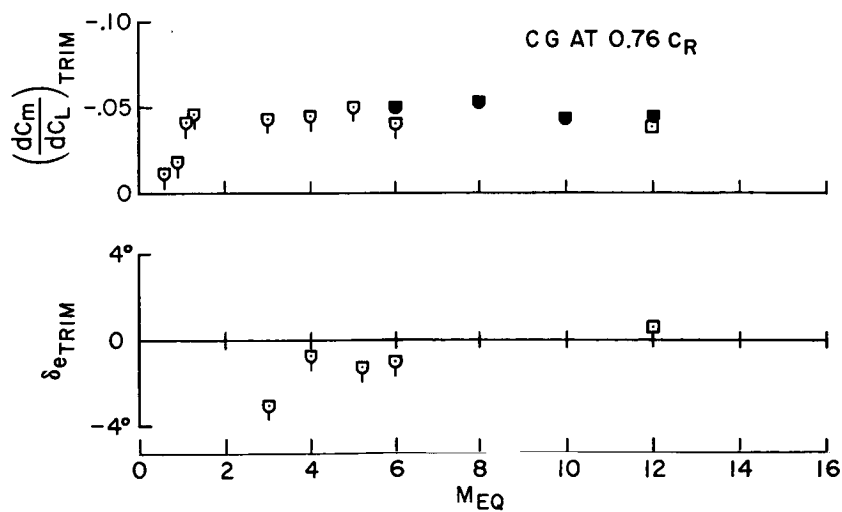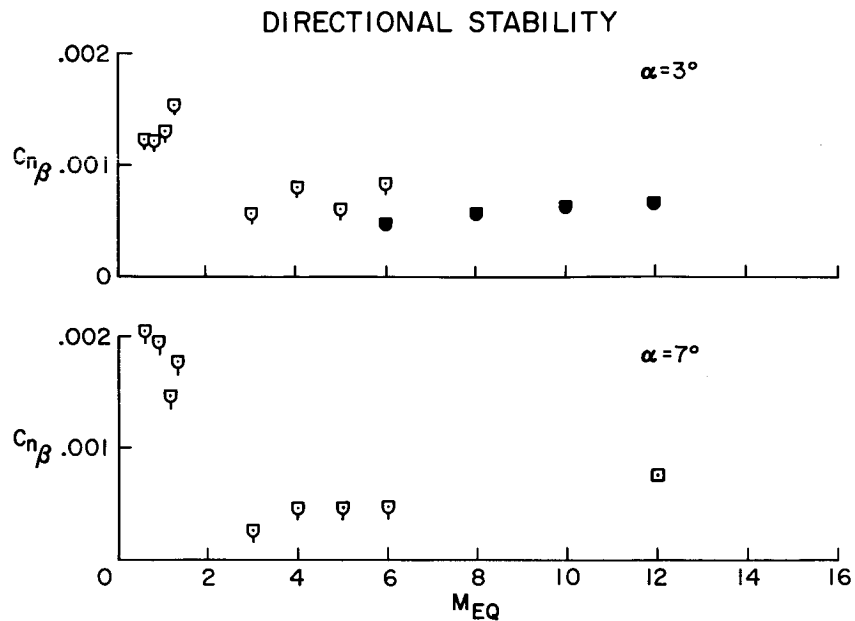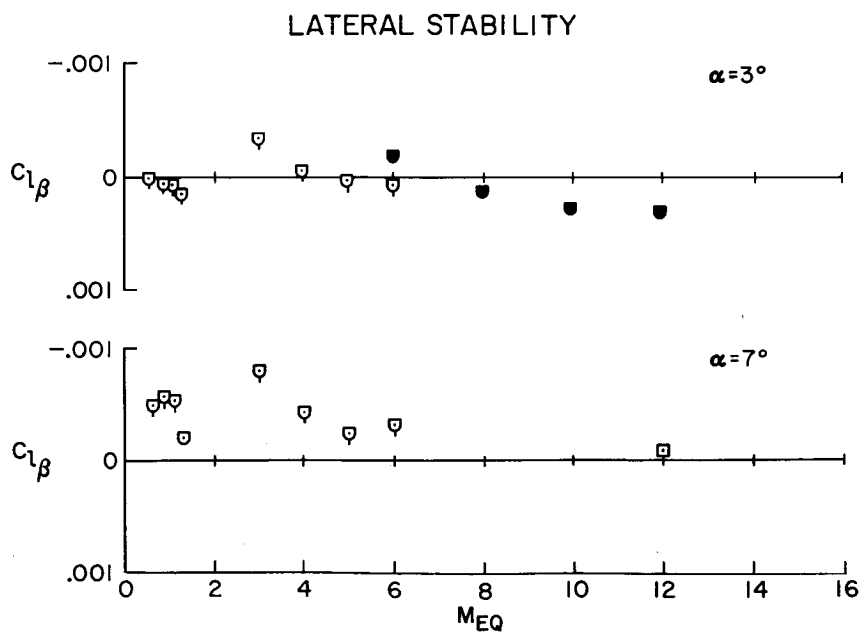


Figure 4

## FLAT-BOTTOM GLIDER
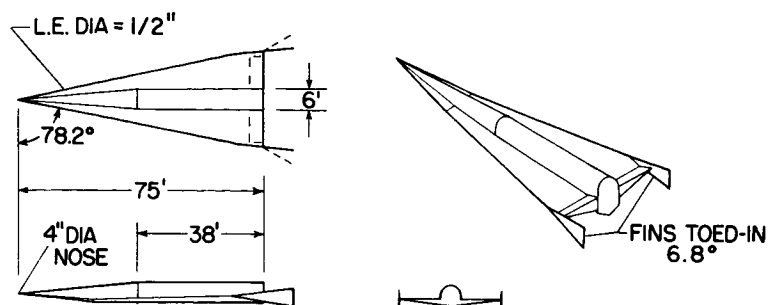


Figure 5

## FLOW FIELDS ASSUMED IN THEORETICAL ANALYSIS
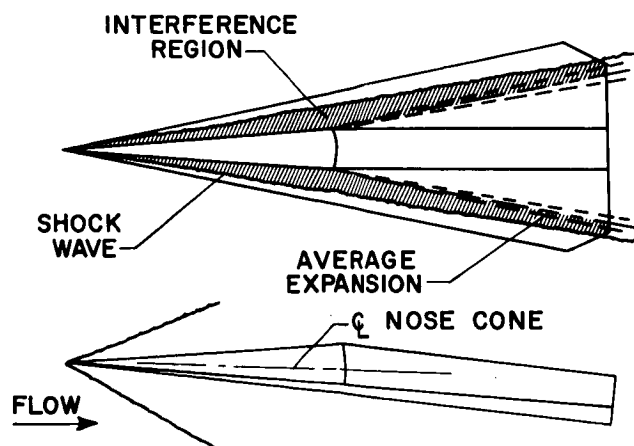


Figure 6

COMPARISON OF CALCULATED AND MEASURED
LONGITUDINAL AERODYNAMIC CHARACTERISTICS

c.g. AT 0.42 $\bar{c}$

| MEAS. | CALC. | $M_\infty$ |
|---|---|---|
| ○ | ——— | 6.9 |
| □ | — — — | 9.6 |
| | - - - - | 15.0 |
| | —·—·— | 18.0 |
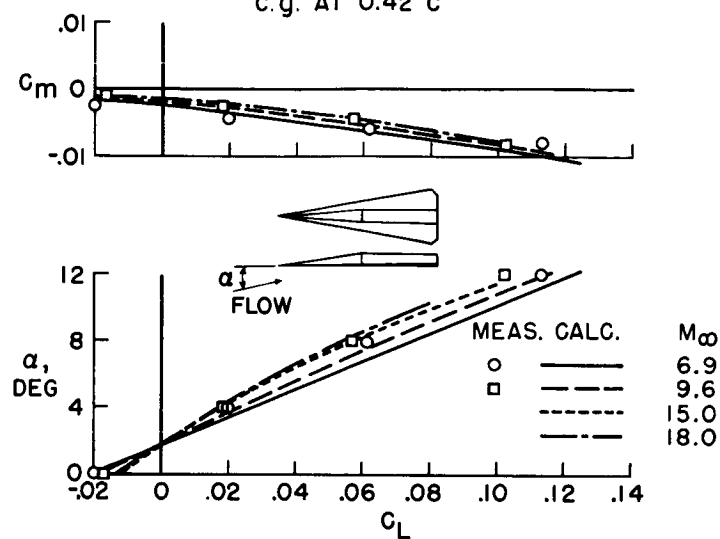
Figure 7

STABILIZING AND CONTROL DEVICES
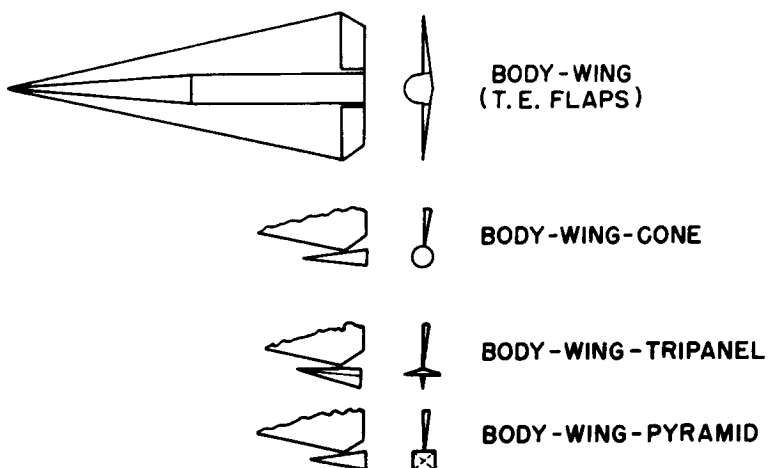
BODY-WING
(T.E. FLAPS)

BODY-WING-CONE

BODY-WING-TRIPANEL

BODY-WING-PYRAMID

Figure 8

EFFECT OF CONTROL ON LONGITUDINAL
AERODYNAMIC CHARACTERISTICS
$M_\infty = 6.9$; c.g. AT 0.42 $\bar{c}$
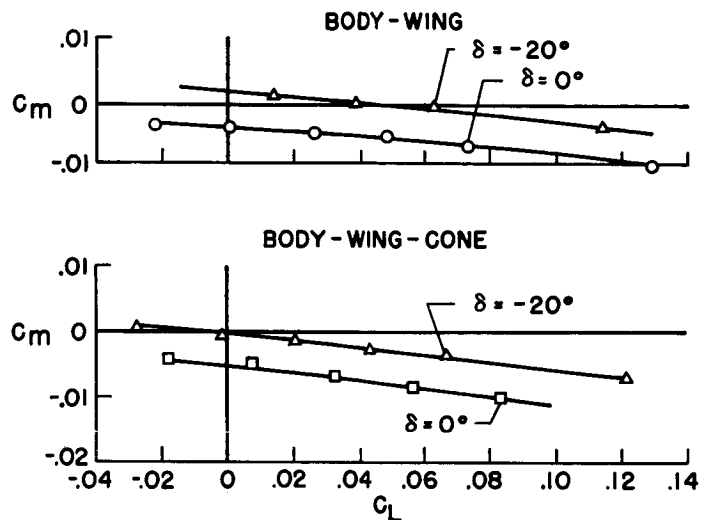
Figure 9

EFFECT OF CONTROL ON LONGITUDINAL
AERODYNAMIC CHARACTERISTICS
$M_\infty = 6.9$; c.g. AT 0.42 $\bar{c}$
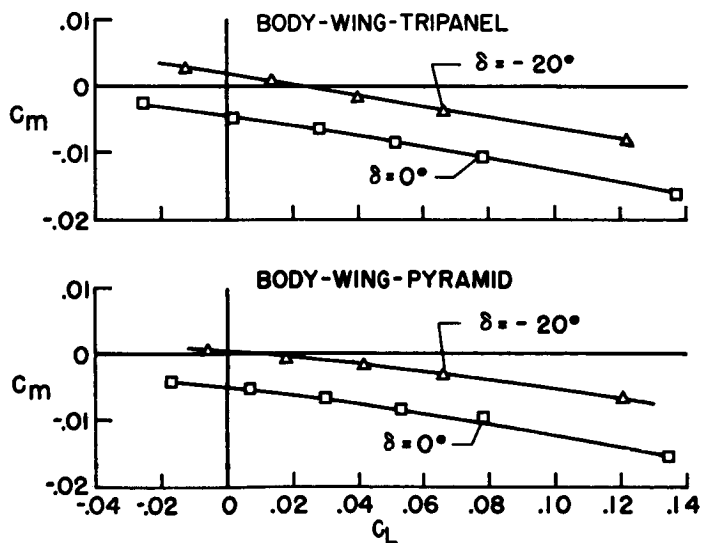
Figure 10

## EFFECT OF NOSE AND FLAP INCIDENCES UPON LONGITUDINAL AERODYNAMIC CHARACTERISTICS

$M_\infty = 6.9$; c.g. AT 0.42 $\bar{c}$

$S_N/S_W = 0.11$

$S_f/S_W = 0.08$

| MEAS. | CALC. | $i_N$, DEG | $\delta$, DEG |
|-------|-------|-----------|---------------|
| ○ | —— | 0 | 0 |
| □ | — — | 5.9 | -5.5 |
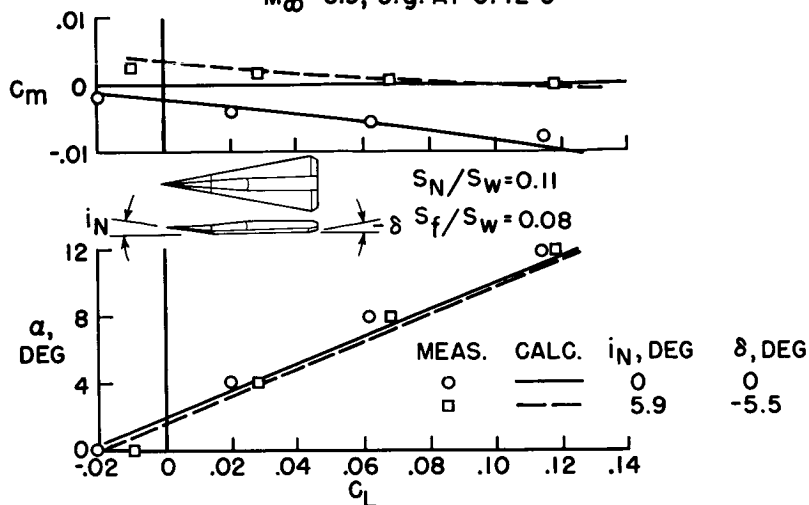
Figure 11

## EFFECT OF TIP CONTROLS ON DIRECTIONAL STABILITY AT $\alpha = 0°$
### c.g. AT 0.42 $\bar{c}$

FINS TOED-IN 6.8°
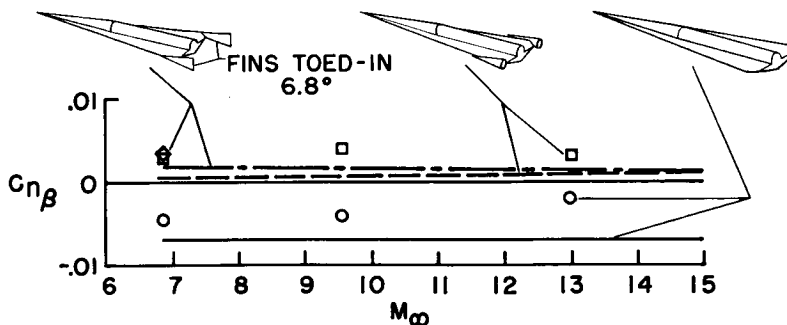
Figure 12

HYPERSONIC BOOST GLIDER
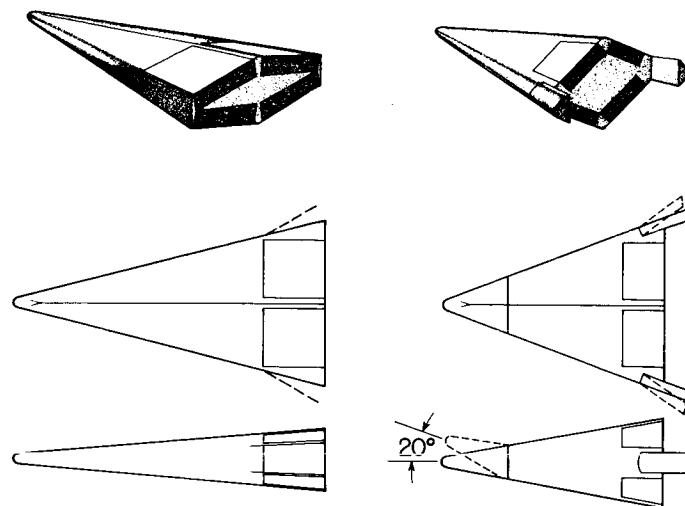


Figure 13

LONGITUDINAL AERODYNAMIC CHARACTERISTICS
OF BOOST-GLIDER WITH LOW LIFT-DRAG RATIO
$M_\infty = 6.9$; c.g. AT $0.40\,\bar{c}$
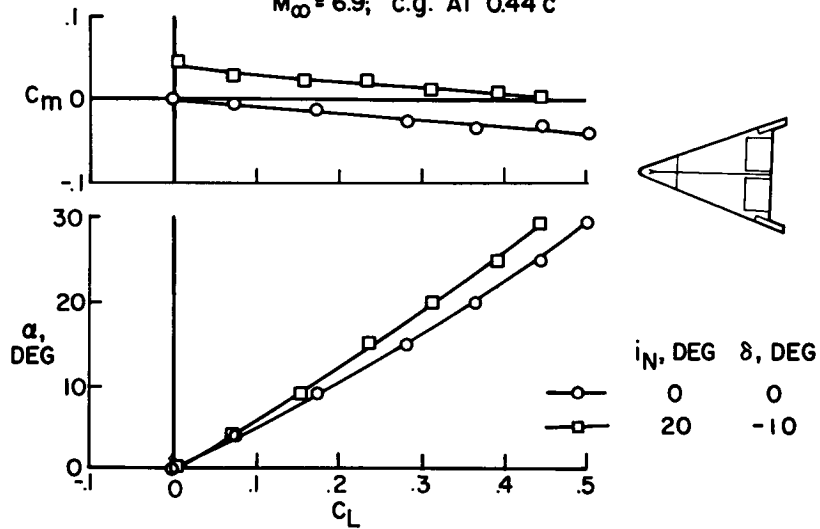


Figure 14

Figure 15

# DYNAMIC LATERAL BEHAVIOR OF HIGH-PERFORMANCE AIRCRAFT

## By Martin T. Moul and John W. Paulson

## Langley Aeronautical Laboratory

## SUMMARY

Several proposed high-performance aircraft have been studied analytically and by model flight tests to define some problem areas in dynamic lateral behavior of high-speed aircraft which require specific attention. In particular, aileron control problems and Dutch roll characteristics with and without artificial damping were considered. The results indicate that effective dihedral and cross-control derivatives can have gross effects on the lateral stability and controllability of hypersonic gliders.

## INTRODUCTION

Hypersonic gliders have been proposed which would extend regions of manned flight to speeds of 20,000 feet per second and altitudes above 200,000 feet. These airplanes, although they would fly to much higher altitudes than current aircraft, experience dynamic motions and control responses similar to those of current aircraft. This is so because the dynamic pressures encountered throughout the flight regime are appreciable; thus, significant aerodynamic forces and moments and airplane natural frequencies comparable to those of today's aircraft are obtained. As a result, dynamic stability and response characteristics remain important. In this paper several possible problem areas related to the lateral behavior of high-performance aircraft are examined.

## SYMBOLS

$b$             wing span

$S$             wing area

$M$           Mach number

$q$      dynamic pressure

$h$      altitude, ft

$k_1$      autopilot gain, $\delta_r/\beta$

$k_2$      autopilot gain, $\delta_r/\delta_a$

$k_3$      autopilot gain, $\delta_a/\dot{\phi}$

$I_x$      moment of inertia about x-axis, slug-ft$^2$

$I_z$      moment of inertia about z-axis, slug-ft$^2$

$t_{1/2}$      time to damp to 1/2 amplitude, sec

$$C_l = \frac{\text{Rolling moment}}{qSb}$$

$$C_n = \frac{\text{Yawing moment}}{qSb}$$

$\alpha$      angle of attack

$\beta$      angle of sideslip

$\dot{\phi}$      rolling velocity

$\delta_a$      aileron deflection

$\delta_r$      rudder deflection

$C_{n_\beta} = \partial C_n/\partial\beta$

$C_{l_\beta} = \partial C_l/\partial\beta$

$C_{n_{\delta_a}} = \partial C_n/\partial\delta_a$

$C_{l_{\delta_a}} = \partial C_l/\partial\delta_a$

$$C_{n_{\delta_r}} = \partial C_n / \partial \delta_r$$

$$C_{l_{\delta_r}} = \partial C_l / \partial \delta_r$$

## DISCUSSION

Several stability and controllability problems related to lateral behavior of high-speed aircraft, such as effects of static lateral derivatives $C_{n_\beta}$ and $C_{l_\beta}$ on Dutch roll stability, aileron divergence criteria, and effects of $C_{l_\beta}$ and cross-control derivatives on damper design, are considered.

In reference to the Dutch roll stability the following expression defines a parameter which is generally a primary factor in determining the undamped natural frequency of the Dutch roll mode. Negative values of this parameter

$$C_{n_\beta,\text{DYN}} = C_{n_\beta} - \frac{I_z}{I_x} \alpha C_{l_\beta} \qquad (1)$$

may lead to a divergence. Although the exact expression for the Dutch roll spring constant includes rotary derivative effects, this approximation which depends only on the static lateral derivatives $C_{n_\beta}$ and $C_{l_\beta}$ is adequate for most cases. For flight conditions in which rotary derivatives are large, these effects must be considered.

The contributing factors in $C_{n_\beta,\text{DYN}}$ are now considered. In addition to the directional stability, there is a contribution of effective dihedral which is proportional to the inertia ratio $I_z/I_x$ and angle of attack. For long, slender, high-speed aircraft, inertia ratios $I_z/I_x$ of 10 or more are common. Thus the term involving $C_{l_\beta}$ can have a predominant effect even at moderate angles of attack. For example, if the aircraft has negative effective dihedral, this term can overcome directional stability and lead to a divergence. In an effort to obtain positive directional stability at high Mach numbers and angles of attack, designers are considering configurations, for example, ventral fins, which may lead to negative effective dihedral. Thus, although $C_{n_\beta}$ is

improved, $C_{n_\beta,DYN}$ may be decreased, and a marginally stable or unstable airplane will result.

Now consider the other condition of positive effective dihedral. With positive effective dihedral this term can compensate for negative directional stability and produce a stable airplane. An illustration of this favorable effect of positive effective dihedral and the importance of $C_{n_\beta,DYN}$ will now be presented.

Figure 1 shows plots of $C_{n_\beta}$ and $C_{n_\beta,DYN}$ for a canard configuration discussed in reference 1. These parameters are plotted against angle of attack.

For this particular configuration having twin inboard vertical tails, $C_{n_\beta}$ decreased with increasing angle of attack and reached large negative values in the high-angle-of-attack range, where negative values of $C_{n_\beta}$ are normally associated with a directional divergence. The loss of $C_{n_\beta}$ is attributed to an effective change in the angle of sideslip of the vertical tail associated with the vortex flow from the canard surfaces. However, the $C_{n_\beta,DYN}$ criterion indicates the airplane to be stable up to an angle of attack of $34^\circ$.

A model of this configuration was tested in the Langley full-scale tunnel by the free-flying-model technique at angles of attack of $28^\circ$ to $35^\circ$. The model flew smoothly and was easy to control, but at the higher angles of attack where $C_{n_\beta,DYN}$ goes to zero, the pilot observed that the model was becoming difficult to control as expected.

The following expressions are criteria that should be satisfied when using rudder and aileron controls to maintain zero bank angle:

For the aileron alone:

$$C_{n_\beta} - C_{l_\beta} \frac{C_{n_{\delta_a}}}{C_{l_{\delta_a}}} > 0 \tag{2}$$

For the aileron plus rudder proportional to sideslip $\left(\delta_r = k_1\beta\right)$:

$$C_{n_\beta} - C_{l_\beta} \frac{C_{n_{\delta_a}}}{C_{l_{\delta_a}}} + k_1\left(\frac{C_{n_{\delta_a}}}{C_{l_{\delta_a}}} C_{l_{\delta_r}} - C_{n_{\delta_r}}\right) > 0 \tag{3}$$

For the aileron plus rudder proportional to aileron $\left(\delta_r = k_2\delta_a\right)$:

$$C_{n_\beta} + C_{l_\beta}\left(\frac{C_{n_{\delta_a}} + k_2 C_{n_{\delta_r}}}{C_{l_{\delta_a}} + k_2 C_{l_{\delta_r}}}\right) \qquad (4)$$

The first expression (eq. (2)) is a divergence criterion when aileron alone is used. This expression must be positive to avoid a lateral divergence. Divergence can result for combinations of (1) positive effective dihedral $\left(-C_{l_\beta}\right)$ and adverse yaw, since $C_{n_{\delta_a}}/C_{l_{\delta_a}}$ would be negative, and (2) negative effective dihedral and favorable yaw with $C_{n_{\delta_a}}/C_{l_{\delta_a}}$ being positive. The importance of this criterion has been demonstrated in flight tests of airplanes having positive effective dihedral and adverse aileron yaw.

Some unconventional controls proposed for preliminary hypersonic configurations have actually produced cross-control derivatives of the same order of magnitude as the basic control derivatives and results have been obtained recently at low speeds with free-flying models of such configurations. Figure 2 shows the ratio of aileron effectiveness parameters (yawing moment to rolling moment) of three hypersonic glider configurations (a flat-top, a flat-bottom, and an all-wing configuration) plotted against angle of attack. Positive direction corresponds to favorable aileron yaw.

Notice that the flat-top and all-wing configurations have aileron yawing moments twice as large as the rolling moments, whereas the flat-bottom configuration has relatively small aileron yaw. All three configurations have positive effective dihedral and in terms of the aileron-alone divergence criterion, the all-wing configuration with large adverse yaw is predicted to be divergent.

Models of these three configurations were flown at angles of attack of $10^o$ to $20^o$ using aileron control only. The flat-bottom model flew smoothly and was easy to control. The flat-top model experienced considerable yawing motion because of the low level of $C_{n_\beta,DYN}$ and the large aileron yaw. The all-wing model was rapidly divergent, as expected, and could not be controlled. After this test, the rudder of the all-wing model was linked to the aileron to reduce the aileron yaw effectively and the model became controllable. In general, when both rudder and aileron are used for control, the two cross-control derivatives, yaw due to aileron and roll due to rudder, are important in determining the divergence characteristics. Two automatic-control schemes for introducing deflections to alleviate this divergence condition have been examined.

The divergence criterion (eq. (3)) when the rudder is used proportional to sideslip angle in order to reduce sideslip has been given. The first part of this equation is identical to that of equation (2) and the second part is a function of the aileron and rudder effectiveness derivatives. For .configurations which would be divergent with aileron-alone control, the possibility exists for stabilizing the system by the effect of the second term. Of course, the second term can be destabilizing too for values of cross-control derivatives having like algebraic signs and exceeding the primary derivatives $C_{l_{\delta_a}}$ and $C_{n_{\delta_r}}$.

The divergence criterion when the rudder is deflected proportional to the aileron in order to counter aileron yaw is given in equation (4). The aileron-alone criterion (eq. (2)) is modified by a $k_2 C_{n_{\delta_r}}$ term in the numerator and a $k_2 C_{l_{\delta_r}}$ term in the denominator. If $k_2$ is set equal to $-\dfrac{C_{n_{\delta_a}}}{C_{n_{\delta_r}}}$, this destabilizing term becomes zero. Thus, feedbacks in the form of rudder deflections proportional to sideslip angle and aileron deflection may be effective in alleviating divergence conditions.

These cross-control derivatives can also have an important effect on damper design. Both yaw and roll dampers may be required to provide satisfactory lateral characteristics at high altitudes. Next, a stability problem arising from the use of dampers with a hypersonic glider configuration is considered.

Figure 3 shows the effects of large variations of the cross-control derivatives on Dutch roll damping for a flat-bottom hypersonic glider configuration for a flight condition of $M = 6.86$ and an altitude of 130,000 feet. The ratio of $C_{n_{\delta_a}}$ to $C_{l_{\delta_a}}$ is plotted as the ordinate. The ratio $C_{l_{\delta_r}}/C_{n_{\delta_r}}$ is plotted as the abscissa. Curves of constant time to damp to 1/2 amplitude of 1, 2, and 5 seconds, and infinity are shown. This figure indicates the variations in the Dutch roll damping for combinations of cross-control derivatives up to ±2 after roll and yaw damper gains were selected to provide a Dutch roll damping just under 2 seconds. Generally large changes in damping can result from variation in these parameters. In particular for the range of cross-control derivatives shown for this airplane, large losses in Dutch roll damping can result for favorable aileron yaw and negative rolling moment due to rudder deflection (first quadrant). In fact, for some combinations of the ratios (1:1, for example) the damping is actually reduced to zero. This is by no means a general result. Other airplanes might experience damping losses for different combinations of these parameters.

In recent designs of damper systems, such problems have already arisen and in one case, for example, the problem was solved by feeding a yaw-rate signal into the roll channel to offset the rolling moment due to the rudder. Also interconnections between rudder and aileron have been used to alleviate the effect of large cross-control derivatives. Since airplanes are being designed to fly through a wider range of flight conditions, it is becoming increasingly difficult to avoid large values of cross-control derivatives, and this problem may become more critical.

In addition to the cross-control derivatives, dihedral effect $C_{l_\beta}$ may also have an important effect on damper design. The effect of positive and negative effective dihedral on Dutch roll frequency has been discussed, and in figure 4 the results of a study to investigate damper-gain requirements for values of $C_{l_\beta}$ of 0.027 and -0.027, are presented. Damping as $\frac{1}{t_{1/2}}$ is shown for the two lateral modes of primary concern, the Dutch roll oscillation and the damping-in-roll mode, as a function of roll-damper gain $k_3$ for a flight condition of $M = 6.86$ and an altitude of 130,000 feet. The cross-control derivatives were considered to be zero. The solid lines on the figure correspond to the case of $C_{l_\beta} = 0.027$ or negative effective dihedral. A yaw-damper gain was selected for which the Dutch roll oscillation would damp to 1/2 amplitude in 2.5 seconds, based on a one degree of freedom in yaw response. With this yaw damper and zero $k_3$, no roll damper, the damping-in-roll mode is unstable and indicated a rapid roll divergence. The Dutch roll oscillation has good damping at this point. As $k_3$ is increased, the damping-in-roll mode is made stable but the damping of the Dutch roll oscillation decreases markedly.

For the case of $C_{l_\beta} = -0.027$, positive effective dihedral, two important differences should be noted. First, the damping-in-roll mode is stable even for $k_1 = 0$, and, secondly, as $k_1$ is increased, the Dutch-roll damping is higher. A comparison of both sets of curves clearly indicates the importance of $C_{l_\beta}$ in determining roll- and yaw-damper gains and the poor damping which may result with negative effective dihedral.

## CONCLUSIONS

In conclusion, some studies of high-performance aircraft have indicated that:

1. For recently proposed high-performance aircraft having high inertia ratio $I_Z/I_X$, the effective dihedral parameter $C_{l_\beta}$ assumes greater importance in affecting the lateral stability characteristics of the airplane. In particular, negative effective dihedral may lead to a divergence.

2. Attention must be given to the cross-control derivatives of hypersonic aircraft in avoiding divergence conditions and adverse effects of dampers.

## REFERENCE

1. Baals, Donald D., Toll, Thomas A., and Morris, Owen G.: Airplane Configurations for Cruise at a Mach Number of 3. (Prospective NACA paper.)

## DIRECTIONAL STABILITY PARAMETERS OF
## CANARD CONFIGURATION
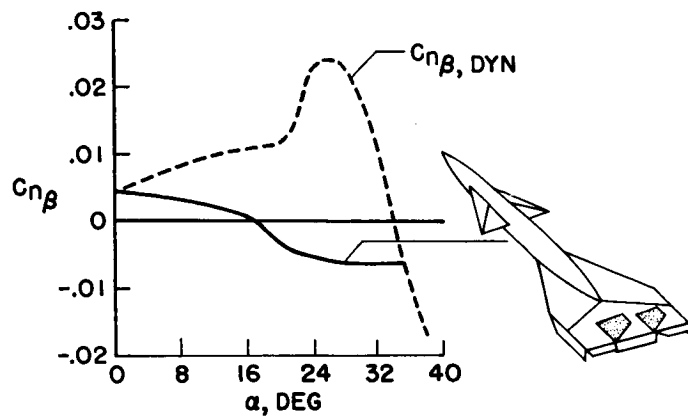


Figure 1

## LOW - SUBSONIC - SPEED LATERAL CONTROL
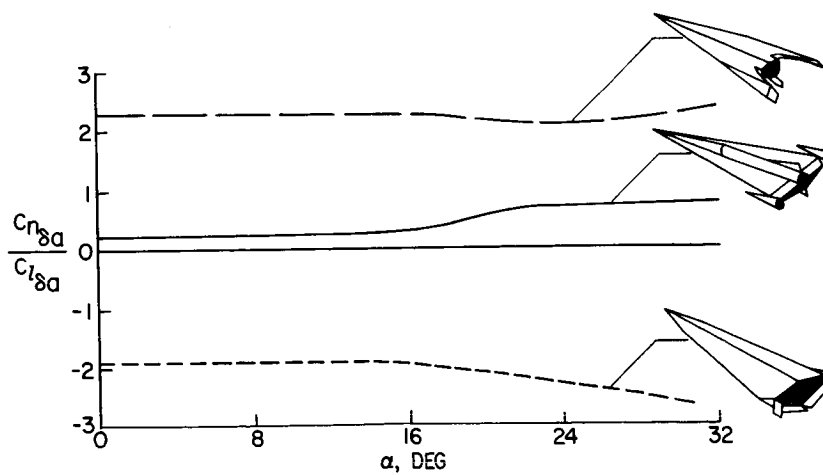


Figure 2

DUTCH ROLL DAMPING WITH ROLL AND YAW DAMPERS
M = 6.86; h = 130,000 FT

$t_{1/2} = 1$    2   5   $\infty$ SEC

$\dfrac{c_{n_{\delta a}}}{c_{l_{\delta a}}}$

$\dfrac{c_{l_{\delta r}}}{c_{n_{\delta r}}}$
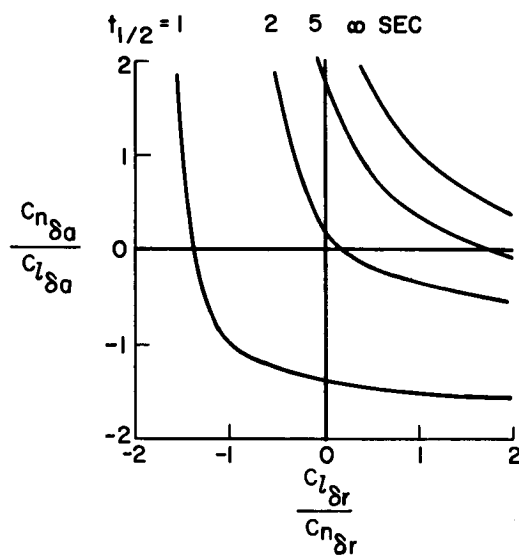
Figure 3

EFFECT OF $C_{l_\beta}$ ON DAMPING CONTRIBUTED BY AUXILIARY DAMPERS
M=6.86; h=130,000 FT

DAMPING IN ROLL

$C_{l_\beta}$
- - -   -0.027
———   .027

$\dfrac{1}{t_{1/2}}$

DUTCH-ROLL MODE

ROLL DAMPER GAIN, $k_3$
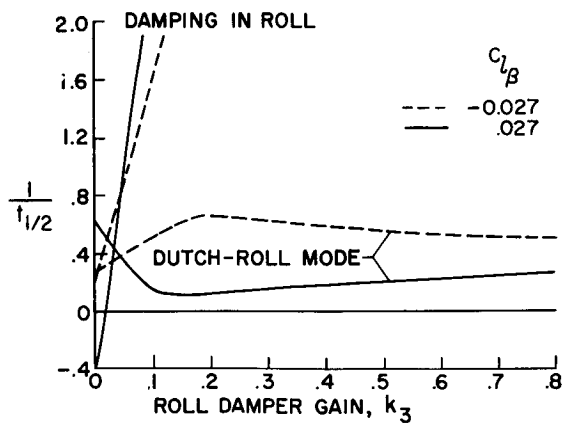
Figure 4

# SIMULATOR INVESTIGATION OF COMMAND REACTION CONTROLS

By Euclid C. Holleman and Wendell H. Stillwell

NACA High-Speed Flight Station

## INTRODUCTION

Exploitation of the ballistic capabilities of present or contemplated manned vehicles requires some form of reaction control so that attitude control will be possible beyond aerodynamic flight limits. Figure 1 shows the pertinent control regions for a plot of altitude against Mach number with an indicated area that represents a dynamic pressure $q$ from 5 to 10 pounds per square foot. In general, it is believed that above this region reaction controls will be required.

Initial investigations of reaction-control usage were made with an analog simulator. These studies investigated on-off acceleration reaction controls which gave adequate control, but which required constant attention to the control task. Such a reaction control system was designed for the X-1B airplane and has been ground-tested with the use of a three-degree-of-freedom simulator. Flight tests of these reaction controls have been initiated.

The purpose of this paper is to evaluate the effectiveness of reaction controls that command velocity and attitude and to compare these systems with the acceleration command system. Although many of the data were obtained for ideal systems at zero dynamic pressure, some results are also available to assess the effects of low dynamic pressure as well as assumed rocket-system lags.

## METHOD

The present study was performed by utilizing a closed-loop simulator consisting of an analog computer, oscilloscope for presentation, control stick, and pilot.

The analog computer was used to solve the differential equations that represented the airplane and control system. Three degrees of freedom were assumed for the zero-dynamic-pressure case, and five degrees of freedom were assumed for the finite-dynamic-pressure case. The mass and basic aerodynamic characteristics of a representative research airplane at a Mach number of 4.5 were used for the assumed problem. A three-axes

control stick (fig. 2), which is similar to the controllers being used in the X-1B airplane, was used. This stick required up-and-down motion for pitch control, side-to-side motion for yaw control, and rotation for roll control. Also shown in the figure is the presentation to the pilot; that is, a trace on an oscilloscope moved up and down to represent pitch and rolled to signify roll whereas yaw was indicated on a meter.

Since it was desired to use these control systems for orientation as well as stabilization in the reaction-control region, several evaluation tasks were employed. The response and precision of control were evaluated by making pitch, yaw, and roll changes in attitude and by coordinating these changes. This task will be referred to as the orientation task. Another control task consisted of attempting to retain initial attitude after the imposition of a sudden constant angular acceleration of 2 degrees per second per second in pitch or yaw, and will be termed the stabilization task.

## RESULTS AND DISCUSSION

Previous studies of acceleration on-off reaction controls have indicated desirable levels of control effectiveness and proportioning. A summary of these results is presented in figure 3, which shows satisfactory control regions that are functions of roll control effectiveness and control effectiveness ratio. Control effectiveness is defined as the angular acceleration produced by full control. Control effectiveness ratio is the ratio of roll control effectiveness to yaw or pitch control effectiveness. For a stabilizing task the on-off acceleration controls were satisfactory in the triangular region shown. Higher control effectiveness resulted in overcontrol tendencies. Also shown is the value presently being flight tested with the X-1B airplane. The limits of the present study are shown by the bars. Although this study was not as comprehensive in determining the limits of satisfactory control as the previous on-off study was, the three systems - proportional acceleration command, velocity command, and attitude command - gave satisfactory control over the range shown, which is a much larger range of control effectiveness than was obtained with the on-off controls. Somewhat arbitrary values of roll control effectiveness of 20 degrees per second per second and a control ratio of 4 were used for all the results presented. The discussion that follows compares the results obtained from proportional acceleration, velocity, and attitude command systems.

For an auxiliary control system such as the reaction control, economical operation is of great importance. The fuel requirements are one indication of the effectiveness of the closed-loop control. Figure 4 shows the effect of feedback gain for the velocity command and the attitude command systems on the relative fuel required for the stabilization

task. The fuel requirements have been normalized to the acceleration command system, which is represented by the intersection at zero gain. For the velocity command system, the relative fuel required decreases with increasing feedback gain. A feedback gain of 1.5 gave good response as well as reasonably good economy for the velocity command system and was used for most of the tests. For the attitude command system, the relative fuel required was rather insensitive to feedback gain in the range from 0.1 to 0.5. A value of 0.25 gave desirable response characteristics for the attitude command system and was used subsequently.

In figure 5 the fuel required to change pitch attitude 30° and stabilize in different time intervals is compared for the three systems. Yaw and roll results are not presented, but these results would be comparable. As might be expected, the slower maneuvers require less fuel than the faster maneuvers. It is apparent that the velocity and attitude command systems are about as economical as the acceleration command system.

The curves shown in figure 5 represent near-minimum fuel requirements for these maneuvers and are much more easily realized with the velocity or attitude system than with the acceleration command system. This is illustrated in figure 6. Note that the pilot control manipulation for the velocity and attitude command systems is much less than for the acceleration command system for satisfactory completion of the orientation task. Initial attempts to change attitude with the acceleration system usually resulted in overcontrol and invariably resulted in more control manipulation.

The results discussed thus far were for ideal systems with ideal rocket characteristics. The effect of practical rocket thrust response on the relative fuel required for the stabilization task is shown in figure 7. Practical rocket response is characterized by a delay and buildup time. Thrust buildup times to 0.4 second were investigated and had no measurable effect on the performance of the systems. Delays up to 0.4 second, which should cover the range of practical delays, had little effect on the relative fuel for any of the three systems. The X-1B had a lag of 0.2 to 0.4 second. For the large delay of 0.8 second the velocity and attitude systems showed only a small increase in relative fuel, but the acceleration system showed a large increase in relative fuel. These trends were even more evident during orientation tasks.

In order to gain some insight into the effect of dynamic pressure on the control task with reaction controls, stabilization tasks were performed at constant dynamic pressure. The results of these tests are shown in figure 8. It can be seen that with the velocity and attitude command

systems, there was little effect of dynamic pressure. With the accelera-
tion command system, dynamic pressure can have a marked effect, depending
on pilot technique and effort expended. With very close attention to the
task, the efficiency of this system can approach that of the velocity or
attitude command systems, but many maneuvers, though not out of control,
resulted in the fuel required that is indicated by the upper bounds of
the cross-hatched area. The dynamic-pressure region of 5 to 10 pounds
per square foot appears to be a very demanding region for precise control
with the acceleration system due to dihedral effect.

In figure 9, these results are extended by simulating the initial
buildup in dynamic pressure during a typical entry without damper
augmentation. Shown are time histories of dynamic pressure, sideslip,
yaw control, bank angle, and roll control for the acceleration (shown
by solid lines) and velocity (shown by dashed lines) command systems.
It was the task of the pilot to recognize a sideslip misalinement, to
zero sideslip, and to maintain control of the airplane during the
dynamic-pressure buildup. Successful entry could be accomplished with
either of the control systems. As dynamic pressure increased, it
became necessary to control the sideslip precisely to prevent large
excursions in roll. The velocity command system minimized this task;
whereas, with the acceleration system, the task was more difficult.
Roll excursions of considerable magnitude were evident especially in
the higher dynamic-pressure range. It should be noted, however, that
in this dynamic-pressure range the aerodynamic controls would be of
increasing importance. With the attitude command system, entry was
accomplished without pilot control.

CONCLUDING REMARKS

In conclusion, it may be said that a velocity or attitude command
reaction control system would facilitate the task of orientation and
stabilization in regions of low dynamic pressure. All the systems were
insensitive to lags that might be encountered in practical rocket systems,
but at large lags the effectiveness of the proportional acceleration sys-
tem deteriorates much more rapidly than does the effectiveness of the
other control systems. Dynamic pressure complicates the stabilization
and orientation problem by aerodynamically coupling yaw and roll, but
this complication only serves to emphasize the superiority of the veloc-
ity and attitude command systems over the acceleration system. The
attitude command system was superior to the velocity command system as a
stabilizing device, but the velocity command system was preferred for
orientation. Finally, additional studies would be desirable to determine
whether the more sophisticated reaction control systems are required
during critical entry conditions.

## PERTINENT CONTROL REGIONS
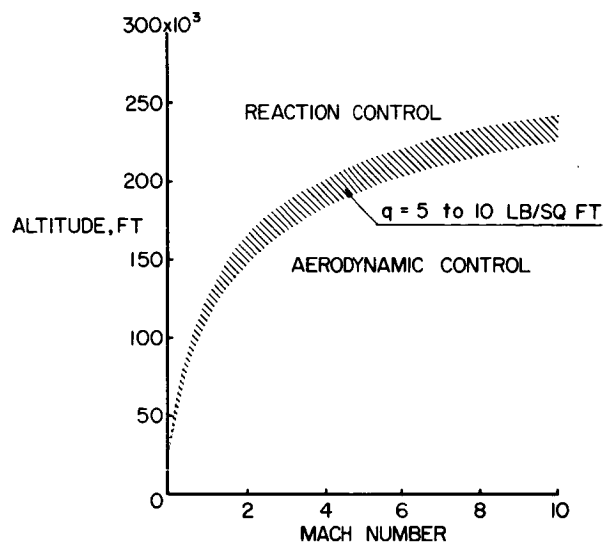


Figure 1

## CONTROL STICK AND PRESENTATION



Figure 2

162
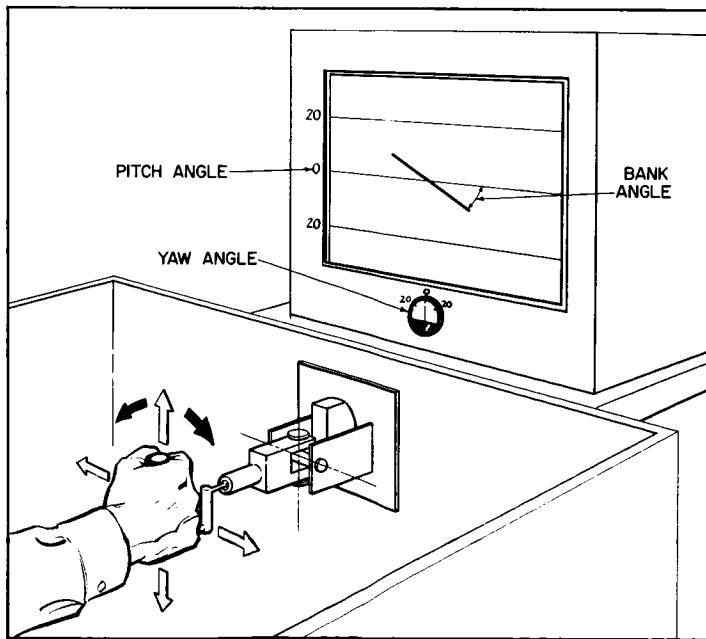
## CONTROL EFFECTIVENESS REGIONS STUDIED

IDEAL SYSTEMS, q=0

CONTROL
EFFECTIVENESS
RATIO,

ROLL
─────────
PITCH OR YAW

X-IB RESEARCH AIRPLANE

SATISFACTORY, ON-OFF
ACCELERATION COMMAND

LIMITS OF PRESENT STUDY,
PROPORTIONAL ACCELERATION,
VELOCITY & ATTITUDE COMMAND

ROLL CONTROL EFFECTIVENESS, DEG/SEC/SEC
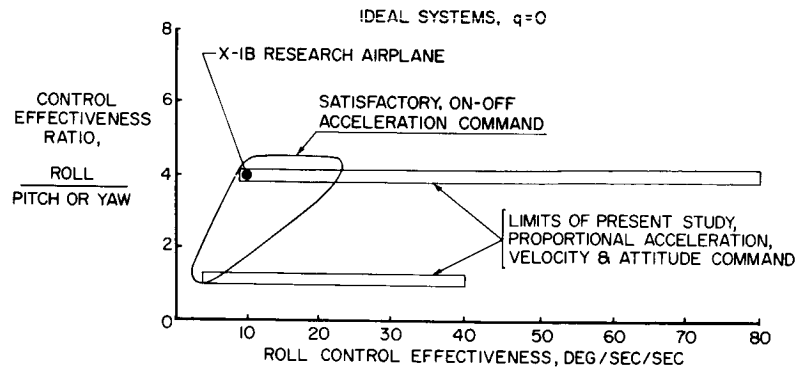
Figure 3

## EFFECT OF SYSTEM GAIN

STABILIZATION TASK, IDEAL SYSTEMS, q = 0

VELOCITY COMMAND

ATTITUDE COMMAND

RELATIVE
FUEL
REQUIRED

$G_V = 1.0$

1.5

VELOCITY FEEDBACK GAIN, $G_V$

ATTITUDE FEEDBACK GAIN, $G_A$
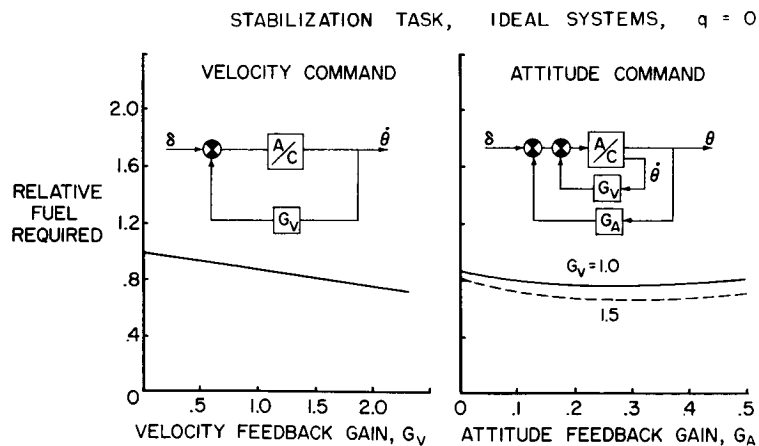
Figure 4

## FUEL REQUIREMENTS FOR 30° ATTITUDE CHANGE

IDEAL SYSTEMS, q = 0
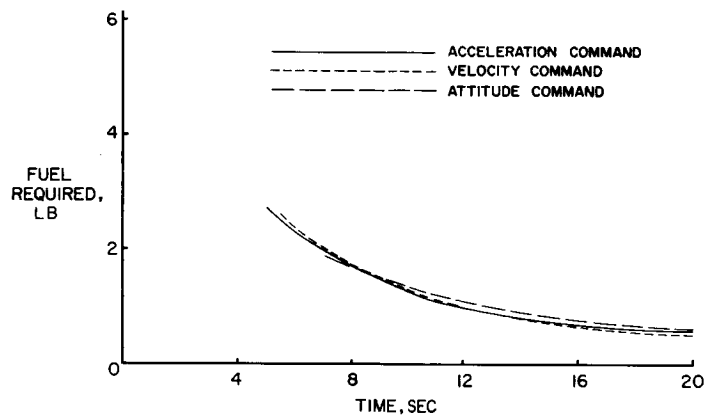


Figure 5

## PILOT CONTROL PROBLEM

ORIENTATION TASK, IDEAL SYSTEMS, q = 0
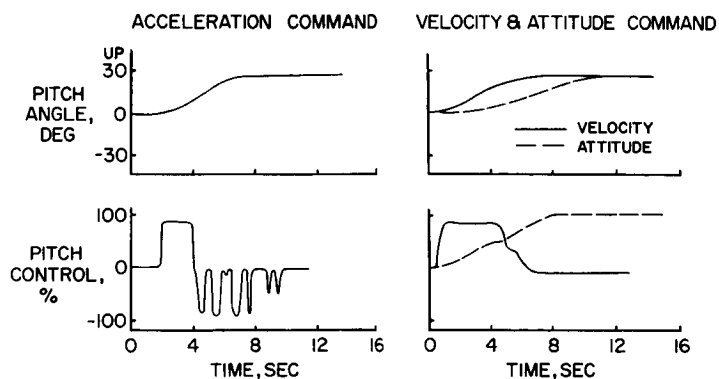


Figure 6

# EFFECT OF THRUST LAG

STABILIZATION TASK, q = 0, BUILDUP = 0.4 SEC
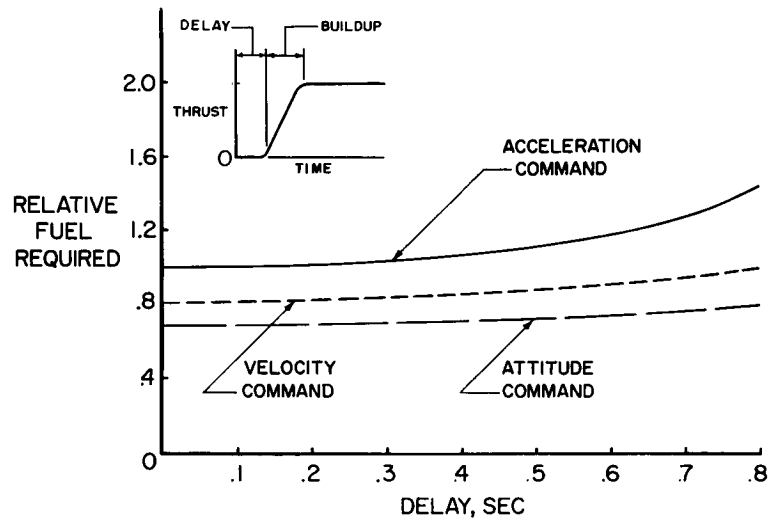
Figure 7

# EFFECT OF DYNAMIC PRESSURE

STABILIZATION TASK, IDEAL SYSTEMS

Figure 8

## CONTROL DURING ENTRY

IDEAL SYSTEMS

q, LB/SQ FT

β, DEG

$\delta_\psi$, %

ACCELERATION COMMAND

φ, DEG

VELOCITY COMMAND

$\delta_\phi$, %

TIME, SEC

Figure 9

13
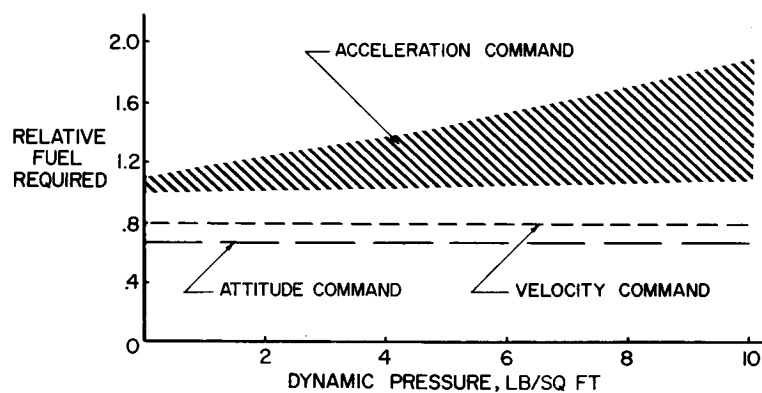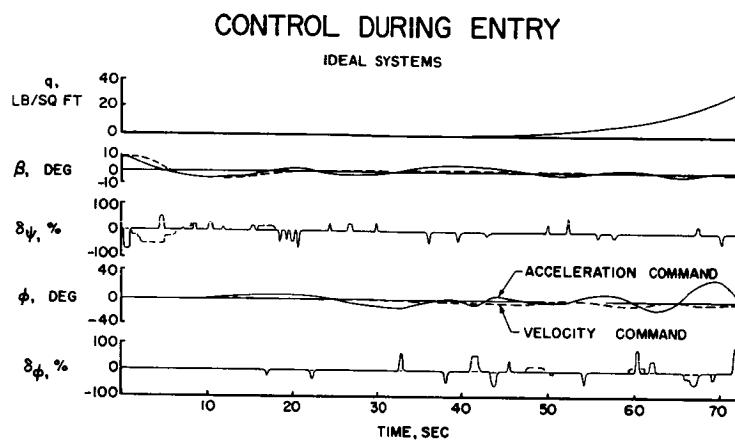
SIMULATION STUDY OF A HIGH-PERFORMANCE AIRCRAFT

INCLUDING THE EFFECT ON PILOT CONTROL OF

LARGE ACCELERATIONS DURING EXIT

AND REENTRY FLIGHT

By C. H. Woodling, James B. Whitten, Robert A. Champine,
and Robert E. Andrews

Langley Aeronautical Laboratory

## SUMMARY

A discussion is given of a simulation study of a high-performance
aircraft conducted on the human centrifuge at the U. S. Naval Air
Development Center, Johnsville, Pa. The centrifuge, in combination with
an analog computer, provided a pilot-controlled simulator which subjected
the pilot to linear accelerations similar to those he would encounter in
exit and reentry flight.

Results of this study indicated that accelerations of the magnitude
considered in this program did not significantly affect the pilot's abil-
ity to carry out his flight task when "flying" the airplane with auxiliary
dampers operating. However, large oscillating acceleration patterns during
reentry flight, such as might be encountered with certain damper failures,
were found to make some reentries marginal and some impossible because
of the effect on the pilot's ability to see and read instruments and
satisfactorily control the airplane.

It is believed that the centrifuge simulator is a significant advance
over static or "fixed-base" simulators for evaluation of pilot restraint,
controls, instrument display, and pilot and airplane response.

## INTRODUCTION

In the past, simulation studies of pilot control capabilities,
including an analog-computer representation of the motion of the air-
plane, have been found to be valuable in the investigation of difficult
piloting problems. For example, simulation studies have been made of

roll coupling, pitch up, and pilot control during landing. In such studies, however, the pilots were not subjected to the sometimes violent motions that the airplane would encounter. At present, studies are being conducted of manned vehicles which will be required to exit from and reenter the earth's atmosphere and in which the pilot will be subjected to large accelerations during the exit and reentry phases. Due to the lack of actual flight experience under such conditions, it is desirable that the vehicle and its flight environment be simulated as closely as possible if the pilot and airplane responses are to be predicted with a certain degree of confidence. The subject of this paper is a discussion of a simulation study of a high-performance aircraft conducted on the human centrifuge at the U. S. Naval Air Development Center, Johnsville, Pa. In this study the pilot was subjected to the large linear accelerations that he would encounter in flight. This study was conducted as a joint effort between NACA and NADC and this opportunity is taken to acknowledge the excellent cooperation of the NADC personnel and particularly Dr. Carl Clark of the Aviation Medical Acceleration Laboratory for his efforts and supervision which contributed largely to the success of this program.

## SYMBOLS

$h$ — altitude, ft

$M$ — Mach number

$a_X$ — longitudinal acceleration, g units

$a_Z$ — normal acceleration, g units

## DESCRIPTION OF SIMULATOR SETUP

A portion of a trajectory, typical of that planned for the North American X-15 research airplane, was considered in this investigation and is shown in figure 1. In this figure, altitude $h$, Mach number $M$, longitudinal acceleration $a_X$, and normal acceleration $a_Z$ are plotted against time which is given in seconds. This part of the trajectory starts at 48 seconds prior to engine burnout at an altitude of 60,000 feet, a Mach number of 2, on a zero lift or zero angle-of-attack flight path, and at a climb angle of $45^\circ$. During the powered phase of the exit, the thrust acceleration increases from 2g to about 4g. While under this acceleration and in the presence of out-of-trim moments in pitch and yaw due to mis-alinement of the thrust, the pilot's task is to fly with the wings level

at zero angle of attack and sideslip. At burnout the acceleration rapidly approaches zero and disturbances are encountered due to the sudden termination of the misalinement moments. As the airplane reaches the higher altitudes, aerodynamic control becomes less effective and reaction control is used to keep the airplane at the proper attitude. If the pilot is able to perform his task properly during exit, the airplane will level out at about 250,000 feet. For reentry, the pilot pulls up to a prescribed angle of attack at about 200,000 feet, holds this angle of attack until the normal acceleration builds up to about 5g because of the increasing dynamic pressure, and then decreases the angle of attack in order to retain nearly constant acceleration until the rate of descent approaches zero. The angle of attack is then further reduced until level flight at 1g is obtained.

The main objectives of the centrifuge program were to answer the following questions:

Can the centrifuge under closed-loop control provide a useful dynamic simulation of a high-performance aircraft under large accelerations?

What are the effects on the pilot's ability to control the dynamic simulator when he is subjected to longitudinal accelerations of the order of 4g during exit and normal accelerations of the order of 5g during reentry?

What is the effect of various angles of attack and associated accelerations on the pilot's ability to fly the reentry?

How well can the pilot perform his task during reentry when subjected to large and rapidly oscillating acceleration patterns, such as might be encountered with certain damper failures?

The human centrifuge is located at the Aviation Medical Acceleration Laboratory at NADC. A photograph of this centrifuge is presented in figure 2.[1] The centrifuge consists of an enclosed gondola mounted in a two-gimbal system on the end of a 50-foot rotating arm. The gimbal system consists of an outer gimbal which rotates about a horizontal axis perpendicular to the centrifuge arm and an inner gimbal which rotates about an axis in the plane of the outer gimbal and perpendicular to the axis of the outer gimbal. The total acceleration of the centrifuge gondola when the arm is set in motion is comprised of a radial component proportional to the square of the angular velocity of the arm, a tangential component proportional to the angular acceleration of the arm, and the vertical acceleration of gravity. The controlled gimbals allow

---

[1]A motion-picture film (L-312) showing the operation of the facility and some results of this study has been prepared and is available on loan from NACA Headquarters, Washington, D. C.

positioning of the centrifuge gondola with respect to these accelerations so that the pilot is subjected to linear accelerations similar to those he would experience in flight. It should be noted that, since the centrifuge has only three degrees of freedom as compared with the six of the airplane, the accurate simulation of the linear accelerations must be done at the expense of angular motions which are not like those experienced in an airplane. However, it was found that under the large linear accelerations that were utilized in this study, the pilots were not significantly disoriented or distracted by these wrong angular motions or accelerations. The design capabilities of this centrifuge are a maximum radial acceleration of 40g with a maximum rate of 10g per second. A more detailed discussion of the centrifuge operation and capabilities is given in references 1 and 2.

Figure 3 shows a diagram of the closed-loop simulator that was used in this program. The simulator included an analog computer, a coordinate converter, and the centrifuge in which the subject pilot was placed. The closed-loop control was accomplished by feeding the three linear accelerations of the pilot, as determined by the analog computer from the equations of motions of the airplane, to a coordinate converter. Here the accelerations were converted to centrifuge commands in the form of gimbal angles and arm angular velocity and acceleration. The centrifuge then subjected the pilot to the three desired accelerations as indicated by the analog computer. While under these accelerations, the pilot observed the instrument panel, on which were displayed necessary quantities from the analog computer, and applied stick and rudder deflections which were fed back as input signals to the analog computer. Thus, the loop was completed, since the pilot's inputs actually controlled the motion of the centrifuge. The two main parts, that is, the analog computer and the centrifuge were located at a distance of approximately 3,500 feet apart and were tied together operationally by telephone lines.

The analog setup included a six-degree-of-freedom representation of the airplane motions, control equations (including auxiliary damper terms and pilot inputs), and computation of the dynamic pressure as a function of altitude and velocity. The aerodynamic characteristics were simulated as a function of both Mach number and angle of attack.

A simulated cockpit was mounted in the centrifuge gondola and included a right-hand console stick, rudder pedals, a left-hand ballistic or reaction control stick, and, for comparative purposes, a standard center control stick. An instrument display panel, which is shown in figure 4, was provided for the pilot. The primary instruments used in this program included an attitude ball indicating roll and pitch angles, and indicators presenting angle of sideslip, angle of attack, normal acceleration, inertial altitude, inertial velocity, inertial rate of climb, roll rate, and heading. Positioned below the panel were damper-malfunction indicator lights and associated switches.

The pilot was secured in the gondola by an integrated harness arrangement. For head restraint the subject's helmet was fastened inside a bucket-type headrest by a steel cable which was attached to the helmet and fixed to the back of the headrest.

## RESULTS AND DISCUSSION

The remaining part of this paper discusses some of the more pertinent findings of this study. Included in these results are some of the pilots' comments and their evaluation of the dynamic simulator.

A typical run on the centrifuge was started by manually bringing the centrifuge up to the initial condition of 2g thrust acceleration. From this initial condition, the pilot would actually start his flight and assume control by turning on the engine switch on the instrument panel. This switch started the integrators of the analog. The angular velocity of the centrifuge would then increase, and the pilot was subjected to the increasing thrust acceleration. During this period of prolonged acceleration, the pilots experienced a drainage of the sinus and a feeling of fullness in the throat which resulted in frequent coughing. Breathing during this time was difficult, usually rapid and shallow. At burnout, oscillations started because of the sudden removal of the thrust misalinement; these oscillations could be stopped by the use of aerodynamic control if the pilot reacted promptly. If the pilot reacted slowly, the oscillations persisted to higher altitudes and the use of reaction control was found necessary. At burnout, the centrifuge, unable to simulate less than 1 g, would come to rest. The pilot would then fly the 0g portion of the trajectory (about 2 minutes duration) statically (with the centrifuge at rest) at 1g. As the airplane reentered the atmosphere, the centrifuge would again rotate in response to the buildup of normal acceleration. The reentry required rapid scanning of a relatively large number of instruments and a high degree of concentration. The high rate of scanning found necessary in this study indicated that the relocation and possibly combining of certain instruments for a more nearly optimum display should be considered. With all dampers operating, three reentry conditions were considered. These were an angle of attack of 15° with an acceleration of 5g until recovery, 20° with 4.5g, and 25° with 4g. Little difference was noted in these reentry conditions except that the 25° case required slightly more control than the 20° or 15° reentries. The difference between 4g and 5g normal acceleration had no noticeable effect on the pilot's ability to reenter. Only moderate "greyout" was experienced during the reentries. Safety stops were included in the simulator which would automatically terminate the run if the commanded acceleration exceeded 8g; however, the subjects rarely received an acceleration over 6g.

It is of interest to note here, before discussing some of the damper failure results, a few comments concerning the comparison of the center control stick with the right-hand stick. The majority of the flights were made with the right-hand stick. However, for the few flights with the center stick, the pilots felt that it was a good controller at low accelerations. Above about 2g, however, two hands were used and the center control stick was considerably more difficult to use than the right-hand stick because of the acceleration effects on the hand and arm positions.

An important part of the investigation was to determine the ability of the pilot to control the airplane during reentry under certain damper failures. Figure 5 shows the effect on reentry of one of the damper failure conditions investigated. Shown are the lateral accelerations during a 25° angle-of-attack reentry (starting 190 seconds after the beginning of the flight) for the case of all dampers operating and the case of a yaw-damper failure. It should be mentioned that in the present investigation the damper system consisted of dampers about all three axes and, in addition, a crossfeed of yaw rate to the roll control surface. In the reentry shown in figure 5, the crossfeed and yaw damper were both not operating. This condition would correspond to a failure of the yaw-rate sensing gyro. With all dampers operating, the pilot was able to maintain practically zero lateral acceleration during reentry. However, with the damper failure a maximum lateral acceleration of about ±2g was encountered. Even though the pilot was able to fly the airplane to recovery under this failure, he experienced some difficulty in reading the instruments during the motion and considered the system used for body and head restraint necessary in avoiding loss of orientation and minimizing distractions from being jostled about.

Another type of damper failure that was simulated is shown in figure 6. Shown in this figure is the normal acceleration during reentry with all dampers operating and with the pitch damper failed. At about 225 seconds, the pilot was unable to cope with the high oscillating accelerations, and the run was automatically terminated when the safety stop was reached at 8g. It is of interest to note the change in frequency of the oscillation as the airplane reenters the atmosphere. It should be mentioned that in the static or "fixed-base" simulation tests, where the pilot was not subjected to normal accelerations, he was able to reenter under this condition of pitch-damper failure about 60 percent of the time. However, the pilots never did reenter successfully in the dynamic tests on the centrifuge. The pilots believed that the oscillating acceleration was such that it did not permit them to control as precisely as required.

Although no specific results will be discussed for reentries with roll-damper failure, reentries with this failure were found to be

extremely difficult. For a small percentage of the cases, recoveries were made with very precise control of a low-angle-of-attack reentry.

## CONCLUDING REMARKS

The centrifuge simulator was found to be a useful dynamic simulation of a high-performance aircraft under large accelerations. It is believed that this simulator is a significant advance over fixed-base simulators for evaluation of pilot restraint, controls, instrument display, and pilot and airplane response.

For the trajectory considered in this study, and with all the dampers operating, the pilots were generally able to carry out successfully their flight task while under longitudinal acceleration of the order of 4g and normal acceleration of the order of 5g, even though some physiological effects were noted. However, large oscillating acceleration patterns, such as might be encountered in the case of certain damper failures, were found to make some reentries marginal and some impossible because of the effect on the pilot's ability to see and read instruments and satisfactorily control the airplane.

## REFERENCES

1. Crosbie, Richard J.: Utilization of a System of Gimbals on the Human Centrifuge for the Control of Direction of Acceleration With Respect to the Subject. Rep. No. 4, Project NM 001 100 303, Aviation Medical Acceleration Lab., U. S. Naval Air Dev. Center (Johnsville, Pa.), Aug. 2, 1956.

2. Clark, Carl, and Crosbie, Richard: Centrifuge Simulation of Flight Accelerations. Project TED ADC AE-1410 (NM 11 02 12.6), Aviation Medical Acceleration Lab., U. S. Naval Air Dev. Center (Johnsville, Pa.), Sept. 17, 1957.
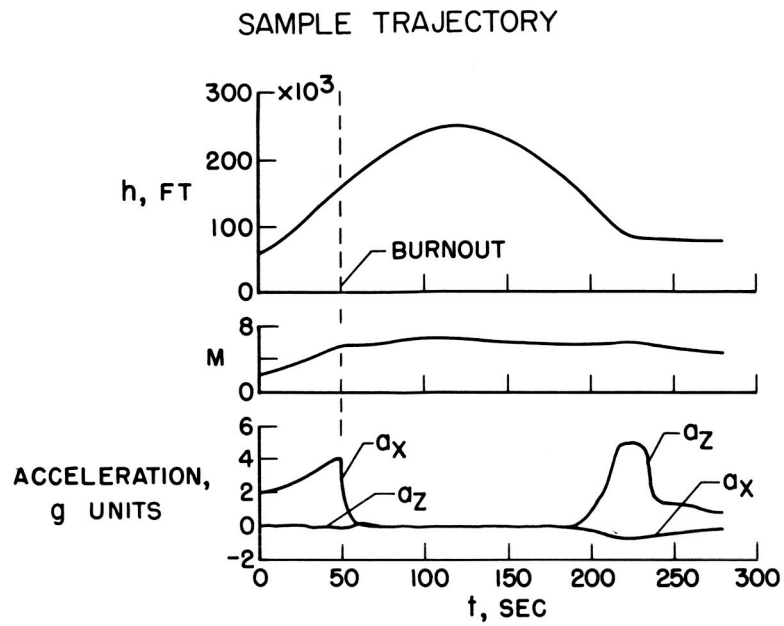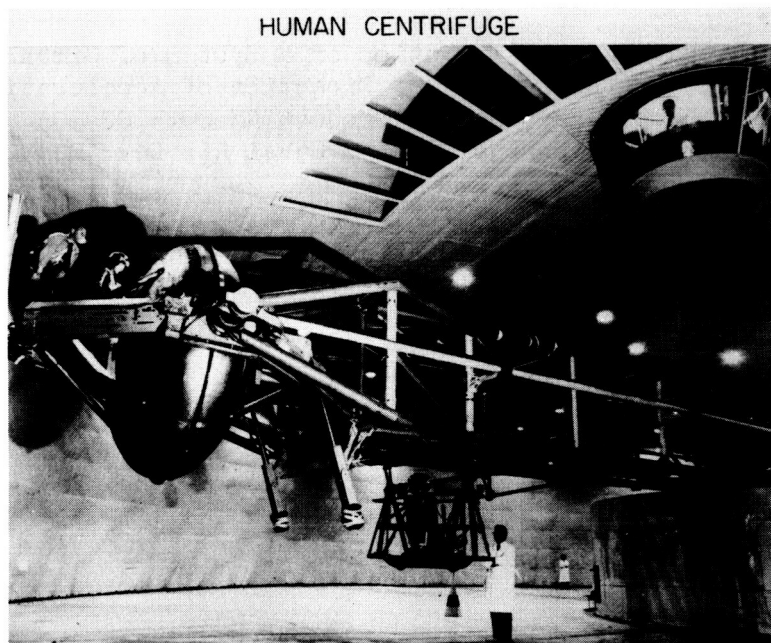
Figure 1



Figure 2

DIAGRAM OF CLOSED-LOOP
ANALOG-CENTRIFUGE-PILOT SIMULATOR



Figure 3



INSTRUMENT-DISPLAY PANEL
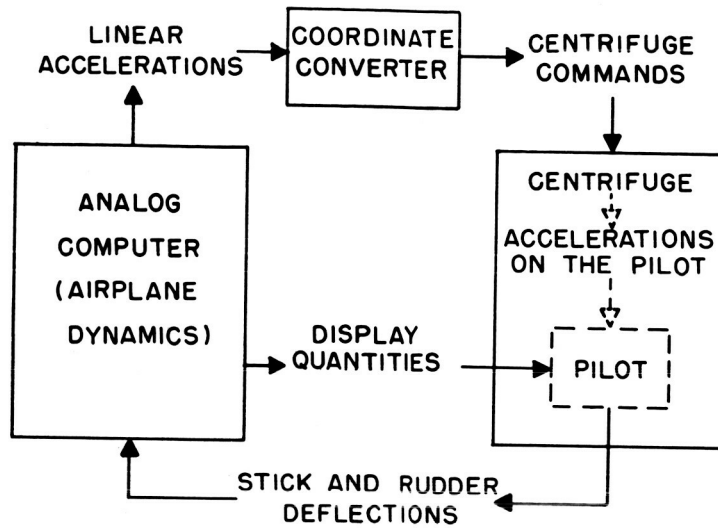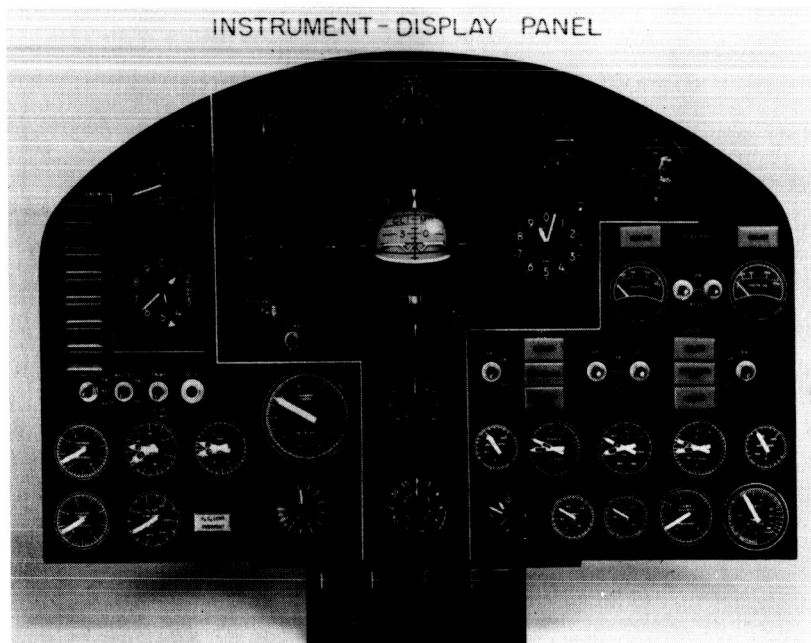
Figure 4

EFFECT OF YAW-DAMPER FAILURE

ALL DAMPERS OPERATING
YAW - DAMPER FAILURE
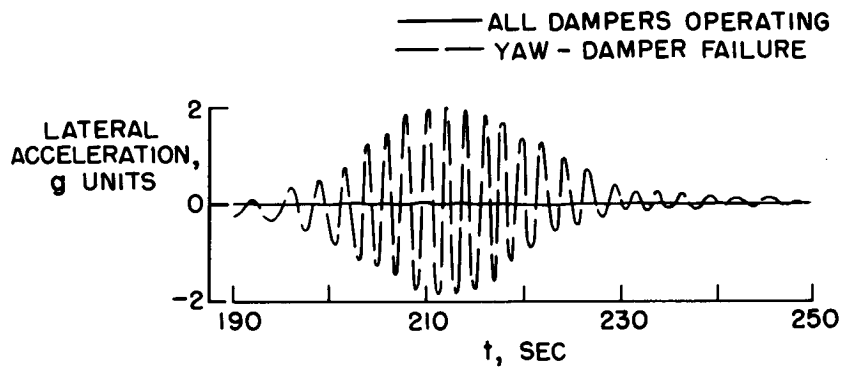
Figure 5

EFFECT OF PITCH-DAMPER FAILURE

ALL DAMPERS OPERATING
PITCH-DAMPER FAILURE

RUN AUTOMATICALLY TERMINATED
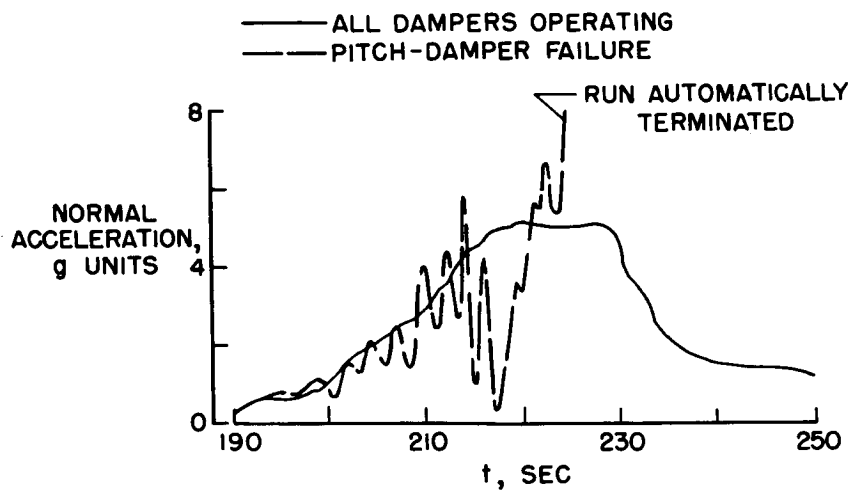
Figure 6

# HYDRODYNAMIC CHARACTERISTICS OF MISSILES

## LAUNCHED UNDER WATER

By John R. Dawson

Langley Aeronautical Laboratory

14

## SUMMARY

Some of the hydrodynamic problems associated with the launching of an air missile from under water are examined briefly. From a limited hydrodynamic investigation that has been made in this field, some experimental results are presented to illustrate the problems that may be expected.

## INTRODUCTION

Much interest is currently being given to the possibility of launching an air missile from a submerged submarine in such a manner that the missile rockets can be fired after the missile emerges from the water surface. In order to examine some of the problems encountered in such launchings, the NACA has made some hydrodynamic experiments in Langley tank no. 2 with a dynamic model of a typical missile.

## SYMBOLS

$d$          depth of launching catapult

$t$          time after emergence

$\phi$          launch angle (cant of launching tube)

$\theta$          angle of deviation of missile from vertical

$\theta_{1\,SEC}$     angle of maximum deviation 1 second after emergence

## APPARATUS AND PROCEDURE

Experiments have been made with a small-scale dynamic model representative of a suitable missile configuration (fig. 1). The weight, moment of inertia, and center-of-gravity location of the model were scaled from representative full-scale values.

The launching method used is illustrated in the sketch included in figure 2. As is shown, the missile was launched by means of a submerged catapult. This simple catapult used compressed air in a manner currently being considered for full-scale launching, but it was not a model of any particular full-scale catapult. The catapult was placed on a small carriage which was towed along underwater rails by means of an electric winch when it was desired to simulate the forward motion of the submarine. A few tests were made with the catapult tube inserted in a streamline body as shown in figure 2, but it was determined that for the submarine speeds under investigation, the effect produced by this body was small, and most of the tests were made with the launching tube alone. The deviation of the model from the vertical after emerging from the water, designated the angle $\theta$, was determined from motion-picture frames.[1]

## RESULTS AND DISCUSSION

The data in figure 1 are for a launching depth of 100 feet and an emergence speed of 90 feet per second. The deviation angle $\theta$ is plotted against time after emergence from the water surface. It is, of course, necessary that the angle $\theta$ be within limits that will permit control by the missile guidance system at the time when the rockets are fired. Each test point shown represents the maximum deviation obtained from a group of test runs made for each condition. In the calm-water condition only random disturbances affect the model, which is statically unstable, and the area shown represents a cross section of the cone of dispersion of $\theta$ values. It is advantageous to fire the rockets as soon as possible after the missile emerges, because of the increase in deviation with time. The value of $\theta$ 1 second after emergence (representing a reasonable delay for rocket firing) is used as a simple figure of interest. The 12-foot wave introduced maximum angular deviations (after 1 second) of about 20° more than the 8° obtained in calm water. The water in a wave crest moves in the direction of the wave train while

---

[1]A short motion-picture film supplement (L-313) illustrating the effects indicated in this paper is available on loan from NACA Headquarters, Washington, D. C.

that in the trough moves in the opposite direction. Accordingly, emergences through the crest and through the trough gave deviation angles in opposite directions but of about the same magnitude.

The effect of the forward speed of the submarine is shown in figure 3, where the maximum angle of deviation 1 second after emergence (designated $\theta_{1 \text{ SEC}}$) in calm water is plotted against the vessel's speed of advance. These data were taken with the launching tube vertical. The launching vessel was traveling on rails and its reactions from the catapulting forces were therefore negligible. In all cases the deviation angle was opposite to the direction of the vessel's forward motion. At 3 knots the deviation was about $45^\circ$ and even at 1 knot the deviation was more than twice that obtained in the static condition. The advantage of getting the submarine speed down to a low value is emphasized by these data.

The curved path of the missile, when the submarine is under way, can be made more nearly tangent to the vertical after emergence by canting the launching tube forward at a launch angle $\phi$ as shown in figure 4. The data in this figure are for a "hovering" speed of 1 knot. Under the conditions shown, the deviation was least at a launch angle of about $6^\circ$, for which case the measured deviation 1 second after emergence was $12^\circ$. Thus, about half the deviation introduced by the 1-knot forward speed has been recovered by canting the launching tube at optimum launch angle. Although the optimum angle is not critical, the practical use of this trend will depend on the accuracy with which the submarine trim can be maintained. Somewhat similar results would be expected if the submarine itself instead of the launching tube in the submarine were inclined at the launch angle.

In figure 5 the effect of launching depth is shown. For these data the launching vessel was fixed and the speed of emergence from the water surface was maintained constant at 90 feet per second. A rapid increase in the deviation angle occurred with increase of depth. At depths greater than 200 feet the model would not consistently emerge from the water.

The model tests reviewed here were made at scale speeds, for which no cavitation occurred. At actual full-scale speeds of the order of 90 feet per second, appreciable cavitation has been observed on a missile of this shape. Force tests made in Langley tank no. 2 and in the Langley high-speed hydrodynamic facility have indicated relatively small effect of this cavitation on static stability. Effects of cavitation on dynamic stability have not yet been evaluated.

While the actual values of deviations indicated in this investigation might perhaps be reduced by refinements in catapulting techniques

that reduce the initial disturbances, there still remain unavoidable disturbances due to motions of the sea and of the launching vessel. These brief experiments have indicated that such environmental disturbances have substantial effects, and the limits in operating conditions for satisfactory missile launching may therefore be imposed by hydrodynamic behavior. Where these operating limits are found to be too restrictive, it would be logical to increase the stability of the missile with tail fins or other devices.

## CONCLUDING REMARKS

The effects of some pertinent operating parameters on the behavior of an air missile when launched from a submerged submarine have been examined experimentally. It was found that for the case of a typical unstable missile, the motions of the sea and of the launching vessel, as well as the depth of the launching catapult, had considerable effect on the attitude that the missile would have at the time its rockets are fired.

MISSILE CONFIGURATION

Figure 1        L-58-1022

## EFFECT OF WAVES ON UNDERWATER LAUNCHING
### SUBMARINE SPEED, ZERO; VALUES ARE FULL SCALE
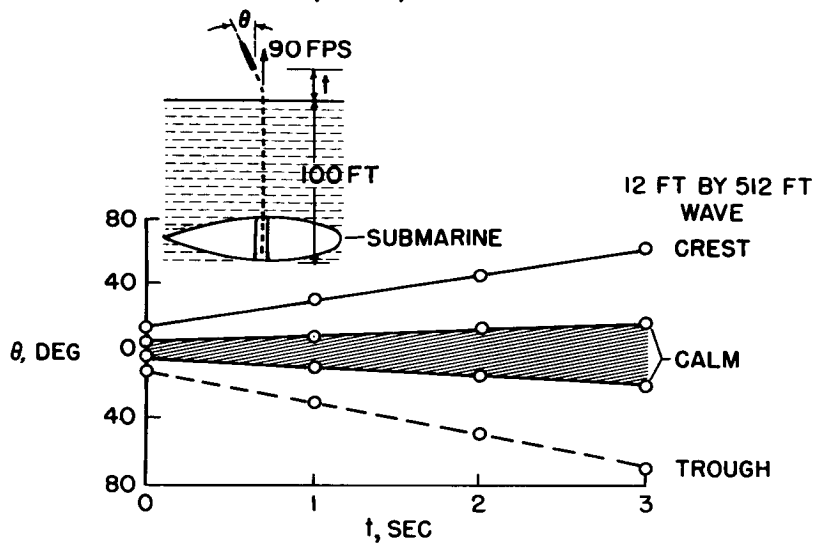
Figure 2

## EFFECT OF SUBMARINE SPEED
## ON VERTICAL UNDERWATER LAUNCHING
### VALUES ARE FULL SCALE
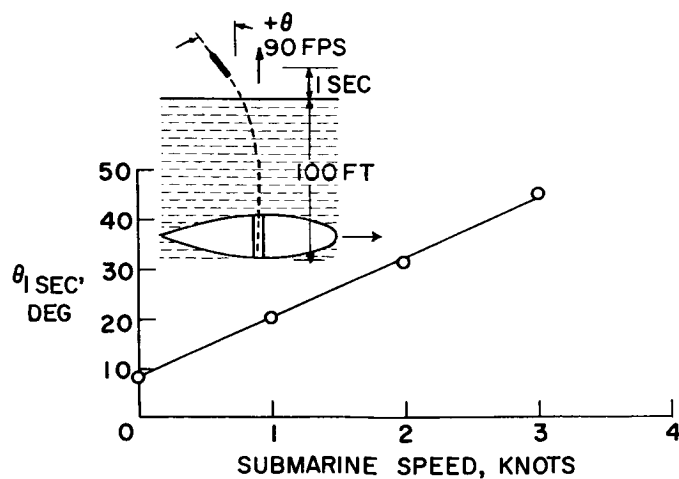
Figure 3

EFFECT OF LAUNCH ANGLE ON UNDERWATER LAUNCHING
SUBMARINE SPEED, I KNOT; VALUES ARE FULL SCALE

$+\theta$
90 FPS
I SEC
100 FT
$\phi$

20

$\theta_{I\,SEC}$, DEG    10

0    3    6    9    12

LAUNCH ANGLE, $\phi$, DEG
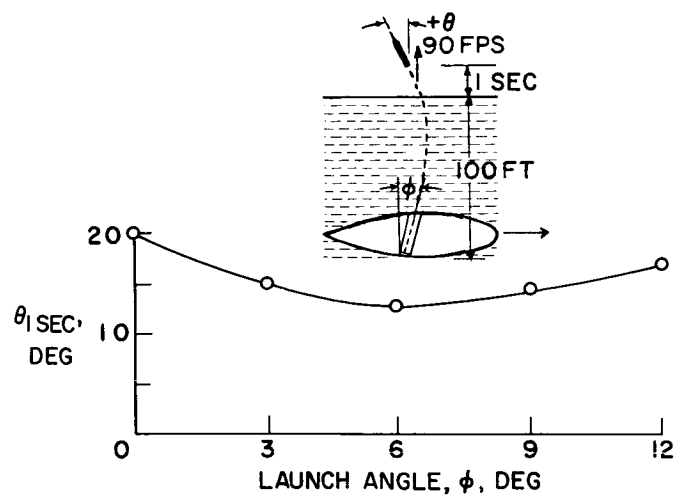
Figure 4

EFFECT OF DEPTH ON UNDERWATER LAUNCHING
SUBMARINE SPEED, ZERO; VALUES ARE FULL SCALE

120

FAILS TO
EMERGE

100

$-\theta$
90 FPS
I SEC

80

$\theta_{I\,SEC}$, DEG    60

d

40

20

0

100    125    150    175    200

DEPTH, d, FT
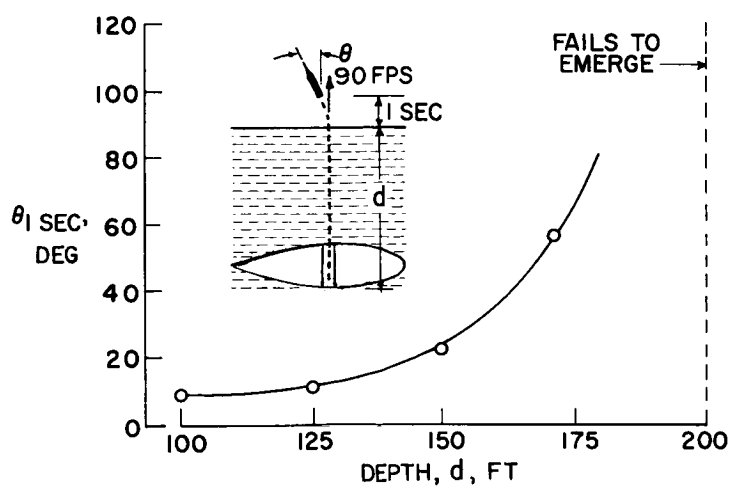
Figure 5

THERMODYNAMIC AND TRANSPORT PROPERTIES AND CHEMICAL

REACTION RATES FOR HIGH-TEMPERATURE AIR

By C. Frederick Hansen and Steve P. Heims

Ames Aeronautical Laboratory

## INTRODUCTION

It is axiomatic that the science of aerodynamics must be based on a good understanding of the atmospheric medium through which vehicles are to fly. It is well known that vehicles traveling at high speed excite the air to high temperatures, with the result that air properties deviate considerably from those of a simple gas which obeys the ideal gas law and which has a constant specific heat. For example, figure 1 shows the major chemical reactions which are produced in the stagnation regions of vehicles traveling at high velocity through the atmosphere. At about 3,000 feet per second the vibrational energy of air molecules begins to become important. Oxygen dissociation begins at 6,000 to 8,000 feet per second, nitrogen dissociation occurs at velocities in excess of 15,000 feet per second, and, finally, ionization of atoms becomes of major importance near escape velocity. The dissociation and ionization reactions are pressure dependent because each particle yields two product particles, and such reactions are inhibited by high pressure. Therefore, higher temperature and, consequently, higher velocity are required to produce the reactions at sea level than at high altitudes where much lower pressures occur. Vibrational energy is excited wherever molecules exist at high temperature, and so the domain in which vibrational excitation is important continues throughout the regions of the dissociation reactions as well. It can be intuitively appreciated that these reactions will affect many of the properties of air. Some of these properties which will not be considered herein may have important aerodynamic effects; for example, the electrical conductivity is a fundamental parameter in magnetohydrodynamics. The present discussion, however, is limited to the thermodynamic and transport properties and to the reaction rates for the chemical processes which occur in air. The thermodynamic properties include the energy, enthalpy, entropy, specific heats, and the speed of sound for air; the transport properties to be considered are the viscosity and thermal conductivity; and the most important reaction rates are those for the chemical processes indicated in figure 1. In the absence of magnetohydrodynamic effects, these parameters are the fundamental ones that determine the characteristics of air flow.

## THERMODYNAMIC PROPERTIES OF AIR

The equilibrium thermodynamic properties of air can be calculated to very high temperatures with considerable confidence, since the molecular and atomic energy levels on which these calculations are based are known very precisely from spectroscopic data (refs. 1 and 2). Gilmore (ref. 3) and later Hilsenrath and Beckett (ref. 4) have prepared accurate tables of thermodynamic functions for air. Before discussing the features of these functions in detail, it will be helpful to review briefly the expressions for energy of atoms and diatomic molecules.

Figure 2(a) shows a ball and spring model for the diatomic molecule which is vibrating and rotating at the same time that it is in translational motion. The energy of this molecule is a function of its velocity $u$, the rotational quantum number $J$, and the vibrational quantum number $n$, as shown in the following equation:

$$e(u,J,n) = \frac{mu^2}{2} + J(J + 1)\frac{h^2}{2I} + nh\nu$$

where

$m$      mass of molecule

$h$      Planck's constant

$I$      moment of inertia

$\nu$      characteristic frequency of molecular bond (the spring)

At high temperatures, the electrons may also be excited to quantum states above the ground state, but this contribution to total energy is generally rather small and, therefore, is omitted herein for purposes of simplification. If one averages this molecular energy over a large number of molecules in an isothermal sample of the gas, the average energy per mole is given by the following equation:

$$E = \frac{3}{2} RT + RT + RT\left(\frac{h\nu}{kT}\right)\left(e^{\frac{h\nu}{kT}} - 1\right)^{-1}$$

The translational motion contributes $\frac{3}{2}$ RT, and the rotation contributes an average energy which asymptotically approaches RT. The characteristic temperature $T_r$ at which rotational energy is half excited is of

the order of $5°$ K, so that, for most practical purposes, air molecules in the gas phase are always fully excited in rotation. On the other hand, the molecular bond is so stiff that at normal temperatures the molecules are essentially rigid rotators. However, as temperature increases, the molecular collisions eventually become energetic enough to set the bond into vibration. The characteristic temperature $T_v$ at which vibrational energy is half excited is rather high, being of the order of $3,000°$ K.

The specific heat at constant density is the derivative of the average energy with respect to temperature. This specific heat for diatomic molecules is shown graphically in figure 2(a). It approaches $5R/2$ at very low temperatures and maintains a relatively constant value throughout the range of temperatures encountered at subsonic and low supersonic flight speeds. As vibrational energy becomes important at higher temperatures, the specific heat approaches $7R/2$.

At still higher temperatures, the molecular impacts become so intense that the bond is often stretched to the breaking point. Figure 2(b) illustrates a collision between two molecules which has just resulted in the dissociation of one of the molecules into two atoms. Again, if electronic energy is neglected, the energy of each atom is its kinetic energy plus one-half the energy stored in the broken bond $e_0/2$, as shown in the following equation:

$$e(u) = \left(\frac{m}{2}\right)\frac{u^2}{2} + \frac{e_0}{2}$$

The average energy for an isothermal mole of atoms is

$$E = \frac{3}{2} RT + \frac{D}{2}$$

As before, the kinetic energy contributes $\frac{3}{2} RT$. The constant $e_0$ is independent of temperature or velocity and contributes to the average energy the heat needed to dissociate 1 mol of the molecules D. The ratio $D/R$ is of the order of $50,000°$ K for oxygen and $100,000°$ K for nitrogen, so that the dissociation energy term is much larger than the average kinetic energy at the temperatures of interest in this study (up to about $15,000°$ K). The specific heat $dE/dT$ of the atoms, from figure 2(b), is about $\frac{3}{2}$ R.

Figure 3 shows the energy and specific heats for molecule-atom mixtures in equilibrium. In the following equations:

Energy:

$$E = (1 - x)E_m + xE_a$$

Specific heat:

$$\frac{\partial E}{\partial T} = (1 - x)\frac{dE_m}{dT} + x\frac{dE_a}{dT} - E_m\frac{\partial x}{\partial T} + (E_a)\frac{\partial x}{\partial T}$$

$E_m$ and $E_a$ are, respectively, the average energy per mol of molecules and of atoms, which has just been considered. The mol fraction of atoms $x$ is a function of the chemical equilibrium constant $K$ and pressure $p$, which can be calculated precisely (ref. 3), and the mol fraction of molecules is $1 - x$. In the equation for specific heat, the first two terms on the right-hand side are the sum of the specific heats for the components of the mixture, whereas the last two terms give the contribution due to the change in mol fractions. The derivative $\partial x/\partial T$, which can be expressed as a function of $x$ and the logarithmic derivative of the equilibrium constant, possesses a rather sharp maximum. The value of $\partial x/\partial T$ is small, but the value of $E_a$ is so large, because of the dissociation energy, that, where the mol fraction derivative is a maximum, the last term in the specific-heat equation is overwhelmingly predominant.

The graph in figure 3 shows the specific heat for air as a function of temperature at a pressure of 0.01 atmosphere and illustrates the striking effect of the chemical reactions. Near 3,000° K the specific heat has a pronounced maximum due to dissociation of oxygen, and again near 5,000° K the nitrogen dissociation is responsible for another peak. The last peak, near 10,000° K, is due to the reactions for single ionization of nitrogen and oxygen atoms. These two reactions occur together in the same range of temperature and a similar set of relations is obtained as for the dissociation reactions, except that the ionization energy $I$ is larger than the dissociation energy ($I/R$ is of the order of 150,000° K). The effect of pressure is that the maximums become larger and more peaked and shift to lower temperatures as pressure decreases.

It is convenient to relate the chemical reactions in air to the compressibility factor $Z$. This factor is the number of moles of gas which arise from a mol of air originally at normal conditions or, alternatively, it is the ratio of the molecular weight of normal air

to the mean molecular weight of the equilibrium gas. It represents the correction factor to the ideal gas equation of state. Figure 4 shows the compressibility factor for air as a function of temperature for pressures of 1.0, 0.01, and 0.0001 atmosphere.

The important reactions in air are also indicated in figure 4. These are: (1) the dissociation of oxygen

$$O_2 \leftrightarrows 2O$$
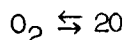
(2) the dissociation of nitrogen

$$N_2 \leftrightarrows 2N$$
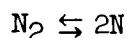
and (3) the reactions for single ionization of nitrogen and oxygen atoms

$$N \leftrightarrows N^+ + e^-$$

$$O \leftrightarrows O^+ + e^-$$
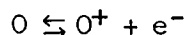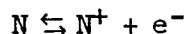
The ionization reactions occur at very nearly the same temperature and with the same energy changes so that they may be classed together as a single reaction, for purposes of approximation.

The foregoing reactions are the ones which largely determine the equilibrium concentration of the major components of air, and these components, in turn, establish the thermodynamic properties. At high pressures, nitric oxide NO becomes a sizable minor component of air but the thermodynamic properties of NO are about the average of those for $N_2$ and $O_2$, and, since the nitric oxide formation does not change the balance between molecules and atoms, it does not greatly influence the thermodynamic functions of air.

The compressibility is not influenced by vibrational excitation and, therefore, is equal to 1.0 until oxygen dissociation begins. Since air contains about 20 percent oxygen, the compressibility approaches 1.2 when oxygen dissociation is complete. It increases further to a value of 2.0 when nitrogen dissociation finishes the conversion of molecules into atoms. Single ionization of the atoms doubles the number of gas particles again, so that the compressibility approaches 4.0 when these reactions are complete.

The effects of the chemical reactions are most intense where the slope of the compressibility is a maximum. The most interesting feature

of these functions is that the slope of Z is nearly zero at the transition from one major reaction to another (fig. 4). This shows that one reaction is essentially complete before the next reaction starts, and in reference 5, for example, complete independence between the reactions is assumed in order to derive analytic solutions for the properties of high-temperature air. It is found that these analytic solutions are generally within 2 percent of the precise answers obtained by iteration (ref. 4). The most time-consuming portion of such calculations is finding the compressibility factor (or its equivalent, the component mol fractions). If less accuracy is sufficient, of the order of 10 percent, the compressibility function can be fitted empirically with hyperbolic tangents. The approximate formulas for compressibility, energy, and the specific heats through the range of the oxygen dissociation reaction (1 < Z < 1.2) are as follows:

$$Z(T,p) \approx 2.5 + 0.1 \tanh\left[\frac{T\left(1 - \frac{1}{8}\log\frac{p}{p_0}\right)}{500} - 7\right] \tag{1}$$

$$\frac{ZE}{RT} \approx (2 - Z)\left[\frac{5}{2} + \frac{3000}{T}\left(e^{3000/T} - 1\right)^{-1}\right] + (Z - 1)\left(3 + \frac{59000}{T}\right) \tag{2}$$

$$\frac{Zc_v}{R} \approx (2 - Z)\left[\frac{5}{2} + \left(\frac{1500/T}{\sinh\frac{1500}{T}}\right)^2\right] + 3(Z - 1) + \left(\frac{T}{2} + 59000\right)\left(\frac{\partial Z}{\partial T}\right)_p \tag{3}$$

$$\frac{Zc_p}{R} \approx \frac{Zc_v}{R} + Z + T\left(\frac{\partial Z}{\partial T}\right)_p \tag{4}$$

(log signifies the logarithm to the base 10). In view of the order of the approximation, an average vibrational frequency is assumed for both oxygen and nitrogen, the particles are treated as though they are all in the ground state of electronic excitation, and the difference between the partial derivatives of compressibility at constant pressure and at constant density is neglected. Note that the displacement of the compressibility function varies as the logarithm of pressure and that the thermodynamic properties are all given as functions of compressibility and temperature. Similar formulas are available, accurate to the order of 10 percent, through the nitrogen dissociation reaction and up to 10 percent ionization (Z < 2.2) and over a range of pressure from 100 to $10^{-4}$ atmospheres. This is a sufficient range of variables for

most practical aerodynamic problems (ref. 5). A complete set of these approximate formulas is as follows:

The compressibility is given by

$$Z \approx 2.5 + 0.1 \tanh\left(\frac{T^*}{500} - 7\right) + 0.4 \tanh\left(\frac{T^*}{1000} - 7\right) + \tanh\left(\frac{T^*}{2500} - 5.8\right) \quad (5)$$

where the reduced temperature is

$$T^* = T\left(1 - \frac{1}{8} \log \frac{p}{p_0}\right) \quad (6)$$

and the reference pressure $p_0$ is 1 atmosphere. The dimensionless energy is

For case I, oxygen dissociation only ($1.0 < Z < 1.2$):

$$\frac{ZE}{RT} \approx (2 - Z)\left[\frac{5}{2} + \frac{3000}{T}\left(\exp \frac{3000}{T} - 1\right)^{-1}\right] + (Z - 1)\left(3 + \frac{59000}{T}\right) \quad (7a)$$

For case II, nitrogen dissociation only ($1.2 < Z < 2.0$):

$$\frac{ZE}{RT} \approx (2 - Z)\left[\frac{5}{2} + \frac{3000}{T}\left(\exp \frac{3000}{T} - 1\right)^{-1}\right] + 0.2\left(3 + \frac{59000}{T}\right) +$$

$$(Z - 1.2)\left(3 + \frac{113000}{T}\right) \quad (7b)$$

For case III, ionization reactions only, up to about 10 percent ionization ($2.0 < Z < 2.2$):

$$\frac{ZE}{RT} \approx (4 - Z)\left(\frac{3}{2} + \frac{51000}{T}\right) + (Z - 2)\left(3 + \frac{220000}{T}\right) \quad (7c)$$

The enthalpy  H  is easily found from the relation

$$\frac{ZH}{RT} = \frac{ZE}{RT} + Z \tag{8}$$

For cases I and II, the entropy  S  is approximately given by

$$Z\left(\frac{S}{R} + \log_e \frac{p}{p_o}\right) \approx (2 - Z)\left\{\frac{7}{2}(\log_e T + 1) - \log_e\left[1 - \exp\left(-\frac{3000}{T}\right)\right] + \right.$$

$$\left. \frac{3000}{T}\left(\exp \frac{3000}{T} - 1\right)^{-1} - \log_e \frac{2 - Z}{Z}\right\} +$$

$$2(Z - 1)\left[\frac{5}{2}(\log_e T + 1) + 2.3 - \log_e \frac{2(Z - 1)}{Z}\right] \tag{9a}$$

and for case III,

$$Z\left(\frac{S}{R} + \log_e \frac{p}{p_o}\right) \approx \frac{5Z}{2}(\log_e T + 1) + 4.6 - (Z - 2)\left(2 \log_e \frac{Z - 2}{Z} + \right.$$

$$\left. 14.2\right) - (4 - Z)\log_e \frac{4 - Z}{Z} \tag{9b}$$

The electronic excitation has been accounted for in the entropy functions by adding constant values equal to the average of the logarithm of the electronic partition function over the temperature range of interest.

For the specific heat, the derivative of compressibility with temperature is required.  It is given by

$$\left(\frac{\partial Z}{\partial T}\right)_p \approx 0.0002\left(1 - \frac{1}{8} \log \frac{p}{p_o}\right)\left[\operatorname{sech}^2\left(\frac{T^*}{500} - 7\right) + 2 \operatorname{sech}^2\left(\frac{T^*}{1000} - 7\right) + \right.$$

$$\left. 2 \operatorname{sech}^2\left(\frac{T^*}{2500} - 5.8\right)\right] \tag{10}$$

If the correction for taking the partial derivative at constant pressure is disregarded, the specific heat at constant density becomes

For case I:

$$\frac{Zc_V}{R} \approx (2 - Z)\left[\frac{5}{2} + \left(\frac{1500/T}{\sinh\frac{1500}{T}}\right)^2\right] + 3(Z - 1) + \left(\frac{T}{2} + 59{,}000\right)\frac{\partial Z}{\partial T} \quad (11a)$$

For case II:

$$\frac{Zc_V}{R} \approx (2 - Z)\left[\frac{5}{2} + \left(\frac{1500/T}{\sinh\frac{1500}{T}}\right)^2\right] + 3(Z - 1) + \left(\frac{T}{2} + 113{,}000\right)\frac{\partial Z}{\partial T} \quad (11b)$$

For case III:

$$\frac{Zc_V}{R} \approx \frac{3Z}{2} + \left(\frac{3T}{2} + 167{,}000\right)\frac{\partial Z}{\partial T} \quad (11c)$$

The specific heat at constant pressure is

$$\frac{Zc_p}{R} \approx \frac{Zc_V}{R} + Z + T\frac{\partial Z}{\partial T} \quad (12)$$

and to the order of these approximations the speed of sound is given by

$$\frac{a^2\rho}{p} \approx \gamma = \frac{\left(\dfrac{Zc_p}{R}\right)}{\left(\dfrac{Zc_V}{R}\right)} \quad (13)$$

The dimensionless energy is shown in figure 5 as a function of temperature for pressures of 0.0001, 0.01, and 1.0 atmosphere. The results given by the approximate formulas compare favorably with more precise calculations (refs. 4 and 5). The greatest errors occur in the region of the ionization reactions, where a simple empirical form for the compressibility function does not seem entirely adequate.

As expected, the accuracy of the approximate formulas for the specific heats is not as good as for energy, since derivatives of compressibility are involved. Still, the ratio of the specific heats is not greatly different from more precise calculations of the speed-of-sound parameter $a^2\rho/p$, as shown in figure 6. This parameter is useful, for example, in computing solutions for air flow by the method of characteristics. The largest deviations occur at the transitions between one reaction and the next, where the speed-of-sound parameter is a maximum.

## TRANSPORT PROPERTIES OF AIR

The transport properties of gases can all be related to the effective size of gas particles during collisions (refs. 6 and 7). The smaller the size, the larger is the mean free path between collisions; then the transport occurs between regions of the gas having greater differences in momentum and energy. Consequently, the coefficients of viscosity and thermal conductivity vary inversely with the size of the gas particles. Figure 7 shows qualitatively the form of the potential functions between the particles from which the collision diameters are determined. Consider first the potential between inert molecules. At long range, the potential has a very shallow minimum which at normal or higher temperature is very small compared with the kinetic energy of the colliding molecules. This is the portion of the potential associated with the weak Van der Waals forces of attraction. At shorter range, the potential rapidly approaches very large positive values and the interparticle forces are strongly repulsive. The path of one molecule with respect to another during collision is shown for two typical cases by the black balls which roll into the potential well, penetrate the positive column, and are deflected back into potential-free space. The depth of the penetration increases with increasing kinetic energy of the relative motion between molecules.

The effective collision diameter $\sigma$ is roughly the diameter of the molecular volume which is not penetrated by the collisions and, on the average, it is approximately the diameter where the molecular potential equals $+kT$. The collision cross section is by definition $\pi\sigma^2$. From the shape of the potential, it can be seen that the collision diameter depends on the energy of the collisions and is, therefore, a function of temperature. At high temperatures, however, the extremely steep portion of the potential is penetrated and the collision cross section is relatively constant, independent of temperature. Then the molecules behave essentially as hard elastic spheres, for which the coefficient of viscosity varies as the one-half power of the temperature. The Sutherland correction to the coefficient of viscosity accounts reasonably

well for the effective increase in collision diameter at low temperatures. Where more precise estimates are required, the methods developed by Hirschfelder and others (ref. 6) are very useful for calculating the transport properties of inert gases.

The transport properties of air at high temperatures are in doubt mainly because of uncertainty about the cross sections for atom-atom and atom-molecule collisions. Two atoms, for example, may approach one another along any one of a number of different potentials depending upon how the electron spin vectors add up. This multiplicity of potentials is indicated by the dashed lines on the atom-atom potential diagram of figure 7. The only one of these potentials which is known quantitatively at present is the lowest lying potential associated with the lowest total electron spin. This is the potential responsible for the vibrational energy levels observed in the stable diatomic molecule. The distinctive feature of this potential is its negative well which is very deep compared with the kinetic energy of collisions at the temperatures of interest herein. In fact, the depth of this well is just the dissociation energy of the diatomic molecules. As pointed out previously this energy corresponds to temperatures of about $50,000°$ K for oxygen and of about $100,000°$ K for nitrogen. Consider the collisions illustrated by the paths of the three black balls rolling into this potential well (fig. 7). The atom, which has a kinetic energy much larger than the absolute value of the potential field through which it traverses, will not be greatly deflected. Now it is the absolute value of the deflection produced by a collision which influences the flux of mass, momentum, or energy through the gas; hence, for practical purposes this collision, which produced only a small deflection, may be considered a miss. On the other hand, an atom which penetrates the volume where the potential change is about equal to its kinetic energy will suffer a considerable deflection, and such a collision will count. It is not essential that the repulsive, positive portion of the potential be penetrated, as in the third collision shown on the right in figure 7. In the subsequent estimates of the transport properties, it will be assumed that the effective diameter for atom-atom collisions is where the lowest lying potential equals  -kT  and that the diameter for atom-molecule collisions is the arithmetic average of the atom-atom and the molecule-molecule diameters. This latter assumption corresponds to the concept that the collision diameter is a measure of the effective range of the electron distribution about the nucleus and that a collision occurs whenever these electron distributions overlap. In the case of collisions between ions or between electrons, the well-known coulomb potential $\pm e^2/r$ may be used in a similar way. For collisions between a neutral and a charged particle, the potential for the interaction between the charge and the induced dipole is used.

The coefficient of viscosity, which is based on the preceding assumption (ref. 5), is shown in figure 8 as a function of temperature for three pressures: 1.0, 0.01, and 0.0001 atmosphere. The ordinate is the ratio of the viscosity coefficient to the value given by a Sutherland type formula

$$\mu_o = 1.46 \times 10^{-5} T^{1/2} \left(1 + \frac{112}{T}\right)^{-1} \tag{14}$$

(in units of g/cm-sec). The ratio is unity until dissociation of molecules becomes appreciable; then the mean free path between molecular collisions becomes larger because the collision diameters for the atoms are smaller than for the molecules, the momentum exchange takes place between more widely separated planes in the gas, and the viscosity increases. On the other hand, the collision diameters become very large in an ionized gas, and then the reverse effect causes the viscosity to drop to very low values. Again, because of the regularity of the functions, it is possible to establish an empirical formula which approximates the temperature and pressure effect on viscosity. Such a formula is

$$\frac{\mu}{\mu_o} = \left\{1 + 0.023 \frac{T}{1000}\left[1 + \tanh \frac{\frac{T}{1000}\left(1 - \frac{1}{8}\log\frac{p}{p_o}\right) - 6.5}{1.5 + \frac{1}{8}\log\frac{p}{p_o}}\right]\right\} \times$$
$$\exp^{-1}\left(\frac{\frac{T}{1000} - 14.5 - 1.5\log\frac{p}{p_o}}{0.9 + 0.1\log\frac{p}{p_o}}\right) \tag{15}$$

(log signifies the logarithm to the base 10). The comparison between equation (15) and the viscosity function is shown in figure 8.

The coefficient of thermal conductivity is shown as a function of temperature for pressures of 1.0 and 0.01 atmosphere in figure 9. Again, the coefficient is referenced to a coefficient of the Sutherland form:

$$k_o = 4.76 \times 10^{-6} T^{1/2}\left(1 + \frac{112}{T}\right)^{-1} \tag{16}$$

(in units of cal/cm-sec-°K). The calculation of these coefficients is based on the method outlined by Hirschfelder (ref. 8) and developed further by Butler and Brokaw (ref. 9). In this method, the energy transfer

through the gas is treated in two independent parts. One part is the energy transferred by collisions as in ordinary thermal conductivity of nonreacting gases. The other part is the energy transferred by diffusion of the gas particles and the reactions which occur to reestablish chemical equilibrium. This latter part predominates wherever the compressibility derivative with respect to temperature becomes a maximum. The effect is very much like the effect on the specific heats. In fact, the thermal conductivity ratio $k/k_O$ is nearly proportional to the specific heat just as for inert gases, so that a reasonably good approximation is

$$\frac{k}{k_O} \approx \frac{c_p}{3.5R} \tag{17a}$$

The comparison between the thermal conductivity and the approximate specific heat given by equation (12) is indicated in figure 9.

The relation given by equation (17a) is good only for the dissociation reactions. Where ionization occurs, the thermal conductivity is greatly increased because of the high thermal velocity of the lightweight electrons. Then the thermal conductivity is approximately given up to about 10 percent ionization by

$$\frac{k}{k_O} \approx 3\left(1 + \frac{1}{4} \log \frac{p}{p_O}\right)\frac{c_p}{3.5R} \tag{17b}$$

It is desirable to check the foregoing theoretical calculations and approximations with experiment. One of the more striking effects predicted by the theory is the pronounced effect on thermal conductivity of gases in which chemical reactions occur. This effect has been observed experimentally in dissociating $N_2O_4$ by Coffin and O'Neal at the Lewis Flight Propulsion Laboratory (ref. 10). As figure 10 shows, their experiments are in very good agreement with the theoretical prediction for the equilibrium gas. The results strongly suggest that the basic relations established by Hirschfelder (ref. 8) are essentially correct. Unfortunately, the thermal dissociation of air cannot be studied at such tractable temperatures as in the case of $N_2O_4$. However, high-temperature air can be produced in the shock tube for short intervals, and figure 11 shows the correlation between measured and theoretical thermal conductivity in air, which has been obtained at the Ames Aeronautical Laboratory. In these experiments, strong shock waves are reflected from the closed end of a shock tube, and a temperature is measured at the interface between the hot stationary air and a quartz glass plug. The temperature is deduced by measuring the change in resistance of a thin film of nickel evaporated onto the glass. If it is assumed that the air is in equilibrium and has a constant thermal diffusivity $k/c_p\rho$, the interface

temperature rises instantaneously to a constant value which is related to the diffusivity of air and of the glass plug (ref. 11). As will be pointed out later, the dissociation of air may be rapid enough to justify the assumption of instantaneous equilibrium. Thermal diffusivity will not be constant in the air, of course, but at least the strong variations in heat capacity and thermal conductivity will cancel each other. In any event, when the experimental data are correlated in this manner, they compare reasonably well with the theoretical predictions. No consistent data exist yet in the really interesting region where a maximum in the coefficient is predicted because of oxygen dissociation.

Ordinarily, the equilibrium thermodynamic and transport properties that have just been discussed would be sufficient to determine the character of gas flow uniquely. However, the chemical reactions in air proceed with a finite rate. When the time required for approach to equilibrium compares with the time needed for a sample of air to pass through a disturbed region of the flow field, the chemical reaction rates become another set of independent parameters on which the flow depends. These parameters are discussed in the following section.

## CHEMICAL REACTION RATES

Before discussing the finite reaction rates, simple flows are compared for the two limiting cases: (1) The reaction is frozen and (2) the reaction is in equilibrium.

The effect of chemical reactions in equilibrium on the flow behind a normal shock wave is well-known (ref. 12) and detailed calculations are available for air (refs. 13, 14, and 15). Figure 12 shows typical effects on the density, pressure, and temperature. If the reactions were infinitely slow, air would behave as an ideal gas, and this condition is designated as frozen flow. However, the reaction rates are finite and, as the flow approaches equilibrium, the temperature is greatly reduced because thermal energy is soaked up in exciting vibrations and in breaking chemical bonds. The pressure is not greatly influenced by the reactions, and the drop in temperature is compensated by a large increase in density.

Reference 16 gives an analysis for flow that maintains chemical equilibrium while expanding around a corner, and a numerical example is given in figure 13 for air which is initially at $6,140^\circ$ K and 1.2 atmospheres. The effect of the reaction in this case is to increase the temperature over the nonreacting value because the recombining gas now gives up the energy that is contained in dissociation and vibration. Thus the gas cools much more slowly during the expansion than a nonreacting gas. From figure 13 it is seen that, during the Prandtl-Meyer

expansion, it is the density which is relatively little affected by the reactions and that it is the pressure which adjusts with the temperature change this time. This is in marked contrast to the effects of reactions on the shock compression.

Now the reaction rates depend on the number of molecular collisions per unit time, and these collisions are more frequent the higher the density and the higher the temperature. At the high densities which occur in low altitude flight, the rates are very rapid and air flows are essentially in complete equilibrium. On the other hand, at very high altitudes where densities are very low, the reaction rates are so slow that flow may be essentially frozen. At intermediate altitudes, it is necessary to consider the reaction rate, from which can be derived the characteristic time in which the gas decays to chemical equilibrium. In a flowing gas, the quantity of interest is a characteristic length obtained by multiplying the time by the flow speed. This characteristic length is used for example in calculations of one-dimensional flows in references 17 and 18.

Figure 14 shows the lengths required to reach vibrational equilibrium in the flow downstream of a normal shock wave at various altitudes and velocities. Relaxation effects are important where this length compares in magnitude with a length such as the shock-detachment distance. At low velocities, where low temperatures occur, the reactions have a trivial effect, as indicated by the shaded portion of the figure. It is seen that, for a wide range of speeds and altitudes, the vibrations may be regarded as being in equilibrium. At altitudes below 150,000 feet, the finite length generally needs to be considered only for vehicles moving slower than 10,000 feet per second. At 240,000 feet, the vibrational relaxation will be important at the stagnation region for vehicles traveling less than 25,000 feet per second. The calculations for these curves are based on Blackman's experimental values for vibrational relaxation (ref. 19). These agree fairly well with the theory of Schwartz and Herzfeld (ref. 20) and the calculations are probably correct within a factor of 5, at least. In contrast, the existing knowledge of dissociation rates is extremely uncertain. The theoretical calculations require some severe mathematical approximations (ref. 21), and experiments have been made only recently which fix the reaction rates within several orders of magnitude (refs. 22 and 23). Despite the value of these recent data, the state of knowledge is still far from satisfactory, as is illustrated in figure 15. This figure shows the three-body recombination rate as a function of temperature for the recombination of oxygen and nitrogen atoms and for the recombination of atoms in air. The third body  M  in the collision serves to carry away the excess energy released by the recombination so that the newly formed molecule can be stable. In view of the uncertainty in the experimental data, the theory developed by Wigner (ref. 21) has been used to calculate the characteristic reaction lengths in dissociating flow. In applying this

theory it has been assumed that the third body in the recombination reaction is a hard elastic sphere and that the potential between atoms is the same one used earlier to evaluate the transport properties. The same expression is used for the recombination rate of both the oxygen and nitrogen atoms.

Figure 16 shows the results for the flow lengths required to reach oxygen dissociation equilibrium downstream of a normal shock. The same functional relations occur as for vibrations; that is, relaxation becomes increasingly important at higher altitudes and lower velocities. For nitrogen dissociation, all curves in figure 16 would be shifted to the left so that the curve for a velocity of 10,000 feet per second for nitrogen roughly coincides with the curve for a velocity of 15,000 feet per second for oxygen; it would fall in the "reaction negligible" region. (See fig. 1.) Similarly, the curve of 15,000 feet per second for nitrogen shifts roughly to the curve of 20,000 feet per second for oxygen.

Above an altitude of 250,000 feet, the typical vehicle enters slip flow and, as the altitude increases further, the shock wave eventually disappears. Under these conditions, molecular impact on surfaces is a more important phenomenon than those associated with the continuum air-flow properties. Thus, in any case, the relaxation effects need to be considered only over a finite range of velocity and altitude.

CONCLUDING REMARKS

It has been found that a fairly satisfactory state of scientific knowledge exists with respect to the equilibrium thermodynamic properties of air, that the knowledge of the transport properties leaves something to be desired, and that the state of theory and experiment on chemical reaction rates is quite inadequate. For example, equilibrium thermo-dynamic properties can be calculated very precisely by iteration methods, to the order of 1/2 percent or better; closed-form analytic solutions for these properties are accurate to the order of 2 to 5 percent; and approximate semiempirical formulas are available for rough engineering estimates which are good to the order of 10 to 20 percent. For transport properties, good theoretical methods for calculating collision cross sections are not yet available; the approximations used have an uncertainty of the order of 50 percent, but the order of magnitude and the functional relationships which have been estimated for these properties are probably correct. Vibrational relaxation rates are approximately known, but the dissocia-tion rates are still uncertain by several orders of magnitude. However, much effort is being focused on these problems, and it is reasonable to anticipate that adequate solutions for aerodynamic purposes will soon be forthcoming.

# REFERENCES

1. Herzberg, Gerhard: Molecular Spectra and Molecular Structure. I. Spectra of Diatomic Molecules. Second ed., D. Van Nostrand Co., Inc., c.1950.

2. Moore, Charlotte E.: Atomic Energy Levels. Cir. 467, Nat. Bur. Standards.
   Vol. I - 1H-23V, June 15, 1949.
   Vol. II - 24Cr-41Nb, Aug. 15, 1952.

3. Gilmore, F. R.: Equilibrium Composition and Thermodynamic Properties of Air to 24,000°K. U. S. Air Force Project RAND Res. Memo. RM-1543, The RAND Corp., Aug. 24, 1955. (Also available from ASTIA as AD 84052.)

4. Hilsenrath, Joseph, and Beckett, Charles W.: Tables of Thermodynamic Properties of Argon-Free Air to 15,000° K. AEDC-TN-56-12, Arnold Eng. Dev. Center, Sept. 1956. (Also available from ASTIA as Doc. No. AD-98974.)

5. Hansen, C. Frederick: Approximations for the Thermodynamic and Transport Properties of High-Temperature Air. NACA TN 4150, 1958.

6. Hirschfelder, Joseph O., Curtiss, Charles F., and Bird, R. Byron: Molecular Theory of Gases and Liquids. John Wiley & Sons, Inc., c.1954.

7. Kennard, Earle H.: Kinetic Theory of Gases. McGraw-Hill Book Co., Inc., 1938.

8. Hirschfelder, Joseph O.: Heat Transfer in Chemically Reacting Gas Mixtures. Jour. Chem. Phys., vol. 26, no. 2, Feb. 1957, pp. 274-281.

9. Butler, James N., and Brokaw, Richard S.: Thermal Conductivity of Gas Mixtures in Chemical Equilibrium. Jour. Chem. Phys., vol. 26, no. 6, June 1957, pp. 1636-1643.

10. Coffin, Kenneth P., and O'Neal, Cleveland, Jr.: Experimental Thermal Conductivities of the $N_2O_4 \rightleftarrows 2NO_2$ System. NACA TN 4209, 1958.

11. Mersman, W. A., Berggren, W. P., and Boelter, L. M. K.: The Conduction of Heat in Composite Infinite Solids. Univ. of California Pub. in Eng., vol. 5, no. 1, 1942, pp. 1-22.

12. Bethe, H. A., and Teller, E.: Deviations From Thermal Equilibrium in Shock Waves. Rep. No. X-117, Ballistic Res. Lab., Aberdeen Proving Ground, 1945.

13. Feldman, Saul: Hypersonic Gas Dynamic Charts for Equilibrium Air. AVCO Res. Lab., Jan. 1957.

14. McKowen, Paul: The Equilibrium Composition and Flow Variables for Air Dissociated by a Strong Shock Wave. Rep. No. 02-984-040, Bell Aircraft Corp., Mar. 8, 1957.

15. Hochstim, Adolf R.: Gas Properties Behind Shocks at Hypersonic Velocities. I. Normal Shocks in Air. Rep. No. ZPh(GP)-002, CONVAIR, Jan. 30, 1957.

16. Heims, Steve P.: Prandtl-Meyer Expansion of Chemically Reacting Gases in Local Chemical and Thermodynamic Equilibrium. NACA TN 4230, 1958.

17. Talbot, L.: The Structure of a Shock Wave in a Gas Having a Long Relaxation Time. Tech. Rep. HE-150-145, Inst. Eng. Res., Univ. of California, Mar. 1957.

18. Heims, Steve P.: Effect of Oxygen Recombination on One-Dimensional Flow at High Mach Numbers. NACA TN 4144, 1958.

19. Blackman, V.: Vibrational Relaxation in Oxygen and Nitrogen. Jour. Fluid Mech., vol. 1, pt. 1, May 1956, pp. 61-85.

20. Schwartz, Robert N., and Herzfeld, Karl F.: Vibrational Relaxation in Gases (Three Dimensional Treatment). Jour. Chem. Phys., vol. 22, no. 5, May 1954, pp. 767-776.

21. Wigner, E.: Calculation of the Rate of Elementary Association Reactions. Jour. Chem. Phys., vol. 5, no. 9, Sept. 1937, pp. 720-725.

22. Camac, M., Camm, J., Feldman, S. Keck, J., and Petty, C.: Chemical Relaxation in Air, Oxygen and Nitrogen. Preprint No. 802, S.M.F. Fund Preprint, Inst. Aero. Sci., Jan. 1958.

23. Christian, R. H., Duff, R. E., and Yarger, F. L.: Equation of State of Gases by Shock Wave Measurements. II. The Dissociation Energy of Nitrogen. Jour. Chem. Phys., vol. 23, no. 11, Nov. 1955, pp. 2045-2049.

## STAGNATION REGION CHEMISTRY

ALTITUDE, THOUSANDS OF FEET

400 — 300 — 200 — 100

VIBRATIONAL ENERGY EXCITED

OXYGEN DISSOCIATES $O_2 \rightarrow 2O$

NITROGEN DISSOCIATES $N_2 \rightarrow 2N$

IONIZATION OF ATOMS
$N \rightarrow N^+ + e^-$
$O \rightarrow O^+ + e^-$

VELOCITY, THOUSANDS OF FT/SEC

0    10    20    30    40
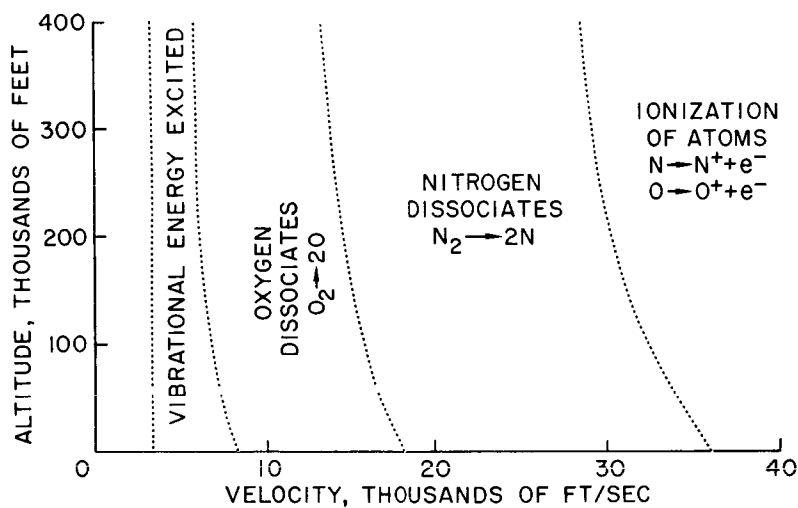
Figure 1

## DIATOMIC MOLECULE

ENERGY

$$e(u,J,n) = \frac{mu^2}{2} + J(J+1)\frac{h^2}{2I} + nh\nu$$

AVERAGE ENERGY

$$E = \frac{3}{2}RT + RT + RT\left(\frac{h\nu}{kT}\right)\left(e^{\frac{h\nu}{kT}}-1\right)^{-1}$$

SPECIFIC HEAT, $\frac{dE}{dT}$

$\frac{7R}{2}$
$\frac{5R}{2}$
$\frac{3R}{2}$

0    $T_V$

TEMPERATURE
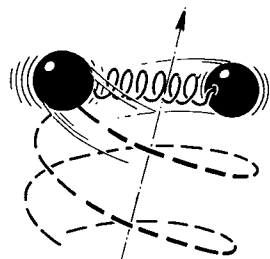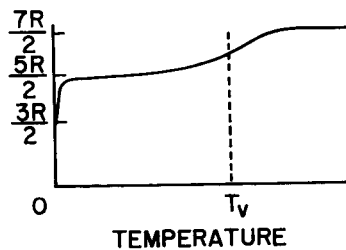
Figure 2(a)

ATOMS
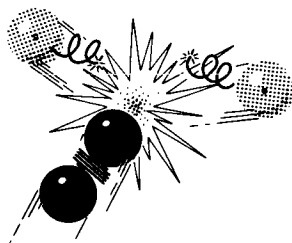
ENERGY

$$e(u)=\left(\frac{m}{2}\right)\frac{u^2}{2}+\frac{e_0}{2}$$

AVERAGE ENERGY

$$E=\frac{3}{2}RT+\frac{D}{2}$$

SPECIFIC HEAT

$$\frac{dE}{dT}=\frac{3}{2}R$$

Figure 2(b)

MOLECULE-ATOM MIXTURES IN EQUILIBRIUM

ENERGY:

$$E=(1-x)E_m+xE_a$$

SPECIFIC HEAT:

$$\frac{\partial E}{\partial T}=(1-x)\frac{dE_m}{dT}+x\frac{dE_a}{dT}$$
$$-E_m\frac{\partial x}{\partial T}+(E_a)\frac{\partial x}{\partial T}$$

mol fraction:

$$x=f(K,p)$$

mol fraction derivative:

$$\frac{\partial x}{\partial T}=g\left(\frac{\partial \log_e K}{\partial T},\ x\right)$$

AIR PRESSURE
.01 ATM

DIMENSIONLESS SPECIFIC HEAT, $\frac{1}{R}\left(\frac{\partial E}{\partial T}\right)\rho$

TEMPERATURE, THOUSANDS °K
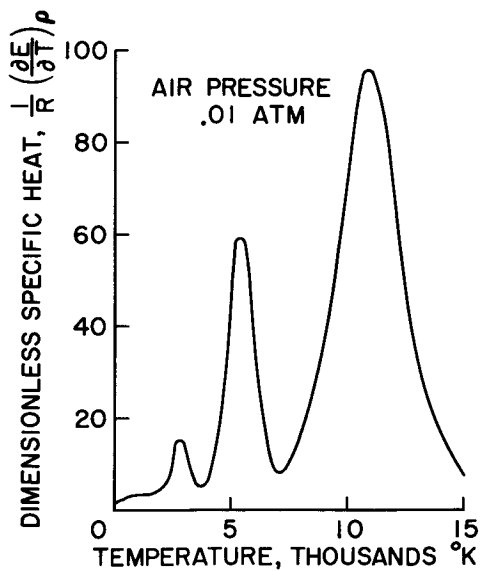
Figure 3

COMPRESSIBILITY FOR AIR IN EQUILIBRIUM
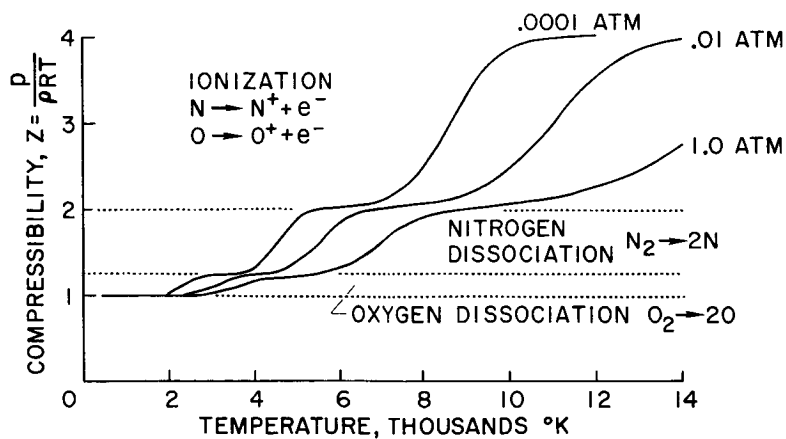


Figure 4

ENERGY OF AIR IN EQUILIBRIUM
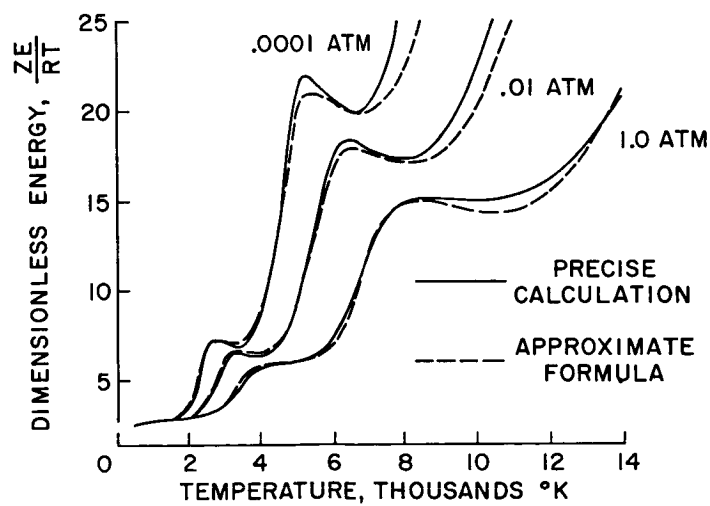


Figure 5

SPEED OF SOUND IN AIR
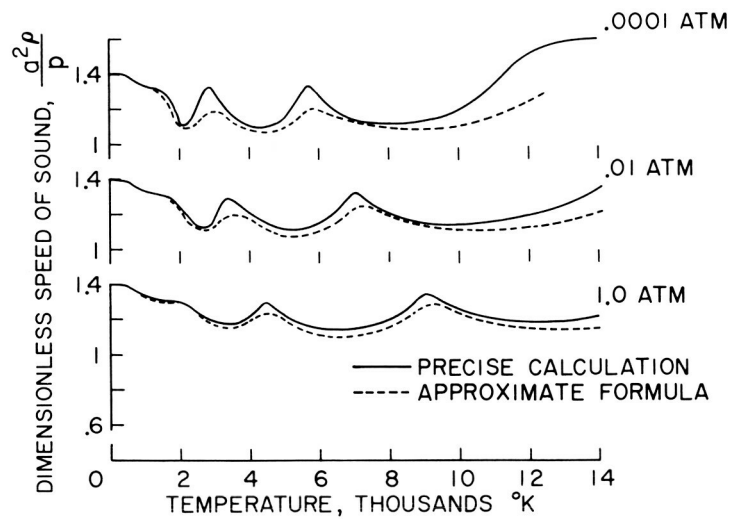


Figure 6
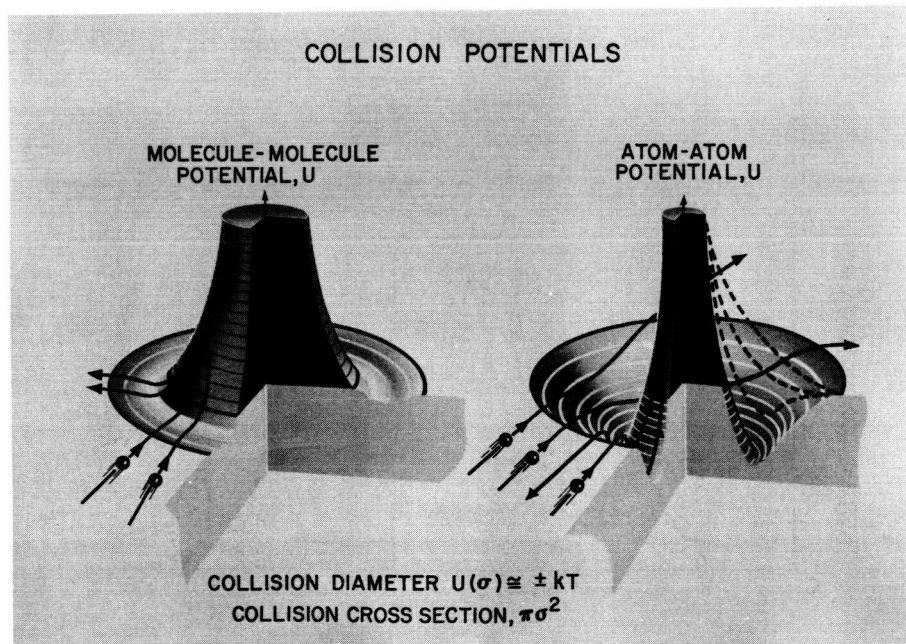


Figure 7

## VISCOSITY FOR AIR
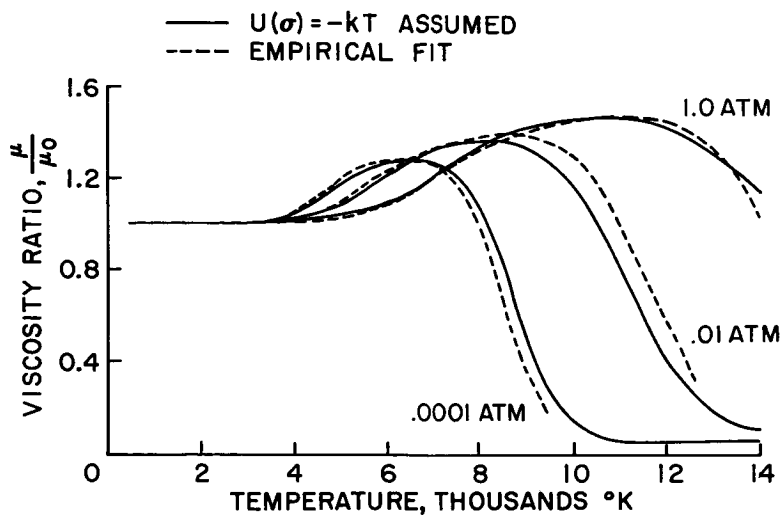


Figure 8

## THERMAL CONDUCTIVITY FOR AIR
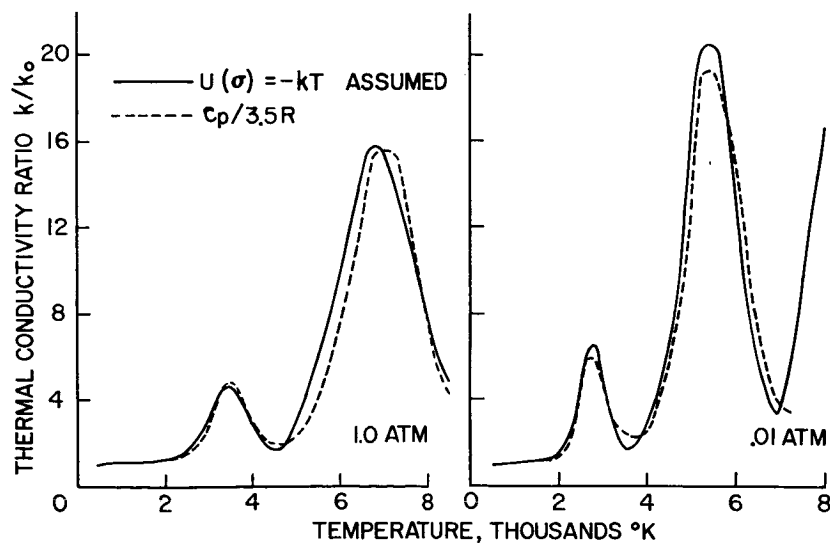


Figure 9

## THERMAL CONDUCTIVITY OF DISSOCIATING $N_2O_4$
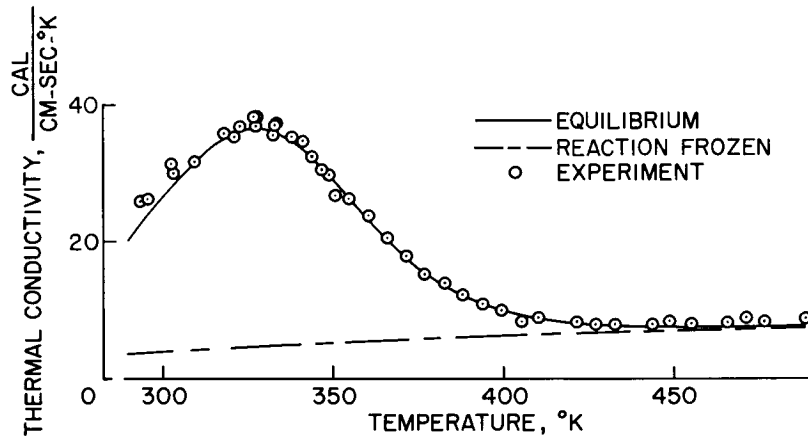


Figure 10

## THERMAL CONDUCTIVITY OF AIR
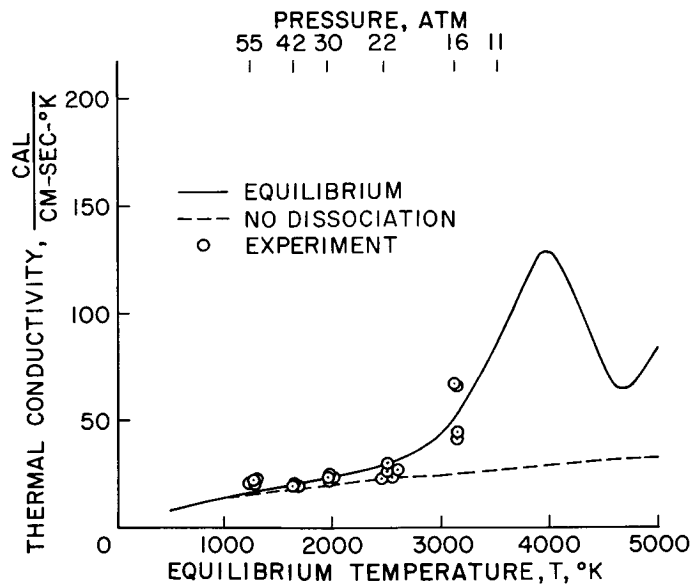


Figure 11

SHOCK COMPRESSION OF AIR



INITIAL CONDITIONS
160,000 FT ALTITUDE
.001 ATM, 288° K
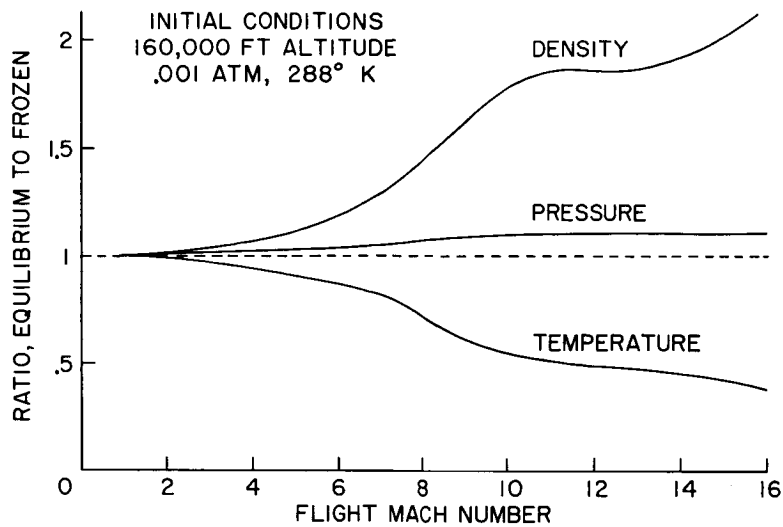
Figure 12

ISENTROPIC EXPANSION OF AIR



INITIAL CONDITIONS
6140° K, 1.2 ATM
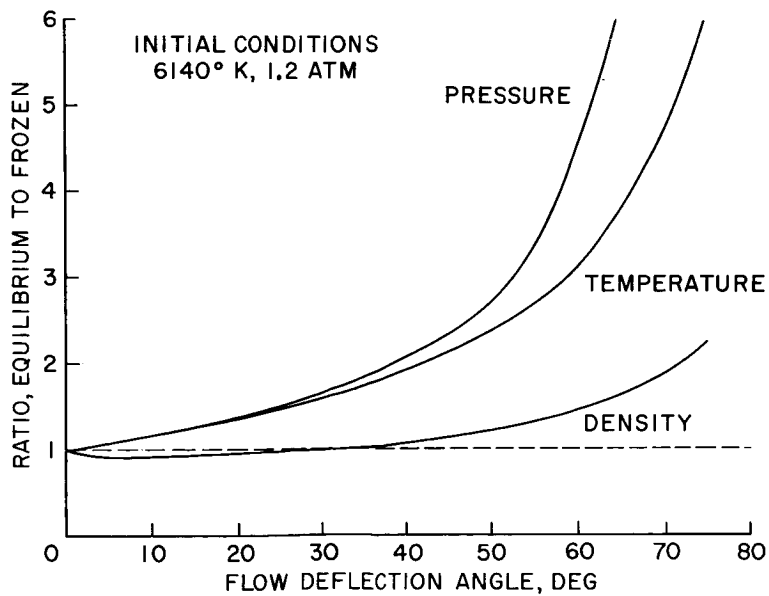
Figure 13

## MOLECULAR VIBRATIONS
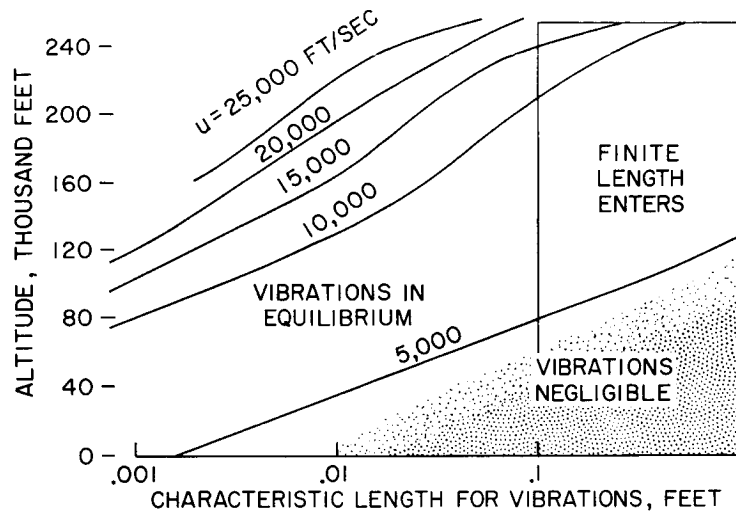
Figure 14

## CHEMICAL RECOMBINATION RATES

Figure 15

OXYGEN DISSOCIATION
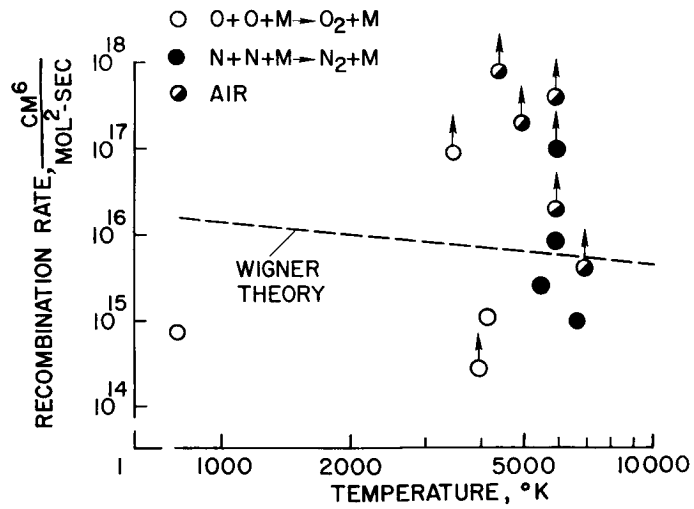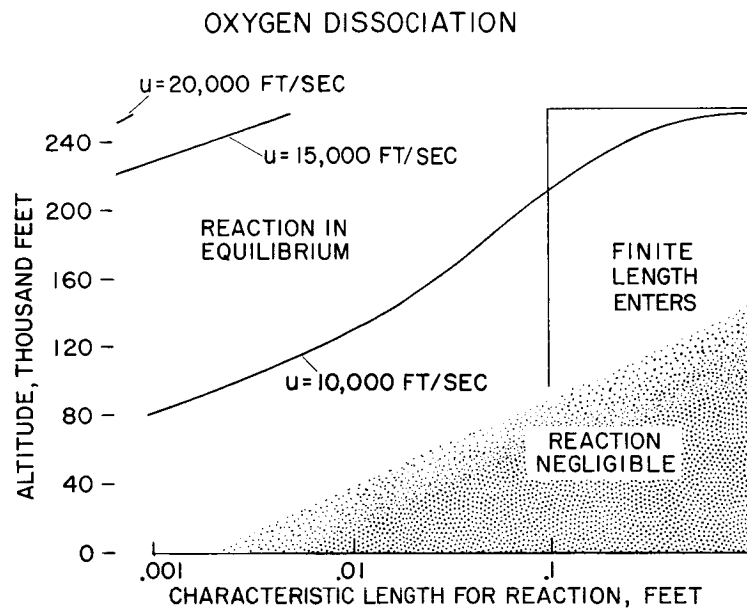


Figure 16

# TRANSITION ON SOME COOLED BLUNT AND SLENDER BODIES

By Richard J. Wisniewski

Lewis Flight Propulsion Laboratory

## INTRODUCTION

The most important requirement in the design of a successful reentry vehicle is an accurate prediction of the heating rates. Since the turbulent heating rates are an order of magnitude greater than the laminar rates, optimum design cannot be accomplished without a knowledge of when, where, and whether transition from laminar to turbulent flow will occur.

The present generation of reentry shapes will be a family of high-drag (blunt) shapes having low values of $W/C_D A$ (where $W$ is weight, $C_D$ is drag coefficient, and $A$ is cross-sectional area of the body). This is a most logical choice from a consideration of aerodynamic heating; since, for a given flow condition, laminar or turbulent, the high-drag shape absorbs less heat than the low-drag shape. Numerous experimental programs have been initiated to determine where transition will occur on the various shapes. At present, analysis of the transition results of these programs has not been too successful.

Although from a heating point of view, the high-drag shape offers more advantages as a reentry shape than the low-drag shape, it may be desirable to attain higher impact velocities and hence less error from wind drift. Therefore, low-drag bodies may be of interest as reentry shapes. In the present paper the prospects for laminar flow with large amounts of cooling for some high-drag (blunt) and low-drag (slender) bodies will be discussed.

## SYMBOLS

A          cross-sectional (frontal) area of body, sq ft

$C_D$        body drag coefficient

D          body diameter, in.

h          enthalpy

T           temperature, $^{\circ}R$

k           roughness height, ft

M           Mach number

$Re_k$      roughness Reynolds number,  $\dfrac{\rho_k U_k k}{\mu_k}$

$Re_{\delta*}$    displacement-thickness Reynolds number,  $\dfrac{\rho_e U_e \delta*}{\mu_e}$

$Re_{TR}$    transition Reynolds number,  $\dfrac{\rho_e U_e s}{\mu_e}$

$Re_\theta$    momentum-thickness Reynolds number,  $\dfrac{\rho_e U_e \theta}{\mu_e}$

d           nose diameter, in.

s           surface distance, ft

U           velocity, ft/sec

W           weight, lb

$\delta*$       boundary-layer displacement thickness, ft

$\theta$           momentum thickness, ft

$\mu$           viscosity, slugs/ft-sec

$\nu$           kinematic viscosity,  $\mu/\rho$, ft$^2$/sec

$\rho$           density, slugs/cu ft

Subscripts:

e           local free-stream conditions at edge of boundary layer

k           at top of roughness

w           conditions at wall

o           stagnation conditions behind shock

∞          free-stream conditions ahead of shock

TR         conditions at transition

## HIGH-DRAG SHAPES

The typical high-drag body that has been chosen for discussion is the hemisphere. Although the hemisphere is generally not considered to represent a realistic reentry shape, it does afford a basic geometric shape on which to study transition. Experimental data on cooled hemispheres are plentiful and any correlation of transition data should provide some sort of basis for correlating transition results on other high-drag shapes.

### Summary of Hemisphere Transition Data

In figure 1 the available transition data for cooled hemispheres from free-flight and wind-tunnel tests are presented as the ratio of wall enthalpy to local stream enthalpy $h_w/h_e$ plotted against the local transition Reynolds number based on momentum thickness $Re_{\theta,TR}$. When these data are analyzed in terms of $h_w/h_e$ and $Re_{\theta,TR}$, no correlation is indicated and, furthermore, no apparent effect of cooling is noted.

The cause of transition on cooled hemispheres is not known, and therefore several correlations have been attempted to determine what parameters strongly influence transition on cooled hemispheres. The most widely attempted correlations have relied on roughness as the correlating parameter.

### Roughness as a Correlation Parameter

Two of the most logical roughness correlation parameters are presented in figure 2. In figure 2(a), the ratio of roughness height to momentum thickness $k/\theta$ is plotted against the transition Reynolds number based on momentum thickness $Re_{\theta,TR}$ for several sets of cooled-hemisphere data. Examination of the NACA Langley data reveals that the highest values of $k/\theta$ yield the smallest values of $Re_{\theta,TR}$, whereas the smaller values of $k/\theta$ yield the largest values of $Re_{\theta,TR}$. Examination of the Lockheed X-17 data, however, shows no evident trend with the value of $k/\theta$. Therefore, although some type of roughness effect is suggested, it appears that $k/\theta$ is an inadequate parameter for correlation.

In figure 2(b), the mean value of the critical roughness Reynolds number for the NACA Langley and the Lockheed X-17 hemisphere flights and for various three-dimensional distributed-roughness tests is presented. The data for the hemispheres are from tests with very large amounts of cooling. The three-dimensional distributed-roughness tests, discussed in greater detail in a subsequent paper by Albert L. Braslow and Elmer A. Horton, are on bodies with little or no cooling. The roughness Reynolds number is defined in terms of the roughness height and local conditions evaluated at the roughness height. The critical roughness Reynolds number is that value of the roughness Reynolds number for which transition first moves from its natural position. In figure 2(b), the mean value of the critical roughness Reynolds number for a subsonic wing, a subsonic hemisphere, and a supersonic cone, is approximately 600. The roughness Reynolds number obtained in flights of cooled hemispheres, evaluated by using the roughness height measured before flight, yields values between 0.05 and 20. Therefore, assuming no large order change in the measured roughness during flight, it must be concluded that the roughness is not large enough to effect transition in the same manner as that found for the three-dimensional distributed-roughness tests of Braslow and Horton.

## Correlation of Hemisphere Data

Since doubtful, or little, success has been achieved with correlation parameters based on roughness, it is reasonable to examine correlation parameters that are independent of roughness. An empirical correlation parameter of this type is presented in figure 3. In figure 3(a), data from smooth hemispheres (1/2 to 6 microin.) are presented on a log-log scale as the ratio of wall enthalpy to total enthalpy $h_w/h_O$ plotted against the ratio of the local displacement-thickness Reynolds number to the local Mach number $Re_{\delta*}/M_e$. Examination of figure 3(a) shows that the transition data are well correlated and that the region between laminar and turbulent flow is well defined. It is also interesting to note in figure 3(a) that, at a constant value of the correlation parameter, cooling will cause the boundary layer to go from laminar flow to turbulent flow.

Presented in figure 3(b) are all the data[1] of figure 1 classified in terms of surface roughness and shown plotted as $h_w/h_O$ against $Re_{\delta*}/M_e$. Again, three regions are clearly defined: laminar, transitional, and turbulent. Now, however, the transition region is seen to

---

[1]The log-log scale restricts the inclusion of additional points that fall on the correlation curve but have negative values of the correlation parameter.

be influenced by the amount of roughness present on the hemisphere. Nevertheless, the data appear to be well correlated.

The method of applying the suggested correlation is presented in figure 4. In addition to the various correlation curves for the various degrees of surface roughness, the variation of the correlation parameter between an angular position of $20^{\circ}$ and $80^{\circ}$ is also included under three different conditions in a trajectory having a constant value of $h_w/h_o$. The correlation indicates that, at a given enthalpy ratio, three regions can be distinguished. When the variation of the correlation parameter along the body is such that it falls in region one, the flow on a body will be laminar even if the surface is quite rough. A second region exists where the flow is transitional. In this region the transition position depends a great deal on the roughness; that is, for a rough body, transition will occur far forward whereas, for a smooth body, transition will occur well back on a body. In a third region, the flow will be turbulent over most of the body even if the body is smooth within practical limits.

This correlation does not represent an answer to the entire problem of transition on cooled blunt bodies. The correlation parameter is of an empirical nature, and no physical model exists to base it on.

Correlation as Applied to Typical Reentry Conditions

In figure 5, the smooth-hemisphere correlation curve has been plotted on a regular scale, and the variation of the correlation parameter between angular positions of $20^{\circ}$ and $80^{\circ}$ is included for a hemispherical intercontinental ballistic missile (ICBM). The trajectory is for a 6-foot-diameter hemisphere having a value of $W/C_DA$ of 130 pounds per square foot. Extrapolating the correlation to the lower enthalpy levels and extending the correlation to include large-diameter bodies, as has been done in figure 5, clearly show that transition will occur on or near the $20^{\circ}$ position during the entire time of reentry. The results presented in this figure indicate a serious question as to the possibility of obtaining extensive laminar flow on a hemisphere under full-scale reentry conditions.

Extension of Correlation Parameter to Other Shapes

Since the actual ICBM reentry nose cones will not be hemispherical, it is desirable to show that the correlation of transition data from other shapes can be attained with the parameter $Re_{\delta*}/M_e$. A plot of the correlation parameter for both the hemisphere and a large blunt cone is

shown in figure 6. This figure shows that the correlation works equally well for the large blunt cone and that two distinct correlation curves are obtained. In fact, at a given enthalpy ratio, the blunt cone shape yields a larger value of $Re_{\delta*}/M_e$ than the hemisphere. This fact should not be interpreted to mean that, insofar as transition is concerned, one shape is superior to the other. Such a conclusion could be made only after studying both configurations under identical trajectories.

At this time it should be pointed out that the hemisphere is by no means the most suitable high-drag body for laminar flow. For example, under the same free-stream conditions, the flat-face body has demonstrated both lower heating rates and more extensive laminar flow than the hemispherical body. Although in this paper no attempt has been made to find the most suitable high-drag body for laminar flow, the parameter which correlates transition on at least two high-drag shapes have been presented.

## LOW-DRAG SHAPES

A typical low-drag shape is the slightly blunted cone. Since it has been demonstrated that transition data on sharp- and blunt-tip cones are in good agreement when local stream conditions are used, considerable data from sharp-tip cones will be considered applicable to blunt cones.

### Cooling Delays Transition on Cones

The ratio of wall temperature to local stream temperature $T_w/T_e$ plotted against the local transition Reynolds number $Re_{TR}$ for the transition data of both sharp- and blunt-tip cones is presented in figure 7. Examination of these data indicates that, with cooling, transition Reynolds numbers as great as $32 \times 10^6$ have been obtained in flight with sharp-tip cones.

At the present time, it appears that long laminar runs on slender reentry bodies are certainly feasible. However, two recent adverse trends have been found which raise questions regarding the possibility of extensive laminar flow on slender reentry shapes: transition reversal and early transition as found with excessive blunting.

## Transition Reversal

Experimental transition data obtained in a wind tunnel on a slightly blunted 9° 30' total-angle cone-cylinder indicate that, under certain conditions, cooling can have an adverse effect on the transition Reynolds number. This phenomenon, termed "transition reversal," is presented in figure 8. The data of this figure reveal the usual increase in the transition Reynolds number with moderate cooling. However, with increased cooling the trend is reversed, and transition occurs far forward on the cooled body. This transition-reversal phenomenon has been substantiated in free flight and in wind-tunnel tests in references 1 to 5. At present, no explanations have been completely successful in explaining all the various transition-reversal data. The data of reference 1 indicate an effect of roughness on transition reversal. However, analysis of all the available reversal data in terms of any roughness parameter suggested to date has not proved to be too successful. Therefore, although roughness certainly affects reversal, roughness as the cause of reversal has not been definitely established as yet. Furthermore, a combination of conditions with cooling are required to obtain transition reversal. At present, it has been established that, on reasonably smooth surfaces (less than 15 microin.), transition reversal has been obtained under a proper combination of local Mach number, unit Reynolds number, and low-temperature ratios.

## Transition as Affected by Blunting

Since all low-drag reentry bodies will require some amount of blunting, a flight program was initiated at the Lewis Flight Propulsion Laboratory to determine the effect of various amounts of blunting on transition. Preliminary results of this program are presented in figure 9. In this figure, the local transition Reynolds number $Re_{TR}$ has been plotted against the ratio of nose diameter to cone base diameter $d/D$ for constant-base-diameter cones under the same ambient conditions. These data show that, beyond a value of $d/D$ of 0.5, transition was observed at transition Reynolds numbers less than $1 \times 10^6$. Similar results at higher Mach number, which show the same trend, have also been obtained but are not presented here. It should be noted that, because full-scale slender reentry bodies will traverse approximately the flight conditions covered herein, the absolute tip size rather than the tip size in percent of cone base diameter is the important dimension. For these flight conditions the apparent limiting diameter was between 2 and 3 inches. Additional data are needed before any firm conclusions can be presented concerning this phenomenon. However, it does appear that there exists some degree of blunting beyond which low transition Reynolds number will be obtained on slender bodies even with

large amounts of cooling. Local conditions on the tip are in the laminar region of the blunt-body correlation when this downstream transition occurs.

## CONCLUDING REMARKS

In conclusion, it has been shown that a reasonable correlation of transition data for a hemisphere and a large blunt cone has been attained. Whether the parameter will be useful for other high-drag shapes remains to be seen. Furthermore, although the correlation does indicate that under certain conditions with cooling, transition will occur on the smoothest practical surfaces, an effect of roughness on transition is noted for the high-drag body.

On the low-drag body, examination of transition data reveals that long laminar runs are feasible, providing a determination can be made of the part transition reversal and blunting play in the transition picture.

## REFERENCES

1. Jack, John R., Wisniewski, Richard J., and Diaconis, N. S.: Effects of Extreme Surface Cooling on Boundary-Layer Transition. NACA TN 4094, 1957.

2. Seiff, Alvin, Sommer, Simon C., and Canning, Thomas N.: Some Experiments At High Supersonic Speeds on the Aerodynamic and Boundary-Layer Transition Characteristics of High-Drag Bodies of Revolution. NACA RM A56I05, 1957.

3. Rabb, Leonard, and Krasnican, Milan J.: Effects of Surface Roughness and Extreme Cooling On Boundary-Layer Transition For 15° Cone-Cylinder in Free Flight at Mach Numbers to 7.6. NACA RM E57K19, 1958.

4. Chauvin, Leo T., and Speegle, Katherine C.: Boundary-Layer Transition and Heat-Transfer Measurements From Flight Tests of Blunt and Sharp 50° Cones at Mach Numbers From 1.7 to 4.7. NACA RM L57D04, 1957.

5. Witt, W. R., Jr., and Persh, J.: A Correlation of Free-Flight Transition Measurements on Various Blunt Nose Shapes by Use of the Momentum-Thickness Reynolds Number. Proc. Aerodynamics Range Symposium, Jan. 1957. Rep. No. 1005, pt. I, Ballistic Res. Labs., Aberdeen Proving Ground, Mar. 1957, pp. 23-43.

# TRANSITION ON COOLED HEMISPHERES



Figure 1

222
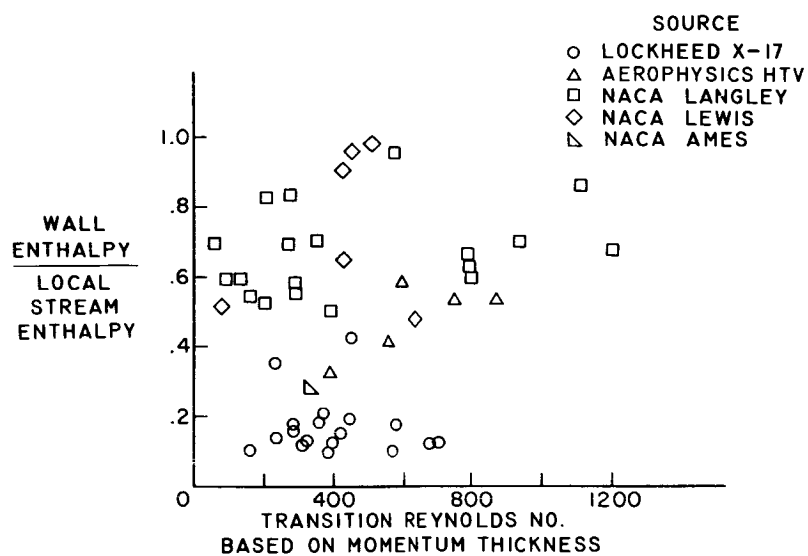
## ROUGHNESS AS A CORRELATION PARAMETER

### RATIO OF ROUGHNESS HEIGHT TO MOMENTUM THICKNESS
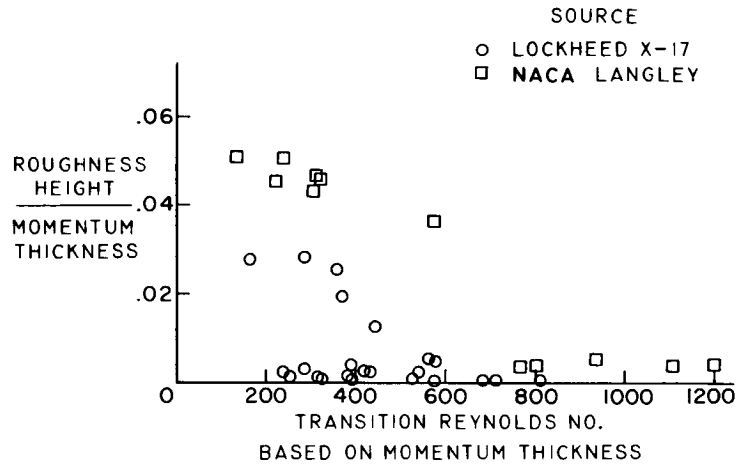


Figure 2(a)

## ROUGHNESS AS A CORRELATION PARAMETER

### CRITICAL ROUGHNESS REYNOLDS NO.
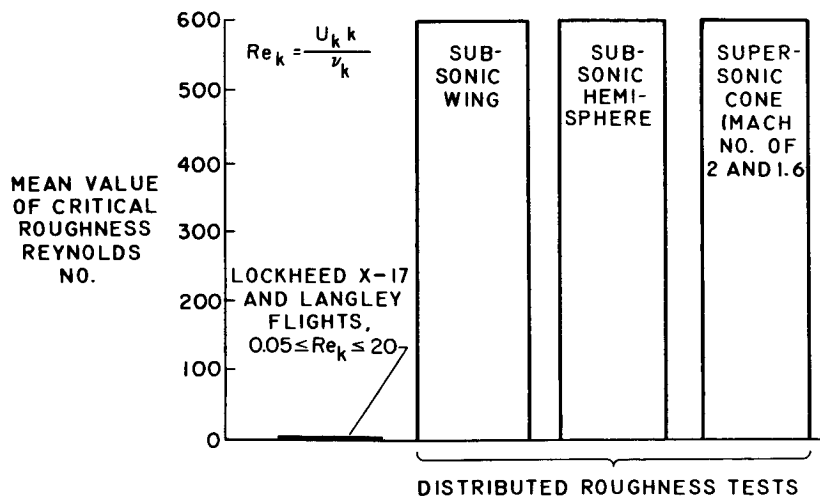


Figure 2(b)

# CORRELATION OF HEMISPHERE DATA
## SURFACES (1/2 TO 6 MICROIN.)

SOURCE
○ LOCKHEED X-17
△ AEROPHYSICS HTV
□ NACA LANGLEY
◇ NACA LEWIS
◺ NACA AMES

WALL ENTHALPY / TOTAL ENTHALPY

LAMINAR

TURBULENT

CORRELATION PARAMETER, $Re_{\delta^*}/M_e$
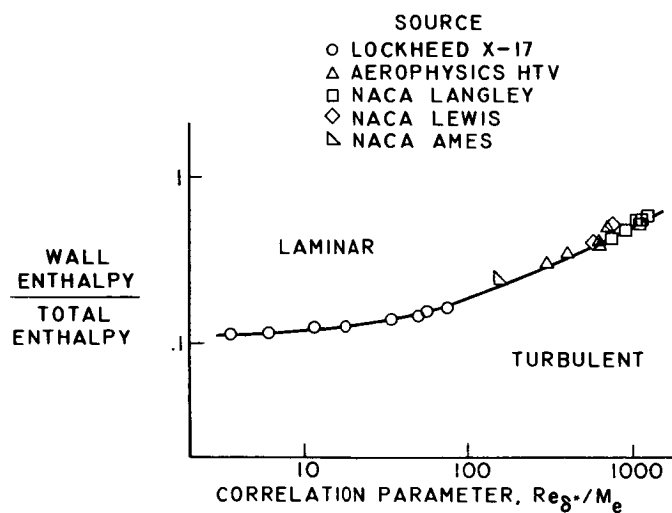
Figure 3(a)

# CORRELATION OF HEMISPHERE DATA
## ROUGHENED SURFACES

|  | SOURCE | SURFACE, MICROIN. RMS |
|---|---|---|
| ● | LOCKHEED X-17 | 20-30 |
| ■ | NACA LANGLEY | 25 |
| ◇ | NACA LEWIS | 145 |
| ▽ | NACA LANGLEY | >140 |

WALL ENTHALPY / TOTAL ENTHALPY

LAMINAR

TURBULENT

SMOOTH HEMISPHERE

CORRELATION PARAMETER, $Re_{\delta^*}/M_e$
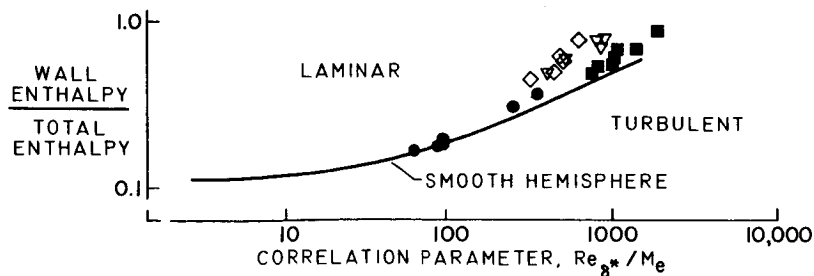
Figure 3(b)

## METHOD OF APPLICATION
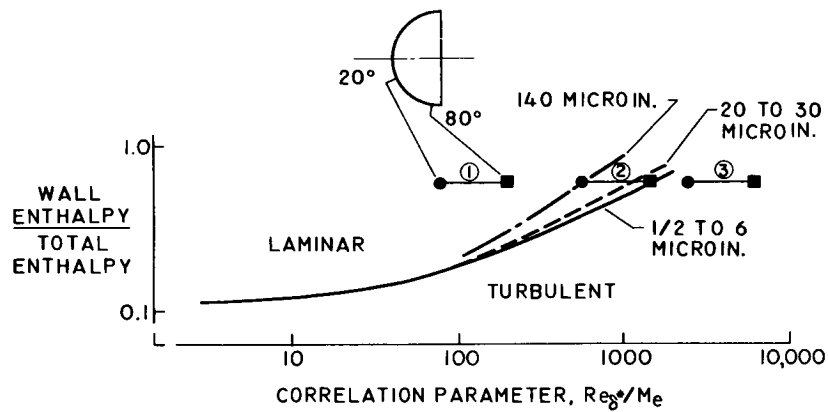


Figure 4

## HEMISPHERICAL ICBM REENTRY BODY

$W/C_D A$, 130 LB/FT$^2$, DIAM, 6 FT; $T_W$, 1000° R
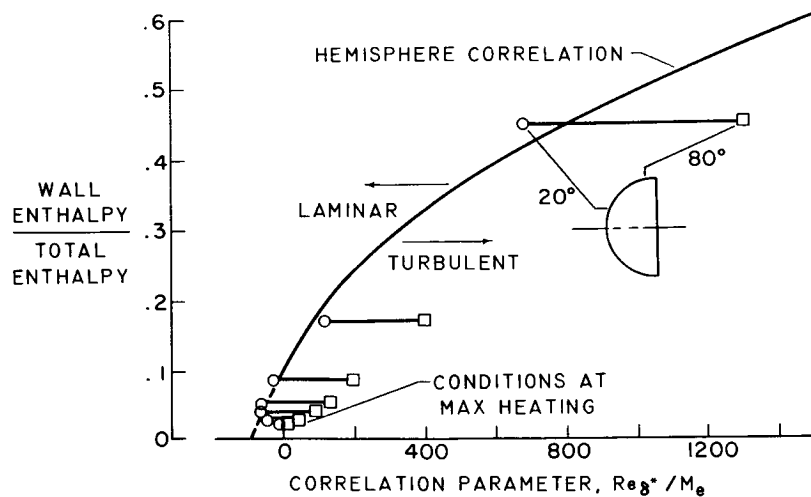


Figure 5

## VARIATION OF CORRELATION WITH BODY SHAPE
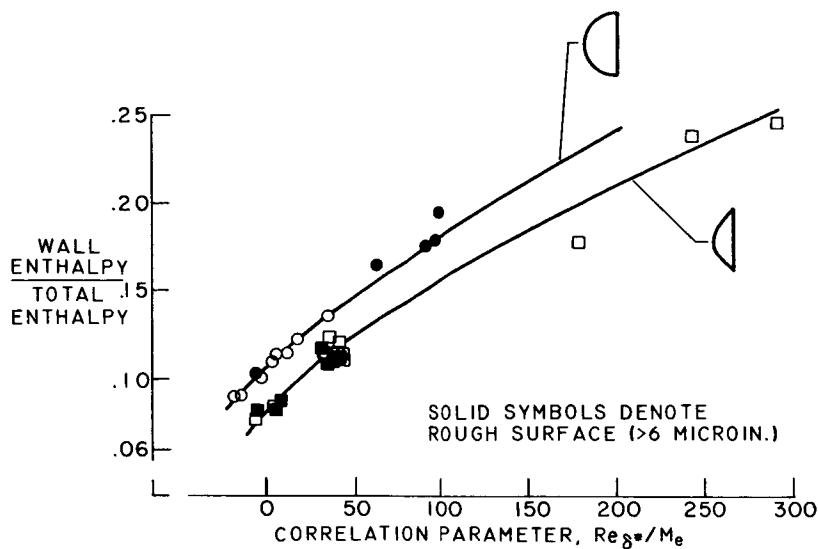


Figure 6

## FAVORABLE EFFECT OF COOLING ON TRANSITION

LOCAL MACH NO. 2 TO 4



Figure 7

226
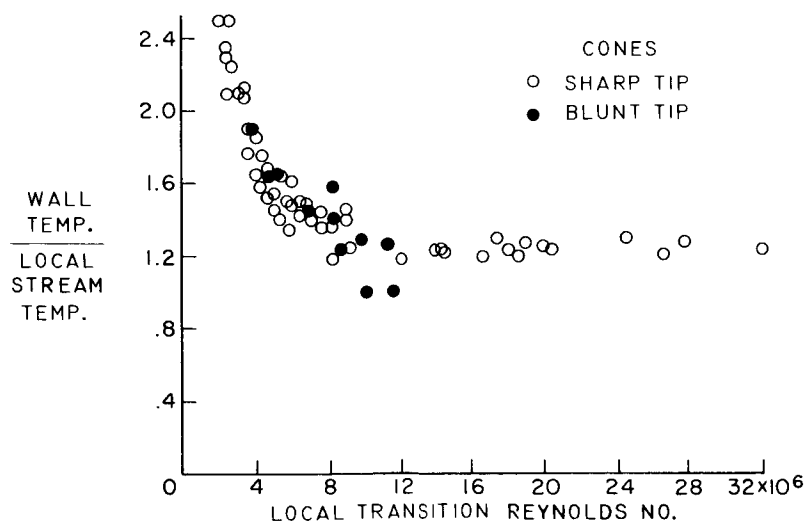
## TRANSITION REVERSAL ON A CONE-CYLINDER

TIP DIAM, 3/16 IN.; M∞, 3.1; ALT, 37,000 FT;
SURFACE, 12 MICROIN.
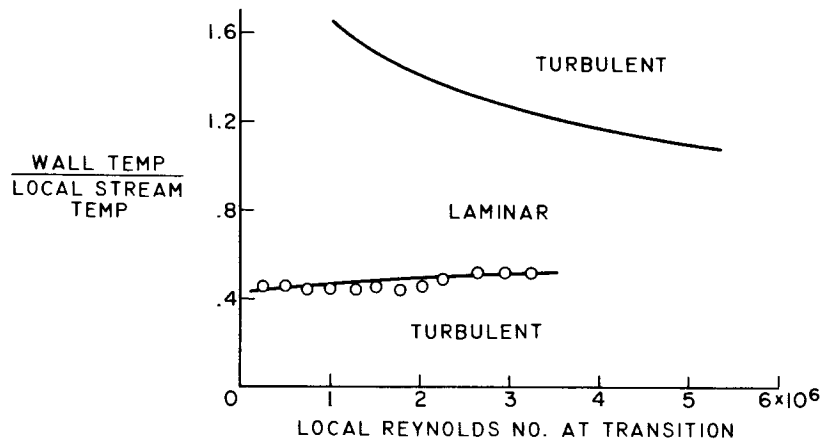


Figure 8

## EFFECT OF TIP DIAMETER ON TRANSITION
## FOR A CONE-CYLINDER

M∞, 3.6; ALT, 40,000 FT; $T_w/T_0 = 0.30$;
SURFACE, <5 MICROIN.
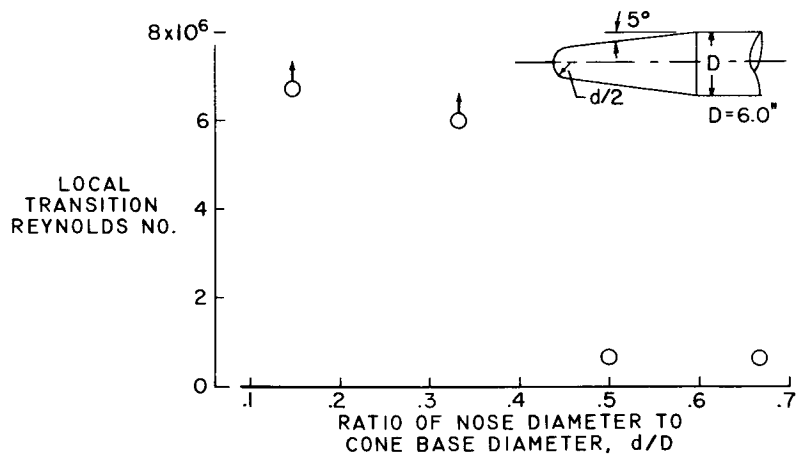


Figure 9

# AERODYNAMIC HEATING OF BLUNT NOSE SHAPES

## AT MACH NUMBERS UP TO 14

By William E. Stoney, Jr.

Langley Aeronautical Laboratory

SUMMARY

Results are presented from recent investigations of the aerodynamic heating rates of blunt nose shapes at Mach numbers up to 14. Data obtained in flight and wind-tunnel tests have shown that the flat-faced cylinder has about 50 percent the stagnation-point heating rates of the hemisphere over nearly the entire Mach number range. Tests made at a Mach number of 2 on a series of bodies made up of hemispherical segments of varying radius of curvature showed that slight amounts of curvature can decrease the local rates at the edge of the flat-faced cylinders with only a slight increase in the stagnation rate. The total heat transfer to such slightly curved bodies is also somewhat smaller than the total heat transfer to flat-faced cylinders.

Comparison of several tests with theoretical heating-rate distributions showed that both laminar and turbulent local rates can be predicted by available theories (given the pressure distribution about the body) reasonably well, although the scatter of the available data still leaves open the choice between the theories at the edge of the bodies, where they usually differ.

Tests on a flat-faced cylinder at a Mach number of 2.49 and at angles of attack up to 15° showed the movement of the apparent stagnation point from the center of the body to the 50 percent windward station at 15° angle of attack. The heat transfer near the windward edge increased about 30 percent while that near the leeward edge decreased about 20 percent at 15° angle of attack.

Preliminary results on a concave nose have indicated the possibility that this type of design may be developed to give heating rates significantly lower than even the flat-faced cylinder rates. The test results have also shown, however, the existence of an unsteady flow phenomenon which can increase the heating rates to extremely high values.

17

CONFIDENTIAL

# INTRODUCTION

The importance of blunt noses as a means of reducing the heat transfer to high velocity missiles has recently received much publicity. The question of just what blunt shape is best is still moot, and it is the purpose of this paper to present and examine some recent experimental results which may throw some light on this problem.

## SYMBOLS

| | |
|---|---|
| $h$ | heat-transfer coefficient |
| $M$ | Mach number |
| $p$ | pressure |
| $Q$ | total heat input |
| $R$ | Reynolds number |
| $r$ | radius |
| $s,x$ | distance along surface measured from center line |
| $s_{TOTAL}$ | total distance along surface measured from center line to edge of body |
| $T$ | temperature |
| $u$ | velocity |
| $\alpha$ | angle of attack |

Subscripts:

| | |
|---|---|
| $d$ | based on diameter |
| $F$ | flat face |
| $HEMIS$ | hemisphere |
| $LAM$ | laminar flow |
| $l$ | local |

TH          theoretical

TURB        turbulent flow

t           stagnation

w           wall

$\infty$    free stream

Superscript:

'(prime)    hemispherical segment


## DISCUSSION


### Stagnation-Point Heating on Hemispherical

### and Flat-Faced Cylinders

Heat is apparently an elusive thing, and the prediction and measurement of its transfer rates is still not the most exact of sciences. This fact is illustrated in figure 1, which presents the heat-transfer coefficients measured at the stagnation points of hemispheres and flat-faced cylinders as a function of free-stream Mach number. All the measured rates are divided by theoretical rates for the hemisphere determined either by the theory of Sibulkin for low Mach numbers (ref. 1) or by the theory of Fay and Riddell for higher Mach numbers (ref. 2). The latter theory includes the real gas effects due to the very high stagnation temperatures obtained at these flight conditions. The measured results were obtained on rocket models (refs. 3 to 6) and in wind tunnels (refs. 7 to 11 and unpublished data).

It is apparent from the scatter shown that both methods of measurement have their troubles. There is the possibility that a variable not accounted for by the theories is responsible for some of the scatter. It seems probable, however, that the scatter in the data is principally the result of heat losses of various types, errors in the measurement of the very thin skins usually used, and, in the case of the flight data, errors in the measurement of the flight conditions of the models. This last type of error is responsible for the fact that heating-rate distributions measured on flight models often show considerably less scatter if they are nondimensionalized by division by the measured stagnation rates rather than by theoretical rates. The agreement of the data taken in this way is due to the invariance of laminar heating-rate distributions with Mach number and Reynolds number.

With these qualifications, it then appears reasonable to say that the measured values support the theoretical values of the stagnation heating rates on the hemispheres throughout the Mach number range and that the stagnation heating rates on the flat-faced cylinder are roughly one-half those on the hemisphere. The markedly lower rates shown for the flat face indicate its possible value as a low-heating-rate shape, but a final evaluation requires the examination of the heating rates over the entire surface.

## Local Heating Rates on a Flat-Faced Cylinder

Local heating rates on a flat-faced cylinder are presented in figure 2. The local heating rates measured in flight (refs. 11 and 12) and in wind tunnels (ref. 10 and unpublished data) are divided by their measured stagnation rates and presented as functions of local distance from the center line divided by the radius of the body. The scatter of some of the data is indicated by the spread of the rails through the symbols. The data are compared with the predictions of two laminar theories, the solid line representing the theory of Lees (ref. 13) and the dashed line, the theory of Stine and Wanlass (ref. 14). For both these theoretical distributions a pressure distribution measured at $M_\infty = 2$ in a wind tunnel (ref. 10) was used. This use is justified by the experimentally obtained fact that the local flow over blunt shapes "freezes" at Mach numbers above about 2, which means that the local Mach numbers do not change significantly with free-stream Mach number above that Mach number. Lees' theory is derived for the condition $\frac{T_w}{T_t} \ll 1$, which is the condition of all high Mach number flight tests. For this condition Lees argues that the direct influence of a local pressure gradient is small and can be neglected. The Stine and Wanlass calculations include a local-pressure-gradient effect, and this is the principal source of the difference shown between the two theories.

In figure 2 the data scatter is again large enough that it is impossible to decide which of the two theories better fits the data. A comparison of the two parts of the figure shows the invariance of the distribution with Mach number and Reynolds number mentioned previously. In spite of the data scatter it is also obvious that the flat-faced cylinder loses some of its advantages over the hemisphere by the increased heating rates at the edge of the face.

## Stagnation-Point Heating Rates on Hemispherical Segments

In an attempt to decrease the edge heating rates while keeping low stagnation rates, a series of bodies were tested which were shaped by

hemispherical segments of different radii. Figure 3 presents the ratio of stagnation-point heating rates measured on these hemispherical segments to the stagnation-point heating rate for the hemisphere of equal body radius plotted (open symbols) as a function of the ratio of body radius to the radius of curvature of the hemispherical segment. The results of two systematic investigations are shown and the agreement between them is fair in spite of the large Mach number and stagnation difference between them. All the results of figure 1 could, of course, be plotted in figure 3 at $\frac{r}{r'} = 0$ to give a band of data from about 0.4 to 0.8. The results of the two investigations shown have the advantage of being parts of a systematic series of tests, and they agree with the general results of figure 1, namely, that the stagnation-point heating rates for the flat face are about 50 percent of those for the hemisphere.

Plotting the solid points which were obtained from pressure measurements (ref. 15) as heating-rate ratios is not strictly honest since these points are actually the square root of the velocity gradient ratios; that is,

$$\frac{\sqrt{(du/dx)'}}{\sqrt{(du/dx)_{\text{HEMIS}}}}$$

However, stagnation-point heating-rate theory shows that the heating rate is a direct function of the square root of the velocity gradient and, thus, the two types of data can be plotted in the same figure with the purpose of allowing the data to reinforce each other. The scatter in the pressure data is smaller, and the data show a small Mach number influence. The combination of pressure and heating-rate data allows a fairly decent line to be drawn through the data to show the effect of changing the nose radius of curvature. The use of theory allows a calculation of heating-rate ratios to be made from the Newtonian pressure principle also and this result is shown by the solid line. The comparison of this solid line with the data is interesting because it shows that the data depart from this line for that body for which Newtonian theory predicts a Mach number of 1 at the shoulder (i.e., slope at the shoulder = 45°).

The bodies tested had sharp or nearly sharp corners, and thus a Mach number of 1 occurred at or very close to the corner. It has been suggested (ref. 15) that for bodies of varying radii of curvature (for example, a body with a flat meridian near the stagnation point faired into the cylinder with a radius of curvature of 25 percent of the cylinder radius), the value of r on a plot such as shown in figure 2(b) should be taken at that point at which the local flow is

sonic, this point to be determined as best as possible, usually by means of pressure distributions. Although the present data can throw no light on the value of this procedure the reader should be aware that the corner can influence the results discussed for this figure and the following local-heating-rate-distribution figures, and that it does this through the mechanism of the sonic-point location. A more general discussion of a closely similar point is given in reference 16, where it is pointed out that the corner shape effects can be felt even if the position of the sonic line is known and is ahead of the corner, at least for Mach numbers less than 3 for bodies of revolution.

## Local Heating Rates on Hemispherical Segments

Again the local heating rates must be examined to permit an evaluation of the various noses tested. In figure 4 the local rates measured on the series of $M = 2$ tunnel models for which the stagnation rates were presented in figure 3 are presented as a function of the ratio of local surface distance from the center line to the total surface distance from the center line. The local rates have been nondimensionalized by division by the stagnation rate of the flat face. The resulting ratios have been adjusted so that the stagnation-point ratios fit the dashed curve shown in figure 3. This has been done in an effort to remove some of the scatter shown in this figure and means that it has been assumed that the difference shown in the stagnation rates was shared by all the measuring stations. This assumption is partially justified at least by the consistency of the measured values of the first two or three stations away from the center line. This consistency appears on the figure as the flatness in the faired curves near the center line. For comparison the laminar-theory distributions of Stine and Wanlass (ref. 14) for the flat-faced cylinder and the hemisphere are also shown (solid lines). (The theory of Stine and Wanlass was used for the flat face since the condition predicted by Lees, namely $\frac{T_w}{T_t} \ll 1$, is not true for the tunnel conditions being compared herein.)

The effect of changing the radius of curvature of the nose is about as might be expected; that is, as the radius of curvature of the nose is increased above that of the hemisphere, the stagnation-point heating rates are reduced but the edge rates are increased. Similarly, as the radius is decreased from the infinite radius of the flat face, the stagnation rate increases and the edge rate decreases. Thus it is possible to reduce the peak local heating rates somewhat by slight amounts of curvature. Although the edge data are not too accurate because of high conduction losses near the corner and because of unknown effects on the local conditions caused by small and varying amounts of radius at the edge, integration of the local rates over the entire surface shows that

small reductions in the total heat-transfer rates are obtainable for bodies with small values of $\frac{r}{r'}$. Note that the hemisphere has about 50 percent more total heat transfer than the flat face, principally because of its 100 percent greater area.

## Comparison of Turbulent and Laminar Rates

## With Theoretical Calculations

Up to this point only laminar flow has been discussed. For hemispheres it has been shown (ref. 7) that turbulent rates as high as three times the laminar stagnation rates can occur. A similar situation exists for the blunter shapes. Figure 5 presents heat-transfer rates measured on a blunt nose of radius ratio $\frac{r}{r'} = 0.50$ for two conditions of the model surface. Again the measured rates have been divided by the measured stagnation rates. The circular and the square symbols give the distributions measured when the body was relatively smooth, while the diamond symbols represent the data obtained when the body was sandblasted to a roughness of about 200 microinches. (The data shown by the square symbols were obtained on the body with a small 1/4-inch spot of 200-microinch roughness at the stagnation point only. The body was 4 inches in diameter.) As on the hemisphere, heating rates as high as three times the stagnation-point values were obtained.

The rough-surface data are compared with flat-plate turbulent theory derived from Van Dreist (see ref. 17, and appendix of ref. 10). The agreement is fairly good and is similar to the agreement shown for flat-plate theory with data from hemispherical noses. (See ref. 7.)

The laminar data are compared with the laminar-distribution theories of Lees (ref. 13) and Stine and Wanlass (ref. 14) based on measured pressure distributions. Again the scatter of the data is just enough to preclude any choice between the theories near the edge where they indicate a marked difference. There is the possibility that the high point (square symbol) is the start of transition. The lateral heat flow around the corner has not been calculated because of the lack of temperature data right in the small-radius corner region, and thus it is possible that the results for the outer two stations are somewhat low. In general, these comparisons are representative of the local measurements made on the remaining bodies of the series shown in figure 3.

## Effect of Angle of Attack

For hemispherical noses the effect of angle of attack on the local heating distributions is fairly small, as can be seen from geometric reasoning alone, but as the body is blunted, the possibility of larger changes due to angle of attack must be considered. Some recent data from the Langley Unitary Plan wind tunnel give an indication of these changes for a flat-faced cylinder for angles up to $15^\circ$.

In figure 6 both the pressure and the heating-rate distributions are plotted as a function of local surface distance from the center line. The local pressures have been divided by the total pressure behind the shock. The lines faired through the data (there were pressure measurements at all the stations indicated by the symbols in the heating-rate plot) indicate that the apparent stagnation point moved from the center to $s/s_{TOTAL} = 0.25$ at $\alpha = 7.5^\circ$ and to $s/s_{TOTAL} = 0.50$ at $\alpha = 15^\circ$ on the windward side.

The local heating rates have been divided by the stagnation rate for the zero-angle-of-attack case. As can be seen in the figure the rates are increased about 30 percent on the windward side and decreased about 20 percent on the leeward at $15^\circ$ angle of attack. These results are also representative of tests at $M = 3.59$ and several other Reynolds numbers of the same order of magnitude.

## Concave Nose

Some rocket-model tests of a series of small specimens indicated the possibility of extremely low heating rates on concave shapes and thus a large-scale flight test was initiated. The flight-test results were so startling that several wind-tunnel investigations were initiated and rushed to completion. The results of all these tests (refs. 18 and 19 and unpublished data) are presented in figures 7 and 8.

A sketch of the configuration, which is simply a concave hemisphere with slightly rounded corners, is presented in figure 7. The ratio of local heating rate to the stagnation-point heating rate of a hemisphere of the same size and flight conditions (calculated by the theory of Fay and Riddell (ref. 2)) is presented as a function of the ratio of local surface distance from the stagnation point to the total distance for both the flight tests (on the left) and the wind-tunnel tests (on the right). The rails indicate the spread of the data.

The low heating rates over most of the inside of the cup increase to only the order of the flat-face stagnation-point heating rates at the inside of the edge (see sketch in fig. 7). The agreement between

the flight and tunnel data in this case is fairly good; however, other wind-tunnel results do not compare so well.

Some of the wind-tunnel tests were made on a small model on which only the stagnation-point heating rates were measured. These tests which are presented in figure 8 indicated unstable flow phenomena in the cup. The schlieren photographs are typical of the two states noted, (1) where the shock was apparently steady, and (2) where the shock was asymmetrical and apparently unsteady in that the asymmetry changed erratically from lip to lip. An independent test at $M = 3.9$ and $R_{\infty,d} = 1.9 \times 10^6$ was made by Robert W. Dunning of the Langley High Mach Number Jet Group on a nose similar to that used in the heat-transfer tests except that the lip was sharp.[1] Motion pictures of this test show one especially interesting feature in that at small angles of attack ($< 2^\circ$) the flow inside the cup appeared to be turbulent even when the shock was apparently symmetrical and steady. This turbulence would then explode for some unknown reason and the apparently unsteady condition would follow.

The stagnation-point heat-transfer data for all the tests are presented in figure 8, again as a ratio of the theoretical hemispherical stagnation-point results and as a function of free-stream Mach number. Note that the flight-test data extend from $M = 2.5$ to $6.5$ and that the heating rates repeat themselves as the model decelerates to $M = 4.0$. As the Mach number increases, the free-stream Reynolds number (based on diameter) changes from $9 \times 10^6$ to $14 \times 10^6$ at the peak $M$ down to $5 \times 10^6$ at $M = 4.0$, indicating little or no effect of Reynolds number on the data.

The wind-tunnel data fall roughly into two groups - the heat-transfer rates when the unsteady shock condition exists (solid symbols) and the rates when the steady shock is formed (open symbols). These data, especially those for the unsteady flow, show a strong Reynolds number dependence which is not shown in the flight data. The triangles presented on the right part of figure 7 show the data obtained in the Unitary Plan wind tunnel for the one case in which the flow was apparently unsteady. This particular case occurred at $M = 2.49$ and $R_{\infty,d} = 1 \times 10^6$ and with the model at an angle of attack of $7\frac{1}{2}^\circ$. Results from some of the tests from the Langley Gas Dynamics Branch and especially the film supplement to the present paper indicated that the instability which in their tests was almost certain to exist at $\alpha = 0$, was gone at

---

[1]A motion-picture film supplement (L-316) has been prepared and is available on loan from NACA Headquarters, Washington, D. C.

$\alpha > 2^{\circ}$. (It should be noted here that the flight model showed no indication of lateral movement on its normal and transverse accelerometers.)

To date the data on the concave shapes have shown that extremely low heat-transfer rates can be obtained over most of the surface of a concave nose; however, the existence of an unsteady state with extremely high rates has also been found. A comparison of all the stagnation-point wind-tunnel and flight-test data for the apparently steady shock case indicates the possibility that other, and as yet unknown, parameters are important in this phenomenon.

Shape is certainly one of these important factors in this phenomenon. Unpublished results from tests made by John O. Reller, Jr., of the Ames Laboratory on a series of cups of different deepness on the front end of an ogive nose at $M = 4$ indicated that the depth of the cup is important in determining the stability of the flow. The depth of the cup was varied by changing the radius of the hemisphere in a manner similar to the method of obtaining the hemispherical segment noses of the present paper. From shadowgraphs of the shock wave it was found that the cup with $\dfrac{r_{body}}{r_{cup}} = 0.76$ remained steady during the tests while the next body in the series for which $\dfrac{r_{body}}{r_{cup}} = 0.95$ exhibited the asymmetrical shock associated with the unsteady flow phenomenon during nearly all the test time.

## SUMMARY OF RESULTS

Recent investigations of the aerodynamic heating rates of blunt nose shapes at Mach numbers up to 14 have yielded the following results:

1. Data obtained in flight and wind-tunnel tests have shown that the flat-faced cylinder has about 50 percent the stagnation-point heating rates of the hemisphere over nearly the entire Mach number range.

2. Tests made at a Mach number of 2 on a series of bodies made up of hemispherical segments of varying radius of curvature showed that slight amounts of curvature can decrease the local rates at the edge of the flat-faced cylinders with only a slight increase in the stagnation rate. The total heat transfer to such slightly curved bodies is also somewhat smaller than the total heat transfer to flat-faced cylinders.

3. Comparison of several tests with theoretical heating-rate distributions showed that both laminar and turbulent local rates can be predicted by available theories (given the pressure distribution about the body) reasonably well, although the scatter of the available data

still leaves open the choice between the theories at the edge of the bodies, where they usually differ.

4. Tests on a flat-faced cylinder at a Mach number of 2.49 and at angles of attack up to $15^{\circ}$ showed the movement of the apparent stagnation point from the center of the body to the 50-percent windward station at $15^{\circ}$ angle of attack. The heat transfer near the windward edge increased about 30 percent while that near the leeward edge decreased about 20 percent at $15^{\circ}$ angle of attack.

5. Preliminary results on a concave nose have indicated the possibility that this type of design may be developed to give heating rates significantly lower than even the flat-faced-cylinder rates. The test results have also shown, however, the existence of an unsteady flow phenomenon which can increase the heating rates to extremely high values.

# REFERENCES

1. Sibulkin, M.: Heat Transfer Near the Forward Stagnation Point of a Body of Revolution. Jour. Aero. Sci. (Readers' Forum), vol. 19, no. 8, Aug. 1952, pp. 570-571.

2. Fay, J. A., and Riddell, F. R.: Theory of Stagnation Point Heat Transfer in Dissociated Air. Jour. Aero. Sci., vol. 25, no. 2, Feb. 1958, pp. 73-85, 121.

3. Tellep, D. M., and Hoshizaki, H.: Summary Analysis of X-17 RTV Program. Aerodynamic Heating and Boundary-Layer Transition. LMSD 2161, Lockheed Aircraft Corp., July 2, 1957.

4. Stoney, William E., Jr., and Swanson, Andrew G.: Heat Transfer Measured on a Flat-Face Cylinder in Free Flight at Mach Numbers up to 13.9. NACA RM L57E13, 1957.

5. Bland, William M., Jr., Swanson, Andrew G., and Kolenkiewicz, Ronald: Free-Flight Aerodynamic-Heating Data at Mach Numbers up to 10.9 on a Flat-Faced Cylinder. NACA RM L57K29, 1958.

6. Rumsey, Charles B., and Lee, Dorothy B.: Heat-Transfer Measurements in Free Flight at Mach Numbers up to 14.6 on a Flat-Faced Conical Nose With a Total Angle of 29°. NACA RM L57L03, 1958.

7. Beckwith, Ivan E., and Gallagher, James J.: Heat Transfer and Recovery Temperatures on a Sphere With Laminar, Transitional, and Turbulent Boundary Layers at Mach Numbers of 2.00 and 4.15. NACA TN 4125, 1957.

8. Crawford, Davis H., and McCauley, William D.: Investigation of the Laminar Aerodynamic Heat-Transfer Characteristics of a Hemisphere-Cylinder in the Langley 11-Inch Hypersonic Tunnel at a Mach Number of 6.8. NACA Rep. 1323, 1957. (Supersedes NACA TN 3706.)

9. Chauvin, Leo T., and Speegle, Katherine C.: Boundary-Layer-Transition and Heat-Transfer Measurements From Flight Tests of Blunt and Sharp 50° Cones at Mach Numbers From 1.7 to 4.7. NACA RM L57D04, 1957.

10. Stoney, William E., Jr., and Markley, J. Thomas: Heat-Transfer and Pressure Measurements on Flat-Faced Cylinders at a Mach Number of 2. (Prospective NACA paper.)

11. Lee, Dorothy B., and Swanson, Andrew G.: Heat Transfer Measured on a Flat-Face Cylinder-Flare Configuration in Free Flight at Mach Numbers From 1.6 to 2.7. NACA RM L58A06, 1958.

12. Speegle, Katherine C., Chauvin, Leo T., and Heberlig, Jack C.: Heat Transfer for Mach Numbers up to 2.2 and Pressure Distributions for Mach Numbers up to 4.7 From Flight Investigations of a Flat-Face-Cone and a Hemisphere-Cone. NACA RM L58B18, 1958.

13. Lees, Lester: Laminar Heat Transfer Over Blunt-Nosed Bodies at Hypersonic Flight Speeds. Jet Propulsion, vol. 26, no. 4, Apr. 1956, pp. 259-269.

14. Stine, Howard A., and Wanlass, Kent: Theoretical and Experimental Investigation of Aerodynamic-Heating and Isothermal Heat-Transfer Parameters on a Hemispherical Nose With Laminar Boundary Layer at Supersonic Mach Numbers. NACA TN 3344, 1954.

15. Boison, J. C., and Curtiss, H. A.: Preliminary Results of Spherical-Segment Blunt Body Pressure Surveys in the 20 Inch Supersonic Wind Tunnel at JPL. RAD Tech. Memo. 2-TM-57-77 (Aerod. Sec. Memo. No. 152), AVCO Res. and Advanced Dev. Div., Oct. 9, 1957.

16. Probstein, Ronald F.: On the Nature of the Sonic Line for Supersonic and Hypersonic Flow Over Blunt Bodies. WADC TN 57-349 (ASTIA Doc. No. AD-142037), Wright Air Dev. Center, U. S. Air Force, Sept. 1957.

17. Van Driest, E. R.: The Problem of Aerodynamic Heating. Aero. Eng. Rev., vol. 15, no. 10, Oct. 1956, pp. 26-41.

18. Markley, J. Thomas: Heat Transfer and Pressure Measurement on a 5-Inch Concave Nose at a Mach Number of 2.0. NACA RM L58C14a, 1958. (Prospective NACA paper.)

19. Cooper, Morton, Beckwith, Ivan E., Jones, Jim J., and Gallagher, James J.: Heat-Transfer Measurements on a Concave Hemispherical Nose Shape With Unsteady-Flow Effects at Mach Numbers of 1.98 and 4.95. (Prospective NACA paper.)

STAGNATION-POINT HEATING RATES MEASURED ON HEMISPHERES
AND FLAT-FACED CYLINDERS

HEMISPHERE DATA
O, □ GAS DYN. (REF. 7)
△ II-IN. HYP. TUN. (REF. 8)
▽ GAS DYN. (UNPUBLISHED)
——— LOCKHEED X-17 (5 FLIGHTS; REF. 3)
—·— PARD (REF. 11)

FLAT-FACED-CYLINDER DATA
◇ PREFLIGHT JET (REF. 10)
◿ UPWT (UNPUBLISHED)
▽ GAS DYN. (UNPUBLISHED)
--- PARD (4 FLIGHTS; REFS. 4, 5, 6, 9)
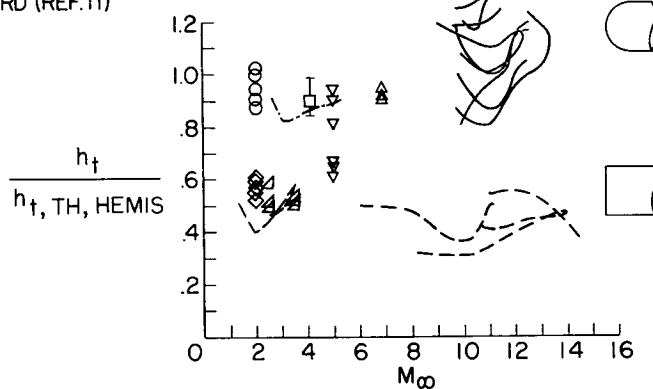
$$\frac{h_t}{h_{t,TH,HEMIS}}$$

Figure 1

LOCAL HEAT-TRANSFER COEFFICIENTS ON A FLAT-FACED
CYLINDER
$M_\infty < 5$

LAMINAR THEORY USING M=2 PRESS. DIST.
————— STINE AND WANLASS (REF. 14)
————— LEES (REF. 13)

TEST
TUNNEL
$M_\infty$                           $R_{\infty,d}$

● ■ 2.0                    $4.7 \times 10^6$          (REF. 10)
▼ 2.5                    .8 AND $1.4 \times 10^6$ } (UPWT
▲ 3.5                    .8 AND $1.3 \times 10^6$ } UNPUBLISHED)

FLIGHT
○ 1.6 to 2.4    3.1 to $4.5 \times 10^6$  (REF. 11)
□ 1.5 to 2.2    7.4 to $11.0 \times 10^6$  (REF. 12)
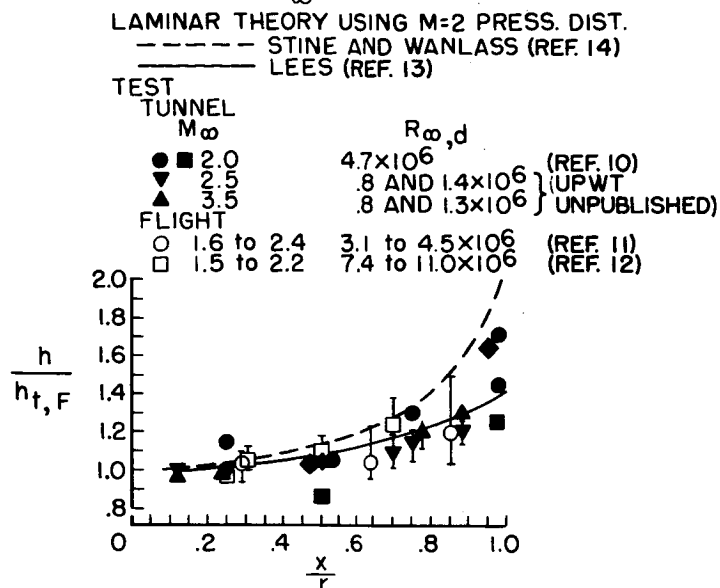


Figure 2(a)

LOCAL HEAT-TRANSFER COEFFICIENTS ON A
FLAT-FACED CYLINDER
$M_\infty > 10$

LAMINAR THEORY USING M=2 PRESS. DIST.
————— STINE AND WANLASS (REF. 14)
————— LEES (REF. 13)

FLIGHT TEST
$M_\infty$                           $R_{\infty,d}$

○ 11.0 to 14.0    1.1 to $1.6 \times 10^6$  (REF. 4)
▽ 11.0 to 14.0    0.8 to $1.6 \times 10^6$  (REF. 6)
△ 10.5 to 11.0    4.7 to $6.8 \times 10^6$  (REF. 5)
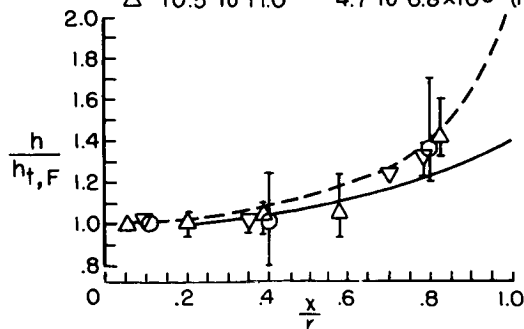


Figure 2(b)

STAGNATION-POINT HEATING RATES ON HEMISPHERICAL
SEGMENTS OF DIFFERENT CURVATURES



HEAT-TRANSFER DATA

| | $M_\infty$ | $T_t, °R$ | |
|---|---|---|---|
| O | 2.0 | 960 | PARD (UNPUBLISHED) |
| □ | 11.5 | ≈1,700 | GAS DYN. (UNPUBLISHED) |

PRESSURE DATA

▼ 2.0 }
▲ 4.8 } JPL (REF. 15)

NEWTONIAN THEORY
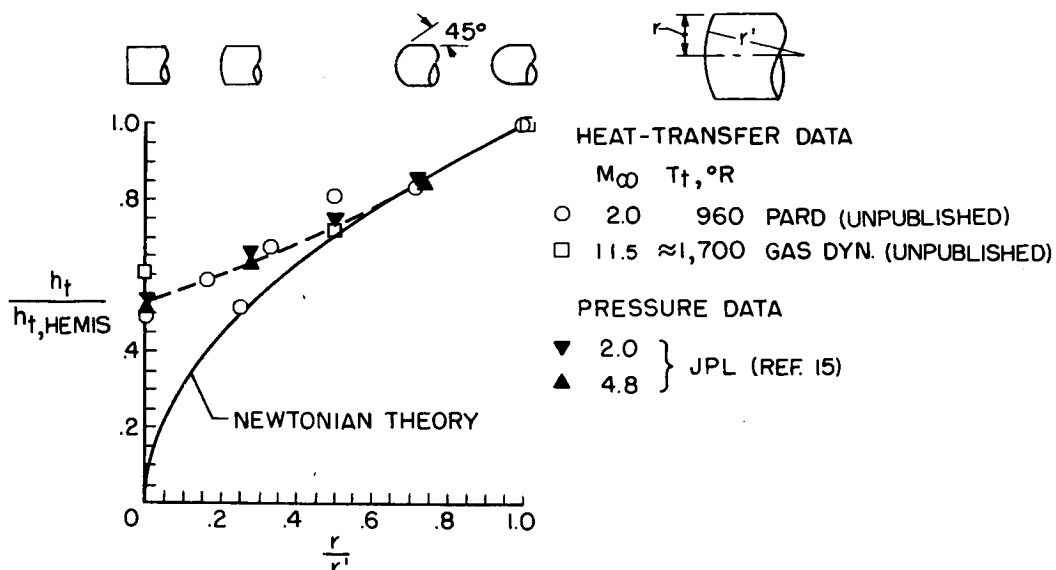
Figure 3

HEMISPHERICAL-SEGMENT LOCAL HEAT-TRANSFER
COEFFICIENTS DIVIDED BY FLAT-FACED STAGNATION VALUES

$M_\infty = 2$ ; $R_{\infty,d} = 4.7 \times 10^6$



| | | $\frac{r}{r'}$ | $\frac{Q}{Q_F}$ |
|---|---|---|---|
| — | | 1.00 | 1.50 |
| -- | | .71 | 1.15 |
| — - | | .50 | 1.00 |
| — | | .33 | .90 |
| --- | | .16 | .90 |
| — | | 0 | 1.00 |
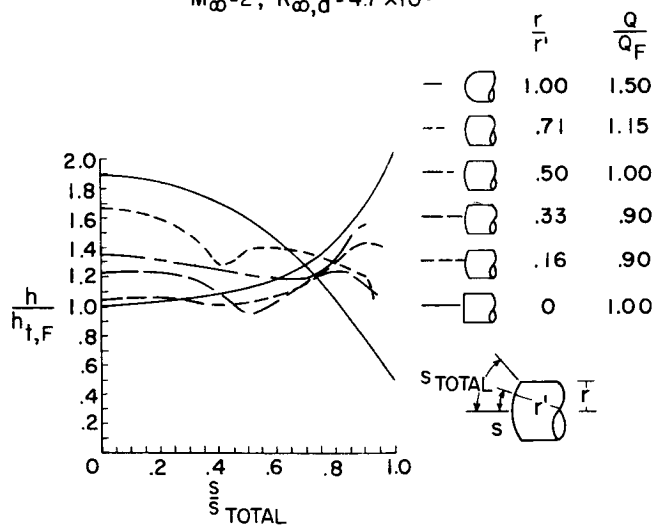
Figure 4

COMPARISON OF MEASURED AND THEORETICAL HEATING RATES
ON A HEMISPHERICAL SEGMENT

$M_\infty = 2$;  $R_{\infty,d} = 4.7 \times 10^6$

TESTS

o □ SMOOTH SURFACE
◇ ROUGH SURFACE
(≈ 200 $\mu$ IN.)

THEORY

LAMINAR { ——— LEES (REF. 13)
{ ----- STINE AND WANLASS (REF. 14)

TURBULENT —·— $\dfrac{h_{TURB}}{h_{LAM}} = 0.04 R_l^{0.3}$

$\dfrac{r}{r'} = 0.50$
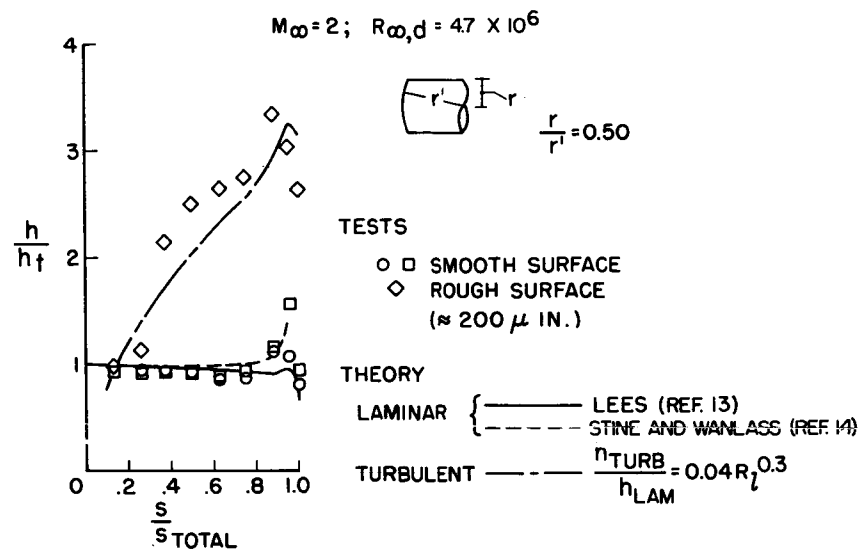
Figure 5

VARIATION OF PRESSURE AND HEAT-TRANSFER COEFFICIENTS
ON A FLAT-FACED CYLINDER WITH $\alpha$

$M_\infty = 2.49$;  $R_{\infty,d} = 1.46 \times 10^6$

APPARENT
STAGNATION
POINT

$\alpha$, DEG
0
7.5
15

LEEWARD

WINDWARD

$\alpha$, DEG

0 ———
7.5 O —— ——
15 □ ----

LEEWARD  x  WINDWARD
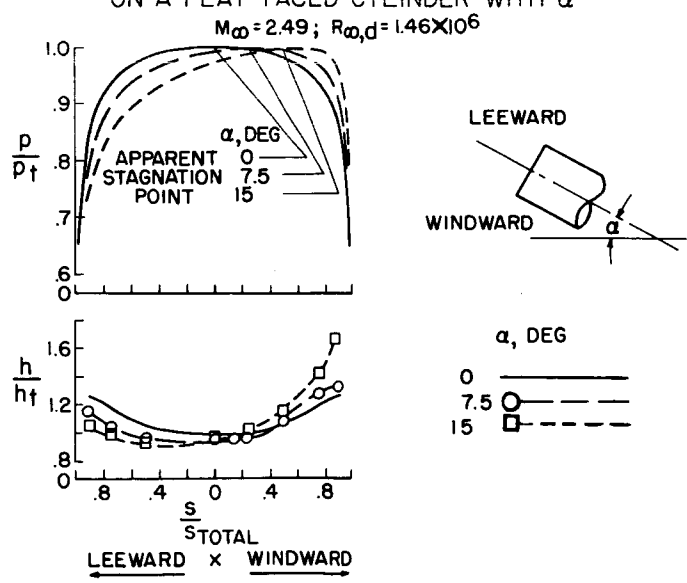
Figure 6

HEATING RATE AND PRESSURE DISTRIBUTIONS
ON A CONCAVE NOSE
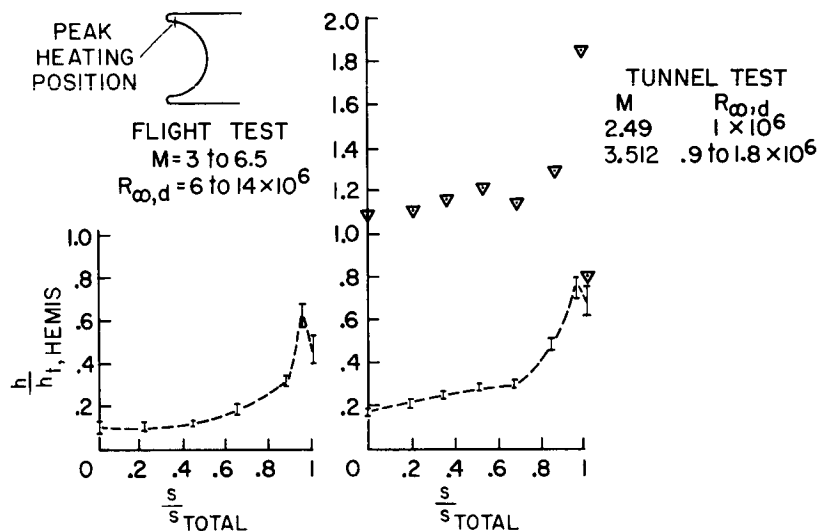


Figure 7

STAGNATION-POINT HEATING RATES MEASURED ON CONCAVE NOSE
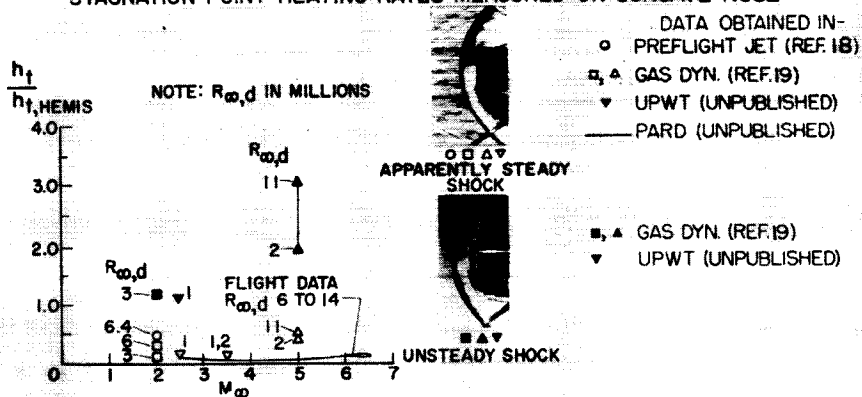


Figure 8

# THE EFFECT OF INJECTION

## OF FOREIGN GASES ON SKIN FRICTION OF THE

### TURBULENT BOUNDARY LAYER

By C. C. Pappas

Ames Aeronautical Laboratory

Transpiration cooling systems may prove to be useful for high-speed aircraft experiencing aerodynamic heating. Fluid injection has an effect on turbulent-boundary-layer skin friction as well as on heat-transfer phenomena. The primary concern in this report is the assessment of the effects of gas injection on the skin friction of the turbulent boundary layer at supersonic speeds. Emphasis should be laid on the fact that the surface heat transfer with transpiration may be obtained directly from the skin friction. Light gases such as hydrogen and helium are attractive because of their known effectiveness; air may be used for convenience, and certain heavy gases will emanate from ablating materials.

Figure 1 gives some idea of the orders of magnitude of the effects of gas injection. The theoretical predictions obtained from NACA TN 4149 (ref. 1) show the influence of foreign-gas injection into a turbulent boundary layer for an isothermal incompressible flow. The ordinate is the ratio of the skin-friction coefficient with injection to the skin-friction coefficient with zero injection. The abscissa is the ratio of the injection parameter $F$ to one-half the zero-injection skin-friction coefficient. The injection parameter $F$ is used subsequently in other figures and is defined as the coolant mass flow rate per unit area normal to the surface divided by the mass-flow rate per unit area of the main stream at the edge of the boundary layer. These coordinates are used because, theoretically for air injection, they largely eliminate the effects of variations in Mach number, Reynolds number, and ratio of wall to free-stream temperature. The results are shown for a Reynolds number of $10^7$ and it is apparent that the light gases hydrogen and helium show marked reductions of the skin friction as compared with air injection; the heavy gas Freon-12 ($CCl_2F_2$) which has a molecular weight of 120.9 shows less reduction in skin friction than does air injection. Similar reductions in heat transfer are indicated by the theory; that is, the heat transfer drops off as shown by the skin friction. Reductions in skin friction of 80 percent are shown for air for injection rates of the order of 3/1000 of the main stream flow. These theoretical results

18

might encourage one to look further into the problem and, of course, this has been done to a somewhat limited scale.

An instrumented test cone was used in this series of experiments to measure the average skin friction with foreign-gas injection. This cone, shown in figure 2, has a 15° total included angle, is $10\frac{1}{2}$ inches long, and has a porous surface of resin-bonded fiber glass. The cone is mounted on one side of a strain gage and the other side of the gage is fixed to the sting support. The injection gas enters the cone through a flexible tube and then passes through the porous wall. Acting in the stream flow direction are the external pressure force and the external skin-friction force. Acting in the opposite direction are the base-pressure force and the indicated strain-gage force. Simple addition of forces yields the desired skin friction.

At this point it might be asked what are the physical effects on the boundary layer when a gas is injected through the porous surface. The boundary layer would be expected to become thicker and a normal laminar boundary layer might be expected to be tripped by the action of the finite jets of injected gas. In figure 3 are shown shadowgraph pictures of a boundary layer on the test cone without a trip. The bottom shadowgraph is of the undisturbed normal boundary layer; this boundary layer is laminar. The other three shadowgraphs show the boundary layer for about equal injection mass-flow rates of Freon-12, air, and helium. It is apparent that the boundary layer is markedly disturbed and thickened. Large swirls or eddies are especially noticeable for the helium injection. The boundary layer with helium injection is eight times as thick as the undisturbed boundary layer. Also, the edge of the boundary layer is much more irregular for helium and air injection. These large swirls may be due to the action of small jets emitting from the porous surface. The nature of the boundary-layer flow is complicated, and it would appear difficult to synthesize a suitable flow model on which a theory might be based.

It has been assumed by many people that injection of gases into a boundary layer would cause the boundary layer to become turbulent from the initial point of injection. Immediate tripping does not occur; however, the transition point of the boundary layer is adversely affected by injection. In figure 4 the location of transition is shown for one set of wind-tunnel test conditions as a function of the injection parameter F. As expected, helium initially causes the largest change in transition location, followed by air and Freon. The movement of transition location per unit change in injection for helium is 3.6 times that for Freon. This comparison should be considered as relative only, because transition location as determined from wind-tunnel tests may be influenced by the individual characteristics of the wind tunnel. The transition location for the Freon tests appears to be asymptotic at a

Reynolds number of about $1.8 \times 10^6$ and complete tripping does not occur. Limitations in viewing the model and the limitation in injection rates for air and helium prevented extension of the respective curves for these wind-tunnel test conditions.

Fundamental to this report were tests to determine skin friction (made with the $15^\circ$ cone model) of a tripped fully turbulent boundary layer using as injected gases helium, air, and Freon-12. The molecular weights of the gases are 4, 28.9, and 120.9, respectively. The results of these tests for a cone Mach number of 3.2 are shown in figure 5. Plotted again is the ratio of the skin-friction coefficient with injection to the zero-injection skin-friction coefficient as a function of the injection parameter F divided by one-half the zero-injection skin-friction coefficient. The curves are faired through the data points. It should be remembered that the skin-friction coefficient for zero injection is a variable with Mach number, Reynolds number, and ratio of wall to free-stream temperature. The relative effectiveness of the light gas, helium, in reducing skin friction is apparent. Less reductions in skin friction were obtained for air and Freon. Model limitations prevented higher injection rates for air and helium.

The experimental results for a turbulent boundary layer for a cone Mach number of 4.3 are presented in figure 6. Higher rates of injection were obtained for these test conditions. Superposed over the data points are the faired curves of the data for a Mach number of 3.2. The reduction in skin friction for helium and air is slightly less for the higher Mach number. Maximum reductions of 40, 54, and 88 percent are shown in this figure for Freon, air, and helium injection. It is of interest to note that for zero injection the laminar skin-friction coefficient is 35 percent of the value for turbulent flow for these test conditions. Three conclusions are evident from the test results: (1) substantial reductions in skin friction are attained with injection; (2) the relative effectiveness of the various gases is in accordance with the theory of reference 1; and (3) heavy gases which may emit from ablating surfaces are not very effective in reducing skin friction. At the present, the experimental data, even for air injection, are very limited and a comparison of available test results with some of the theories is warranted.

This comparison is made in figure 7 for air injection. The conditions for comparison are for a wall temperature approximately equal to the stagnation temperature of the flow, for a Mach number range from 0 to 5, and within a Reynolds number range of $3 \times 10^6$ to $10^7$. The two theories, that of Dorrance and Dore (ref. 2), and that of Rubesin (ref. 3), cover the shaded regions as indicated in the figure. The dashed curves indicate the experimental skin-friction results. The low-speed (M $\approx$ 0) results are from reference 4. The skin-friction data for a Mach number of 2.55 (ref. 5) were obtained on a cone with a rough

surface, and the zero-injection skin-friction coefficients are high. For the higher injection rates the influence of surface roughness diminishes; therefore, the skin-friction coefficients should be referenced to smooth-cone values consistent with those of the present tests. The ratio of the skin-friction coefficients has been adjusted upward as indicated by the two vertical arrows. Note that neither theory predicts the variation with Mach number of the skin-friction ratio as obtained from experiment from a Mach number of zero to a Mach number of 4.3. Also, the major change in skin-friction ratio occurs in the range of Mach number from zero to 2.55. Small changes due to Mach number are shown at the higher Mach numbers and the injection is least effective at the highest Mach number where transpiration systems will find their probable application.

Surface heat transfer for a transpiration system should follow the trends indicated for skin friction. Caution should be exercised when applying the available theories to predict heat transfer and skin friction with transpiration. Additional experimental results will be needed to clarify the effect of Mach number on skin friction with foreign-gas injection.

## REFERENCES

1. Rubesin, Morris W., and Pappas, Constantine C.: An Analysis of the Turbulent Boundary-Layer Characteristics on a Flat Plate With Distributed Light-Gas Injection. NACA TN 4149, 1958.

2. Dorrance, William H., and Dore, Frank J.: The Effect of Mass Transfer on the Compressible Turbulent Boundary-Layer Skin Friction and Heat Transfer. Jour. Aero. Sci., vol. 21, no. 6, June 1954, pp. 404-410.

3. Rubesin, Morris W.: An Analytical Estimation of the Effect of Transpiration Cooling on the Heat-Transfer and Skin-Friction Characteristics of a Compressible, Turbulent Boundary Layer. NACA TN 3341, 1954.

4. Mickley, H. S., and Davis, R. S.: Momentum Transfer for Flow Over a Flat Plate With Blowing. NACA TN 4017, 1957.

5. Tendeland, Thorval, and Okuno, Arthur F.: The Effect of Fluid Injection on the Compressible Turbulent Boundary Layer - The Effect on Skin Friction of Air Injected Into the Boundary Layer of a Cone at M = 2.7. NACA RM A56D05, 1956.

## EFFECT OF GAS INJECTION ON TURBULENT SKIN FRICTION

**TN 4149**

$$M \approx 0, \quad R_x = 10^7, \quad F = \frac{\rho_w V_w}{\rho_1 U_1}$$
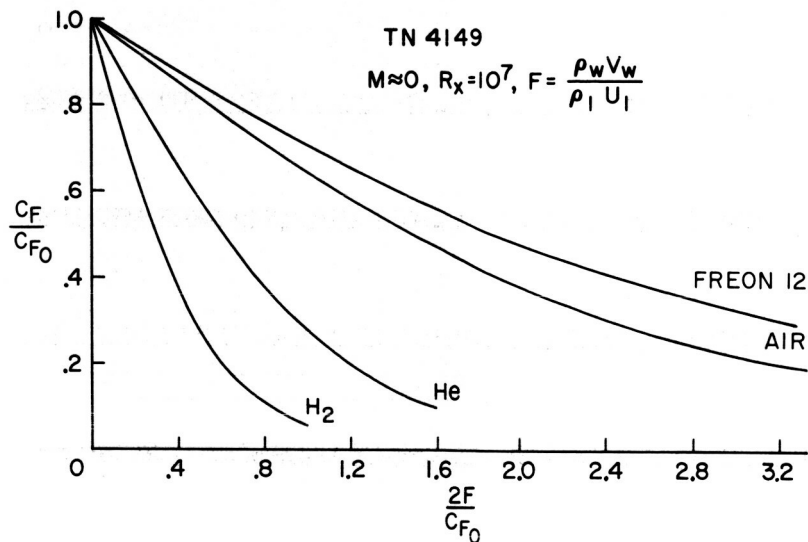
Figure 1

## TEST MODEL
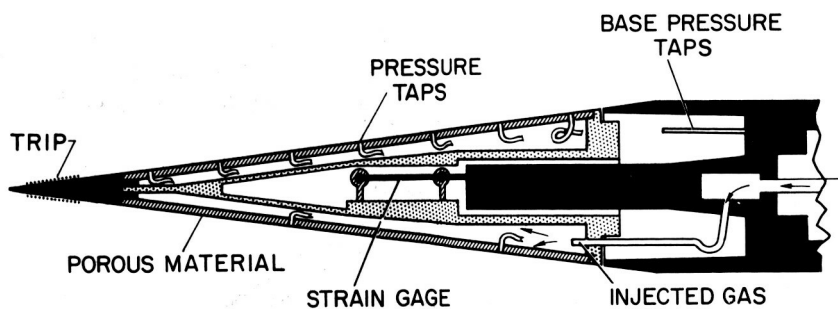
Figure 2

## COMPARISON OF BOUNDARY LAYER WITH
## INJECTION OF VARIOUS GASES

**NO TRIP    $R_C = 4.7 \times 10^6$**
**LOCAL M=4.3**
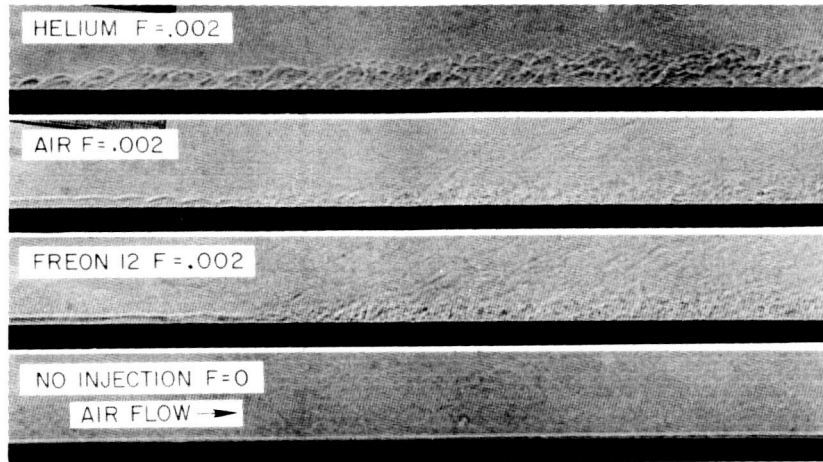


Figure 3

## MOVEMENT OF TRANSITION POINT WITH INJECTION



Figure 4

EFFECT OF INJECTION ON AVERAGE SKIN FRICTION

$M_c = 3.2$
$2.9 \times 10^6 \leq R_c \leq 5.8 \times 10^6$
$T_w \approx T_r$

FREON 12

AIR

HELIUM

$\dfrac{c_F}{c_{F_0}}$

$\dfrac{2F}{c_{F_0}}$
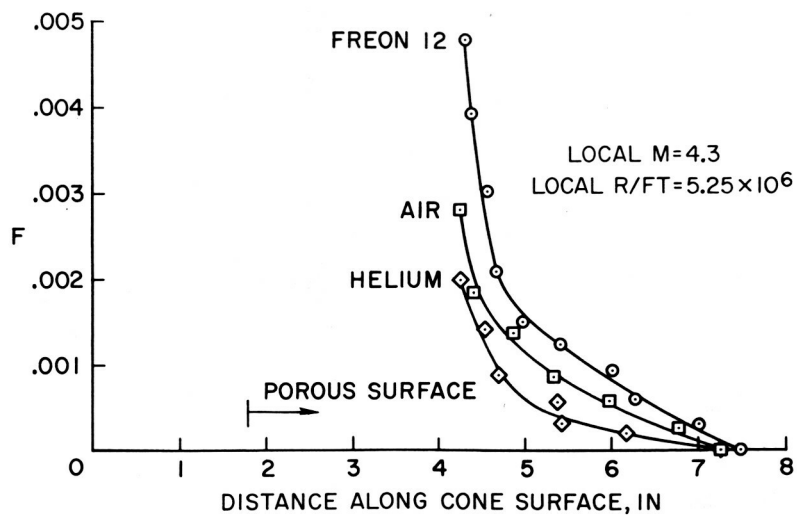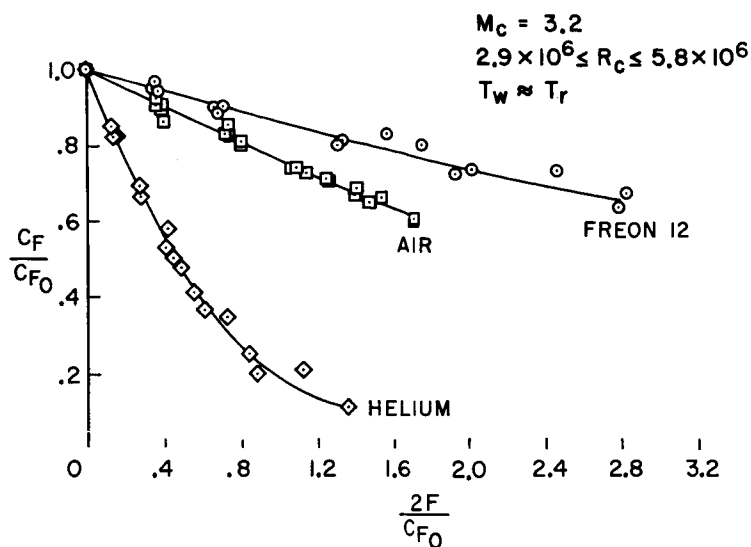
Figure 5

EFFECT OF INJECTION ON AVERAGE SKIN FRICTION

$M_c = 4.3$
$3.2 \times 10^6 \leq R_c \leq 4.6 \times 10^6$
$T_w \approx T_r$

FREON 12

AIR

HELIUM

$\dfrac{c_F}{c_{F_0}}$

$\dfrac{2F}{c_{F_0}}$

Figure 6

COMPARISON OF EXPERIMENT WITH THEORY
FOR AIR INJECTION
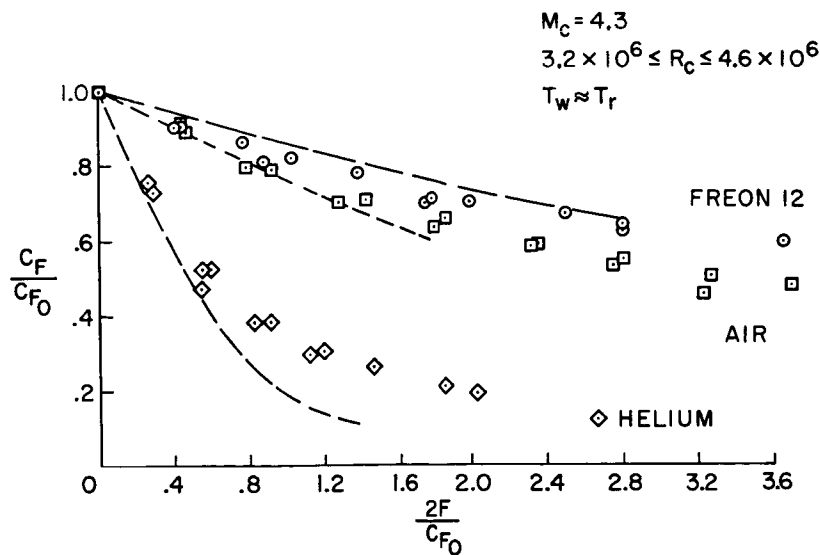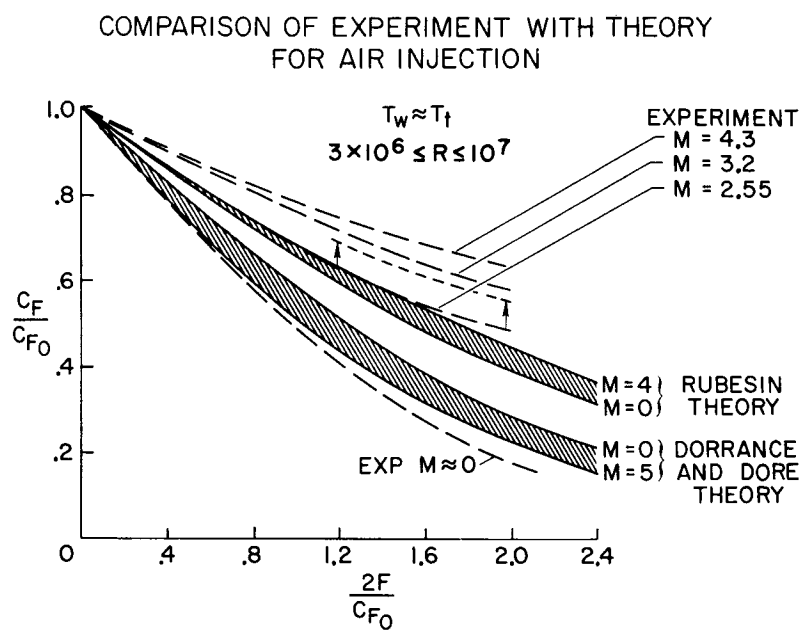


Figure 7

# A THEORETICAL STUDY OF NOSE ABLATION

By Leonard Roberts

Langley Aeronautical Laboratory

## INTRODUCTION

It is now well-known that an important feature of an atmospheric reentry vehicle is the bluntness of its nose. Such a shape causes a thickened boundary layer so that a shield of air over the nose reduces heat transfer to the body. This reduction in heat transfer is not in itself sufficient to achieve desirable body temperatures, however, and further shielding of some sort is required.

This shielding is accomplished by providing an expendable material which soaks up heat; thus, a copper nose of sufficient thickness soaks up enough heat to shield the interior of the body. Alternatively, the material may be supplied as a fluid which is injected through a porous nose into the boundary layer and allowed to flow over the body. If the injection could be made in a controlled way and only when needed, it would be an improvement over the solid copper shield since it causes a reduction in one source of heat - skin friction. However, the structural problems involved in devising such a porous wall may outweigh the advantages.

The third alternative is to let ablation take place. This is not just a negative approach of allowing heat to expend itself in the sublimation or depolymerization of unimportant material; it is also an extension of the original blunt-nose idea of using the thickened boundary layer to shield the nose. The convection of heat by the foreign gas produced can make the main contribution to the shielding at sufficiently high temperatures.

Previous theoretical studies of ablation have been concerned mainly with the melting of glass and the melting of ice, and solutions of the boundary-layer equations have been obtained by Sutton (ref. 1). These solutions involved a seventh-order system of differential equations with appropriate boundary conditions. A simplified analysis has been made by Lees (ref. 2) when there is no gaseous phase of the material.

When the general problem of shielding by ablation is considered, the following question arises: Which material will have the best

19

overall heat capacity per pound?  In order to answer this question it is necessary to look into the mechanism of shielding and to ask why one material can absorb more heat than another.

The purpose of this paper is to show that these questions may be answered by a simplified analysis provided it contains all the correct physical ingredients of the problem.  The analysis presented herein avoids the solution of a seventh-order system of differential equations but nevertheless respects all heat-transfer and mass-transfer boundary conditions.  It shows in a very simple way the important properties that make a good heat shield.  Only the case in which the nose sublimes directly to the gaseous state is considered here, although the extension to the more general case of solid-liquid-gas ablation is easily made.

A comparison with experimental results for the material Teflon shows that the theory is useful and may be used in the evaluation of the effective heat capacities of other materials.

## SYMBOLS

| | |
|---|---|
| $B$ | burning heat |
| $c_b$ | specific heat of body material |
| $c_p$ | specific heat of mixture |
| $D$ | coefficient of diffusivity |
| $H_{EFF}$ | effective heat capacity |
| $k$ | conductivity |
| $L$ | latent heat |
| $\dot{m}$ | rate of mass loss |
| $N_{Nu}$ | Nusselt number |
| $N_{Pr}$ | Prandtl number, $\dfrac{\mu c_p}{k}$ |
| $N_{Sc}$ | Schmidt number, $\dfrac{\mu}{\rho D}$ |
| $q$ | rate of heat transfer per unit area |
| $R$ | Reynolds number |

T            temperature

U            tangential velocity at edge of boundary layer

$\dot{u}$, v       velocity components

V            velocity

W            concentration of foreign gas

$\dot{w}$            rate of weight loss per unit area

x, y         coordinate axes

Z            value of  z  outside boundary layers

$$z = \int_0^y \frac{\rho}{\rho_w}\, dy$$

β            shape factor

δ            boundary thickness

μ            coefficient of viscosity

ρ            density

τ            time

Subscripts:

0            stagnation conditions

1            foreign gas

2            air

b            body

o            no ablation

T            temperature

u            velocity

w            wall

W            concentration

ANALYSIS

Experiments carried out at the Langley Aeronautical Laboratory show that the nose of a body in ablation soon achieves a blunt shape even if it was not initially blunt and then recedes steadily due to ablation without further appreciable change in shape. Because of this effect, the main features of the flow can be obtained by considering only the region in the near vicinity of the stagnation point. It is convenient to fix the coordinate system in the ablation surface so that the interior of the nose moves toward its surface with a constant velocity $V_b$ equal to the unknown ablation rate. (See fig. 1.) The problem of heat conduction in the solid is first considered and attention is then turned to the problem of heat transfer and mass transfer in the boundary layer of constant thickness near the stagnation point.

Conduction of Heat in the Solid Nose

The transfer of heat in a solid moving with constant velocity $V_b$ in the y-direction is governed approximately by the following equation:

$$\rho_b V_b c_b \frac{dT}{dy} = \frac{d}{dy}\left(k_b \frac{dT}{dy}\right) \tag{1}$$

where heat transfer is considered to take place normal to the constant-temperature surface.

The solution of equation (1) which satisfies the conditions $T = T_w$ at $y = 0$ and $T = T_b$ as $y \to -\infty$ is

$$T = T_b + \left(T_w - T_b\right)\exp\left(\frac{c_b \rho_b V_b}{k_b} y\right) \tag{2}$$

From equation (2) the rate of heat transfer at $y = 0$ is

$$k_b\left(\frac{dT}{dy}\right)_w = \rho_b V_b c_b\left(T_w - T_b\right) \tag{3}$$

and the heat content of the nose is approximately

$$\frac{k_b}{V_b}\left(T_w - T_b\right) \tag{4}$$

per unit cross-sectional area which must be supplied before ablation starts.

## The Integrated Boundary-Layer Equations

The integral forms of the boundary-layer equations are written as follows:

For heat transfer,

$$-c_{p,2}\left(T_0 - T_w\right)V(Z) = \beta \int_0^Z c_p\left(T - T_w\right)\frac{u}{U}\,dz + \frac{k_w}{\rho_w}\left(\frac{dT}{dz}\right)_w \tag{5}$$

which expresses the heat balance in the boundary layer.

For mass transfer,

$$-V(Z) + V_w = \beta \int_0^Z \frac{u}{U}\,dz \tag{6}$$

The left-hand side of equation (6) denotes the rate of introduction of mass into the boundary layer whereas the right-hand side is the convection of mixture in the x-direction in the boundary layer.

For foreign-gas transfer,

$$V_w = \beta \int_0^Z W \frac{u}{U}\,dz \tag{7}$$

The rate of introduction of foreign gas is balanced by the convection of foreign gas in the boundary layer. In equations (5), (6), and (7)

$$V = \frac{\rho}{\rho_w}\,v$$

$$z = \int_0^y \frac{\rho}{\rho_w}\,dy$$

and

$$\beta = \frac{dU}{dx} = \frac{U}{x} \tag{8}$$

and is the velocity gradient at the stagnation point. The specific heat of the mixture is

$$\overline{c_p} = c_{p,1}W + c_{p,2}(1 - W) \tag{9}$$

The transfer boundary conditions at the ablation surface are

$$\rho_b V_b = \rho_w V_w = \dot{m} \tag{10}$$

$$-\rho_w D\left(\frac{dW}{dz}\right)_w = (1 - W_w)\rho_w V_w \tag{11}$$

$$k_w\left(\frac{dT}{dz}\right)_w = (L - B)\rho_w V_w + c_b\left(T_w - T_b\right)\rho_b V_b \tag{12}$$

The following simple profiles are now inserted into the integral equations:

$$\left.\begin{aligned} 1 - \frac{u}{U} &= \left(1 - \frac{z}{\delta_u}\right)^2 \\[2ex] \frac{T_0 - T}{T_0 - T_w} &= \left(1 - \frac{z}{\delta_T}\right)^2 \\[2ex] \frac{W}{W_w} &= \left(1 - \frac{z}{\delta_W}\right)^2 \end{aligned}\right\} \tag{13}$$

where $\delta_u$, $\delta_T$, and $\delta_W$ are, respectively, the thicknesses of the velocity, temperature, and concentration boundary layers.

The boundary-layer thickness when ablation takes place is greater than that of the corresponding no-ablation thickness and is given by

$$\frac{2}{3}\delta_u = \frac{2}{3}(\delta_u)_o + \frac{V_w}{\beta} \tag{14}$$

and the no-ablation thickness $(\delta_u)_o$ is related to the dimensionless heat-transfer parameter by equations (5) and (13) by

$$(\delta_u)_o = \frac{15}{2}\left(\frac{\mu}{\rho\beta}\right)_w^{1/2}\left(\frac{N_{Nu}}{R_w^{1/2}}\right)_{N_{Pr},w=1}$$ (15)

The value $\left(\dfrac{N_{Nu}}{R_w^{1/2}}\right)_{N_{Pr},w=1} = 0.72$ was taken from the exact solution of reference 3.

The integral equation for the transfer of foreign gas (eq. (7)) together with the boundary condition (eq. (11)) gives the following approximate expression for the concentration of foreign gas at the wall:

$$W_w = \frac{N_{Sc,w}^{2/3}\dfrac{\dot{m}}{(\rho\mu\beta)_w^{1/2}}}{\left(\dfrac{N_{Nu}}{R_w^{1/2}}\right)_{N_{Pr},w=1} + \dfrac{1}{5}\dfrac{\dot{m}}{(\rho\mu\beta)_w^{1/2}}}$$ (16)

which may now be used in the calculation of the specific heat $c_p$ of the mixture.

In a similar way the heat-transfer integral equation (eq. (5)) together with the boundary conditions (eqs. (10) and (12)) gives the approximate relation

$$\frac{1}{N_{Pr,w}}\left(\frac{N_{Nu}}{R_w^{1/2}}\right) + \frac{1}{5}N_{Pr,w}^{-2/3}\frac{\dot{m}}{(\rho\mu\beta)_w^{1/2}} = \left\{1 + \frac{L - B + c_b\left(T_w - T_b\right)}{c_{p,2}\left(T_o - T_w\right)} + \right.$$

$$\left.\left(\frac{c_{p,1}}{c_{p,2}} - 1\right)\left[1 - \frac{3}{2}N_{Sc,w}^{2/3}\left(N_{Pr,w}^{-1/3} - \frac{5}{7}\right)\right]\right\}\frac{\dot{m}}{(\rho\mu\beta)_w^{1/2}}$$ (17)

In terms of the rate of heat transfer $q_o$ to the unshielded nose,

$$\frac{q_0}{(\rho\mu\beta)_w^{1/2}} = \frac{q_{0,2}(T_0 - T_w)}{N_{Pr,w}}\left(\frac{N_{Nu}}{R_w^{1/2}}\right)_0 \text{ , equation (17) may be expressed in the}$$

form

$$\frac{\dot{m}}{(\rho\mu\beta)_w^{1/2}}\left[L - B + c_b(T_w - T_b) + \frac{\overline{c_p}}{c_{p,2}}\frac{N_{Pr,w}}{\left(\dfrac{N_{Nu}}{R_w^{1/2}}\right)_0}\frac{q_0}{(\rho\mu\beta)_w^{1/2}}\right]^{-1} \tag{18}$$

where

$$\overline{c_p} = \left[\frac{3}{2}N_{Sc,w}^{2/3}\left(N_{Pr,w}^{-1/3} - \frac{5}{7}\right) - \frac{1}{5}N_{Pr,w}^{-2/3}\right]c_{p,2} +$$

$$\left[1 - \frac{3}{2}N_{Sc,w}^{2/3}\left(N_{Pr,w}^{-1/3} - \frac{5}{7}\right)\right]c_{p,1} \tag{19}$$

is interpreted as an effective specific heat for the mixture in the boundary layer.

The effective heat capacity $H_{EFF}$ is given by

$$H_{EFF} = \frac{q_0}{\dot{m}} = L - B + c_b(T_w - T_b) + \frac{\overline{c_p}}{c_{p,2}}\frac{N_{Pr,w}}{\left(\dfrac{N_{Nu}}{R_w^{1/2}}\right)_0}\frac{q_0}{(\rho\mu\beta)_w^{1/2}} \tag{20}$$

It is seen that $H_{EFF}$ increases linearly with $\dfrac{q_0}{(\rho\mu\beta)_w^{1/2}}$. For high

heating rates $\dfrac{\dot{m}}{(\rho\mu\beta)_w^{1/2}} \rightarrow \dfrac{c_{p,2}}{\overline{c_p}}\dfrac{\left(\dfrac{N_{Nu}}{R^{1/2}}\right)_w}{N_{Pr,w}}$, a finite limit, although $\dot{m}$

continues to increase slowly because of the increase in $(\rho\mu\beta)_w^{1/2}$.

Thus at high heating rates the effective heat capacity continues to increase even though the rate of mass loss is almost constant. (See figs. 2 and 3.)

The effective specific heat $\overline{c_p}$ is seen to be a function of $c_{p,1}$, $c_{p,2}$, $N_{Pr,w}$, and $N_{Sc,w}$ so that it depends on the thermal and diffusive properties of the mixture of gas and air. Typical curves showing the variation of $\overline{c_p}/c_{p,2}$ with $c_{p,1}/c_{p,2}$, $N_{Pr,w}$, and $N_{Sc,w}$ are shown in figure 4.

## DISCUSSION OF RESULTS

The steady nondimensional rate of mass loss $\dfrac{\dot{m}}{(\rho\mu\beta)_w^{1/2}}$ is shown in figure 2 as a function of $\dfrac{q_0}{(\rho\mu\beta)_w^{1/2}}$, which has units Btu/lb and is independent of the nose shape. The effective heat capacity $H_{EFF}$ is also plotted against $\dfrac{q_0}{(\rho\mu\beta)_w^{1/2}}$. (See fig. 3.) In order to make a comparison with experimental results, the experimental values were corrected to take account of the time $\tau$ required to heat up the body before ablation could take place; this corrected value is given by equation (4) as

$$\tau = \frac{k_b}{V_b} \frac{T_w - T_b}{q_0}$$

The results presented here do not differ appreciably when other boundary-layer profiles are used; this agreement shows that the important conditions are the mass-transfer and heat-transfer boundary conditions at the surface of the nose. Since these conditions have been respected, it is not surprising that good agreement with the experimental results is obtained. (See figs. 2 and 3.)

The effective specific heat of the mixture $\overline{c_p}$ given by equation (19) is shown in figure 4 as a function of $c_{p,1}/c_{p,2}$ for different values of $N_{Pr,w}$ and $N_{Sc,w}$. Figure 4 shows that, for $c_{p,1}/c_{p,2} > 1$, $\overline{c_p}$ increases as the Schmidt number $N_{Sc,w}$ decreases but, for $c_{p,1}/c_{p,2} < 1$, $\overline{c_p}$ increases as $N_{Sc,w}$ increases.

An increase in Prandtl number $N_{Pr,w}$, however, causes an increase in $\overline{c_p}$ for both $c_{p,1}/c_{p,2} > 1$ and $c_{p,1}/c_{p,2} < 1$. These diffusive effects are explained very simply in the following way.

When the Prandtl number $N_{Pr,w}$ is large, the velocity boundary-layer thickness is greater than the thermal-layer thickness so that most of the convection in the x-direction takes place in the hot fast-moving layers of gas and the effective specific heat of the layer is high (see fig. 5); this is true for any value of $c_{p,1}/c_{p,2}$.

The Schmidt number effect is explained by noting that the highest $\overline{c_p}$ is obtained when the gas of higher specific heat is convected in the hot fast-moving layers furthest from the wall; thus, for $c_{p,1} > c_{p,2}$, a low value of the Schmidt number gives a high value of $\overline{c_p}$ since the foreign gas diffuses easily away from the wall before being convected. When $c_{p,1} < c_{p,2}$ and the Schmidt number is large, however, a high value of $\overline{c_p}$ is obtained; thus, the foreign gas does not diffuse easily but rather pushes the air into the hot fast-moving layers. (See fig. 5.)

## CONCLUDING REMARKS

The shielding of a body by ablation of a suitable material at the nose is a very effective method; the mechanism is such that the effective heat capacity increases with heat transfer and, as the theory shows, the rates of mass loss tend to increase only very slowly even when the rate of heat transfer increases considerably. The very simplicity of this method suggests that it deserves a great amount of effort in the processing of materials which have the appropriate thermal properties in the solid and gaseous state.

# REFERENCES

1. Sutton, George W.:  The Hydrodynamics and Heat Conduction of a Melting Surface.  Jour. Aero. Sci., vol. 25, no. 1, Jan. 1958, pp. 29-32, 36.

2. Lees, Lester:  Similarity Parameters for Surface Melting of a Blunt-Nosed Body in a High Velocity Gas Stream.  GM-TM-184 (Contract No. AF 18(600)-1190), The Ramo-Wooldridge Corp., July 29, 1957.

3. Reshotko, Eli, and Cohen, Clarence B.:  Heat Transfer at the Forward Stagnation Point of Blunt Bodies.  NACA TN 3513, 1955.

ABLATION CONFIGURATION
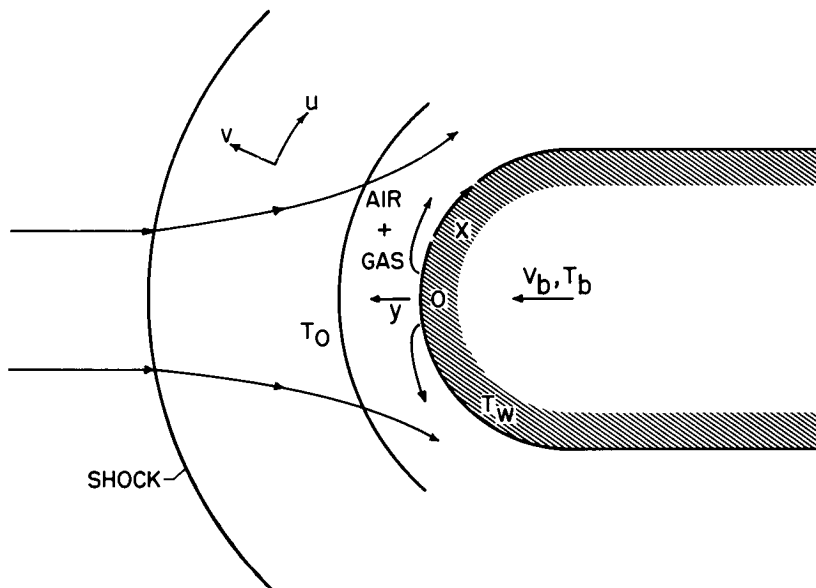


Figure 1

COMPARISON WITH EXPERIMENTAL RESULTS FOR TEFLON MODELS
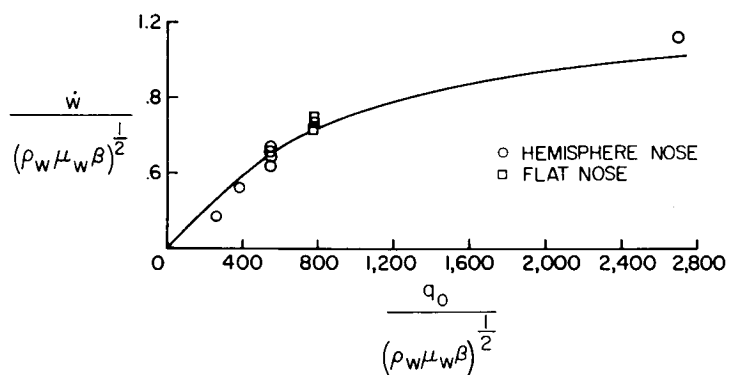


Figure 2

COMPARISON WITH EXPERIMENTAL RESULTS FOR TEFLON MODELS
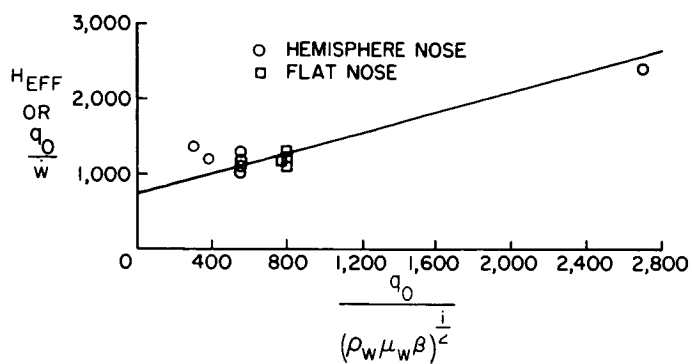


Figure 3

EFFECTIVE SPECIFIC HEAT OF THE MIXTURE
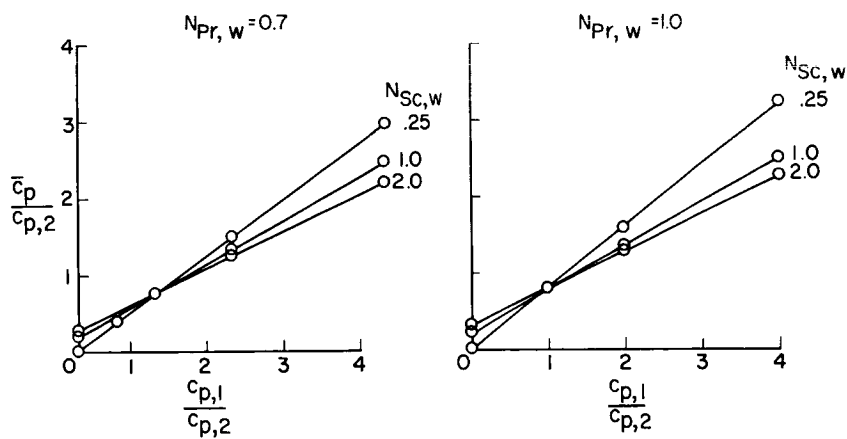


Figure 4

EXPLANATION OF SHIELDING

IF $c_{p,1} > c_{p,2}$, THEN $N_{Sc,w} < 1$ AND $N_{Pr,w} > 1$ GIVE

LEAST MASS LOSS



IF $c_{p,1} < c_{p,2}$, THEN $N_{Sc,w} > 1$ AND $N_{Pr,w} > 1$ GIVE

LEAST MASS LOSS



Figure 5

CONFIDENTIAL
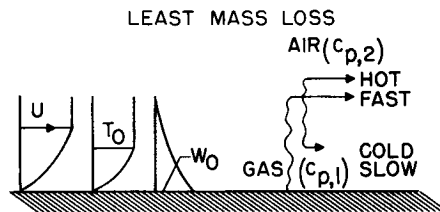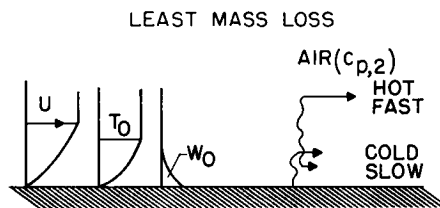
EXPERIMENTAL ABLATION COOLING

By Aleck C. Bond, Bernard Rashis,
and L. Ross Levin

Langley Aeronautical Laboratory

## SUMMARY

This paper presents the results of an experimental investigation on the ablation of a number of promising materials for heating conditions comparable to those which may be encountered by unmanned reentry satellite vehicles, as well as for higher heating conditions comparable to those associated with reentry ballistic missiles. Materials tested included the plastics Teflon, nylon, and Lucite; the inorganic salts ammonium chloride and sodium carbonate; graphite; a phenolic resin and fiber glass composition; and the commercial material Haveg Rocketon. Results of these tests indicated heat-absorption capabilities which are several times greater than those of current metallic heat-sink materials. The results with Teflon showed that for hemispherical noses there was no apparent effect of size or stagnation-point pressure on ablation rate for the range of variables covered in the tests. For flat-faced configurations, however, there was a definite increase in the ablation rate with increased stagnation-point pressure. The results for the several materials tested at heating rates associated with reentry ballistic missiles showed considerable increase in the effective heats of ablation over the results obtained at lower heating rates. This trend of increased effectiveness with increased heating potential is in agreement with the predictions of ablation theories. Comparisons of the results for several materials tested at the higher heating rates showed graphite to have the lowest ablation rate of all materials tested.

## INTRODUCTION

Ablating surface materials appear to hold considerable promise as a cooling or heat-shielding system for high-speed vehicles, from the standpoint of simplicity as well as efficiency. A theoretical treatment by Leonard Roberts of the Langley Laboratory, for ablating materials which sublime rather than melt, has indicated the desirable properties for such materials. Likewise the theoretical treatments of ablation systems with materials which exhibit the intermediate liquid phase by such investigators as Lees (ref. 1) and Sutton (ref. 2) have also indicated the prime requisites for such systems. Further, these studies have all shown that

the absorption of heat by ablation involves a number of complex mechanisms which require considerable knowledge of material properties in the various states (solid, liquid, and gaseous) for complete analytical treatment, and therefore detailed experimental investigation of the ablation phenomena is necessary. The purpose of this paper is to present some recent experimental data on the ablation of a number of promising materials for conditions of medium to high aerodynamic-heating rates. These data were obtained in three hot-air jet facilities of the Langley Laboratory.

## SYMBOLS

$h_{EFF}$ — effective heat of ablation, $\dfrac{\bar{q}}{\bar{w}/S}$, Btu/lb

$M_\infty$ — free-stream Mach number

$p_{t,2}$ — surface pressure at model stagnation point, lb/sq in. abs

$\bar{q}$ — average aerodynamic heating rate (for a nonablating surface) for flat face or hemispherical nose at a surface temperature equal to the melting or decomposition temperature of the material, Btu/(sq ft)(sec)

$S$ — surface area of flat face or hemispherical nose, sq ft

$T_w$ — surface temperature, $^\circ$F

$T_t$ — stagnation temperature, $^\circ$F

$t$ — time, sec

$W$ — weight, lb

$\bar{w}$ — average rate of weight loss from nose of model, $(\Delta W)_{NOSE}/\Delta t$, lb/sec

## TEST FACILITIES AND MODELS

The ceramic-heated jets (laboratory scale model and pilot model) of the Langley Pilotless Aircraft Research Division and the 700-kw electric-arc-powered air jet of the Langley Structures Research Division were used to conduct the present tests. The laboratory scale model, which is a $M_\infty = 2.0$ jet (ref. 3), was utilized to make exploratory

tests at moderate heating rates on the materials Teflon, Lucite, nylon, ammonium chloride, sodium carbonate, phenolic resin and fiber glass, and Haveg Rocketon. Hemispherical-nosed models 1/2 and 5/8 inch in diameter were used in these tests. The pilot model jet, which is a similar but larger facility $(M_\infty = 3.65)$, was used to investigate the effect of such factors as size, shape, and surface pressure, as well as heating rate, on Teflon. Both hemispherical and flat-faced models from 1/2 to 2 inches in diameter were tested in this facility. The electric-arc-powered air jet $(M_\infty = 2.0)$ was used to investigate the performance of nylon, Teflon, Rocketon, and graphite at extremely high heating rates. The test stagnation temperature was approximately $11,000^\circ$ F in this facility and hemispherical-nosed models of 1/4-inch diameter were employed in the tests.

## TEST TECHNIQUE AND DATA REDUCTION

The method of data reduction employed in these tests is illustrated in figure 1. The sketches at the top of the figure indicate the mode of ablation which was generally observed for both the hemispherical and flat-faced models. The hemispherical noses tended to maintain their hemispherical shape, and likewise the flat-faced models tended to maintain their flat face with some slight rounding at the corners. The weight loss of the nose was determined in most cases by weighing the model before and after testing to obtain a total weight loss and applying a correction to account for the material loss from the sides of the model. In some cases the nose weight loss was determined by calculating volumetric changes from enlargements of high-speed motion-picture film. It was found that this latter method agreed rather closely with the weighing method except for the materials which have high coefficients of expansion.

The average ablation rate of the nose $\bar{w}$ was determined by simply dividing the nose weight loss by the elapsed test time. Test times of 2 to 7 seconds were used for the ceramic-heated jet tests, and for the electric-arc-powered-jet tests the test times were 1/2 to 2 seconds except for the graphite test which was conducted for a period of about 4 seconds. In order to compare the several materials, the data were reduced to an effective-heat-of-ablation parameter $h_{EFF}$, defined as $\dfrac{\bar{q}}{\bar{w}/S}$.

Laminar heating distributions were assumed for all the ceramic-heated-jet tests since the Reynolds number (based on diameter) for the largest model tested was less than 600,000. Also, the nose surfaces eroded as would be expected with laminar heating distributions. Integration of the laminar heating distribution at $M_\infty = 2.0$ on a hemisphere

gives the result that the average heating rate to a hemisphere is equal to 1/2 the stagnation-point heating value. Likewise, integration of the laminar heating distribution for a flat face at $M_\infty = 2.0$ from the results of reference 4 yielded the result that the average heating rate to the flat face is about 3/4 of the stagnation-point heating ratio of a hemisphere of the same diameter. The theory of reference 5, modified for conditions behind the normal shock and including the appropriate velocity gradient, has been found to agree quite well with calorimeter measurements of the stagnation-point heating of hemispherical noses in these two facilities and was thus used to obtain the stagnation-point heating rates.

In the case of the electric-arc-powered air jet the average heating rate to the hemispherical-nosed models was obtained by converting calorimeter measurements of the heating rates to a copper model. Since the test Reynolds number (based on model diameter) is also quite low in this facility, and since the models here too eroded as would be expected with laminar heating distributions, it was assumed that the heating to these models was also laminar.

Surface temperatures used in calculating heat transfer for the various materials are given in the following table:

| Materials | Melting or decomposition temperature, $^\circ$F |
|---|---|
| Teflon | 1,000 |
| Phenolic resin and glass | 2,000 |
| Haveg Rocketon | 2,000 |
| Nylon | 600 |
| Lucite | 250 |
| Ammonium chloride ($NH_4Cl$) | 635 |
| Sodium carbonate ($Na_2CO_3$) | 1,560 |

Current literature on properties of Teflon (refs. 6 and 7, for example) does not give any fixed sublimation or decomposition temperature for this material, but indicates that it tends to become soft and jellylike at temperatures approaching $600^\circ$ F. Some data on mass loss rate with temperature are given in reference 7, from which it may be deduced that for high heating rates the decomposition temperature may be in the range from $1,000^\circ$ to $1,200^\circ$ F. Some simple laboratory tests were conducted in an attempt to determine the stabilization temperature of a metallic plate heated electrically at relatively high heating rates and covered on both sides with pieces of Teflon. When this stabilization temperature was extrapolated to eliminate the effect of the

gas layer produced between the heated plate and the Teflon, the resulting temperature was approximately 1,000° F.

The surface-temperature values used in the calculations for the phenolic resin and glass and for Haveg Rocketon were estimated from static-test measurements. Some recent measurements made with an optical pyrometer with models tested in the jets have substantiated the estimated values. The melting temperature of nylon was obtained through private correspondence with E. I. du Pont de Nemours & Company, Inc. Surface temperatures for the remaining materials, Lucite, ammonium chloride, and sodium carbonate, are handbook values and were obtained from reference 8.

## RESULTS AND DISCUSSION

### Exploratory Tests

Results of the exploratory ablation tests conducted at moderate heating rates in the laboratory scale model ceramic-heated air jet and at high heating rates in the electric-arc-powered air jet, all at a Mach number of 2.0, are shown in figure 2. The data are presented as the effective-heat-of-ablation parameter $h_{EFF}$ plotted against the average aerodynamic heating rate and were obtained with 1/2- and 5/8-inch-diameter models in the ceramic-heated jet and 1/4-inch-diameter models in the arc-powered jet. The heating-rate scale is broken in this figure in order that the trends in the lower range of heating will not be obscured. The lower heating-rate range (75 to about 350 Btu/(sq ft)(sec)) is comparable to the heating rates which may be encountered by unmanned reentry satellite vehicles, whereas the higher heating rate ($\approx$1,570 Btu/(sq ft)(sec)) is in the category of heating rates associated with reentry ballistic missiles. Another range of heating rates exists for the manned reentry satellite vehicle, from 0 to about 75 Btu/(sq ft)(sec), as has been indicated in heating studies for such vehicles of reference 9. It is felt that caution should be used in extending the present data to this lower range of heating, since these materials may be affected by heat conduction and hence exhibit deterioration of physical strength under prolonged low heating rates.

For the lower heating rates the plastic materials Teflon, nylon, and Lucite show a decreasing effectiveness with increasing heating rate. The high values of effectiveness indicated for these materials at the lower heating rates are believed to be influenced somewhat by conduction into the solid and hence do not reflect values of effectiveness for steady ablation. This conduction effect was investigated experimentally for Teflon by testing a series of models at an approximately constant heating rate ($\bar{q} \approx 68$ Btu/(sq ft)(sec)) for successively longer periods

of time in order to determine the elapsed time at the actual beginning of ablation. At this low heating rate it was found that approximately 0.7 second elapsed before noticeable ablation began. At approximately 2.0 seconds the ablation rate was 90 percent of the leveling-off or asymptotic value. Applying this data correction to the value of $h_{EFF}$ (3,100 Btu/lb) at $\bar{q} \approx 76$ Btu/(sq ft)(sec) results in $h_{EFF} = 2,830$ Btu/lb. Therefore, conduction accounts for only about 10 percent of the uncorrected value of $h_{EFF}$. The correction for conduction would, of course, decrease with increasing heating rate and should be well within the experimental accuracy at heating rates of 200 to 300 Btu/(sq ft)(sec).

In the case of the phenolic resin and fiber glass composition and the Haveg Rocketon, which is a resin-asbestos composition, it is seen that $h_{EFF}$ increases with increasing heating rate. This can be explained by the fact that the resin in these materials burns readily, and hence at the lower heating rates the heat of combustion of the resin must counteract a significant portion of the shielding effect. However, as the heat input is increased the shielding effect apparently also increases.

Both sodium carbonate and ammonium chloride displayed higher average effective heats of ablation than any of the other materials at the lower heating values at which they were tested. The ammonium chloride has an effectiveness more than twice as great as that of the other materials at a heating rate of about 200 Btu/(sq ft)(sec). It should be mentioned that both these materials displayed low resistance to thermal shock, possibly because of the method of manufacture, which consisted of simply cold-pressing crystals of these materials to form the test specimen. This difficulty might be overcome by the use of suitable binders or reinforcement materials during manufacture.

The values of $h_{EFF}$ for Teflon, nylon, and Rocketon at the higher heating rates of the arc-powered jet show an increasing trend of effectiveness with heating rate. The Rocketon and nylon show more than a 200 percent increase in effectiveness over the values at lower heating rates; however, Teflon does not show such a marked increase in performance. This larger increase for nylon and Rocketon may be due to the more complete vaporization of the liquid layer which was seen to form on these materials at the lower heating rates. Teflon, on the other hand, did not display this liquid phase at any of the test heating rates but went directly from the solid to the gaseous state.[1] The trend of increased effectiveness with increased heating rate agrees with the theory of Lees

---

[1]These observations can be seen in a motion-picture film supplement L-296 which is available on loan from NACA Headquarters, Washington, D. C.

(ref. 1) which predicts increased effectiveness with higher enthalpy potentials. The trend of increased effectiveness for Teflon at higher heating rates is also predicted by the previously mentioned theory of Leonard Roberts, which was specifically developed for materials which sublime rather than melt.

A photograph showing several materials after test in the laboratory scale model ceramic-heated jet is given as figure 3. It can be seen that the plastic materials Teflon, nylon, and Lucite ablated quite uniformly with relatively small change in the hemispherical-nose shape. The Rocketon does not show as uniform ablation as the plastics and exhibits some charring at the nose due to burnout of the resin binder. The specimen of phenolic resin and fiber glass shown here was tested for a shorter period of time than the other materials and hence shows practically no effect. Other models of this material, tested for longer periods of time, showed considerable charring action as the resin binder was consumed.

The effect of the resin content of the phenolic resin and glass specimens on the average effective heat of ablation was investigated by testing specimens of different resin content for constant stagnation temperature or constant heating rate. Results of these tests for stagnation temperatures of 2,900° and 3,800° F are shown in figure 4. These results indicate decreasing effectiveness with increased resin content, due of course to the lower effectiveness of the resin binder itself. Indications are (private correspondence with the General Electric Company) that at higher heat fluxes (from 1,000 to 1,500 Btu/(sq ft)(sec)), the trend is reversed. The chemical breakdown of resin at these high heating rates apparently results in the formation of light gases which are relatively efficient in their shielding action.

Further Teflon Tests

In the initial tests at the moderate heating rates of the laboratory model ceramic-heated jet, the models utilized were all essentially the same size (1/2 and 5/8 inch in diameter), the stream total pressure was maintained constant for all the tests, and the aerodynamic heating rate was varied simply by changing the stagnation temperature. In order to investigate the effect of such test conditions as temperature, pressure, and model size and shape, a program was laid out for a somewhat systematic variation of these test conditions. Teflon was chosen as the material, since it is relatively easy to handle and fabricate, it ablates rather uniformly, and it also has the characteristic of going directly from the solid to the gaseous state without any intermediate liquid phase. The program as outlined for this series of tests is shown in figure 5, and includes the previously discussed initial tests. As previously stated, the

initial tests in the laboratory scale model ceramic-heated jet were all conducted at constant stream total pressure, and hence $p_{t,2}$, which is the surface pressure at the model stagnation point, is constant in all of these tests. In the pilot model ceramic-heated jet, systematic variations of heating rate were accomplished for 1-inch-diameter flat-faced models by varying stagnation temperature for two levels of stagnation pressure. Likewise the effect of size on both flat-faced and hemispherical-nosed models was investigated at the higher pressure level and at near-constant stagnation temperature. The test conditions for the electric-arc-powered air jet are also included here.

The data from these various tests on Teflon are presented in figure 6 as the average rate of ablation per unit surface area as a function of the average aerodynamic heating rate. The open symbols denote the data for hemispherical-nosed models and the partially and completely filled symbols denote the data for the flat-faced models. In general, the points for the hemispherical-nosed models tend to lie along one line without any discernible effects resulting from changes in model size or stagnation-point pressure. It should be noted that here again the heating-rate scale has been broken and, hence, the one data point for the highest test heating rate, if plotted on an unbroken scale, would show a reduction in slope of the average rate of ablation at the higher heating rates. The points for the flat-faced models at the lower pressure level (denoted by the half-filled squares) also tend to agree with the trend of the data for the hemispherical-nosed models; however, the data for the flat-faced models at the higher pressure level show a pronounced effect of pressure on ablation rate.

The ablation-rate data of figure 6 have been reduced to the effective-heat-of-ablation parameter $h_{EFF}$ and are presented in figure 7 again as a function of the average aerodynamic heating rate $\bar{q}$. All the data for the hemispherical-nosed models show essentially the same trend with $\bar{q}$, and the flat-faced models tested at the lower stagnation-pressure level (denoted by the half-filled squares) also agree with this trend. The three points for the flat-faced models at the higher stagnation-point pressure (denoted by the filled squares) gave lower values of $h_{EFF}$, but tend to approach the trend established by the other data at the higher heating rates. The data point at the higher heating rate of the electric-arc-powered jet, which is the same as that presented previously for Teflon in figure 2, indicates the gradually increasing trend of effectiveness with heating rate for rates greater than about 250 Btu/(sq ft)(sec).

It is known that the heat of depolymerization of Teflon decreases with increased pressure, and hence the reduction in effectiveness for the flat-faced models at the lower heating rates may possibly be a result of the higher pressure loading on the flat face. As heating rate

is increased the heat of depolymerization becomes a less significant part of the total effectiveness, since the shielding effect is becoming more predominant.

Photographs of several typical Teflon models after test in the pilot model ceramic-heated jet are shown in figure 8. In general, these photographs show that the smaller models, up to 1 inch in diameter, ablated quite uniformly with little change in basic shape. Both the flat-faced and the hemispherical-nosed model of 2-inch diameter showed some local pitting or cratering which may be attributed to transition to turbulent flow, or possibly to increased heating due to impact of ceramic dust with the model surface.

As a matter of interest a comparison is made in figure 9 of the experimental effective heat of ablation of Teflon (presented in fig. 7 for hemispherical-nosed models) with the effectiveness for a nitrogen-transpiration-cooled hemispherical nose shape of the same diameter as the Teflon models. The lower curve for nitrogen was calculated for a surface temperature of $1,000^\circ$ F, the temperature used in the calculation of heating rates for Teflon. The upper transpiration-cooling curve was calculated for a surface temperature of $1,500^\circ$ F, which is considered a practical limit of surface temperature for porous stainless-steel materials employed in transpiration cooling systems, and thus represents the most effective cooling that can be achieved with nitrogen for the aerodynamic heat fluxes to which the Teflon models were subjected.

Both nitrogen curves indicate less cooling effectiveness than those for Teflon for the range of $\bar{q}$ from about 75 to 225 Btu/(sq ft)(sec). At the very high heating rate of 1,570 Btu/(sq ft)(sec), however, the nitrogen transpiration effectiveness is calculated to be more than twice the effectiveness of Teflon. It should be noted that the calculations of the nitrogen values were based on the theoretical curve of Stanton number ratio as a function of the flow-rate parameter given in Lees' analysis (ref. 1) and not on experimental values. The theoretical curves are based on the assumption that the exiting coolant has properties identical to those of the local stream flow. For the electric-arc-powered air jet, the local stream properties may very well be substantially different from those of the transpired coolant.

If a lighter gas such as helium had been chosen for the comparison, it would have been shown to be considerably more effective than the Teflon ablating system. Nitrogen was chosen for the comparison since it was estimated that the properties of the Teflon gas resemble those of nitrogen. Likewise, the comparison could have been made with some of the other ablating materials which show considerably higher effectiveness than Teflon.

## Graphite Test

Considerable interest has been expressed in the use of carbon as an ablating material in view of its extremely high heat of vaporization. Reference 10 indicates values of about 26,000 Btu/lb for the heat of vaporization of carbon. In order to take advantage of these high heats of vaporization, carbon or graphite should be used at conditions where the surface can reach the vaporization or sublimation temperature of these materials. Test temperatures in the ceramic-heated jets are not high enough to achieve surface vaporization; however, the test temperature ($\approx 11,000^\circ$ F) of the electric-arc-powered air jet is more than adequate. A test was conducted in this facility with a 1/4-inch-diameter hemisphere-cylinder model, made of AGR graphite, and the measured ablation-rate data are shown in figure 10 and are compared with the previously discussed ablation-rate data for the several other materials tested in this facility. The graphite model was tested for a period of 4 seconds in order to obtain a measurable weight loss. As can be seen from this bar-graph presentation, the graphite is considerably better than any of the other materials tested at these high heating conditions. It has only about 1/8 the erosion rate of the better of the other materials, Rocketon.

Some additional tests conducted with graphite in the laboratory scale model ceramic-heated jet at a stagnation temperature of $4,000^\circ$ F showed that in spite of the fact that graphite suffers from oxidation at such temperatures, the ablation rate was only about 1/2 that measured in the arc-powered jet.

## CONCLUDING REMARKS

The experimental results given in this paper have indicated several ablating materials that have effective heat-absorption capabilities several times greater than those of current metallic heat-sink materials. Since the ablating materials investigated herein are rather unconventional, the choice of a given material for application to an actual vehicle should, of course, involve consideration of strength, workability, ease of manufacture and handling, and so forth. The results with Teflon showed that for hemispherical-shaped noses there was no apparent effect of size or stagnation-point pressure on the trend of ablation rate for the range of variables covered in the tests. For the flat-faced configuration, however, there was a definite increase in the magnitude of ablation rate with increased stagnation-point pressure. The results for the several materials tested at heating rates comparable to those encountered by a reentry ballistic missile showed considerable increase in the effective heats of ablation over the results obtained

at lower heating rates.  This trend of increased effectiveness with increased heating potential is in agreement with the prediction of theory.  Comparisons of the results for several materials tested at the higher heating rates of the electric-arc-powered air jet showed graphite to have the lowest ablation rate of all materials tested in this facility.

CONFIDENTIAL

# REFERENCES

1. Lees, Lester: Similarity Parameters for Surface Melting of a Blunt-Nosed Body in a High Velocity Gas Stream. GM-TM-184 (Contract No. AF 18(600)-1190), The Ramo-Wooldrige Corp., July 29, 1957.

2. Sutton, George W.: The Hydrodynamics and Heat Conduction of a Melting Surface. Jour. Aero. Sci., vol. 25, no. 1, Jan. 1958, pp. 29-32, 36.

3. Fields, E. M., Hopko, Russell N., Swain, Robert L., and Trout, Otto F., Jr.: Behavior of Some Materials and Shapes in Supersonic Free Jets at Stagnation Temperatures up to 4,210° F, and Descriptions of the Jets. NACA RM L57K26, 1958.

4. Stoney, William E., Jr.: Aerodynamic Heating of Blunt Nose Shapes at Mach Numbers up to 14. (Prospective NACA paper.)

5. Sibulkin, M.: Heat Transfer Near the Forward Stagnation Point of a Body of Revolution. Jour. Aero. Sci. (Readers' Forum), vol. 19, no. 8, Aug. 1952, pp. 570-571.

6. Levitt, A. P., and Wong, A. K.: A Survey of the Elevated Temperature Properties of Teflon and Kel-F. Rep. No. WAL 397/9, Watertown Arsenal Labs. (Watertown, Mass.), Aug. 24, 1956.

7. Madorsky, S. L., Hart, V. E., Straus, S., and Sedlak, V. A.: Thermal Degradation of Tetrafluoroethylene and Hydrofluoroethylene Polymers in a Vacuum. Nat. Bur. Standards Jour. Res., vol. 51, no. 6, Dec. 1953, pp. 327-333.

8. Hodgman, Charles D., ed.: Handbook of Chemistry and Physics. Thirty-sixth ed., Chemical Rubber Publishing Co., 1954-1955.

9. Faget, Maxime A., Garland, Benjamine J., and Buglia, James J.: Preliminary Studies of Manned Satellites - Wingless Configuration: Nonlifting. (Prospective NACA paper.)

10. Bloxsom, Daniel E., Jr.: Cooling of Solid Surfaces With Heat Power Inputs Over $10^5$ Watts/$cm^2$. 1957 Heat Transfer and Fluid Mechanics. Institute (Held at C.I.T.), Stanford Univ. Press, June 1957, pp. 159-172.

CONFIDENTIAL

## DATA REDUCTION
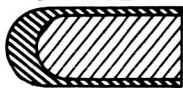
**HEMISPHERE-CYLINDER**  **FLAT-FACED CYLINDER**

$$(\Delta W)_{NOSE} = (\Delta W)_{TOTAL} - (\Delta W)_{SIDES}$$

$$\bar{w} = (\Delta W)_{NOSE}/\Delta t$$

$$h_{EFF} = \frac{(\bar{q})_{NOSE}}{\left(\frac{\bar{w}}{S}\right)_{NOSE}}$$

Figure 1

## EFFECTIVE HEATS OF ABLATION OF SEVERAL MATERIALS
### $\frac{1}{4}$-IN., $\frac{1}{2}$-IN. AND $\frac{5}{8}$-IN. DIAM. HEMISPHERE NOSES

$h_{EFF} = \frac{\bar{q}}{\bar{w}/s}$, BTU/LB

$NH_4Cl$, TEFLON, $Na_2CO_3$, PHENOLIC+GLASS, LUCITE, ROCKETON, NYLON

$\bar{q}$, BTU/(SQ FT)(SEC)

Figure 2

## SEVERAL MATERIALS AFTER TEST

### 5/8" DIA. MODELS

TEFLON

NYLON

LUCITE

ROCKETON

1/2" DIA. PHENOLIC RESIN AND GLASS
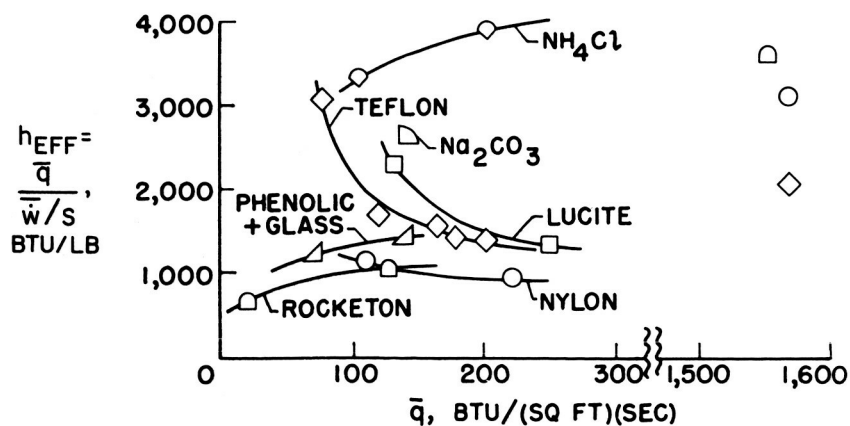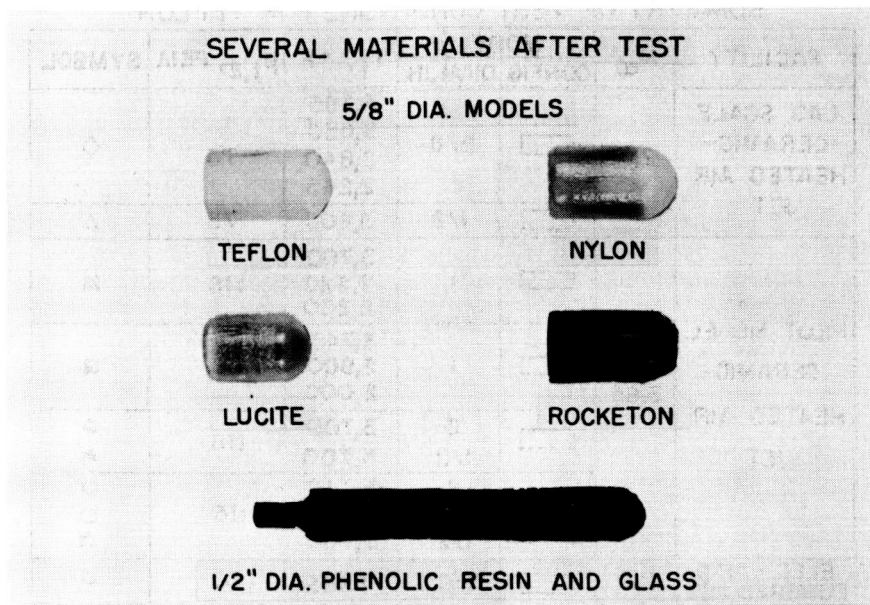
Figure 3

## EFFECT OF RESIN CONTENT ON EFFECTIVE HEAT OF ABLATION

GLASS–REINFORCED PHENOLIC RESIN;
$\frac{1}{2}$ –IN.– DIAM. HEMISPHERICAL NOSES

$T_t = 3,800\,°F$
$\bar{q} = 140 \dfrac{BTU}{(SQ\,FT)(SEC)}$

$h_{EFF}$, BTU/LB

$T_t = 2,900\,°F$
$\bar{q} = 70 \dfrac{BTU}{(SQ\,FT)(SEC)}$

RESIN CONTENT, PERCENT
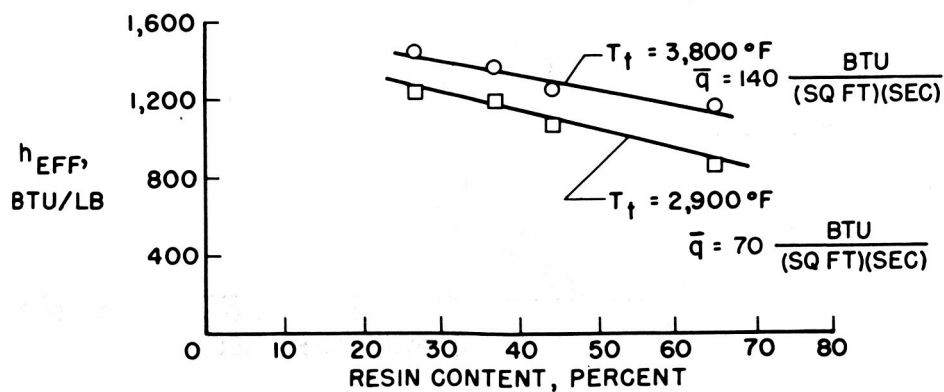
Figure 4

### SUMMARY OF TEST CONDITIONS FOR TEFLON

| FACILITY | $M_\infty$ | MODEL | | $T_t$, °F | $p_{t,2}$, PSIA | SYMBOL |
|---|---|---|---|---|---|---|
| | | CONFIG. | DIAM., IN. | | | |
| LAB. SCALE CERAMIC-HEATED AIR JET | 2.0 | ▭ | 5/8 | 3,755 3,550 2,840 2,245 | 75 | ◇ |
| | | ▭ | 1/2 | 3,800 | 75 | △ |
| PILOT MODEL CERAMIC-HEATED AIR JET | 3.65 | ▭ | 1 | 3,700 2,820 2,200 | 116 | ■ |
| | | ▭ | 1 | 3,740 2,900 2,000 | 58 | ◪ |
| | | ▭ | 2 1/2 | 3,700 3,700 | 116 | ● ▲ |
| | | ▭ | 2 1 1/2 | 3,710 3,710 3,730 | 116 | ○ □ ◁ |
| ELEC.-ARC-POWERED JET | 2.0 | ▭ | 1/4 | 11,000 | 70 | ◿ |

Figure 5

## AVERAGE RATE OF ABLATION OF TEFLON
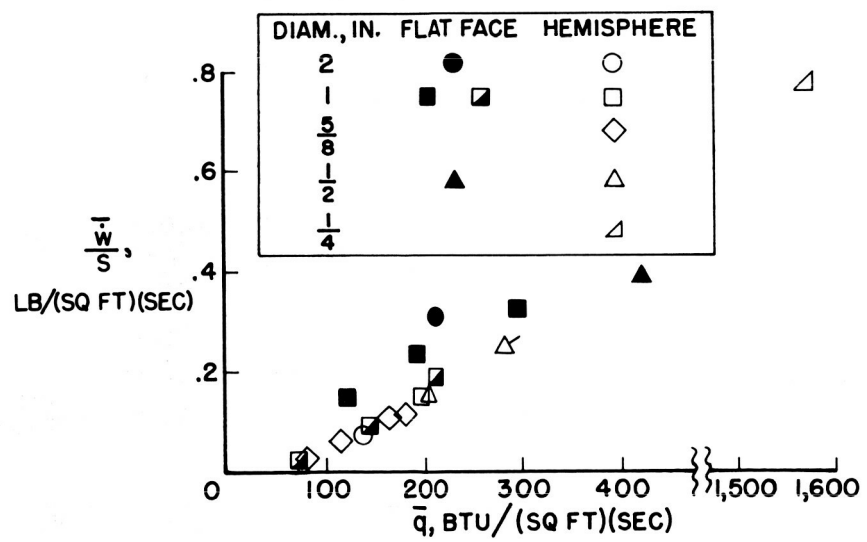


Figure 6

## EFFECTIVE HEAT OF ABLATION OF TEFLON



Figure 7



SEVERAL TYPICAL TEFLON MODELS AFTER TEST
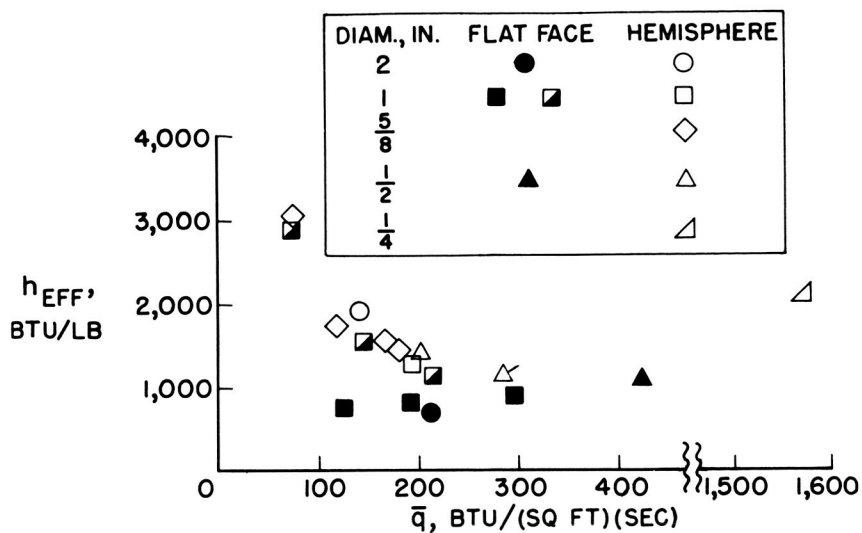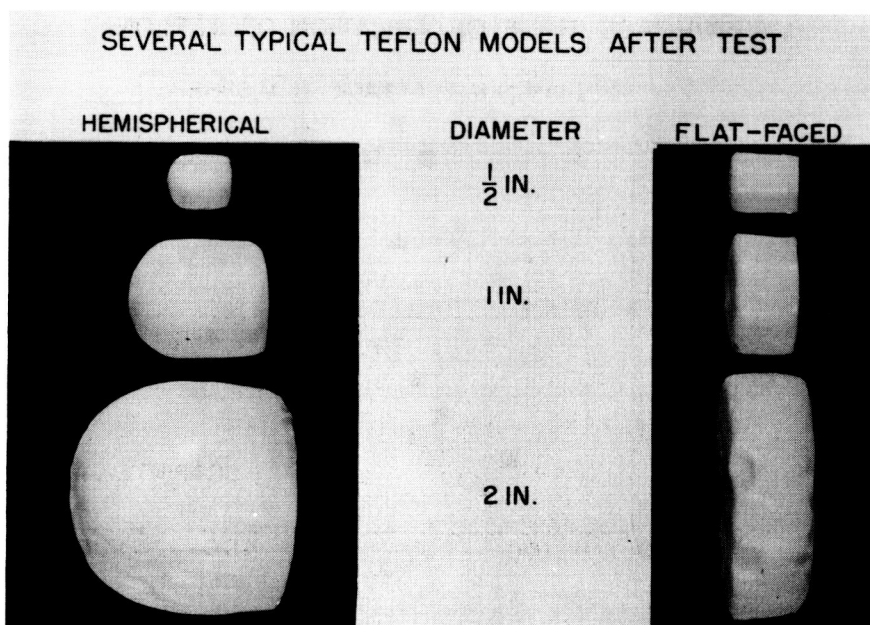
Figure 8

## COMPARISON OF EFFECTIVENESS OF ABLATION
## AND TRANSPIRATION COOLING
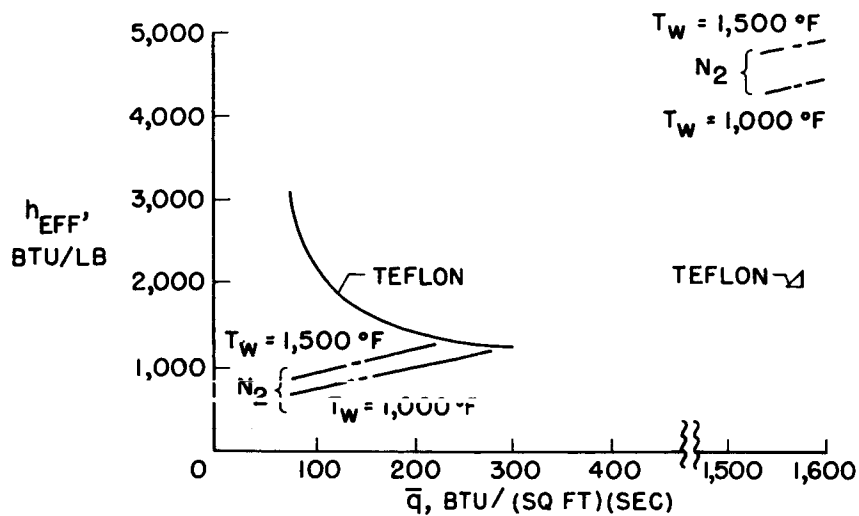


Figure 9

## AVERAGE RATE OF ABLATION OF SEVERAL
## MATERIALS IN ELECTRIC-ARC-POWERED AIR JET

$M_\infty \approx 2.0$; $T_f \approx 11,000$ °F
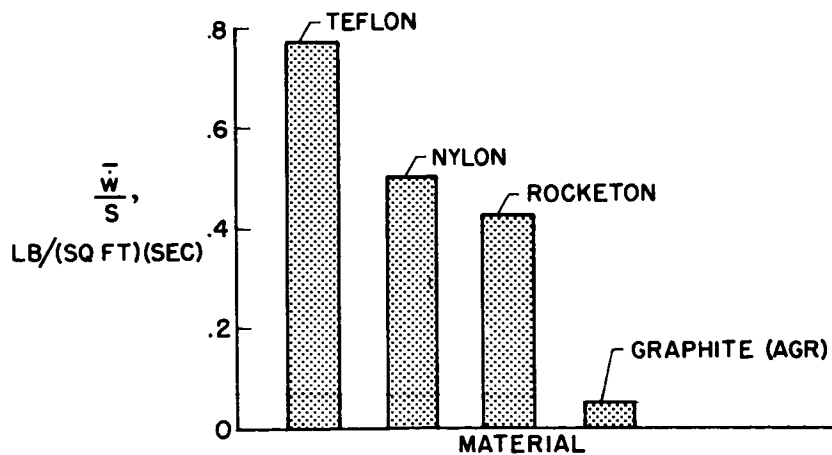


Figure 10

# PRELIMINARY EXPERIMENTAL STUDY OF ENTRY HEATING

## USING THE ATMOSPHERIC ENTRY SIMULATOR

By Stanford E. Neice

Ames Aeronautical Laboratory

## INTRODUCTION

The continuing interest in long-range missiles has stimulated the search for new experimental techniques which can reproduce in the laboratory the effects of aerodynamic heating associated with the missile's flight. One of the new experimental techniques which has been developed at the Ames Aeronautical Laboratory is the atmospheric entry simulator in which the total heat per unit mass as well as thermal stresses associated with the atmospheric entry of a ballistic missile can be duplicated in a scaled model launched upstream through a specially designed supersonic nozzle.

A schematic diagram of the apparatus, indicating the component parts, is presented in figure 1. The apparatus consists of four main parts: pressure tank, test section, vacuum tank, and model launcher. The pressure tank is initially separated from the test section by a diaphragm which can be ruptured to permit high-pressure air to flow through the test section into the vacuum tank. The model launcher serves to put models into flight, at the speed desired, upstream along the axis of the test section. Models can be recovered in a catcher located in the pressure reservoir. As the model proceeds through the test section, a time-distance history is deduced from electronic counters which operate on photobeam signals "triggered" by the model's passage. From the time history, a velocity record can be obtained. The photobeam signal also operates through a time-delay circuit to take spark shadowgraphs of the model at a point downstream of each photobeam station. Conditions of flight can be adjusted to simulate the total convective heat per unit mass associated with the atmospheric entry of a ballistic missile.

The theoretical basis for simulation was discussed in reference 1. A subsequent report, reference 2, presented the practical significance of the method. Also included in reference 2 were the results of an investigation of the atmospheric entry of a cylindrical shape employing

the heat-sink principle whereby the entire heat imparted to the model during atmospheric entry is to be absorbed in an outer shell of high heat capacity and conductivity.

In the case of the heat-sink vehicle, the required amount of heat absorbing material can become prohibitive; hence, the interest in a second method whereby the latent heat of vaporization of a lightweight, nonconducting material is utilized as the heat-absorbing process. Thus the outer shell would be continuously diminished during descent through the atmosphere.

An examination of the factors involved in establishing a given temperature distribution in a material - namely, dimensionless parameters which include heat-transfer coefficient, time, dimension, and diffusivity - indicates that the conditions previously used to duplicate total convective heat input per unit mass and thermal stress will also tend to duplicate the vaporization-ablation process. The model will experience ablation due to convection heating to the same degree as the missile; the percent weight loss of the model from such ablation during traverse through the simulator will duplicate that of the missile during atmospheric entry.

## SYMBOLS

| | |
|---|---|
| A | cross-sectional area of body, sq ft |
| $C_D$ | drag coefficient |
| D | body diameter, ft |
| R | nose radius, ft; also, range from launch, nautical miles |
| $V_E$ | entrance velocity, ft/sec |
| W | weight, lb |
| $\theta_E$ | entry angle, deg |

## METHOD

In the current tests, solid models are used. Since missiles will employ ablating materials only as an outer shell, the similarity

relating to internal conditions merits explanation. The ablation process, including thermal stresses, is confined only to the outermost portion of the surface. Any shell, therefore, where the thickness is large in comparison with the "disturbed region" of the surface should very nearly produce the same results as the so-called "infinitely thick shell." Any surface phenomenon such as ablation or spalling should therefore be duplicated by a solid model. Structural failures occurring near the surface tend to be transmitted throughout the particular material. The initial surface consequence of such failure should also be duplicated, whereas the end effect, such as complete destruction of the model, would not.

Certain phenomena which may not be simulated in these experiments should be mentioned. In particular, there are the reaction times for such processes as the sublimation of surface material as well as chemical processes taking place in the boundary layer. Sufficient data to determine these times for synthetic long-chain molecules, such as nylon and Teflon, do not appear to be available. These reaction-rate phenomena, therefore, remain a subject for future study. Radiation phenomena are not simulated. For the velocity range of the current tests, the total heating by radiation to the body from the hot gases surrounding the body as well as from the body to the surrounding medium is much smaller than the total convective heating. The lack of simulation of radiation, therefore, is not important in these present tests.

## DISCUSSION

The shapes used in this investigation are shown in figure 2. The first shape was the blunt spherical-nosed cone-cylinder with a nose radius about one-quarter of the body diameter and having a one-half-caliber cylindrical afterbody. The second shape was the one-half-caliber cylinder, as shown. The first series of models weighed 110 milligrams and the second, 77 milligrams. Both models had diameters of 0.222 inch and were constructed of nylon. In figure 3, the corresponding missiles that these models simulate are shown. The simulated missiles have a diameter of 2.70 feet. The spherical-nosed cone-cylinder has a nose radius of 0.65 foot, a cylindrical afterbody of 1.35 feet in length, and a weight of 710 pounds; the cylinder, on the other hand, has an overall length of 1.35 feet and weighs 540 pounds. The ratio $W/C_D A$ for both simulated vehicles is also presented. According to an analysis reported in reference 3, both missiles should have a total range of 1,620 nautical miles when launched at an angle of $38^\circ$ to the horizontal with a velocity of 15,800 feet per second.

In this first series of tests all models were launched at velocities between 15,200 and 15,800 feet per second. A typical velocity profile as obtained for a spherical-nosed cone-cylinder is shown in figure 4. In this figure the theoretical velocities for the simulated missile along with the experimental model velocities are plotted according to simulated altitude. The altitude range duplicated by the simulator is as shown. The agreement between theoretical and experimental values demonstrates that one of the requirements for simulation has been satisfied; namely, that the velocity at corresponding points in the trajectory be the same for model and missile.

A spherical-nosed cone-cylinder model, as recovered, after completed flight is shown in figure 5 and is compared with a similar model which has not been fired. Noticeable features of the recovered model are the appearance of a small crater at the stagnation point and the pattern of cracks which emanate from that point. Contrast this with figure 6 which shows a cylindrical model as recovered after having completed traverse through the simulator. The appearance of pits on the surface can readily be seen. There are, however, no surface cracks or other indications of failure as have been observed on the spherical-nosed cone-cylinder.

The failure of the spherical-nosed model, as seen here, was not always sufficiently extensive to cause complete destruction during simulation. This is illustrated in the spark shadowgraphs presented in figure 7, which shows the model in a completed flight at three representative locations in its traverse through the simulator. For this model, the point of maximum convective heat-transfer rate to the stagnation point occurs at an altitude of about 108,000 feet. In the second shadowgraph, the model has passed the altitude of maximum heating rate and thermal stress at the stagnation point. The lower shadowgraph shows the model intact and adequately centered in the airstream.

In contrast to this particular test, a series of shadowgraphs showing an abortive flight is presented in figure 8. Launching and flight conditions were nearly identical to those in the successful flight. Of all models launched, about two-thirds failed in the manner shown here. Such failure might be caused by the launching forces. The intact appearance of the model in the upper shadowgraph would tend to preclude such failure. Damage to the model in the form of small cracks would, however, not show in the shadowgraphs and hence launching as a factor contributing to model failure cannot be ruled out. The stresses encountered at impact into the catcher, where the model was embedded only a fraction of an inch in balsa wood, would scarcely produce such failure. The remaining possibility is, of course, the thermal stress encountered during flight.

The recovered spherical-nosed models, no matter how they were cracked, were in sufficiently good condition for weighing and measuring. Recovered cylindrical models were, of course, quite suitable. The results obtained from simulator tests of five spherical-nosed (blunt) cone-cylinders and five half-caliber cylinders (each constructed of nylon and launched at velocities between 15,200 and 15,800 feet per second) indicated that the percentage weight loss was 2.6 percent for the blunt cone-cylinders and 1.4 percent for the half-caliber cylinders. In both cases, the weight loss in launching, corresponding to the diameter decrement, has been subtracted from the total loss. For the spherical-nosed cone-cylinder, the weight loss to the simulated missile would amount to about 18 pounds corresponding to a uniformly distributed loss of about 0.4 inch of nylon over the entire front portion. For the cylindrical shape, the full-scale weight loss would be 7.5 pounds corresponding to a uniformly distributed loss of about 0.2 inch of nylon over the entire front face.

In the final tests with nylon, an attempt was made to determine the maximum velocity at which the spherical-nosed model would remain entirely intact throughout flight. Several launchings were performed at continuously reduced velocities until models were recovered intact. The velocities for each of these launchings were 10,300 feet per second after prior abortive runs at 11,700 feet per second. A recovered model, initially launched at 10,300 feet per second, is shown in figure 9 and is compared with a similar model launched at 15,800 feet per second. The intact appearance of the lower velocity model is evident. From the standpoint of material loss, nylon appears to be quite satisfactory. The failure of models launched at velocities greater than 10,300 feet per second causes doubt as to whether nylon would survive the thermal loading. Results in this respect are not conclusive, since the effects of launching forces must still be assessed. However, these particular nylon shapes will survive the thermal stresses during atmospheric entry for entrance velocities of at least 10,300 feet per second.

## CONCLUDING REMARKS

Tests using other materials are proceeding. Recent results of launching spherical-nosed Teflon models at velocities near 14,100 feet per second indicate a percentage weight loss of about $3\frac{1}{2}$ percent with the models remaining intact through the flight. Efforts are continuing to augment this velocity to values near 20,000 feet per second. Such velocities would permit the simulation of atmospheric entry of intercontinental ballistic missiles. Other materials will also be considered.

Tests, similar to those considered here, will be repeated with graphite and boron nitride and such other materials as may appear feasible.

REFERENCES

1. Eggers, A. J., Jr.:  A Method for Simulating the Atmospheric Entry of Long-Range Ballistic Missiles.  NACA RM A55I15, 1955.

2. Neice, Stanford E., Carson, James A., and Cunningham, Bernard E.: Experimental Investigation of the Simulation of Atmospheric Entry of Ballistic Missiles.  NACA RM A57I26, 1957.

3. Eggers, Alfred J., Jr., Allen, H. Julian, and Neice, Stanford E.: A Comparative Analysis of the Performance of Long-Range Hyper-velocity Vehicles.  NACA TN 4046, 1957.  (Supersedes NACA RM A54L10.)

## SMALL-SCALE ATMOSPHERIC ENTRY SIMULATOR

TEST SECTION
(SUPERSONIC NOZZLE)

PHOTOBEAM
STATION

VACUUM TANK

HELIUM GUN
(MODEL LAUNCHER)

CAMERA STATION
(TYPICAL)

PRESSURE
TANK

8        8        12

29

DIMENSIONS IN FEET
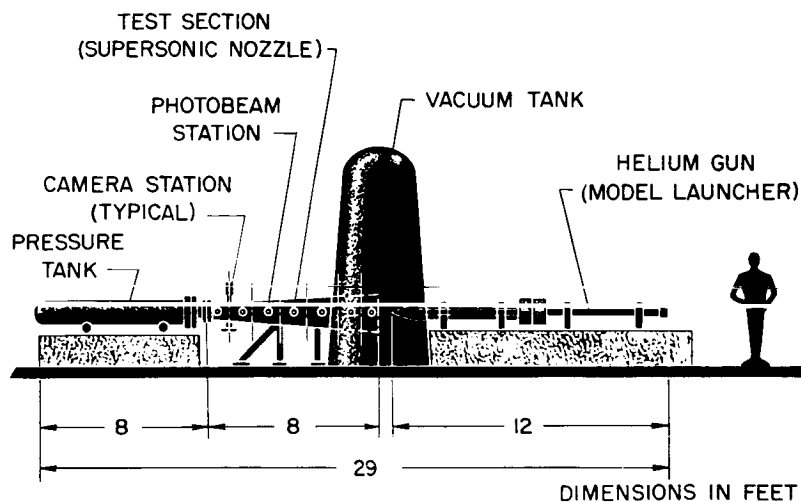
Figure 1

## TEST MODELS

MATERIAL, NYLON

.110"

.110"

51°

.222"D

.053"R

.222"D

SPHERICAL-NOSED CONE-CYLINDER
WT = .110 GMS

CYLINDER
WT = .077 GMS

Figure 2

## MISSILES SIMULATED



SPHERICAL-NOSED CONE-CYLINDER
WT = 710 LB
$\dfrac{W}{C_D A} = 100$
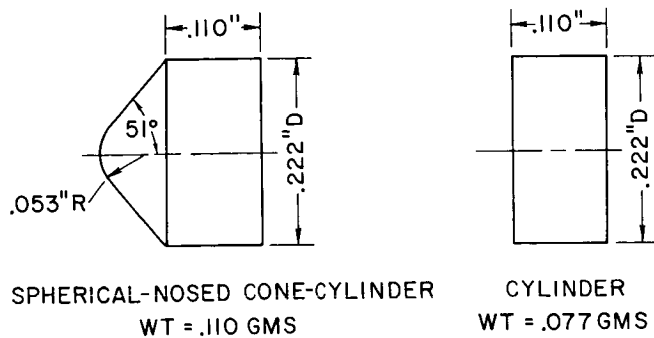
CYLINDER
WT = 540 LB
$\dfrac{W}{C_D A} = 51$
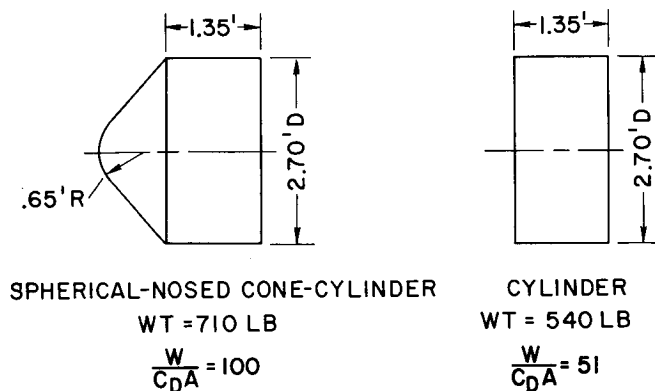
Figure 3

## VELOCITY OF SPHERICAL-NOSED CONE-CYLINDER MODEL
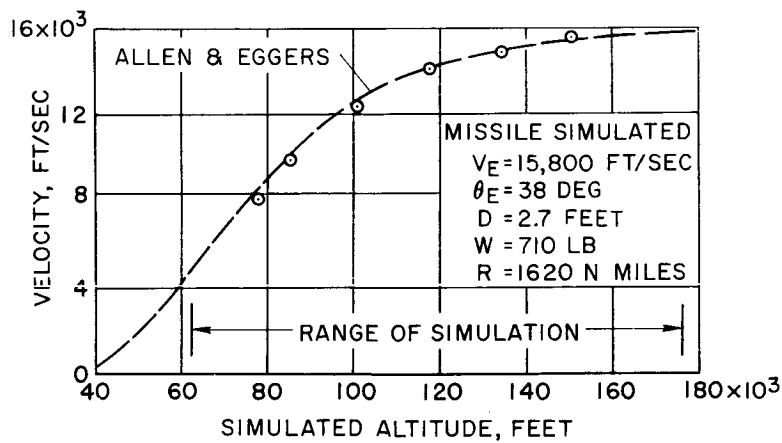


Figure 4

SPHERICAL-NOSED CONE-CYLINDER
LAUNCHED THROUGH SIMULATOR



BEFORE

AFTER
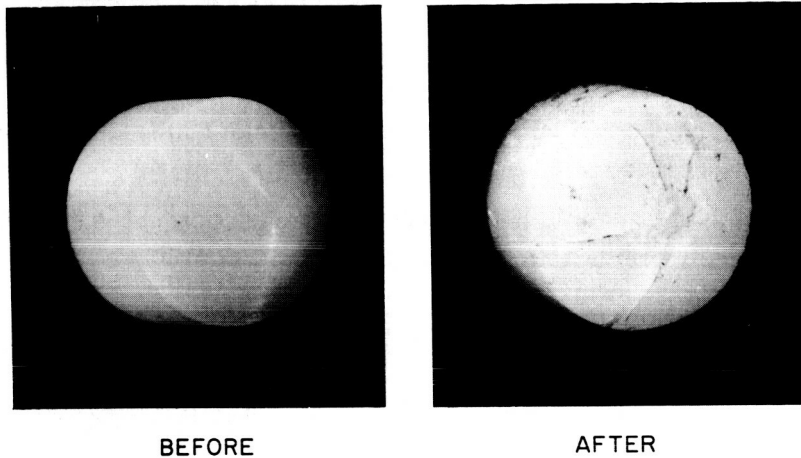
Figure 5

CYLINDERS LAUNCHED THROUGH SIMULATOR



BEFORE

AFTER
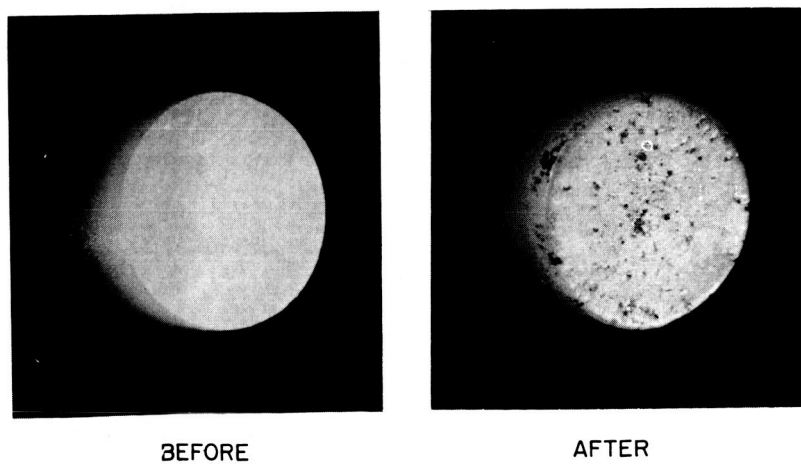
Figure 6

## COMPLETED FLIGHT OF SPHERICAL-NOSED
## CONE-CYLINDERS THROUGH SIMULATOR
$$V_E = 15,800 \text{ FT/SEC}$$
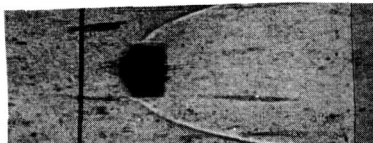
VELOCITY: 14,900 FT/SEC

SIMULATED
ALTITUDE: 134,500 FT

VELOCITY: 9,860 FT/SEC

SIMULATED
ALTITUDE: 85,900 FT

VELOCITY: 5,600 FT/SEC

SIMULATED
ALTITUDE: 70,600 FT

Figure 7

## ABORTIVE FLIGHT OF SPHERICAL-NOSED
## CONE-CYLINDERS THROUGH SIMULATOR
$$V_E = 15,800 \text{ FT/SEC}$$
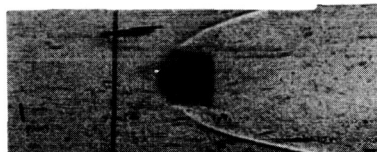
VELOCITY: 14,900 FT/SEC

SIMULATED
ALTITUDE: 134,500 FT

VELOCITY: 9,860 FT/SEC

SIMULATED
ALTITUDE: 85,900 FT

VELOCITY: 5,600 FT/SEC

SIMULATED
ALTITUDE: 70,600 FT

Figure 8

MODELS AFTER FIRING IN SIMULATOR
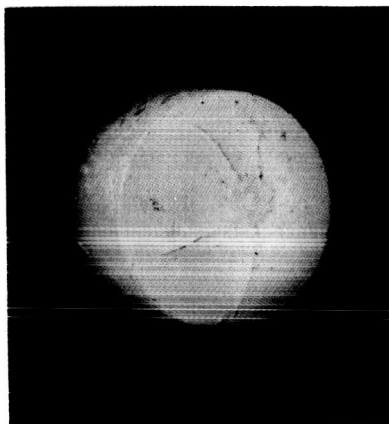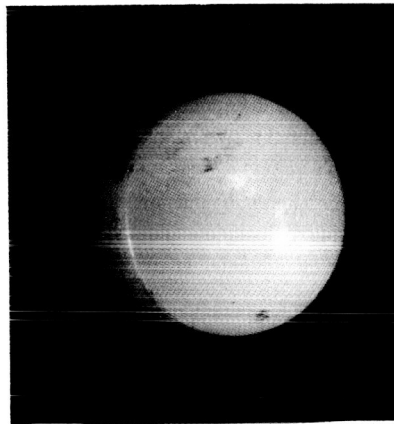


$V_E$ = 15,800 FT/SEC          $V_E$ = 10,300 FT/SEC

Figure 9

# HEAT TRANSFER TO SURFACES AND PROTUBERANCES IN A

## SUPERSONIC TURBULENT BOUNDARY LAYER

By Paige B. Burbank and H. Kurt Strass

Langley Aeronautical Laboratory

## SUMMARY

The presence of large protuberances that are only partially immersed in a turbulent boundary layer effects a large increase in heat transfer upstream and on each side of the protuberance wake. Extreme care must be taken in locating a protuberance in the influence of another one. The ratio at a particular thermocouple of the heat-transfer coefficient for the flat plate with the protuberance to the heat-transfer coefficient of the flat plate alone can be as great as 12 in the more adverse location.

## INTRODUCTION

The importance of minimum weight and maximum fuel volume has led in some cases to the location of major piping on the outer shell of large missiles. In the absence of a suitable theory for calculating the heat transfer to protuberances totally or partially immersed in a turbulent boundary layer, tests were conducted to determine experimentally the distribution of heat transfer to the protuberance and the adjacent skin area. Tests were conducted on several configurations with circular cylinders mounted normal to a flat plate to simulate antennas or externally mounted pipes.

## SYMBOLS

$N_{St}$      Stanton number

d      diameter, 2.8 in.

h      heat-transfer coefficient

$h_L$          heat-transfer coefficient based on free-stream conditions for laminar flow on cylinder of infinite length

$h_o$          heat-transfer coefficient of flat plate alone

M          Mach number

R          Reynolds number

T          wall temperature

$\delta$          boundary-layer thickness

$\psi$          meridian angle

Subscript:

x          distance from leading edge of flat plate

## MODEL DESIGN

The perspective drawing in figure 1 illustrates the instrumented cylinder mounted on the 4- by 10-foot flat plate that spans the test section along the horizontal center plane of the Langley Unitary Plan wind tunnel. A 1-inch-wide band of No. 60 carborundum grains located 4 inches rearward of the leading edge was used to insure a turbulent boundary layer. The leading-edge wedge was alined so that no flow deviation occurred on the test surface, and pneumatic seals prevented flow around the edges of the plate.

The instrumented portion of the flat-plate surface is composed of two interchangeable panels, each instrumented with iron-constantan thermocouples, having a uniform skin thickness of 0.050-inch stainless steel, and insulated from the support structure by a 1/2-inch honeycomb of Fiberglas. The panel used for a protuberance support has 84 thermocouples; the filler panel, 9 thermocouples.

The instrumented cylinder also constructed of stainless steel has a height of $12\frac{1}{2}$ inches, a diameter of 2.8 inches, and a uniform skin thickness of 0.050 inch. The cylinder is insulated from the flat plate by a 0.11-inch sheet of Micarta. Twenty-four thermocouples were located along the stagnation line and 45° and 90° from the stagnation line, as shown in figure 1.

## METHOD OF DATA REDUCTION

The heat-transfer coefficients are obtained from the basic heat-transfer equation by using the transient temperatures resulting from a stepwise increase in the stagnation temperature. The individual ratios of equilibrium temperature to stagnation temperature are determined prior to the stagnation temperature bump. The transient thermocouple measurements are obtained every 1/2 second for 1 minute on a Consolidated Engineering Corporation Millisadic.

## RESULTS AND DISCUSSION

The heat-transfer coefficients were first determined for the flat plate alone at Reynolds numbers per foot varying from $1.33 \times 10^6$ to $3.98 \times 10^6$ and at free-stream Mach numbers of 2.65 and 3.51. The resultant Stanton numbers for locations within 5 inches of the center line of the flat plate are shown for $M = 2.65$ at $R = 2.58 \times 10^6$ per foot and $M = 3.51$ at $R = 2.86 \times 10^6$ per foot in figure 2. The experimental Stanton numbers for the plate are somewhat lower (8 to 25 percent) than predicted by the Van Driest theory. Similar differences have frequently been noted by others.

The results of the protuberance tests are presented as a ratio at a particular thermocouple of the heat-transfer coefficient for the flat plate with the protuberance to the heat-transfer coefficient of the flat plate alone. This ratio will be referred to hereinafter as $h/h_o$.

The heat-transfer distribution is shown in figure 3 for a single cylinder mounted on the flat plate for a free-stream Mach number of 3.51 and a Reynolds number of $23.4 \times 10^6$.

The boundary-layer thickness, calculated by the method outlined in reference 1, at the position of the cylinder is 43 percent of the cylinder diameter. The distribution of thermocouple locations, denoted by crosses, permits considerable freedom in determining the location of the $h/h_o$ contours; the regions, therefore, are representative rather than exact. The influence of the cylinder is propagated upstream on the flat plate a distance of 2 diameters and the ratio $h/h_o$ increases to 8 at the stagnation line of the cylinder. The region of high heat transfer is washed downstream on each side of the cool region of the wake. The low heat transfer in the region of low-density separated flow in the wake is confined to a distance of less than 1 diameter; then $h/h_o$ increases to almost 2.

Increasing the Reynolds number per foot by a factor of $2\frac{1}{2}$ at a Mach number of 3.51 as shown in figure 4 has a negligible effect on the area influenced by the cylinder but decreases $h/h_o$ at the stagnation point (of the cylinder) from $8\frac{1}{2}$ to $6\frac{1}{2}$.

The Mach number was varied with a constant Reynolds number per foot. The most significant effect was shown to be an increase of $h/h_o$ at the stagnation line of the cylinder from 5 at a Mach number of 2.65 to 8 at 3.51 with no systematic effect in the wake.

The heat transfer on the cylinder is presented in figure 5 as the ratio of the measured heat-transfer coefficient to the calculated heat-transfer coefficient based on free-stream conditions for laminar flow on a cylinder of infinite length as presented in reference 2. This ratio will be referred to hereinafter as $h/h_L$. The ratio is shown for $M = 2.65$ and $3.51$ at the stagnation line; at three vertical distances from the flat plate the variation of the ratio about the forward $90^o$ of the cylinder is shown. The shock pattern caused by the interaction of the cylinder bow shock with the flat plate, as shown in figure 16 of reference 3, causes a high-density separated flow and a resultant thickening of the boundary layer that causes a region of high heat transfer whose proximity to the flat plate increases with increasing Mach number. The portion of the cylinder uninfluenced by the flat plate is in good agreement with theory. There is no measurable effect of Reynolds number on the distribution of $h/h_L$ on the cylinder.

The effect of locating the instrumented cylinder at several positions in the wake of a second cylinder was investigated at a Mach number of 3.51 and approximately $R = 2.8 \times 10^6$ per foot. The contour plot in figure 6 illustrates the heat-transfer distribution resulting from placing the instrumented cylinder 3.2 diameters downstream of a dummy cylinder. The region of high heating upstream of the dummy cylinder should be of the same magnitude as that for the single cylinder; the comparatively low indicated value of $h/h_o$ of 5 is due to the lack of instrumentation about this cylinder. The resultant wake and very mixed flow cause a reduction in heat transfer upstream of the instrumented cylinder. The thermocouple in the flat plate at the stagnation point indicates a value of $h/h_o$ of less than 4 in comparison with a value of 8 for the single cylinder. Figure 7 illustrates that the separated flow reduces the heat-transfer coefficient on the second cylinder; the value of $h/h_L$ varies from 0.3 to 0.8 along the stagnation line. The circumferential plots indicate flow reattachment resulting in a value of $h/h_L$ 25 to 50 percent higher than that predicted at the $45^o$ and $90^o$ stations.

In figure 8, the result of positioning the instrumented cylinder 6.4 diameters downstream of the dummy cylinder is shown. The relatively large distance between the two cylinders permits the flow field to reestablish a heat-transfer distribution similar to that for the single cylinder. The thermocouple on the flat plate at the stagnation line of the cylinder indicates a value of $h/h_0$ of 6 as compared with the value of 8 for the single-cylinder configuration. The heat-transfer distribution on the instrumented cylinder in figure 9 indicates that the large influence of the wake of the dummy cylinder on the stagnation line noted in the preceding configuration is considerably damped and the overall distribution is similar to that for the single cylinder. The reattached flat-plate boundary layer is thinner and the region of high heating is closer to the flat plate than with the single-cylinder configuration. The circumferential distribution of $h/h_L$ on the portion of the cylinder uninfluenced by the flat plate indicates that the measured values are less than predicted, and the deviation increases with increasing $\psi$.

Figure 10 shows the $h/h_0$ distribution resulting from placing the instrumented cylinder 3.2 diameters downstream of the dummy cylinder and offset so that a line connecting the centers of the cylinders forms an angle of $26\frac{1}{2}^{\circ}$ with the free stream. Superposing the contour plot for the single cylinder on the dummy cylinder indicates that the instrumented cylinder is just downstream of the region of high heat transfer associated with the bow shock of the leading cylinder, and the thermocouple reading at the stagnation line is only slightly higher than that of the preceding configuration. The distribution of $h/h_L$ on the cylinder shown in figure 11 indicates that the leading cylinder bow shock produces a slight increase in heat transfer closer to the flat plate than that associated with the single cylinder with maximum heating occurring at the edge of the boundary layer. The portion of the cylinder not influenced by the flat plate is in good agreement with theory.

In figure 12, the instrumented cylinder is 3.2 diameters downstream of the dummy cylinder, a line connecting the centers of the cylinders from an angle of $45^{\circ}$ with the free stream. The region of elevated heating from the leading cylinder bow shock impinges on the instrumented cylinder between 0 and $90^{\circ}$ and results in extremely high values of $h/h_0$ ranging from 9 to 12 adjacent to the cylinder. The cylinder heat transfer shown in figure 13 indicates that the region of maximum heating along the stagnation line occurs some distance from the flat plate with a maximum $h/h_L$ of $2\frac{3}{4}$. The circumferential plots indicate a value of $h/h_L$ of 2 for angles up to $45^{\circ}$.

Exploratory tests have also been conducted on roughness elements that are small compared with the boundary-layer thickness. Figure 14 illustrates the skin of a sandwich-construction element that had been deformed by abnormal heating rates. A model was constructed to duplicate this surface with the bottom of the dimples 0.020 inch below the surface. Tests were conducted in the ceramic-heated jet (pilot model) with a free-stream Mach number of 4 and stagnation temperatures of approximately 2,500° F. The test specimen was the surface of a 30° wedge and resulted in a surface Mach number of 3 and a free-stream Reynolds number of $6 \times 10^6$ per foot. Detailed temperature measurements failed to indicate any significant change in the level of the heating in the region of the dimpled surface as compared with that of a smooth surface.

Similar tests were conducted on stainless-steel Phillips-type screwheads in a stainless-steel surface. The location of the screws in relation to the model surface is shown in the upper sketch in figure 15. In order to simulate normal manufacturing tolerances, the surfaces of the screws were 0.015 inch above the model surface, flush, and 0.015 inch below the surface. Thermocouples on the back face of the screwheads and temperature measurements of the surface made by a photographic technique showed that all the screwheads reached temperatures which averaged approximately 100° hotter than those of the adjacent skin. The photograph of the model in figure 16 was taken during the latter portion of the test; the luminescence is a function of temperature. With the assumption that the high screw temperatures resulted from the fact that the mass of the screw is substantially less than that for a cylinder of skin of equal face area, the screwhead temperature time history was computed, with consideration of the conduction across the metal-to-metal interface as outlined in reference 4 and the assumption that the heat transfer was the same as that of the adjacent skin. The results in figure 17 show good agreement with theory. In order to check the assumption that the screwhead temperature is dependent upon the area exposed to aerodynamic heating and the conduction across the interface, a second model, illustrated in the lower portion of figure 15, was constructed. All three plugs have the same volume, one plug was cylindrical, the other two plugs were tapered with a ratio of two to one. On face areas with the same test conditions as those used on the honeycomb deformed skin, the plug with the large area outboard had a temperature 100° greater and the inverted plug had a temperature of 100° cooler than the cylindrical plug that had the same temperature as the model skin.

## CONCLUDING REMARKS

In conclusion, the presence of large protuberances that are only partially immersed in a turbulent boundary layer effects a large increase in heat transfer upstream and on each side of the protuberance wake.

Extreme care must be taken in locating a protuberance in the influence of another one. The ratio at a particular thermocouple of the heat-transfer coefficient for the flat plate with the protuberance to the heat-transfer coefficient of the flat plate alone can be as great as 12 in the more adverse location.

# REFERENCES

1. Tucker, Maurice: Approximate Calculation of Turbulent Boundary-Layer Development in Compressible Flow. NACA TN 2337, 1951.

2. Goodwin, Glen, Creager, Marcus O., and Winkler, Ernest L.: Investigation of Local Heat-Transfer and Pressure Drag Characteristics of a Yawed Cylinder at Supersonic Speeds. NACA RM A55H31, 1956.

3. Bloom, Martin H., and Pallone, Adrian: Heat Transfer to Surfaces in the Neighborhood of Protuberances in Hypersonic Flow. 1957 Heat Transfer and Fluid Mechanics Institute (Held at C.I.T.), Stanford Univ. Press, June 1957, pp. 249-278.

4. Barzelay, Martin E., Tong, Kin Nee, and Holloway, George F.: Thermal Conductance of Contacts in Aircraft Joints. NACA TN 3167, 1954.

## FLAT-PLATE HEAT-TRANSFER MODEL
## AND PROTUBERANCE
### LANGLEY UNITARY PLAN WIND TUNNEL
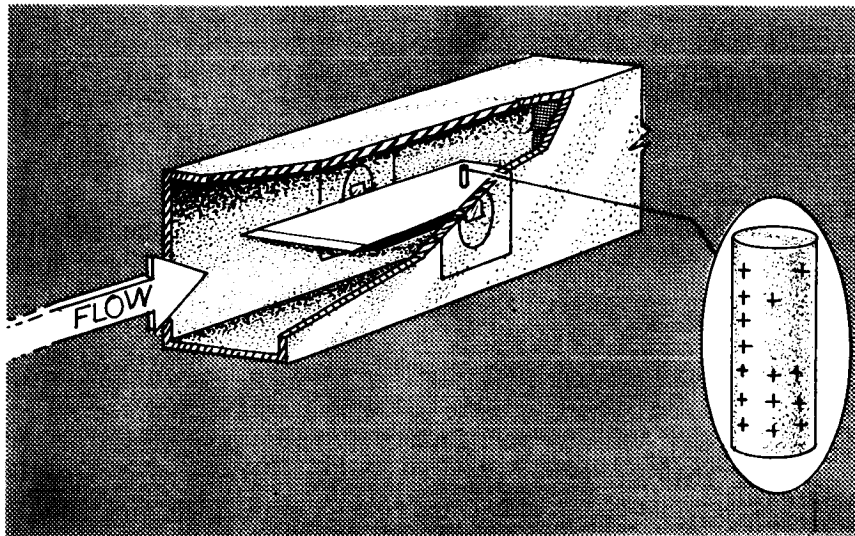


Figure 1

DISTRIBUTION OF STANTON NUMBER ALONG MODEL CENTER LINE
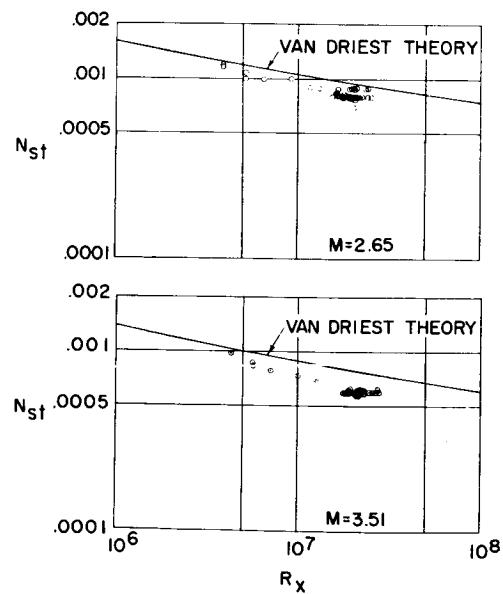


Figure 2

FLAT-PLATE HEAT TRANSFER

SINGLE CYLINDER; M = 3.51; $R_X$ = 23.4 X $10^6$
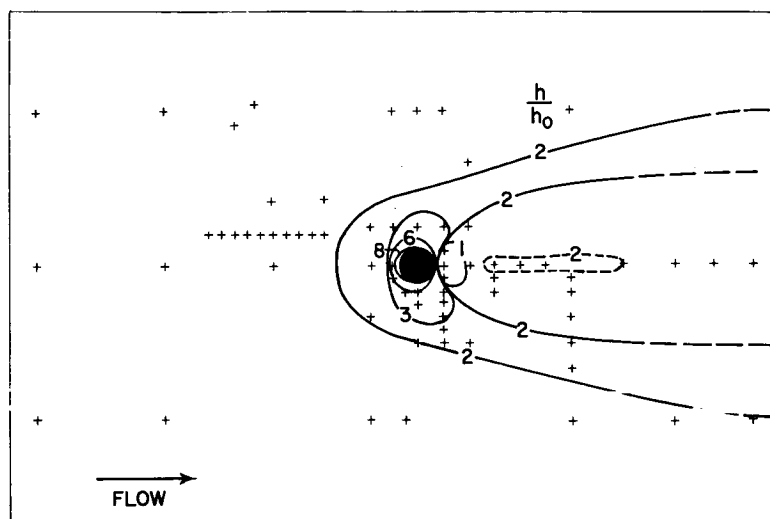


Figure 3

EFFECT OF REYNOLDS NUMBERS ON FLAT-PLATE HEAT TRANSFER

M = 3.51
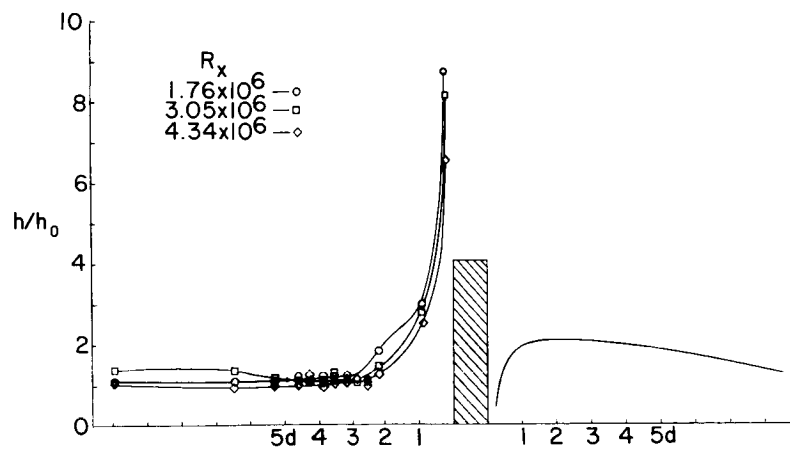


Figure 4

# CYLINDER HEAT TRANSFER
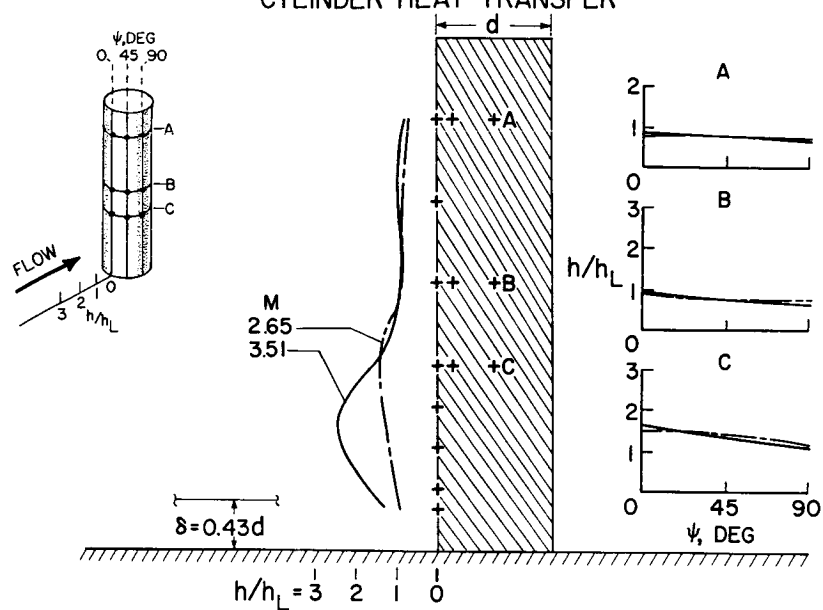


Figure 5

# FLAT-PLATE HEAT TRANSFER
## TANDEM CYLINDERS 3.2 d APART; M=3.51; $R_x$=21.6×10$^6$



Figure 6

## CYLINDER HEAT TRANSFER



Figure 7

## FLAT−PLATE HEAT TRANSFER
### TANDEM CYLINDERS SPACED 6.4d APART; $M=3.51$; $R_x = 21.6 \times 10^6$
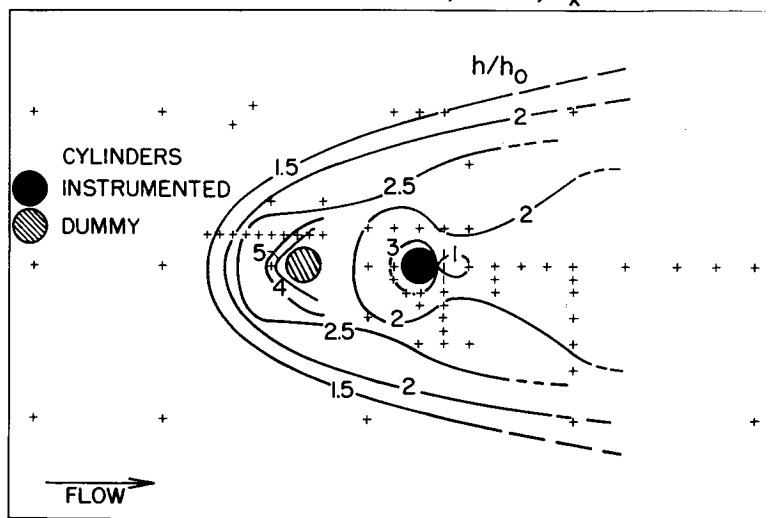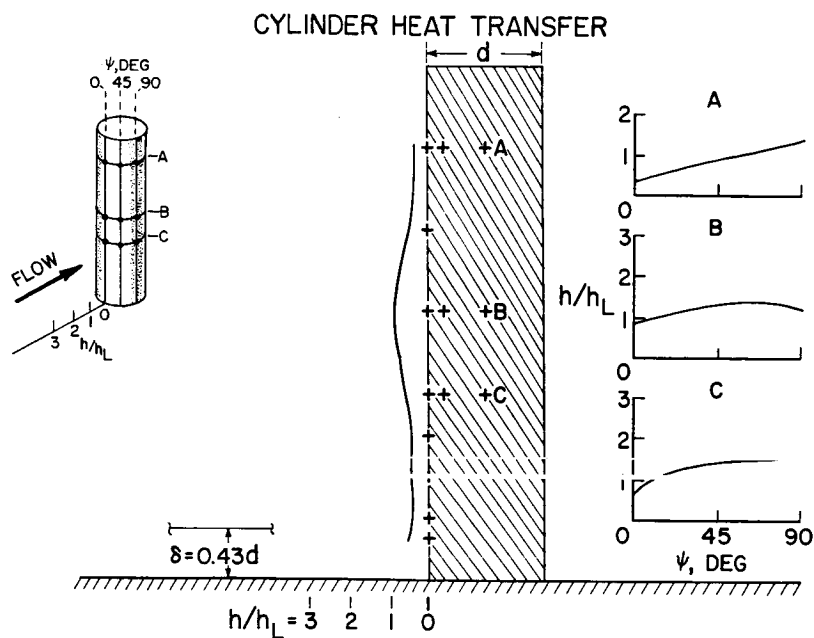


Figure 8
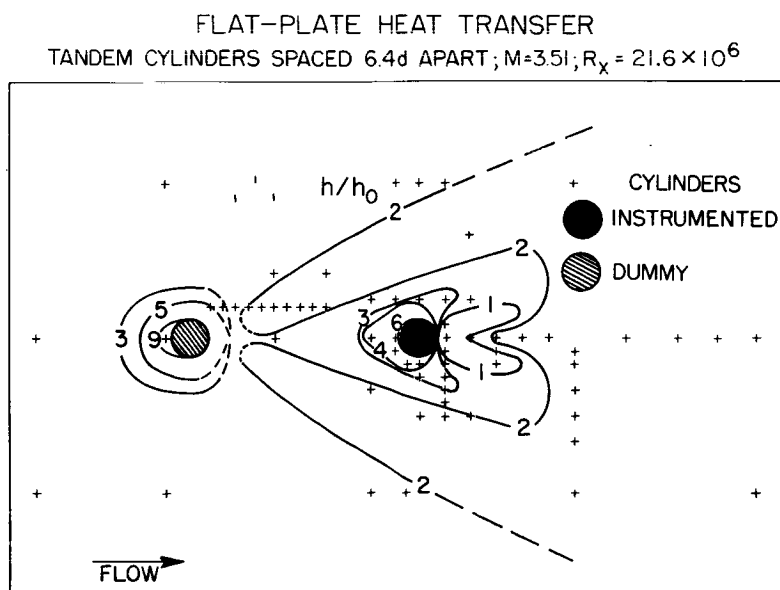
CYLINDER HEAT TRANSFER
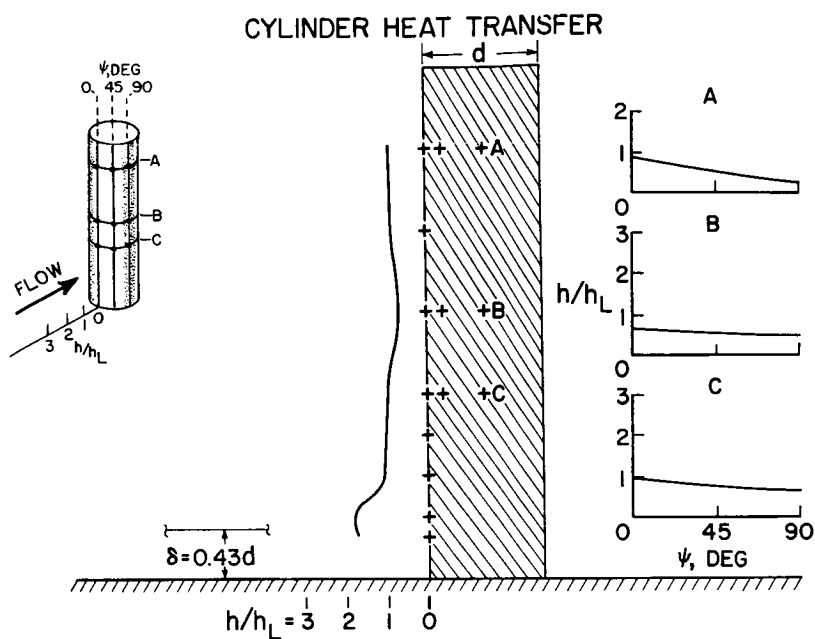
Figure 9



FLAT-PLATE   HEAT   TRANSFER
CYLINDERS WITH 26.5° OFFSET; M=3.51; $R_x$ =21.9x10⁶
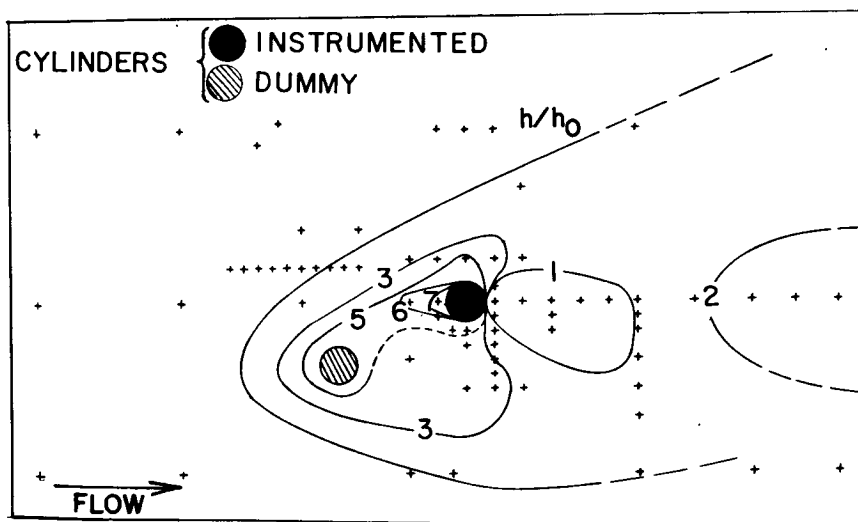
Figure 10

CYLINDER HEAT TRANSFER
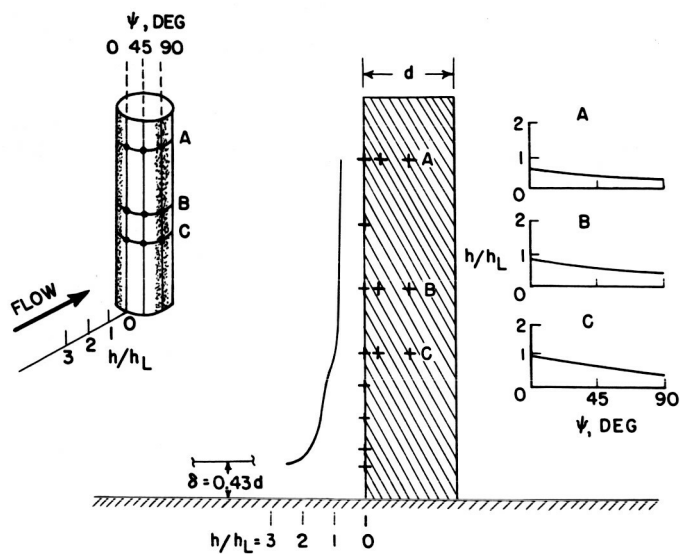


Figure 11

FLAT-PLATE HEAT TRANSFER
CYLINDERS WITH 45° OFFSET; M = 3.51; $R_X$ = 22.1 X $10^6$



Figure 12

310

CYLINDER HEAT TRANSFER



Figure 13

HONEYCOMB STRUCTURE AFTER HEATING
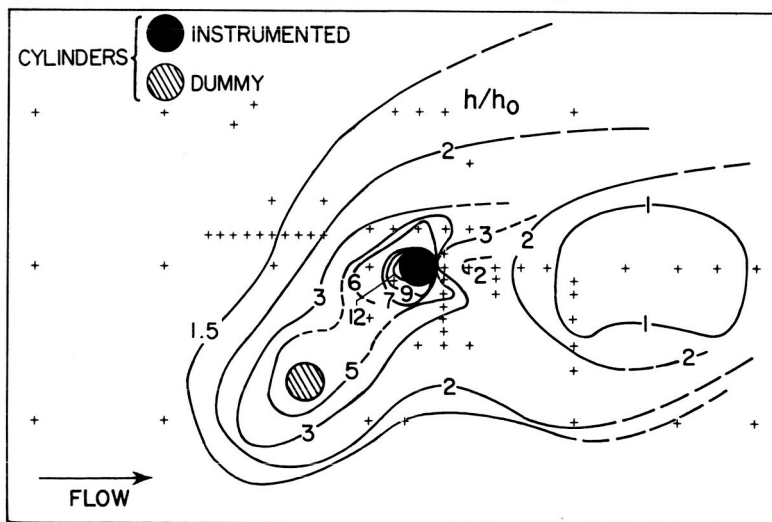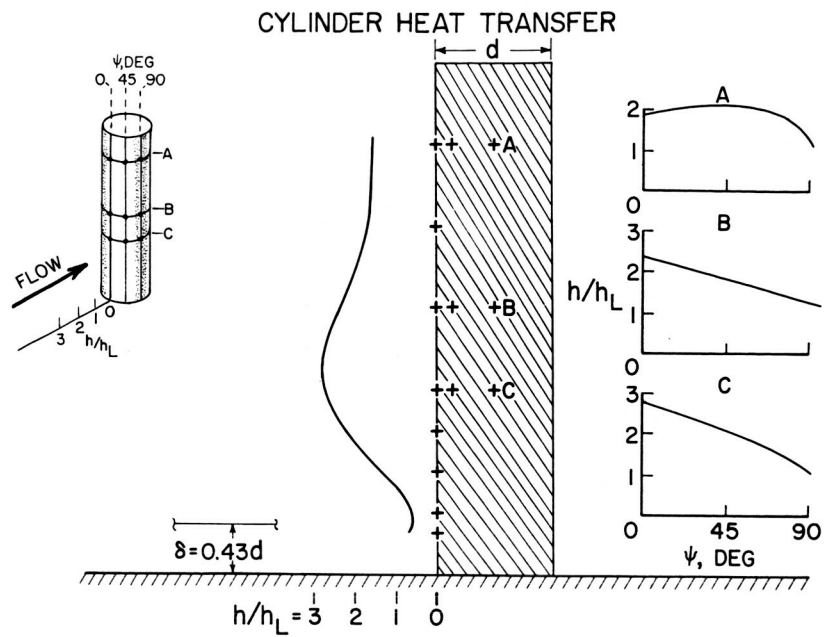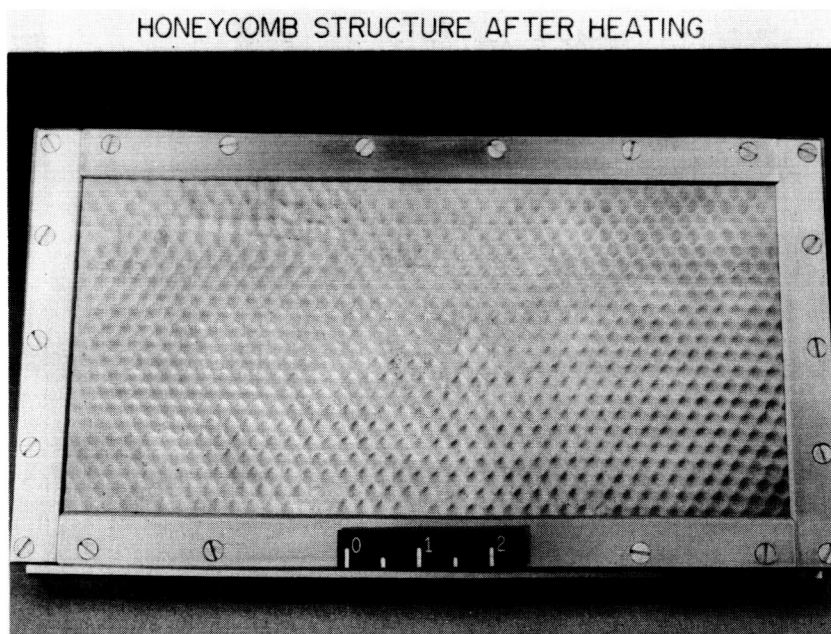


Figure 14

SPECIMENS TESTED IN PILOT-MODEL
CERAMIC-HEATED AIR JET

M=4
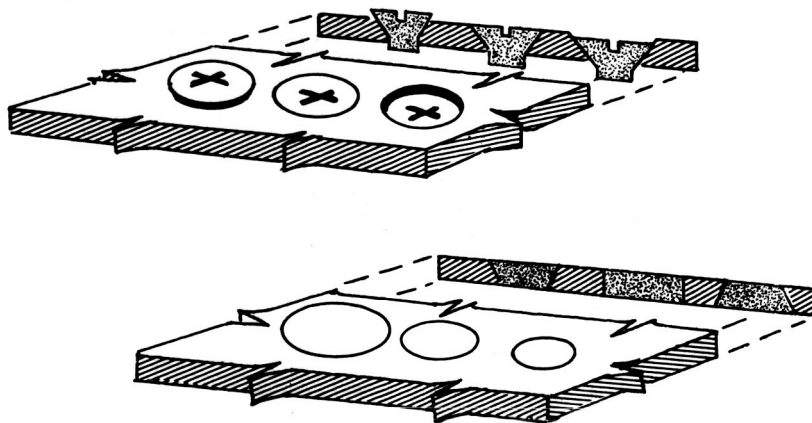


Figure 15



SCREWHEAD MODEL AT ELEVATED TEMPERATURE
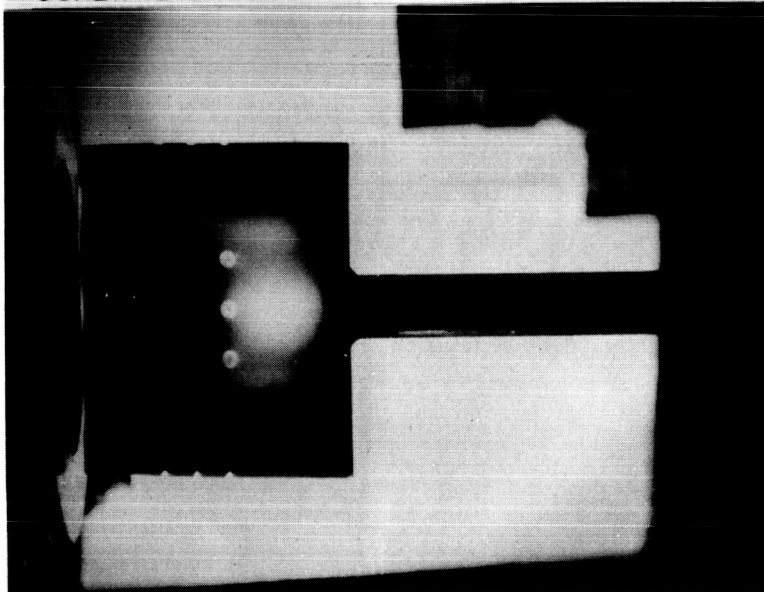
Figure 16

COMPARISON OF CALCULATED AND MEASURED
TEMPERATURE TIME HISTORY OF SCREWHEADS
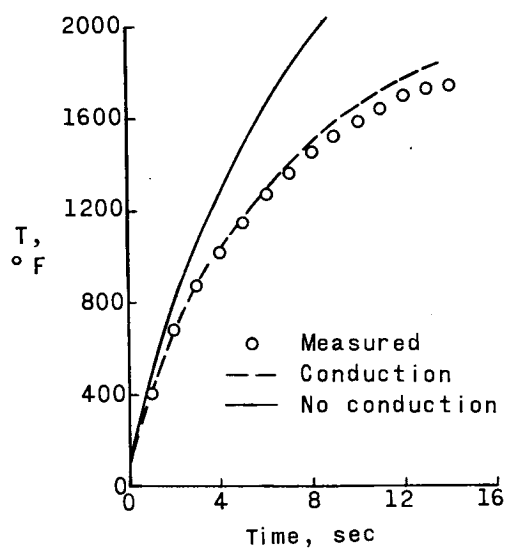


Figure 17

# EXPERIMENTAL STUDY OF BALLISTIC-MISSILE

## BASE HEATING WITH OPERATING ROCKET

By J. Cary Nettles

Lewis Flight Propulsion Laboratory

Early attempts to launch IRBM- and ICBM-type missiles indicated that a very probable cause of malfunction of the missile was excessive temperature in the motor compartment. The existence of this condition was evident in failures of the motor directional drives and premature shutdown of the rocket-motor fuel supply. Current successful firings are made with missiles that have closed-in bases and insulation around all of the vital parts. Although this arrangement does make the missile operational, it is not considered satisfactory because the base closure and insulation add weight that reduces the final velocity of the missile and, consequently, its range. In addition, the closing-in of the motor compartment makes this cavity highly susceptible to explosions due to fuel and oxygen leaks.

A rocket of the 1,000-pound-thrust class was installed in the Lewis 8- by 6-foot supersonic tunnel to permit a controlled study of some of the factors affecting the heating of a rocket-missile base. Liquid oxygen and JP-4 fuel were used as propellants. A photograph of the rocket in operation is shown in figure 1. The model body diameter is 7.875 inches, and the rocket-nozzle discharge diameter is 3.4 inches with a throat-to-discharge area ratio of 8. The nozzle was contoured according to present large-scale motor designs. All of the test firings reported herein were made with a chamber pressure of 500 pounds per square inch absolute. The duration of firing was controlled by the time required to reach an apparent stable temperature in the base region. Average firings were about 45 seconds in duration.

A simplified diagram that depicts the flow in the base of a typical missile is shown in figure 2. The idea that bound-vortex flow exists in a base such as this has been advanced in numerous references dealing with the study of base pressure. The generation of vortex flow is associated with mixing profiles that are found between the base region and both the stream and jet flow. Quantities of stream and exhaust gas are transported into the base and mixed together to create a base temperature. The gas that enters the base from the jet also contains unburned products that become potentially combustible when mixed with the stream air.

A calorimetric process for the base was assumed, and the resulting computed temperatures are shown in figure 3. The values of jet-gas concentration $w_j/w_a$ of 0.03 and 0.06 that were selected for the computations were based on experimental measurements made with an NACA fuel-air ratio meter. For the mixing calculations, all the jet gas was assumed to arrive in the base at jet temperature. The curves indicate that with mixing alone the base temperature can range from $300^\circ$ to $500^\circ$ F for the jet-gas concentrations considered. The change of temperature with oxygen-fuel ratio is small. For the case where burning is occurring, the additional assumption was made that all the heat of combustion available in the jet gas was released in the base. The values of temperature indicated, therefore, are theoretical limits and have no special significance.

It is important to note from the curves of mixing plus burning that large temperature rises can occur even with moderate concentrations of jet gas if the mixture is ignited. Also, with burning, the trend is toward reduced temperature rise as the oxygen-fuel ratio is increased toward the stoichiometric value of 3.4. In fact, the reason that the computed temperature rise due to burning does not coincide with the mixing value at an oxygen-fuel ratio of 3.4 is that the rocket-motor combustion efficiency is less than unity.

Data are shown in figure 4 for firings made with an open base that simulates a missile configuration. Each test point shown represents an individual rocket firing. The temperatures presented are the maximum values observed with thermocouples mounted to measure air temperature; however, the spread between the maximum and the minimum was not great. The temperatures are the result of operation of the rocket motor only; the effect of accessory discharge will be discussed later. In spite of the apparent scatter, the data at a Mach number of 2.0 (circles) and a Mach number of 1.6 (squares) tend to fall in two categories. One is a relatively low level, and the other is much higher - the higher level being about $1,200^\circ$ F at a Mach number of 2.0. Photographic observations confirm that the high-temperature data coincide with visual burning in the base. A trend of decreasing temperature with increasing oxygen-fuel ratio is observed in most of the high-temperature data.

The base of the missile was closed, and the data from this configuration are shown in figure 5. Temperatures inside the closed cavity were just slightly above stream stagnation temperature and are not shown in this figure. The temperature outside the closed base was somewhat different from that in the open base, but the overall level was about the same.

The data presented in the previous figures were obtained with nitrogen as the pressurizing gas for the liquid oxygen. Nitrogen dissolves in liquid oxygen and causes a deterioration of the combustion efficiency

at a given indicated oxygen-fuel ratio.  The use of nitrogen was an
expedient, and the reduction in combustion efficiency was not at first
considered to be important.  Data obtained with helium as the pressur-
izing gas are shown in figure 6, where it can be seen that the improved
combustion efficiency has reduced the temperature, presumably because
a smaller quantity of combustibles is present.  The difference in com-
bustion efficiency is about 8 points.

If the simplified base flow of figure 2 is recalled, it is logical
to surmise that one way of reducing the amount of jet gas entrained in
the base is to move the jet rearward so that the mixing zone intercepted
by the base streamlines is reduced.  The data that were obtained with
the motor extension increased from 0.32D to 0.59D, where  D  is the
diameter of the base, are presented in figure 7.  It is apparent that
moving the motor relative to the base was very effective in reducing the
temperature, even though the base was open.  Pursuing the idea that, if
a little helps, a lot is better, the motor was extended to 0.78D, and
the data for this configuration are presented in figure 8.  The tempera-
tures indicated in figure 8 are essentially the stagnation values for
the tunnel.  Independent measurements of the jet-gas concentration in
the base indicated that the amount of jet gas in the base was also
greatly reduced, being essentially zero for the 0.78D configuration.

Extending the motor out of the base introduces the possibility
of increased pressure on the motor, especially as the trailing shock
is approached in the supersonic case.  Typical pressures measured on the
motor shroud at a Mach number of 2.0 are presented in figure 9.  The
computed expansion angle for flow around the base corner into the base
pressure region is shown schematically for reference.  The pressure rise
indicated for the two extended-motor cases is probably due to a feeding
forward of the pressure rise of the trailing shock.  It is apparent that
an estimate of loads on a motor actuator would be very difficult because
of the complex flow field.

Four configurations of turbine exhaust are shown in figure 10.
Propane was used to simulate the fuel-rich turbine discharge gas.  The
configuration at the upper left is an early design that proved to be
very poor from the base-heating standpoint.  The temperatures measured
were well above 1,500° F, and violent burning was observed in the base.
The configuration at the lower left was an attempt to keep the burning
downstream of the base in the hope that the hot gas would be swept away
instead of being trapped in the base.  The temperature and burning with
this configuration was, if anything, worse than with the first configu-
ration.  The configurations on the right were a result of a more compre-
hensive study of the base flow.  The discharge at the upper right is
located outboard of the base by an amount that was believed to be out-
side of the base stagnation streamline.  This configuration showed no

increase in base temperature even when hydrogen was discharged. Another version of this same concept is shown at the lower right. This configuration also showed no temperature rise with propane.

This work, to date, can be summarized as follows:

1. With single rocket-type missiles, very high temperatures can occur in the base region because of ignition of burnable rocket gases. One might presume that multiple rocket installations will suffer from the additional complication caused by jets impinging on adjacent jets.

2. The spacing between the end of the base and the end of the rocket motor is a very important parameter affecting the base temperature. Rational methods for selecting the proper spacing are not readily apparent.

3. The estimation of airloads on the rocket motor is difficult because a pressure rise feeds forward from the trailing shock.

4. Combustibles that are dumped into the base by accessories seriously aggravate the base-burning temperature rise. Discharges that extended well past the base radius or that were located in such a manner as to protrude outside of the base stagnation streamline were effective in eliminating the burning of accessory exhaust in the base.

ROCKET INSTALLATION IN 8×6
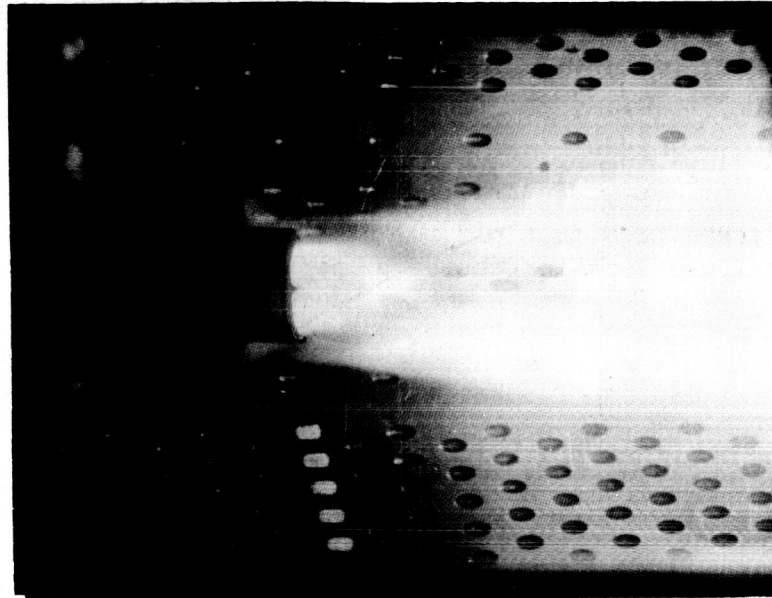


Figure 1

# FLOW IN BASE REGION
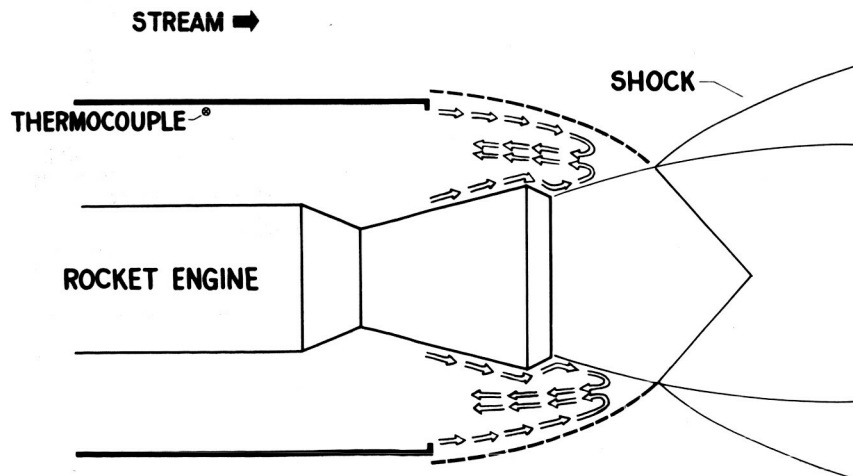


Figure 2

## TEMPERATURE COMPUTED
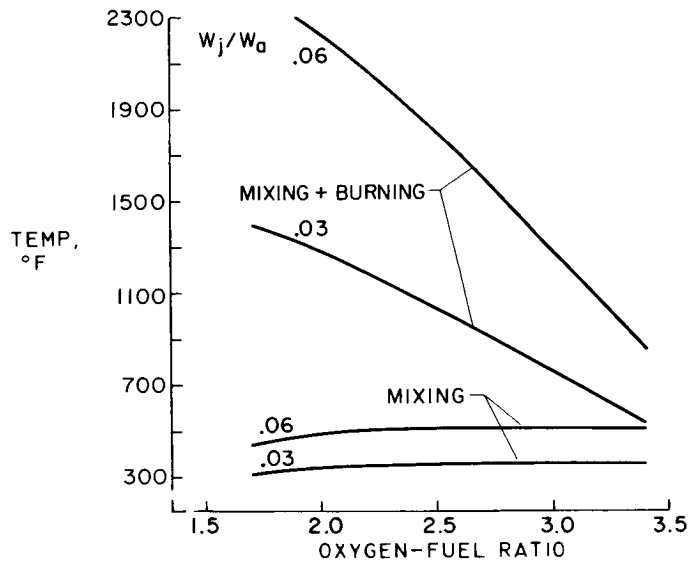


Figure 3

## TEMPERATURE INSIDE OPEN BASE
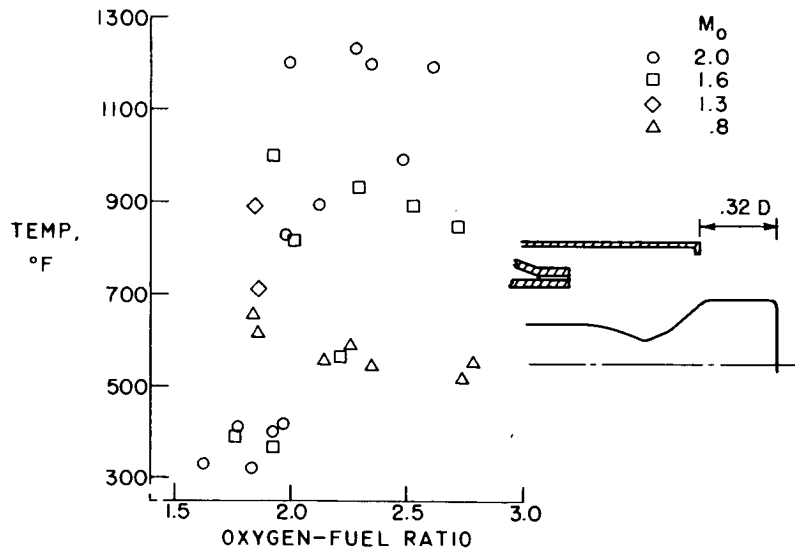


Figure 4

## TEMPERATURE OUTSIDE CLOSED BASE
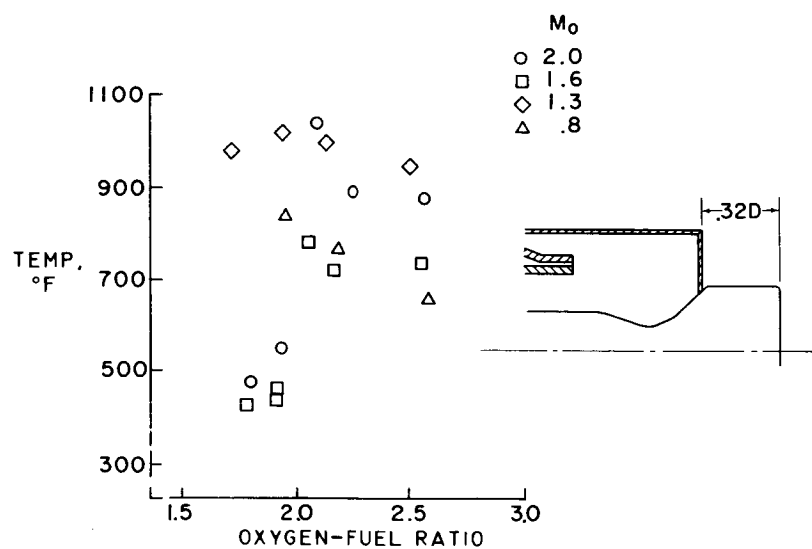


Figure 5

## TEMPERATURE OUTSIDE CLOSED BASE
## IMPROVED ROCKET COMBUSTION
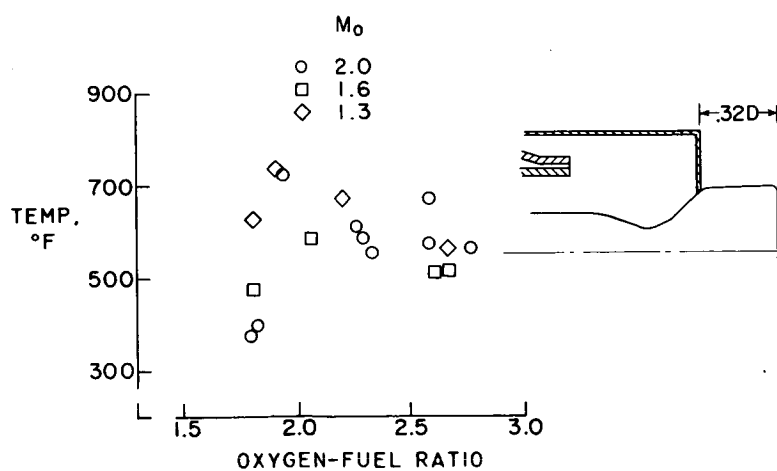


Figure 6

# INCREASED MOTOR EXTENSION
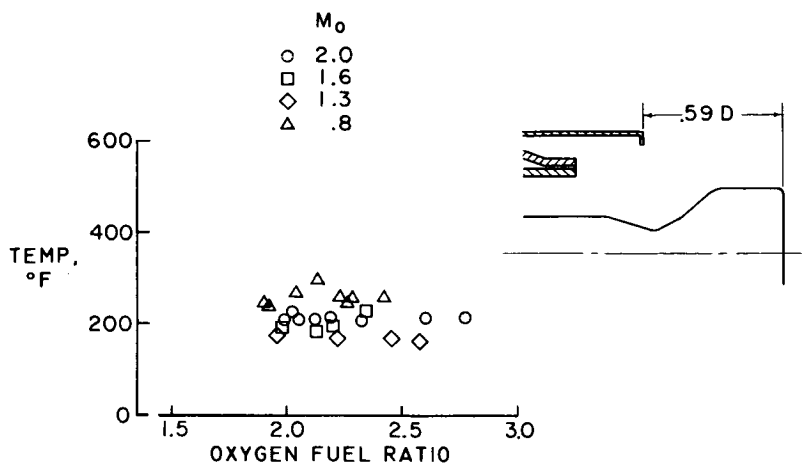
Figure 7

# INCREASED MOTOR EXTENSION
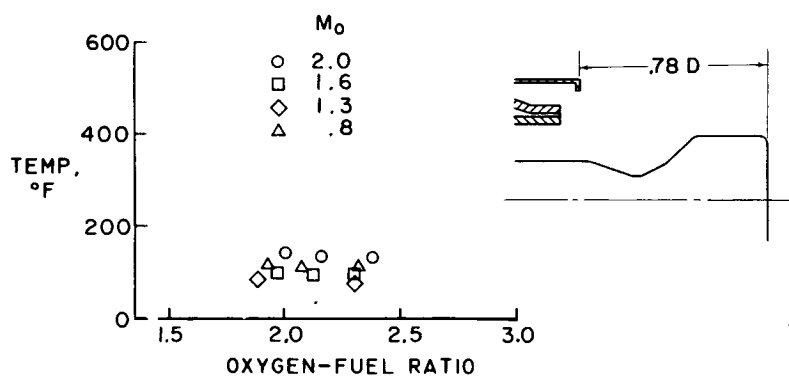
Figure 8

## PRESSURE ON MOTOR

$M_0 = 2.0$

PRESSURE
RATIO
$p/p_0$

COMPUTED

$r/D$

.32 D

.59 D

.78 D

DISTANCE TO JET EXIT, X/D
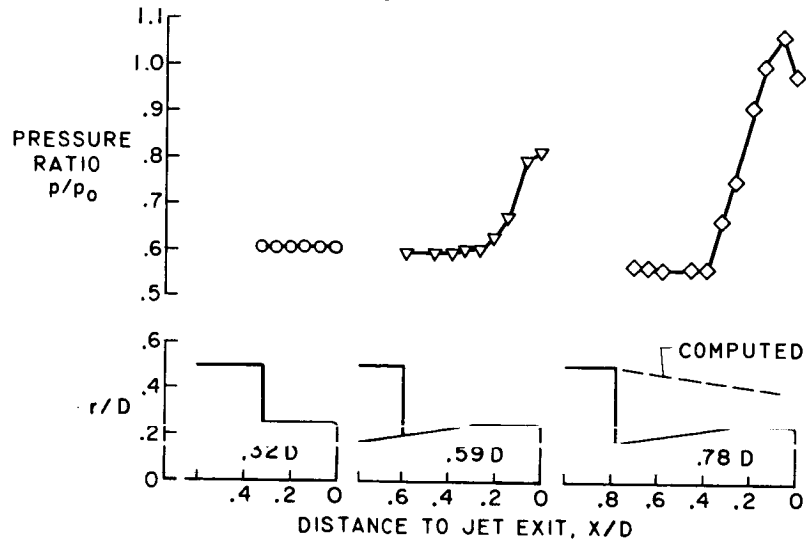
Figure 9

## TURBINE EXHAUST CONFIGURATIONS

$T_b > 1500°$ F

$T_b$ NORMAL

8°

30°

30°
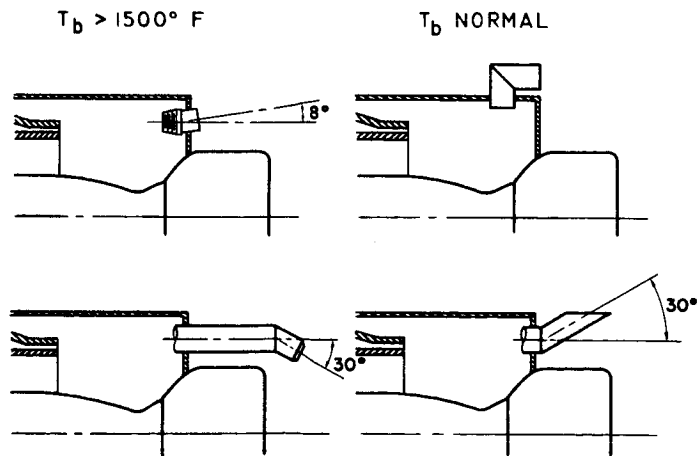
Figure 10

# PRESSURE RISE FOR INCIPIENT SEPARATION

## OF TURBULENT BOUNDARY LAYERS

By Donald M. Kuehn

Ames Aeronautical Laboratory

## INTRODUCTION

Any aerodynamic device which has boundary layer flowing through an adverse pressure gradient can experience boundary-layer separation if the gradient and pressure rise are sufficiently severe. This separation can exist for a number of common devices, such as deflected flaps, ailerons, compressor blades, supersonic diffusers, and spoilers. Since some design procedures depend on the flow being attached, it is essential that designers have data available to estimate the operating limits of the devices which are subject to boundary-layer separation. A continuing program is being performed at the Ames Aeronautical Laboratory to study laminar, transitional, and turbulent separated boundary layers. One phase of the program will be described. It is concerned with the pressure rise which a turbulent boundary layer will tolerate with no separation. The purpose of this paper is to present a brief résumé of the design data obtained and to point out significant physical trends.

The experiments were conducted in the Ames 1- by 3-foot supersonic tunnel No. 1 over a Mach number range of approximately 1.6 to 4.2 and a Reynolds number range, based upon boundary-layer thickness, of about $1.5 \times 10^4$ to $7.5 \times 10^4$. The investigation was restricted to turbulent boundary layers, and the boundary-layer flow approaching the interaction region was one of essentially zero pressure gradient. Models used were two-dimensional compression corners (to simulate the flow over deflected flaps or ailerons), curved surfaces (to simulate the flow over a compressor blade), and incident shocks (to simulate the type of pressure rise common with supersonic diffusers).

## SYMBOLS

M         Mach number of flow approaching pressure rise

p         static pressure

r           radius of curved portion of curved surface model

$R_\delta$       boundary-layer Reynolds number

$\delta$           boundary-layer thickness at beginning of pressure rise

Subscripts:

0           conditions upstream of pressure rise

1           conditions downstream of pressure rise

## RESULTS

The results of the investigation indicate three variables to be of considerable importance as affecting the pressure rise which is required to cause a turbulent boundary layer to separate. They are Mach number, Reynolds number, and body shape. Typical data are presented which illustrate the trend of incipient-separation pressure rise with these three variables.

Static-pressure distributions along a curved surface and the corresponding shadowgraphs for separated and attached turbulent flows are shown in figure 1. The left portion of this figure illustrates the hump in the pressure distribution which is characteristic of separated regions for all body shapes of this investigation. The point of boundary-layer separation is indicated in the figure. The right portion of this figure shows the pressure distribution and corresponding shadowgraph for an attached flow. The first occurrence of separation was detected by decreasing Mach number from a condition of no separation until the characteristic hump in the pressure distribution first appeared. The pressure rise for incipient separation is thus defined as that pressure ratio achieved just before separation is evident $\left(\text{indicated as } \left(p_1/p_0\right)_{INCIP}\right.$ in fig. 1$\Big)$. An important point to be observed is the widely different flow fields and pressure distributions possible for only a slight difference in Mach number; that is, a Mach number of 3.74 as compared with a Mach number of 3.86.

Figure 2 shows the effect of Reynolds number on the pressure ratio for the incipient separation of turbulent boundary layers in compression corners. Pressure ratio is plotted as a function of Reynolds number, based upon boundary-layer thickness, for Mach numbers varying from 2 to 4. This Reynolds number effect is predominant in the high Mach number range and in the low Reynolds number range. The Reynolds number effect shown for compression corners is typical of that found for curved sur-

faces and incident shock models. A possibly surprising feature of this
Reynolds number effect, and one that is opposite to that for subsonic
flow, is the ability of a turbulent boundary layer at low Reynolds num-
ber to tolerate a larger pressure rise with no separation than can a
boundary layer at high Reynolds number. This trend is opposite to the
generally accepted idea that adverse flow conditions, resulting from low
Reynolds number effects, can usually be improved by increasing the
Reynolds number. This same trend has, however, been noted in previous
work (ref. 1) with respect to other pressure ratios associated with
separation and was attributed to the decrease of local skin-friction
coefficient with increasing Reynolds number. It is possible that the
Reynolds number trend noted herein is also associated with this skin-
friction variation.

The effect of Mach number on the pressure ratio for incipient turbu-
lent separation for several body shapes at a constant Reynolds number is
shown in figure 3. The pressure ratio for incipient separation is plotted
as a function of Mach number approaching the pressure rise. In a previous
publication (ref. 2), comparison of compression-corner data obtained at
Ames Laboratory with incident shock data obtained by Bogdonoff at
Princeton University indicated a large difference to exist between these
two models with respect to the pressure rise required for separation
above a Mach number of 2. Reynolds number was not constant in the com-
parison. Incipent separation data at constant Reynolds number obtained
in the present investigation, however, show the compression-corner and
incident-shock-model data to be quite similar. In view of the Reynolds
number effect observed in this investigation, the apparent difference
(fig. 3) between these two models is believed to be due to Reynolds num-
ber. The curved-surface models demonstrate the large gains to be real-
ized in the pressure-rise ratio with no separation by decreasing the
pressure gradient. Values of radii, expressed in terms of boundary-
layer thickness, of approximately 10, 20, and 30 are represented and
pressure ratios up to 16 are shown with no separation. In the upper
Mach number range, body shape, Reynolds number, and Mach number are
important variables affecting the incipient separation pressure ratio.
However, as Mach number is decreased to a value less than 2, a pressure
ratio of approximately 1.8 will suffice to describe incipient separation
conditions for all body shapes and Reynolds numbers of this investigation.
These data show clearly that the pressure rise which will cause a turbu-
lent boundary layer to separate can be considerably higher than the values
of about 2 to 3 which have been used in various design methods.


CONCLUDING REMARKS


Three main variables have been pointed out as having considerable
influence on the pressure rise for incipient turbulent separation. First,

there was a Reynolds number effect which had not been detected in previous supersonic data and which is opposite in trend to that for subsonic flow; second, there was an extremely large effect of Mach number for all body shapes; and third, reduction of the pressure gradient by increasing the radius of the curved surface had a large influence on the pressure rise possible with no separation.

## REFERENCES

1. Chapman, Dean R., Kuehn, Donald M., and Larson, Howard K.: Investigation of Separated Flows in Supersonic and Subsonic Streams With Emphasis on the Effect of Transition. NACA TN 3869, 1957.

2. Chapman, Dean R., Kuehn, Donald M., and Larson, Howard K.: Preliminary Report on a Study of Separated Flows in Supersonic and Subsonic Streams. NACA RM A55L14, 1956.

## SEPARATED AND ATTACHED TURBULENT FLOWS
## FOR A CURVED SURFACE $R_\delta \approx 5 \times 10^4$
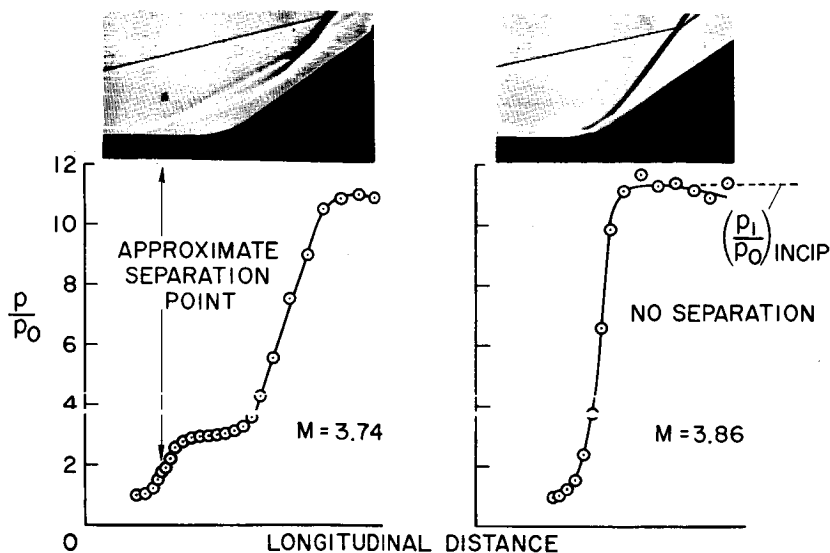


Figure 1

## EFFECT OF REYNOLDS NUMBER ON PRESSURE
## RATIO FOR INCIPIENT TURBULENT SEPARATION



Figure 2

CONFIDEN...
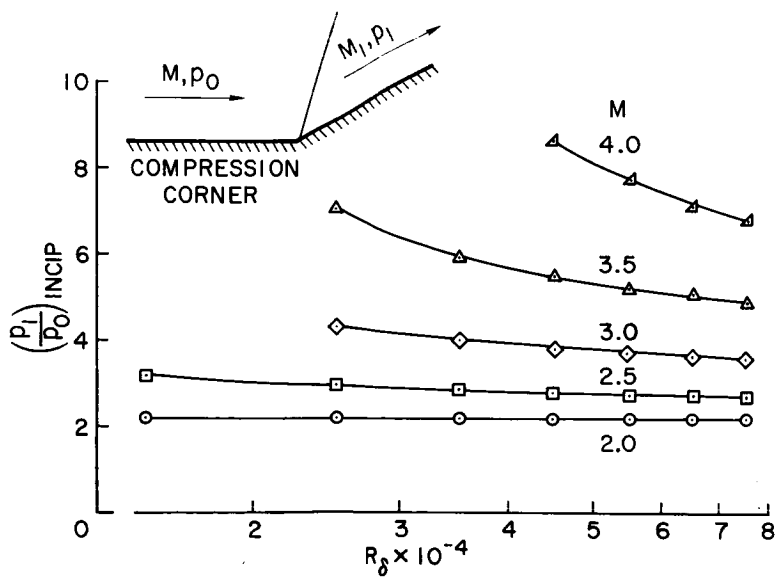
EFFECT OF MACH NUMBER ON PRESSURE RATIO FOR
INCIPIENT TURBULENT SEPARATION $R_\delta \approx 5 \times 10^4$
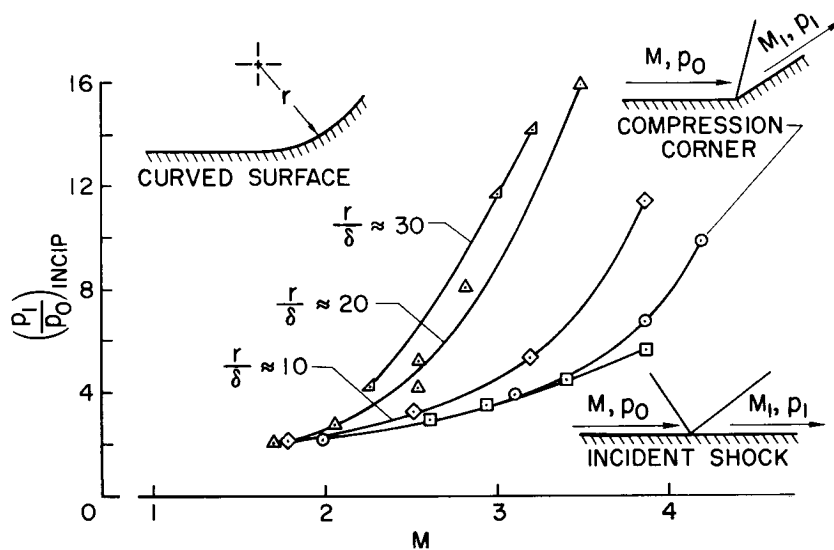


Figure 3

# EFFECTS OF BOUNDARY-LAYER DISPLACEMENT AND LEADING-EDGE

# BLUNTNESS ON PRESSURE DISTRIBUTION, SKIN FRICTION,

# AND HEAT TRANSFER OF BODIES AT HYPERSONIC SPEEDS

By Mitchel H. Bertram and Arthur Henderson, Jr.

Langley Aeronautical Laboratory

## SUMMARY

Results are presented of an investigation to determine the effect of boundary-layer displacement and leading-edge bluntness on surfaces in hypersonic flow. The presence of the boundary layer and the blunt leading edge induce pressure gradients which in turn affect the skin friction and heat transfer to the surface. Methods for predicting these phenomena on two-dimensional surfaces are given and a brief review of recent three-dimensional results is presented.

## INTRODUCTION

In hypersonic flow large pressure and temperature gradients can be induced on a plate without the plate itself having an inclination. In pure form two main types of induced effects may be detected. One is the pressure gradient induced by the presence of thick boundary layers on sharp leading-edge plates and the other is the pressure gradient induced on surfaces following very blunt leading edges. These induced effects, together with the manner in which they are influenced by plan form and angle of attack, are the main consideration of this investigation. In addition, since purity is not often attained and the cases in which the two induced effects act simultaneously are often of more practical significance, the case of mixed effects is also considered. The important progress that has been made in these areas is demonstrated.

## SYMBOLS

a'          skin-friction constant in viscous-interaction theory

A           aspect ratio

$C_c$          chord-force coefficient

$\overline{C}_{c,p}$       inviscid pressure chord-force coefficient

$\Delta C_{c,p}$      increment in pressure chord-force coefficient due to boundary-layer-displacement effects

$C_{c,t}$       pressure-chord-force-coefficient contribution due to finite thickness of leading edge

$C_{D,N}$      nose drag coefficient based on forward projected area of nose

$C_F$         average skin-friction coefficient for one side of flat plate including boundary-layer-displacement effects

$\Delta C_F$       increment in average skin-friction coefficient due to boundary-layer-displacement effects

$\overline{C}_{F,T}$      total skin-friction coefficient of flat plate with zero pressure gradient

$C_{F,T}$       total skin-friction coefficient of flat plate including boundary-layer-displacement effects

$$C_\mu = \frac{\mu_w T_\infty}{\mu_\infty T_w}$$

$$C_{\mu,e} = \frac{\mu_e T_\infty}{\mu_\infty T_e}$$

$C_{N_\alpha}$      flat-plate normal-force-curve slope including boundary-layer-displacement effects

$\overline{C}_{N_\alpha}$      flat-plate normal-force-curve slope (inviscid)

$d$          nose diameter

$L$          plate length

$M_\infty$        free-stream Mach number

$M_a$        asymptotic Mach number on flat plate (inviscid sharp-leading-edge value)

| | |
|---|---|
| $N_{St}$ | Stanton number including pressure-gradient effects |
| $\bar{N}_{St}$ | Stanton number on flat plate with zero pressure gradient |
| $N_{St,\infty}$ | Stanton number based on free-stream conditions |
| $p$ | local pressure |
| $\Delta p_\Lambda$ | local pressure rise due to blunting with sweep |
| $p_\infty$ | free-stream pressure |
| $p_a$ | asymptotic pressure on flat plate (inviscid sharp-leading-edge value) |
| $p_c$ | theoretical inviscid pressure on cone surface |
| $p_w$ | surface pressure |
| $R_{a,x}$ | Reynolds number based on asymptotic conditions on flat plate (inviscid sharp-leading-edge values) |
| $R_{\infty,c}$ | Reynolds number based on free-stream conditions and root chord of delta wing |
| $R_{\infty,d}$ | Reynolds number based on free-stream conditions and nose diameter |
| $R_{\infty,t}$ | Reynolds number based on free-stream conditions and nose thickness |
| $R_{\infty,x}$ | Reynolds number based on free-stream conditions and streamwise distance |
| $R_S$ | Reynolds number based on sharp-cone surface conditions and surface distance from the nose |
| $S$ | distance along surface |
| $t$ | nose thickness |
| $T_e$ | recovery temperature |

$T_w$        wall temperature

$T_0$        stagnation temperature

$x$        streamwise distance along axis

$\alpha$        angle of attack

$\delta$        plate deflection angle

$\Lambda$        sweepback angle

$\gamma$        ratio of specific heats

$\mu_w$        dynamic viscosity at wall temperature

$\mu_e$        dynamic viscosity at recovery temperature

$\overline{\chi}_\infty$        viscous interaction parameter based on free-stream conditions, $M_\infty{}^3 \sqrt{C_\mu} \Big/ \sqrt{R_{\infty,x}}$

$\overline{\chi}_{\infty,S}$        viscous interaction parameter based on free-stream conditions and using the square root of the plate area as the characteristic length in the Reynolds number

## RESULTS FOR TWO-DIMENSIONAL CONFIGURATIONS

### Boundary-Layer-Displacement Effects

Surface pressures.- The effect of the boundary layer in displacing the flow around flat plates is most familiar through its effect on the pressure distribution. Recently high Mach number data have become available for pressure distributions on flat plates with very sharp leading edges. Published data of this type are given in references 1 and 2. More recent data are given by some measurements in the Mach number 9.6 nozzle of the Langley 11-inch hypersonic tunnel to test both changes in Reynolds number and angle of attack shown in figure 1. These results were obtained with, for this setup, an unavoidable heat transfer. The abscissa in figure 1 is a parameter first shown by Lees and Probstein (ref. 3) to be that for which correlation of boundary-layer induced effects should be obtained. In it Mach number, Reynolds number, and coefficient in the linear formula for viscosity are used at the local asymptotic flow conditions, that is, the conditions that would be

obtained on the plate at each angle of attack were there no boundary layer present. Also the viscosity coefficient $C_\mu$ is evaluated at estimated recovery conditions designated $C_{\mu,e}$. The pressure parameter in the ordinate is the pressure rise above asymptotic pressure divided by the asymptotic pressure.

Large pressure rises are obtained as the leading edge is approached. Although all the angles of attack correlate well, the original data (the open symbols) fall below the line given by insulated-plate theory (Lees' first-order strong interaction, ref. 4) due to heat transfer from the boundary layer to the plate wall during these transient tests. The inset in figure 1 shows the measured temperatures along the plate normalized with respect to stagnation temperature, together with the polynomial fitted to these data for use with the theoretical method of modifying the data to insulated-plate conditions. In the same manner that was found to be successful in reference 2, the original data were modified to the insulated-plate case. The result is shown by the solid symbols in figure 1 and is in general agreement with the theoretical line.

Skin friction.- These large pressures, of course, have an effect on both skin friction and heat transfer. The results of strong-interaction theory and the hypersonic equations for pressure as a function of plate deflection angle are used to obtain figure 2, which shows the contribution of each surface of a two-dimensional wedge wing to the total skin friction. This contribution of each surface is normalized with respect to the total skin friction of a flat-plate wing (both surfaces) with a zero pressure gradient at zero angle of attack. The hypersonic boundary-layer-interaction parameter is evaluated at undisturbed free-stream conditions ahead of the plate. So long as the wall temperature is constant the plot is independent of the wall temperature. The constant $a'$ is a function of wall temperature and is tabulated and plotted graphically in reference 2. When $\overline{X}_\infty = 0$, the classical flat-plate skin-friction values result.

Utilizing these same equations but adapting them to the delta wing according to reference 2 permits a similar plot to be constructed for a delta wing. Such a plot is shown in figure 3. For the delta wings the Reynolds number utilizes the square root of the projected wing area as the characteristic length. This is done to facilitate the use of area as a comparison basis.

As an illustration of the use of the results from figures 2 and 3, figure 4 has been prepared. Figure 4 gives the total skin friction for a two-dimensional and a delta-plan-form flat plate as a function of the hypersonic similarity parameter for various values of the

hypersonic interaction parameter. Of course, a similar plot can be constructed for a wing of given wedge angle from figures 2 and 3. Note the appreciable increases in total skin friction due to boundary-layer-displacement effects, even at moderate values of the hypersonic interaction parameter.

Both flat-plate and delta-wing data for skin friction at $M_\infty = 6.8$ have been presented in reference 2. The magnitude of the increase in skin friction which could be ascribed to boundary-layer-displacement effects was correctly predicted. Recent data obtained at Mach number 9.6 for the variation of chord force with angle of attack for a delta-wing—half-cone combination obtained by W. O. Armstrong in the Langley 11-inch hypersonic tunnel are shown in figure 5. For the present purposes the presence of the half-cone complicates but need not obscure the comparison. The lines at the bottom of this figure outline the various contributions to the pressure chord force such as the inviscid-pressure chord force $\left(C_{c,p}\right)$, the increment in pressure chord force due to boundary-layer-displacement effects $\left(\Delta C_{c,p}\right)$, and the leading-edge-thickness contribution to the chord force $\left(C_{c,t}\right)$. The large area immediately above the pressure contributions is the skin friction for a delta-plan-form flat plate with zero pressure gradient $\left(\overline{C}_F\right)$, and the area above this $\left(\text{designated } \Delta C_F\right)$ is the increment in skin friction calculated to be due to boundary-layer-displacement effects. This increment alone is, in general, larger than the pressure drag from all sources on this model. Because of the shielding effect on the cone, the negative angles of attack are relied upon for comparison between theory and experiment. Throughout the entire range, however, the prediction of theory is considered good.

Normal force.- The results discussed have been concerned with the effect on the skin friction attributable to boundary-layer displacement; however, there is a corresponding effect on the normal force, so that the $L/D$ of the wing is probably less affected than would be indicated by displacement effects on skin friction alone. The predicted effect on normal force for a two-dimensional insulated flat plate is compared in figure 6 with data obtained by Tellep in the University of California low-density tunnel at a Mach number of about 4 (ref. 5). Shown are Tellep's original data for various aspect ratios and the data modified to infinite aspect ratio according to Tellep. The increases in normal force can be large, and one factor illustrated in figure 6 is the need of more attention to the effect of aspect ratio.

Blunt-Leading-Edge Effects

Blast-wave theory correlation of surface pressures at zero sweep and zero angle of attack.- Thus far, only the viscous or boundary-layer induced effects have been treated. As mentioned previously, the conditions on a plate with a blunt leading edge represent another example of an induced effect that assumes significance at hypersonic speeds. The increase in pressures on a plate following a blunt leading edge has been known for some time and has been demonstrated both theoretically and experimentally (refs. 6 to 8). Cheng and Pallone (ref. 9) and Lees and Kubota (ref. 10) more recently have given the proper correlating parameters for this phenomenon. Their work stems from the so-called "blast-wave" theory in which the two-dimensional blunt leading edge is taken as the origin of an explosion in which the energy released is proportional to the leading-edge drag. The theoretically predicted correlation parameter has been found to correlate the results from characteristics theory where a sonic wedge is utilized as the blunt leading edge (ref. 11). This correlation of surface pressures over an extended range of Mach number in air and helium is shown in figure 7. The correlation parameter from blast-wave theory is the abscissa in the figure. This correlation parameter combines the effect of distance from the leading edge, Mach number, and nose drag. The ordinate is the nondimensionalized wall pressure rise above free-stream pressure induced by the blunt leading edge. The correlation is good except very near the nose (within the first 3 to 4 nose diameters) where the theory is not expected to apply. First-order blast-wave theory is also shown on this plot. Note the departure of this theory from the characteristics solutions at large values of $x/t$. This first-order blast-wave theory again is not expected to apply at these larger values of the distance parameter.

Effect of angle of attack on surface pressures at zero sweep.- For comparison of the theory with experiment, Princeton helium-tunnel data obtained at $M_\infty = 11.4$ with viscous effects believed to be negligible have been utilized, and the data were found to be in reasonable agreement with theory (ref. 11). Some recent data bearing on this problem have been obtained by W. V. Feller on a hemicylinder leading-edge plate in the Langley 11-inch hypersonic tunnel. Although the Mach number is somewhat low $\left(M_\infty = 6.9\right)$ a number of test variables are covered, and for this reason the data are valuable. Experimental and theoretical data for the zero-yaw plate are presented in figure 8 for several angles of attack. The ordinate in this figure is the increment in pressure ratio due to the blunt leading edge at each angle of attack. A positive angle of attack refers to the windward surface of the plate, while a negative angle of attack indicates the leeward or shielded side of the plate. The abscissa is distance from the leading edge in terms of leading-edge thickness. The theoretical

lines are the result of the characteristics solutions for the sonic-wedge leading-edge plate. Note that the trend with angle of attack is well predicted by theory.

In order to determine trends to be expected from similar results at a higher Mach number, figure 9 has been prepared from characteristics solutions for the flat plate with sonic-wedge leading edge at a Mach number of 20. This figure presents the pressure rise on the wing surface due to a combination of angle of attack and leading-edge bluntness as a function of surface distance. The rise in pressure above the asymptotic pressure (the sharp-leading-edge plate pressure) is considerably reduced, percentagewise, as the angle of attack is increased. Note the large induced pressures, especially on the low-pressure side of the plate. At $\alpha = -10°$, pressure-difference ratios as high as the order of 10 are predicted while the inviscid pressure for a sharp-leading-edge plate is essentially zero absolute.

Effect of sweep on surface pressures.- The effect of sweep on the blunt-leading-edge induced pressures is also of considerable practical significance. Sweep has been investigated by again resorting to blast-wave theory and assuming that the induced pressures are a function only of the cross-flow component of the Mach number. At zero angle of attack the induced-pressure rise at a given streamwise location on a wing with sweep is found to be reduced from the pressure rise on an unswept wing by a factor equal to the cosine of the sweep angle to the 8/3 power. This relationship is shown in figure 10. The effects of sweep can be large; for example, at a sweep angle of 60° the induced-pressure rises are predicted to be about 1/7 of those for zero sweep.

Figure 11 presents the pressure data for the hemicylinder-leading-edge plate at zero angle of attack at $M_\infty = 6.9$ in a form designed to test this prediction of the effect of sweep. The pressure rise modified by the cosine function is plotted against streamwise distance in terms of nose thickness. The cosine function is found to correlate the pressure-rise data for 0° and 40° sweep with excellent accuracy. However, the data for 60° sweep are about 15 percent higher than the data for the two lower sweep angles. This discrepancy is that which would be expected were viscous effects present, inasmuch as the cosine function is not a correlating factor for viscous effects. The agreement with theory, from the sonic-wedge leading-edge correlation by blast-wave theory presented earlier, is considered good.

The effect of sweep at an angle of attack of 5° is shown in figure 12. Again the cosine function correlates the pressures for each side. Here again the pressure is presented as the increment in pressure due to the blunt leading edge. The positive values of $\alpha = 5°$

refer to the windward side of the plate while -5° refers to the leeward side. The main exception to correlation is for the 60° swept plate on the leeward side.

## Combined Viscous and Leading-Edge-Bluntness Effects

Thus far, the viscous and blunt-leading-edge effects have been treated separately. In actual applications, however, they will probably more often than not be found to be acting simultaneously. A fair amount of pressure data of this type has been obtained in the Princeton helium tunnel (refs. 8 and 12). Recently pressure data of this mixed viscous and blunt-leading-edge type have been obtained on a flat plate in a 2-inch helium jet at the Langley Laboratory, in which the available data are extended to very high Mach numbers (Mach numbers in the range 17 to 23). Some Princeton data are shown in figure 13(a) and some Langley data in figure 13(b). By choice, the pressure-rise parameter has been plotted against the viscous-correlation parameter. For clarity only the highest and lowest Mach numbers and Reynolds numbers for the Langley tests have been shown. A simple linear addition of the pressure predictions of viscous theory and sonic-wedge characteristics theory modified according to blast-wave theory is presented for comparison with the data. The viscous theory was obtained by the method of reference 13 with a continuously variable Mach number gradient. There is no large consistent disagreement between theory and experiment. The very large pressure rises that can be obtained on a flat plate at zero angle of attack from a combination of viscous and blunt-leading-edge effects should be noted.

## Heat Transfer

The next problem to be considered is that of heat transfer to these surfaces. A simple solution to the problem of laminar heat transfer to surfaces on which pressure gradients occur in hypersonic flow is available from similarity theory. This solution which is restricted to power-law variations of pressure with surface distance was pointed out by Li and Nagamatsu (ref. 14), who worked out in detail the case of the strong-interaction self-induced pressure gradient by this method. M. H. Bertram of the Langley Laboratory has determined the results from this solution for general use. The result for Stanton number is shown in figure 14, where $\bar{N}_{St}$ represents the Stanton number with zero pressure gradient and $N_{St}$ represents the point values of heat-transfer coefficient normalized by the same conditions as the $\bar{N}_{St}$ values.

Note that the pressure gradient reduces the heat transfer but a high

local pressure increases the heat transfer. The value of n = -0.875 corresponds to infinitely favorable velocity gradient in the transformed plane with $\gamma = 7/5$.

This theory has been utilized for comparison with some available data, namely, that of Crawford and McCauley (ref. 15) and Creager (ref. 16) shown in figure 15. Crawford and McCauley's data were obtained on hemisphere-nosed cylinder at Mach number 6.8. For purpose of analysis, these data were assumed to be equivalent to flat-plate data. Creager's data were obtained on a hemicylinder-leading-edge flat plate at zero angle of attack and Mach number 3.9. In order to obtain the curves from similarity theory, power laws were fitted to the measured pressure distributions. In general, good fits to the pressure data could be obtained. The exception was Creager's pressure data which at the higher values of x/t showed a variation of pressure with inverse distance higher than the 2/3 power so that lateral and trailing-edge effects were indicated. Thus, for these data only the lower values of x/t were theoretically evaluated. The correlation parameter for laminar theory $N_{St,\infty}\sqrt{R_{\infty,x}}$ is plotted in figure 15 against the streamwise distance in terms of nose thicknesses. The data from reference 15 and from reference 16 (in the range considered) are found to be well predicted by similarity theory. These pressure-gradient effects will of course assume greater importance at very high Mach numbers where the induced pressures are much larger.

## THREE-DIMENSIONAL CONFIGURATIONS

### Pressures on Blunted Rods

In the discussion of the effects considered thus far, three-dimensional bodies in general have not been considered. A short review of some recent results on simple bodies at high Mach numbers will now be presented. In figure 16 are shown surface-pressure results from blunt-nose rods immersed in hypersonic helium flow. Data from two sources are shown: results from the Princeton helium tunnel (ref. 17) and unpublished results from the Langley 2-inch helium jet. The pressure-rise parameter is shown plotted against the blast-wave-theory correlating parameter for a given nose shape, that is, distance (in rod diameters) divided by Mach number squared. In figure 16(a) are the results for the hemisphere tipped rod. These data appear to separate into two main groups; one, the Mach number 12 to 14 data, the other the Mach number 17 to 21 data. From flat-plate calculations based on the Mach number 21 data, the difference between the two sets of data appears, roughly, to be attributable to boundary-layer-displacement effects.

The data for the flat-nosed rod in figure 16(b) show somewhat better correlation at the higher values of $x/d$, although the Mach number 11.7 data are somewhat lower than the rest of the data. At the low value of $x/d$ the familiar phenomenon of overexpansion around the $90^\circ$ corner is noted.

## Pressures on Blunted Cones

A next step in this study is to investigate a blunt-nosed body with finite afterbody angle. Pressure measurements have been obtained on a flat-nosed $10^\circ$ half-angle cone in a 2-inch helium jet at the Langley Laboratory. These results are shown in figure 17 for Mach numbers of 17 and 23 and various nose diameter Reynolds numbers. The pressure change from inviscid sharp-cone pressure divided by the sharp-cone pressure is plotted against distance in nose diameters along the cone axis. Before the data are examined in detail, note the general level of the measured pressure rises, which are quite small compared with data from flat plates in both air and helium presented earlier in figures 1 and 13. The magnitude of these pressure changes is in tenths whereas the flat-plate pressure rises ranged from values as high as 10 to 40. The theory shown in figure 17 is Probstein's for hypersonic laminar-boundary-layer interaction over a cone (ref. 18). Only sharp cones are considered in the theory.

For the two lowest Reynolds numbers, the agreement of experiment with theory is considered good, that is, at least for the region beyond about 17 diameters of the nose. Here viscous effects appear to be dominant. However, the picture changes at the two highest Reynolds numbers. The inviscid flow field in the vicinity of the nose exerts its influence and the pressure distributions resemble those measured on flat-nosed cones in air at Mach number 6.85 (ref. 19) with a characteristic overexpansion in the region of 10 diameters which is qualitatively similar to the pressure distributions predicted by Chernyi (ref. 20). Viscous effects, though present, appear to be considerably modified or even subordinate to the inviscid flow field effects.

## Heat Transfer to Sharp and Blunted Cones at $\alpha = 0^\circ$

Heat-transfer data have been obtained in air at a free-stream Mach number of 6.7 on cones similar in configuration to those tested for surface pressures in helium. These cones had a $10^\circ$ half-angle with sharp, flat, and tangent sphere tips. The tests were conducted at a stagnation temperature of about $1,120^\circ$ R with a ratio of wall (essentially isothermal) to stagnation temperature close to $1/2$. The experimentally determined recovery factor for laminar flow was 0.843 (based

on sharp-cone surface conditions). This value of recovery factor was used throughout in determining values of Stanton number from the temperature data.

Results at zero angle of attack are shown in figure 18. The ordinate is the laminar-heat-transfer correlation parameter in which Stanton number, Reynolds number $R_S$, and the coefficient in the linear formula for viscosity $C_\mu$ are evaluated at the theoretical surface conditions on the sharp-tip cone at zero angle of attack. The abscissa is the same Reynolds number used in the correlation parameter of the ordinate.

Although experimental values for the sharp-tip cone are somewhat higher than the laminar-theory values, the Stanton number parameter is essentially independent of the surface Reynolds number up to the Reynolds number at which the start of transition is indicated (about $4.5 \times 10^6$). When the tip of the cone is blunted, this insensitivity of the Stanton number parameter to Reynolds number no longer applies. There is a decided decrease in heat transfer relative to the heat transfer on the sharp-tip cone as the blunt tip is approached. The effect of blunting on the geometry alone (pressure assumed constant) when the Mangler transformation is used appears to account for substantially all of this decrease in heat transfer. In the theory the boundary layer is assumed to start two-dimensionally from the shoulder at the blunt nose and to approach the cone value asymptotically. Note that the blunt nose delays transition to surface Reynolds numbers of from $5 \times 10^6$ to $6 \times 10^6$.

### Heat Transfer to Sharp and Blunted Cones at $\alpha = 5^\circ$

Next to be considered is the effect of angle of attack on the heat transfer to these cones. Shown in figure 19 are the heat transfers to the $0^\circ$, $90^\circ$, and $180^\circ$ meridians of the sharp- and flat-faced cones at $5^\circ$ angle of attack in the same Stanton number parameter form as were given the zero-angle-of-attack results. All parameters are normalized or computed from the cone theory at zero angle of attack and thus are directly comparable to the zero-angle-of-attack results. As expected, the heat transfer over most of the length was highest along the most windward meridian ($0^\circ$) and more or less continuously decreased to the top meridian ($180^\circ$). The results at the side meridian ($90^\circ$) were not greatly different from the zero-angle-of-attack results which are shaded in this figure. The effect of blunting is similar to that obtained at zero angle of attack. The most striking effect is that of angle of attack on transition and thus on the heat transfer to the $180^\circ$ meridian. (Compare figs. 19(a) and 19(b).) Transition occurs

along this meridian first, and on the sharp cone (fig. 19(a)) the heat transfer becomes equal to or slightly higher than the heat transfer to the most windward meridian at the rearward stations (highest values of $R_S$). The $90^\circ$ meridian has an increase in heat transfer well above the other two meridians at the most rearward station. Bluntness appears to delay transition along the $180^\circ$ meridian, but the trend of the data appears to be much the same for the blunted cone as for the sharp-tipped cone. The initial points on the $180^\circ$ meridian are believed to have a high indicated heat transfer because of lateral heat conduction, which was not taken into account in the analysis of the data since it was negligible in most instances.

## CONCLUDING REMARKS

The results presented indicate that much of the viscous and nose-blunting phenomena that have been studied in the past in a rather academic way are now understood to the point where engineering estimates of many of their effects are now possible. However, a large area for additional research remains to be explored.

███████AL

REFERENCES

1. Kendall, James M., Jr.: An Experimental Investigation of Leading-Edge Shock-Wave - Boundary-Layer Interaction at Mach 5.8. Jour. Aero. Sci., vol. 24, no. 1, Jan. 1957, pp. 47-56.

2. Bertram, Mitchel H.: Boundary-Layer Displacement Effects in Air at Mach Numbers of 6.8 and 9.6. NACA TN 4133, 1958.

3. Lees, Lester, and Probstein Ronald F.: Hypersonic Viscous Flow Over a Flat Plate. Rep. No. 195 (Contract AF 33(038)-250), Aero. Eng. Lab., Princeton Univ., Apr. 1952.

4. Lees, Lester: Hypersonic Flow. Fifth International Aeronautical Conference (Los Angeles, Calif., June 20-23, 1955), Inst. Aero. Sci., Inc., 1955, pp. 241-276.

5. Tellep, D. M.: Lift on Flat Plates in Low Density Supersonic Flow. Rep. No. HE-150-131 (Ser. No. 20-104, Contract N7-onr-295-Task 3), Inst. Eng. Res., Univ. of California, Aug. 30, 1955.

6. Bertram, Mitchel H.: Viscous and Leading-Edge Thickness Effects on the Pressures on the Surface of a Flat Plate in Hypersonic Flow. Jour. Aero. Sci. (Readers' Forum), vol. 21, no. 6, June 1954, pp. 430-431.

7. McLellan, Charles H., Bertram, Mitchel H., and Moore, John A.: An Investigation of Four Wings of Square Plan Form at a Mach Number of 6.9 in the Langley 11-Inch Hypersonic Tunnel. NACA Rep. 1310, 1957. (Supersedes NACA L51D17.)

8. Hammitt, A. G., and Bogdonoff, S. M.: Hypersonic Studies of the Leading Edge Effect on the Flow Over a Flat Plate. Jet Propulsion, vol. 26, no. 4, Apr. 1956, pp. 241-246.

9. Cheng, H. K., and Pallone, A. J.: Inviscid Leading-Edge Effect in Hypersonic Flow. Jour. Aero. Sci. (Readers' Forum), vol. 23, no. 7, July 1956, pp. 700-702.

10. Lees, Lester, and Kubota, Toshi: Inviscid Hypersonic Flow Over Blunt-Nosed Slender Bodies. Jour. Aero. Sci., vol. 24, no. 3, Mar. 1957, pp. 195-202.

11. Bertram, M. H., and Baradell, D. L.: A Note on the Sonic-Wedge Leading-Edge Approximation in Hypersonic Flow. Jour. Aero. Sci. (Readers' Forum), vol. 24, no. 8, Aug. 1957, pp. 627-628.

12. Hammitt, Andrew G.: The Hypersonic Viscous Effect on a Flat Plate With Finite Leading Edge. Rep. No. 378 (WADC TN 57-105), Dept. Aero. Eng., Princeton Univ, Mar. 1957.

13. Bertram, Mitchel H.: An Approximate Method for Determining the Displacement Effects and Viscous Drag of Laminar Boundary Layers in Two-Dimensional Hypersonic Flow. NACA TN 2773, 1952.

14. Li, Ting-Yi, and Nagamatsu, H. T.: Hypersonic Viscous Flow on Non-insulated Flat Plate. Proc. Fourth Midwestern Conference on Fluid Mechanics, held at Purdue Univ. Sept. 8-9, 1955, Res. Ser. No. 128, Purdue Eng. Experiment Station, 1956, pp. 273-287.

15. Crawford, D. H., and McCauley, W. D.: Investigation of the Laminar Aerodynamic Heat-Transfer Characteristics of a Hemisphere-Cylinder in the Langley 11-Inch Hypersonic Tunnel at a Mach Number of 6.8. NACA Rep. 1323, 1957. (Supersedes NACA TN 3706, 1956.)

16. Creager, Marcus O.: Effects of Leading-Edge Blunting on the Local Heat Transfer and Pressure Distributions Over Flat Plates in Supersonic Flow. NACA TN 4142, 1957.

17. Vas, I. E., Bogdonoff, S. M., and Hammitt, A. G.: An Experimental Investigation of the Flow Over Simple Two-Dimensional and Axial Symmetric Bodies at Hypersonic Speeds. Rep. No. 382 (WADC TN 57-246), Dept. Aero. Eng., Princeton Univ., June 1957.

18. Probstein, Ronald F.: Interacting Hypersonic Laminar Boundary Layer Flow Over a Cone. Tech. Rep. AF 2798/1 (Contract AF 33(616)-2798), Div. Eng., Brown Univ., Mar. 1955.

19. Bertram, Mitchel H.: Tip-Bluntness Effects on Cone Pressures at M = 6.85. Jour. Aero. Sci., vol. 23, no. 9, Sept. 1956, pp. 898-900.

20. Chernyi, G. G.: Hypersonic Flow Around a Slender Blunt Cone. Morris Friedman Foreign Translations C-113. (From Doklady Akademii Nauk USSR, vol. 115, no. 4, 1957, pp. 681-683.)

BOUNDARY-LAYER INDUCED PRESSURES ON FLAT PLATE
AIR; $M_\infty = 9.6$; $26 < R_{\infty,t} < 50$
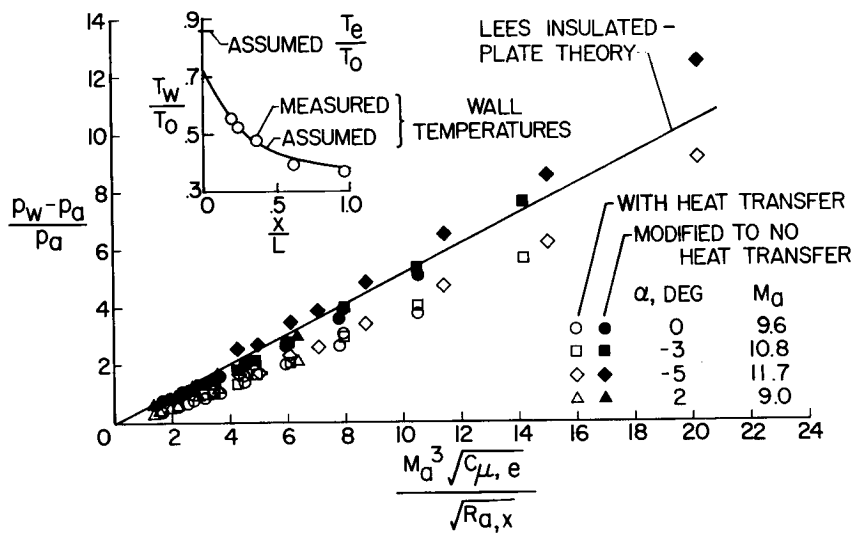


Figure 1

BOUNDARY-LAYER-INDUCED AND ANGLE-OF-ATTACK EFFECTS ON SKIN
FRICTION OF FLAT PLATE
TWO-DIMENSIONAL PLAN FORM; $\gamma = \frac{7}{5}$
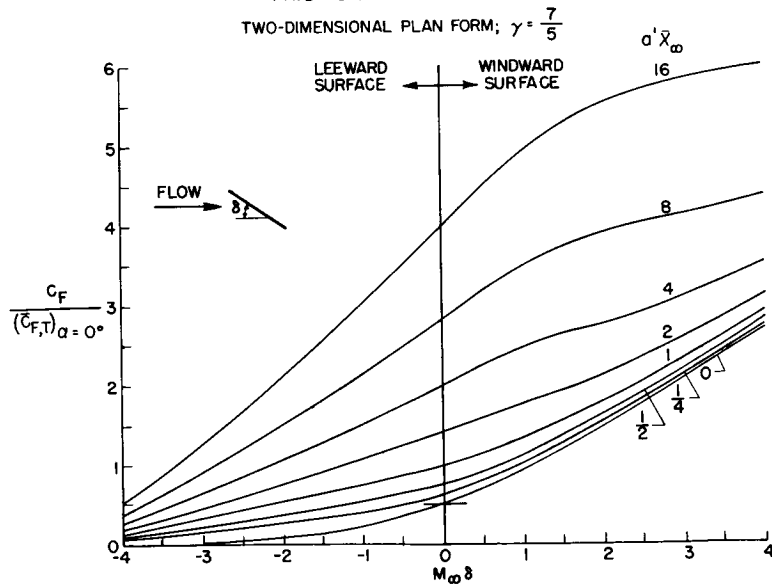


Figure 2

BOUNDARY-LAYER-INDUCED AND ANGLE-OF-ATTACK
EFFECTS ON SKIN FRICTION OF FLAT PLATE
DELTA PLAN FORM; $\gamma = \frac{7}{5}$
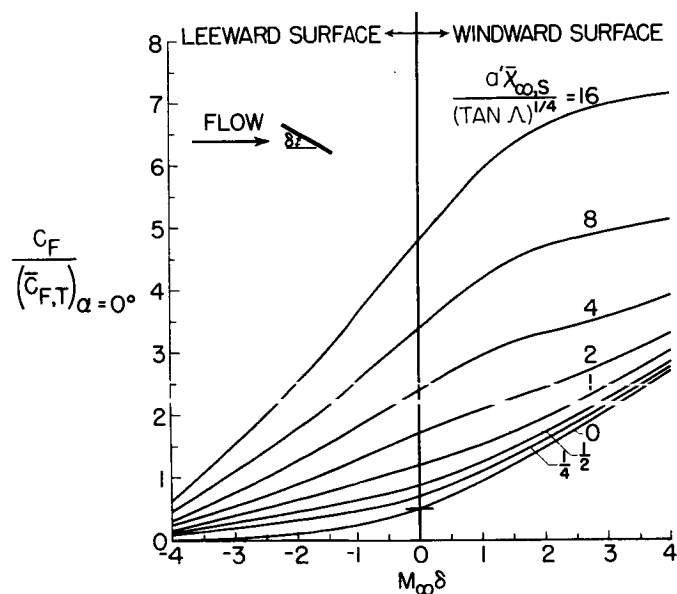


Figure 3

HYPERSONIC BOUNDARY-LAYER-INDUCED AND ANGLE-OF-
ATTACK EFFECTS ON TOTAL SKIN FRICTION OF FLAT PLATES
$\gamma = \frac{7}{5}$
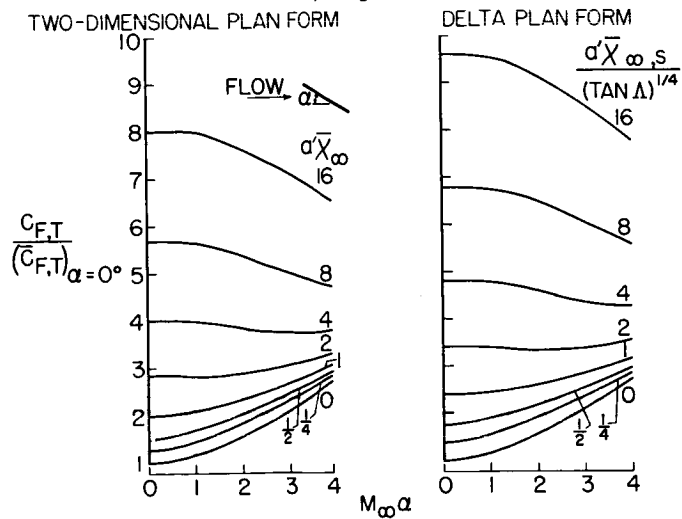


Figure 4

## CHORD FORCE FOR DELTA-WING-HALF-CONE COMBINATION

### AIR; $M_\infty = 9.6$; $R_{\infty,c} = 0.66 \times 10^6$

—— THEORY
○ EXPERIMENT
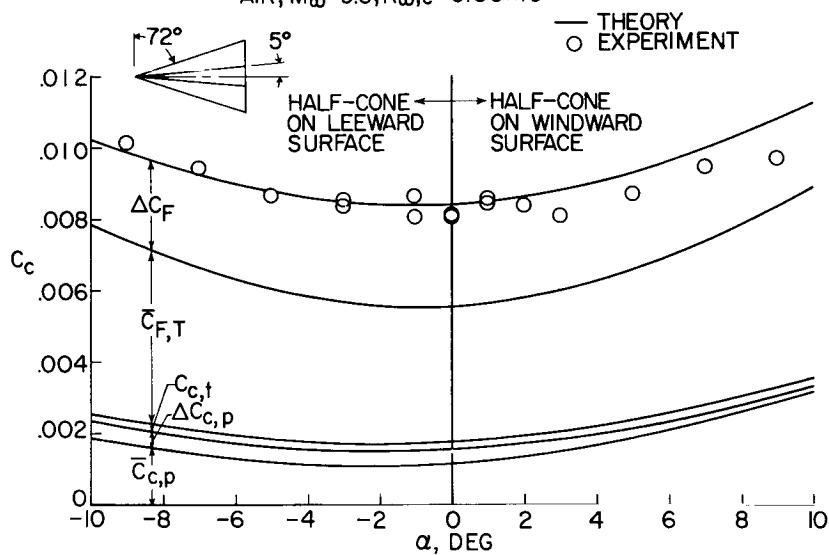
Figure 5

## EFFECT OF VISCOUS INTERACTION AND ASPECT RATIO ON $C_{N_\alpha}$ OF RECTANGULAR WINGS

### TELLEP, UNIV. OF CALIF; $3.7 < M_\infty < 4.1$; AIR

| TEST | MODEL | ASPECT RATIO, A | MODIFIED TO A=∞ |
|------|-------|------------------|------------------|
| ○ | A | 1.0 | ● |
| □ | B | 1.2 | ■ |
| ◇ | C | 1.6 | ◆ |
| △ | D | 2.0 | ▲ |
| ◺ | 1 | 1.6 | ◤ |
| ◁ | 2 | 1.6 | ◀ |

VISCOUS THEORY
INSULATED PLATE;
$M_\infty \to \infty$; $A = \infty$; $\alpha = 0°$

Figure 6

CORRELATION OF PRESSURES INDUCED BY BLUNT L.E.
$\alpha = 0°; \Lambda = 0°; \gamma = 7/5$



Figure 7(a)

CORRELATION OF PRESSURES INDUCED BY BLUNT LEADING EDGE
$\alpha = 0°; \Lambda = 0°; \gamma = \frac{5}{3}$



Figure 7(b)

EFFECT OF $\alpha$ ON FLAT PLATE WITH BLUNT L.E.
AIR; $\Lambda = 0°$; $M_\infty = 6.9$
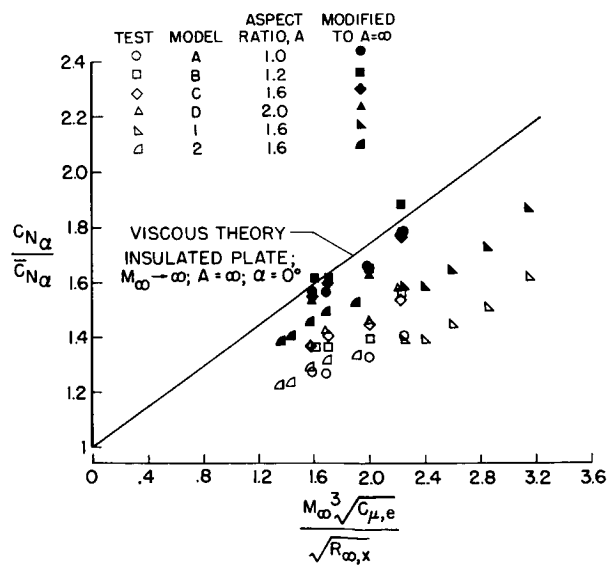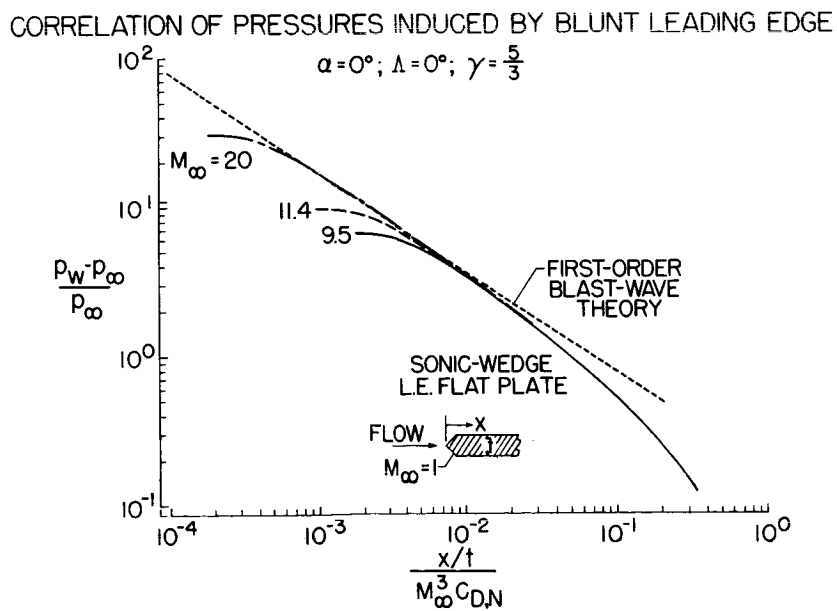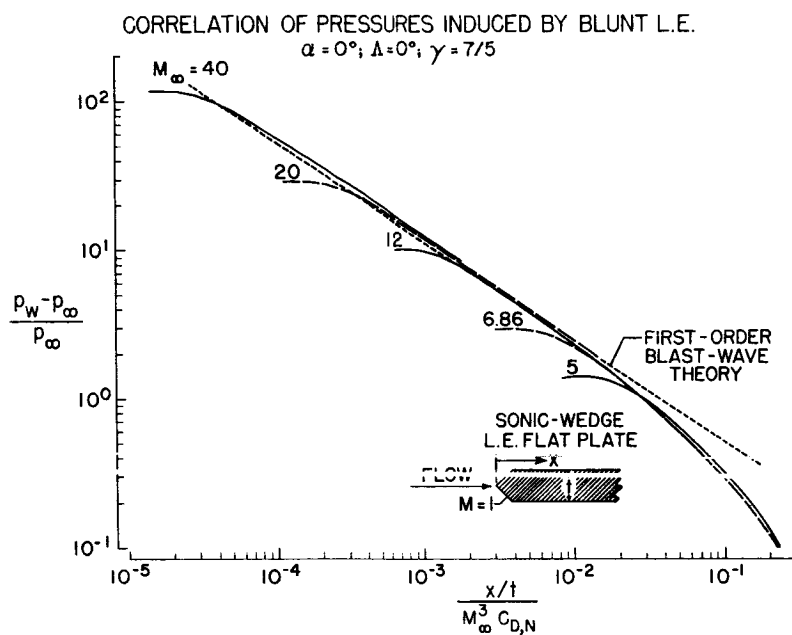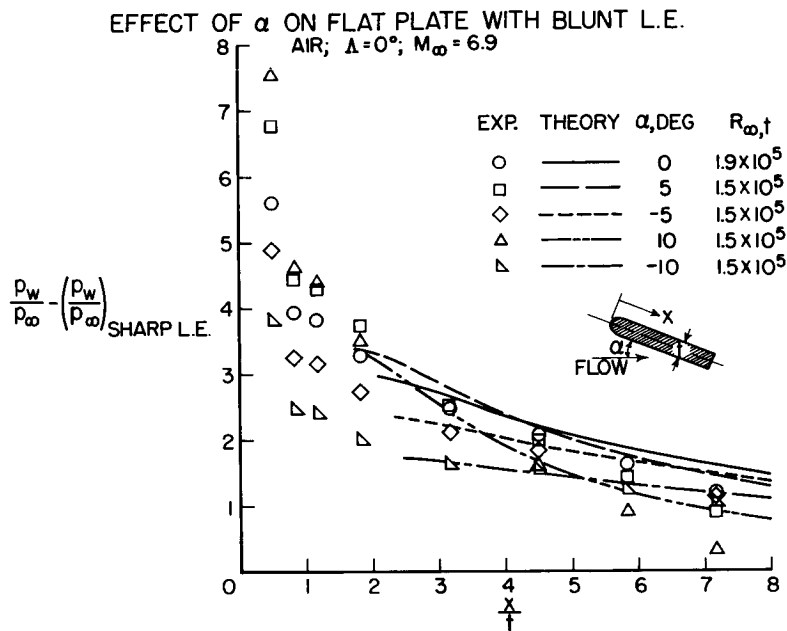


Figure 8

EFFECT OF $\alpha$ ON BLUNT L.E. INDUCED PRESSURES ON FLAT PLATE
$\Lambda = 0°$; $\gamma = 7/5$; $M_\infty = 20$
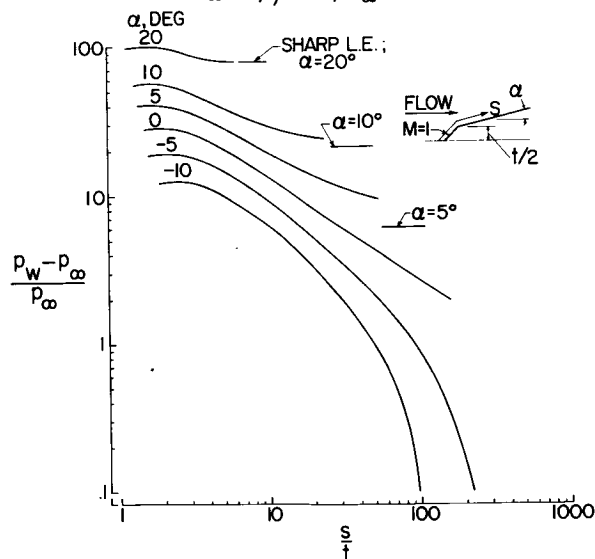


Figure 9

EFFECT OF L.E. SWEEP ON BLUNT L.E. INDUCED PRESSURES

$\alpha = 0°$
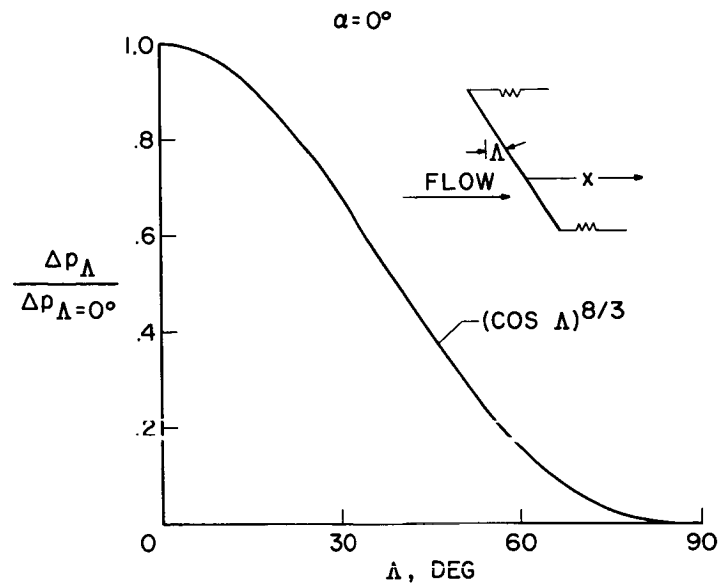


Figure 10

CORRELATION OF PRESSURES ON A FLAT PLATE WITH A HEMICYLINDER L.E.

$\alpha = 0°$; $M_\infty = 6.9$; $R_{\infty, i} = 2.2 \times 10^5$
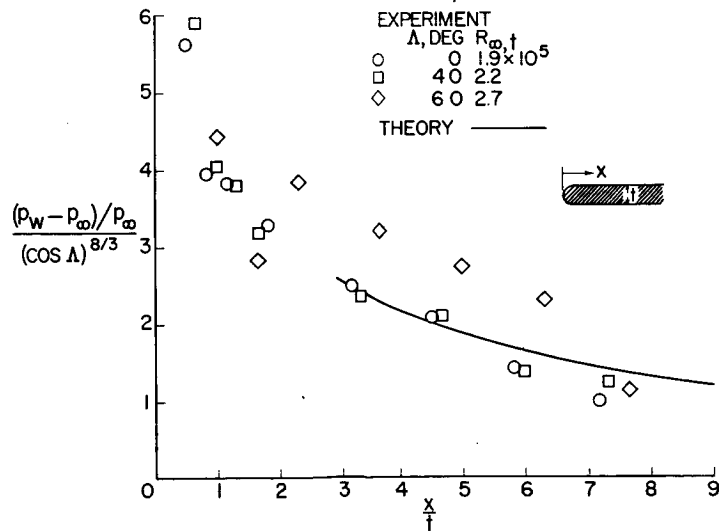


Figure 11

EFFECT OF SWEEP ON PRESSURES ON FLAT PLATE WITH
HEMICYLINDER L. E.

AIR;  $M_\infty = 6.9$ ;  $R_{\infty,t} = 1.5 \times 10^5$



Figure 12

COMBINED VISCOUS AND L.E. BLUNTNESS EFFECTS
ON FLAT-PLATE PRESSURES
PRINCETON HELIUM TUNNEL; $M_\infty = 11.4$



Figure 13(a)

COMBINED VISCOUS AND L.E. BLUNTNESS EFFECTS
ON FLAT-PLATE PRESSURES
HELIUM
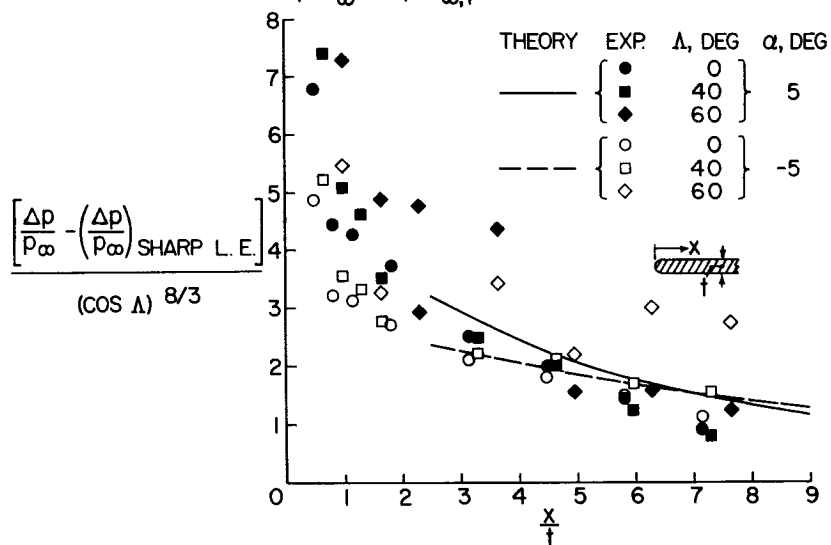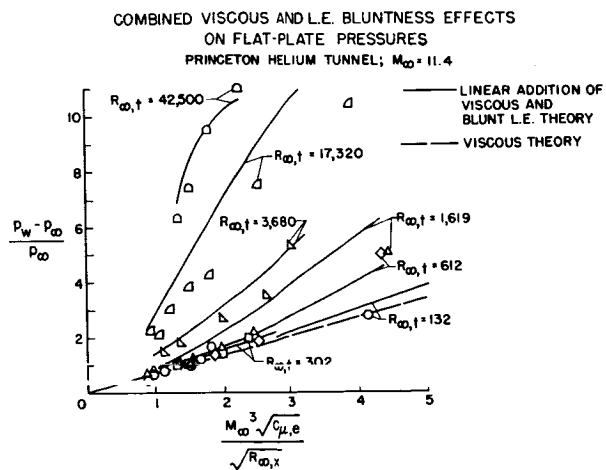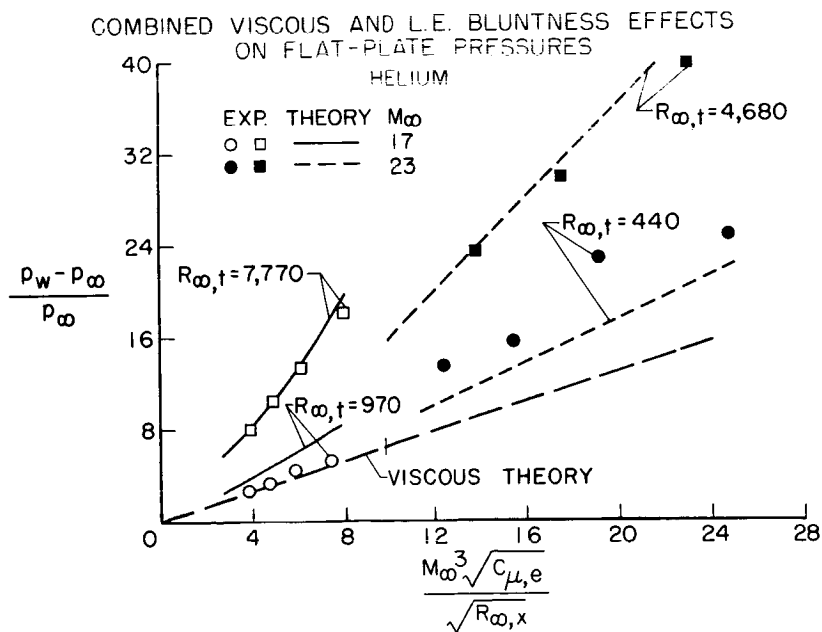


Figure 13(b)

EFFECT OF PRESSURE GRADIENT ON STANTON NUMBER
METHOD OF HYPERSONIC SIMILAR SOLUTIONS; $\gamma = 7/5$
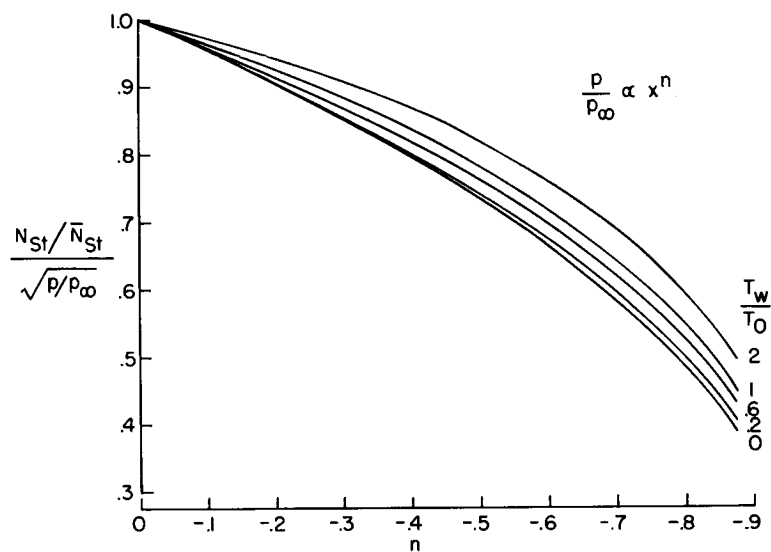


Figure 14

HEAT TRANSFER TO A BLUNTED ROD AND TO A BLUNTED FLAT PLATE
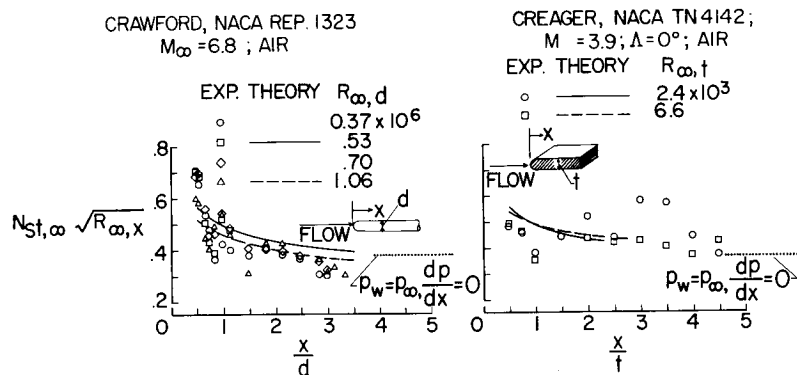


Figure 15

## PRESSURE DISTRIBUTION ON A BLUNTED ROD
### HELIUM; HEMISPHERICAL NOSE

| | $M_\infty$ | $R_{\infty,d}$ | |
|---|---|---|---|
| ○ | 12.1 | $3.3 \times 10^5$ | PRINCETON |
| □ | 12.7 | 3.1 | HELIUM |
| ◇ | 13.7 | 2.7 | TUNNEL |
| ∧ | 16.9 | 2.8 | |
| ◁ | 18.8 | 2.3 | |
| ⊿ | 21 | 0.6 | LANGLEY 2-INCH HELIUM JET |

$\frac{p_w - p_\infty}{p_\infty}$

$(x/d)/M_\infty^2$
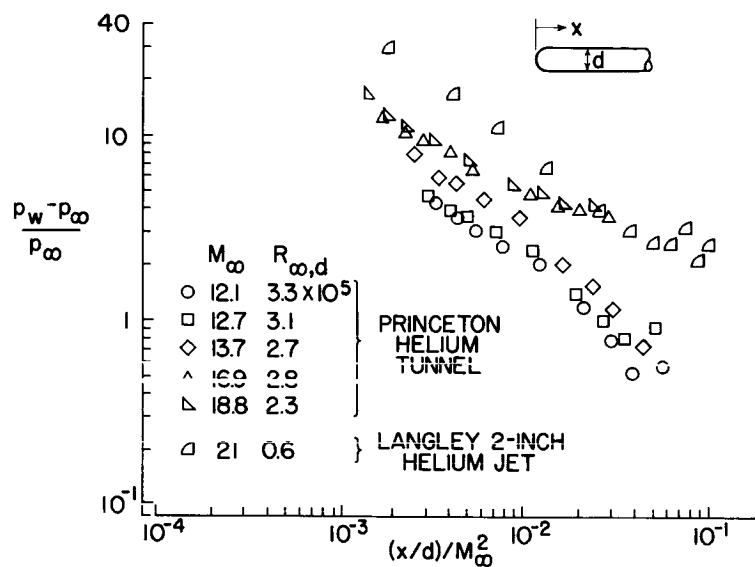
Figure 16(a)

## PRESSURE DISTRIBUTION ON A BLUNTED ROD
### HELIUM; FLAT NOSE

| | $M_\infty$ | $R_{\infty,d}$ | |
|---|---|---|---|
| ○ | 11.7 | $3.4 \times 10^5$ | PRINCETON |
| □ | 12.6 | 3.0 | HELIUM |
| ◇ | 13.9 | 2.6 | TUNNEL |
| ⊿ | 21 | 0.6 | LANGLEY 2-INCH |
| ◁ | 21 | .9 | HELIUM JET |

$\frac{p_w - p_\infty}{p_\infty}$

$(x/d)/M_\infty^2$
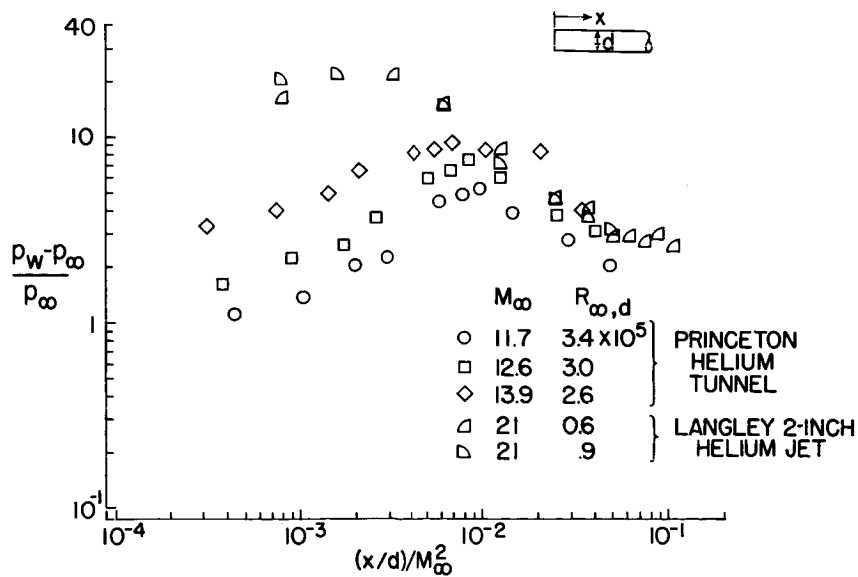
Figure 16(b)

## PRESSURE DISTRIBUTION ON A BLUNTED CONE
### HELIUM

$M_\infty = 17$

$$\frac{p_w - p_C}{p_C}$$

$M_\infty = 23$

| EXP. | VISCOUS THEORY | $R_{\infty,d}$ |
|------|---------------|-----------|
| ○ | ——— | 2,300 |
| □ | — — — | 6,500 |
| ◇ | - - - - | 13,000 |
| △ | —··—·· | 28,000 |

$$\frac{x}{d}$$
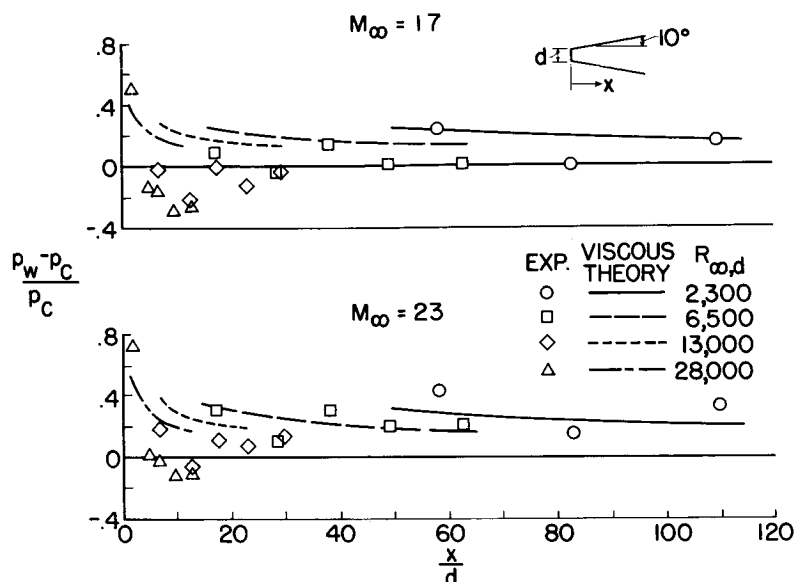
Figure 17

## HEAT TRANSFER TO SHARP AND BLUNTED CONES
### $\alpha = 0°$; 10° HALF-ANGLE CONE; $M_\infty = 6.7$; AIR

ESSENTIALLY SHARP CONE

$R_{\infty,d} = 430$ — 1,240 — 1,690 — 3,210

SHARP-CONE THEORY

$$\frac{N_{St}\sqrt{R_S}}{\sqrt{C_\mu}}$$

FLAT-TIP CONE

$R_{\infty,d} = 7,600$ — 23,000 — 43,000

CONE THEORY WITH MANGLER TRANSFORMATION FOR PRESENCE OF BLUNTED TIP

HEMISPHERE-TIP CONE

$R_{\infty,d} = 8,600$ — 20,000 — 48,000

$R_S$

Figure 18

HEAT TRANSFER TO SHARP-TIPPED CONE
$\alpha = 5°$; $10°$ HALF-ANGLE CONE; $M_\infty = 6.7$; AIR



Figure 19(a)

HEAT TRANSFER TO BLUNTED CONE
$\alpha = 5°$; $10°$ HALF-ANGLE CONE; $M_\infty = 6.7$; AIR
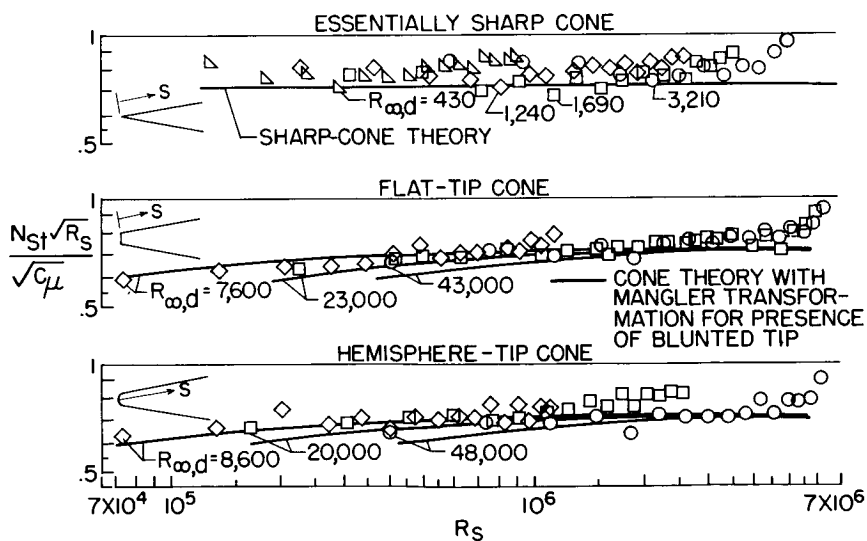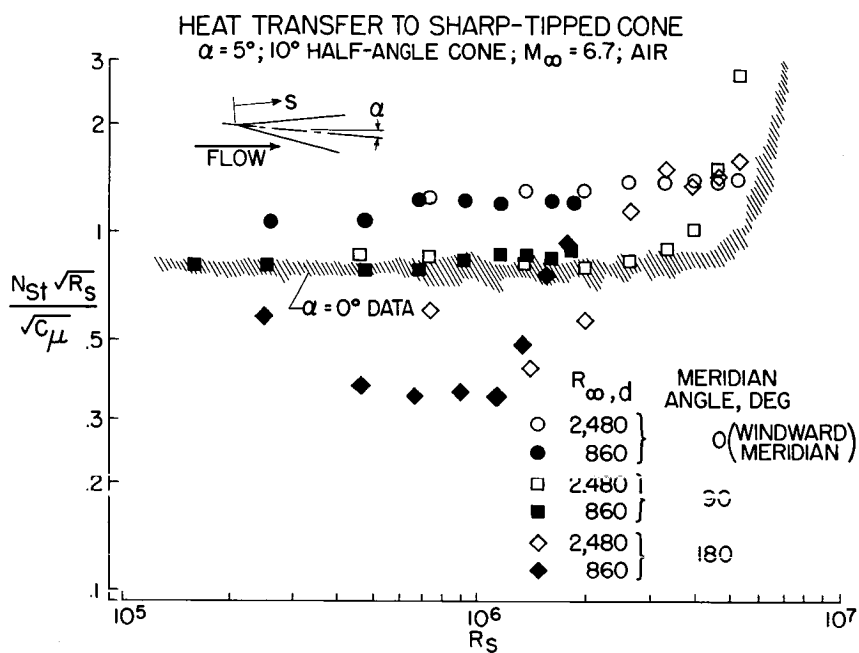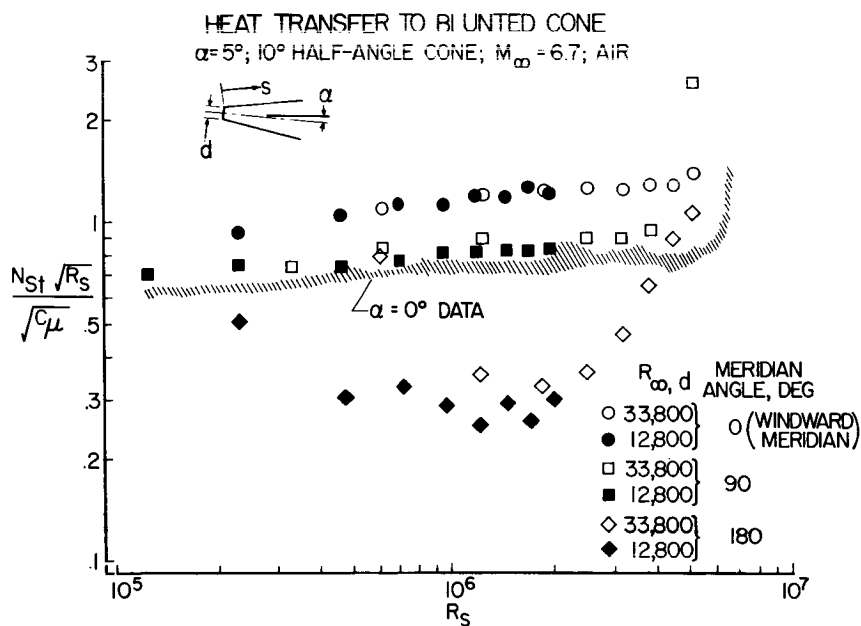


Figure 19(b)

# AERODYNAMIC HEATING OF HYPERSONIC CONFIGURATIONS

By Leo T. Chauvin, B. Leon Hodge,
and Andrew G. Swanson

Langley Aeronautical Laboratory

## INTRODUCTION

At a time when rocket-airplane and missile speeds are rapidly increasing, the need for the ability to predict correctly the heating rates on all exposed surfaces is evident. Heat-transfer data so far available have been primarily for isolated components at zero angle of attack. The aim of the present paper is to present component heat-transfer data at high angle of attack and especially to present configuration data for the important regions where the mutual aerodynamic interference of configuration components affects the heating rates.

## SYMBOLS

| | |
|---|---|
| $\Lambda$ | angle of sweep |
| $\alpha$ | angle of attack |
| $x$ | distance along nose |
| $d$ | diameter |
| $N_{St}$ | Stanton number |
| $R_\infty$ | free-stream Reynolds number |
| $\psi$ | meridian angle |
| $c$ | chord |
| $M_\infty$ | free-stream Mach number |
| $R_{\infty,c}$ | free-stream Reynolds number based on chord |
| $r$ | radius |
| $\rho$ | density of air |
| $c_p$ | specific heat of air |
| $V$ | velocity |

26

_l_          length of body

b          span

s          distance from leading edge

## OGIVE-CYLINDER WING-BODY CONFIGURATION

In figure 1 are shown two ogive-cylinder bodies having sweptback wings of $39°$ and $75°$. The two configurations were mounted on the front of a Nike rocket motor in a fork-like arrangement such that the models were at an angle of attack of $8°$. Further description of the test vehicle and basic measurements for evaluating the heat transfer have already been published and are presented in reference 1.

Some heat-transfer data typical of those measured at other Mach numbers are shown for the nose section of the configuration having a swept wing of $39°$ in figure 2 (for the windward and leeward sides of the nose). The Stanton number expressed as a free-stream condition is plotted as a function of the ratio $x/d$ where $x$ is the distance from the nose tip to the measurement station and $d$ is the body diameter. The measurements are presented for $M_\infty = 4.4$ and a unit Reynolds number of $19 \times 10^6$. Indicated in the figure by the solid line is the theory of reference 2 for heat transfer to yawed cones, which is in good agreement with the measurements for both sides of the body. The dashed line represents the theory of reference 3 for turbulent heat transfer to cones at zero angle of attack. Fair agreement is obtained with the measurements when the local conditions for an equivalent tangent cone and distance from the nose tip to measurement station are used in the theory. For comparison, the estimated Stanton number for $\alpha = 0°$ at $\frac{x}{d} = 1.0$ and 2.5 is $2 \times 10^{-3}$ and $1 \times 10^{-3}$, respectively. These estimates were derived from reference 3 and local conditions obtained by the method of characteristics. For a simple body free of protuberances such as the one at an angle of attack of $8°$, the figure shows that the theory gives a good prediction of the heating.

The influence of the wing on the heat transfer to the body is shown in figure 3 where the measurements are presented as plots of the free-stream Stanton number as a function of distance along the configuration for $M_\infty = 4.2$, $\alpha = 8°$, and for various meridian stations $\psi$. At $\psi = 0$ (at the windward station), the measurements are about constant. At $\psi = 67°$ the Stanton number decreases behind the leading edge and then rises to a magnitude of twice that at $\psi = 0$. Heat transfer on the leeward side is less than half the value for $\psi = 0$. For comparison,

the calculated Stanton number for zero angle of attack (no interference being assumed) is approximately $0.7 \times 10^{-3}$. Measurements made on the wing-body configuration with $75^\circ$ sweep showed the same heat-transfer rise. It appears from these tests that severe heating might be experienced in the wing-body junctures and that a better understanding of the complex flow fields in the wing-body region may be required before the heat transfer can be predicted.

Heat-transfer measurements made on the wing are presented in figure 4 as plots of the free-stream Stanton number as a function of $x/c$. Measurements are presented for both sides of the $39^\circ$ and $75^\circ$ swept wings at $\alpha = 8^\circ$ for $M_\infty = 4.4$ and $R_{\infty,c} = 16 \times 10^6$ based on the chord of the wing at the measurement station. The data are compared with the Van Driest theory (ref. 3) based on sharp-wedge flow conditions parallel to the body axis and distance from the leading edge to the measured point. For this angle of attack, previous tests (ref. 4) have shown that for an isolated wing good agreement was obtained. For these tests, however, the effects of the body on the wing were such as to reduce the heating on the windward side by approximately 20 percent and by a considerable amount on the leeward side.

## X-15 AIRPLANE

Shown in figure 5 is a sketch of the North American X-15 airplane. A 1/15-scale model of this research airplane has been tested in the Langley Unitary Plan wind tunnel at $M_\infty = 3.0$ and a Reynolds number per foot of $4.4 \times 10^6$. Note the large external fairings on both the top and side views which alter local flow conditions and thereby alter the heat transfer. A complete heat-transfer investigation of this configuration has been made; however, only the data at the forward station at $x/l = 0.13$, and further back along the body at $x/l = 0.50$ and along the wing chord at 50-percent semispan are presented. In order to provide testing in a turbulent boundary-layer, roughness (No. 60 carborundum) was added along the bottom of the model.

In figure 6 is shown the distribution of the measured free-stream Stanton number around the body at $x/l = 0.13$ for $M_\infty = 3.0$ and for angles of attack of $0^\circ$, $15^\circ$, and $28^\circ$. For zero angle of attack the distribution of the measured Stanton number is symmetrical about the fuselage and is in agreement with the turbulent cone heat-transfer theory of reference 3 except for the point at $\psi = 0$ where the measurement is higher, probably owing to the influence of the roughness strip. For an increase in angle of attack to $15^\circ$, the heat transfer at the stagnation point is increased by a factor of 2.0 at $\psi = 0$ and decreases around

the model to a value of 1/5 that at $\psi = 0°$ (windward) at $\psi = 180°$ (leeward). Although increasing the angle of attack to 15° doubled the heating at $\psi = 0$, a further increase to 28° made little change on the entire heating distribution. This has also been observed in similar tests (ref. 5) when the crossflow Mach number approaches 1. The theory of reference 2, which was compared with a similar body in figure 2 but for a lower angle of attack, now greatly underestimates the heating for these large angles of attack.

At station $x/l = 0.5$ where the body is cylindrical, figure 7 shows the distribution of the measured Stanton number around the fuselage and fairing. At zero angle of attack the distribution around the fuselage is symmetrical and agrees with the turbulent flat-plate theory of reference 3. As the angle of attack is increased to 15° the heating at $\psi = 0°$ is increased about 2.5 times and the heating remains high around the fuselage until the side of the fairing (at $\psi = 90°$) is reached. On the leeward side the Stanton number is about half of that on the windward side. Increasing the angle of attack to 28°, the heat transfer on the windward side is further increased to about 3.5 times that of zero angle of attack, and the heating remains high along the windward side up to the side of the fairing. On the leeward side the heat transfer for 28° is about the same as that for 0° and 15°. The theory of Ivan E. Beckwith (unpublished) for turbulent heat transfer for an infinite swept cylinder is presented for the windward side. This theory is based on Reynolds number (based on body diameter) and local crossflow conditions and applies only at the stagnation point. The theory shows only fair agreement at an angle of attack of 15° but gives perfect agreement at 28° where truer crossflow conditions prevail. These data indicate that, for high angles of attack, crossflow theory predicts the heat transfer very well.

The measured heat transfer for the wing of the airplane is shown in figure 8 for the 50-percent semispan where the data are presented as plots of free-stream Stanton number as a function of $x/c$ for $M_\infty = 3.0$ and $R = 2.2 \times 10^6$ based on wing chord. The wing had an NACA 66-005 airfoil section and roughness added close to the leading edge to trip the boundary layer. Tests were made at angles of attack of 0°, 15°, and 28°. The measurements at zero angle of attack are in good agreement with the turbulent flat-plate heat-transfer theory of reference 3 where the Reynolds number in the theory is based on distance from the leading edge parallel to the axis of the body. For the windward side the measured heat transfer for an angle of attack of 15° is about 15 percent higher than that for the theory and for an angle of attack of 28° is 20 percent higher than that for theory. For the leeward side, experiment and theory are in good agreement. The theory for these tests was based on wedge flow, a sharp leading edge being assumed and the distance being that from the leading edge parallel to the body to the measured point. It appears

that, for even a simple shape such as a wing, as the angle of attack is increased to large angles, the theory underestimates the heat transfer on the windward side.

## HYPERSONIC GLIDER TESTS

In figure 9 are shown two rocket glider shapes that were simulated by rocket-propelled model tests at $M \approx 10$ and a Reynolds number per foot of $1.2 \times 10^6$. The arrangement of the flat surfaces on the test vehicle was such that three of these surfaces formed a pyramid nose shape. On the right-hand side of the figure is shown one of the flat surfaces having a sweptback leading edge of $75^\circ$ at an angle of attack of $8^\circ$. The sketch on the left-hand side of the figure is the same flat surface with a conical body, which simulates a wing at an angle of attack of $8^\circ$ with an underbody. Shown in figure 9 are the stations at which heat-transfer measurements were made. The Reynolds number for these tests is such that the test model simulates the first 30 feet of the full-scale airplane at an altitude of 160,000 feet.

The experimental heat transfer to the simulated glide vehicles was obtained from temperature-time histories measured in free-flight rocket-model tests. The temperatures were measured with thermocouples welded to the inside surface of the skin of the test model. These inside temperatures were used to compute outside surface temperatures which in turn were used to compute heating rates; the method of reference 6 was used for these computations. The leading-edge heating data were corrected for lateral conductive heat flow to the cooler flat surface of the simulated wings.

The theoretical leading-edge heating rates were computed from a modified three-dimensional stagnation-point theory. The basic theory used was that of Fay and Riddell (ref. 7) which was evaluated by using a Lewis number of 1.0, a Prandtl number of 0.71, the Sutherland viscosity variation with temperature, and ideal-gas-flow properties. The validity of this method of evaluation of the Fay and Riddell theory is discussed in reference 8. This three-dimensional heating rate was multiplied by $1/\sqrt{2}$ to convert it to a two-dimensional stagnation-line heating rate as was done in reference 9. This heating rate was then reduced, to account for the alleviating effects of sweep, by the factor $(\cos \Lambda)^{3/2}$. This factor has theoretical justification for $M \to \infty$ (ref. 10, for example), although some experimental data from wind-tunnel tests have indicated that the heating reduction due to sweep is more nearly proportional to $\cos \Lambda$. Heating rates were reduced to free-stream Stanton numbers by using the free-stream stagnation temperature as adiabatic wall temperature.

It can be seen (fig. 10) that the experimental data obtained from both of the simulated glide vehicle tests are in reasonable agreement with the theoretical prediction obtained from the method outlined above. It is interesting to note that, for the high sweep of the configurations tested, the use of $\cos \Lambda$ in the theory would result in a theoretical level almost twice as high as that obtained using $(\cos \Lambda)^{3/2}$. Some recent experimental data obtained by Cunningham and Kraus (ref. 11) have also indicated that the $(\cos \Lambda)^{3/2}$ parameter is the more valued one; these data were obtained, however, at very low Reynolds numbers and the possible existence of slip flow must be suspected. Data from references 10 and 12 have also shown the validity of $(\cos \Lambda)^{3/2}$ at the lower sweep angles although the agreement is better with $\cos \Lambda$ at the higher sweep angles.

The experimental heat-transfer rates to the flat-undersurface glider configuration were determined by the same general procedure as those for the leading edge and are given in figure 11. The data, however, were reduced to free-stream Stanton numbers by using local adiabatic wall temperatures. Theoretical Stanton numbers were computed from the Van Driest theories for flat plates (refs. 3 and 13) for laminar and turbulent flow, respectively. The modified Reynolds analogy $C_h = 0.6 C_f$ (ref. 14) was used. Local flow conditions were those for an $8°$ wedge having an oblique shock at the leading edge. Local adiabatic wall temperatures and free-stream values of $c_p \rho V$ were again used to obtain the free-stream Stanton numbers.

The data are correlated on the basis of length from the glider wing leading edge measured parallel to the surface center line. The data show better correlation when plotted in this manner than when correlated on the basis of ray length from the model nose (or wing apex). The data indicate that the flow was laminar over the flat surface.

The experimental heat-transfer rates to the body of the conical under-body configuration were determined by the same method as used for the leading-edge and flat-surface heating and are given in figure 12 as a function of azimuth angle around the body. The rates were reduced to free-stream Stanton numbers by using the stagnation temperature as the adiabatic wall temperature. In order to determine local flow conditions for calculation of theoretical heating rates, a pressure distribution for yawed cones (ref. 15) was assumed to exist over the conical underbody. By using the pressure distribution and the ideal gas relation and assuming a normal shock at the model nose, local flow conditions were computed. These local flow conditions were used with the theory for laminar and turbulent heat transfer for cones (ref. 3) to compute local Stanton numbers which were then converted to free-stream Stanton numbers. The data are plotted on polar coordinates with Stanton number given as a function

of azimuth position on the body. The dashed line is the turbulent theory for a cone and the solid line is the laminar theory. For the 4.5-inch station the experimental data are as high as those of the turbulent theory, except for a point close to the wing where the measurement is lower than that of the laminar theory. At the 8.5-inch station the measurements are higher than the value given by laminar theory. At this low Reynolds number the agreement with turbulent theory appears to be entirely fortuitous. The reason for these high heating rates is not known at this time.

## CONCLUSIONS

From a number of wing and body components tested separately and in combination, the following conclusions were reached:

1. As might be expected, good agreement between theory and experiment was obtained for slender nose shapes and wing surfaces at low angles of attack when not subject to mutual interference. However, substantial discrepancies occurred even in these simple cases at high angles of attack. For the cylindrical portion of a body, crossflow theory correctly predicted the heat transfer only at high angles of attack. The leading-edge heat transfer to a wing swept 75° was in good agreement with theory which indicates a reduction of leading-edge heating that is proportional to the cosine of the angle of sweep to the 3/2 power.

2. When wing-body combinations were subjected to mutual interference, important discrepancies between theory and experiment were found in almost every case; for example:

(a) Heat transfer on portions of a cylindrical fuselage in the vicinity of a wing was about twice as high as that predicted by theory, and the heat transfer on a conical body under a low-aspect-ratio delta wing was similarly about twice as high as the theoretical values.

(b) Conversely, heat transfer to a wing in the vicinity of a cylindrical fuselage was found to be substantially alleviated.

CONFIDENTIAL

REFERENCES

1. Chauvin, Leo T.: Temperature Measurements From a Flight Test of Two Wing-Body Combinations at $7^\circ$ Angle of Attack For Mach Numbers to 4.86 and Reynolds Numbers to $19.2 \times 10^6$. NACA RM L57F27, 1957.

2. Braun, Willis H.: Turbulent Boundary Layer on a Yawed Cone in a Supersonic Stream. NACA TN 4208, 1958.

3. Van Driest, E. R.: The Problem of Aerodynamic Heating. Aero. Eng. Rev., vol. 15, no. 10, Oct. 1956, pp. 26-41.

4. Carter, Howard S.: Heat Transfer on the Lifting Surfaces of a $60^\circ$ Delta Wing at Angle of Attack for Mach Number 1.98. NACA RM L56C23, 1956.

5. Feller, William V.: Heat Transfer to Bodies at Angles of Attack. NACA RM L57D19c, 1957.

6. Hill, P. R.: A Method of Computing the Transient Temperature of Thick Walls From Arbitrary Variation of Adiabatic-Wall Temperature and Heat-Transfer Coefficient. NACA TN 4105, 1957.

7. Fay, J. A., and Riddell, F. R.: Theory of Stagnation Point Heat Transfer in Dissociated Air. Jour. Aero. Sci., vol. 25, no. 2, Feb. 1958, pp. 73-85, 121.

8. Stoney, William E., Jr., and Swanson, Andrew G.: Heat Transfer Measured on a Flat-Face Cylinder in Free Flight at Mach Numbers up to 13.9. NACA RM L57E13, 1957.

9. Lees, Lester: Laminar Heat Transfer Over Blunt-Nosed Bodies at Hypersonic Flight Speeds. Jet Propulsion, vol. 26, no. 4, Apr. 1956, pp. 259-269.

10. Goodwin, Glen, Creager, Marcus O., and Winkler, Ernest L.: Investigation of Local Heat-Transfer and Pressure Drag Characteristics of a Yawed Circular Cylinder at Supersonic Speeds. NACA RM A55H31, 1956.

11. Cunningham, Bernard E., and Kraus, Samuel: Experimental Investigation of Rates of Heat Transfer to Transverse Circular Cylinders in a 6500 Feet Per Second Hypersonic Air Stream. (Prospective NACA paper.)

12. Eggers, A. J., Jr., Hanson, C. Frederick, and Cunningham, Bernard E.: Theoretical and Experimental Investigation of the Effect of Yaw on Heat Transfer to Circular Cylinders in Hypersonic Flow. NACA RM A55E02, 1955.

CONFIDENTIAL

13. Lee, Dorothy B., and Faget, Maxime A.:  Charts Adapted From Van Driest's Turbulent Flat-Plate Theory for Determining Values of Turbulent Aerodynamic Friction and Heat-Transfer Coefficients.  NACA TN 3811, 1956.

14. Rubesin, Morris W.:  A Modified Reynolds Analogy for the Compressible Turbulent Boundary Layer on a Flat Plate.  NACA TN 2917, 1953.

15. Savin, Raymond C.:  Application of the Generalized Shock-Expansion Method to Inclined Bodies of Revolution Traveling at High Supersonic Airspeeds.  NACA TN 3349, 1955.

## HEAT TRANSFER TO AN OGIVE-CYLINDER—WING-BODY COMBINATION
### $\alpha = 8°$; $M_\infty = 4.4$; FLIGHT; PARD
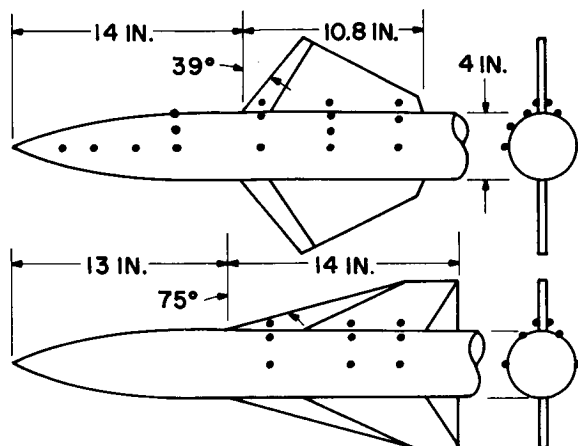


Figure 1

## HEAT TRANSFER TO AN OGIVE CYLINDER
### $\alpha = 8°$; $M_\infty = 4.4$; $\frac{R_\infty}{FT} = 19 \times 10^6$
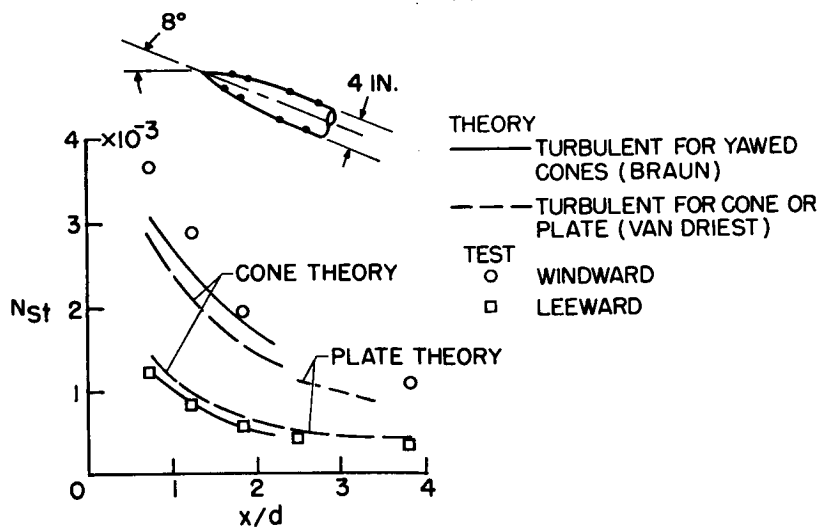


Figure 2

## HEAT TRANSFER TO BODY IN WING-BODY REGION

$\alpha = 8°$; $M_\infty = 4.2$
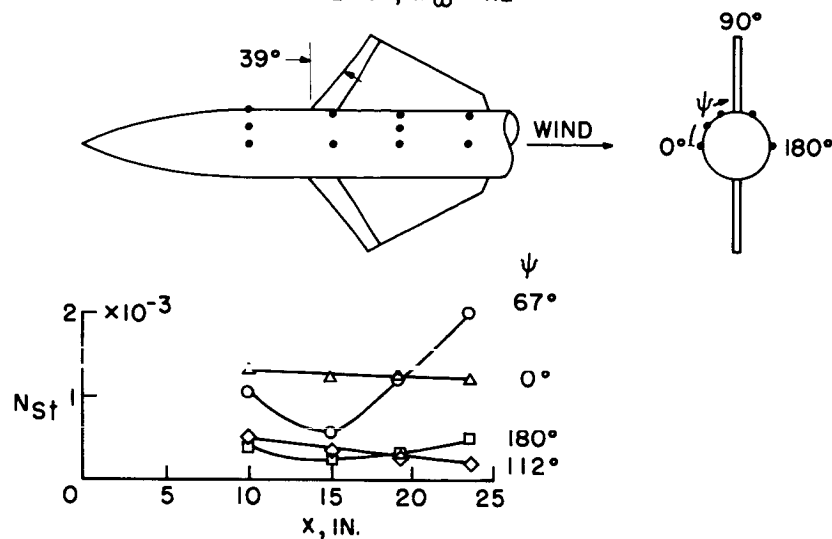


Figure 3

## AERODYNAMIC HEATING TO WINGS NEAR A WING-BODY JUNCTURE

$\alpha = 8°$; $M_\infty = 4.4$; $R_{\infty,c} = 16 \times 10^6$



Figure 4

CONFIDENTIAL
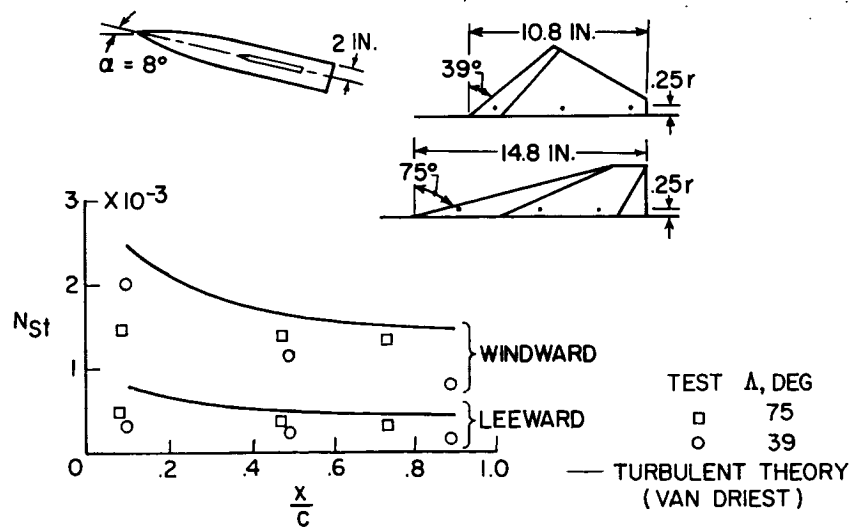
X-15 HEAT-TRANSFER MODEL

$M_\infty = 3; \dfrac{R_\infty}{FT} = 4.4 \times 10^6;$ LANGLEY UNITARY TUNNEL



TOP VIEW

SIDE VIEW

$l = 39.2$ IN.
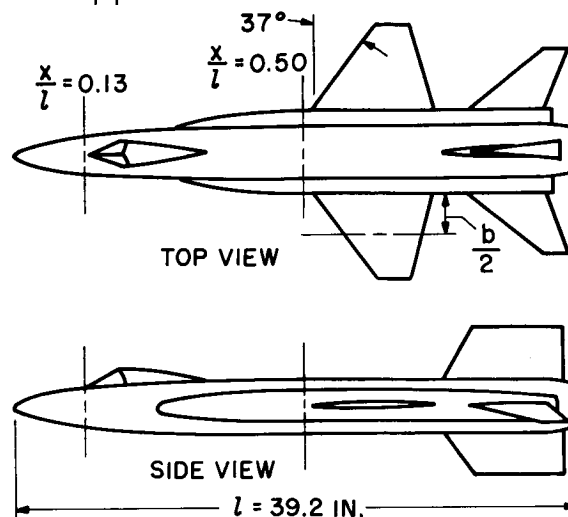
Figure 5

HEAT TRANSFER TO X-15 AIRPLANE FUSELAGE

$\dfrac{x}{l} = 0.13; \quad M_\infty = 3.0; \quad \dfrac{R_\infty}{FT} = 4.4 \times 10^6$



Figure 6

HEAT TRANSFER TO X-15 AIRPLANE FUSELAGE
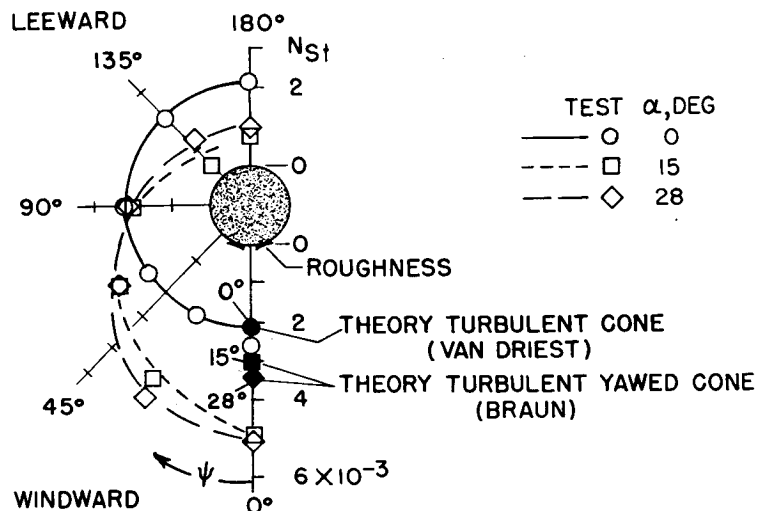
$$\frac{x}{l} = 0.5; \quad M_\infty = 3.0; \quad \frac{R_\infty}{FT} = 4.4 \times 10^6$$
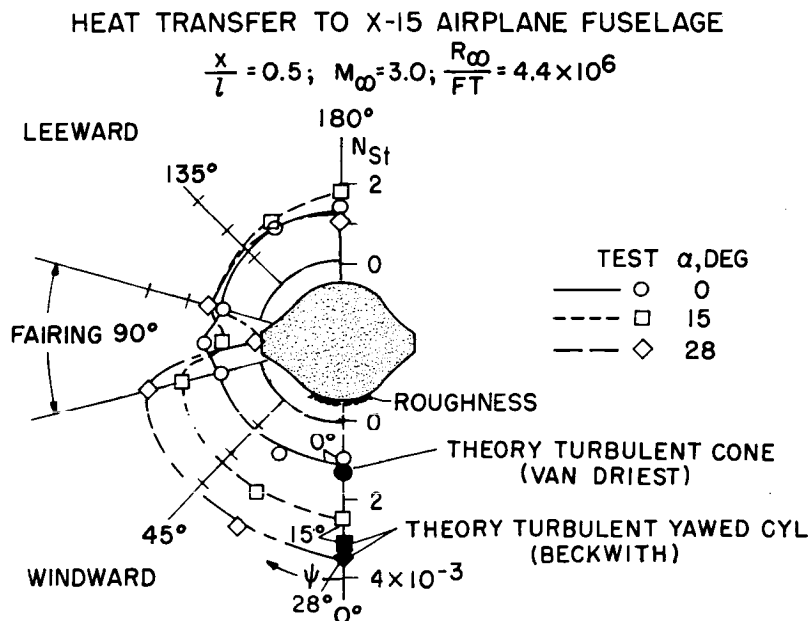


Figure 7

AERODYNAMIC HEATING TO A 37°
SWEPT WING AT VARIOUS ANGLES OF ATTACK
NACA 66-005 AIRFOIL SECTION; $M_\infty = 3.0$; $R_{\infty,c} = 2.2 \times 10^6$
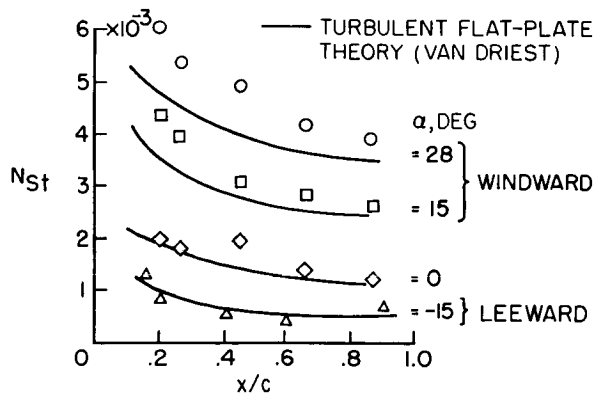


Figure 8

## HYPERSONIC ROCKET GLIDER TESTS

$\bar{\alpha} = 8°$; $M \approx 10$; $R/FT \approx 1.2 \times 10^6$; FLIGHT; PARD

CONICAL
UNDERBODY

FLAT
SURFACE

FLOW
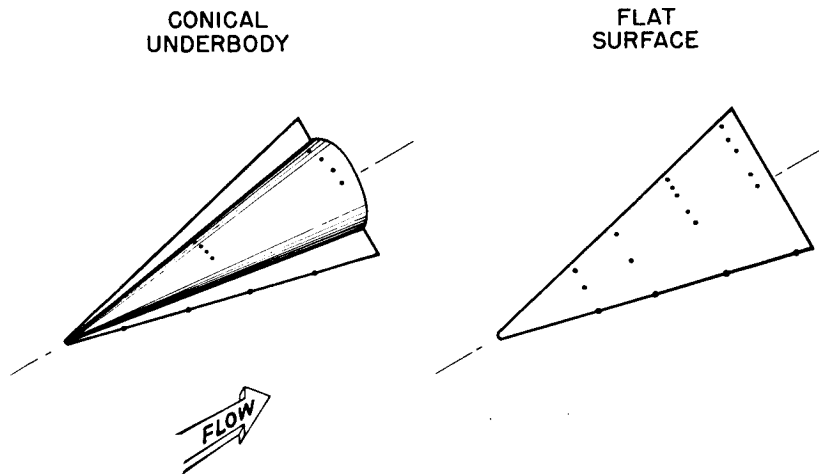
Figure 9

## AERODYNAMIC HEATING OF LEADING EDGE
## OF 75° SWEPT WING

$M_\infty = 10.3$;    $R/FT \approx 1.5 \times 10^6$

THEORY FOR INFINITE CYLINDER

$(FAY\ AND\ RIDDELL) \times \dfrac{1}{\sqrt{2}} (COS\ \Lambda)^{\frac{3}{2}}$

$\dfrac{N_{St,EXP}}{N_{St,TH}}$

△ CONICAL-UNDERBODY WING
□ FLAT-SURFACE WING

DISTANCE ALONG LEADING EDGE, IN.
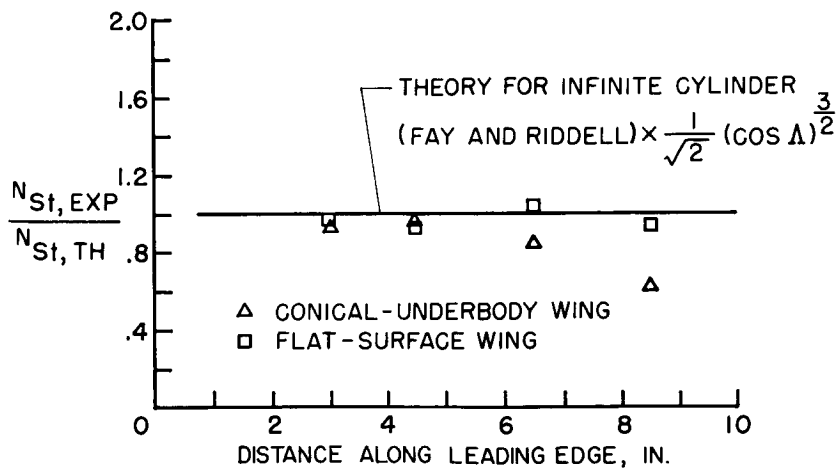
Figure 10

AERODYNAMIC HEATING OF 75° SWEPT WING

$\alpha = 8°; M_\infty = 10; R_\infty / FT = 1.7 \times 10^6$



VAN DRIEST FLAT-PLATE THEORY
- - - - LAMINAR
——— TURBULENT
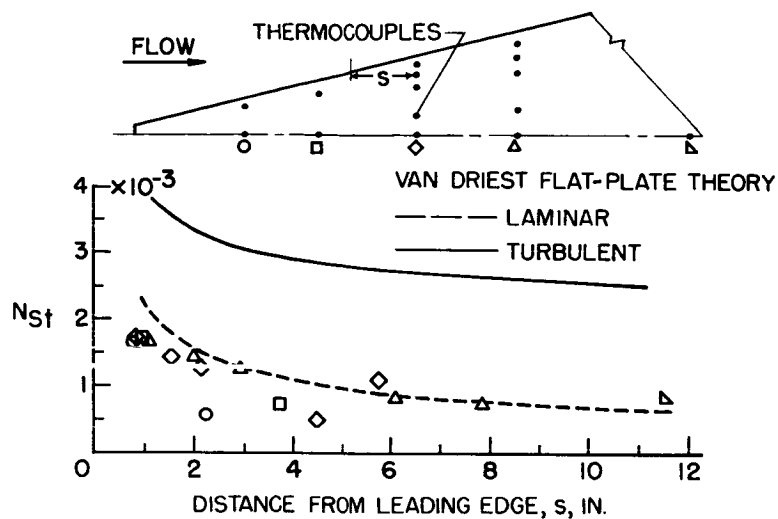
Figure 11

HEATING ON AN 8.4° CONE MOUNTED ON A WING

$\alpha = 8°; M_\infty = 10.3; \frac{R_\infty}{FT} = 1.2 \times 10^6$

VAN DRIEST CONE THEORY
- - - - TURBULENT
——— LAMINAR
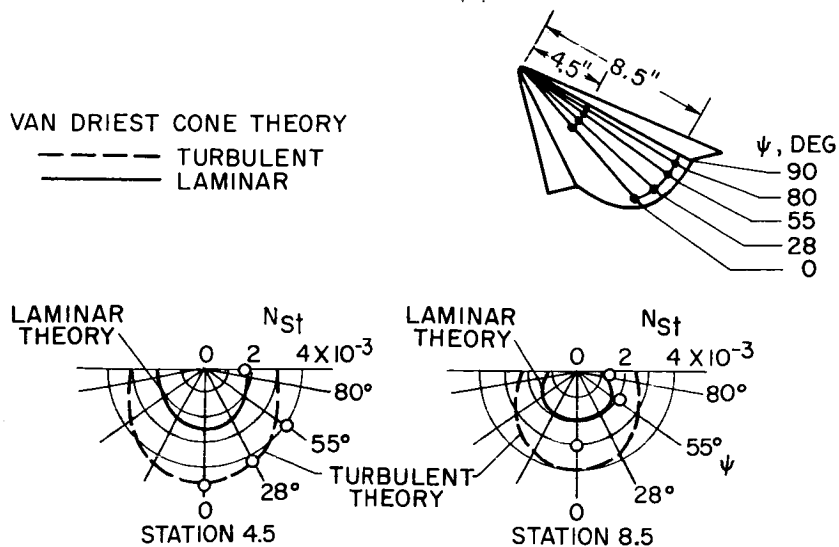


Figure 12

# OPTIMIZATION THEORY FOR TIME-VARIANT MISSILE SYSTEMS

## AND NONSTATIONARY INPUTS

By Elwood C. Stewart and Gerald L. Smith

Ames Aeronautical Laboratory

## INTRODUCTION

The design of automatic control systems is often based on the response to standard inputs such as a step or ramp. However, the actual inputs to most systems can only be described statistically. For example, the problem of target interception must be treated statistically for two reasons: (1) Target motions can only be described statistically, since quite obviously the target may maneuver in many possible ways, and (2) in most systems information about the target is obscured by unwanted signals called noise, which are also statistical in nature. Consequently, it is necessary to base design of guidance systems on statistical concepts.

Three previous papers (refs. 1 to 3) have dealt with the design of guidance systems from the viewpoint of statistical filter theory, specifically the Wiener filter theory and certain of its modifications. Two main assumptions which are generally made in this and similar work are: (1) the systems are time-invariant and (2) the inputs can be represented by stationary random time series. Although certain problems can be described without violating these assumptions, others cannot. Therefore, the purpose of this paper is to discuss how the theory can be extended so that these assumptions need not be made.

## TIME-VARIANT MISSILE SYSTEMS

The first assumption to be considered is that the guidance system be non-time-varying. There are many classes of guidance systems which must be considered as essentially time-varying because of their mode of operation. For example, in figure 1 is shown a homing missile attacking a target. Guidance of this missile is accomplished by employing line-of-sight information which therefore involves range. Since the range changes continuously during an attack, the equations describing this problem are necessarily time-varying. In contrast, a beam-rider-type

27

guidance system, also shown in figure 1, is non-time-varying because range is not normally transmitted to the missile, and therefore the missile merely flies down the beam. The time-varying problem shown in figure 1 is a general one, typical of many guidance problems. Later, however, in order to be specific, the discussion will be confined to examples of a short-range, air-to-air homing missile attacking a large bomber.

Such problems as the time-varying one illustrated in figure 1 can be described in terms of time-varying differential equations or, as is completely equivalent, in terms of the block diagram shown in figure 2. The essential feature of this diagram is the box shown as $1/R(t)$ which represents the time-varying nature of the problem. The problem to be solved can be stated simply as follows: Given the time-varying range, the statistical properties of the target motion, and the noise, find the optimum control system which will minimize the error $\epsilon$ at the interception time $T$ and yet not exceed the available control-motion capabilities of the missile at any time $t_2$ during the flight. Mathematically, such problems are handled by minimizing the error with a restriction on control motion as indicated by the following expression:

$$\overline{\epsilon^2(T)} + \lambda\ \overline{\delta^2(t_2)}$$

where $T$ is time of interception, $t_2$ is any time during flight, and $\lambda$ is the Lagrangian multiplier. From physical reasoning, the restriction on control motion should be constant at the maximum permissible value throughout the entire flight.

There are four distinct steps involved in the solution of the problem as stated. The _first_ step is to convert the solution of differential equations in the real time domain to a new kind of time called adjoint time. It is known that for time-varying systems the mean-square-ensemble average of the error is given by the following equation:

$$\overline{\epsilon^2(t_2)} = \int_{-\infty}^{t_2} h^2(t_2, t_1)dt_1 \tag{1}$$

where $h$ represents the error response at time $t_2$ due to an impulse introduced at time $t_1$. (See fig. 3.) For example, if an impulse is introduced into the system at time $t_1'$, the error response shown would be obtained. The value of $h$ for this case is indicated in figure 3. If the impulse were introduced at another time $t_1''$ as shown, a different

response would be obtained, and so forth. Note that these responses are plotted as a function of time $t$ for a fixed time $t_1$. However, in equation (1) it is necessary to have $h$ as a function of $t_1$ for a fixed $t$ since the integration is with respect to $t_1$. Such a response could be obtained by cross-plotting the curves given, and the result would appear as given at the bottom of figure 3. However, this procedure is not only unwieldy, but it is simply not adapted to the synthesis problem.

The basic trouble in this approach is that too much information is contained in the solution of the differential equations, that is, the response at all times $t$, whereas only the response at a very particular time $t_2$ is of interest. This extraneous information can be discarded by transforming the real-time differential equations to what is known as adjoint differential equations. Such a transformation is related to the principles of reciprocity which are familiar in many other fields such as aerodynamic flow, mechanics, and circuit theory. It will suffice here to point out that, physically, the transformation amounts to interchanging the inputs and outputs positionwise, and also timewise by running time backwards, starting from the end of flight and proceeding backwards to the beginning of flight. The end result of the transformation is that the solution of the adjoint differential equations or the error output of the adjoint block diagram gives the desired response $h$ as a function of $t_1$.

By following such a line of attack, the differential equations or the block diagram in figure 2 can be converted to the corresponding adjoint equations or diagram. Although these representations are not shown, the analysis would be concerned with the adjoints of the guidance system and control system rather than the systems themselves. The second step in the solution now is to utilize the adjoint equations or block diagram to write expressions for both the error and the control motion in terms of the adjoint of the unknown control system. From the expression $\overline{\epsilon^2(T)} + \lambda \overline{\delta^2(t_2)}$, the following adjoint differential equations which give the desired response $h$ can be written:

For miss distance:

$$\overline{\epsilon^2(T)} = \int_0^\infty \left( \left[ \int_0^\infty h(\tau-x)h_N(x)dx \right]^2 + \left\{ \int_0^\infty \left[ u_0(\tau-x) - h(\tau-x) \right] h_T(x)dx \right\}^2 \right) d\tau \qquad (2a)$$

$$h(\tau) = \frac{1}{\tau} \iint k_a c(\tau) d\tau \, d\tau - \frac{1}{\tau} \int_0^\tau h(\xi) \iint k_a c(\tau,\xi) d\tau \, d\tau \, d\xi \qquad (2b)$$

For control-motion requirements:

$$\overline{\delta^2(t_2)} = \int_0^\infty \left( \left[ \int_0^\infty g(\tau-x,\tau_1)h_N(x)dx \right]^2 + \left\{ \int_0^\infty \left[ u_0(\tau-x-\tau_1) - g(\tau-x,\tau_1) \right] h_T(x)dx \right\}^2 \right) d\tau \qquad (3a)$$

$$g(\tau,\tau_1) = \frac{c(\tau,\tau_1)}{\tau} - \frac{1}{\tau} \int_0^\tau g(\xi,\tau_1) \iint k_a c(\tau,\xi)d\tau \, d\tau \, d\xi \qquad (3b)$$

Although it will not be necessary to understand all of the details of these equations there are certain points of interest. It can be seen that there are two equations describing the miss distance and two equations describing the control motion. The first miss-distance equation (eq. (2a)) is due to noise and the second is due to the target motion. The only unknown in equation (2a) is the impulse response h which represents the adjoint of the guidance system. The second equation (eq. (2b)) is an integral equation with two unknowns h and c, where c represents the impulse response of the adjoint of the control system. These miss-distance equations suffice to relate miss distance to the unknown control system c by means of the intermediate parameter h. An examination of the two control-motion equations reveals a similar

situation. Consequently, the quantity to be minimized $\overline{\epsilon^2(T)} + \lambda \overline{\delta^2(t_2)}$ is expressed in terms of the unknown control system by means of the four equations given.

Now, the problem is one of finding the optimum control system which will minimize the quantity $\overline{\epsilon^2(T)} + \lambda \overline{\delta^2(t_2)}$. Unfortunately, these equations have not been solved. As a consequence, some approximate solution has been sought. A clue to such a solution can be found when the control-motion restriction is eliminated by allowing the missile to have unlimited acceleration capability. In this case $\lambda = 0$, and the equations can be solved for the minimum theoretical miss distance. For illustration, the solution for a typical air-to-air homing-missile situation is given in figure 4 by the dashed curve where the minimum miss distance is plotted against one of the important parameters, the magnitude of the noise spectral density. The important clue is that this curve is identical with that which is obtained for a constant-coefficient guidance system as indicated by the solid curve. This result for no restrictions suggests that even with a restriction on control motion, the performance of both systems would be the same. There are many compelling arguments to support this view. For example, when both problems are defined in terms of a similar coordinate system, it can readily be seen that both systems are attempting to solve the same problem. That is, both missiles are attempting to fly the same constant-true-bearing course, although neither

one can quite succeed in doing so. Furthermore, both systems have a missile with the same acceleration capability, and both systems have available the same input information. After the answer is obtained, a back check would verify that the approximation is a good one.

It is interesting to compare these results with the performance which would be obtained by disregarding noise theory in the design. As an example, the upper curve in figure 4 shows the noise performance of a system optimized for a target motion with no noise present. A comparison of this curve with the curves with restrictions and without restrictions shows that a significant reduction in miss distance should be possible.

The third step in the solution is to synthesize the guidance system to achieve the desired miss-distance performance indicated in figure 4. From the first miss-distance equation (eq. (2a)), it can be seen that only the impulse response  h  need be the same as for the equivalent constant-coefficient guidance system. Then, from the second miss-distance equation (eq. (2b)), it can be seen that the desired  h  can be achieved by solving this integral equation for the control-system adjoint  c. However, there is another difficulty here, and it appears to be in the manner of representing the control system by a single impulse response. Systems which are physically very simple often have impulse responses which are quite complicated. Consequently, it has been necessary to find another representation.

A more suitable representation for the control system is shown in figure 5, where the control system has been broken up into three parts: a time-varying multiplying part, and two non-time-varying parts representing the radar and the servo system. This representation not only makes the system easy to construct, but it is exactly the formulation which is needed in order to synthesize an optimum control system. An equation quite similar to the second miss-distance equation can now be derived - one that relates  h  not to  c, but to the components of the control system as it has been broken up in figure 5. This equation is

$$h(\tau) = \frac{1}{\tau}\mathcal{L}^{-1}\left\{Y_2(s)\mathcal{L}\left[f(\tau)\mathcal{L}^{-1}\left(\frac{k_aY_1(s)}{s^2}\right)\right]\right\} - \frac{1}{\tau}\mathcal{L}^{-1}\left\{Y_2(s)\mathcal{L}\left[f(\tau)\int_0^\tau h(\tau-x)\iint k_aY_1(x)dx \; dx \; dy\right]\right\} \quad (4)$$

For certain time-varying functions  $f(\tau)$, this equation can be solved for the optimum control system. Thus, the desired miss-distance performance which is given in figure 6 can be achieved. Actually, there are a great many control systems which satisfy equation (4), and so a whole class of systems is generated all of which have that miss-distance performance.

The <u>fourth</u> and last step is to satisfy the desired control-motion restriction which has been temporarily ignored. This can be done as follows: Of all the homing systems which satisfy the miss-distance performance in figure 6, it is clear that each system will have different control-motion requirements throughout flight. Thus, from this whole class of systems, the one or more having the desired restriction can be chosen. If a system with uniform control requirements is chosen, the level of control motion, of course, is identical with that for the constant-coefficient guidance system.

As an example, the method just given can be illustrated by showing the performance of a couple of very simple homing systems. For the first system, take f(t) to be a constant, which means that the control system is constant-coefficient; for the second, take a time-varying control system in which f(t) equals range, that is, a range-multiplication-type control. On solving the necessary equations it is found that the first control system turns out to be proportional navigation. Furthermore, for both systems the form of required radar is such that under static or very low-frequency operation, the radar would measure rate of rotation of the line of sight. This result is very gratifying because it is precisely this quantity which all radars do measure.

It is clear that the miss-distance performance of both these systems is the same and is given by the dashed curve in figure 6, provided that the allowable or desired control restriction is not exceeded. As seen in figure 7, however, the control-motion requirements are quite different. For the proportional-navigation control system, it is seen that in close to the target, the demands on the missile considerably exceed its capabilities, as indicated by the design value. Consequently, limiting would occur, and the miss-distance curve in figure 6 would tend to move up, the exact amount of increase depending on the specific situation. On the other hand, the demands on the range-multiplication control system are essentially uniform. Note that the level is virtually identical with that for the constant-coefficient guidance systems indicated by the dashed curve. It is clear also that since the level of required control is the same as the design value, no limiting would occur, and the desired miss-distance performance indicated in figure 6 would be obtained. Thus, an approximate solution to the optimization problem has been achieved.

## NONSTATIONARY INPUTS

Consider now the other assumption generally made in filter theory - the assumption of stationarity. There are principally two ways in which the inputs may not be stationary, and the Wiener theory can be extended to apply to these cases.

The first case is illustrated in figure 8 by a target maneuver process which is stationary and which therefore must extend in both directions to infinity as indicated. However, a real target maneuver will have a finite beginning and a finite end. For this reason the process is certainly nonstationary, although it might be classified as "stationary within a certain interval." The usefulness of the stationary theory in such cases might be questioned; however, it can readily be shown that it is. The reason is that if the impulse response time of the missile guidance system is shorter than the flight time of the missile, maneuvers which occur before the beginning of the flight have no effect on the miss at the interception time. Fortunately, in the interception problem practically all situations fall into this category. Thus, although all real missile problems are nonstationary according to the strict mathematical definition of the term, in practice such problems can be handled with the stationary theory.

The second case of interest is one in which the input process is nonstationary even within the interval of interest, that is, the flight time of the missile. An interesting example of such an input is a step of target acceleration as indicated in the following sketch, where the beginning of the step is equally likely to occur anywhere within the flight interval 0 to T:



TARGET
ACCELERATION

Wiener's theory can be extended to this and similar nonstationary processes. This extension can be accomplished by utilizing the adjoint theory discussed previously to write an expression for the mean-square-ensemble miss distance. By making certain simplifications, the following expression for the nonstationary input can be derived:

$$\overline{\epsilon_T^2(T)} = \int_{-\infty}^{\infty} \left|1 - Y(\omega)\right|^2 \left(\frac{a^2}{2\pi T\omega^6}\right) d\omega$$

The $Y(\omega)$ refers to the guidance-system transfer function, and the factor in parentheses will always be related to the nonstationary input. In this case it refers to the step maneuver. The corresponding expression for a stationary process is

$$\overline{\epsilon_T^2(T)} = \int_{-\infty}^{\infty} \left| 1 - Y(\omega) \right|^2 \Phi(\omega) d\omega$$

From comparison of these two expressions, it is apparent that the factor in parentheses for the nonstationary process behaves exactly as does the spectral density $\Phi(\omega)$ for the stationary process. Thus this factor may be used in the Wiener theory to derive minimum miss distances and optimum transfer functions even though the process is distinctly nonstationary.

## CONCLUDING REMARKS

It is important to emphasize that optimization theory does not eliminate all problems in the design of guidance systems. There may be so many factors involved in the design of a particular system that application of the theory to all of them would be very difficult. Nevertheless, it is clear that filter theory must be enlarged in scope to encompass more and more such factors. In this paper two very important factors have been considered - time-varying systems and nonstationary inputs. Although emphasis has been on the short-range homing-missile problem, it is clear that many other important problems can be cast in a similar form - the fire-control problem, for example. In fact, all systems utilizing active radars would have a similar problem. Finally, on a broader scale it can be seen that in the filter-theory field and in many other diverse fields such as rocket staging, trajectory optimization, and so forth, the problems are strikingly similar.

## REFERENCES

1. Stewart, Elwood C.: Application of Statistical Theory to Beam-Rider Guidance in the Presence of Noise. I - Wiener Filter Theory. NACA RM A55E11, 1955.

2. Stewart, Elwood C.: Application of Statistical Theory to Beam-Rider Guidance in the Presence of Noise. II - Modified Wiener Filter Theory. NACA RM A55E11a, 1955.

3. Stewart, Elwood C., Druding, Frank, and Nishiura, Togo: The Effects of Target and Missile Characteristics on Theoretical Minimum Miss Distance for a Beam-Rider Guidance System in the Presence of Noise. NACA RM A57F26, 1958.

## TWO CLASSES OF MISSILE SYSTEMS

RADAR BEAM ₵

CONSTANT-COEFFICIENT
BEAM-RIDER MISSILE SYSTEM

TIME-VARYING HOMING—
MISSILE SYSTEM

Figure 1

## HOMING–MISSILE GUIDANCE SYSTEM

NOISE

TARGET
POSITION

ERROR $\epsilon$

$\dfrac{1}{R(t)}$

CONTROL
COMMAND SYSTEM

MISSILE
POSITION

AERODYNAMICS

CONTROL MOTION $\delta$
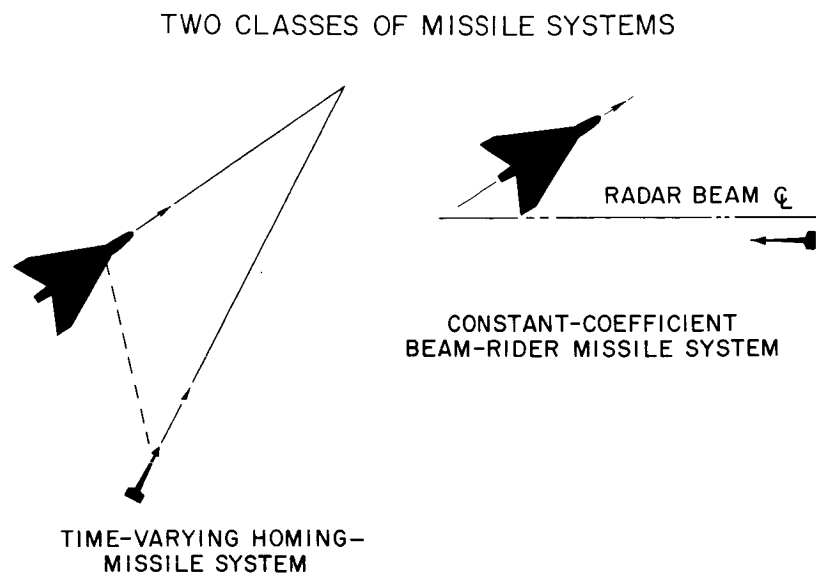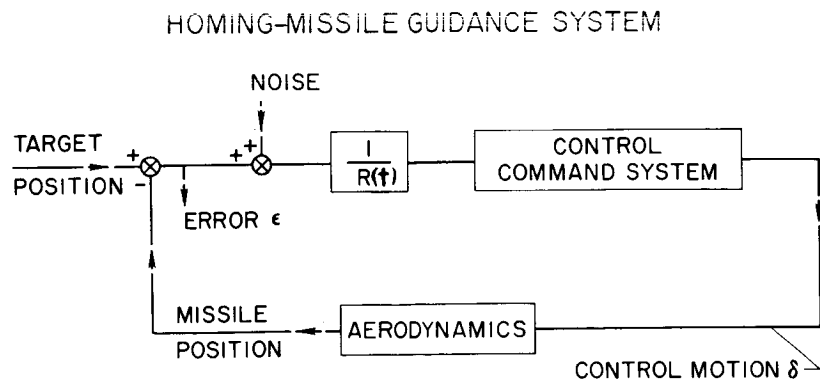
MINIMIZE: $\overline{\epsilon^2(T)} + \lambda \, \overline{\delta^2(t_2)}$

WHERE: T = INTERCEPTION TIME
$t_2$ = ANY TIME DURING FLIGHT
$\lambda$ = LAGRANGIAN MULTIPLIER

Figure 2

## EVALUATION OF MISS DISTANCE

$$\overline{\epsilon^2(t_2)} = \int_{-\infty}^{t_2} h^2(t_2, t_1)\, dt_1$$
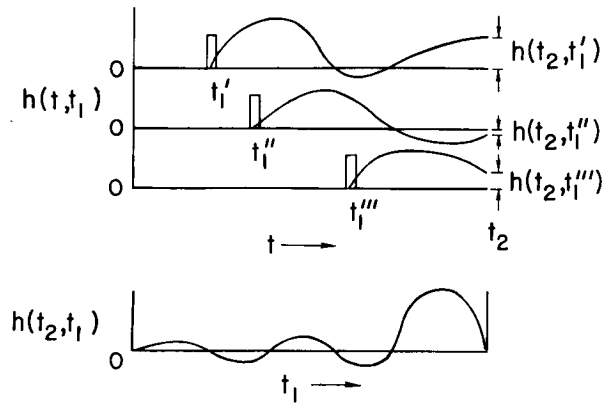


Figure 3

## MINIMUM MISS–DISTANCE PERFORMANCE
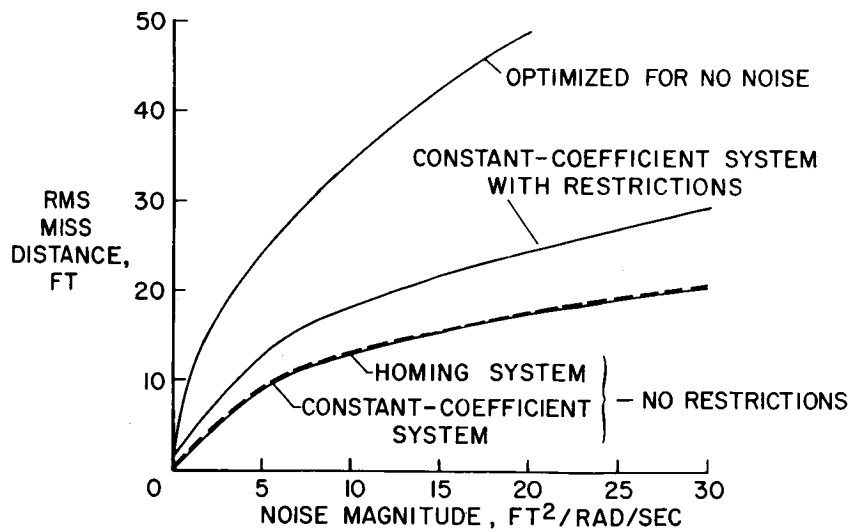


Figure 4

HOMING-MISSILE GUIDANCE SYSTEM
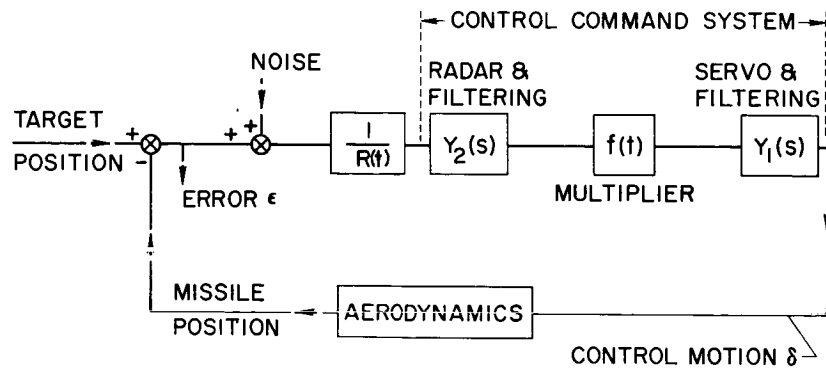
Figure 5

MINIMUM MISS DISTANCE WITH CONTROL RESTRICTIONS
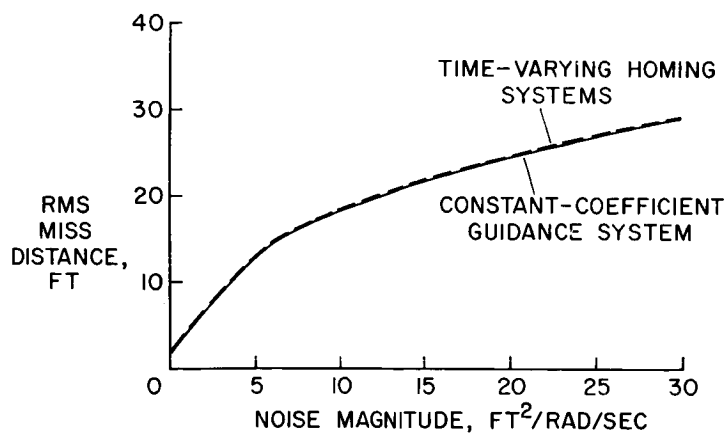
Figure 6

CONTROL-MOTION REQUIREMENTS FOR HOMING SYSTEMS
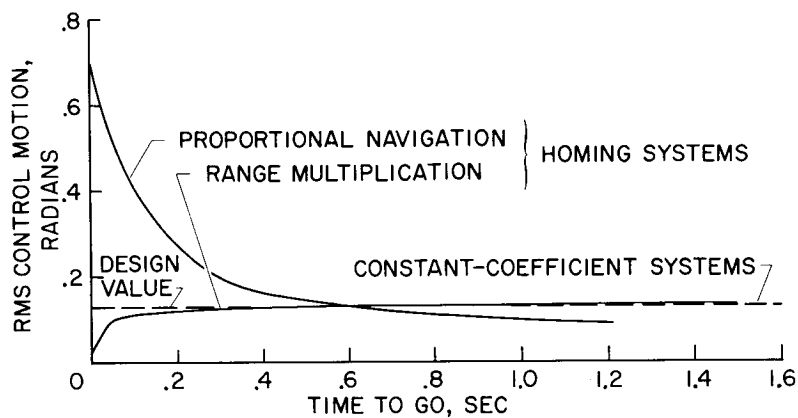


Figure 7

EFFECT OF MANEUVER ON MISS DISTANCE
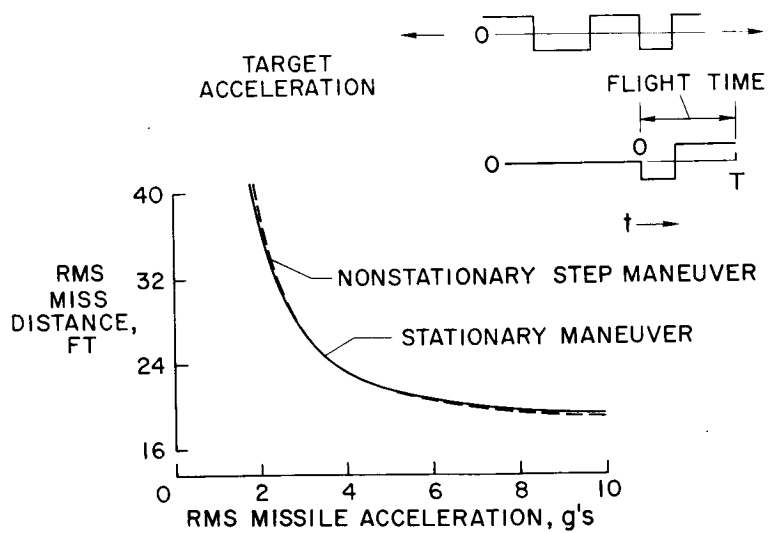


Figure 8

RESEARCH ON THE ROTARY DERIVATIVES

By Benjamin H. Beam, Henry C. Lessing,
and Bruce E. Tinling

Ames Aeronautical Laboratory

## INTRODUCTION

Analysis of the dynamic motions of vehicles designed to fly within the atmosphere depends upon a knowledge of the aerodynamic stability derivatives. The stability derivatives which depend on the rate of rotation of the aircraft about its center of gravity, commonly called the rotary derivatives, have an important influence on the divergence or subsidence of oscillatory motions. It is difficult to generalize as to the importance of aerodynamic rotary derivatives in the overall suitability and flying qualities of an aircraft. Much depends on the type of aircraft under discussion and on whether deficient aerodynamic damping can be supplemented by some other means. There is general agreement, however, that knowledge of the rotary derivatives is a necessary starting point in most cases and certainly desirable in all cases.

On reviewing the literature on the subject of rotary derivatives at supersonic speeds, it is impressive to note the number of theoretical reports that were written from 5 to 10 years ago. The state of development of the theory, at least for idealized configurations in linearized supersonic flow, is well advanced. References to experimental studies of the derivatives are encountered much less frequently. The tests are difficult and the data necessary for an appraisal of the theory are accumulated much more slowly. The data on the rotary derivatives presented in this paper were gleaned from the results of oscillation tests conducted on a number of specific airplane configurations in several of the Ames Aeronautical Laboratory wind tunnels over the past few years. A description of this method of testing with a discussion of its advantages and limitations may be found in reference 1. The primary aim of the present paper is to correlate theory and experiment in such a way as to bring out important features which are well defined and which have wide application.

## SYMBOLS

Forces, moments, and deflections are referred to a body system of axes defined in figure 1.

A        aspect ratio, $b^2/S$

a        lift-curve slope of a lifting surface in undisturbed flow referred to its plan-form area

b        wing span

$C_l$        rolling-moment coefficient, $\dfrac{\text{Rolling moment}}{\frac{1}{2}\rho V^2 Sb}$

$$C_{l_p} = \frac{\partial C_l}{\partial(pb/2V)}$$

$$C_{l_r} = \frac{\partial C_l}{\partial(rb/2V)}$$

$$C_{l_\beta} = \frac{\partial C_l}{\partial\beta}$$

$$C_{l_{\dot\beta}} = \frac{\partial C_l}{\partial(\dot\beta b/2V)}$$

$C_m$        pitching-moment coefficient, $\dfrac{\text{Pitching moment}}{\frac{1}{2}\rho V^2 S\bar c}$

$$C_{m_\alpha} = \frac{\partial C_m}{\partial\alpha}$$

$$C_{m_{\dot\alpha}} = \frac{\partial C_m}{\partial(\dot\alpha\bar c/2V)}$$

$$C_{m_{i_H}} = \frac{\partial C_m}{\partial i_H}$$

$$C_{m_q} = \frac{\partial C_m}{\partial(q\bar c/2V)}$$

$C_N$     normal-force coefficient, $\dfrac{\text{Normal force}}{\frac{1}{2}\rho V^2 S}$

$C_{N_\alpha} = \dfrac{\partial C_N}{\partial \alpha}$

$C_n$     yawing-moment coefficient, $\dfrac{\text{Yawing moment}}{\frac{1}{2}\rho V^2 S b}$

$C_{n_p} = \dfrac{\partial C_n}{\partial (pb/2V)}$

$C_{n_r} = \dfrac{\partial C_n}{\partial (rb/2V)}$

$C_{n_\beta} = \dfrac{\partial C_n}{\partial \beta}$

$C_{n_{\dot\beta}} = \dfrac{\partial C_n}{\partial (\dot\beta b/2V)}$

$\bar{c}$     wing mean aerodynamic chord

$G\left(\dfrac{\tan \delta}{\tan \mu}\right)$     function defined in reference 14

$i_H$     incidence angle of horizontal tail

$l$     projection on longitudinal axis of distance of center of
lift of tail behind moment reference

M     Mach number

p     rolling velocity

q     pitching velocity

r     yawing velocity

S     wing plan-form area; other areas are indicated by subscripts
on   S

V     velocity

X,Y,Z     coordinate axes

$X_b$     projection on longitudinal axis of distance of base of fuse-
lage behind moment reference

$\alpha$     angle of attack, radians except where noted

$\beta$     angle of sideslip, radians except where noted

$\delta$     semiapex angle of wing

$\epsilon$     angle of downwash

$\eta$     tail efficiency factor

$\lambda$     taper ratio

$\mu$     Mach angle

$\rho$     mass density

$\sigma$     angle of sidewash

Subscripts:

a.c.     referred to aerodynamic center of wing

b     fuselage base

F     fuselage

H     horizontal tail

V     vertical tail

W     wing

A dot over a symbol indicates the first derivative with respect to time.

## DISCUSSION

### Damping in Pitch and Yaw of Bodies of Revolution

The starting point in the analysis of the rotary derivatives of elongated bodies of revolution is the "slender body" theory (ref. 2). The method has been generalized and extended to compressible flows

(e.g., refs. 3, 4, and 5). Results of these analyses indicate that the damping in pitch or yaw of pointed bodies depends only on the area of the base and the distance from the base to the pitching or yawing axis of the body. Similar analyses using unsteady source-sink potentials for compressible flows (ref. 6) result in the same expressions for the damping in pitch of slender bodies of revolution at low angles of attack performing oscillations in which the wave length is long compared with the body length.

The equation is

$$\left(C_{m_q} + C_{m_{\dot{\alpha}}}\right)_F = \frac{\bar{c}^2}{b^2}\left(C_{n_r} - C_{n_{\dot{\beta}}}\right)_F = -\frac{4S_b X_b^2}{S\bar{c}^2} \tag{1}$$

Equation (1) provides a basis for comparing the results of a number of tests on different fuselage configurations over a wide range of Mach numbers. The slender-body-theory damping from equation (1) is represented by a value of unity in figure 2. The experimental points, representing the ratio of measured damping to that estimated from equation (1), were obtained from a number of recent tests of different fuselage arrangements. The fuselage configurations were not strictly bodies of revolution and included canopies, side fairings along the fuselage, and in some cases wing surfaces where the contribution of these surfaces was estimated to be negligible. The motions included both pitching and yawing. The scatter in the data is largely that between different fuselage configurations or between yawing and pitching modes with the same fuselage.

It is immediately obvious from a study of the damping-in-pitch and damping-in-yaw data in figure 2 that the slender-body theory underestimates the measured damping by a considerable margin at supersonic speeds. At subsonic speeds the theoretical and measured values of damping are in better agreement. At Mach numbers between 2 and 3, however, the measured damping increases to two or three times the estimated value.

An explanation for these differences is found in a study of the limitations of the theory in predicting the force characteristics of elongated bodies at very small angles of attack. Some data on the slope of the normal-force curve with angle of attack for these conditions are shown in the lower part of figure 2. Here again the slender-body theory has been used as a basis of comparison and is represented by a value of unity in the figure. The experimental data were obtained from references 7 and 8 and apply to bodies of revolution having ogival noses and cylindrical afterbodies. The fineness ratio of the afterbodies is 6. The effects of viscosity on the normal forces which may become significant at higher angles of attack (ref. 9)

are negligible for the data presented in figure 2. These data then indicate the differences which can be expected in estimating the normal-force characteristics of bodies of revolution by the slender-body theory. The differences are not so great as they are for damping in pitch but are in the same direction and have the same trend with Mach number. Syvertson and Dennis, reference 8, have obtained extremely good agreement with experiment by accounting for the differences in normal force at small angles of attack on the basis of second-order effects. It can be presumed that these second-order effects also account for the differences noted in the damping-in-pitch data. Second-order calculations for damping in pitch and damping in yaw have not as yet been made.

At speeds beyond the range of the present data, it is expected that the damping would gradually approach the values given by the Newtonian impact theory. This probable trend has been indicated by the dashed line at the top of figure 2.

### Damping in Pitch of Horizontal Tail

The contribution of a horizontal tail to damping in pitch has always been significant. In fact, in the past for subsonic speeds it has generally been found that a reasonably good estimate of total airplane damping in pitch could be made by merely increasing the estimated tail contribution by an arbitrary factor of about 25 percent to account for the contribution of the other parts of the airplane. One instructive way of approaching the damping contribution of a horizontal tail is to consider first the tail contribution to static stability (ref. 10), which can be expressed in terms of tail length, tail normal-force-curve slope, tail efficiency, and the downwash at the tail as

$$\left(C_{m_\alpha}\right)_H = -\left(\frac{l_H}{\bar{c}_H}\right) a_H \frac{S_H}{S} \eta_H \left(1 - \frac{d\epsilon}{d\alpha}\right) \tag{2}$$

By following a line of reasoning analogous to that used in expressing the static stability, it can be shown that the dynamic stability derivative becomes

$$\left(C_{m_q} + C_{m_{\dot\alpha}}\right)_H = -2\left(\frac{l_H}{\bar{c}}\right)^2 a_H \frac{S_H}{S} \eta_H \left(1 + \frac{d\epsilon}{d\alpha}\right) \tag{3}$$

The two equations have a strong similarity. In fact, they contain the same terms but are arranged in different ways. The tail-length term is

squared in the equation for damping so that its sign is always positive, which implies that both canard and conventional tails will have similar damping characteristics.

Another significant point is illustrated in figure 3. In this figure is presented the contribution of a horizontal tail to the static stability and damping in pitch of an unswept-wing interceptor-type airplane having a high horizontal tail. This configuration is interesting because of the impingement on the horizontal tail of the shock and expansion field from the wing, as shown in the sketch, in the range of Mach numbers from 1.5 to 3.5.

The experimental values of horizontal-tail contribution are the differences in static stability and damping with the tail on and off. The theoretical values were calculated from equations (2) and (3). It can be shown from linearized-supersonic-flow theory that where the tail is outside the field enclosed by the Mach lines from the leading and trailing edges of the wing the downwash term $d\epsilon/d\alpha$ will be zero. Where the tail is completely inside Mach lines from the wing leading and trailing edges $d\epsilon/d\alpha$ should be 1.0. In between these two extremes intermediate values of $d\epsilon/d\alpha$ should apply.

At a Mach number of approximately 1.5 the leading edge of the horizontal tail is just behind the Mach wave from the wing trailing edge. The downwash here should be near zero and, as shown in figure 3, the static stability $\left(C_{m_\alpha}\right)_H$ is near the theoretical value for zero downwash. According to theory $\left(C_{m_\alpha}\right)_H$ and $C_{m_{i_H}}$ should also be equal for zero downwash, and, as shown in figure 3, the theoretical value for $d\epsilon/d\alpha = 0$, if $\eta_H$ is assumed to be 0.90, is very near the experimental values of $C_{m_{i_H}}$. Further increases in Mach number bring the tail inside the expansion field from the wing and, as indicated by equations (2) and (3), result in decreased static stability and decreased dynamic stability in accordance with the increased values of $d\epsilon/d\alpha$. At a Mach number of approximately 3.5 the horizontal tail emerges ahead of the wing flow field, and it is seen that the experimental values of the tail contribution at this Mach number correspond quite closely with those obtained for zero downwash.

Values of $d\epsilon/d\alpha$ calculated from the differences between theory and experiment for $\left(C_{m_\alpha}\right)_H$ can be used to obtain the second theoretical curve for damping in pitch in figure 3, which corresponds reasonably well with the experimental data. For Mach numbers between 1 and 1.5 the agreement between theory and experiment is rather poor. Part of the

discrepancy is clearly caused by secondary effects, such as impingement of shock waves from the tail on the fuselage, which would exist between Mach numbers of about 1 to 1.2. At subsonic speeds the theoretical values again agree with experiment (ref. 11).

### Damping in Yaw of a Vertical Tail

The contribution of a vertical tail to the damping in yaw is estimated by a procedure exactly analogous to that for damping in pitch of a horizontal tail, and it is therefore of interest to consider the vertical tail at this point. The equations for static directional stability and damping in yaw, by following the same reasoning employed in obtaining equations (2) and (3) and also assuming $\cos \alpha = 1$, became

$$\left(C_{n_\beta}\right)_V = -\frac{l_V}{b_W} a_V \frac{S_V}{S} \eta_V \left(1 + \frac{d\sigma}{d\beta}\right) \tag{4}$$

$$\left(C_{n_r} - C_{n_{\dot\beta}}\right)_V = 2\left(\frac{l_V}{b_W}\right)^2 a_V \frac{S_V}{S} \eta_V \left(1 - \frac{d\sigma}{d\beta}\right) \tag{5}$$

The rate of change of sidewash angle with sideslip angle $d\sigma/d\beta$ enters into these equations in the same way that the downwash parameter $d\epsilon/d\alpha$ enters into equations (2) and (3). The sidewash at the vertical tail is primarily due to the presence of the fuselage. Various investigators (refs. 12 and 13) exploring the effects of the presence of a lifting fuselage ahead of the vertical tail have shown that a pair of vortices shed by the fuselage results in sidewash at the vertical tail which is unfavorable to static stability. This sidewash effect becomes, in general, more adverse with increasing angle of attack. The vortex position at a transverse cross section through the vertical tail is illustrated in figure 4. The effect of these vortices on the variation of the experimental tail contribution to $\left(C_{n_\beta}\right)_V$ with angle of attack, also shown in figure 4, is as expected from the vortex distribution.

Theoretical values of $\left(C_{n_\beta}\right)_V$ and $\left(C_{n_r} - C_{n_{\dot\beta}} \cos \alpha\right)_V$ calculated from equations (4) and (5), assuming $d\sigma/d\beta = 0$ and $\eta_V = 1$, are also shown in figure 4. It is seen that these estimates are rather poor and that some consideration must be given to the sidewash to account for the variation in the derivatives with angle of attack.

The explanation for the poor agreement between theory for zero sidewash and experimental data for the static stability derivative $\left(C_{n_\beta}\right)_V$ has been considered elsewhere (refs. 12 and 13). It is therefore assumed that $\left(C_{n_\beta}\right)_V$ is known either from theoretical calculations or from experimental data. The point to be made here is the close relationship between the static directional stability and the damping in yaw with regard to the sidewash effects. The difference between the theoretical values of $\left(C_{n_\beta}\right)_V$ for $d\sigma/d\beta = 0$ and the experimental values can be taken as a measure of the sidewash term in equation (4). At each angle of attack these values of $d\sigma/d\beta$ can be used to revise the previously estimated value of $\left(C_{n_r} - C_{n_{\dot\beta}} \cos\alpha\right)_V$ for $d\sigma/d\beta = 0$. This process has been employed to obtain the additional theoretical curve for damping in yaw in figure 4 which is in reasonable agreement with the experimental values. Methods of considering sidewash which have been found applicable for steady flow at lower speeds are evidently applicable to dynamic phenomena at supersonic speeds.

Before leaving the subject of the tail surfaces there is one further point to be made that is illustrated in figure 5. At subsonic and transonic speeds the vertical-tail contribution to the damping in yaw is of major importance. For Mach numbers above 2, however, the increased damping contribution of the fuselage and the decreased tail effectiveness combine to reduce the importance of the vertical tail. As shown in figure 5, the contribution of the vertical tail at a Mach number of 3.5 is of secondary importance. At these Mach numbers the damping of the fuselage emerges as the most important item.

## Damping in Pitch of Wings

The direct contribution of the wing to damping in pitch is small for airplanes having horizontal tails and wings with small sweep. The indirect effect of the wing due to its downwash and sidewash acting on the tail surfaces has been considered previously in connection with the tail. In the case of the tailless airplane, however, the contribution of the wing to the total damping in pitch becomes important. In fact, for the notched-triangular-wing configuration shown in figure 6, the damping would be almost entirely due to the wing.

An abundance of theoretical work has been done on the contribution of plane wings to damping in pitch at supersonic speeds (refs. 14, 15, and 16, e.g.), and the comparisons between theory and experiment indicate reasonably good agreement (refs. 17 and 18). Application of previous theoretical results to the configuration shown in figure 6 is

made difficult because of the drooped wing tips and partial span sweep of the trailing edge. These factors are considered in the following manner. The expression for damping in pitch about the aerodynamic center of a triangular wing can be shown from reference 14 to be equivalent to

$$\left(C_{m_q} + C_{m_{\dot{\alpha}}}\right)_{a.c.} = -\frac{\pi}{4} \frac{b}{c} G\left(\frac{\tan \delta}{\tan \mu}\right) \tag{6}$$

The aerodynamic center was selected since the test data indicated that the model was very nearly statically balanced about the actual point of rotation. In the application of equation (6) to the notched-triangular-wing configuration shown in figure 6, the value of the mean aerodynamic chord $\bar{c}$ was that for the configuration shown. The drooped wing tips were considered by decreasing the span $b$. Values of $G$ as a function of $\tan \delta/\tan \mu$ were obtained from reference 14.. The results of this calculation are shown as the dashed line in figure 6. The correspondence between theory and experiment shown in figure 6 is reasonably good. However, this agreement may be somewhat fortuitous and more detailed theoretical calculations for the actual geometry and more corroborating experimental data would be desirable. The importance of figure 6 is that it illustrates a method of applying the extensive theoretical results of triangular- and arrow-wing configurations to plan forms that depart slightly from these idealized shapes.

## Rolling Derivatives

The rolling wing has been studied extensively by linearized-supersonic-flow theory and numerical results are available for a wide variety of plan forms having arbitrary sweep, taper, and tip rake. Many of these results are summarized in reference 19.

Some results comparing theoretical and experimental values of damping in roll are presented in figure 7. The theoretical values were obtained from the sources summarized in reference 19 and are shown as dashed lines in figure 6. Experimental data were obtained from oscillation tests on the three wing-fuselage combinations sketched in figure 7 and the results are shown as solid lines.

The agreement between theory and experiment is rather good for the unswept wing having a taper ratio of 0.4 and somewhat less satisfactory for the unswept wing with a taper ratio of 0.2. In determining the theoretical values, the effects of the fuselage on the damping in roll have been assumed to be negligible. Although ordinarily it would seem

that this assumption is justified, the extended side fairings along the fuselage of the model having a wing with a taper ratio of 0.2 may contribute some interference effects which would account for some of the differences shown between theory and experiment.

The data for the notched triangular wing shown in figure 7 require additional explanation. As indicated in the sketch, the tips of the wings of the test model, from about 65 percent of the span outboard, were drooped 45°. Analysis shows that (for a roll axis located below the plane of the wing) this droop reduces the pressures due to rolling velocity at the surface of the drooped section by the cosine of the droop angle, and the rolling moment about the longitudinal axis due to the surface pressures is also reduced by the cosine of the droop angle. For a droop angle of 45° the incremental rolling moments from the tip sections are reduced by 50 percent. Since much of the loading from a rolling wing is confined to the tip sections, it becomes obvious that wing-tip droop can have a powerful influence on the damping in roll.

These effects can be illustrated in the following manner: The theoretical curve for a plane notched triangular wing having the same developed span and plan-form area as the test model is indicated in figure 7 by the plane notched triangle. The theoretical curve for the notched triangular wing having drooped tips was obtained by first evaluating the damping in roll for a notched triangular wing having the same span and notch span as the projected plan form of the test model and, second, referring the damping-in-roll derivatives to the developed span and plan-form area of the test model. The agreement with the experimental data, which was also referred to developed span and plan-form area, is reasonably good.

The comparison of the two theoretical curves illustrates the powerful effects on damping in roll that seemingly innocuous geometrical changes can produce. In figure 8 a small sketch of the cross section of the notched-triangular-wing test model is shown. The inclination of the pressure force vectors at the drooped tips under rolling conditions is shown and it is seen that the component at the drooped wing tips which produces roll is reduced from that for the plane wing. It is also apparent that the vertical location of the center of gravity can be very important in determining damping in roll for wings having very low aspect ratio. If the vertical location of the center of gravity were above the wing plane, in approximately the position shown in the phantom view in the sketch, the damping in roll for a triangular wing with drooped tips would be greater than that for a plane triangular wing rather than less as in the data shown in figure 7.

Wing-tip droop can have powerful effects on other lateral-directional derivatives. Large side forces and yawing moments result from rolling

because the lateral component of the pressures at the drooped tips acts in the same direction for each tip, as indicated in the sketch in figure 8. The situation is thus quite different from that for the plane wing which, at $0°$ angle of attack, experiences no side force or yawing moments due to rolling. Experimental data for this configuration at a Mach number of 3.5 reveal that the magnitude of the yawing moment due to rolling $C_{n_p} + C_{n_{\dot{\beta}}} \sin \alpha$ can be larger than the damping in roll $C_{l_p} + C_{l_{\dot{\beta}}} \sin \alpha$, as shown in figure 8. It seems clear from these data that the most important influence on the yawing moment due to rolling is that due to the drooping of the wing tips. Although not presented in this paper, similar results would be expected and are apparent in the data for the rolling moment due to yawing derivative $C_{l_r} - C_{l_{\dot{\beta}}} \cos \alpha$ for this configuration.

## CONCLUDING REMARKS

The foregoing discussion of the results of recent research on the rotary derivatives is intended to place in better perspective some of the problems encountered in estimating these derivatives for current and future aircraft. It must be said frankly that the subjects were deliberately selected to emphasize certain points. Other aspects, even those for which appreciable experimental data are available, are not well enough understood at the present time to discuss with any clarity. In this category are the derivatives which depend on sideslip and sideslip velocity at higher angles of attack. Those who have studied the rolling moment due to sideslip derivative $C_{l_{\beta}}$ will recognize the important influence that viscous and interference effects can have on the sideslip derivatives, even to the point that the theoretically predicted trends are masked by these other effects. Some anomalous influences of the wing on the tail surfaces under rolling conditions have been noted. An understanding of these and other related problems depends on further investigation.

## REFERENCES

1. Beam, Benjamin H.: A Wind-Tunnel Test Technique for Measuring the Dynamic Rotary Stability Derivatives at Subsonic and Supersonic Speeds. NACA Rep. 1258, 1956. (Supersedes NACA TN 3347.)

2. Munk, Max M.: The Aerodynamic Forces on Airship Hulls. NACA Rep. 184, 1924.

3. Jones, Robert T.: Properties of Low-Aspect-Ratio Pointed Wings at Speeds Below and Above the Speed of Sound. NACA Rep. 835, 1946. (Supersedes NACA TN 1032.)

4. Sacks, Alvin H.: Aerodynamic Forces, Moments, and Stability Derivatives for Slender Bodies of General Cross Section. NACA TN 3283, 1954.

5. Bryson, Arthur E., Jr.: Stability Derivatives for a Slender Missile With Application to a Wing-Body-Vertical-Tail Configuration. Jour. Aero. Sci., vol. 20, no. 5, May 1953, pp. 297-308.

6. Dorrance, William H.: Nonsteady Supersonic Flow About Pointed Bodies of Revolution. Jour. Aero. Sci., vol. 18, no. 8, Aug. 1951, pp. 505-511, 542.

7. Grimminger, G., Williams, E. P., and Young, G. B. W.: Lift on Inclined Bodies of Revolution in Hypersonic Flow. Jour. Aero. Sci., vol. 17, no. 11, Nov. 1950, pp. 675-690.

8. Syvertson, Clarence A., and Dennis, David H.: A Second-Order Shock-Expansion Method Applicable to Bodies of Revolution Near Zero Lift. NACA TN 3527, 1956.

9. Allen, H. Julian, and Perkins, Edward W.: A Study of Effects of Viscosity on Flow Over Slender Inclined Bodies of Revolution. NACA Rep. 1048, 1951. (Supersedes NACA TN 2044.)

10. Perkins, Courtland D., and Hage, Robert E.: Airplane Performance - Stability and Control. John Wiley and Sons, Inc., 1949, p. 220.

11. Buell, Donald A., Reed, Verlin D., and Lopez, Armando E.: The Static and Dynamic-Rotary Stability Derivatives at Subsonic Speeds of an Airplane Model With an Unswept Wing and a High Horizontal Tail. NACA RM A56I04, 1956.

12. Spearman, M. Leroy, and Henderson, Arthur, Jr.: Some Effects of
    Aircraft Configuration on Static Longitudinal and Directional
    Stability Characteristics at Supersonic Mach Numbers Below 3.
    NACA RM L55L15a, 1956.

13. Nielsen, Jack N., and Kaattari, George E.: The Effects of Vortex
    and Shock-Expansion Fields on Pitch and Yaw Instabilities of
    Supersonic Airplanes. Preprint No. 743, S.M.F. Final Preprint,
    Inst. Aero. Sci., June 1957.

14. Ribner, Herbert S., and Malvestuto, Frank S., Jr.: Stability
    Derivatives of Triangular Wings at Supersonic Speeds. NACA
    Rep. 908, 1948. (Supersedes NACA TN 1572.)

15. Brown, Cinton E., and Adams, Mac C.: Damping in Pitch and Roll of
    Triangular Wings at Supersonic Speeds. NACA Rep. 892, 1948.
    (Supersedes NACA TN 1566.)

16. Malvestuto, Frank S., Jr., and Margolis, Kenneth: Theoretical
    Stability Derivatives of Thin Sweptback Wings Tapered to a Point
    With Sweptback or Sweptforward Trailing Edges for a Limited Range
    of Supersonic Speeds. NACA Rep. 971, 1950. (Supersedes NACA
    TN 1761.)

17. Henderson, Arthur, Jr.: Investigation at Mach Numbers of 1.62,
    1.93, and 2.41 of the Effect of Oscillation Amplitude on the
    Damping in Pitch of Delta-Wing - Body Combinations. NACA
    RM L53H25, 1953.

18. Tobak, Murray: Damping in Pitch of Low-Aspect-Ratio Wings at Sub-
    sonic and Supersonic Speeds. NACA RM A52L04a, 1953.

19. Jones, Arthur L., and Alksne, Alberta: A Summary of Lateral-
    Stability Derivatives Calculated for Wing Plan Forms in Super-
    sonic Flow. NACA Rep. 1052, 1951.

## BODY SYSTEM OF AXES
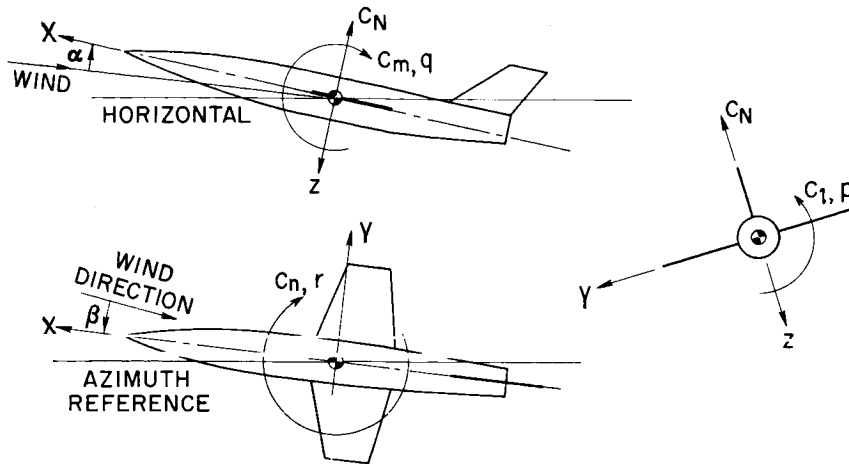


Figure 1

A COMPARISON OF EXPERIMENTAL DATA FOR SEVERAL
FUSELAGE ARRANGEMENTS WITH SLENDER-BODY
THEORY, $\alpha=0°$



○ OGIVE CYLINDER
□ PITCH DATA, BODY-WING
◇ PITCH DATA, BODY ALONE
△ YAW DATA, BODY-WING
◁ YAW DATA, BODY-WING
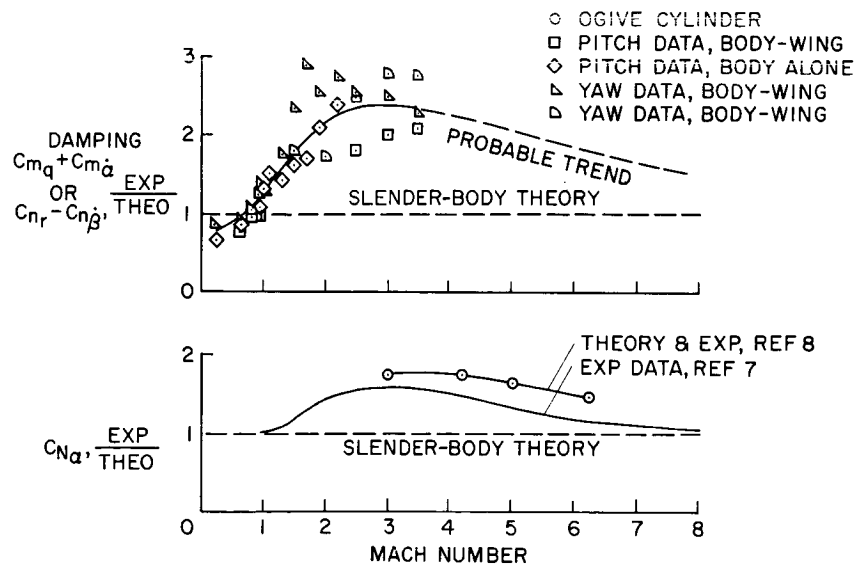
Figure 2

A COMPARISON OF EXPERIMENTAL DATA WITH THEORY FOR
THE CONTRIBUTION OF A HIGH HORIZONTAL TAIL BEHIND A
WING, $\alpha = 0°$

STATIC-LONGITUDINAL-STAB. DERIVATIVE

$C_{m_{i_H}}$ FROM EXPERIMENT

THEORY, $d\epsilon/d\alpha = 0$, $\eta_H = .9$

$(C_{m_\alpha})_H$

$-.024$
$-.016$
$-.008$
$0$

○ OSCILLATION DATA
□ STATIC-FORCE DATA

DAMPING-IN-PITCH DERIVATIVE

$(C_{m_q} + C_{m_{\dot\alpha}})_H$

$12$
$8$
$4$
$0$

THEORY, $d\epsilon/d\alpha$ INCLUDED

THEORY, $d\epsilon/d\alpha = 0$, $\eta_H = .9$

$0 \qquad 1 \qquad 2 \qquad 3$

M
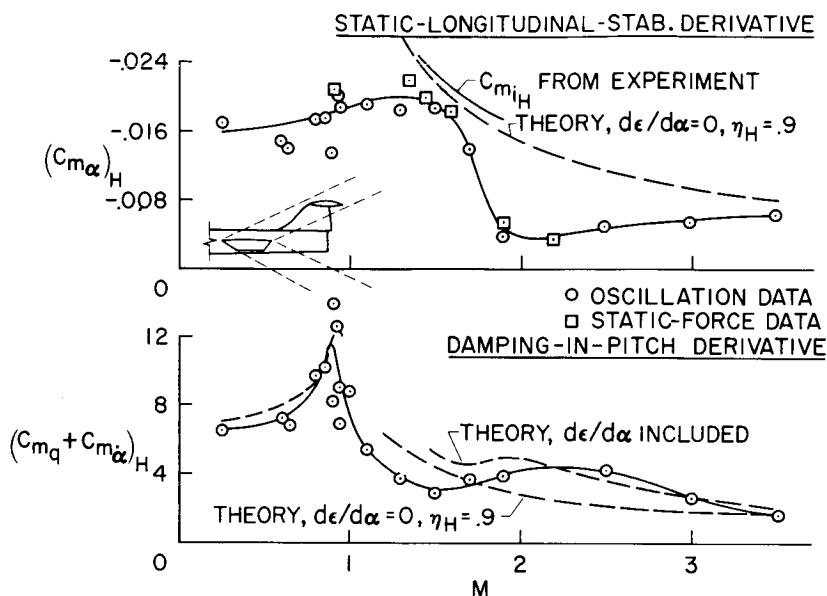
Figure 3

CONTRIBUTION OF VERTICAL TAIL TO THE
STATIC–DIRECTIONAL–STABILITY AND DAMPING–IN–
YAW DERIVATIVES

M = 3.0

THEORY, $\dfrac{d\sigma}{d\beta} = 0$, $\eta_V = 1$

$(C_{n_\beta})_V$

$.006$
$.004$
$.002$
$0$

THEORY, $\dfrac{d\sigma}{d\beta}$ INCLUDED

$(C_{n_r} - C_{n_{\dot\beta}} \cos \alpha)_V$

$-.6$
$-.4$
$-.2$
$0$

THEORY, $\dfrac{d\sigma}{d\beta} = 0$, $\eta_V = 1$

$-8 \quad -4 \quad 0 \quad 4 \quad 8 \quad 12 \quad 16$

$\alpha$, DEG
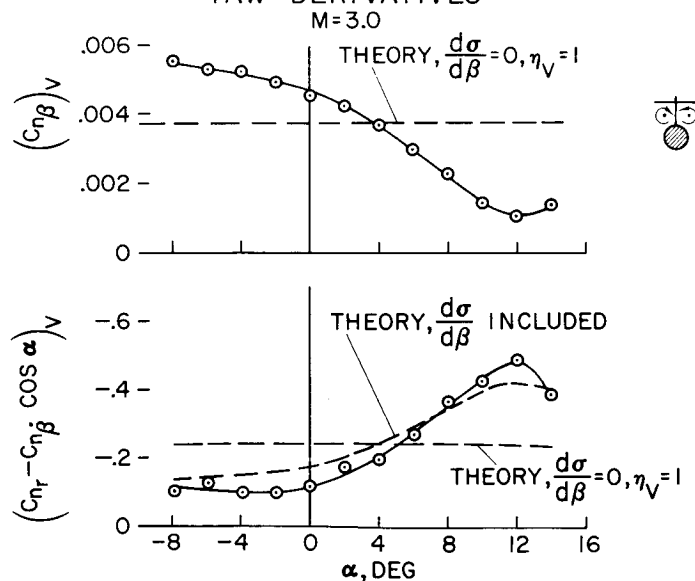
Figure 4

DAMPING IN YAW OF AIRPLANE MODEL
WITH AND WITHOUT VERTICAL TAIL



FLAGGED SYMBOLS — TAIL OFF
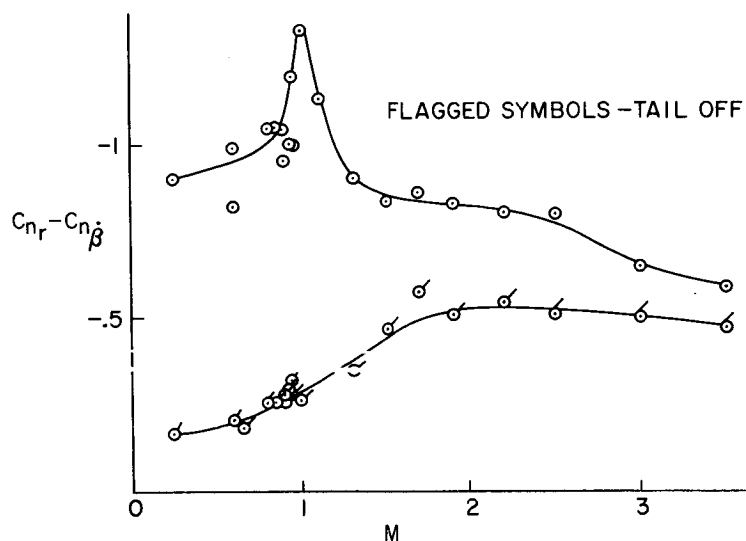
Figure 5

DAMPING IN PITCH OF A NOTCHED-TRIANGULAR-
WING CONFIGURATION, $\alpha = 0°$



$$\left(C_{m_q} + C_{m_{\dot{\alpha}}}\right)_{a.c.} = \frac{\pi}{4} \frac{b}{c} G\left(\frac{\text{TAN } \delta}{\text{TAN } \mu}\right)$$
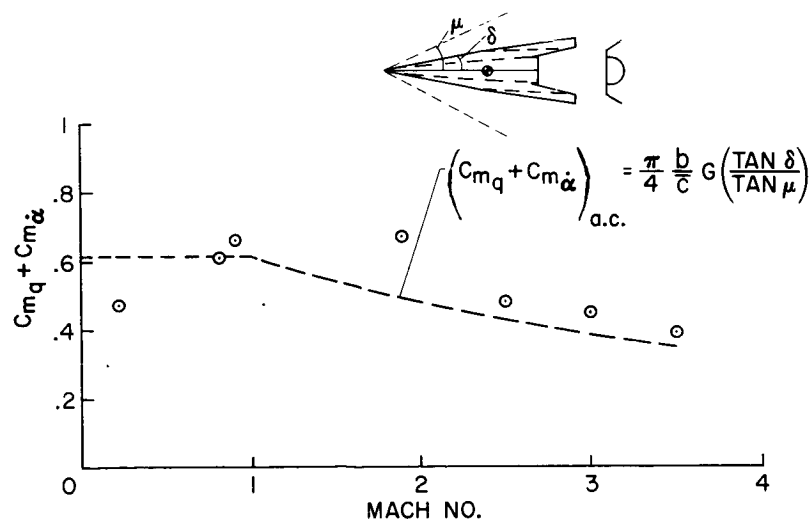
Figure 6

CORRELATION OF DAMPING-IN-ROLL PARAMETER WITH
ASPECT-RATIO PARAMETER FOR SEVERAL WING PLANFORMS
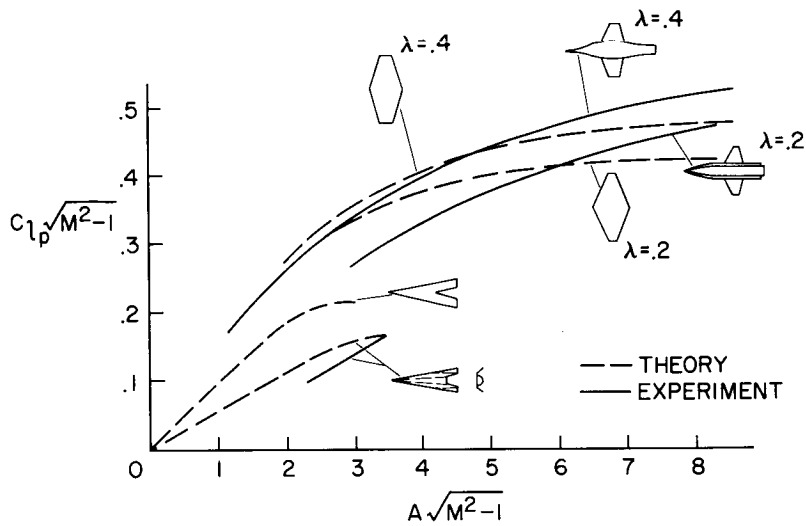


Figure 7

ROLLING DERIVATIVES FOR NOTCHED-TRIANGULAR-WING-
CONFIGURATION HAVING DROOPED TIPS
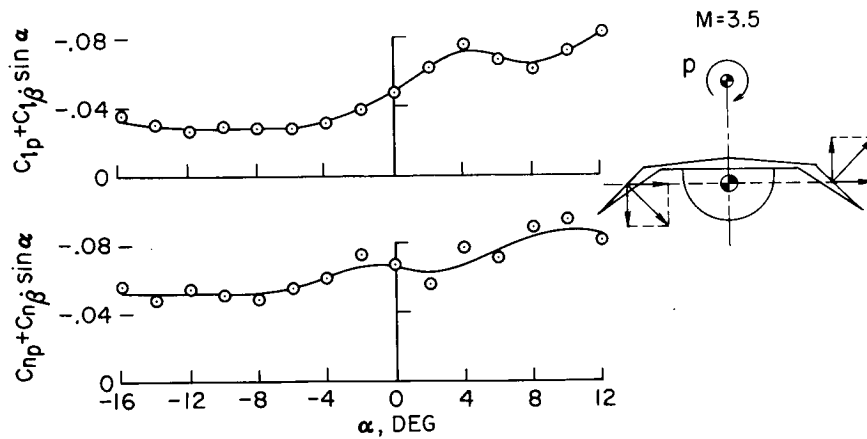


Figure 8

EVALUATION OF SOME AERODYNAMIC CONTROLS FOR A

MISSILE HAVING LOW ASPECT RATIO

By Warren Winovich and Nancy S. Higdon

Ames Aeronautical Laboratory

## INTRODUCTION

The selection of a particular control for a given missile is frequently a compromise over conflicting requirements. From the control viewpoint, the inherent advantage of the small center-of-pressure travel that is characteristic of delta configurations having low aspect ratio places a premium on control types that preserve or improve this feature.

The purpose of this paper is to discuss the results of a static-stability-controls investigation carried out with the missile configuration shown in figure 1. Besides small center-of-pressure travel with Mach number, the low-aspect-ratio configuration was chosen because of the inherently small induced rolling moment developed during maneuvering conditions. The basic wing-body combination (fig. 1) consists of a 3-caliber ogive nose with a cylindrical afterbody fitted with a cruciform wing. Overall body length is 10 diameters. The cruciform wing has a delta plan form with an aspect ratio of 3/8. Wing panels consist of flat plates with leading and trailing edges beveled. The model was tested with three basic control types (fig. 1): a tail control, a canard control, and a nose control. The center-of-gravity positions to allow a static margin of 0.2 diameter at Mach number 2 resulted in shorter moment arms for the canards; all center-of-gravity stations are in the range of 45 to 55 percent of the body, which represents realistic values.

## DISCUSSION

The details of the controls are shown in figure 2. Three types were tested: a diamond-plan-form control with a balanced hinge line; a rectangular control with a balanced hinge line; and a swiveling nose control. The planar types both have wedge-shaped cross sections to reduce center-of-pressure movement on the control. The swivel nose control consists of a forward position of the ogive nose that pivots in the pitch plane relative to the body axis. The swiveling portion was designed to have the

29

same plan-form area as two of the planar surfaces to make control effects comparable on an area basis.

For the diamond-plan-form cases, the controls were tested interdigitated with respect to the wings as well as inline with the wings. Hence, all four panels were deflected, and the effective control area in the pitch plane was increased by a factor equal to the square root of 2. This factor should be recognized when comparisons are made between inline and interdigitated controls, particularly in the case of control effectiveness.

An assessment of control adequacy depends on prerequisites established by the intended mission. Among the desirable control qualities of an interceptor type of missile is that of possessing stable equilibrium over its operational range with regards to angle of attack as well as Mach number. For simplicity of the guidance system, there should be no control reversal. Further, the missile should be able to fly at trimmed conditions without unduly high trim-drag penalties. Also, control effectiveness should be sufficiently high to allow for development of large normal forces to yield rapid response rates.

The criteria just given are satisfied for a missile that is able to operate at a small static-stability margin with no inherent control reversal introduced by configuration nonlinearities and one which possesses a control with high effectiveness. This discussion specifies for the given configuration which control type, tail control or canard control, inline or interdigitated, or nose control, has the best qualities.

The effect of the addition of controls to the basic wing-body combination is shown in figure 3. The center of pressure measured from the nose of the missile $x/d$ is plotted as a function of angle of attack $\alpha$ for $0^\circ$ control deflection at Mach number 3. The small center-of-pressure travel for the basic wing-body combination is retained up to Mach number 5. For comparison, the body-alone center-of-pressure travel is also shown to illustrate the advantage gained by using a low-aspect-ratio wing. Adding canard surfaces in the interdigitated position causes an increase in the center-of-pressure travel at small angles of attack. On the other hand, adding the tail control in the interdigitated position improves the center-of-pressure travel of the basic wing-body combination. For this case, center-of-pressure travel is independent of angle of attack and lies on the centroid of plan-form area. Thus, for the configuration of the present test, addition of control area behind the centroid of area of the basic wing-body combination reduces center-of-pressure travel whereas addition of control area ahead of the centroid of area increases the center-of-pressure travel.

The extremely small center-of-pressure travel shown for the interdigitated tail controls results in linear pitching-moment curves that,

in turn, allow the missile to be trimmed to small values of static margin with no inherent control reversal. On the other hand, the center-of-pressure travel indicated for the canard case results in nonlinearities in the pitching moment at small angles of attack, and therefore yields higher trim penalties.

In figure 4 the control effectiveness at Mach number 2 for the canard and tail controls is shown. The incremental pitching-moment coefficient $\Delta C_m$ is plotted against control deflection $\delta$ for angles of attack of $0^\circ$ and $14^\circ$. At $0^\circ$, as would be expected, the incremental pitching-moment coefficient for the interdigitated cases is greater than that for the inline case by a factor approximately equal to the square root of 2. A comparison of the canard and tail-rearward types shows that the canards are much more effective at small control deflections. This indicates that, for this specific canard configuration where the control span is the same as the wing span, unexpected favorable interference occurs. When operating at combined angle of attack and control deflection at this Mach number, the canard configurations show a reduction of control effectiveness which is of the order of 50 percent at an angle of attack of $14^\circ$ and large control deflection. This is caused by the stalling of the canard surfaces which are deflected positively to trim. For the interdigitated tail control, however, there is essentially no change in control effectiveness at combined angle of attack and control deflection. The inline tail controls exhibit a constant control-effectiveness reduction of about 15 percent at combined angle of attack and control deflection owing to their location in the wake of the wing. Therefore, the interdigitated tail realizes a gain in control effectiveness which is greater than the square-root-of-2 factor.

In figure 5, the effect of Mach number on control effectiveness is shown for the canard and tail controls. The arrangement is the same as that for the preceding figure except that the Mach number is 3. At $0^\circ$ angle of attack, the incremental pitching-moment coefficient is

decreased by the inverse ratio of $\beta = \sqrt{M^2 - 1}$ in accordance with linear theory. This holds for all of the planar control types tested. At combined control deflection and angle of attack at Mach number 3, the interdigitated canard control exhibits favorable interference, just the opposite of the effect found at Mach number 2. The interdigitated tail control, however, shows a negligible effect of angle of attack at both Mach numbers.

The rectangular-plan-form tail control develops the same control effectiveness at small angles of attack as does the diamond-plan-form control. At combined angle of attack and control deflection the rectangular-plan-form control with one-quarter-chord gap retains control effectiveness. The effect of decreasing the gap from one-quarter chord to zero was to linearize the pitching moment. The linearizing effect of the zero-gap rectangular-plan-form tail control can be attributed to

viscous effects which prevent the flow from passing through the wing-control gap as the control unports initially. The more linear variation of pitching-moment coefficient resulted in slightly higher trim normal-force coefficients than were obtained for both the inline diamond configuration and the one-quarter-chord gap rectangular tail configuration.

For the swivel nose control it was found that control effectiveness increased slightly between Mach numbers 2 and 3. An analysis in which control effectiveness was calculated, assuming that the swiveling ogive can be replaced by a cone, predicts such an increase. However, the effectiveness of the nose control is low; for example, at Mach number 3 it is less than half the value corresponding to the interdigitated tail control.

The effect of bank angle on pitching-moment effectiveness is shown in figure 6. For the case shown, the missile receives a command to maneuver toward a target that is at an angle $\phi$ relative to the missile. The maneuver is accomplished by deflecting all four control panels to go directly to the target without rolling. The control effectiveness $C_{m_\delta}$ shown on the ordinate is developed in the plane of the target. The dashed lines represent linear theory with no regard for interference effects. The points are results of wind-tunnel tests at Mach number 3 and an angle of attack of $12^\circ$.

The theory indicates no advantage for either type of control owing to symmetry at $45^\circ$. However, at $45^\circ$ the inline configuration does not realize the theoretical prediction because of the location of the control panels in the wakes of the wings. The interdigitated control, which is positioned more favorably, has no wake interference effects and develops practically as much pitching effectiveness as the inline control at $45^\circ$. Thus, the interdigitated control has a slight advantage in this maneuver over a wider angle range.

For the long-chord low-aspect-ratio configuration at combined angles of attack and sideslip, tests at the Langley Aeronautical Laboratory and the Ames Aeronautical Laboratory have shown that there is adequate roll control up to Mach number 6.

In figure 7, the trim capabilities of the control types are compared. In this figure trim normal-force coefficient $C_{N_{TRIM}}$ is plotted as a function of the trim control deflection $\delta_{TRIM}$ at Mach number 3. All types were trimmed to the same static margin to make this comparison. Owing to the excellent center-of-pressure characteristics the interdigitated tail control develops the highest normal force for a given control deflection. Although the interdigitated canard showed the largest center-of-pressure travel, the favorable interference that was observed to exist enables this control type to develop high normal forces also. The lowest curve

represents the swivel-nose-control case as well as the inline diamond and rectangular tail and canard controls. As shown, the maximum trim normal-force coefficient for this group is only slightly greater than 2. By resorting to interdigitation of the control panels it is possible, therefore, to develop over twice the trim normal force relative to the inline types.

The trim lift-drag polars are shown in figure 8. The trim lift coefficient is shown as a function of the trim drag coefficient at Mach number 3 for the various configurations. The dashed line represents the untrimmed case which is essentially the same for all control types. The minimum drag for the canard types is slightly higher than that for the tail-rearward types. For any given lift coefficient the plot shows that the drag penalty is least for the interdigitated-tail-control types.

In figure 9 the comparison is made of the agreement between experimental and predicted control effectiveness as a function of Mach number. The dashed curve is the result of linear theory which has been modified to account for panel-body interference. The circles represent experimental data for the interdigitated tail control. Theory overpredicts control effectiveness by an almost constant percentage. The trend predicted by linear theory of the falloff of effectiveness with Mach number holds for Mach numbers up to 6. Although the control effectiveness decreases with Mach number, the good moment characteristics of the interdigitated tail control at combined control deflection and angle of attack still allow large trim forces to be developed at the higher Mach numbers.

In figure 10 the same comparison is shown for the interdigitated canard control. For this case, theory underpredicts the experimental values. This occurs over the entire Mach number range and illustrates that favorable interference acts to increase the control effectiveness at 0° angle of attack for this particular canard surface. However, at combined control deflection and angle of attack it has been noted that the interference can be unfavorable. The decrease of control effectiveness with Mach number is again closely predicted by linear theory.

## CONCLUDING REMARKS

For the delta configuration having low aspect ratio tested in this investigation, the interdigitated tail control comes closest to satisfying the criteria given. This control actually improves the stability of the basic wing-body combination. Small center-of-pressure travel allows trimming at small stability margin with subsequent small trim-drag penalties. Larger trim normal forces can be developed for this control than can be developed for inline-control types. Finally, the favorable location

of the control panels away from the wing wake minimizes interference effects so that the control effectiveness is maintained over wide limits.

REFERENCES

1. Jorgensen, Leland H., and Katzen, Elliott D.:  Wing-Body Combinations With Wings of Very Low Aspect Ratio at Supersonic Speeds.  NACA RM A56G16, 1956.

2. Pitts, William C., Nielsen, Jack N., and Kaattari, George E.:  Lift and Center of Pressure of Wing-Body-Tail Combinations at Subsonic, Transonic, and Supersonic Speeds.  NACA Rep. 1307, 1957.

MODELS

10d

3d

$A = \dfrac{3}{8}$

d

BASIC WING-BODY

TAIL CONTROL        CANARD CONTROL        NOSE CONTROL

Figure 1

CONTROLS

DIAMOND                    RECTANGULAR

SWIVEL NOSE
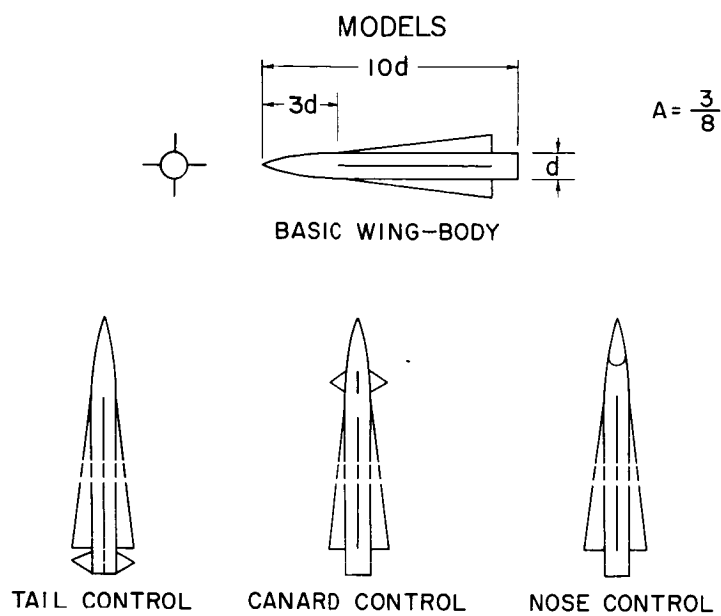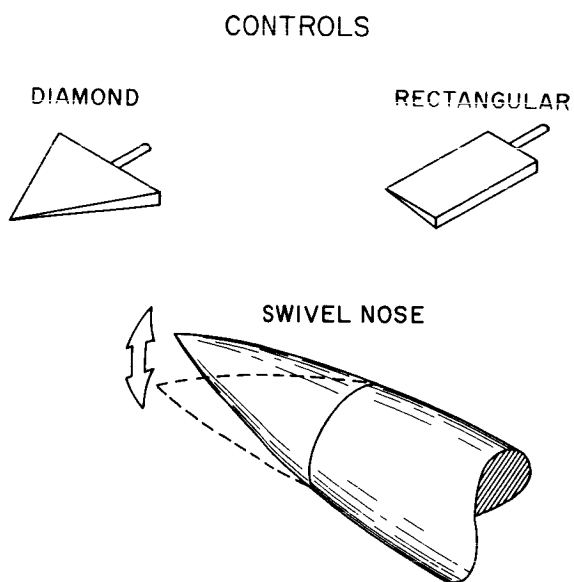
Figure 2

EFFECT OF CONTROL ON CENTER OF PRESSURE
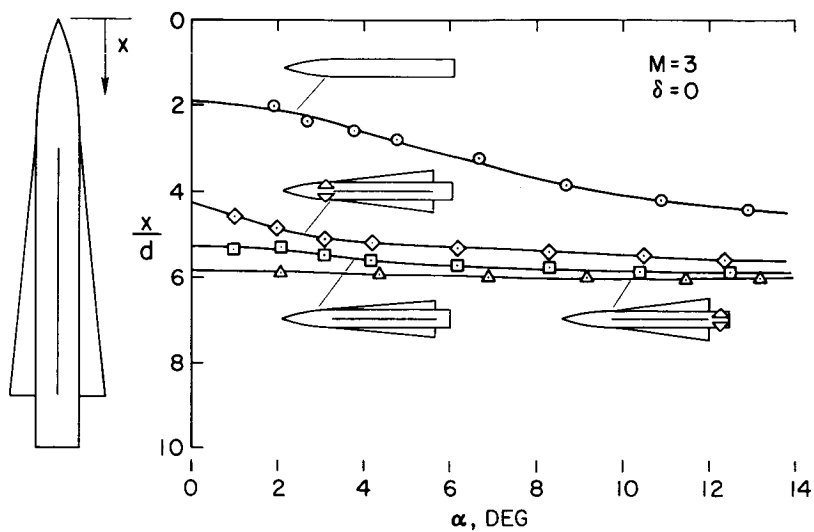


Figure 3

CONTROL EFFECTIVENESS
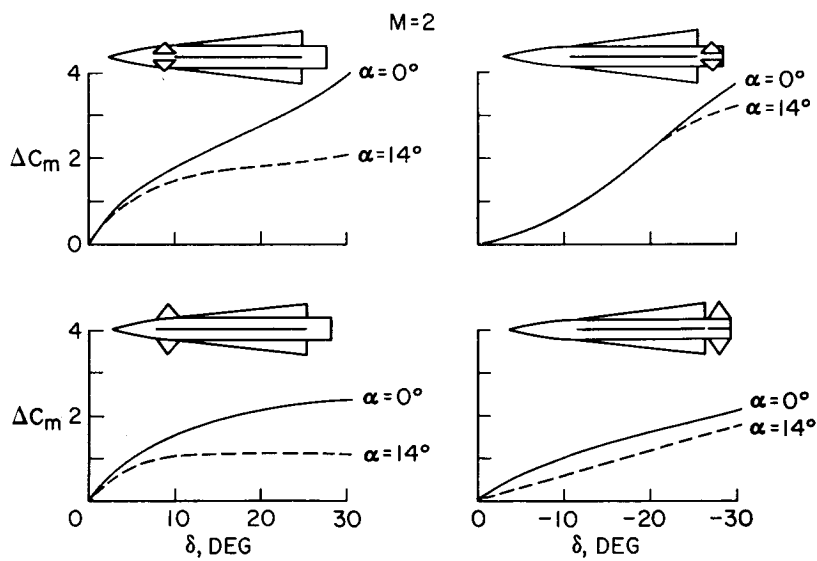


Figure 4

## CONTROL EFFECTIVENESS

M = 3
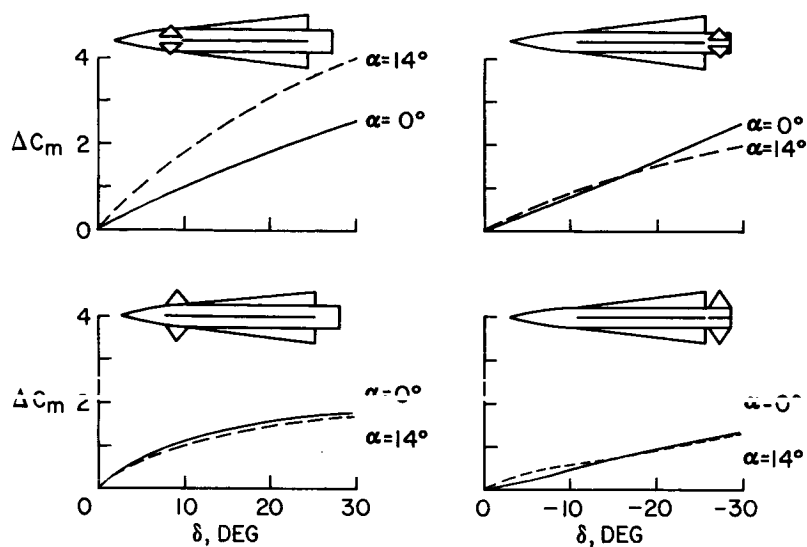


Figure 5

## EFFECT OF BANK ANGLE ON CONTROL EFFECTIVENESS

M = 3, α = 12°



Figure 6

## TRIM ABILITIES

M = 3



Figure 7

## TRIM LIFT—DRAG POLARS

M = 3
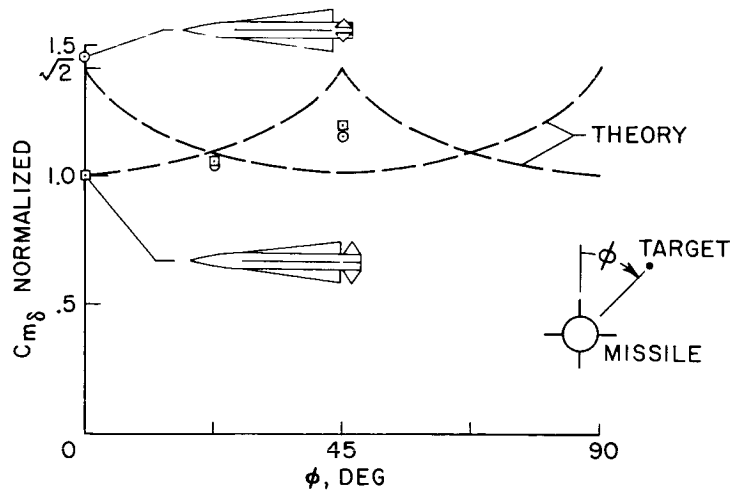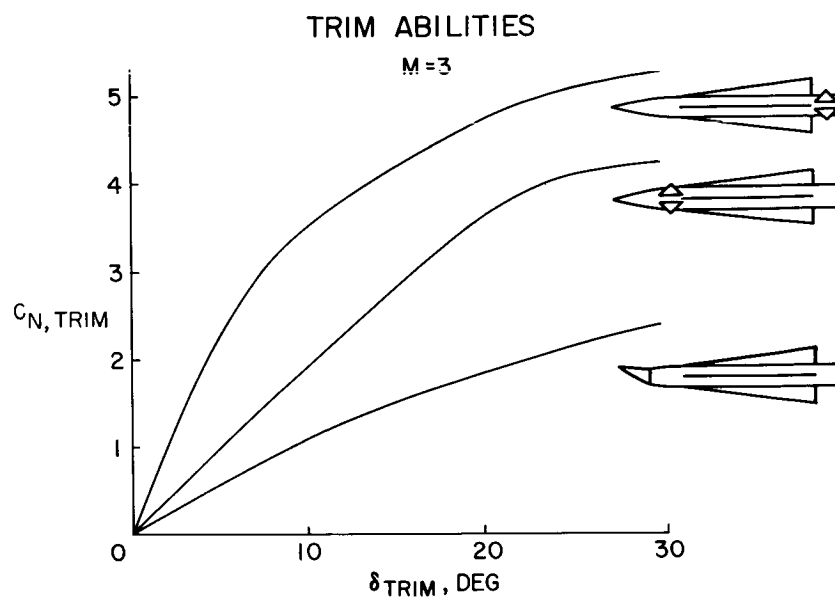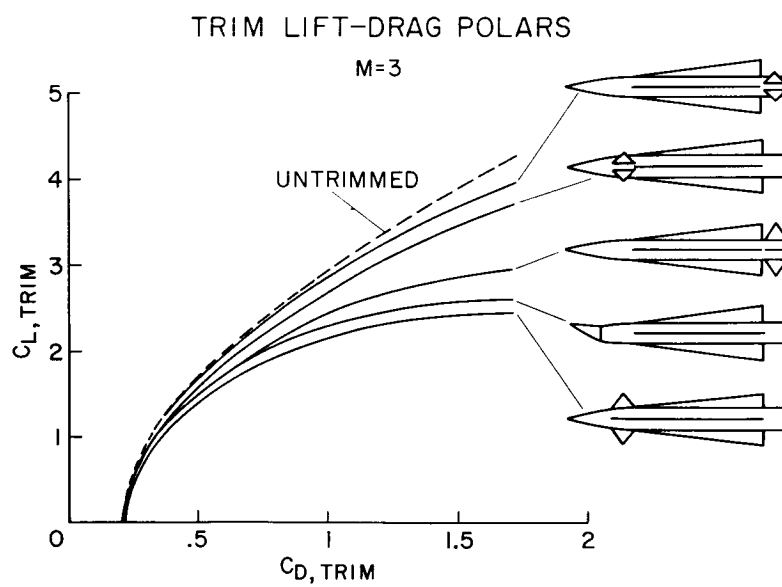


Figure 8

PREDICTION OF TAIL CONTROL EFFECTIVENESS

$\alpha = 0°$
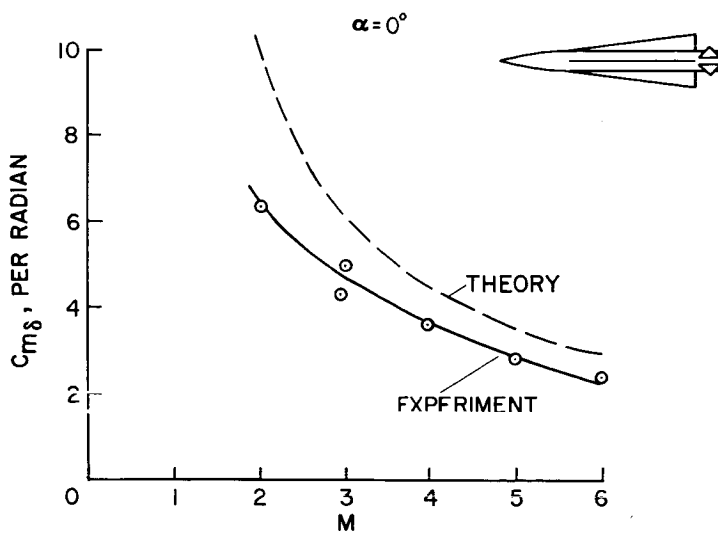


Figure 9

PREDICTION OF CANARD CONTROL EFFECTIVENESS

$\alpha = 0°$
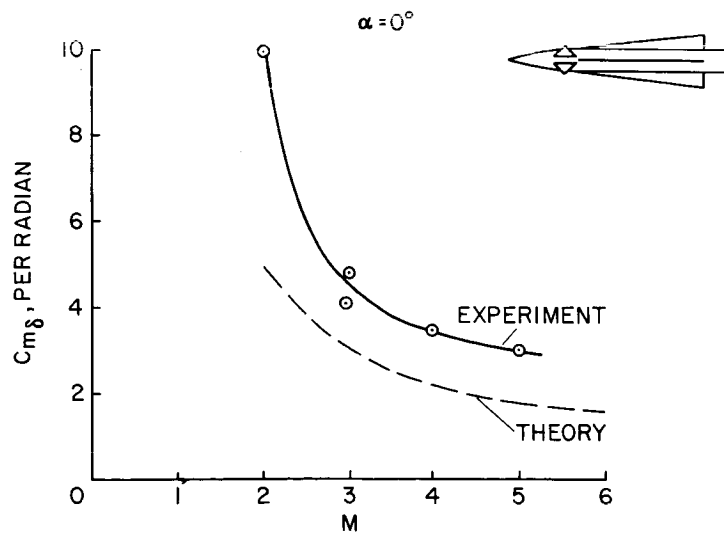


Figure 10

# MANEUVER PERFORMANCE OF INTERCEPTOR MISSILES

## By David G. Stone

### Langley Aeronautical Laboratory

## SUMMARY

From an analysis of a point defense against ballistic missiles with an intercept near an altitude of 140,000 feet, a lift coefficient from 2 to 3 is shown to be required of the antimissile missile. This lift is readily obtained from missile configurations having small low-aspect-ratio surfaces and even from bodies alone at higher angles of attack. Preliminary wind-tunnel tests at Mach numbers of 4.65 and 6.8 have indicated trailing-edge controls to be poor in trimming a low-aspect-ratio configuration to the required lift, whereas an all-movable forward surface with a short lever arm on a flared-skirt configuration shows adequate trim lift characteristics. These preliminary analyses and wind-tunnel tests indicate that more research should be done on controls, either aerodynamic or reaction type, so that interceptor-missile configurations may be trimmed to the angles of attack required to develop the necessary turning force.

## INTRODUCTION

The performance criterion for an interceptor missile to defend against ballistic missiles is turning force sufficient to intercept the target as well as drag characteristics that do not degrade the ability of the rocket motor to obtain high altitude and range in a short length of time.

## SYMBOLS

$C_L$          lift coefficient

$C_N$          normal-force coefficient

$C_{N,TRIM}$          trim normal-force coefficient

g          acceleration due to gravity

L/D        lift-drag ratio

$(L/D)_{TRIM}$   trim lift-drag ratio

$l$           length of missile

M          Mach number

t           time, sec

$\Delta t$         incremental time, sec

x          distance from nose to center of gravity

$x/l$       center-of-gravity location

$\alpha$         angle of attack, deg

$\alpha_{TRIM}$    trim angle of attack, deg

$\delta$, $\delta_c$     deflections of control surface, deg

## DISCUSSION

In order to aid in determining the aerodynamic lifting force that may be required of an antimissile missile, a purely arbitrary problem of intercepting an intercontinental ballistic missile (ICBM) was set up. A point-defense problem was considered. Figure 1 presents the conditions, trajectories, and requirements for an antimissile missile that is maneuvered by aerodynamic forces and aerodynamic controls. The arbitrary conditions for point defense were to intercept an ICBM warhead at an altitude of 140,000 feet at a minimum range from launch of 40 nautical miles. The missile considered consisted of a so-called aerodynamic steerable stage that places the warhead stage at 140,000 feet in 40 seconds so that the warhead stage may make the final correction to intercept (in the order of 2 nautical miles) in several more seconds. In the figure, altitude is shown plotted against horizontal range. The ICBM path enters at 20° and the antimissile launch point is somewhere beneath this path. If atmosphere is not considered, the zero point on the range is the extension of the ICBM path to theoretical impact. The curved trajectories illustrate the paths of the antimissile for two different turning forces or lift. In detail, the missile is launched at 70° and

boosted to a Mach number of 6 between altitudes of 20,000 and 30,000 feet in nonguided flight. Then the missile coasts and makes an "aerodynamic turn." For example, two turns are shown: one for a lift coefficient of 2 for a duration of 15 seconds and another for $C_L = 3$ for a duration of 5 seconds. A value of $C_L$ of 3 causes the missile to turn too much for this 70° launch angle; however, if the launch angle were 80°, a value of $C_L$ of 3 would be required to obtain a trajectory similar to the one shown fully. At the end of this "aerodynamic turn" the sustainer rocket is fired to accelerate the missile to $M = 10$ so that the desired intercept point may be reached in time. The latter part of the path is a ballistic trajectory to the point of near intercept.

The important point of this trajectory analysis is that lift coefficients, based on body cross-sectional area, in the range of 2 to 3 are required for maneuver performance. This represents normal accelerations in the order of 30g. Also, note that when the missile is at high angles of attack in the denser air the Mach number is not excessive.

Configurations that are capable of producing lift forces of this magnitude have been tested in wind tunnels and are reported in references 1 to 5. Two configurations having different aerodynamic controls and their trim capabilities will be shown for Mach numbers of 4.65 and 6.8 as obtained in the Langley Unitary Plan wind tunnel and in the Langley 11-inch hypersonic tunnel. The two configurations are shown in figure 2. Based on body length, the Reynolds number is $12.5 \times 10^6$ for the data at $M = 4.65$ and $3 \times 10^6$ for the data at $M = 6.8$. Figure 3(a) summarizes the results at $M = 4.65$ for a low-aspect-ratio long-chord delta cruciform configuration having trailing-edge controls. Plotted as the ordinate is the trim normal-force coefficient based on body cross-sectional area against the center-of-gravity location for two deflections of the controls. These data show that in order to reach required values of normal-force coefficient from 2 to 3, the static stability must be quite low, in fact, near neutrally stable. The boundary mark indicates the position of neutral stability. This is realistic because neutral stability should be no problem inasmuch as the moment characteristics of long-chord configurations are so nearly linear and have no adverse static stability characteristics. Note that trim angles of attack around 15° are required. The static margin to obtain values of $C_N$ from 2 to 3 is in the order of 0.2 body diameters, the value at which Warren Winovich and Nancy S. Higdon in the preceding paper compared various controls. Shown again in figure 3(b) is the trimmed lift effectiveness at $M = 6.8$. Note the severe reduction in effectiveness of the trailing-edge controls that are directly behind the wing. Of course, at a Mach number of 6.8 the trailing-edge controls are incapable of producing the required values of $C_N$ from 2 to 3. If these controls were all-movable and interdigitated with respect to the wings, the large reduction in effectiveness

would not occur at $M = 6$ as pointed out in the paper by Winovich and Higdon.

The drag penalty which goes with these trim lift conditions is shown in figure 4 as the trim lift-drag ratio plotted against center-of-gravity location for a Mach number of 4.65. These results also emphasize the need for low static margin to obtain better values of $(L/D)_{TRIM}$. The untrimmed $L/D$ capabilities of this configuration are slightly better than 3 as compared with $(L/D)_{TRIM}$ of slightly over 2. Therefore, the trailing-edge controls are incapable of producing the full $L/D$ capabilities of the configuration.

A different configuration is presented in figure 5(a). Shown is $C_{N,TRIM}$ plotted against center-of-gravity location for a flared-skirt-stabilized configuration with an all-movable surface just in front of the center of gravity. Data for two deflections of the control surface are presented. Again for even this configuration the static stability must be quite low at $M = 4.65$ to obtain the required values of $C_{N,TRIM}$ from 2 to 3. Note that the trim angles of attack are near $12^{\circ}$. The control lift effectiveness is quite high, accounting for the trim capabilities. Shown in figure 5(b) is the trimmed lift effectiveness at $M = 6.8$. At this higher Mach number, ample $C_{N,TRIM}$ capabilities are available for this configuration at trim angles of attack near $14^{\circ}$.

The trimmed lift-drag characteristics of the flared-skirt configuration under these conditions are shown in figure 6(a) for $M = 4.65$ and in figure 6(b) for $M = 6.8$. The trimmed lift-drag characteristics are no better than for the long-chord delta configuration, but the untrimmed lift-drag ratio for the flared-skirt configuration is only slightly better than 2. Therefore, the all-movable forward surface develops $(L/D)_{TRIM}$ capabilities that are the maximum available from the configuration.

The preceding data indicate that aerodynamic controls may be a problem for the antimissile missile. That is, the all-movable-surface configurations may have severe heating and interference effects, and the trailing-edge controls are ineffective at high supersonic speeds. However, the aerodynamic lifting capabilities are adequate. Therefore, this suggests some form of nonaerodynamic or reaction control for trimming.

For purposes of comparison, another analysis was made for a hypothetical wingless missile to do the same arbitrary point-defense job as the winged aerodynamic-controlled missile. The basic premise of this analysis was that the turning force would come from the body lift and the component of the thrust vector due to angle of attack only.

Therefore, the booster or sustainer rocket motors must be active during the entire 50 seconds of flight to 140,000 feet. Figure 7 presents the trajectory and requirements for this wingless configuration. Plotted is the altitude against the horizontal range for the trajectory shown. The missile is launched at an angle of 70° and at an altitude of about 20,000 feet the turn begins while the booster is burning. This turn requires a lift coefficient of about 2 (based on body cross-sectional area). Most of the turn is accomplished during boost where the Mach number varies slowly between 4 and 6 in the denser air, the interval between 13 seconds and 30 seconds. Then, the booster drops off near 80,000 feet and the missile, still utilizing body lift and using a two-step-thrust or dual-thrust sustainer motor, completes the turn into the required trajectory in the required time to place the warhead stage at 140,000 feet in 50 seconds. Above the trajectory plot in figure 7 is shown the effective lift-drag ratio experienced during this particular programed turn. The solid line indicates the total effective lift-drag ratio, which is the sum of the aerodynamic lift-drag ratio and the components attributed to the rocket thrust. The dashed line shows the aerodynamic lift-drag ratio of the body alone involved. Also shown is the angle of attack to develop the required lift coefficient and the tilting of the thrust vector. Note that at the beginning of the turn most of the turn is accomplished with body lift whereas, as the altitude increases (that is, as the aerodynamic lift and drag in pounds become smaller), the tilting of the thrust vector is of greater importance.

## CONCLUDING REMARKS

From these preliminary wind-tunnel tests of interceptor missile configurations and the analysis of point defense against ballistic missiles, it is concluded that adequate aerodynamic lift is readily available and should be utilized when operating under high-dynamic-pressure conditions and that more work should be done on controls, either aerodynamic or reaction type, so that the configurations may be trimmed to the angles of attack required to develop the necessary turning force.

CONFIDENTIAL

## REFERENCES

1. Jorgensen, Leland H., and Katzen, Elliott D.: Wing-Body Combinations
   With Wings of Very Low Aspect Ratio at Supersonic Speeds. NACA
   RM A56G16, 1956.

2. Katzen, Elliott D., and Jorgensen, Leland H.: Aerodynamics of Mis-
   siles Employing Wings of Very Low Aspect Ratio. NACA RM A55L13b,
   1956.

3. Turner, Kenneth L., and Appich, W. H., Jr.: Investigation of the
   Static Stability Characteristics of Five Hypersonic Missile Con-
   figurations at Mach Numbers From 2.29 to 4.65. NACA RM L58D04,
   1958.

4. Robinson, Ross B.: Wind-Tunnel Investigation at a Mach Number of
   2.01 of the Aerodynamic Characteristics in Combined Angles of Attack
   and Sideslip of Several Hypersonic Missile Configurations With Vari-
   ous Canard Controls. NACA RM L58A21, 1958.

5. Robinson, Ross B., and Bernot, Peter T.: Aerodynamic Characteristics
   at a Mach Number of 6.8 of Two Hypersonic Missile Configurations,
   One With Low-Aspect-Ratio Cruciform Fins and Trailing-Edge Flaps
   and One With a Flared Afterbody and All-Movable Controls. NACA
   RM L58D24, 1958. (Prospective NACA paper.)

CONFIDENTIAL

## AERODYNAMIC-PERFORMANCE REQUIREMENTS

MIN. INTERCEPT CONDITIONS

ALTITUDE        140,000 FT
FLIGHT TIME     50 SEC
RANGE           40 NAUT. MILES

WARHEAD STAGE

AERODYNAMIC STAGE

LAUNCH ANGLE = 70°

ICBM PATH

M = 8.8        20°

$C_L = 2$ ; $\Delta t = 15$ SEC

M = 10
M = 4.5

ALTITUDE, FT

M = 4.5        $C_L = 3$ ; $\Delta t = 5$ SEC
M = 6          40 NAUT. MILES

RANGE, FT
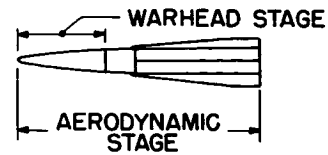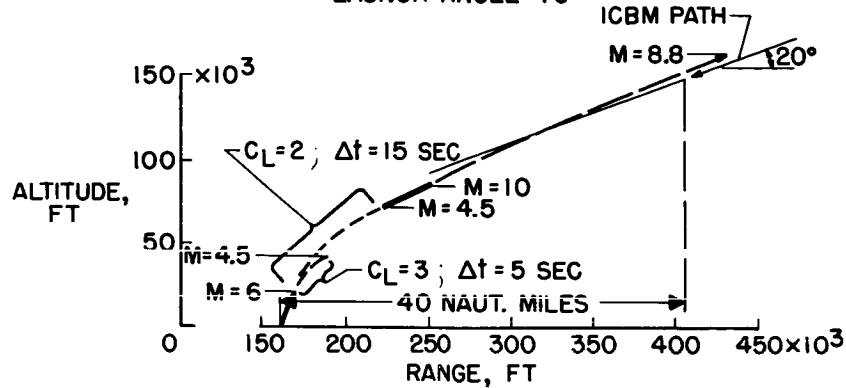
Figure 1

## LOW-ASPECT-RATIO LONG-CHORD DELTA MISSILE CONFIGURATION

Hinge line
.333D
5°
Nose fineness ratio = 5
D   1.855D
.1 D radius
.427D
D
6.375D
10D
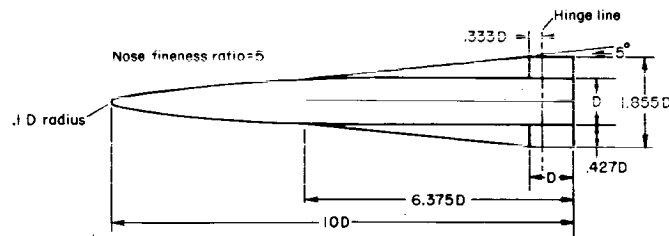
## FLARED-SKIRT-STABILIZED MISSILE CONFIGURATION WITH ALL-MOVABLE FORWARD SURFACE

Hinge line    .1068D
Nose fineness ratio = 5
.74D    D    10°
1.705D
.1 D radius
.667D
2.48D    2D
2.125D
5.327D
10D

Figure 2

## TRIMMED LIFT EFFECTIVENESS
### M = 4.65



Figure 3(a)
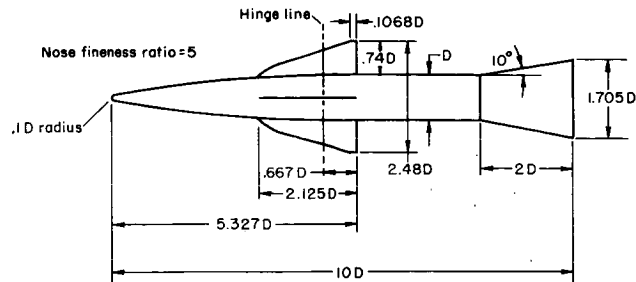
## TRIMMED LIFT EFFECTIVENESS
### M = 6.8
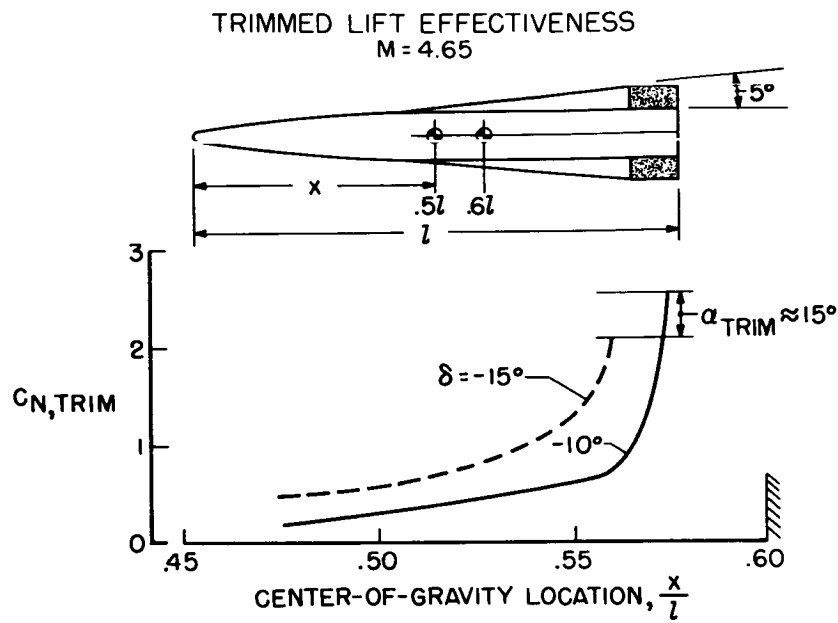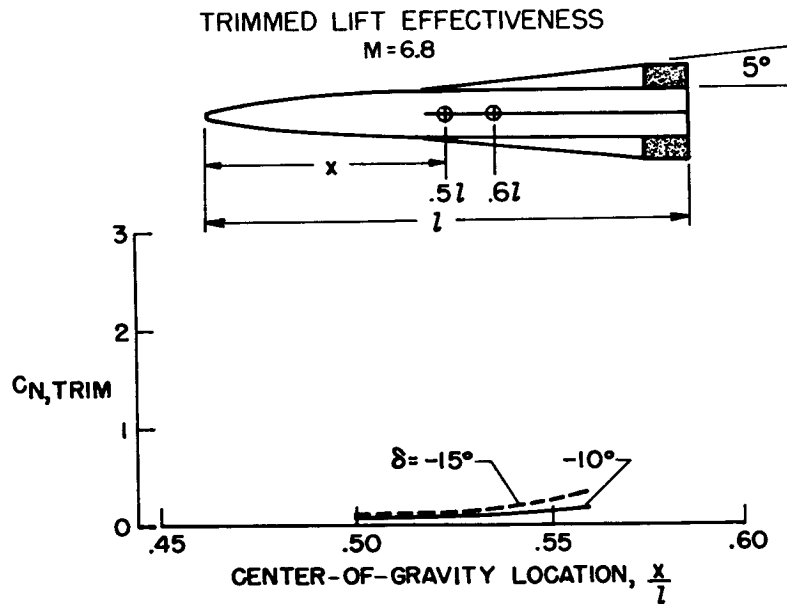


Figure 3(b)

## TRIMMED LIFT-DRAG CHARACTERISTICS
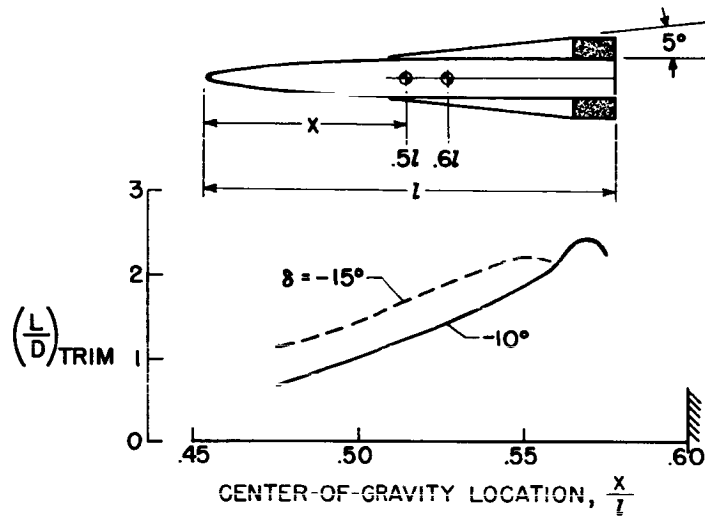
### M = 4.65



Figure 4

TRIMMED LIFT EFFECTIVENESS
M = 4.65
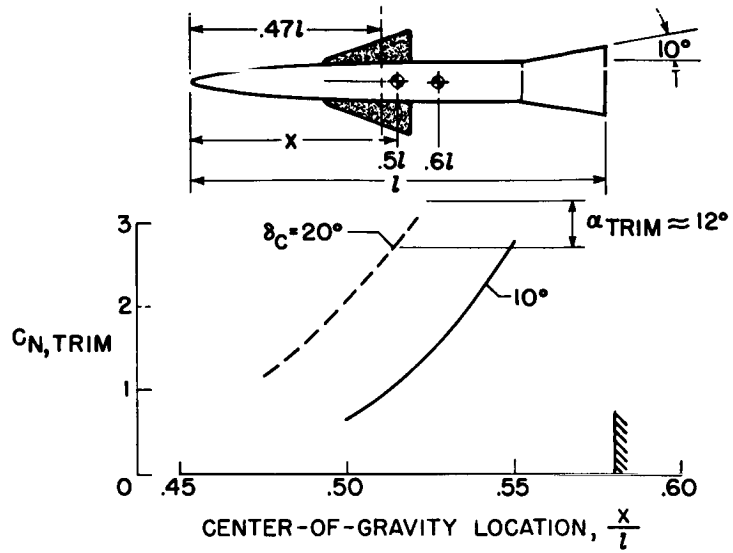


Figure 5(a)

TRIMMED LIFT EFFECTIVENESS
M = 6.8
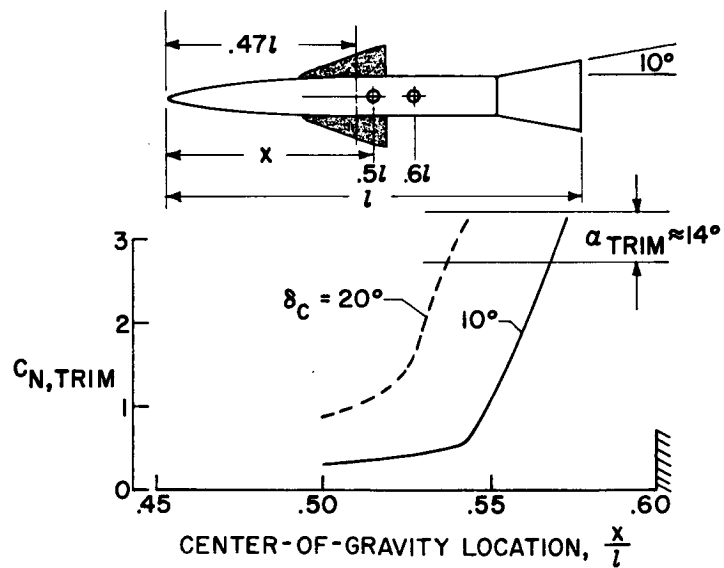


Figure 5(b)

TRIMMED LIFT-DRAG CHARACTERISTICS
M = 4.65
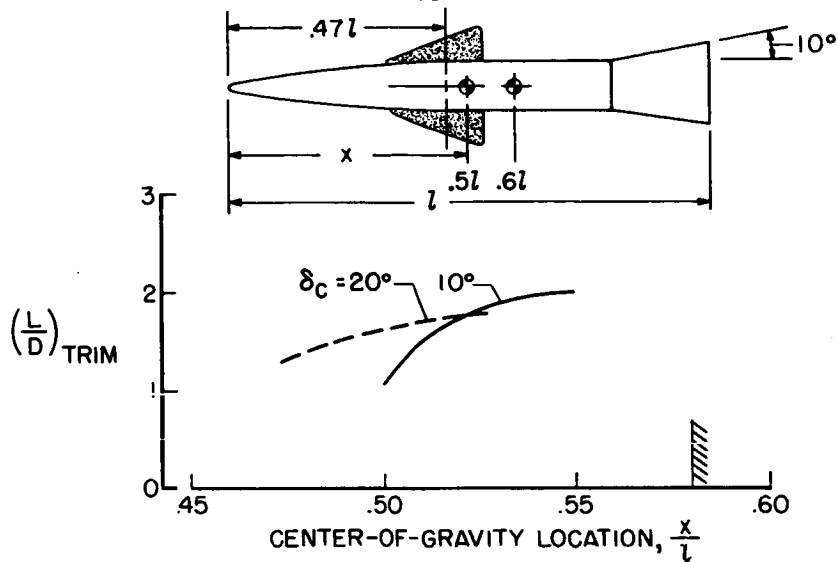


Figure 6(a)

TRIMMED LIFT-DRAG CHARACTERISTICS
M=6.8
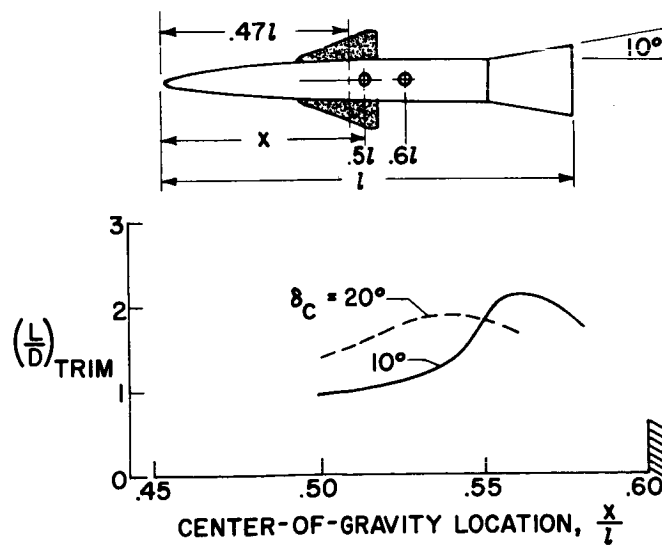


Figure 6(b)

WINGLESS CONFIGURATION
CONTINUOUS – BURNING ROCKET MOTORS
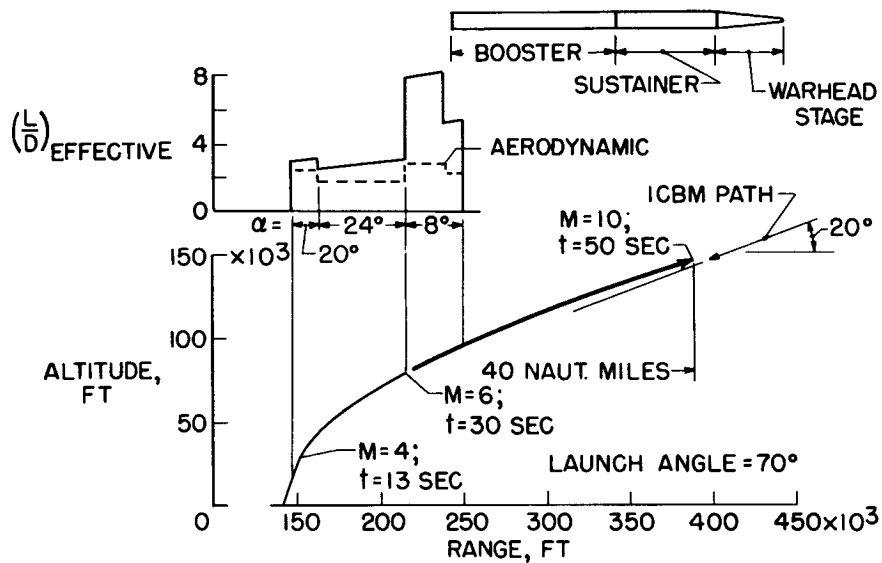


Figure 7

SOME PRELIMINARY EXPERIMENTS ON HIGH-SPEED IMPACT WITH

APPLICATION TO THE PROBLEM OF DEFENSE AGAINST

INTERCONTINENTAL BALLISTIC MISSILES

By A. C. Charters

Ames Aeronautical Laboratory

INTRODUCTION

The intercontinental ballistic missile (ICBM) has been called "an ultimate weapon" because it appears next to impossible to stop once it has been launched. In truth the ICBM is a difficult quarry. Destroying it in flight is like shooting down a rifle bullet. On the other hand, this weapon is sure to be used in any major conflict, as recent events have demonstrated conclusively, and it is vital for our own welfare that we pursue the development of an adequate defense.

If an engineering problem is unusually difficult, a fruitful approach sometimes is to seek a special solution which is strictly valid only for limited conditions. Often, partial answers will point the way to a solution of the whole problem. This approach is taken here. A special solution to the defense problem is being sought out; a particular method, as it were, of attacking and destroying the ICBM as it approaches its target.

The essence of the method is to destroy the ICBM by perforating its heat shield with a small projectile. Its impact on the shield will open up a hole having a diameter greater than the thickness and will expose the interior to a stream of hot gas similar to the flame of an oxyacetylene cutting torch. It is reasonable to suppose that a cutting-torch flame played on the delicate nuclear warhead would wreak havoc in short order. Although it is not definite that perforation of the heat shield will be lethal, this will be the underlying hypothesis.

The ICBM will supply the velocity for the impact, of course, and it is only necessary to place the projectile in its path. The impact will take place at ICBM entry speed, and engineering calculations must be based on a knowledge of impact at velocities of 20,000 ft/sec and above. Unfortunately, little is known about impact at these speeds, and a limited program of research is being carried out by the NACA to fill the gap.

The purpose of this paper is twofold:  first, to present the results from the impact program to date; second, to apply these to roughing-out the general dimensions of a weapons system.

PRELIMINARY RESULTS OF HIGH-SPEED IMPACT RESEARCH

Experimental Procedure

The program of research has consisted of firing small spheres at thick copper plates, since it is believed that copper is a material whose properties may make it suitable for an ICBM heat shield.  The test apparatus is shown in figure 1.  The spheres were fired from the gun at the left, traversed several chambers, and struck the target at the right. All spheres were made of metal and had a diameter of 1/8 inch, except in one series of tests.  They were fired in a sabot, shown in the sketch, which separated into two halves on leaving the muzzle and were trapped in the blast tank.  Spark photographs were taken in the velocity chamber, and a typical example is shown in the bottom right-hand corner of the figure.  The targets were mounted with their surfaces perpendicular to the trajectory and all were massive compared to the cavities, so that in effect they were semi-infinite solids.

Results and Discussion

The primary purpose of the impact program was to obtain information on the depth of penetration, and the number of tests are really inadequate for any conclusions about the physics of impact.  However, at risk of oversimplification, a few remarks will be made.

Comments on the impact process.- For small spheres fired at normal incidence into heavy metal targets, the impact will fall into one of three categories, as illustrated in figure 2.  This figure shows the results of firing 1/8-inch tungsten-carbide spheres into lead targets at various speeds.  The ordinate of the graph is the penetration in diameters; the abcissa of the graph is a parameter proportional to the velocity.  The solid line at the right represents the correlation of all the impact data from the remainder of the program.  Representative target blocks were sectioned and photographs of the sections are inserted above the portions of the graph to which they belong.

At low velocities, the strength of the sphere's material is greater than the dynamic pressure of impact, and the sphere penetrates the target as a nondeformable projectile.  At high velocities the dynamic pressure of impact is much greater than the strength of the material of either the

sphere or target, and the sphere and target act as though they were liquids - hence, the designation "fluid impact." In between these regions, there is a transition zone.

The graph in figure 2 is a sort of pirate's treasure map, and, if you're to find the treasure, you have to know where you are on the map. In other words, when in the nondeformable-projectile region, penetration prediction can be made throughout this region, but the point at which transition will occur cannot be predicted and the penetration in the fluid region cannot be described. The converse is true when in the fluid region.

All the tests of this program, except this special series, fall in the fluid region. The name "fluid impact" comes from the hydraulic model used to explain shaped-charge penetration, because this model appears to give a correct picture of the physical processes taking place. The cavity starts to form as the sphere flows into the target and sets some of the target material in motion. The cavity continues to grow as the target material flows away from the point of impact and reaches its full size when the flow is stopped by plastic shear.

If the hydraulic model is correct, then the sphere would be expected to flow out as a thin coating over the outside of the cavity. And this is just what happens, as shown in figure 3. Figure 3 is a photograph of the cavity formed by the impact of a lead sphere on a copper target. The entire surface of the cavity is covered with a smooth silver-colored coat of lead, which is seen to contrast strongly with the red color of the copper block.

Lead is a ductile metal, of course, and it might be expected to behave like a liquid under the action of very great forces. However, the same process takes place even though the material of the sphere is a hard, brittle metal. This is illustrated in figure 4, which shows the cavity produced by a high-carbon steel ball impacting a copper target. The steel sphere does not flow smoothly as lead does. Rather it fragments into many small pieces which float on top of the flow of target metal during the formation of the cavity as though they were blocks of ice floating on a river.

The use of lead as a target material to simulate high-speed impact in copper.- Copper was chosen as the target material of primary interest in these preliminary tests, and it was desired to study impact in copper at ICBM entry velocities of 20,000 ft/sec and above. Unfortunately, the guns available at the time could not fire at these speeds, and a low-speed analog was sought as a means of investigating high-speed impact in copper.

The key to a low-speed analog comes from a suggestion of J. H. Huth and his associates, based on an analysis of experiments at the University of Utah and the Naval Research Laboratory. Huth found that penetrations could be correlated on the basis of the speed of sound in the target metal and suggested that the correct dimensionless parameter was the ratio of the velocity of impact to the speed of sound in the target material, which he called the "impact Mach number." If his hypothesis is correct, lead is a good target material for a low-speed analog, because its speed of sound is only a third of that of copper. Consequently, impact in copper at 20,000 ft/sec could be simulated by lead at 7,000 ft/sec, a velocity within reach of the guns used for these tests.

Huth's hypothesis was tested by firing lead spheres into lead targets and copper spheres into copper targets. A comparison of the target blocks is shown in figure 5. The lead targets are shown at the top of the figure and the copper targets, at the bottom. The impact Mach number scale is shown in the center. The first three targets on the left were selected to compare cavities in the two metals at the same Mach number, and the similarity is quite evident. The lead target at the right shows the hole that would be struck in the copper heat shield of an ICBM by the 1/8-inch sphere shown at the bottom of the figure.

Dependence of penetration on impact Mach number.- The measurements of penetration are shown in figure 6. This graph is a log-log plot of penetration in diameters against impact Mach number. As can be seen, the data for lead and copper are correlated satisfactorily.

The impact Mach number was used to analyze the data from all the tests of this program, but a note of caution should be introduced at this point. The impact Mach number stems from a dimensional analysis rather than from a theoretical treatment of the basic physics of impact, and there may be some doubt as to whether the speed of sound is a truly fundamental variable in the physics of the process.

Effect of sphere material on penetration.- A series of tests were carried out to answer the question: "What material should the sphere be made of to produce the greatest penetration for a given weight?" The results are shown in figure 7, as a graph of penetration against the density of the sphere. The material of the sphere was varied from a magnesium alloy, on the one hand, to a tungsten compound on the other. The weight of the sphere and its velocity were kept constant. Firings were made into both lead and copper targets.

The answer to the question can be seen at once. The deepest cavity is made by the sphere with the greatest density. In other words, weight for weight, the best material is the densest available.

Correlation of all impact data.- The linear plots of data shown
in figures 6 and 7 suggest that the penetration may be a function of a
single parameter. This was found to be the case, as shown in figure 8.
The parameter in question is the product of the density ratio and the
impact Mach number, where $\rho_P$ is the density of the sphere and $\rho_T$ is
the density of the target. All of the data from the impact program are
shown on this log-log plot of the penetration against the impact param-
eter. It can be seen that all the data are fitted reasonably well by
a straight line, the formula for which is given in the upper right-hand
corner. This formula provides an engineering basis for predicting the
effects of high-speed impact.

## APPLICATION TO ANTIMISSILE WEAPONS SYSTEM

The results of the impact program will now be applied to the study
of an antimissile weapons system. The impact formula will be used to
compute the diameter of the sphere required to perforate the heat shield
of the ICBM. In making this calculation the penetration will be equated
to the thickness of the heat shield, although strictly speaking the for-
mula does not apply to the case in which penetration is comparable to
the target thickness. Actually, using the formula in this way is con-
servative, as recent tests at the Langley Aeronautical Laboratory have
shown, because "thin" targets are penetrated more deeply than "thick"
targets under the same conditions of impact. Also, the Langley tests
have shown that heating the target material increased the penetration.
So, here again, the formula is conservative, if the ICBM is struck part
way through the atmosphere and its heat shield is hot.

### General Plan for Counterattack

The plan for counterattack is shown in figure 9. The ICBM approaches
its target along a straight line inclined to the horizon at about 20°.
After it is identified and located, an interceptor missile is launched
and directed to intercept the ICBM at a safe distance from its intended
target.

The warhead of the missile is loaded with small spheres. As a
point of interception is approached, the spheres are spread out into a
symmetrical pattern which lies like a screen athwart the path of the
onrushing ICBM. The spacing is held close enough so that a strike is
certain if the ICBM flies through the pattern.

## Design of Interceptor Missile

The computation of the total weights of spheres required and sizes of interceptor missiles must be based on a definite attack situation. Consequently, a hypothetical attack is considered, although this is done purely for the purpose of illustrating the magnitude of hardware required to implement the proposed weapons system. The conditions of the counterattack are set forth in figures 9 and 10.

Let the spacing between spheres be one unit. Then the diameter of the pattern is taken to be 1,000 units. Consequently, approximately 1,000,000 spheres will be the total number needed. The spheres are considered to be made of tungsten to give the greatest penetration for the least weight. The impact Mach number is assumed to be 2, which is believed to be representative.

Two materials are considered for the heat shield of the ICBM: one with a specific gravity of 10, representative of the "heat-sink" type of shield, and the other with a specific gravity of 2, representative of the "ablating" type of shield. The shield, or "skin," thickness is varied from 0.1 inch, which may be typical of a satellite, through 1 inch, which may be representative of a long-range, ballistic missile, to 10 inches, which might be possible for a heavily armored vehicle, called a "space dreadnought."

The graph in figure 10 is a plot of the weight of 1,000,000 spheres against the skin thickness to be perforated. The top line corresponds to the case where the specific gravity is 10 and the bottom line, to the case where the specific gravity is 2. A rough calculation indicated that the total weight of the pursuit missile will be about 10 times the weight of the spheres which it must carry. Accordingly, the total missile weights are given by the ordinates at the right of the graph.

It is evident that weights of spheres and missiles depend critically on the skin thickness, for these range over 6 orders of magnitude to cover the skin thicknesses considered. Consequently, attention is focused on three cases.

First, the satellite: Here, only a few pounds of spheres will be needed and the pursuit missile is correspondingly light. Destruction by impact looks very promising in this case.

Second, the ICBM: Here, the sphere weights will range in the hundreds or thousands of pounds, and the missile weights, in the thousands or ten-thousands of pounds. So, in this case it may be reasonable to conclude that the weapons system promises to be feasible and merits further study.

Third, the space dreadnought:  Here, the sphere weights will range
from a hundred thousand to a million pounds and the missile weights from
a million to ten million pounds.  These values are very large, even com-
pared to the weights of ballistic missiles, and it is probably fair to
state that a heavily armored vehicle is safe from destruction by the
impact of a relatively small sphere.

## CONCLUDING REMARKS

This paper has been concerned with defense from the ICBM.  It may
be of interest to conclude the discussion by reversing positions for a
moment and studying the effects of countermeasures on the design of the
attacking ICBM, for there is a corollary to be drawn from the results
of this investigation.

Now, the recipients of an ICBM are certain to regard its delivery
as a most unfriendly gesture and will act with the utmost of vigor to
intercept it en route.  It is possible they will throw up a screen of
pellets, as proposed in this paper.  At least, the designer of the ICBM
should be prepared for this eventuality in the design of his heat shield.

If the heat shield is the ablating type, the defense will be pre-
dicted on the lower curve of figure 10 with the shield thickness probably
being a few inches.  It was shown that a relatively light pursuit missile
could bring about the destruction of the ICBM.  Consequently, the ICBM
designer may feel it necessary to back up his ablating heat shield with an
inner shield of armor heavy enough to defeat any attempt at perforation.

The corollary to be drawn from the present study is this:  The heat
shield of an ICBM may have to be a shield in an older military sense; that
is, a device for warding off the blows of one's opponent.  The shield of
the ICBM must ward off the heat of high-speed entry into the earth's
atmosphere.  It may also have to ward off the impact of a screen of pro-
jectiles intercepting its path.

## TEST APPARATUS



Figure 1

## BASIC TYPES OF IMPACT
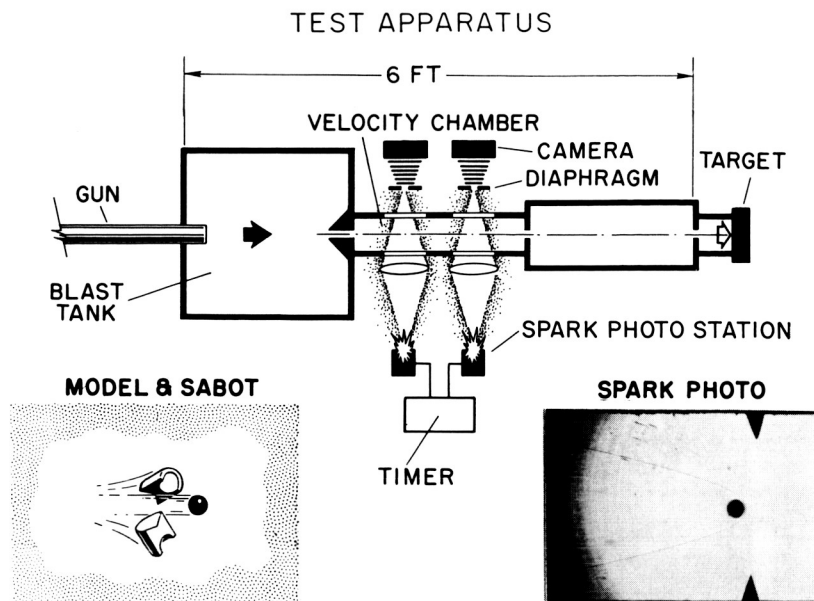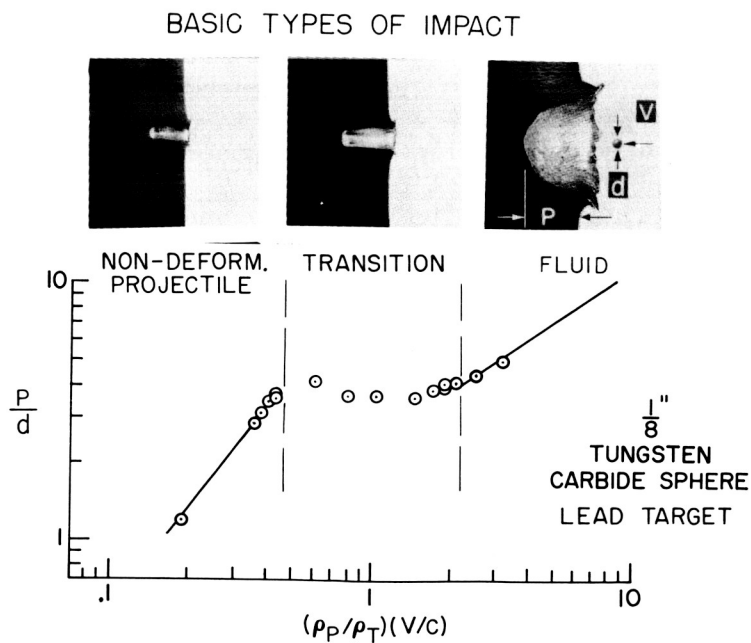


Figure 2

## CAVITY PLATING FROM IMPACT OF LEAD SPHERE ON COPPER TARGET
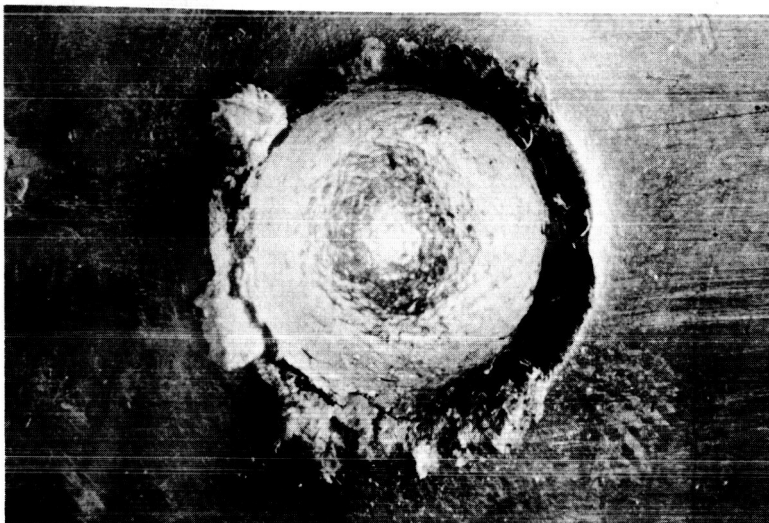


Figure 3

## CAVITY PLATING FROM IMPACT OF STEEL SPHERE ON COPPER TARGET



Figure 4

CAVITIES FROM IMPACTS OF LEAD SPHERES ON LEAD TARGETS AND COPPER SPHERES ON COPPER TARGETS

Figure 5



PENETRATION VS IMPACT MACH NUMBER FOR LEAD INTO LEAD AND COPPER INTO COPPER

□ LEAD (c = 4,025 FT/SEC)
△ COPPER (c = 11,670 FT/SEC)
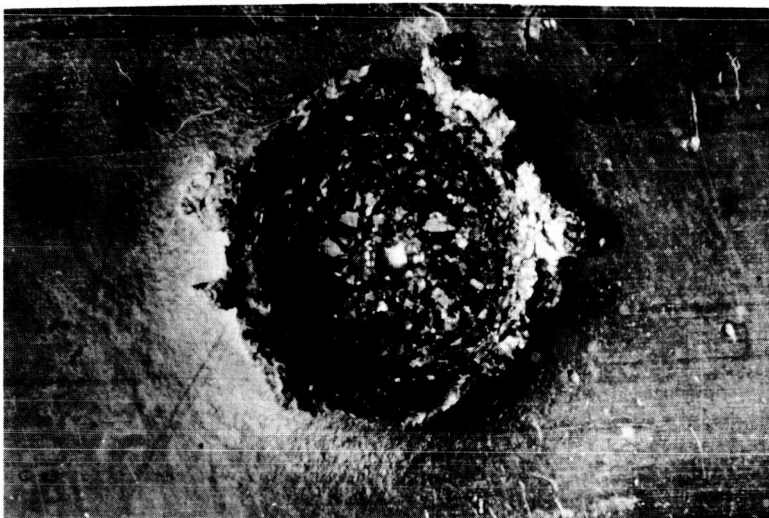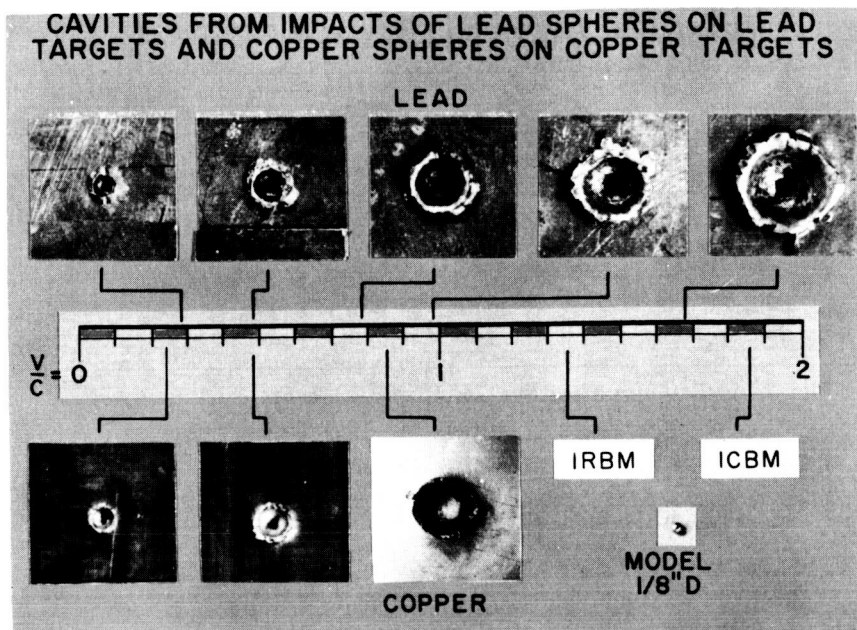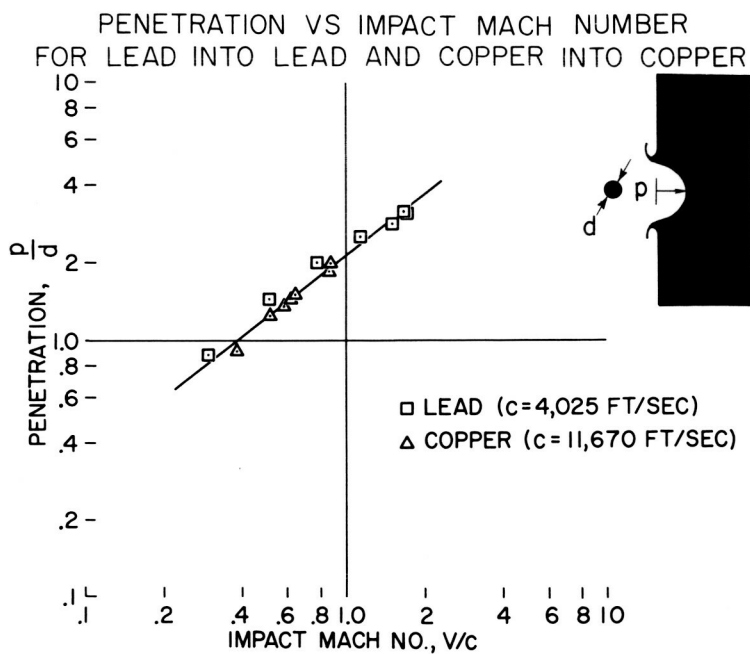
Figure 6

PENETRATION VS DENSITY FOR SPHERES
HAVING CONSTANT MASS AND IMPACT VELOCITY

COPPER

STEEL — LEAD

ALUMINUM —

Mg ALLOY —

TUNGSTEN

Pb TARGET —

PENETRATION, P (INCHES)

Cu TARGET —

V = 7000 FT/SEC
SPHERE WEIGHT
.130g

PROJECTILE DENSITY, $\rho_P$ (LBS/INCH$^3$)
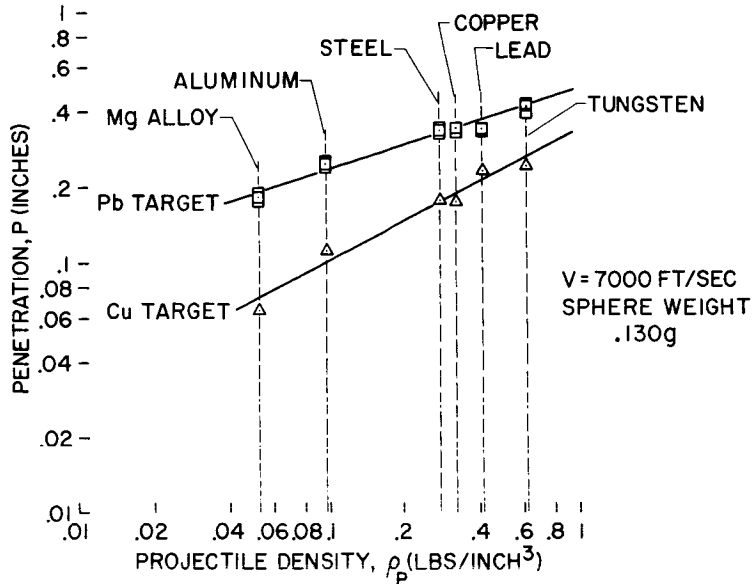
Figure 7

PENETRATION VS IMPACT PARAMETER

$$P/d = 2.28 \left(\frac{\rho_P}{\rho_T}\right)^{.69} \left(\frac{V}{c}\right)^{.69}$$

c = 4,025 FT/SEC Pb

c = 11,670 FT/SEC Cu

P/d

| TARGET | | TEST |
|---|---|---|
| Pb | Cu | |
| △ | △ | d, m CONST |
| ○ | ○ | V, d CONST |
| □ | □ | V, m CONST |

$$\left(\frac{\rho_P}{\rho_T}\right)\left(\frac{V}{c}\right)$$
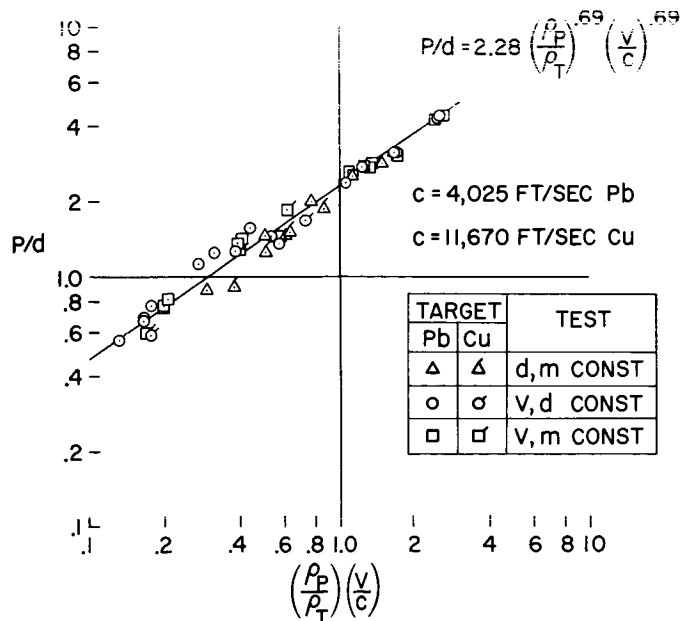
Figure 8

Figure 9



Figure 10

# EFFECTS OF SURFACE ROUGHNESS ON TRANSITION

By Albert L. Braslow and Elmer A. Horton

Langley Aeronautical Laboratory

## INTRODUCTION

It is known, at least qualitatively, how such factors as pressure gradients and leading-edge sweep influence the ability to maintain laminar flow over smooth configurations. If, after a study of such effects, laminar flow still appears possible, the next hurdle to be overcome is the adverse effect of surface roughness on transition. This paper will review recent results obtained at supersonic speeds as well as subsonic on the size of roughness required to promote premature transition.

## DISCUSSION

For discrete particles of roughness, that is, particles of a three-dimensional nature such as sand grains or rivets or spattered bugs, a critical size has been found to exist below which the roughness has no influence on the natural transition and above which the roughness causes premature transition. This is shown in figure 1 by means of several observations of the variation of streamwise boundary-layer velocity fluctuations with time. These measurements were made with the use of a hot-wire anemometer on a $10^O$ included-angle cone at a Mach number of 2.01 in the Langley 4- by 4-foot supersonic pressure tunnel.

In figure 1 the vertical location of the trace indicates the corresponding Reynolds number per foot of the stream. The left group of traces was obtained through a Reynolds number range for a smooth cone. The bottom trace indicates completely laminar flow. The next higher trace indicates occasional bursts of turbulent flow. The next higher indicates laminar flow a small part of the time, and the top one, fully turbulent flow. All traces were made with the hot wire at the same location. This change in the character of the boundary layer with changes in Reynolds number is consistent with the concept of the origin of turbulence as turbulent spots of the type shown by Schubauer and Klebanoff (ref. 1) for subsonic speeds. A recent investigation at the Ames Laboratory (ref. 2) verifies the existence of turbulent spots at supersonic speeds.

In the upper right part of the figure are shown hot-wire traces taken behind some granular roughness on the cone. This roughness was 0.003 inch high but had no effect on the natural transition as seen by the fact that the turbulence was initiated at the same value of stream unit Reynolds number. In contrast, the traces in the lower right part of the figure, taken behind a larger size roughness, show a large reduction in stream unit Reynolds number for the initiation of turbulence. This comparison clearly indicates that a critical size of three-dimensional roughness does exist.

With measurements of this kind, a criterion has been determined with which the size of roughness required to cause transition can be predicted. This critical size of three-dimensional roughness has been correlated on the basis of a critical local roughness Reynolds number similar to that used previously at subsonic speeds (ref. 3).

The critical roughness Reynolds number $R_{k,t}$ was formed with the height of the particle and the local flow conditions existing at the top of the particle when the particle began to introduce turbulent spots into the boundary layer. It should be remembered that at supersonic speeds, there are large variations in kinematic viscosity through the boundary layer due to the temperature distribution; therefore, in order to reduce the effect of Mach number on the roughness Reynolds number, local values of density and viscosity at the top of the particle were used as well as the velocity at the particle height (fig. 2). Results are presented for various sizes of granular-type roughness located at various distances from the model leading edge. The circular symbols represent data obtained on the $10^\circ$ cone at Mach numbers of 1.61 and 2.01 (ref. 4) and the square and diamond symbols represent an airfoil and a sphere tested at low speeds in the Langley low-turbulence pressure tunnel and the Langley full-scale tunnel, respectively. The square root of the roughness Reynolds number was chosen as the variable because this value is more nearly proportional to the critical projection height than is $R_{k,t}$. For supersonic Mach numbers as well as subsonic, the value of the critical roughness Reynolds number parameter is about constant for the granular roughness.

The effect of the geometry of the particle is shown in figure 3 in which $\sqrt{R_{k,t}}$ is plotted against the ratio $d/k$ of the particle width or diameter to the particle height. The circular symbols represent spherical roughness particles; the square symbols, granular particles; and the diamond symbols, surface craters with a raised rim around the circumference. For the craters, the overall diameter of the crater and not the width of the raised rim was used for the value of $d$ and the height of the raised rim above the undisturbed surface was used for the value of $k$. Some systematic variation is shown between $\sqrt{R_{k,t}}$ and $d/k$

which is similar to a trend previously obtained with cylindrical projections (ref. 5) where the cylinders resembling upright telephone poles, that is, small ratios of d to k, showed an increase in $\sqrt{R_{k,t}}$. For all shapes, it made no difference whether transition was initiated by an individual particle of roughness or by a group of particles.

The values of $\sqrt{R_{k,t}}$ shown in these two figures cover a 12-fold range in roughness height, a 30-fold range in distance from the model leading edge, a 30-fold range in the ratio of roughness width to height, variations in roughness shape, and a range of speeds from low subsonic to a Mach number of 2. The values of $\sqrt{R_{k,t}}$ vary from about 15 to 30, a correlation close enough to indicate the magnitude of a three-dimensional type of roughness necessary to cause transition within a factor of 2. With this parameter, it is also possible to determine the minimum size of three-dimensional roughness required to fix transition intentionally for model tests in which it is important to minimize the drag contribution of the roughness itself. More about this application will be found in a subsequent paper by Albert E. von Doenhoff.

Another point to be made is the fact that the existence of a fixed value of the critical local roughness Reynolds number is based on the concept of similar flows about the roughness. This condition is very nearly fulfilled for various ratios of roughness height to boundary-layer thickness if the roughness is well submerged in the boundary layer. For roughness protruding through the boundary layer, a constant value of $\sqrt{R_{k,t}}$ would not be expected. Observations at both subsonic and supersonic speeds for this condition have indicated that the critical roughness parameter is substantially greater.

In figure 4 is presented an indication of the magnitude of the critical size of roughness associated with the critical roughness Reynolds number parameter. An example is given of the maximum roughness size permissible for the maintenance of laminar flow for roughness located at various distances from the leading edge of a thin wing for flight at a Mach number of 3 at altitudes of 100,000 feet and 50,000 feet. At 100,000 feet, the permissible roughness height is of the order of 1/16 inch, certainly large enough to be easily found. At 50,000 feet, however, the allowable roughness is of the order of 0.010 inch, a height that would be difficult to detect on a large area with a reasonable degree of inspection. It should be emphasized that it is not the root-mean-square value of the surface roughness that determines the onset of transition due to roughness but rather the individual projections of maximum height. These tallest particles reach the critical value of roughness Reynolds number first. Because of a lateral spread of turbulence behind the roughness, a few strategically placed particles larger

than the root-mean-square roughness can cause turbulent flow over most of the surface for conditions where laminar flow might be expected if only the root-mean-square value were considered.

The possible effects of laminar boundary-layer stability on the critical roughness size are next considered. It is known that boundary-layer cooling, boundary-layer suction, and favorable pressure gradients have a stabilizing effect on the laminar layer for theoretically small disturbances. In a stable laminar layer, these theoretically small disturbances damp out as they move downstream and the extent of laminar flow over a smooth surface can be greater than for the unstable case. (The effectiveness of cooling and of continuous suction is shown in references 6 to 9 and 10, respectively.) In figure 5 are presented additional hot-wire traces behind three-dimensional roughness elements of finite size. The measurements were made in the Langley 4- by 4-foot supersonic pressure tunnel on a $10^0$ cone for a Mach number of 2.01 (fig. 5(a)) and in the Langley Unitary Plan wind tunnel at a Mach number of 4.21 (fig. 5(b)). In each figure, the left group of traces was made with the model surface at equilibrium temperature and the right group for the same surface roughness but with the model cooled. The wall-temperature distributions for the cooled model are shown in the upper right-hand corner. At both Mach numbers, the wall temperature varied from almost stagnation temperature near the cone apex to about $-50^0$ F ahead of the roughness.

It is clearly demonstrated that for the stream unit Reynolds number at which the roughness was just critical, that is, when turbulent spots began to appear with the surface at equilibrium temperature, cooling the cone surface resulted in a completely turbulent boundary layer. In fact, for the cooled condition, it was necessary to decrease appreciably the stream unit Reynolds number in order to return the boundary layer to the laminar condition. Associated with the surface cooling for given values of roughness size and location and stream Reynolds number and Mach number is an increase in the actual roughness Reynolds number $R_k$ caused by (1) an increase in velocity at the top of the particle due to a thinning of the boundary layer and an increase in convexity of the velocity profile and (2) an increase in local density and a decrease in local viscosity due to the lowered boundary-layer temperature. The fact that transition resulted from this increase in roughness Reynolds number indicates that the critical value of roughness Reynolds number was not increased to any important extent by the theoretical increase in laminar boundary-layer stability resulting from the surface cooling. This conclusion is verified with the aid of figure 6. The circular symbols represent values of the roughness parameter $\sqrt{R_{k,t}}$ for the cooled cone where the values are based on the cooled conditions at the top of the roughness. Comparison of these points with the circular symbols shown previously in figure 2 for the cone at equilibrium temperature shows that the values of

$\sqrt{R_{k,t}}$ are about the same for the surfaces whether warm or cooled. Also presented in figure 6 are values of the roughness parameter obtained with cylindrical roughness on an airfoil where the laminar layer was stabilized by means of continuous suction (ref. 11), as indicated by the square symbols. In addition, the diamond symbols represent values obtained with spherical roughness on the large sphere in the Langley full-scale tunnel where the laminar boundary layer was stable because of the favorable pressure gradient. For this large variety of conditions, an increase in laminar boundary-layer stability, whether by favorable pressure gradients, boundary-layer suction, or surface cooling, had very little effect on the roughness Reynolds number parameter for transition.

For two-dimensional roughness, such as spanwise ridges or grooves, however, laminar stability can have a beneficial effect on the allowable roughness. Recent evidence of this can be found in a paper by Van Driest and Boison (ref. 9) for the laminar layer made stable by means of surface cooling and, secondly, from some tests of spanwise wires on the large sphere where an increase in stability resulted from the favorable pressure gradient. This difference in the effect of laminar boundary-layer stability on the initiation of turbulence caused by two- or three-dimensional type roughness is associated with a basic difference in the triggering mechanism of turbulence for the two types of roughness. Hot-wire measurements have shown that for the three-dimensional roughness, the turbulent spots are initiated at the roughness when the local Reynolds number becomes critical. For two-dimensional roughness, turbulent spots are first noted at a rearward position with no turbulence forward and a further increase in Reynolds number is required to move the transition gradually forward. (For example, see ref. 12.) The disturbances produced by the two-dimensional roughness, therefore, appear to be of the Tollmein-Schlichting type and are subject to amplification theories during their movement downstream. For the three-dimensional roughness, however, transition is initiated directly at the roughness and the stability arguments are not applicable.

A final point to be made consists of the effect of laminar stability on the lateral spread of the turbulence behind a roughness particle. The lateral spread of turbulence was measured on the sphere behind roughness located at various positions, where the location determined the degree of stability due to the favorable pressure gradient. Measurements were also made on a flat plate where the stability was increased by surface cooling. In neither case did an increase in laminar boundary-layer stability have any appreciable effect on the spread of turbulence.

444

## CONCLUDING REMARKS

The transition-triggering mechanism of three-dimensional-type surface roughness appears to be the same at supersonic and subsonic speeds. In either case, the important parameter is a Reynolds number based on the height of the roughness and the local flow conditions at the top of the roughness. With a value of this roughness parameter $\sqrt{R_{k,t}}$ of about 22, it is possible to predict with reasonable accuracy the height of three-dimensional roughness required to cause transition. Neither the critical three-dimensional roughness Reynolds number nor the lateral spread of turbulence behind the roughness is changed to any important extent by increasing the laminar boundary-layer stability to theoretically small disturbances. Therefore, for a given stream Mach number and Reynolds number, surface cooling, boundary-layer suction, or a favorable pressure gradient will, in the presence of roughness, promote rather than delay transition. A favorable effect of stability on permissible two-dimensional-type disturbances, however, is possible.

# REFERENCES

1. Schubauer, G. B., and Klebanoff, P. S.: Contributions on the Mechanics of Boundary-Layer Transition. NACA Rep. 1289, 1956. (Supersedes NACA TN 3489.)

2. James, Carlton S.: Observations of Turbulent Burst Geometry and Growth in Supersonic Flow. NACA TN 4235, 1958. (Prospective NACA paper.)

3. Von Doenhoff, Albert E., and Horton, Elmer A.: A Low-Speed Experimental Investigation of the Effect of a Sandpaper Type of Roughness on Boundary-Layer Transition. NACA TN 3858 (Corrected copy), 1956.

4. Braslow, Albert L.: Effect of Distributed Granular-Type Roughness on Boundary-Layer Transition at Supersonic Speeds With and Without Surface Cooling. NACA RM L58A17, 1958.

5. Loftin, Laurence K., Jr.: Effects of Specific Types of Surface Roughness on Boundary-Layer Transition. NACA WR L-58, 1946. (Formerly NACA ACR L5J29a.)

6. Diaconis, N. S., Jack, John R., and Wisniewski, Richard J.: Boundary-Layer Transition at Mach 3.12 as Affected by Cooling and Nose Blunting. NACA TN 3928, 1957.

7. Diaconis, N. S., Wisniewski, Richard J., and Jack, John R.: Heat Transfer and Boundary-Layer Transition on Two Blunt Bodies at Mach Number 3.12. NACA TN 4099, 1957.

8. Czarnecki, K. R., and Sinclair, Archibald R.: An Investigation of the Effects of Heat Transfer on Boundary-Layer Transition on a Parabolic Body of Revolution (NACA RM-10) at a Mach Number of 1.61. NACA Rep. 1240, 1955. (Supersedes NACA TN's 3165 and 3166.)

9. Van Driest, E. R., and Boison, J. Christopher: Experiments on Boundary-Layer Transition at Supersonic Speeds. Jour. Aero. Sci., vol. 24, no. 12, Dec. 1947, pp. 885-899.

10. Braslow, Albert L., Burrows, Dale L., Tetervin, Neal, and Visconti, Fioravante: Experimental and Theoretical Studies of Area Suction for the Control of the Laminar Boundary Layer on an NACA 64A010 Airfoil. NACA Rep. 1025, 1951. (Supersedes NACA TN 1905 by Burrows, Braslow, and Tetervin and NACA TN 2112 by Braslow and Visconti.)

11. Schwartzberg, Milton A., and Braslow, Albert L.: Experimental Study of the Effects of Finite Surface Disturbances and Angle of Attack on the Laminar Boundary Layer of an NACA 64A010 Airfoil With Area Suction. NACA TN 2796, 1952.

12. Dryden, Hugh L.: Review of Published Data on the Effect of Roughness on Transition From Laminar to Turbulent Flow. Jour. Aero. Sci., vol. 20, no. 7, July 1953, pp. 477-482.

## HOT-WIRE MEASUREMENTS IN BOUNDARY LAYER
### EFFECT OF GRANULAR ROUGHNESS ON TRANSITION R; M=2.01
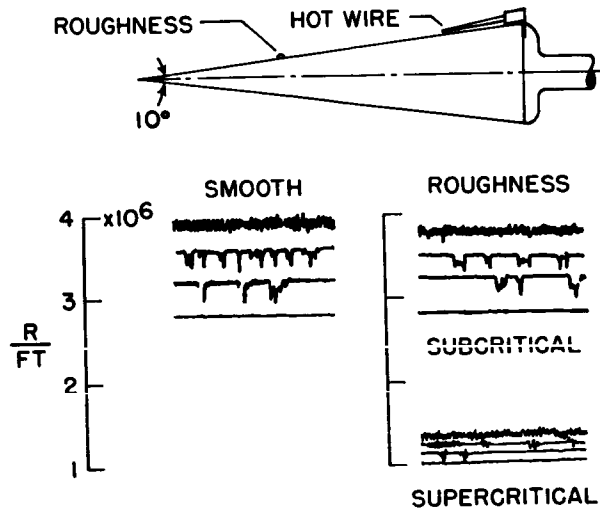


Figure 1

## ROUGHNESS REYNOLDS NUMBER PARAMETER
## AS FUNCTION OF CONFIGURATION VARIABLES
### GRANULAR ROUGHNESS

| ROUGHNESS HEIGHT, k, IN. | CONFIG. | M |
|---|---|---|
| O  0.005 - 0.023 | 10° CONE | 1.61, 2.01 |
| □   .009 - .018 | AIRFOIL | 0.10 |
| ◇   .020 - .062 | SPHERE | 0.10 |



ROUGHNESS LOCATION FROM L.E., IN.

Figure 2

448
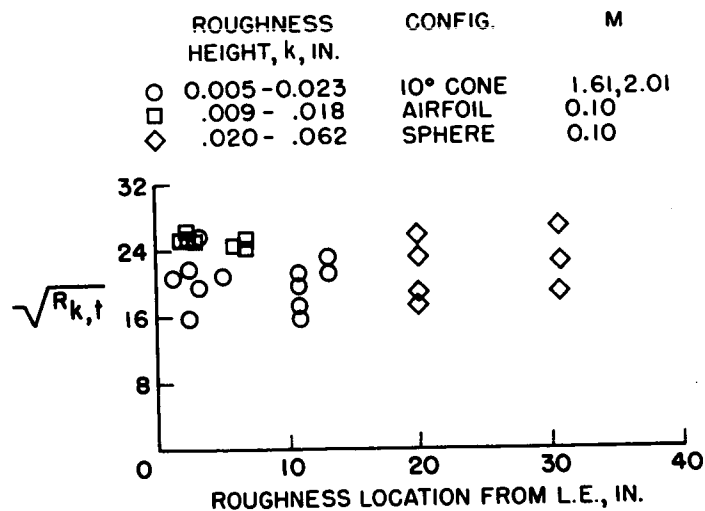
ROUGHNESS REYNOLDS NUMBER PARAMETER
AS FUNCTION OF ROUGHNESS GEOMETRY
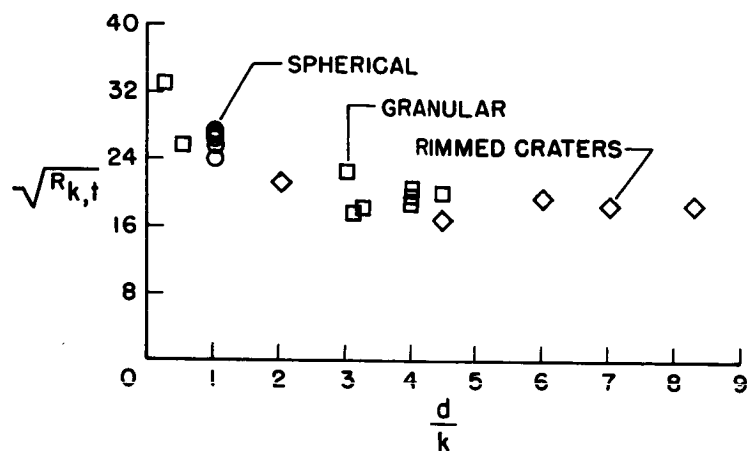


Figure 3

EXAMPLE OF MAXIMUM ROUGHNESS HEIGHT
PERMISSIBLE FOR LAMINAR FLOW
M = 3
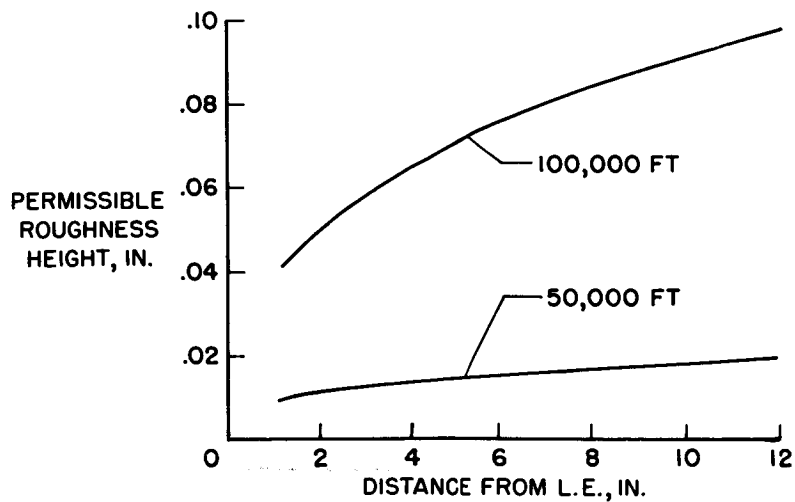


Figure 4

## HOT-WIRE MEASUREMENTS BEHIND ROUGHNESS
### EFFECT OF SURFACE COOLING ON TRANSITION R; M=2.0l
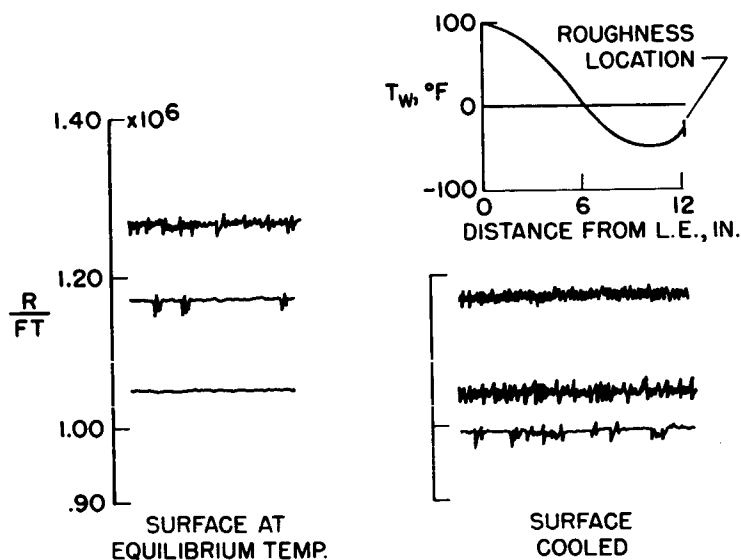


Figure 5(a)

## HOT-WIRE MEASUREMENTS BEHIND ROUGHNESS
### EFFECT OF SURFACE COOLING ON TRANSITION R; M=4.2l
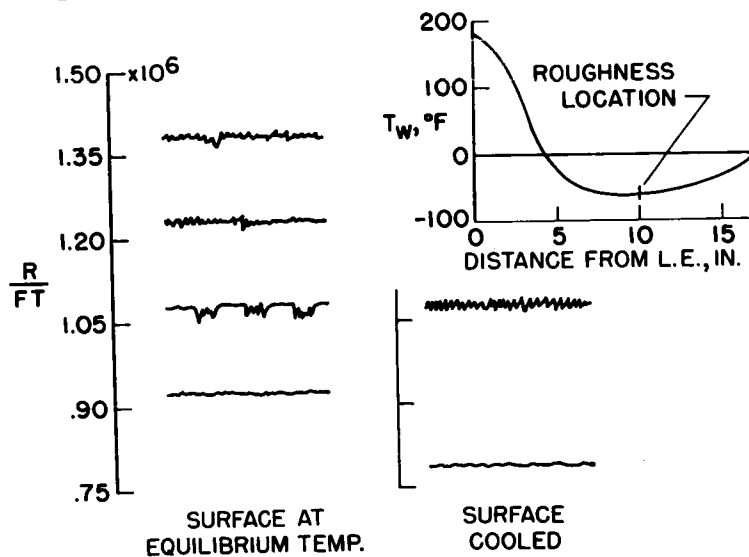


Figure 5(b)

ROUGHNESS REYNOLDS NUMBER PARAMETER AS AFFECTED
BY LAMINAR-BOUNDARY-LAYER STABILITY

| | ROUGHNESS HEIGHT, k, IN. | CONFIG. | ROUGHNESS TYPE | M |
|---|---|---|---|---|
| COOLING | | | | |
| CONTINUOUS SUCTION | | | | |
| FAVORABLE ○ | 0.010-0.019 | 10° CONE | GRANULAR | 1.61,2.01 |
| PRESSURE □ | .004- .012 | AIRFOIL | CYLINDRICAL | .10 |
| GRADIENT ◇ | .015- .062 | SPHERE | SPHERICAL | .10 |
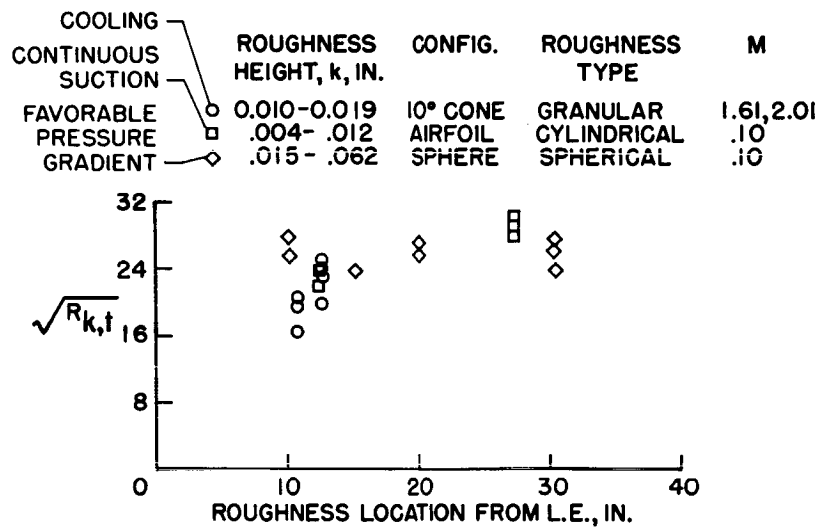


Figure 6

# THE PROSPECTS FOR LAMINAR FLOW ON HYPERSONIC AIRPLANES

By Alvin Seiff

Ames Aeronautical Laboratory

## FACTORS AFFECTING EXTENT OF LAMINAR FLOW

Ordinarily, it is desired to obtain a maximum amount of laminar flow on airplanes for hypersonic flight in order to cut down the aerodynamic heat input and to improve aerodynamic efficiency. If an attempt is made to determine where boundary-layer transition will occur on a complete airplane, a number of factors are considered, some of which are listed in figure 1. An airplane which has the highly swept and blunt-leading-edge airfoil which is required for aerodynamic efficiency and control of the leading-edge temperatures is shown in this figure. The first factor listed is the Reynolds number which is well-known to be the most important factor. If the Reynolds number is exceptionally low, laminar flow will occur without regard for the other factors; conversely, if the Reynolds number is exceptionally high, fully turbulent flow will approximate what is obtained. In the intermediate region the extent of laminar flow depends on the other factors, and it is in this region of Reynolds number that hypersonic lifting flight can occur. The other factors listed are the ratio of wall temperature to boundary-layer recovery temperature, which is well-known to have important influence on transition and which will be treated in other papers of this volume; the surface roughness, which has been known to be important as long as boundary-layer transition has been known; angle of attack which affects the boundary layers on both wings and bodies but not necessarily in the same way; sweepback of the wing leading edge, which is known to have adverse effects on laminar stability; and aerodynamic interference. The configuration of figure 1 is chosen to be particularly bad from the standpoint of interference. The possibility of such effects as the discharge of a turbulent wake by the canard onto the surface of the wing, the crossing of the wing surface by the shock wave generated by the vertical tail, and the intersection of the leading-edge shock waves of all lifting surfaces onto the body boundary layer is noted. All these interactions might be expected to cause transition to occur at flight Reynolds numbers. An additional and general type of aerodynamic interference is the influence on the wing boundary layer of the pressure distribution generated by the body and vice versa.

Undoubtedly, other factors such as the pressure gradient, important parts of which are included in the category of aerodynamic interference, could be added to this list. The main point, however, is that all these factors must be considered if a rational attempt is to be made to maximize the laminar flow or to predict the extent of the laminar flow.

## SYMBOLS

$$C = \frac{\delta}{x} \sqrt{R}$$

$C_D$          drag coefficient

$C_{D_0}$      minimum drag coefficient

$C_L$          lift coefficient

d              maximum diameter

$l$            representative airplane length

M              Mach number

R              Reynolds number

$R_h$          roughness Reynolds number for two-dimensional roughness

$R_k$          roughness Reynolds number for three-dimensional roughness

T              temperature, $^O R$

u              velocity

$u_s$          satellite velocity

W/S            wing loading

x              longitudinal distance

$x_n$          nose length

$\alpha$       angle of attack

$\overline{\alpha_R{}^2}$   mean-square angle of attack for three-wing model

$\beta = \sqrt{M^2 - 1}$

$\delta$   boundary-layer thickness

$\theta$   body angular position

$\Lambda$   angle of sweep of leading edge

$\mu$   free-stream viscosity

$\rho$   airstream mass density

Subscripts:

e   boundary-layer edge

k   top of roughness

r   recovery

T   transition

w   wall

$\infty$   free stream

## DISCUSSION

Closer examination of the flight Reynolds number shows that it is largely determined by the wing loading and the flight speed as indicated by the equation presented in figure 2, which represents the fact that for equilibrium flight the aircraft weight must be counterbalanced by the sum of lift and centrifugal force due to the curvature of flight around the earth. A low value of the wing loading permits a high equilibrium altitude and, consequently, a low Reynolds number. Similarly, as the speed becomes appreciable compared with satellite velocity, less aerodynamic lift is required and the altitude is again permitted to increase. The result is that the flight Reynolds number decreases with increase in flight speed. For a wing loading of 25 pounds per square foot and an airplane 50 feet long, the Reynolds numbers based on length are moderate and range from $15 \times 10^6$ at a Mach number of 4 to $7 \times 10^6$ at a Mach number of 20. This result indicates that full-scale hypersonic flight can occur in a region of Reynolds number where laminar flow has

been observed in flight tests and in wind tunnels. It should be noted, however, that, by doubling the wing loading and the length, Reynolds numbers four times as great as those shown were obtained and therefore are considerably less desirable.

How smooth must an airplane surface be in order to give laminar flow at flight conditions such as those of figure 2? Subsonic experience was that the surfaces had to be exceedingly smooth to permit much laminar flow at flight conditions. In order to indicate whether this will be the case at high supersonic speeds as well, available data on critical roughness are shown in figure 3 as a function of Mach number at the boundary-layer edge. Data from references 1 to 3 on three-dimensional roughness, such as would be given by sandpaper or carborundum grains on the surface or sandblasting of the surface, are shown in figure 3(a) and are correlated by using the Reynolds number based on roughness height and local properties in the boundary layer at the top of the roughness elements. Data from reference 4 for distributed two-dimensional roughness in the form of transverse grooves are presented in figure 3(b) in terms of the Reynolds number based on roughness height and air properties outside the boundary layer divided by the parameter C $(C = (\delta/x)\sqrt{R})$ which is constant on the surface of a flat plate and indicates the effect of Mach number and wall temperature ratio on the boundary-layer growth rate. This latter type of correlation for distributed roughness has been discussed in reference 5. However, the present purpose is not to enter into detailed discussion of methods of correlating roughness effect but rather to point out the trend common to figures 3(a) and 3(b), namely, a large increase in permissible roughness with increasing boundary-layer-edge Mach number. Since figure 3(a) is based on local properties inside the boundary layer for a constant external-flow Reynolds number, there will be a further effect of Mach number on the permissible three-dimensional roughness, as indicated by the equation

$$\frac{R_e}{R_k} = \left(\frac{u_e}{u_k}\right)\left(\frac{T_e}{T_k}\right)^{1.7}$$

where the subscript e identifies properties at the boundary-layer edge and the subscript k identifies properties at the top of the roughness. As the Mach number increases, $T_k$ increases and, as a result, the permissible three-dimensional roughness increases with Mach number at a rate faster than is indicated in the figure. As an example, the permissible heights of distributed roughness at a Mach number of 7 for the flight conditions of figure 2 are predicted to be greater than 0.2 inch for both two- and three-dimensional roughness.

Another factor which can lead to early occurrence of transition, at least for the case of slender bodies of revolution, is angle of attack. Figure 4, which is taken from reference 6, shows data for the sheltered side of a slender body at angle of attack, the windward side remaining laminar in this case over the entire range. The position at which transition occurred is plotted against the angle of attack in degrees. As the angle goes above about $0.5^\circ$, transition comes onto the body at about 27 calibers from the nose and moves forward progressively with increasing angle. This effect is probably a result of transverse pressure gradients on the body which cause the boundary-layer profiles to become three-dimensional, a situation similar to that which occurs on sweptback wings. The curves shown in figure 4 were obtained from the assumption that transition occurs at a fixed angular position on the sheltered side of the cylindrical cross section and, if the assumed angular positions of $120^\circ$ and $180^\circ$ are taken, the observed points are bracketed. These curves provide a basis for extrapolating the data to higher angles of attack. Of course, the presence of wings on the body would tend to modify the effect and might, in fact, help to suppress it, since the wings act like boundary-layer fences and tend to prevent the body crossflow which leads to transition. At any rate, the adverse effect of angle of attack on bodies should be held in mind.

Sweepback of the wing leading edge has been known to be adverse in subsonic flow since 1952, when flight tests and wind-tunnel tests made in England (for example, ref. 7) brought this to light. Subsonic data (unpublished) recently obtained by Boltz, Kenyon, and Allen in the Ames 12-foot pressure tunnel also show this adverse effect and are reproduced in figure 5. Whenever early transition due to sweep has been observed, there has also been observed on the surface a number of parallel lines or streaks with streamwise direction that were made visible by the use of subliming agents on the surface as in the photograph of figure 6. This photograph is a view of the bottom surface of the airfoil in the wind tunnel with the flow direction from left to right. The streaks develop on the airfoil in the laminar region and lead individually to separate wedges of turbulence. The white spanwise stripe on the airfoil was painted on the surface to indicate the chordwise station and was rubbed smooth. It does not influence this result as has been proved by many observations of the phenomenon in which these marks were absent. It was suspected very early that the streaks were traces of streamwise vortices in the boundary layer, and a rake survey of the transverse-flow components in the boundary made by Boltz confirms this.

It was first suggested by P. R. Owen and D. G. Randall of the Royal Aircraft Establishment, Farnborough, England, that the instability causing transition was due to the three-dimensionality of the boundary layer. Velocities in the transverse direction are induced by transverse pressure gradients present on the surface of even two-dimensional swept wings because of the spanwise "shearing" of the chordwise pressure distribution.

Owen and Randall noted that the transverse velocity profile contains an
inflection point near its outer edge and would therefore be unstable.
The instability leads initially to streamwise vortices and finally to
turbulence.  This hypothesis was given further weight by the analysis
of reference 8 which considered the stability of a boundary layer with
three-dimensional profiles when subjected to transverse periodic dis-
turbances and the instability was found to occur above a critical
Reynolds number.  It was found by Owen and Randall that the onset of
vortices on the subsonic airfoils occurred when the Reynolds number,
based on the maximum value of the transverse velocity component and the
boundary-layer thickness, exceeded a critical value of 125.  For the
particular airfoils of these subsonic tests, this Reynolds number was
found to vary approximately with the square root of the chord Reynolds
number and the square root of the nose radius.  At values of 130 to 190,
transition occurred near the leading edge.  In tests in the Ames 12-foot
pressure tunnel, transition near the leading edge occurs at a value of
about 170 and is in agreement with the British results.

From the explanation of Owen and Randall, it might be expected that
sweep would continue to destabilize the boundary layer at supersonic
speeds.  There is, however, no indication from presently available theory
as to the effect that compressibility and heat transfer might have on
the stability of supersonic boundary layers to this type of disturbance.
The data which are shown in figure 7, however, indicate end results gen-
erally similar to those of the subsonic tests.  It might be expected that
a way of combating this instability is to choose wings of constant sur-
face pressure so that no transverse pressure gradients exist.  This type
of pressure distribution is obtained on triangular wings with wedge sec-
tions and sharp leading edges when the flow component normal to the leading
edge is supersonic.  Tests at this condition were made by Dunning and
Ulmann (ref. 9) at a Mach number of 4 and are indicated in figure 7 by
the circles.  Surprisingly, an adverse effect of sweepback was still
obtained.  This effect might be due to the finite thickness of the leading
edge which is necessarily present in experimental models so that in the
vicinity of the leading edge the flow is three-dimensional; or, it might
be a result of some other factors of an as yet unknown character present
in the tests.  When the wing section in these tests was changed to a sub-
sonic wing section so that pressure-distribution effects were introduced,
the effect of sweepback became more pronounced and thus is consistent
with the hypothesis of Owen and Randall.  A test on a triangular wing
with 74° sweepback (unpublished) was made in the Ames supersonic free-
flight tunnel, again using a relatively flat wing section.  The leading
edge was made blunt intentionally to simulate a leading-edge thickness
of 1.8 inches at a full-scale length of 50 feet.  The result obtained,
when compared with an earlier datum point for a body of revolution, shows
a somewhat similar trend to that obtained on the wedge-section wings in
the wind-tunnel test except at a higher level of Reynolds number.  This
increase in transition Reynolds number can be attributed to the reduced

wall temperature ratio and the reduction in stream turbulence for the flight test.

The effect of a cylindrical leading edge on the transition due to sweepback has been investigated (ref. 10 and recent unpublished data). The results obtained from tests of yawed circular cylinders are shown as diamond symbols in figure 7. The Reynolds number for transition at the stagnation line has been reduced from over $4 \times 10^6$ at zero sweep to the order of $2 \times 10^5$ at $40^\circ$ of sweepback, based on free-stream properties and diameter, although the data do not indicate definitely the level of the curve at the higher angles of sweepback. However, Feller, from tests at a Mach number of 6.9, has found that the cylinder flow was fully laminar at a Reynolds number of $1.3 \times 10^5$. (See ref. 11.) For the flight Reynolds numbers shown in figure 2, these results would imply turbulent flow only for leading edges larger than about 1 foot diameter. The instabilities generated on smaller leading edges, although they do not cause transition on the leading edge, might cause early transition back on the wing. This possibility will require further investigation.

Owen and Randall's transition criterion has not been evaluated for these supersonic data. To do so requires lengthy calculations of the twisted velocity profiles. In one supersonic experiment for a Mach number of 1.6 (ref. 12), the transverse critical Reynolds number was found to be smaller than that at subsonic speeds. The promising correlation obtained subsonically makes it appear to be well worthwhile to make further calculations of this kind for supersonic experiments.

If the complete configurations are again considered and one is selected which offers some opportunity for maximizing the laminar flow, it might look like the three-wing design (ref. 13) which is shown in figure 8. This arrangement, which has the wing, vertical tail, and fuselage originating at a common point, avoids having shock waves or wakes cross any surface. In addition, the full-length wing panels might be expected to suppress the crossflow effects and transition due to angle of attack. The wing leading edges are swept back $74^\circ$, and the wing surfaces are flat in order to avoid transverse pressure gradients. However, the pressure field due to the body nose induces a transverse pressure variation onto the surface of the wings and the leading edge of the wing is extremely blunt. This bluntness corresponds to a thickness of 3 inches at a full-scale length of 50 feet. Thus, three-dimensionality has been introduced into the boundary layer. (The high degree of bluntness was required to permit gun-launching the models without incurring buckling failure of the leading edge.)

Models of this design were tested in the Ames supersonic free-flight tunnel at a Mach number of 6 and a ratio of wall temperature to recovery temperature of 0.25. Since the boundary-layer condition could not be

visually observed by any available technique, it was decided to obtain information on the amount of laminar flow from drag measurements. The data were collected in the manner shown in figure 8, the mean-square angle of attack being used as the independent variable in order to correlate the variations in drag due to lift. In this presentation, the measurements for a constant boundary-layer condition should lie along a straight line through $C_{D_0}$ with a slope equal to the lift-curve slope; two such lines are shown, $C_{D_0}$ being calculated for all laminar boundary layers and all turbulent boundary layers. The experimental points obtained may be compared with these two lines.

The models were tested with various degrees of surface roughness, as noted in the key to figure 8. The purpose of this was twofold: One class of surfaces, indicated by the solid symbols, was made very rough in order to generate an all-turbulent boundary layer to establish the accuracy of the theoretical drag curve. These models had scratches 600 microinches deep (corresponding to 1/8 inch deep on the 50-foot airplane) and the scratches were applied particularly across the face of the leading edge with the thought that these scratches would be effective in causing immediate transition. The results obtained fell along the turbulent line in a very satisfactory fashion. The other models, the open symbols, had surface roughnesses which were well below the critical values indicated by figure 3, and the roughness was varied in this region to determine whether corresponding variations in drag would be observed. Within the scatter, no dependence of the drag on smoothness was observed. The roughest of these surfaces would correspond to a surface covered with broad scratches 1/32 inch deep at full scale.

The open symbols, with the exception of one point, define a line roughly parallel to the theoretical lines at a level about one-fourth to one-third of the way between the laminar and turbulent lines. This result indicates that the boundary layer is laminar over two-thirds to three-fourths of the model surface. Figure 7 showed, for the case of a $74^\circ$ swept wing alone in the same test facility, a transition Reynolds number of $3.3 \times 10^6$. If transition is assumed to occur on the airplane model at this value of the Reynolds number at all spanwise stations, there results a triangular area of turbulent flow of about one-half the length of the model, and therefore of about one-fourth the wetted area; thus three-fourths of the wetted area is laminar. The present result with the airplane model is therefore consistent with the result for the wing alone (fig. 7). This correspondence of the two results would imply that there are no seriously unfavorable effects of configuration on the airplane as tested compared with the wing alone. It also appears that in both cases sweepback was the predominant factor leading to transition. The effect of angle of attack, at least for the angles represented on the figure which range up to $6.5^\circ$ root mean square, was evidently small or compensating on opposite surfaces of the model; thus, if transition

moved forward on one surface, it moved back on the opposite surface and led to the same mean value of the minimum drag coefficient.

At higher Reynolds numbers, the results indicated in figure 9 were obtained. As would be expected, at Reynolds numbers between $12 \times 10^6$ and $13 \times 10^6$, the measured drag was closer to the turbulent curve and corresponded to laminar boundary layer on perhaps 45 percent of the surface. This condition continues to correspond to transition at a streamwise Reynolds number of $3.3 \times 10^6$.

## CONCLUDING REMARKS

In conclusion, some of the factors which must be considered in relation to boundary-layer transition on hypersonic airplanes have been reviewed. It appears that the Reynolds numbers for full-scale flight will be moderate, for vehicles of the size of fighter aircraft, if low wing loadings are employed. Roughness effects give promise of being much less severe than those in lower speed flight; however, this statement does not mean that roughness can be ignored altogether as a factor at hypersonic speeds. Angle of attack and aerodynamic interference effects are of sufficient importance to warrant attention in designs which seek to obtain the maximum extent of laminar flow. The principal deterrent to fully laminar flow is the adverse effect of sweepback of the wing leading edge. Up to the present time, transition has been observed to occur at Reynolds numbers no higher than $3.3 \times 10^6$ on a $74^\circ$ swept wing with a blunt leading edge at a Mach number of 6 under temperature conditions similar to those of flight. This condition was sufficient to give a laminar boundary layer on from one-half to three-fourths of the model surface at flight Reynolds numbers (for a wing loading of 25 pounds per square foot). The effect on this result of further refinements in design cannot be foretold inasmuch as transition due to sweepback is only beginning to be understood. Further changes in the results might also be anticipated from increasing the Mach number well above 6 and correspondingly reducing the ratio of wall temperature to recovery temperature. These possibilities must await further study.

REFERENCES

1. Von Doenhoff, Albert E., and Horton, Elmer A.:  A Low-Speed Experimental Investigation of the Effect of a Sandpaper Type of Roughness on Boundary-Layer Transition.  NACA TN 3858 (corrected copy), 1956.

2. Braslow, Albert L.:  Effect of Distributed Granular-Type Roughness on Boundary-Layer Transition at Supersonic Speeds With and Without Surface Cooling.  NACA RM L58A17, 1958.

3. Carros, Robert J.:  Effect of Mach Number on Boundary-Layer Transition in the Presence of Pressure Rise and Surface Roughness on an Ogive-Cylinder Body With Cold Wall Conditions.  NACA RM A56B15, 1956.

4. Seiff, Alvin:  A Review of Recent Information on Boundary-Layer Transition at Supersonic Speeds.  NACA RM A55L21, 1956.

5. Seiff, Alvin, Sommer, Simon C., and Canning, Thomas N.:  Some Experiments at High Supersonic Speeds on the Aerodynamic and Boundary-Layer Transition Characteristics of High-Drag Bodies of Revolution. NACA RM A56I05, 1957.

6. Jedlicka, James R., Wilkins, Max E., and Seiff, Alvin:  Experimental Determination of Boundary-Layer Transition on a Body of Revolution at  M = 3.5.  NACA TN 3342, 1954.

7. Gregory, N., and Walker, W. S.:  Brief Wind Tunnel Tests on the Effect of Sweep on Laminar Flow.  Rep. No. 14,928, British A.R.C., May 21, 1952.

8. Gregory, N., Stuart, J. T., and Walker, W. S.:  On the Stability of Three-Dimensional Boundary Layers With Application to the Flow Due to a Rotating Disk.  Phil. Trans. Roy. Soc. (London), Ser. A, vol. 248, no. 943, July 14, 1955, pp. 155-199.

9. Dunning, Robert W., and Ulmann, Edward F.:  Effects of Sweep and Angle of Attack on Boundary-Layer Transition on Wings at Mach Number 4.04.  NACA TN 3473, 1955.

10. Beckwith, Ivan E., and Gallagher, James J.:  Experimental Investigation of the Effect of Boundary-Layer Transition on the Average Heat Transfer to a Yawed Cylinder in Supersonic Flow.  NACA RM L56E09, 1956.

11. Feller, William V.: Investigation of Equilibrium Temperatures and Average Laminar Heat-Transfer Coefficients for the Front Half of Swept Circular Cylinders at a Mach Number of 6.9.  NACA RM L55F08a, 1955.

12. Scott-Wilson, J. B., and Capps, D. S.:  Wind Tunnel Observations of Boundary Layer Transition on Two Sweptback Wings at a Mach Number of 1.61.  Tech. Note Aero. 2347, British R.A.E., Dec. 1954.

13. Seiff, Alvin, and Allen, H. Julian:  Some Aspects of the Design of Hypersonic Boost-Glide Aircraft.  NACA RM A55E26, 1955.

FACTORS AFFECTING EXTENT OF LAMINAR FLOW
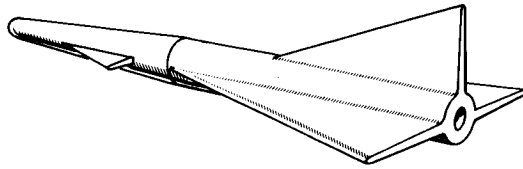


1. REYNOLDS NUMBER
2. WALL TEMP RATIO
3. ROUGHNESS
4. ANGLE OF ATTACK
5. SWEEPBACK
6. AERODYNAMIC
     INTERFERENCE

Figure 1

FLIGHT REYNOLDS NUMBERS OF HYPERSONIC AIRPLANE

$$\frac{\rho u l}{\mu} = \frac{21(W/S)(1-u^2/u_s^2)}{\mu C_L u}$$



$\frac{\rho u l}{\mu}$ MILLIONS

W/S = 25 LB/FT$^2$
$l$ = 50 FT
$C_L = \frac{4}{\beta} \times 0.1$

VELOCITY, FT/SEC

Figure 2

EFFECT OF MACH NO ON ALLOWABLE ROUGHNESS

3-DIMENSIONAL ROUGHNESS



⊙ VON DOENHOFF
△ BRASLOW
▫ CARROS
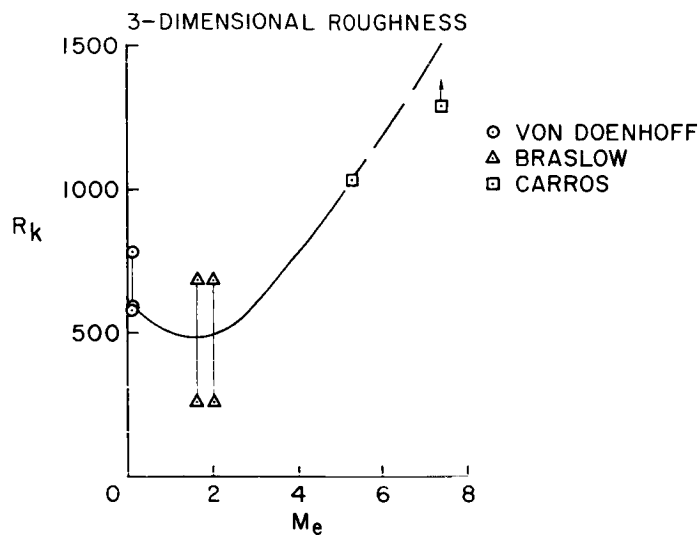
Figure 3(a)

EFFECT OF MACH NO ON ALLOWABLE ROUGHNESS

2 - DIMENSIONAL ROUGHNESS
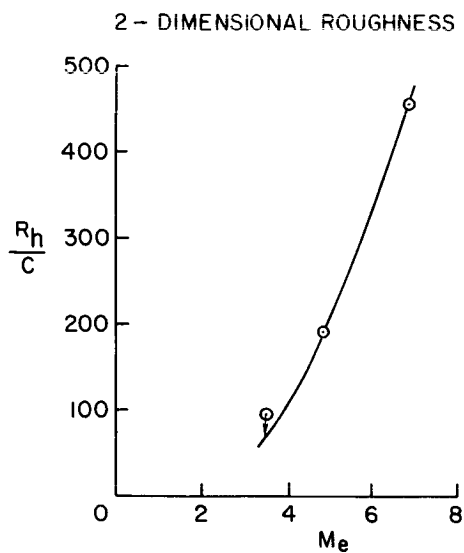


Figure 3(b)

SHELTERED-SIDE TRANSITION ON BODY
AT ANGLE OF ATTACK

$M = 3.5$
$R = 11 \times 10^6$

$\theta_T = 120°$   $= 180°$

$$\frac{x_T}{d} = \frac{x_n}{d} + \frac{\sin(\theta_T - 90)}{2\alpha}$$

$\alpha$, DEG
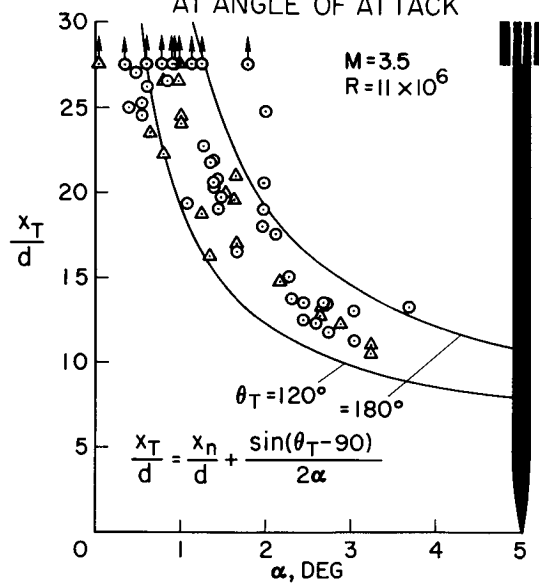
Figure 4

EFFECT OF SWEEPBACK, SUBSONIC DATA

$64_2$A015 AIRFOIL
AMES 12-FOOT W T

$R_T$, MILLIONS

$\alpha = 2°$, LOWER SURFACE

$\alpha = 0$

$\alpha = 2°$, UPPER SURFACE

$\Lambda$, DEG
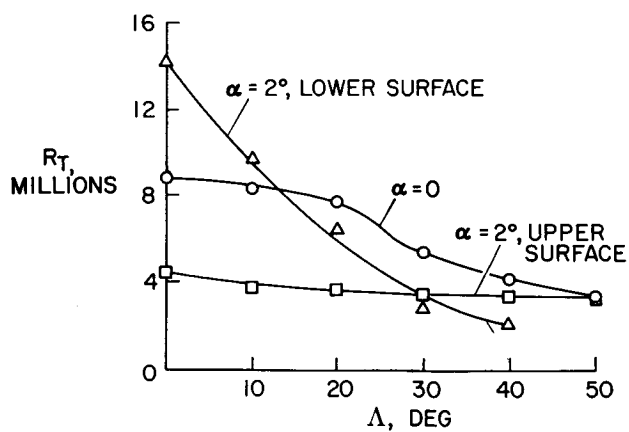
Figure 5

## TRANSITION PATTERN ON SUBSONIC AIRFOIL
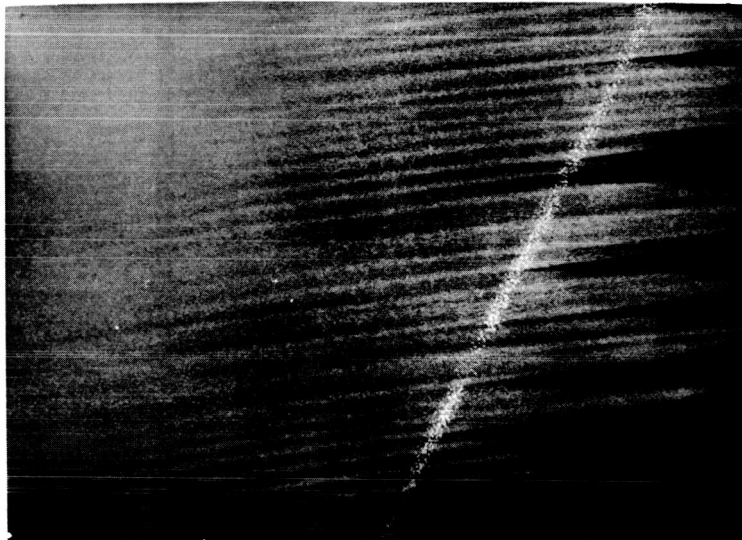


Figure 6
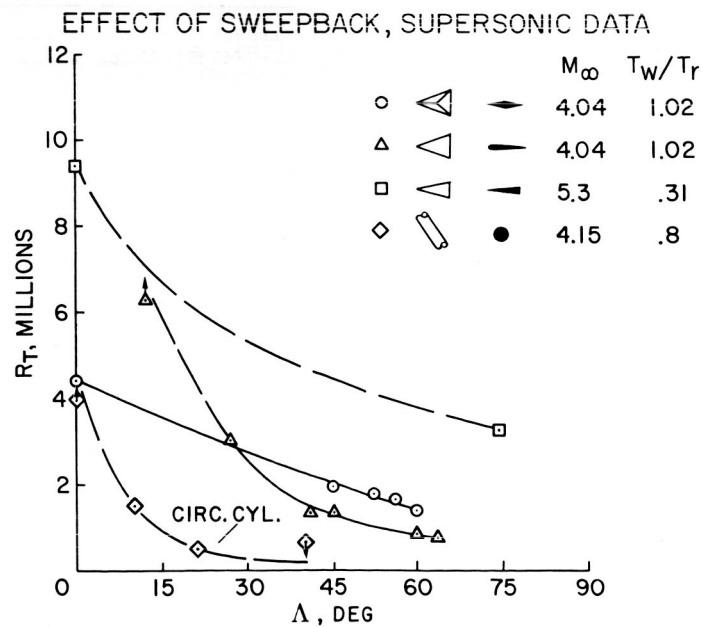


Figure 7

## COMPARISON OF DRAG MEASUREMENT WITH THEORY FOR 3-WING AIRPLANE MODEL

CALCULATED
TOTAL DRAG

TURBULENT

LAMINAR

$C_D$

M = 6
R = 5.7 TO 7.6 x 10$^6$

3"

○ BUMPS, < 5 $\mu$ INCH
△ SCRATCHES, 30 $\mu$ INCH
□       "       , 150 $\mu$ INCH
▼       "       , 600 $\mu$ INCH
◆ SCRATCHES, NOTCHED L.E.

$\overline{a_R}^2$, RAD$^2$
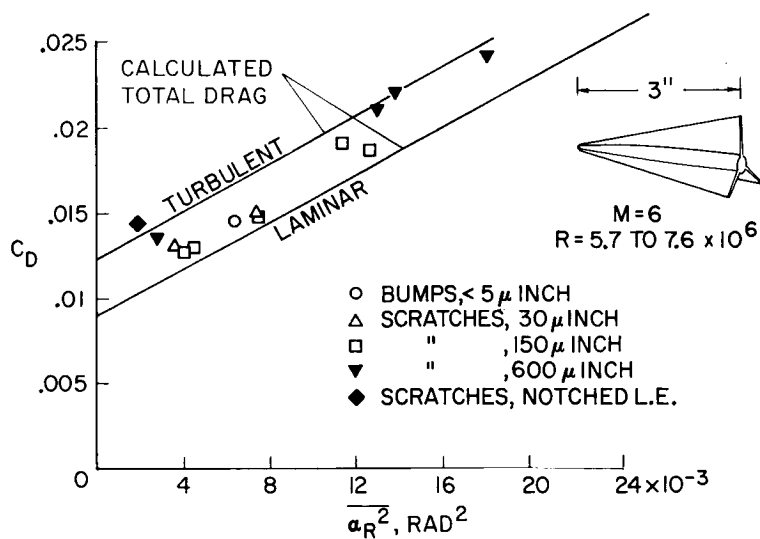
Figure 8

## VARIATION OF MINIMUM DRAG WITH REYNOLDS NUMBER

M = 6

$C_{D_0}$

TURBULENT

LAMINAR

REYNOLDS NUMBER, MILLIONS
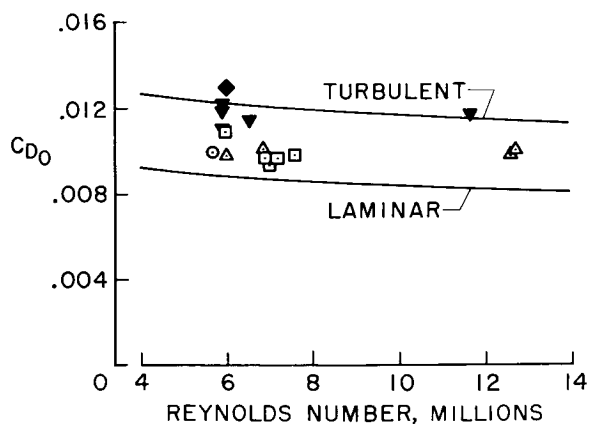
Figure 9

# BOUNDARY-LAYER TRANSITION IN FULL-SCALE FLIGHT

By Richard D. Banner, John G. McTigue,
and Gilbert Petty, Jr.

NACA High-Speed Flight Station

## INTRODUCTION

Because of the greatly increased need for knowledge of full-scale boundary-layer transition and the difficulty of simulating actual flight conditions, a program has been initiated to provide a better understanding of the boundary-layer flow as it exists in supersonic flight. This paper shows the results obtained in the early flight tests which determined the extent of laminar flow that could be obtained with practical wing-surface conditions.

## SYMBOLS

$R$       Reynolds number per foot, $V_\infty/\nu$, per ft

$V_\infty$       free-stream velocity, ft/sec

$\nu$       kinematic viscosity

$R_x$       nondimensional Reynolds number based on $x$

$x$       distance from leading edge

$\Lambda$       sweep angle

$\alpha$       angle of attack

$h_p$       altitude

$M$       Mach number

$\tau$       thickness, in.

## DISCUSSION

An F-104 airplane was instrumented, as shown in figure 1, for transition investigations on the wings. The basic wing has a modified biconvex airfoil with a thickness ratio of 3.4 percent, a sharp leading edge, and a slight amount of sweep (about $27^{\circ}$). A 1/10-inch-thick Fiberglas glove was installed on the right wing and was instrumented with one row of transition detectors on both the top and bottom surfaces. These detectors provided continuous monitoring of the laminar and turbulent boundary-layer-flow conditions (ref. 1).

Chemical sublimation was employed for boundary-layer-flow visualization on both wings, and cameras (fig. 1) were installed for recording the chemical indications. Many investigators have used the chemical sublimation technique in both wind tunnels and in flight (refs. 2, 3, and others). These tests have extended the use of this technique in flight to speeds near a Mach number of 2.0.

The transition-detector signals (see fig. 2) were multiplexed and recorded on an oscillograph. The sequencing was scheduled to conform to the locations of the detectors on the wing. This arrangement allowed location of the laminar and turbulent flow areas, within about 5 percent of the chord, by inspection of the records. The reasons for using flow visualization are illustrated in figure 2. Turbulent wedges, originating upstream of the detectors, cause local areas of turbulent flow. As can be seen, the third detector indicates turbulent flow in an area that would otherwise be laminar.

From the 35-millimeter flight film of the chemical indications, photographic enlargements have been made and a typical in-flight photograph of the lower surface of the Fiberglas covered wing is shown in figure 3. The white chemical remaining in the vicinity of the leading edge indicates the extent of laminar flow being experienced on the wing. The field of view of the camera includes the area of the wing from the leading edge rearward to just behind the aileron hinge in the outboard area and some of the inboard area of the wing. In all the tests no laminar flow had been observed in the inboard area, and for that reason this area is omitted in subsequent photographs of this presentation. The area shown is outboard of the 47-percent-exposed-span station.

In some cases the airplane returned from the flight with a chemical indication remaining on the wing. It will be of interest to look at one such indication before proceeding with the main part of the discussion. Figure 4 presents an enlargement of the leading-edge region of the wing. The section seen is about 1 square foot. Note the striations that can be seen in the chemical. Other investigators have also observed these striations in a laminar boundary layer, both in wind-tunnel tests (for

instance, Alvin Seiff's paper) and in flight (ref. 4) at subsonic speeds. The striations have been attributed to the presence of vortices which are shed from the swept leading edges and contribute to the breakdown of the normally laminar flow. Although it could not be determined when this phenomenon occurred during the flight, it is believed to be worth mentioning since it appears to be a problem that must be considered in determining the extent of laminar flow that could be expected on swept wings.

Turning now to the flight photographs that were taken during the tests, figure 5 shows the effect of the leading-edge-flap "piano type" hinge on producing transition. As can be seen, the hinge tripped the laminar boundary layer producing turbulent wedges which merge rearward of the hinge to form completely turbulent flow over the remainder of the wing. The laminar area is approximately 15 percent of the test area. This condition of the wing is referred to as unfinished. In improving the wing-surface conditions the flap hinge was filled to eliminate any abrupt discontinuities. Also, all rivetheads and screwheads were ground flush with the wing skin and filler material was applied to fill any pits or small depressions, and then the whole surface was sanded. This condition of the wing is referred to as the finished wing. Following the tests with the finished wing, the wing was painted and polished.

The effect of these improvements can be seen by comparing figure 6 with figure 5. Although the Mach number for the test with the painted wing is slightly different, the variation in the altitudes resulted in the same free-stream Reynolds number and the same angles of attack.

In comparing the unfinished and finished wing lower surfaces, it can be seen that considerably more laminar flow was obtained on the finished wing. This is primarily due to smoothing over the leading-edge-flap hinge. Painting the wing surface reduced the average roughness from about 25 to 13 microinches, but the effect on transition was not appreciable on either the top or bottom surface. The extent of laminar flow on the painted wing is about 25 percent of the test area for the upper surface and about 35 percent of the test area for the lower surface.

Realizing that the standards that had been set for roughness were rather arbitrary and that they might differ from those set in the wind tunnel, it was felt, nevertheless, that the maximum in practical improvements to the wing surface had been reached. The extent of laminar flow that was observed on the finished and painted wing is considered to be representative of the maximum that might reasonably be expected for these flight conditions. This conclusion was arrived at because the extreme care that was taken in producing the Fiberglas surface finish had resulted in an average roughness of only 7 microinches.

A comparison of the finished and painted wing and the Fiberglas covered wing is shown in figure 7. For clarity, the leading edges are all shown to the left. Covering the wing with Fiberglas had slightly altered the wing profile, and the leading edge had been rounded to 1/10-inch radius, instead of the sharp leading edge of the basic wing. Also, waviness measurements at 1/2-inch increments indicated an average deviation of about 0.003 inch on the Fiberglas covered wing as compared with 0.006 inch on the basic wing. Exactly what effect these changes produced locally could not be determined; however, as can be seen, no large differences in the overall extent of laminar flow is evidenced. In order to determine the effect of Mach number and altitude on the extent of laminar flow, the transition-detector installation on the Fiberglas covered wing was utilized.

Tests were conducted at speeds from a Mach number of 1.2 to a Mach number of 2.0 at altitudes from 35,000 to 56,000 feet. The free-stream Reynolds number varied from 1.3 to 4.3 $\times$ $10^6$ per foot. The maximum transition Reynolds numbers (based on free-stream conditions and the distance to the point of transition) that were obtained on the Fiberglas test area are shown in figure 8.

Data obtained at all angles of attack, from near $0^0$ to near $10^0$, have been used to construct the curves. As can be seen, the maximum transition Reynolds number on the top surface of the wing varied from about 2.5 $\times$ $10^6$ at a Mach number of 1.2 to about 4 $\times$ $10^6$ at a Mach number of 2.0. The trend on the lower surface is generally to more laminar flow, with the maximum transition Reynolds number varying from about 2 $\times$ $10^6$ at a Mach number of 1.2 to about 8 $\times$ $10^6$ at a Mach number of 2.0.

Although no attempt has yet been made to separate the effects of the variables that contribute to the results presented herein, the results are encouraging in that laminar flow has been obtained over extensive areas of a wing surface at supersonic speeds with practical wing-surface conditions.

CONCLUDING REMARK

Further flight testing should include investigations to determine what effects on the boundary layer are experienced when the leading edge is altered, when the angle of attack is varied, when shock-wave—boundary-layer interaction takes place, and when other factors enter the problem as important variables.

# REFERENCES

1. Richardson, Norman R., and Horton, Elmer A.: A Thermal System for Continuous Monitoring of Laminar and Turbulent Boundary-Layer Flows During Routine Flight. NACA TN 4108, 1957.

2. Main-Smith, J. D.: Chemical Solids as Diffusible Coating Films for Visual Indications of Boundary-Layer Transition in Air and Water. R. & M. No. 2755, British A.R.C., Feb. 1950.

3. Gray, W. E.: Visual Transition Tests in Flight on a Griffith Suction Wing, 16% Thick. Rep. No. Aero.2076, British R.A.E., Oct. 1950.

4. Owen, P. R., and Randall, D. G.: Boundary Layer Transition on a Sweptback Wing. Rep. No. Aero 277, British R.A.E., May 1952.

# F-I04 AIRPLANE – TRANSITION TEST AREAS

RADIUS = O.1"

DETECTORS
(TOP & BOTTOM)

FIBERGLAS ($\tau$ = O.1)

I"

CAMERA LOCATIONS
(TOP & BOTTOM)

$\Lambda$ = 26.9

SHARP

PRODUCTION WING

I"
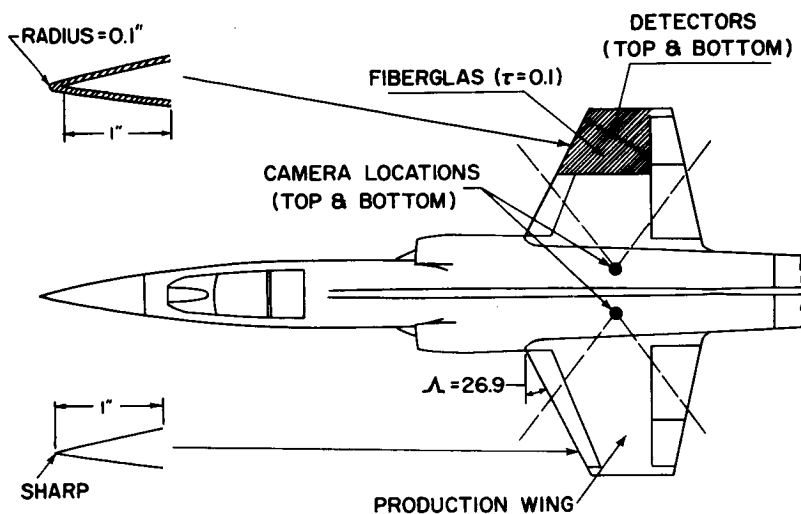
Figure 1

# TRANSITION TEST METHODS
## CHEMICAL SUBLIMATION

TURBULENT

LAMINAR

### TRANSITION DETECTORS

TURBULENT

GALVANOMETER
DEFLECTION

LAMINAR

X, FT
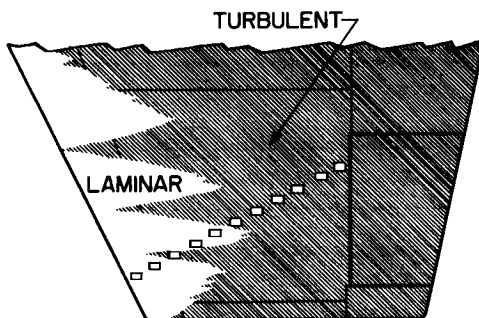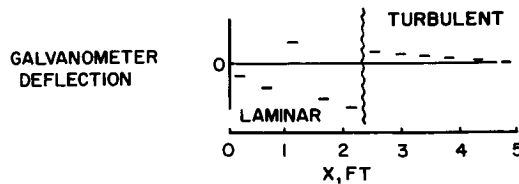
Figure 2

## IN-FLIGHT PHOTOGRAPHS

TYPICAL 35-MM ENLARGEMENT
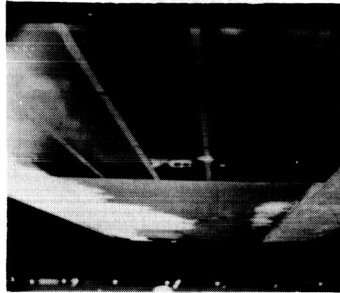
ARTIST'S CLARIFICATION

THIS AREA OMITTED
SUBSEQUENTLY
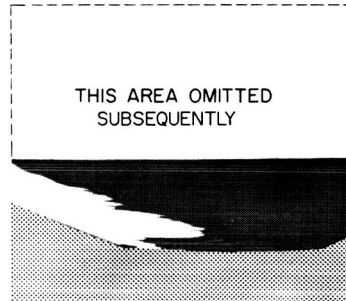
Figure 3

## INDICATION OF THE PRESENCE OF VORTICES
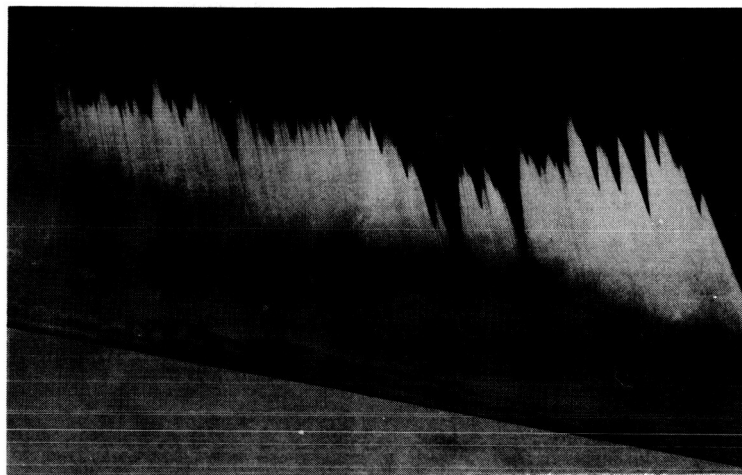
Figure 4

LAMINAR FLOW ON UNFINISHED WING

M= 2.0, $h_p \approx$ 56,000 FEET
$\alpha$ = 4.5°, R=1.8x10⁶ PER FOOT

L.E. FLAP HINGE LINE
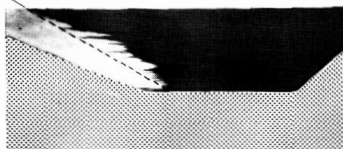


LOWER SURFACE LEFT WING

Figure 5

EFFECTS OF SURFACE CONDITIONS
R=1.8x10⁶ PER FOOT

FINISHED WING; M=2.0
ROUGHNESS = 25 $\mu$ in.
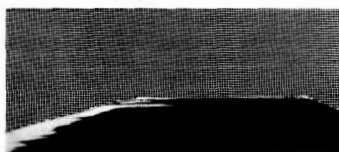
FINISHED & PAINTED WING; M=1.8
ROUGHNESS=13 $\mu$ in.
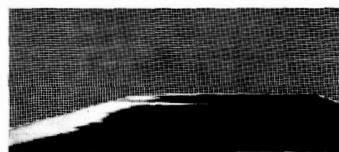


UPPER SURFACE



UPPER SURFACE



LOWER SURFACE



LOWER SURFACE

Figure 6

## COMPARISON OF LEFT-& RIGHT-WING TRANSITION
## M=1.8, R=1.8×10⁶ PER FOOT

LEFT WING
FINISHED & PAINTED

ROUGHNESS=13μ in.

RIGHT WING
FIBERGLAS TEST AREA

ROUGHNESS=7μ in.

UPPER SURFACE

UPPER SURFACE

LOWER SURFACE

LOWER SURFACE
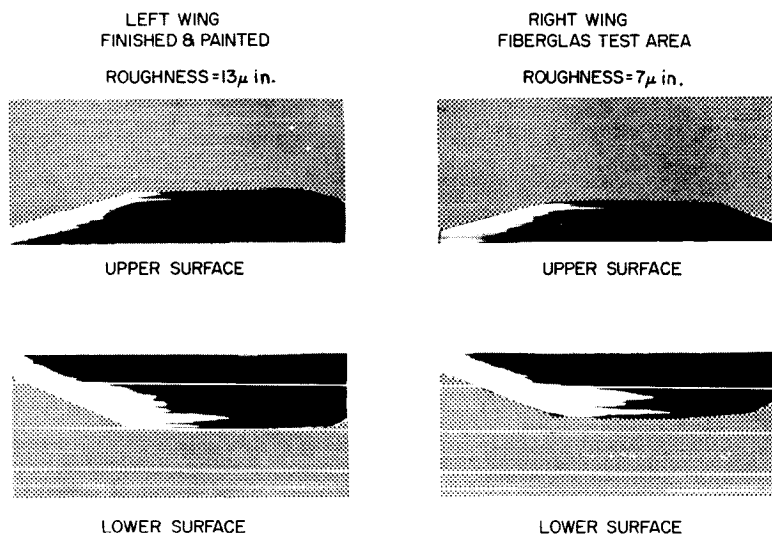
Figure 7

## MAXIMUM TRANSITION REYNOLDS NUMBERS
### FIBERGLAS TEST AREA- RIGHT WING
$10° > \alpha > 0°$

TOP SURFACE

BOTTOM SURFACE
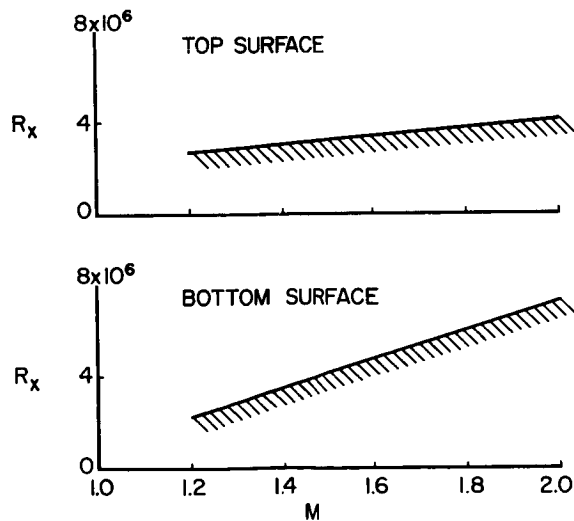
Figure 8

# TURBULENT SKIN FRICTION AT HIGH MACH NUMBERS

## AND REYNOLDS NUMBERS

### By Fred W. Matting

### Ames Aeronautical Laboratory

For a number of years now, people have been making measurements of skin friction. Formerly the main interest was at low Mach numbers; later, measurements were made at supersonic Mach numbers. However, almost all of these measurements were over a limited range of Reynolds numbers. On the other hand, these measurements fairly well determined the effects of Mach number and heat transfer on skin friction.

The purpose of this paper is to give the results of skin-friction measurements in turbulent boundary layers at high Mach numbers and high Reynolds numbers where data have not previously existed. The equipment used was expressly designed to give high Mach numbers and high Reynolds numbers. It is difficult to obtain high Mach numbers and high Reynolds numbers simultaneously with air in a wind tunnel. In order to avoid condensation, it is necessary to heat the air. As a result there is a loss in density and, hence, in Reynolds number. It seemed desirable, then, to use a gas that does not condense at high Mach numbers. This suggested helium, which was used as a working fluid in addition to using air. It was, of course, necessary to determine the equivalence of air and helium in the turbulent boundary layer. At high Mach numbers in a given wind tunnel, higher Reynolds numbers can be obtained with helium than with air. This is mainly due to the fact that no heating of the helium is required. The different ratios of specific heats also contribute to the increase.

Figure 1 is a sketch of the Ames 1- by 10-inch boundary-layer channel. The test section is 10 inches wide and has a nominal height of 1 inch. These proportions assure an essentially two-dimensional flow. Although this is called a "channel," studies were not made of channel flows. There was always a core of potential flow between the top and the bottom boundary layers. The nozzle block is adjustable which allows the setting off of different Mach numbers and different pressure gradients. Up to the present, only the zero-pressure-gradient case has been studied. Direct measurements of local skin friction were made by means of the skin-friction element shown. This element consists of a disc $2\frac{1}{4}$ inches in diameter suspended from flexures. The force on the disc is measured by means of a differential

transformer. Corrections were made for buoyancy forces surrounding the disc. These corrections were generally found to be negligible. The disc was flushed to its housing to within a half-wavelength of light by means of an optical interferometer. Both the disc and the top plate have very smooth finishes, the disc being finished to 4 microinches and the top plate to 15 microinches. Not shown in figure 1 is a heater which allows control of the stagnation temperature of the working fluid. To date, the stagnation temperature was always set in relation to the wall temperature, so that the boundary layers were adiabatic. Experiments to date, then, consisted of direct measurements of local skin friction in turbulent boundary layers on a smooth flat plate at zero pressure gradient. These boundary layers were adiabatic. The speed was varied from low subsonic Mach numbers up to a Mach number of 6.7. The Reynolds number range was from $1 \times 10^6$ to $120 \times 10^6$. At the highest Reynolds number, the stagnation pressure was 700 lb/sq in. In calculating the Reynolds number, the length used was from the center line of the element back to the virtual origin of turbulence as best it could be determined. Boundary-layer surveys were made at a number of upstream stations to determine the point of transition as a function of Mach number and Reynolds number for this tunnel. Over most of the range of Reynolds numbers it was found that the virtual origin was very near to the nozzle throat.

Figure 2 is a plot of Mach number against Reynolds number showing the test domain of the boundary-layer channel, which is everything to the left of the hatched line. For purposes of comparison, also shown is the so-called corridor of continuous flight, which is the approximate Mach number-Reynolds number regime for steady continuous level flight of airplane-like configurations. A characteristic length of 50 feet was used in the calculation. Most previous skin-friction data were taken in the area to the left of and below the corridor of continuous flight. It can be seen that this equipment has extended the Mach number-Reynolds number range into a regime of considerable interest. Even a further extension would be desirable. It should also be mentioned that certain noncontinuous flying vehicles, such as ballistic missiles, actually operate outside (and above) the corridor of continuous flight. The shaded area at the bottom of the figure shows the regime in which tests have been conducted to date. Air was used as the working fluid up to a Mach number of 4.2, and helium from a Mach number of 4.2 up to a Mach number of 6.7.

On the question of the equivalence of air and helium in the turbulent boundary layer, a dimensional analysis of the differential equations of motion and energy for the turbulent boundary layer (at constant pressure) shows that, in order to get dynamically similar boundary layers with two different gases, it is necessary to match a certain parameter. This parameter is $M\sqrt{\gamma - 1}$, where $\gamma = C_p/C_v$. This parameter is also

valid for the laminar boundary layer. It is only a boundary-layer parameter, though, and should not be used for other flows. Figure 3 shows the equivalence relation used:

$$M_a = M_{He} \sqrt{\frac{\gamma_{He} - 1}{\gamma_{AIR} - 1}}$$

where $M_a$ is the equivalent air Mach number for a helium flow at the actual Mach number $M_{He}$. The value of $\sqrt{\frac{\gamma_{He} - 1}{\gamma_{AIR} - 1}}$ is approximately 1.29. Figure 3 shows a comparison of air and helium flows at actual Mach numbers of 4.20 and 3.25, respectively. Both of these flows are at an equivalent air Mach number of 4.20. Therefore, one would expect these two flows to be dynamically similar in the turbulent boundary layer. Referring to the plot in figure 3 of the local skin-friction coefficient against Reynolds number, it is seen that the air and helium points do fall on one curve. Also, for comparison, is shown the curve for $M_a = 0$. It is noted that the sizable reduction of $C_f$ (which is a measure of compressibility effects) is the same for the two gases. This is the experimental verification of the equivalence of air and helium in the turbulent boundary layer.

It was stated previously that at high Mach numbers in a given wind tunnel one can obtain higher Reynolds numbers with helium than with air. To illustrate this, in the Ames 1- by 10-inch boundary-layer channel at an equivalent air Mach number of 15, a Reynolds number of $25 \times 10^6$ can be expected if helium is used. To obtain this same Reynolds number with air would require a test section 150 feet long and the air would have to be heated to 4,600° R; in other words, at this Mach number the Reynolds number factor is about 75 to 1.

Figure 4 largely summarizes the data taken to date. It is a plot of the local skin-friction coefficient against Reynolds number at Mach numbers ranging from 0.2 to 6.70. These are all equivalent air Mach numbers. It is noted that the subsonic data agree well with those taken by other experimenters. The broken line represents data taken in the Ames 12-foot pressure tunnel (ref. 1). The dotted line is the Kármán-Schoenherr incompressible curve. The important thing about the subsonic data is that it shows no roughness effects or roughness "bend-up." When appreciable roughness exists, the subsonic skin-friction curve will bend up with Reynolds number and will eventually become horizontal. No such effects are seen here. This is mentioned because it is seen that there is a slight bend-up in the supersonic curves at the highest Reynolds numbers. It is believed that this bend-up is not due to roughness. All

the data were taken with the same top plate and the same skin-friction element. A number of investigators have shown that high Mach number boundary layers are less sensitive to roughness than are subsonic boundary layers. (This is probably due to the fact that the high Mach number boundary layers have thicker laminar sublayers.) Therefore, since no roughness effects in the subsonic measurements are to be seen, it is felt that the supersonic measurements are free from roughness effects.

Figure 5 is a plot of the ratio of the local skin-friction coefficient to the incompressible local skin-friction coefficient at the same Reynolds number $C_f/C_{f_i}$ plotted against Reynolds number. The dashed lines represent calculated values of $C_f/C_{f_i}$ calculated by the T' or intermediate enthalpy method. This method uses a mean reference temperature to evaluate the physical properties of the gas. The method was originally used by Rubesin and Johnson (ref. 2) for laminar flows and was adapted to turbulent flows by Eckert, Sommer and Short, and others. The constants used in the calculations are those determined by Sommer and Short (ref. 3). (Constants obtained by other investigators do not change the results much.) It is noted that the experimental data and the T' calculations agree quite well; however, the trends are slightly different with Reynolds numbers. To date, no satisfactory explanation of the bend-up in $C_f/C_{f_i}$ at the highest Reynolds numbers has been found. However, this effect is actually small, as is seen by referring back to figure 4. The large effect on $C_f$ is due to Mach number, as shown on figure 4. (There is another large effect due to heat-transfer conditions, but this was not in the scope of the present investigation.) It has been known for some time that the T' method gives good predictions for the effects on skin friction of Mach number and heat transfer at moderate Reynolds numbers. It is now seen that the T' method gives good answers over a surprisingly large Reynolds number range. This is probably the most important result of this paper.

It should be emphasized again that these data were taken in adiabatic boundary layers. To calculate $C_f$ in a nonadiabatic boundary layer, one could start with $C_{f_i}$, say the Kármán-Schoenherr value, and then use the T' method. This method will give good predictions for the effects of Mach number and heat transfer on $C_f$, and, as has been shown, the T' method will also give a fairly good prediction for the effect of Reynolds number on skin friction.

# REFERENCES

1. Smith, Donald W., and Walker, John H.:  Skin-Friction Measurements in Incompressible Flow.  NACA TN 4231, 1958.

2. Rubesin, M. W., and Johnson, H. A.:  A Critical Review of Skin-Friction and Heat-Transfer Solutions of the Laminar Boundary Layer of a Flat Plate.  Trans. A.S.M.E, vol. 71, no. 4, May 1949.

3. Sommer, Simon C., and Short, Barbara J.:  Free-Flight Measurements of Turbulent-Boundary-Layer Skin Friction in the Presence of Severe Aerodynamic Heating at Mach Numbers From 2.8 to 7.0.  NACA TN 3391, 1955.

## 1-BY 10-INCH BOUNDARY-LAYER CHANNEL
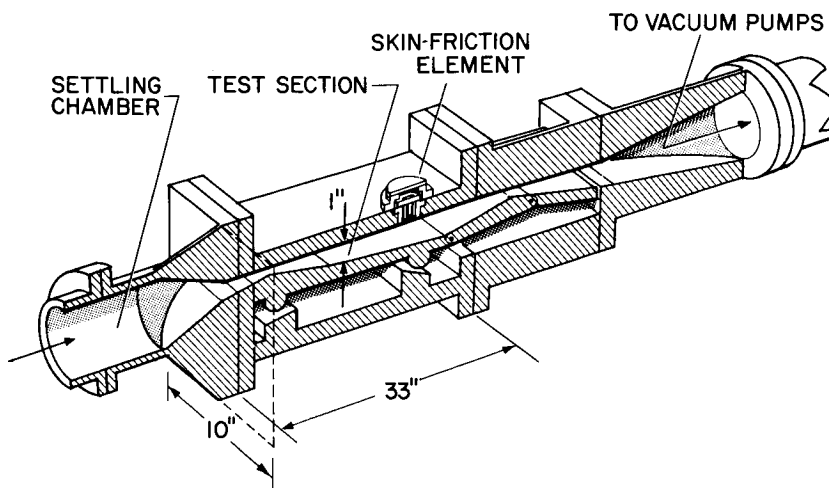


Figure 1

## TEST DOMAIN
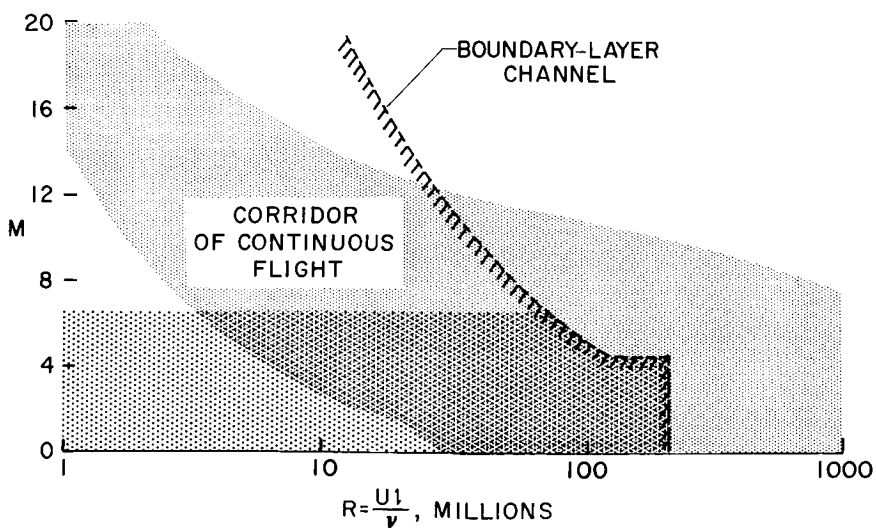


Figure 2

## EQUIVALENCE OF AIR AND HELIUM
## TURBULENT SKIN FRICTION

$$\text{EQUIVALENT AIR MACH NO.} \equiv M_a \equiv M_{He} \sqrt{\frac{\gamma_{He}-1}{\gamma_{AIR}-1}} \approx 1.29\, M_{He}$$
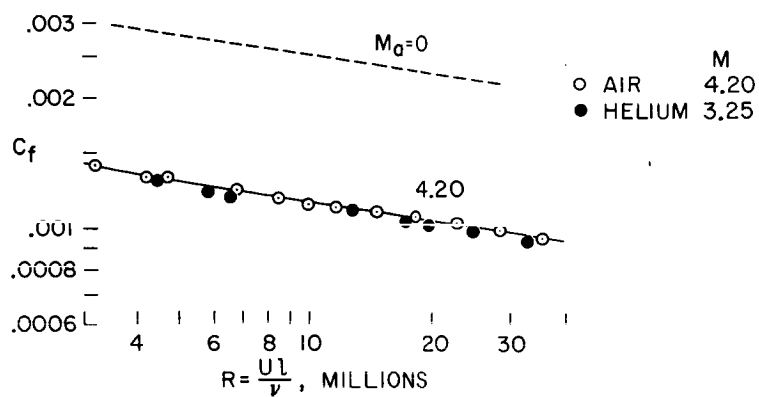


Figure 3

## FLAT PLATE TURBULENT SKIN FRICTION



Figure 4

EFFECT OF R ON $C_f/C_{f_i}$

$M_a = 2.95$

.6 —

.5 —

$\dfrac{C_f}{C_{f_i}}$ .4 —

4.20

——— T' METHOD

.3 —

6.70

.2 —

.1 ⌊

3   4      6   8  10        20        40        80    120

R, MILLIONS
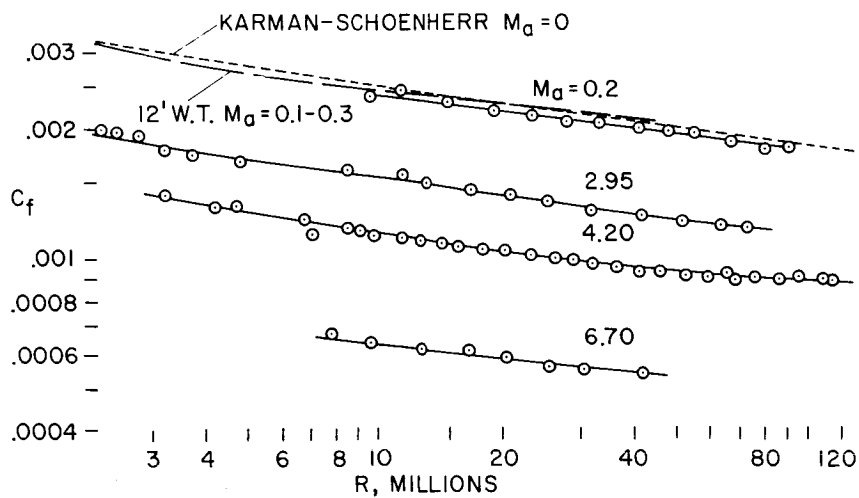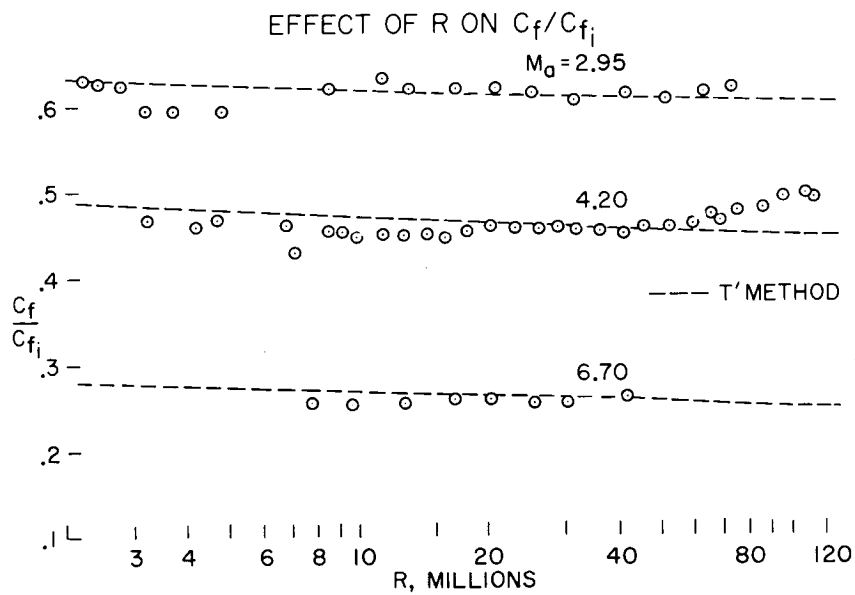
Figure 5

EFFECTS OF FABRICATION-TYPE ROUGHNESS ON TURBULENT

SKIN FRICTION AT SUPERSONIC SPEEDS

By K. R. Czarnecki, John R. Sevier, Jr.,
and Melvin M. Carmel

Langley Aeronautical Laboratory

SUMMARY


An investigation has been made of the effects of fabrication-type
surface roughness on turbulent skin-friction drag at supersonic speeds.
Insofar as the present data are concerned, it was found that fabrica-
tion of the thin-skin constructions (sandwich or honeycomb) could be
done sufficiently well in practice so as to cause no increase in drag
over the smooth body; however, the juncture-type roughnesses (gaps,
steps, etc.) produced significant increases in drag as compared with the
smooth body. The results indicate that the effects of both Reynolds
number and Mach number can be correlated on the basis of changes in
flow characteristics within the inner parts of the boundary layer.
Consequently, increasing the unit Reynolds number has a detrimental
effect and increasing Mach number has a powerful alleviating effect on
drag due to surface roughness.

36

INTRODUCTION


As the designs of supersonic aircraft become more refined the
proportion of the airplane drag assignable to skin friction generally
increases. This fact makes it imperative, from the standpoint of
obtaining optimum performance in speed and range, that the airplane
skin friction be maintained at the lowest practicable value by keeping
the airplane surfaces aerodynamically smooth. In actual practice the
aerodynamically smooth surface is difficult to achieve and a certain
amount of surface roughness in the form of waviness, steps, grooves,
and similar protuberances must be accepted. This paper will review
briefly some results from recent tests made to evaluate the magnitude
and other drag characteristics of a few of these types of fabrication
roughnesses in a turbulent boundary layer at supersonic speeds.

## SYMBOLS

$C_f$      skin-friction drag coefficient based on wetted surface area of basic smooth body and free-stream flow conditions

$C_{D,r}$      roughness drag coefficient based on total frontal area of roughness and free-stream flow conditions

$k$      critical or allowable roughness height

$k_{M=1.61}$      critical or allowable roughness height at $M = 1.61$

$M$      Mach number

$R_{FT}$      free-stream unit Reynolds number

$R_{FT,CR}$      free-stream unit Reynolds number at which drag due to roughness first appears

$\delta_L$      laminar sublayer thickness

$\left(\delta_L\right)_{M=1.61}$      laminar sublayer thickness at $M = 1.61$

## BASIC PROBLEM

The basic problem is illustrated by the sketch in figure 1. This sketch shows a three-quarter front view of a supersonic airplane configuration and some of the external details that create the problem. First, because of high surface temperature requirements, the airplane will be built of sandwich construction and these sandwich panels probably will cover most of the airplane surface. If the sandwich panels contain a honeycomb core, the external surface may have a "waffle" like appearance after exposure to heat as illustrated for the panel on the wing. If the panel is constructed of a stringer core, the seam welding of the external skin may leave lines of dents and protuberances resembling "hemstitching" as indicated for the panel on the fuselage. Further, the joining of the panels one to another and the provision of access doors, as exemplified by the thin lines in the airplane sketch, will generally result in some local surface imperfections. These imperfections can be in the form of steps, grooves, waves, creases, or combinations thereof. These types of surface roughness, however, will not saturate the surface but will occur only at fairly large intervals.

Whereas the sandwich-panel-type roughness distribution is measured in square feet, the juncture-type roughness is measured in lineal feet.

## MODELS AND TESTS

In order to determine the effects of fabrication-type roughness on skin-friction drag at supersonic speeds the investigation had to be carried out on a simple model wherein the various components of total drag could be readily measured and/or separated; thus, the incremental drag due to roughness is isolated. Consequently, the investigation was carried out on the basic ogive-cylinder body illustrated in figure 2. This basic body had a length of 50 inches and a diameter of about 4.1 inches, which gave the body a fineness ratio of 12.2. The ogival nose was 3 calibers in length and faired tangentially into the constant-diameter cylindrical afterbody.

For simplicity in construction, the fabrication roughnesses were built into the cylindrical portion of the model only. In order to obtain measureable increments in drag due to roughness in these tests, the drag was determined for a number of the steps, grooves, or waves set apart at intervals judged to be sufficiently large to eliminate the effects of mutual interference. These intervals range from 1 inch for the grooves to two inches for stepped models.

Sixteen bodies representing different types or heights of fabrication-type roughness were investigated, exclusive of the smooth body. Some details of the juncture-type roughnesses are shown in figure 2. Included are 0.050-inch-square grooves and two heights each of forward- and rearward-facing steps, of protruding waves and transverse creases, and of combinations of steps and grooves. Three of the models had waffle-like surfaces representative of sandwich-construction panels with honeycomb cores, and two had surfaces representative of sandwich-construction panels with the external skin seam-welded to stringers along lines resembling hemstitching. Since it is difficult to describe the waffle or hemstitching type of roughnesses, no sketches are shown for these configurations. It should be mentioned, however, that the smooth waffle model had a rather gently wavy surface with waves approximately 0.002 inch in height, whereas the coarse waffle models had rather sharp ridges approximately 0.005 to 0.006 inch in height.

All of the models were tested at Mach numbers of 1.61 and 2.01 in the Langley 4- by 4-foot supersonic pressure tunnel and seven representative models were tested in the Langley Unitary Plan wind tunnel at $M = 2.87$. The range of free-stream unit Reynolds numbers varied from about $0.5 \times 10^6$ to $9 \times 10^6$. For all tests, transition was fixed near

the nose of the model by means of narrow strips of carborundum or sand grains. Skin friction was determined by measuring the total drag on the models by means of an internal strain-gage balance and subtracting measured values of forebody and base pressure drags. All tests were limited to zero angle of attack.

## BACKGROUND INFORMATION

Before the results of the present investigation are discussed, it appears appropriate to mention some of the physical concepts that are involved. To begin with, a large number of investigations of surface roughness have been made at subsonic speeds. (See ref. 1.) These tests indicate that when the roughness did not protrude beyond the laminar sublayer there was little if any drag due to roughness. If the roughness protruded beyond this height, it created an additional form drag above and beyond the skin-friction drag of the basic smooth surface. For protrusions well beyond the laminar sublayer, the drags of roughnesses of similar shape could be readily correlated with the use of a drag coefficient based on the height of the roughness and the average dynamic pressure existing within the boundary layer over the height of the roughness. Lastly, since changes in sublayer thickness are indicative to a first order of the changes in local conditions in the inner portion of the boundary layer and this thickness changes but little with increase in model length at constant free-stream unit Reynolds number, the free-stream unit Reynolds number obviously is the controlling parameter.

It may be expected that the basic concepts just discussed for low speeds will also apply at supersonic speeds. Thus, it was possible in the present investigation to test full-scale roughness at full-scale unit Reynolds number. For example, an airplane flying at $M = 3$ at about 70,000 feet altitude would be operating at a Reynolds number per foot of about $1.5 \times 10^6$. This Reynolds number lies in the lower part of the test range.

## RESULTS AND DISCUSSION

### Smooth Bodies

Some skin-friction results for the reference smooth body and for some typical models having the type of roughness insufficiently large to cause any measurable penalty in drag are shown in figure 3 for the

lowest test Mach number of 1.61. The ordinate in this figure is the effective skin-friction coefficient based on the smooth body wetted surface area and the abscissa is the free-stream Reynolds number per foot. As may be seen, there is little or no difference in drag for the smooth body or the bodies with hemstitching or smooth waffle type of roughness. This result does not necessarily mean that the dents or protuberances on the models with roughness do not produce drag, but that the number and size of the surface irregularities may be so small and the smooth part of the surface relatively so large that the drag produced by the roughness is well within the accuracy of measurement. The main conclusion to be derived from figure 3 is that, for the well distributed type of roughness associated with the construction of sandwich panels which may cover a large portion of the airplane, it appears readily feasible to maintain the surface sufficiently smooth with normal fabrication procedures to escape any measurable drag due to roughness.

The straight line in the figure is an average "smooth" body curve drawn through the composite data which will be used for reference in figures 4 and 5.

## Configurations With Roughness

Some typical basic test results for configurations with roughness of the type insufficiently large to cause any measurable penalty in drag are presented in figures 4 and 5 for M = 1.61 and 2.87. The ordinate and abscissa are the same as in figure 3 and the average smooth body curve is the reference previously described. Note that the coarse waffle surfaces show a sizable increment in drag and are therefore representative of the types of sandwich-panel surfaces that must be avoided in fabrication or after exposure to heat.

The results of the investigation indicate, as illustrated by the typical plots in these figures, two items of significance. First, the smaller is the increment in drag due to roughness, defined as the difference in effective drag coefficient between the curves for the models with roughness and that for the smooth bodies, the more closely the curves for the models with roughness parallel the smooth body curve. This result suggests the possibility of correlating the effects of changes in drag increment with Reynolds number on the basis of some parameter involving the unit Reynolds number. Second, the data in general do not indicate the existence of a critical Reynolds number below which the drag of the bodies with roughness merge with the smooth body drag curve as was illustrated supersonically for distributed surface roughness in references 2 and 3. The explanation is that the roughnesses protrude through the laminar sublayer, usually by a substantial margin, even at the lowest test Reynolds number.

## Critical Roughness

As an item of interest at this point, it may be pointed out that, as the Mach number increases, the temperature of the boundary layer near the surface also increases rapidly and the density decreases while viscosity increases. The laminar sublayer thickness, therefore, increases rapidly with M and it may be expected that the critical or allowable roughness height, below which no drag due to roughness appears, will also increase. This statement is shown to be true in figure 6. The allowable roughness is defined as indicated by the sketch on the right of the figures as the maximum roughness which will not cause an increase in skin-friction drag below some arbitrary critical Reynolds number. For larger values of roughness, the skin-friction curve for the model with roughness will diverge from the smooth body curve at lower values of $R_{FT}$ and create a drag increment at the reference Reynolds number such as is evident above the critical Mach number. In the plot on the left of figure 8 is presented the ratio of critical or allowable roughness height at the test Mach number to allowable roughness height at M = 1.61 as a function of M at constant Reynolds number for distributed sand-grain type of roughness. The experimental points are plotted as circular symbols while the theoretical curve, which assumes that the first appearance of the drag due to roughness occurs at a constant value of the ratio of roughness height to laminar sublayer thickness, is shown as a dotted line.

The results of figure 6 indicate excellent agreement between theory and experiment. The accuracy of the experimental data is probably on the order of ±10 or ±15 percent so that the nearly perfect agreement may be somewhat fortuitous. Still, the data do show that the basic concept is probably correct and that increasing the Reynolds number has a powerful alleviating effect on the critical or allowable roughness height.

## Reynolds Number Correlation

In the form presented thus far the results for the juncture-type roughnesses are not in a form suitable for application to model configurations other than the ogive-cylinder tested. In figures 7 and 8, therefore, some of the results obtained at M = 1.61 and 2.87 have been reduced to a more useful form wherein the increment in drag coefficient due to roughness is based on free-stream flow conditions and the total frontal area of the roughnesses investigated. At the same time this drag increment has been divided by $\sqrt[5]{R_{FT}}$. The minus 1/5th power of the Reynolds number per foot corresponds to the slope of the skin-friction curve of the smooth bodies. The test points in these figures

represent average values of drag increment picked from data such as shown in figures 4 and 5 at the various Reynolds numbers indicated.

The results indicate that the effects of Reynolds number can be predicted quite well except possibly at the lowest Reynolds numbers. In this range, however, the accuracy of measurement is quite low due to low tunnel dynamic pressure and the problem of fixing transition. Also, only a few of the many configurations investigated show this disagreement at low Reynolds numbers per foot and all have been included here. It should be noted, however, that the correlation must eventually break down at low Reynolds numbers if a critical Reynolds number is to exist. A similar Reynolds number correlation is obtained for the distributed type of roughnesses except that the drag generally cannot be expressed in terms of roughness dimensions because of the difficulty of measuring the roughness height or density of distribution.

For subsonic speeds Hoerner (ref. 1) has demonstrated that the drag of the juncture-type roughnesses increases approximately as $\sqrt[18]{R_{FT}}$ because of the combined effects of decreasing boundary-layer thickness and the consequent projection of the roughness into a higher dynamic pressure region within the boundary layer. In these tests the increase is only as $\sqrt[5]{R_{FT}}$. The reason for this faster increase is not known at present, inasmuch as there is no change in this factor in the Mach number range from 1.61 to 2.87. The final answer awaits completion of the breakdown of the roughness drag into its components of wave and vortex drag. The correlation of the results for the various roughness heights also awaits completion of this analysis.

In using the data of figures 7 and 8, the procedure requires that the type and size of roughness on an airplane be identified. The drag coefficient parameter based on roughness frontal area can then be estimated from these data for the proper Mach number. This parameter is multiplied by the flight $\sqrt[5]{R_{FT}}$ and the drag coefficient converted from roughness frontal area to wing area on the basis of the number of lineal feet of roughness existing on the airplane and the height of the roughness. Thus the smaller the number and heights of juncture-type roughness on an airplane the smaller is the increment in drag due to roughness in terms of airplane coefficients.

Mach Number Effects

The effects of Mach number on drag due to roughness are illustrated in figure 9. In this figure, the ordinate is the drag parameter

$\dfrac{C_{D,r}}{\sqrt[5]{R_{FT}}}$ as was used in figures 7 and 8 and the abscissa is the test Mach number. Results are shown for only a few cases but are representative of configurations not shown. The results show that, as the Mach number is increased, the drag coefficient decreases. The rate of decrease appears to be roughly proportional to the magnitude of the coefficient involved.

Inasmuch as changes in drag due to roughness with Mach number can logically be expected to vary in direct proportion to the changes in the flow characteristics of the inner parts of the boundary layer and these changes can be described to a first order by the changes in laminar sublayer thickness, a correlation of the Mach number effects was made on the basis of the expected changes in sublayer thickness with Mach number. The results for a few typical cases are shown in figure 10. In this figure the ordinate is the roughness drag parameter multiplied by the ratio of the thickness of the laminar sublayer at the test Mach number to that at $M = 1.61$ $\dfrac{\delta_L}{\left(\delta_L\right)_{M=1.61}}$. The correlation exhibits a considerable amount of scatter, but the corrections for Mach number effects appear to be correct.

## CONCLUDING REMARKS

The results of this investigation of the effects of fabrication-type surface roughness on turbulent skin-friction drag at supersonic speeds indicate that the effects of both Reynolds number and Mach number can be correlated on the basis of changes in flow characteristics within the inner parts of the boundary layer. Consequently, increasing the unit Reynolds number has a detrimental effect and increasing Mach number has a powerful alleviating effect on drag due to surface roughness. The correlation of the effects of changes in roughness height or shape requires a more comprehensive analysis than was attempted in this paper. Further investigation must be made of the effects of roughness sweep and possibly mutual interference effects.

# REFERENCES

1. Hoerner, Sighard F.: Aerodynamic Drag. Publ. by the author (148 Busteed, Midland Park, N. J.), 1951.

2. Czarnecki, K. R., Robinson, Ross B., and Hilton, John H., Jr.: Investigation of Distributed Surface Roughness on a Body of Revolution at a Mach Number of 1.61. NACA TN 3230, 1954.

3. Sevier, John R., Jr., and Czarnecki, K. R.: Investigation of Effects of Distributed Surface Roughness on a Turbulent Boundary Layer Over a Body of Revolution at a Mach Number of 2.01. NACA TN 4183, 1958.

SOURCES OF ROUGHNESS

"HEMSTITCHING"

"WAFFLE"

ACCESS HATCHES

JUNCTURE-TYPE ROUGHNESSES
GROOVES
STEPS
TRANSVERSE CREASES
PROTRUDING WAVES
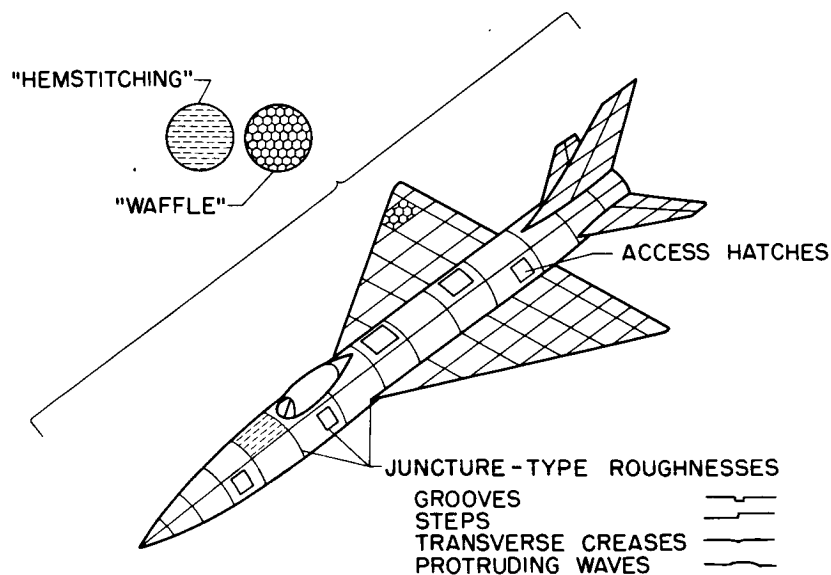
Figure 1

BASIC MODEL AND DETAILS OF JUNCTURE-TYPE ROUGHNESSES
BASIC MODEL; ALL DIMENSIONS IN INCHES

4.1

12.3

50

TRANSVERSE GROOVES     FORWARD STEPS     REARWARD STEPS

.050          .010          .010
              OR           OR
       .050   .020   2     .020    2

GROOVES AND STEPS   TRANSVERSE CREASES   PROTRUDING WAVES
.010 OR .020

.050   2    .020   .017   1.5   .024          1.5
                   OR          OR
                   .050        .050
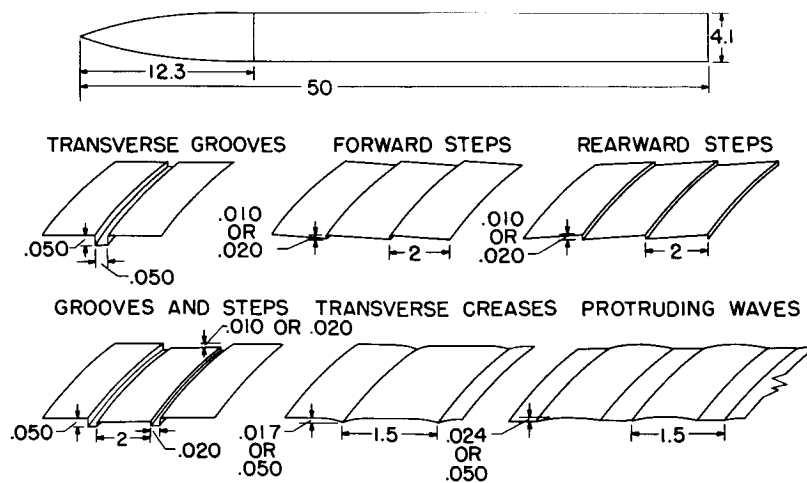
Figure 2

SKIN-FRICTION DRAG COEFFICIENT OF "SMOOTH" BODIES

M = 1.61
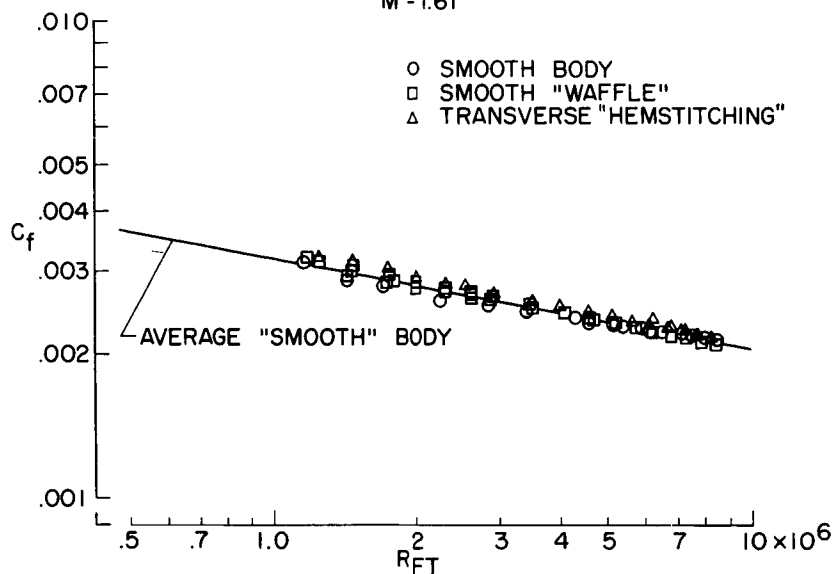


Figure 3

EFFECTS OF ROUGHNESS ON SKIN FRICTION
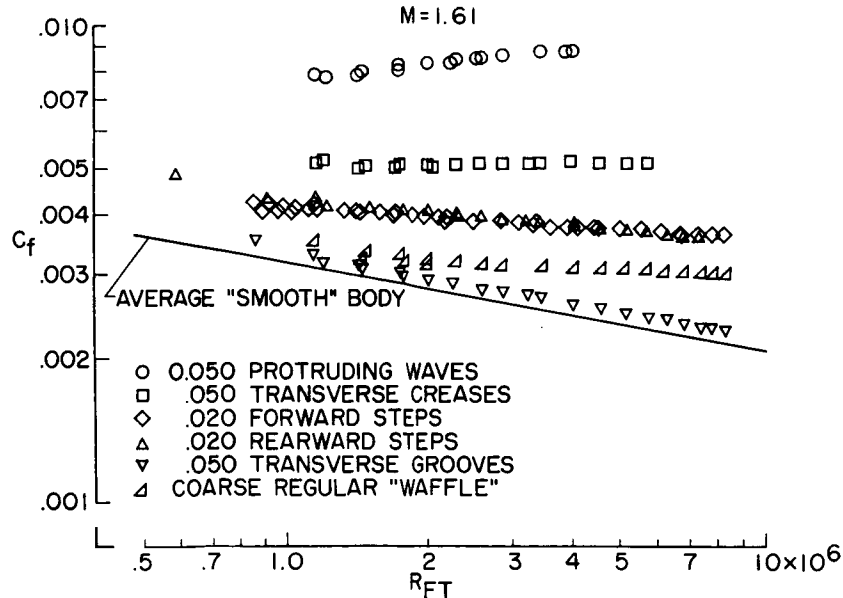
M = 1.61



Figure 4(a)
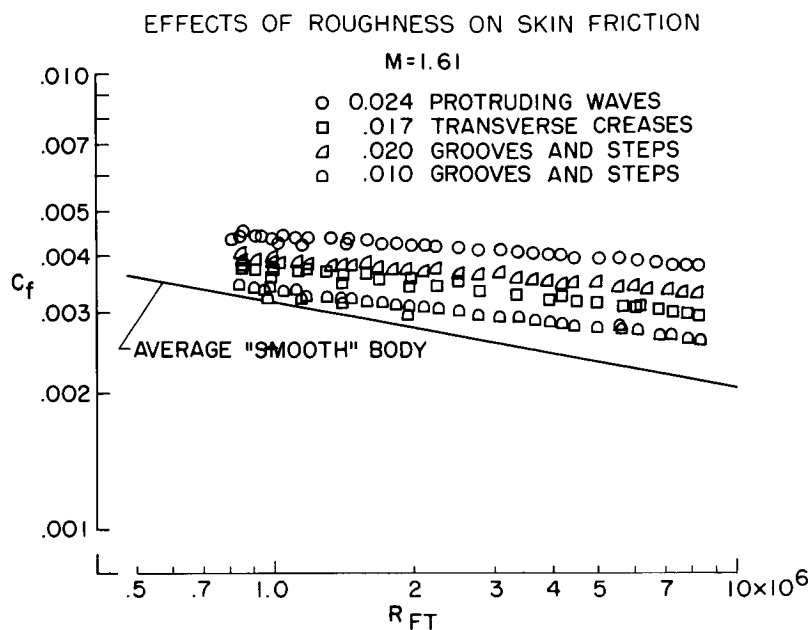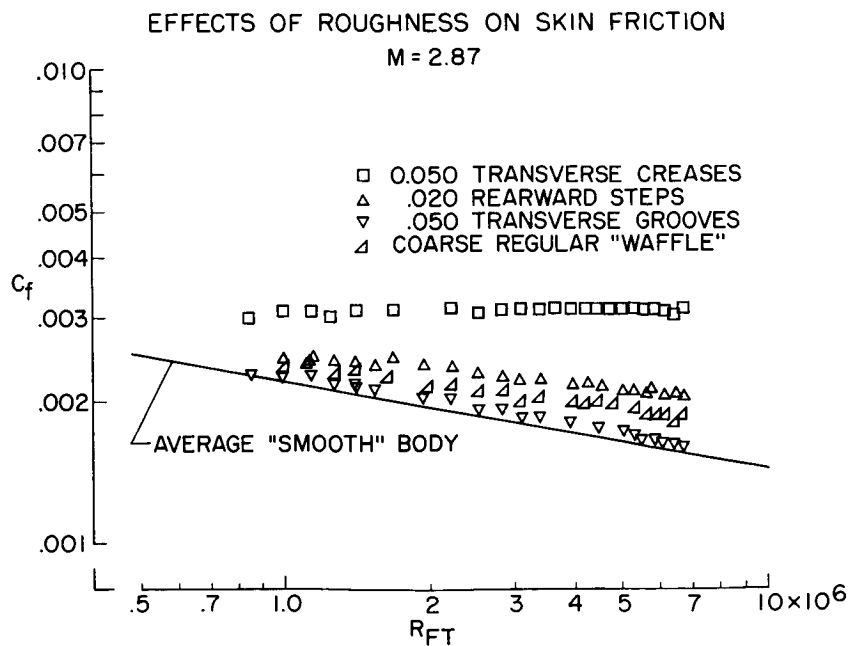
CONFIDENTIAL

EFFECTS OF ROUGHNESS ON SKIN FRICTION

M = 1.61

○ 0.024 PROTRUDING WAVES
□ .017 TRANSVERSE CREASES
◁ .020 GROOVES AND STEPS
▱ .010 GROOVES AND STEPS

AVERAGE "SMOOTH" BODY

$C_f$

Figure 4(b)

EFFECTS OF ROUGHNESS ON SKIN FRICTION

M = 2.87

□ 0.050 TRANSVERSE CREASES
△ .020 REARWARD STEPS
▽ .050 TRANSVERSE GROOVES
◁ COARSE REGULAR "WAFFLE"

AVERAGE "SMOOTH" BODY

$C_f$

Figure 5(a)

EFFECTS OF ROUGHNESS ON SKIN FRICTION

M = 2.87

□  0.017 TRANSVERSE CREASES
◿   .020 GROOVES AND STEPS
◹   .010 GROOVES AND STEPS

AVERAGE "SMOOTH" BODY

Figure 5(b)

EFFECT OF MACH NUMBER ON CRITICAL ROUGHNESS

○   EXPERIMENT
---  THEORY
     (NACA TN
       4183)

$\dfrac{k}{k_{M=1.61}}$

$R_{FT,CR}$

WITH ROUGHNESS

$C_f$

SMOOTH BODY

$R_{FT}$

Figure 6

REYNOLDS NUMBER CORRELATION

M = 1.61



Figure 7

REYNOLDS NUMBER CORRELATION

M = 2.87
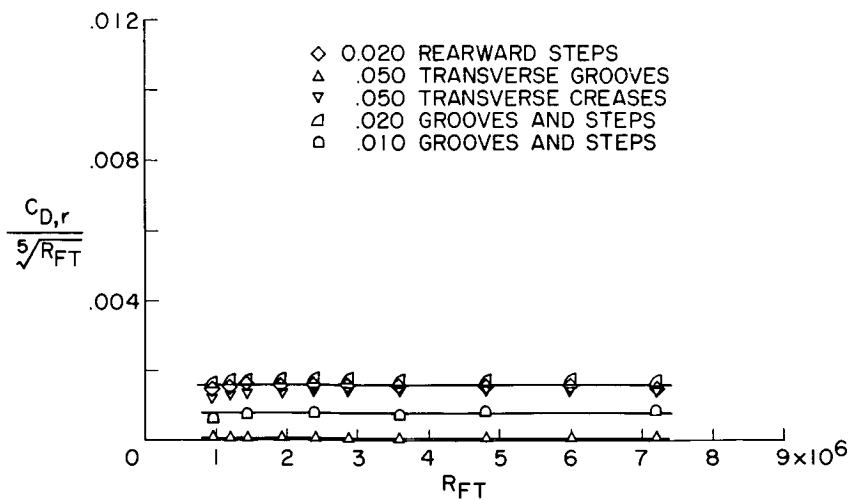


Figure 8

EFFECT OF MACH NUMBER ON ROUGHNESS-DRAG PARAMETER
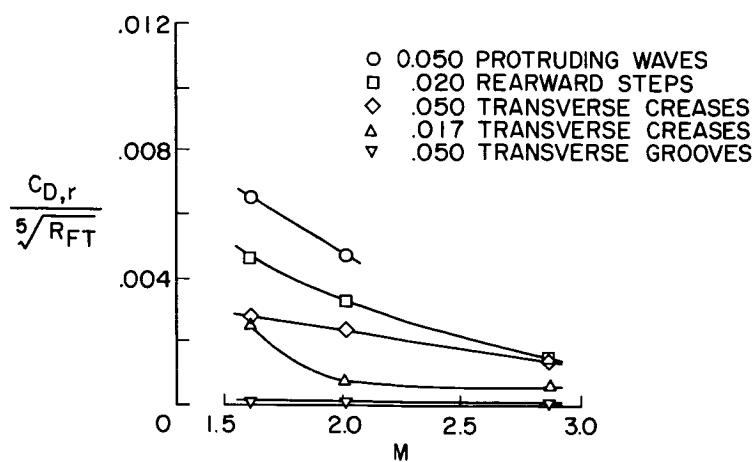


Figure 9

MACH NUMBER CORRELATION
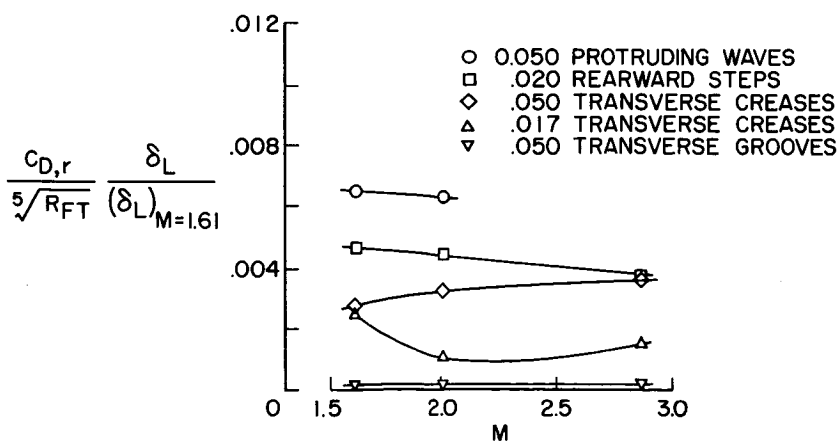


Figure 10

# PREDICTION OF FULL-SCALE SKIN-FRICTION DRAG

By Albert E. von Doenhoff

Langley Aeronautical Laboratory

## INTRODUCTION

The problem of predicting full-scale flight drag from wind-tunnel tests has been of interest for many years and appears to be giving rise to as much heated debate now as it ever did.  One approach to the problem would be to collect flight drag data for a number of airplanes and to compare these data with wind-tunnel drag data for models of these air-planes.  Such a comparison would presumably lead to the setting up of certain empirical correction procedures.  Unfortun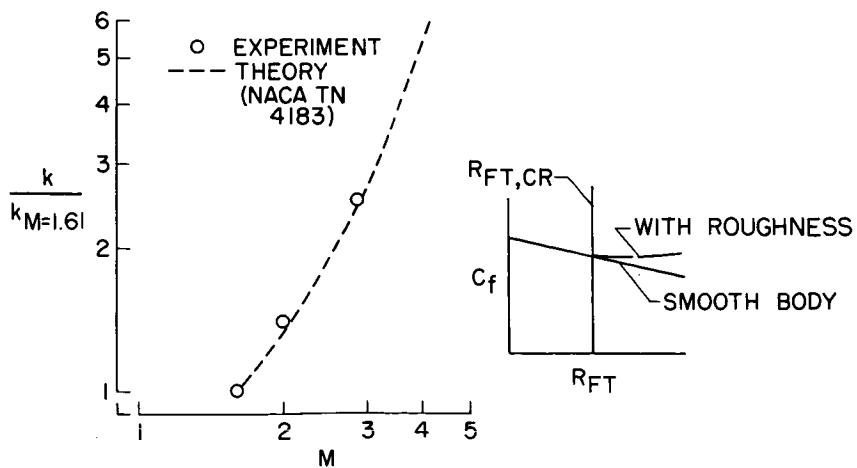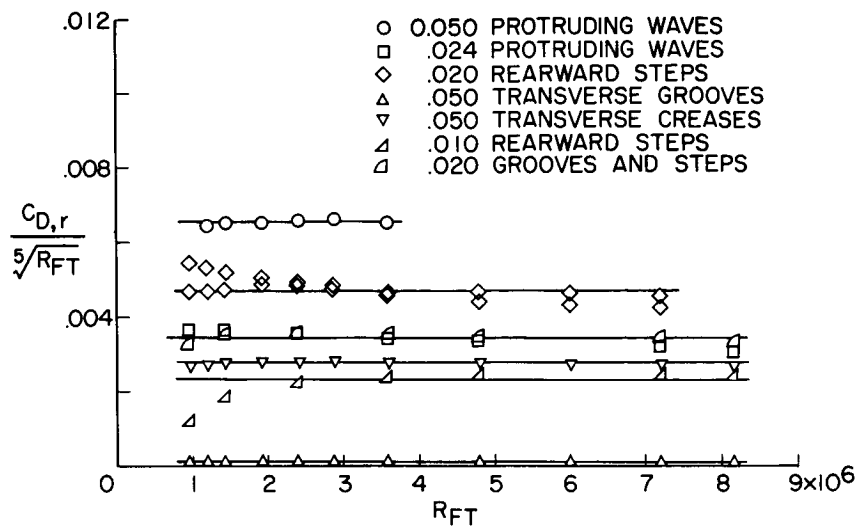ately, flight drag data are difficult to obtain with accuracy sufficient for this purpose and, in addition, the actual flight configuration usually differs sig-nificantly from the corresponding model configuration, with the result that available data suitable for making the empirical correlation are extremely limited.

On the other hand, the basic skin-friction laws for laminar and turbulent flow are well known and firmly established over a very wide range of Reynolds numbers and Mach numbers (ref. 1).  Some additional data on turbulent skin friction were presented in a previous paper by Fred W. Matting.  Another obvious approach is, therefore, to make use of this knowledge in attempting to predict flight characteristics from the tunnel data.  As a matter of fact recent NACA research on skin friction has been planned in such a way as to implement this approach.

37

## PROCEDURE

The proposed procedure is not particularly new.  The main purpose here is to present what is considered to be the rational approach to this problem.  The procedure based on this conception of the problem is given schematically in figure 1.  The upper line is the curve for the all-turbulent flat-plate skin friction for the proper Mach number.  The lower curve is the one for the corresponding laminar flat plate.

It is presumed that the model test has been made with transition fixed.  More will be mentioned later about the method of fixing transition.

This value of the friction drag of the model is then reduced by the decrease in turbulent skin friction of a flat plate over the Reynolds number range from model conditions to flight conditions. If the airplane designer feels confident, after a realistic appraisal of the situation, that certain areas of the airplane have laminar rather than turbulent flow, he would be justified in reducing the extrapolated drag to allow for this effect.

Finally, examination of any actual airplane will reveal a myriad of defects in the surface - for example, rivets, wrinkles, butt joints, and control-surface gaps - that were not simulated on the model. An allowance must be included for such drag-producing elements in order to arrive at a reasonable value for the airplane drag coefficient. This, in brief, is the proposed procedure. It should be noted that the value of the drag measured in the wind tunnel may be very nearly equal to the predicted flight value. This fact can be quite confusing unless it is realized that a number of compensating influences are involved.

## DISCUSSION

It is necessary to examine the feasibility of carrying out the procedure. The first step in the process is to fix transition for the model test. In doing this, it is desirable to use a device that has a negligible intrinsic drag of its own. In accomplishing this aim, research of the type discussed in a previous paper by Albert L. Braslow and Elmer A. Horton has been a big help. In order to bring transition up to a given point it is only necessary to glue some granular particles to the surface, the size of the particles being governed by the condition that $\sqrt{R_k}$ be greater than about 25, where $R_k$ is the roughness Reynolds number formed with local values of the density, velocity, and viscosity at the top of the roughness and the height of the roughness. It should be emphasized that the number of such particles need not be very large. A typical example of the application of such particles to a $10^\circ$ cone is given in figure 2. It is evident that, if a turbulent wedge originated at each of the particles, these wedges would overlap a very short distance downstream of the particles. The optimum distribution of particles is, of course, a line of particles spaced a uniform distance apart. In practice, however, it has not been found necessary to be so careful.

Figure 3 illustrates this point. The drag polar of a typical high-speed fighter configuration at a Mach number of 1.57 obtained in the Langley Unitary Plan wind tunnel is given for the model without roughness, with 0.003 to 0.005 inch roughness, and with 0.011-inch size roughness applied. The density of application was about as shown in figure 2. It is evident that even the larger size of roughness had no effect on the

drag. The reason for the agreement of the smooth-model data with the data with roughness in place is that, in this particular case, the flow was turbulent at the position of the roughness without the transition trip. In fact, it was desirable to choose a model having this characteristic in order to avoid the extraneous effect, so far as the roughness drag is concerned, of moving the position of transition. The point to be made is that roughness large enough to cause transition does not necessarily result in a significant increment in the drag if the roughness is properly applied. In this case the No. 60 roughness was definitely large enough to cause transition, as indicated by criteria based on the results of a previous paper by Albert L. Braslow and Elmer A. Horton. There are limits, of course. At very low test Reynolds numbers it becomes increasingly difficult to trip the laminar layer without causing significant extra drag due to the trip, but for wing Reynolds numbers of the order of $10^6$ or more, no trouble is experienced.

The second step is to justify the allowance for the decrease in turbulent skin friction between the model and the full-scale airplane. Not much doubt exists regarding this effect on flat plates or simple body configurations. Some questions have been raised occasionally as to whether the same rules apply to a complex complete airplane configuration. Several investigations have indicated that the normal turbulent scale effect is experienced at transonic speeds. (See, for example, ref. 2.) A comparison of the results from tunnel and rocket-propelled model tests of a complete airplane configuration at widely different Reynolds numbers is given in reference 2. In order to try to answer the question at supersonic speeds, figure 4 has been prepared. These data are for a complete configuration, which is discussed in reference 3. The model was tested with transition fixed near the leading edge over a wide Reynolds number range in the Langley Unitary Plan wind tunnel.

In figure 4 a first-order estimate of the skin friction was taken as the ratio of wetted area to wing area times the skin friction for a flat plate at the proper Mach number, 3.0. It was assumed that the difference between the measured data and the estimated skin friction at the highest test Reynolds number was a measure of the wave drag. This quantity was then subtracted from the data at lower Reynolds numbers. It is evident that the measured scale effect is just about equal to that estimated on the basis of flat-plate skin friction. These data are typical of many other cases that could have been cited to justify the scale effect correction on turbulent skin friction.

A word now about the allowance for laminar flow. Although the mechanism of transition at supersonic speeds appears to be very similar to that in incompressible flow, there are some factors that deserve special mention in connection with obtaining extensive laminar flow at supersonic speeds. Experience has indicated that it is very difficult, if not impossible, at practical Reynolds numbers, to obtain laminar flow behind the intersection

of a shock wave with the surface. The effect of cooling the surface as shown in a previous paper by Albert L. Braslow and Elmer A. Horton is to increase the sensitivity of the boundary layer to roughness; that is, cooling decreases the maximum allowable roughness height. There is some evidence, as indicated in a previous paper by Richard D. Banner, John G. McTigue, and Gilbert Petty, Jr., that increasing Mach number makes the unfavorable influence of leading-edge sweep more severe. Aside from these effects, the factors affecting the possible extent of laminar flow are qualitatively very much the same as for incompressible flow. All of these factors must be very carefully and realistically studied if significant extents of laminar flow are actually to be achieved.

Third, to obtain an estimate of the airplane drag, the allowance previously mentioned for surface roughness and excrescences must be made. In making this estimate, the order of magnitude of the roughness which is just large enough to affect turbulent skin friction must be kept in mind. This critical roughness is usually somewhat smaller than that necessary to cause transition. In incompressible flow a quick crude estimate of the critical roughness size can be obtained from the relation that the critical roughness Reynolds number, formed with the free-stream velocity, density, and viscosity, and the height of the roughness, is about 100. The allowable height of the roughness has been shown by Czarnecki, Sevier, and Carmel (ref. 4) to increase with Mach number. It may be expected to decrease with surface cooling.

A large amount of data has been accumulated at low speeds through the years and has been conveniently summarized in reference 5. An estimate of the extra drag items on a North American F-86 airplane based on these data and a close examination of the airplane are given in table I. It has been shown that no laminar flow exists on this airplane and thus no laminar flow was assumed in this analysis. As is evident, the number of different kinds of items is fairly large and the drag contribution of most of them is rather small. Leakage may also be a significant drag item, although the magnitude of this effect could not be estimated from a visual inspection of the airplane. Nevertheless the sum of all the items considered represents an important fraction of the total drag.

Sufficient data to make this sort of a drag analysis at supersonic speeds have not been available. The data presented in reference 4 represent a significant contribution in this respect and represent part of a continuing program. It seems reasonable to expect, however, that, except for the very smallest grade of roughness, the drag contributions at supersonic speeds will be at least as large as at subsonic speeds because of the production of wave drag. The classes of items of greatest importance on future airplanes may be different from those considered in the case of the F-86 airplane.

## CONCLUDING REMARKS

A rational procedure has been presented for predicting full-scale airplane drag from fixed-transition model data. It has the advantage of taking into account all the pertinent factors in as accurate a manner as available data permit. For example, as opposed to the previously mentioned empirical approach, the present procedure allows for any possible decreases in drag associated with improved construction methods and surface condition. It would be very difficult to do this without analyzing the problem in terms of a number of distinct phenomena as has been done in the present proposed procedure.

## REFERENCES

1. Schlichting, Herman (J. Kestin, trans.): Boundary Layer Theory. McGraw-Hill Book Co., Inc., 1955.

2. Howell, Robert R., and Braslow, Albert L.: Experimental Study of the Effects of Scale on the Absolute Values of Zero-Lift Drag of Aircraft Configurations at Transonic Speeds. NACA RM L56J29, 1957.

3. Baals, Donald D., Toll, Thomas A., and Morris, Owen G.: Airplane Configurations for Cruise at Mach Number 3. (Prospective NACA paper.)

4. Czarnecki, K. R., Sevier, John R., Jr., and Carmel, Melvin M.: Effects of Fabrication-Type Roughness on Turbulent Skin Friction at Supersonic Speeds. (Prospective NACA paper.)

5. Hoerner, Sighard F.: Aerodynamic Drag. Publ. by the author (148 Busteed, Midland Park, N. J.), 1951.

TABLE I

ROUGHNESS-DRAG ESTIMATE FOR A NORTH AMERICAN F-86 AIRPLANE

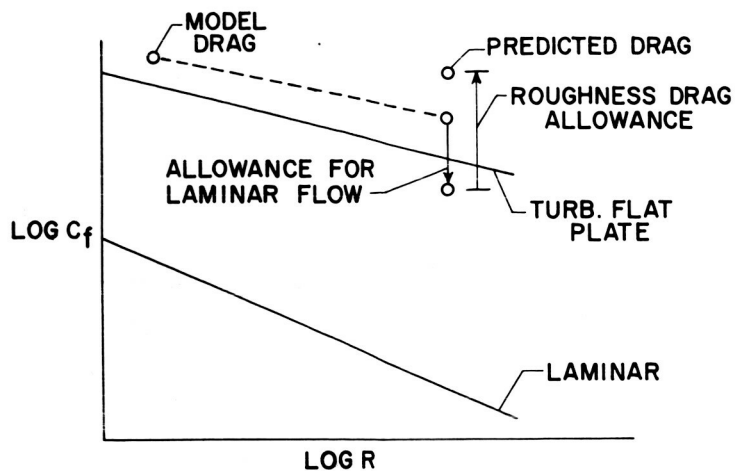| Roughness item | Drag coefficient |
|---|---|
| Scratches | 0.0006 |
| Leading-edge slat gaps | .00144 |
| Control-surface gaps | .00027 |
| Butt joints | .00049 |
| Cover plates | .0002 |
| Rivets | .00017 |
| Projections | .00015 |
| Slots (screw heads) | .000002 |
| Holes | .00001 |
| Gouges | .000002 |
| Total | 0.0033 |

## PROCEDURE FOR PREDICTING DRAG
## FROM MODEL TESTS



Figure 1

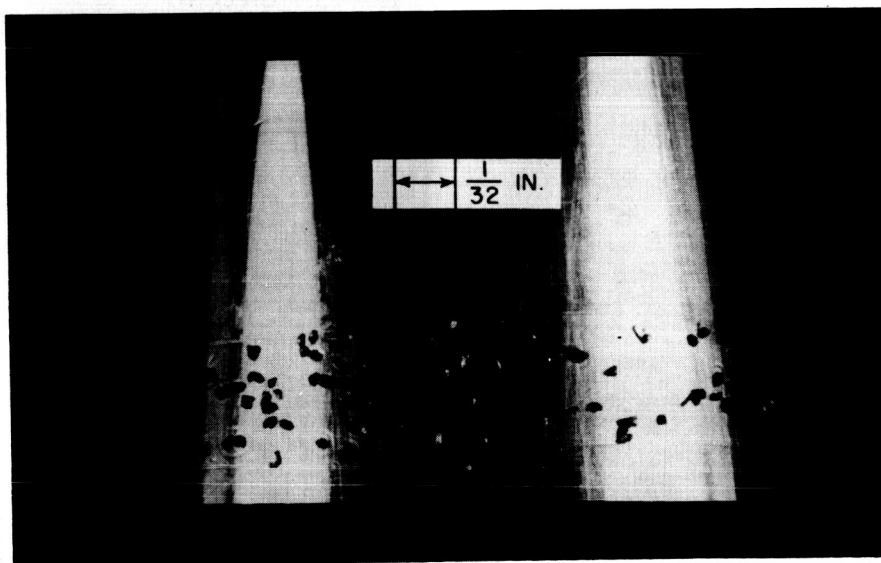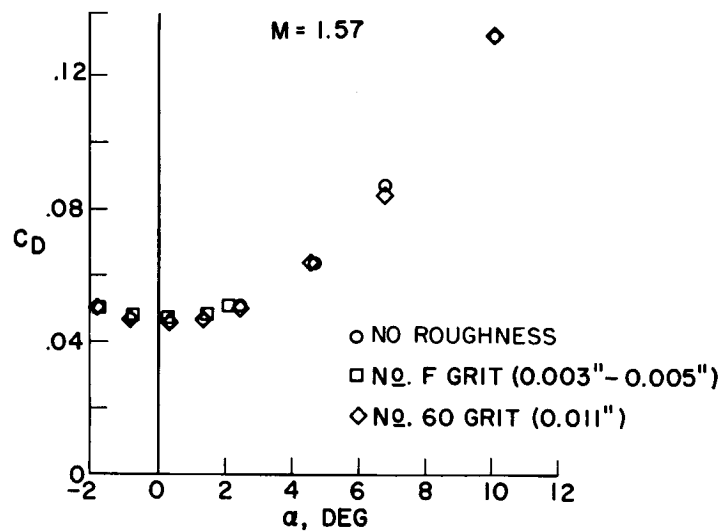## TYPICAL DISTRIBUTED-ROUGHNESS TRANSITION TRIP



Figure 2

EFFECT OF TRANSITION TRIPS ON FULLY
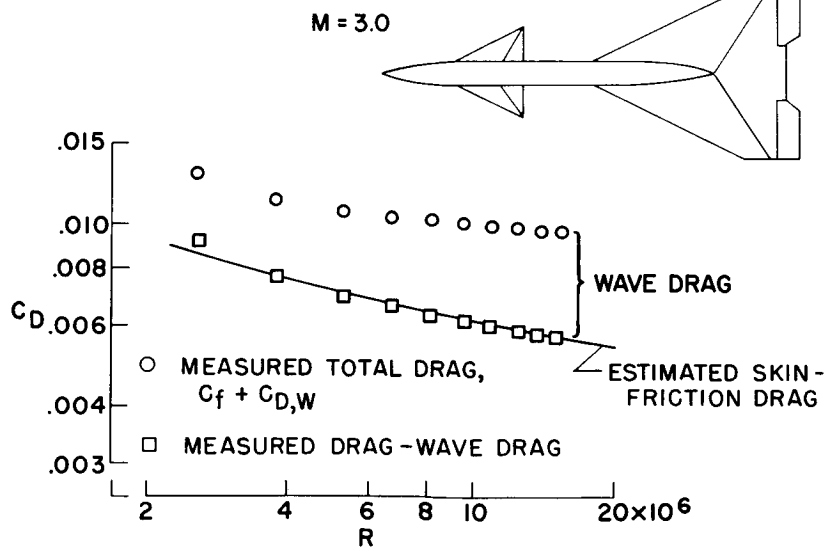TURBULENT MODEL DRAG



Figure 3

DRAG SCALE EFFECT ON CANARD
DELTA-WING CONFIGURATION



Figure 4

# IDEALIZED WINGS AND WING-BODIES AT A MACH NUMBER OF 3

## By Elliott D. Katzen

### Ames Aeronautical Laboratory

## THEORETICAL CONSIDERATIONS

Theoretical possibilities for obtaining high lift-drag ratios at $M = 3$ are given, and some experiments which were designed to exploit the theory are described. In discussing the theoretical maximum lift-drag ratios of idealized arrangements, it is convenient to consider, as a standard of comparison, the lifting flat plate.

Included in figure 1 are the maximum lift-drag ratios for flat plates having two types of plan forms, the delta and the arrow. The maximum lift-drag ratios have been computed for $M = 3$ (for symbols, see appendix) and for an assumed minimum drag coefficient of 0.005. These values correspond to those for a very large airplane flying at a high Reynolds number so that the friction drag coefficient would be relatively low.

The maximum lift-drag ratios are shown as a function of the slenderness parameter $\beta \tan \epsilon$ where $\beta$ is defined as $\sqrt{M^2 - 1}$ and $\epsilon$ is the semiapex angle of the leading edge of the wing. In addition to the results for flat plates, the improvement in lift-drag ratio predicted by cambering and twisting the wings is shown. For both types of plan forms with super-sonic leading edges and for the subsonic–leading-edge delta wings, the drag-due-to-lift results of references 1 and 2 were used to compute the improved lift-drag ratios. For the arrow wings with subsonic leading edges, the drag due to lift was optimized by using a four-term load distribution in the manner of references 3 and 4. The calculations were made at one point, $\beta \tan \epsilon = 0.5$. The curve of lift-drag ratio was then faired from this calculated point to the points calculated for arrow wings with supersonic leading edges.

It can be seen from figure 1 that $(L/D)_{MAX}$ for the arrow wings is higher than that for the delta wings. The improvement caused by warping decreases as the slenderness is decreased, and for wings with highly supersonic leading edges the improvement becomes negligible. These trends would be the same if a higher minimum drag coefficient had been assumed, but the magnitudes would be different. For example, if $C_{D_0} = 0.015$ had been chosen, the $(L/D)_{MAX}$ for the very slender arrow wing would be about 7 instead of over 11, as shown in figure 1. For the very slender

arrow wing, $\beta \tan \epsilon = 0.5$, relatively high lift-drag ratios are predicted for either the flat plate with subsonic flow or for the same plan form cambered and twisted. Experiments were designed then in an attempt to attain this high lift-drag ratio.

## EXPERIMENTAL INVESTIGATION

Four models are shown in figure 2 which were cambered and twisted for low drag due to lift. (See refs. 3 and 4.) Models 1 and 2 were designed for a lift coefficient of 0.1; therefore, the wings are rather extreme, as can be seen from sections taken at various stations along the wing. The forward part of the wing is raised considerably above the Z = 0 plane. Since the trailing edge of the root chord lies in the Z = 0 plane, the resulting angle of attack of the root section is relatively high, about $7.5^{\circ}$, compared with the tips which lie in the Z = 0 plane at about zero angle of attack.

Model 2 has the same camber and twist as model 1, but the dihedral has been changed in an attempt to change the separation pattern on the wing. At the midchord station it is seen that model 2 is turned below the Z = 0 plane, compared with model 1 which is above the Z = 0 plane. This change in dihedral with no changes of camber and twist leaves the forward part of the wing "dished out." One method of adding volume to the wing is, therefore, suggested, and model 3 is simply model 2 with volume added as shown.

Model 4 was designed for a lift coefficient of 0.05. The optimum lift is, therefore, to be obtained half by camber and twist and half by angle of attack. The wing is less extreme than that of the previous models; the forward portion is only half as far above the Z = 0 plane as is model 3.

The wings, except for model 3, have 12-percent-thick sections normal to the leading edge. The wing section used, normal to the leading edge, is the Clark Y. For the models shown, the symmetrical part of the Clark Y was wrapped around the calculated mean lines. The resulting sections, in the stream direction, are about 3.4 percent thick. With this thickness, for this very slender shape, the wings resemble bodies more than wings, especially in the forward region.

Experimental results for models 1 and 4 are shown in figures 3 and 4. It can be seen in figure 3 that reducing the design lift coefficient reduces the lift at a fixed angle of attack with little change in lift-curve slope. The less extreme wing (model 4) has less drag than the wing designed for a lift coefficient of 0.1 (model 1). It can be seen that with the pitching moments taken about an axis at 35 percent of the mean

aerodynamic chord, model 1 trims at the optimum lift coefficient.  Model 4, however, trims at a lower lift coefficient; therefore, a control surface or flap would have to be deflected, and a trim drag penalty would result.  Both models are stable throughout the test range of lift coefficients, but there is a tendency for the pitching-moment curve to flatten at the higher lift coefficients.

Figure 4 shows that the maximum lift-drag ratio for model 4, the less extreme wing, is 8.4 compared with about 7.4 for model 1 which was designed for a lift coefficient of 0.1.  Model 2, also designed for a lift coefficient of 0.1, had a different separation pattern but had about the same maximum lift-drag ratio as model 1.  Increasing the volume of model 2, as shown in figure 2, reduced the maximum lift-drag ratio from 7.4 to about 6.0.

Calculated drag coefficients for models 1 and 4 at their design lift coefficients are shown by solid symbols (fig. 3).  Calculated maximum lift-drag ratios are shown in the same manner (fig. 4).  It is seen that for the wing designed for a lift coefficient of 0.05, theory and experiment are in good agreement at the design point.  This is not the case for the wing designed for a lift coefficient of 0.1.

The results shown in figure 5 are for the maximum test Reynolds number of $3.5 \times 10^6$, based on the wing mean aerodynamic chord.  At this Reynolds number and lower test Reynolds numbers separation occurs on the wing as shown in the figure.  In this figure, results of visual-flow studies made by using the liquid-film and vapor-screen techniques are presented.  The evaporation pattern of a film of white lead applied to the upper surfaces of model 1 shows two rows of bubbles, indicating separation, near the leading edge and further inboard.  Sketches made from vapor-screen studies also indicate separation.  In the vapor-screen technique, light is made to shine through the wind-tunnel windows in a plane perpendicular to the model axis.  Water vapor introduced into the wind tunnel shows regions of separation and vortices as dark areas in the plane of light.  Regions of separation for the light plane near the mid-chord station of the model are shown in figure 5.  The separated region approximately corresponds to the region between the two rows of bubbles seen in the liquid-film pattern.  Further downstream the region of separation is wider and raised higher off the wing.  Still further downstream, the separated region rolls up into discrete vortices.

Calculations made by C. E. Brown of the Langley Laboratory indicate that even for the very slender wing with a Mach number normal to the leading edge of 0.5, the local Mach number on the upper surface of the wing exceeds the critical Mach number.  Thus, transonic effects including shock waves may combine with viscous effects and cause the separation

shown on the wing. Supersonic wing theory, the basis for the design of the wings studied, does not take account of these effects, and differences between theory and experiment are thus to be expected.

Additional visual-flow studies using sublimation and shadowgraph techniques indicate that the boundary layer was turbulent on both upper and lower surfaces of the wing except for a narrow region (enough to support laminar separation) near the leading edge. For these highly sweptback wings the transition pattern was constant for the angle-of-attack and Reynolds number ranges of the tests; thus, the results presented herein are for an essentially turbulent boundary layer.

Figure 6 shows two wings, models 5 and 6, of the same plan form as the previous models, but the camber and twist are different. Model 5 is untwisted and has a cambered wing section. The section normal to the leading edge is the Clark Y (12 percent thick). Model 6 is the same wing twisted in the direction indicated by theory for the previous models; the tips are "washed out."

The experimental results for models 5 and 6 are presented in figures 7 and 8. It can be seen in figure 7 that washing out the tips reduces the lift at fixed angles of attack with little change in lift-curve slope. There is also little change in the minimum drag coefficient, but the drag polar is shifted and, therefore, the maximum lift-drag ratio is increased from 8.4 to 9 (fig. 8). Twisting the wing had a large effect on the pitching moments; for the untwisted wing there would be a drag penalty involved in trimming the wing. The twisted wing trims at optimum lift coefficient.

The effect of adding volume to model 6 is shown in figure 9. Volume was added by placing the wing on a circular-cylindrical body and also by placing wedges under the wing in order to obtain favorable interference lift at the same time the volume was increased. The wedge height for the model shown is 4 percent of the total wing length. In addition, the wing was tested with a wedge having a height of 2 percent of the total wing chord. The maximum lift-drag ratio and volume for the latter wing-wedge model were approximately the same as for the wing with the circular-cylindrical body.

Model 6 (the wing alone) has a large volume. If the wing had as large an area as is currently being considered for some airplanes, for example, 5 or 6 thousand square feet, the volume would be about 10 thousand cubic feet, almost that of the Boeing B-52 fuselage.

Also shown in figure 9 are the lift-drag ratios for a series of delta-wing models (ref. 5). For these models the maximum lift-drag ratio reaches a peak for the wing with a sonic leading edge. Further increases in wing aspect ratio, or area, result in decreased lift-drag ratios.

In figure 10 the calculated and experimental maximum lift-drag ratios for model 6 are shown as a function of Reynolds number. The only change with Reynolds number in the calculated curve is the result of skin friction. Experimental results given by Fred W. Matting in a previous paper on turbulent boundary layers were used in the calculations. Also shown in figure 10 is a calculation in which a drag increment is added to that of model 6, and the results are extrapolated to high Reynolds numbers in a manner to be expected from skin-friction considerations. The added drag increment includes an estimated allowance for vertical fins to provide directional stability and for nacelles. If additional volume were needed, the drag increment would be increased and the lift-drag ratio decreased further.

It can be seen from figure 10 that the experimental lift-drag ratios for model 6 increase at a faster rate with increasing Reynolds number than is to be expected from skin-friction considerations alone. It is believed that this increased rate is caused by changes in separation effects as the Reynolds number is increased.

## CONCLUDING REMARKS

In summary, it is seen that the relatively high lift-drag ratios calculated are only partly realized at low wind-tunnel Reynolds numbers. Further experiments are desirable where conditions closer to actual flight can be obtained.

# APPENDIX

## SYMBOLS

C       wing root chord

$C_D$       drag coefficient

$C_{D_O}$       drag coefficient caused by air friction and wave production due to volume

$C_L$       lift coefficient

$C_m$       pitching-moment coefficient

L/D       ratio of lift to drag

M       Mach number

R       Reynolds number

Z       body ordinate, measured perpendicular to the flight axis at the design attitude

$\alpha$       angle of attack

$\beta = \sqrt{M^2 - 1}$

$\epsilon$       semiapex angle of the wing leading edge

Subscripts:

DES       design conditions

MAX       maximum

## REFERENCES

1. Zhilin, Yu. L.: Wings of Minimum Drag. Prikladnaia Matematika i Mekhanika (Moscow, Leningrad), vol. XXI, 1957, pp. 215-220.

2. Cohen, Doris: The Warping of Triangular Wings for Minimum Drag at Supersonic Speeds. Jour. Aero. Sci. (Readers' Forum), vol. 24, no. 1, Jan. 1957, pp. 67-68.

3. Tucker, Warren A.: A Method for the Design of Sweptback Wings Warped to Produce Specified Flight Characteristics at Supersonic Speeds. NACA Rep. 1226, 1955. (Supersedes NACA RM L51F08.)

4. Grant, Frederick C.: The Proper Combination of Lift Loadings for Least Drag on a Supersonic Wing. NACA Rep. 1275, 1956. (Supersedes NACA TN 3533.)

5. Jorgensen, Leland H.: Experimental Lift-Drag Ratios for Two Families of Wing-Body Combinations at Supersonic Speeds. NACA RM A58A08, 1958.

$(L/D)_{MAX}$ FOR ASSUMED $C_{D_0} = .005$

$M = 3$

——— FLAT, NO L.E. THRUST
- - - FLAT, L.E. THRUST
—·— WARPED

$\beta = \sqrt{M^2 - 1}$

SUBSONIC ←→ SUPERSONIC L.E.

$\beta \tan \epsilon$
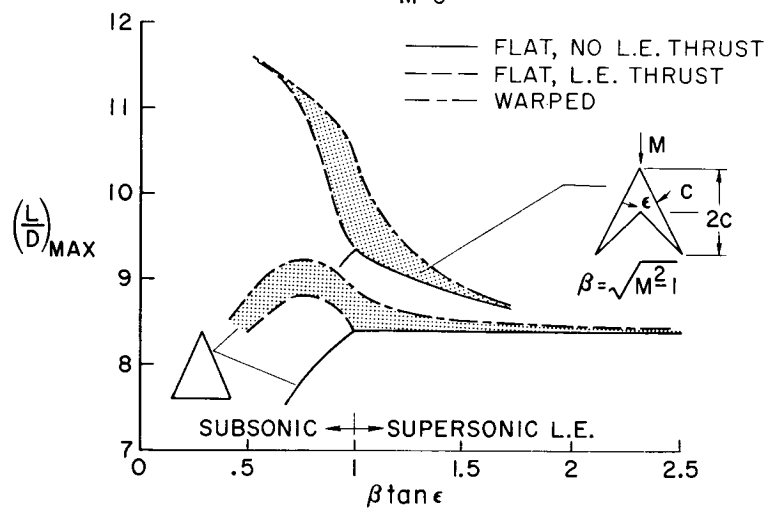
Figure 1

WARPED WINGS
$M_{DES} = 3$

$\beta \tan \epsilon = .5$

$C_{L_{DES}} = .1$   .1   —   .05

$10°$

$7"$

$14"$

$19.5°$

$5"$

1   2   3   4
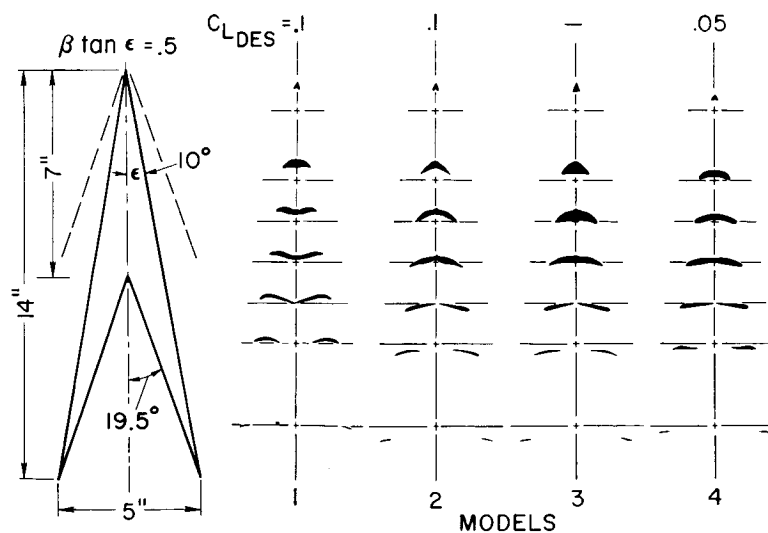
MODELS

Figure 2

## CHARACTERISTICS OF WARPED ARROW WINGS
### $\beta \tan \epsilon = .5$  M=3  R=3.5×10⁶

o MODEL 1, $C_{L_{DES}} = .1$
□ MODEL 4, $C_{L_{DES}} = .05$
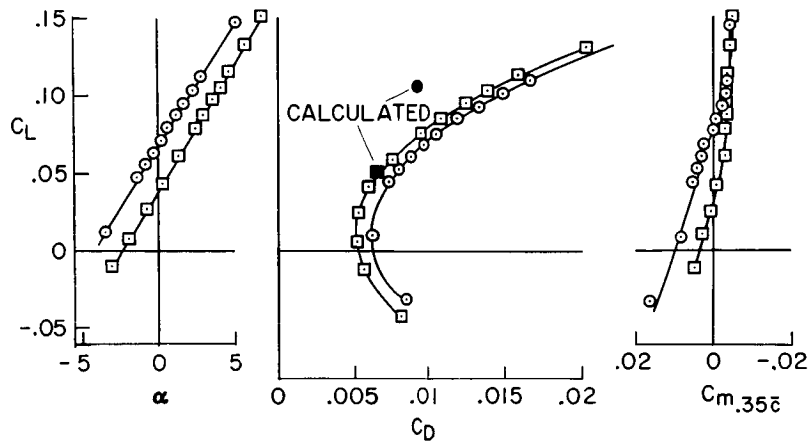


Figure 3

## L/D OF WARPED ARROW WINGS
### $\beta \tan \epsilon = .5$  M=3  R=3.5×10⁶
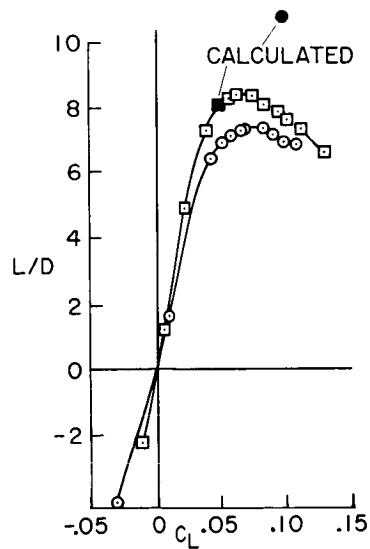


Figure 4

## VISUAL FLOW STUDIES
$\beta \tan \epsilon = .5$     $M = 3$     $\alpha = 0$
$C_L = .07$
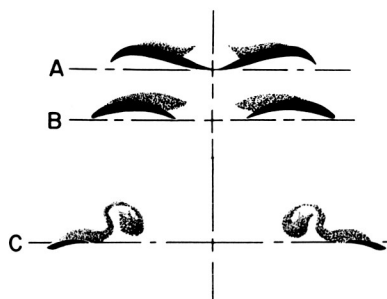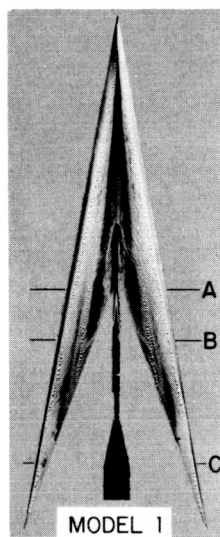


MODEL 1

Figure 5

## CAMBERED ARROW WINGS

$\beta \tan \epsilon = .5$     UNTWISTED     TWISTED



7"

14"

10°

$\epsilon$

19.5°

5"

5     MODELS     6
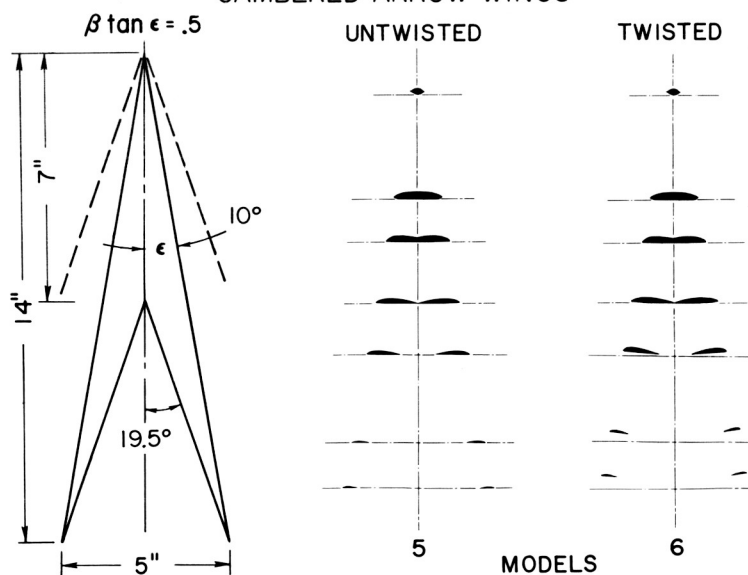
Figure 6

CHARACTERISTICS OF CAMBERED ARROW WINGS
$\beta \tan \epsilon = .5$   M $= 3$   R $= 3.5 \times 10^6$

□ MODEL 5, UNTWISTED
○ MODEL 6, TWISTED
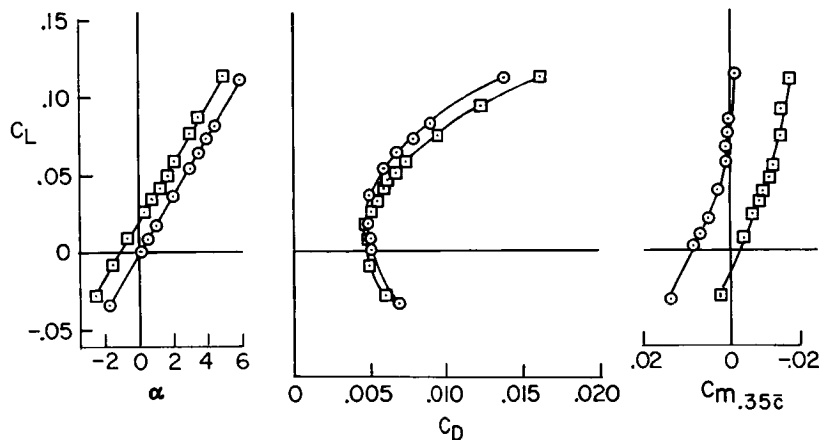


Figure 7

L/D OF CAMBERED ARROW WINGS
$\beta \tan \epsilon = .5$   M $= 3$   R $= 3.5 \times 10^6$

□   MODEL 5, UNTWISTED

○   MODEL 6, TWISTED



Figure 8

VOLUME EFFECT

$M = 3$     $R = 3.5 \times 10^6$

RM A58A08

$(L/D)_{MAX}$

$(VOLUME)^{2/3}/PLAN\ AREA$

Figure 9

SCALE EFFECT

$M = 3$

$\left(\dfrac{L}{D}\right)_{MAX}$

CALCULATED

MODEL 6

PROPULSION AND
STABILITY ALLOWANCE

R, MILLIONS

Figure 10

# AIRPLANE CONFIGURATIONS FOR CRUISE AT A MACH NUMBER OF 3

By Donald D. Baals, Thomas A. Toll, and Owen G. Morris

Langley Aeronautical Laboratory

## SUMMARY

Relative to the problem of efficient cruise at a Mach number of 3, wind-tunnel tests have been made of four complete configurations based on widely different aerodynamic approaches and giving promise of high lift-drag ratios. These designs included a highly cambered arrow-wing configuration with $75^\circ$ of sweep, a $70^\circ$ swept-wing configuration with control surfaces on booms outboard of the wing tip, a canard configuration 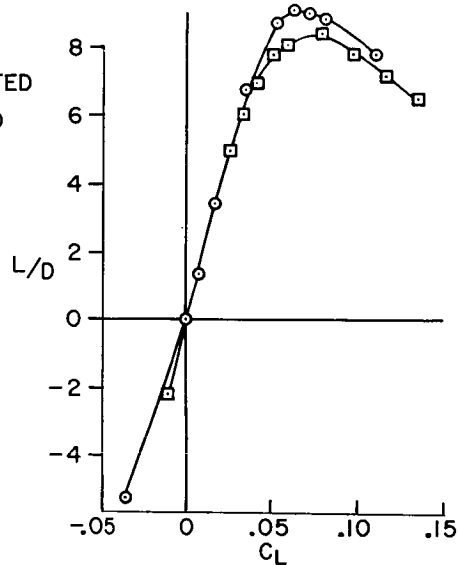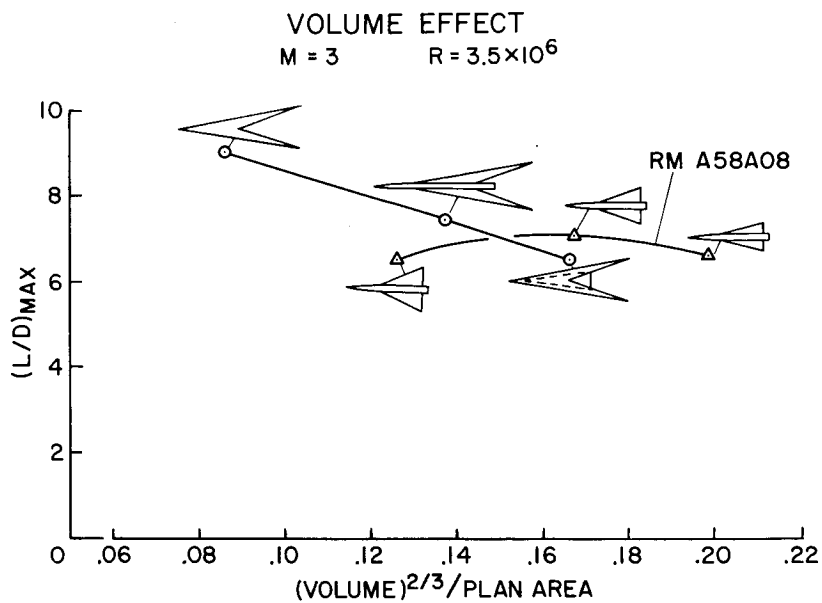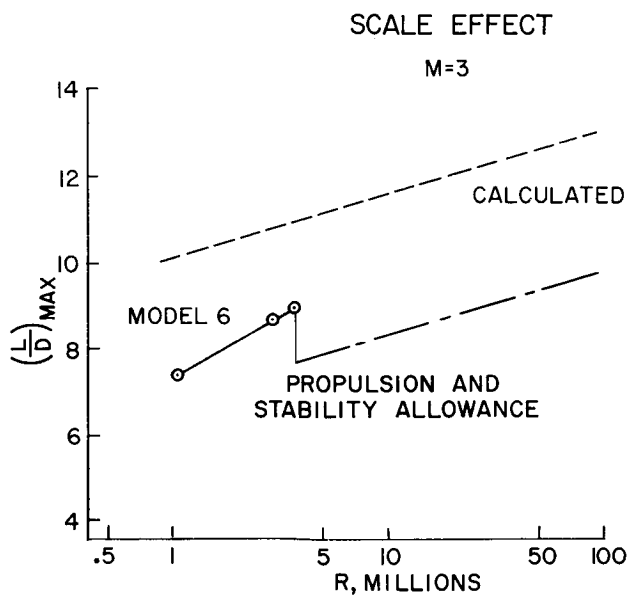with a low-aspect-ratio clipped delta wing employing tip ventrals, and a delta-wing configuration having an aspect ratio of 3. These model designs met, in most cases, minimum requirements of volume, engine simulation, stability and trim applicable to a long-range bomber design. The design concepts and results, however, are believed to be generally applicable.

Although the experimental programs were not sufficiently complete for an evaluation of the special features, high lift-drag ratios were obtained in all cases. Maximum lift-drag ratios of about 6 were measured at a Mach number of 3 for conditions of fixed transition at test Reynolds numbers of 2 to 4 million. These values extrapolate to maximum lift-drag ratios on the order of 7.5 for full-scale Reynolds numbers of about 100 million. The various configurations differed appreciably in minimum drag and in drag due to lift. There is reason to believe that significant performance improvements can still be achieved, perhaps by combining some of the more attractive features of the different configurations.

## INTRODUCTION

The problem of efficient cruise at a Mach number of 3 has placed great emphasis on the achievement of high lift-drag ratios. Relative to this problem, certain aerodynamic approaches appear to have merit. These approaches include optimumizing the total lift distribution for minimum induced drag, the development of favorable lift interference, and the decrease of minimum drag through component design.

39

For the most part, experimental support at a Mach number of 3 for these approaches has been limited to rather elementary models; that is, studies involving wing-body combinations or single components. During the last year the National Advisory Committee for Aeronautics has made experimental studies wherein essentially complete configurations incorporating some of the more promising ideas were investigated in the Mach number range near 3.

Results of four of these model studies are presented. To provide a valid basis for comparison, these model designs usually met minimum requirements of volume, engine simulation, stability, and trim. In general, these configurations were laid out to meet requirements for a long-range-bomber design; however, the design concepts and results should be generally applicable. All test results were obtained under conditions of transition fixed near the leading edges of all surfaces. Inlet air flow was provided for all models, and a drag correction was made for the measured internal momentum losses.

It should be noted that the configurations presented in the present study are not regarded as optimum, and comparative results should not be considered indicative of the ultimate potential of each approach.

SYMBOLS

The lift, drag, and pitching-moment results are given with respect to the wind-axes system; whereas, lateral stability results correspond to body axes. All of the basic moment data are nondimensionalized in terms of wing areas, wing spans, and assumed center-of-gravity locations as given for the various models in the following table.

| Model | Wing area, $S$, sq ft | Wing span, $b$, ft | Wing mean aerodynamic chord, $\bar{c}$, ft | Center-of-gravity location | |
| --- | --- | --- | --- | --- | --- |
| | | | | Distance from nose, ft | Fraction $\bar{c}$ |
| Arrow-wing | 3.49 | 2.50 | 1.70 | 2.33 | ---- |
| Outboard-tail | 1.74 | 2.00 | 1.08 | 2.37 | 0.65 |
| Canard | 4.18 | 1.94 | 2.25 | 3.36 | .24 |
| Delta-wing | .13 | .625 | .277 | .277 | .50 |

The coefficients and symbols are defined as follows:

$C_L$      lift coefficient, $\dfrac{\text{Lift}}{qS}$

$C_{L,OPT}$      lift coefficient at maximum $\dfrac{L}{D}$

$C_D$      drag coefficient, $\dfrac{\text{Drag}}{qS}$

$C_{D,MIN}$      minimum drag coefficient

$C_{D,0}$      zero-lift drag coefficient

$C_{D,0}'$      nominal zero-lift drag coefficient

$C_m$      pitching-moment coefficient, $\dfrac{\text{Pitching moment}}{qS\bar{c}}$

$C_{m,0}$      zero-lift pitching-moment coefficient

$C_f$      skin-friction coefficient

$\dfrac{L}{D}$      lift-drag ratio

$\left(\dfrac{L}{D}\right)_{MAX}$      maximum lift-drag ratio

$q$      dynamic pressure, lb/sq ft

$S$      wing area, sq ft

$A$      wing aspect ratio, $\dfrac{b^2}{S}$

$\lambda$      wing taper ratio, $\dfrac{\text{Tip chord}}{\text{Root chord}}$

$\Lambda$      leading-edge sweep angle, deg

$b$      wing span, ft

$\bar{c}$      wing mean aerodynamic chord, ft

$\dfrac{t}{c}$        ratio of section thickness to section chord

$\left(\dfrac{t}{c}\right)_r$        ratio of wing-root thickness to wing-root chord

R        Reynolds number based on $\bar{c}$

M        Mach number

$\delta_h$        incidence of wing-tip horizontal trimming surface, relative to adjacent wing chord line, deg

$\delta_c$        incidence of canard trimming surface, deg

$\alpha$        angle of attack, deg

$C_{n_\beta}$        directional stability derivative

$C_{l_\beta}$        effective dihedral derivative

$\dfrac{\partial C_D}{\partial C_L{}^2}$        drag-due-to-lift parameter

$\dfrac{\partial C_m}{\partial C_L}$        longitudinal stability parameter

## PRESENTATION OF RESULTS

### The Arrow-Wing Model

Figure 1 shows the configuration characteristics of the arrow-wing model. This model is an application of the arrow-wing approach to the problem of obtaining a high lift-drag ratio. This approach was discussed by Elliott D. Katzen in the previous paper. For the complete configuration presented herein, the wing leading edge has a $75^{\circ}$ angle of sweep. A minimum fuselage is employed with the main volume in the wing. Engine simulation is provided by six separate nacelles, each alined with the local streamlines for minimum drag. All moving control surfaces are located at the wing tips in order to provide longitudinal and directional stability and control.

The wing was designed on the basis of linear theory by using an optimum combination of four loads based on an adaptation of methods presented in references 1 and 2. The wing plan form and idealized

loading distribution were modified in the region of the wing tip in an attempt to reduce the local lift coefficients. The foregoing analytical procedures provided theoretical values for the drag due to lift and the lift-curve slope. The zero-lift wave drag for the complete configuration was estimated from linear theory as the sum of the individual drag of the various components without correction for interference effects. To this value was added the theoretical skin-friction drag (ref. 3) for a turbulent boundary layer at test Mach number and Reynolds number conditions for evaluation of the minimum drag.

Figure 2 shows the basic longitudinal characteristics of the arrow-wing model at $M = 2.87$ for two control deflections (ref. 4). The computed linear-theory values are also shown. The minimum drag coefficient of 0.0110 agrees well with the estimate, but the experimental drag due to lift is considerably higher than calculated. This high induced drag caused the $\left(\frac{L}{D}\right)_{MAX}$ to fall considerably below the estimate, but the value of 6.2 obtained is still relatively high.

The arrow-wing model has a positive value of $C_{m,0}$ due to the "washout" at the wing tips, and the configuration trims at $\left(\frac{L}{D}\right)_{MAX}$ with a very small control deflection. The pitching-moment curves are fairly linear up to the test limit of about $0.2C_L$, although it appears that some reduction in stability has begun at that point.

Outboard-Tail Model

The configuration of figure 3 is referred to as the outboard-tail model. The underlying aerodynamic approach resembles, in some respects, that of the previous arrow-wing design. The lifting surfaces are contained essentially within the Mach cone from the wing apex with the lifting outboard tails providing variation in spanwise as well as longitudinal loading distributions. Favorable drag due to lift is expected to result from the upwash field at the horizontal tails, which allows them to carry an upload at negative tail incidence. Similarly, the sidewash field at the vertical tails can be utilized to provide some additional drag reduction.

This particular arrangement of components was influenced by research directed at obtaining favorable lift characteristics in take-off and landing as well as acceptable stability characteristics through the speed range. A detailed discussion of the design concept is given in reference 5. Engine simulation is provided by a "three-over-three" engine pack exhausting at the fuselage base.

Figure 4 shows the longitudinal characteristics of the outboard-tail configuration at $M = 2.97$ for two control deflections. All coefficients and the given aspect ratio are based on wing plus horizontal-tail area and on the total span. The results presented were obtained as a part of the investigation reported in reference 6.

The maximum lift-drag ratio is about 5.85, with a minimum drag coefficient of about 0.0150. This high value of minimum drag results in part from the fact that this model has approximately double the specified minimum volume. The agreement of experimental with the estimated characteristics is shown to be reasonably good up to maximum $\frac{L}{D}$ but only fair at higher lifts.

In estimating the model lift, only the wing and the horizontal tails were considered. For each of these components, the linear-theory lift slope of the isolated surface was calculated. Also, a calculation of the wing-generated flow field at the tails indicated a rate of change of effective upwash angle with angle of attack of 0.7. This interference effect along with the characteristics of the isolated surfaces yielded the lift estimate shown for the model. Drag due to lift was assumed to be determined by the reciprocal of the lift-curve slope of the wing and of the horizontal tail, with appropriate consideration again given to the vector components of the upwash field. Zero-lift drag was obtained by simple addition of the wave and skin-friction contributions of the components, as in the case of the arrow-wing model.

The outboard-tail model has a positive value of $C_{m,0}$ caused by $3^{\circ}$ of washout at the wing tip and this model trims at $\left(\frac{L}{D}\right)_{MAX}$ for essentially zero control deflection. In its present form, however, this configuration at $M = 2.97$ becomes longitudinally unstable somewhat above the cruise lift coefficient. Subsonic tests, however, indicate that no serious problem exists through the range of take-off lift coefficients. A modified configuration with a $60^{\circ}$ sweep has been developed in an attempt to alleviate this supersonic stability problem.

### Canard Model

Figure 5 shows the configuration characteristics of the canard model. The engine-wing combination is designed to optimumize interference lift at $M = 3$ by positioning the shock from the inlet wedge just behind the leading edge of the wing lower surface. Wing-tip fins are used to reflect these shocks for a further lift increment and to provide directional stability at angles of attack. On the upper surface of the wing the location of the wing ridge line and the shape of the fuselage afterbody have been selected to improve lift-drag interference.

Canard controls along with a modified elliptical fuselage having a nose cant of about $3^O$ have been incorporated in order to achieve efficient trim characteristics.

Figure 6 presents the basic longitudinal characteristics plotted against lift coefficient at M = 3. These results were obtained for a configuration revised from the preliminary model reported in reference 7. The revision consisted of the upward nose cant and addition of upper-surface area to the wing tip fins. The maximum value of lift-drag ratio for the canard configuration is about 6.0, and the minimum drag coefficient is about 0.0120. The configuration is trimmed at maximum $\frac{L}{D}$ with a very small canard deflection but with a low stability margin. Note that the pitching-moment curves are essentially linear over the test lift-coefficient range.

The evident correlation with the estimated characteristics, shown as dashed curves, is an indication that the configuration is performing as anticipated. The estimates are admittedly approximate, however. The configuration lift was estimated as the sum of the isolated canard lift plus the lift of the wing assumed to be a full delta wing in an attempt to approximate the effect of the tip fins. A linear-theory calculation of the interference lift and drag of an undersurface wedge which simulated the solid volume of the engine pack was also included in the estimate. Drag due to lift was assumed equal to the reciprocal of the lift-curve slope, while the zero-lift drag was obtained by simple addition of the component contributions of wave and skin-friction drag.

### Delta-Wing Model

Figure 7 shows the configuration characteristics of a delta-wing model having a leading-edge sweep of $53^O$. The configuration chosen was the result of a systematic study made of a family of wings in the Langley 9-inch supersonic tunnel, the initial phases of which are reported in reference 8. The 2-percent-thick wing is of relatively high aspect ratio, and its leading edge is supersonic at M = 3. This configuration was designed to obtain high lift-drag ratios by a simple combination of low-drag elements. A small $\frac{2}{3}$-power body was located on the underside of the wing with engine simulation provided by six separate internal-compression nacelles.

It should be noted that this configuration is not strictly comparable to the previous models. It has only about one-third the equivalent internal volume of the canard and arrow-wing models, and no control surfaces are provided for trim. The rather large base area has been corrected to free-stream static-pressure conditions.

Figure 8 presents the longitudinal characteristics at $M = 2.91$. The maximum lift-drag ratio for the untrimmed delta-wing configuration is about 6.3, with a minimum drag coefficient of 0.0094 which is the lowest of all configurations tested. The experimental agreement with the theoretical estimates for the delta-wing model is very good. The lift-curve slope was assumed equal to the linear-theory value of $\dfrac{4}{\sqrt{M^2 - 1}}$, which is applicable to delta wings with supersonic leading edges. Drag due to lift was assumed equal to the reciprocal of the lift-curve slope, while the zero-lift drag was estimated by methods similar to those for the previous models.

## Lateral Characteristics

Lateral characteristics of the four models that have already been discussed are summarized in figure 9. This figure shows the directional stability derivative $C_{n_\beta}$ and the effective dihedral derivative $C_{l_\beta}$ plotted against angle of attack for the test Mach number nearest 3.0. Note that all models are directionally stable at the test angles of attack. The arrow-wing, outboard-tail, and canard models have fairly substantial values to angles of attack of at least $10^\circ$; whereas, at the single test condition of a $0^\circ$ angle of attack, the delta-wing model was marginally stable. The derivative $C_{l_\beta}$ ranged from essentially zero in the cruise range for the outboard-tail model to fairly large positive effective dihedral (negative $C_{l_\beta}$) for the arrow wing. No results were obtained for the delta-wing model.

## ANALYSIS OF RESULTS

### Variation of $\left(\dfrac{L}{D}\right)_{MAX}$ With Mach Number

Figure 10 presents the variation of experimental maximum lift-drag ratio with Mach number for the four basic configurations. In general, $\left(\dfrac{L}{D}\right)_{MAX}$ decreases with increasing Mach number, as would be expected from the theoretical increase in drag due to lift.

The most rapid decrease in $\left(\dfrac{L}{D}\right)_{MAX}$ with Mach number occurs for the arrow-wing configuration. This rapid decrease near $M = 3$ is believed to result from a combination of insufficient sweep and the use of air-foil sections having excessive thickness. This combination leads to

local transonic shocks and attendant flow separation. The arrow-wing configuration accordingly exhibits much more favorable $\frac{L}{D}$ characteristics at the lower test Mach number.

The canard configuration, on the other hand, shows a marked peak in $\left(\frac{L}{D}\right)_{MAX}$ at M = 3. This might be expected, since the inlet-wing combination was designed for peak efficiency at this Mach number. Supplementary data, wherein the Mach number and angle of leading-edge sweep were varied, show that the peak may occur rather abruptly near M = 3. It should be noted that although the canard configuration has a relatively low aspect ratio of 0.9, values of $\frac{L}{D}$ comparable to those of the configuration of much higher aspect ratio are obtained.

It will be noted that at Mach numbers near 3, all configurations have a maximum lift-drag ratio of about 6. This fact is more of a coincidence than a general conclusion, for the resulting lift-drag ratios are shown later to result from widely differing characteristics.

Drag Polar Analysis

In order to achieve a better understanding of the lift-drag ratio trends, it is necessary to study the elements that contribute to the form of the drag polar. Figure 11 shows the method that has been adopted in this study. The objective is to divide the total drag into a drag coefficient at zero lift and a drag-due-to-lift term. The experimental drag data are plotted against $C_L^2$. As is generally true with wings having camber, twist, or some means for obtaining favorable lift interference, $C_D$ does not vary linearly with $C_L^2$. Therefore, in a strict sense the drag due to lift cannot be defined precisely by a single term proportional to $C_L^2$.

For practical purposes, however, a single-term method can be devised to represent the most significant portion of the drag polar by drawing a straight line tangent to the experimental curve of $C_D$ plotted against $C_L^2$ at the point corresponding to $\left(\frac{L}{D}\right)_{MAX}$. The slope of the tangent gives the value of $\frac{\partial C_D}{\partial C_L^2}$, and the intercept at zero lift is a nominal drag value of $C_{D,0}'$ usually slightly less than the experimental minimum drag but close to the minimum drag that would be measured for a

symmetrical model with the twist and camber removed. With the parameters $\frac{\partial C_D}{\partial C_L{}^2}$ and $C_{D,0}'$ determined, the effects of independent variation of the

parameters on $\left(\frac{L}{D}\right)_{MAX}$ and on the optimum lift coefficient can be studied through simple equations such as those shown in figure 11. These equations form the basis for estimating the effects of Reynolds number on $\frac{L}{D}$ and $C_{L,OPT}$ presented later. For the subsequent analysis, values of $C_{D,0}'$ are not presented, but data are given for $C_{D,MIN}$ which, for the configurations considered, is generally only slightly greater than $C_{D,0}'$.

$$\text{Variation of } C_{D,MIN} \text{ and } \frac{\partial C_D}{\partial C_L{}^2} \text{ With } M$$

Figure 12 shows the variation in $C_{D,MIN}$ and $\frac{\partial C_D}{\partial C_L{}^2}$ with Mach number for the four basic configurations. Relative to the minimum drag at $M = 3$, it will be noted that there is about a 50-percent variation in $C_{D,MIN}$, from the low value for the delta-wing model to the high value for the outboard-tail model. This difference is caused, in part, by the greatly differing levels of internal volume. The delta-wing model has about one-third the volume of the arrow-wing and canard models, while the outboard-tail model has about twice their volume.

Relative to the minimum drag of these configurations, the skin friction at test Reynolds numbers is the major component and ranges from about $1\frac{1}{2}$ to 3 times the value of the estimated pressure drag. These values indicate the great importance of testing under known boundary-layer conditions, for any variation in skin friction can completely mask the pressure drag.

The drag-due-to-lift characteristics are also shown in figure 12. In all cases the drag due to lift increases with increasing Mach number as predicted by linear theory. The outboard-tail configuration is shown to have the lowest value of all configurations tested, which indicates the effectiveness of its design concept. The low drag due to lift compensates for the high minimum drag of this configuration in determining its lift-drag ratio.

The arrow wing, however, has a drag due to lift which increases rapidly with Mach number and attains a maximum value of about 0.7 at $M = 3$. This value is about 40 percent greater than the theoretical estimate and corresponds in theory to that of a plane wing with supersonic leading edges such as for the delta-wing model.

The arrow-wing approach, however, is considered to have merit, for the design deficiencies of the initial model are now better understood and are capable of improvement. Although this configuration has attractive characteristics near $M = 3$, the optimum application may be found to occur at somewhat lower Mach numbers.

It should be noted that there are considerable additional wing-body data available at Mach numbers of about 3 which bear on the general problem of lift-drag ratio but which are not included herein. Although no positive statement can be made concerning their potential as to complete configurations, the drag-due-to-lift factors are, in general, less attractive than those of the complete configuration presented here.

$$\text{Variation of Trim } \frac{L}{D} \text{ With } \frac{\partial C_m}{\partial C_L}$$

Thus far mainly maximum lift-drag ratio characteristics of the various configurations have been considered. The cost of trimming over a range of stability margins is now considered. Figure 13 shows the variation in trim $\left(\frac{L}{D}\right)_{MAX}$ with stability level $\frac{\partial C_m}{\partial C_L}$ for values of test Mach number nearest 3. The curves were established from experimental data for which different control settings were used. For any of the configurations shown, trim at rather large stability margins can be obtained for rather small penalties in $\left(\frac{L}{D}\right)_{MAX}$. The trim $\left(\frac{L}{D}\right)_{MAX}$ for the canard model, however, begins to decrease at a somewhat lower stability margin than for the other models.

At the bottom of figure 13 are noted the supersonic stability margins required for neutral subsonic stability. These margins were determined from subsonic tests of the basic configurations and merely represent the shift of the aerodynamic center with Mach number. The plot shows that the experimental stability levels at $M \approx 3$ for the arrow-wing and outboard-tail models are higher than needed in order to maintain neutral subsonic stability. The particular canard configuration shown, however, would require an increase in supersonic stability level from the test conditions. Some performance penalty would result, therefore, unless special aerodynamic or mechanical methods are employed. The shift of the aerodynamic center shown is believed more a function of body-wing-inlet design rather than any inherent characteristic of the canard control. Canard models have been tested which have shown considerably less shift than that indicated here. (For example, see reference 9 and the paper by Charles F. Hall and John W. Boyd.)

Figure 14 shows the predicted extrapolation to full-scale Reynolds numbers of the $\left(\frac{L}{D}\right)_{MAX}$ values for a Mach number of 3. A theoretical variation of skin friction with Reynolds number for adiabatic conditions (ref. 3) is assumed as well as the constancy of drag due to lift with Reynolds number. The experimental values of $\frac{L}{D}$ have been adjusted to M = 3 and are shown plotted at their respective test Reynolds numbers.

The dashed line is the theoretical extrapolation in lift-drag ratio starting from a mean test value of about 6 at a Reynolds number of 3 million. A ±10-percent spread from the theoretical turbulent skin-friction variation is also shown. This variation is indicative of the range from a small amount of laminar flow to all-turbulent flow with some roughness drag. As pointed out in the paper by K. R. Czarnecki, John R. Sevier, Jr., and Melvin M. Carmel, and in the paper by Albert E. von Doenhoff, such an extrapolation presumes extreme care has been exercised in minimizing the drag due to protuberances, air leakage, and auxiliary inlets and outlets in order to justify limiting the model scale corrections to skin friction only. The problem of exit drag is discussed in a following paper by John M. Swihart and William J. Nelson.

The extrapolation is considered to provide evidence that values of $\left(\frac{L}{D}\right)_{MAX}$ of the order of 7.5 may be achieved at M = 3 for complete configurations at a Reynolds number of about 100 million. This value represents an attractive level of lift-drag ratio and results in a product of $M \times \frac{L}{D}$ for the basic range equation which exceeds the value for the best subsonic configurations.

An extrapolation of the lift coefficient at which $\left(\frac{L}{D}\right)_{MAX}$ occurs $\left(\text{that is, } C_{L,OPT}\right)$, when made on the basis of conditions identical with those used for $\left(\frac{L}{D}\right)_{MAX}$, shows that the full-scale values of $C_{L,OPT}$ would be expected to fall within the range from 0.09 to 0.11 for the configurations investigated.

## CONCLUDING REMARKS

Results have been presented for essentially complete airplane configurations based on widely differing aerodynamic approaches to the problem of obtaining a high lift-drag ratio. Although the experimental programs were not sufficiently complete for an evaluation of the special features, high lift-drag ratios were obtained in all cases.

Maximum lift-drag ratios of about 6 were measured at a Mach number of 3 for test Reynolds number conditions. These values extrapolate to a maximum lift-drag ratio value on the order of 7.5 for full-scale Reynolds numbers of about 100 million.

The various configurations differed appreciably in minimum drag and in drag due to lift. There is reason to believe, therefore, that significant performance improvements can still be achieved, perhaps by combining some of the more attractive features of the different configurations.

Certain deficiencies noted for the various configurations, particularly with regard to trim and stability characteristics, do not appear to present prohibitive problems of solution.

534

REFERENCES

1. Tucker, Warren A.:  A Method for the Design of Sweptback Wings Warped to Produce Specified Flight Characteristics at Supersonic Speeds. NACA Rep. 1226, 1955.  (Supersedes NACA RM L51F08.)

2. Grant, Frederick C.:  The Proper Combination of Lift Loadings for Least Drag on a Supersonic Wing.  NACA Rep. 1275, 1956.  (Supersedes NACA TN 3533.)

3. Van Driest, E. R.:  Turbulent Boundary Layer in Compressible Fluids. Jour. Aero. Sci., vol. 18, no. 3, Mar. 1951, pp. 145-160,216.

4. Hallissy, Joseph M., Jr., and Hasson, Dennis F.:  Aerodynamic Characteristics at Mach Numbers 2.36 and 2.87 of an Airplane Configuration Having a Cambered Arrow Wing With a 75° Swept Leading Edge. (Prospective NACA paper.)

5. Sleeman, William C., Jr.:  Preliminary Study of Airplane Configurations Having Tail Surfaces Outboard of the Wing Tips.  NACA RM L58B06, 1958.

6. Church, James D., Hayes, William C., Jr., and Sleeman, William C., Jr.: Investigation of Aerodynamic Characteristics of an Airplane Configuration Having Tail Surfaces Outboard of the Wing Tips at Mach Numbers of 2.30, 2.97, and 3.51.  NACA RM L58C25, 1958.  (Prospective NACA paper.)

7. Kelly, Thomas C., Carmel, Melvin M., and Gregory, Donald T.:  An Exploratory Investigation at Mach Numbers of 2.50 and 2.87 of a Canard Bomber-Type Configuration Designed for Supersonic Cruise Flight.  NACA RM L58B28, 1958.

8. Mueller, James N.:  An Investigation of the Effect of Varying the Maximum-Thickness Position Upon the Aerodynamic Characteristics of a Series of $3\frac{1}{2}$-Percent-Thick Delta Wings.  NACA RM L55D26, 1955.

9. Spearman, M. Leroy, and Driver, Cornelius:  Some Factors Affecting the Stability and Performance Characteristics of Canard Aircraft Configurations.  NACA RM L58D16, 1958.  (Prospective NACA paper.)
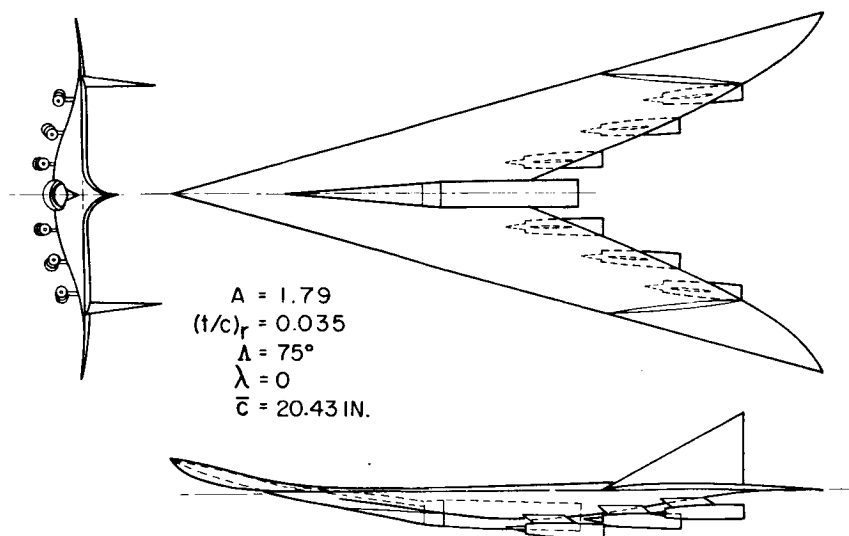
ARROW-WING MODEL



$A = 1.79$
$(t/c)_r = 0.035$
$\Lambda = 75°$
$\lambda = 0$
$\bar{c} = 20.43$ IN.

Figure 1

LONGITUDINAL CHARACTERISTICS OF ARROW-WING MODEL
M = 2.87; R = 4×10⁶
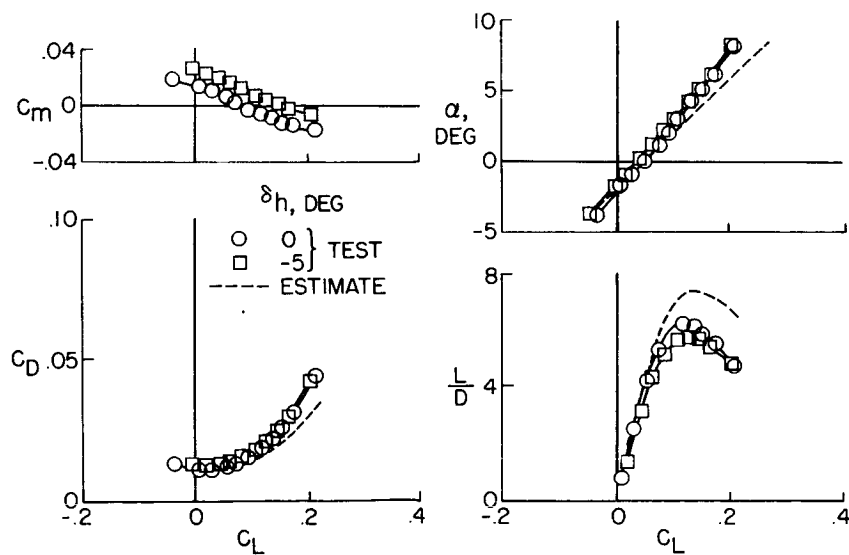


Figure 2

OUTBOARD-TAIL MODEL



A = 2.3
t/c = 0.04
Λ = 70°
λ = 0.127
c̄ = 12.95 IN.

Figure 3

LONGITUDINAL CHARACTERISTICS OF OUTBOARD-TAIL MODEL
M = 2.97; R = 2×10⁶



Figure 4

## CANARD MODEL



$$A = 0.904$$
$$t/c = 0.025$$
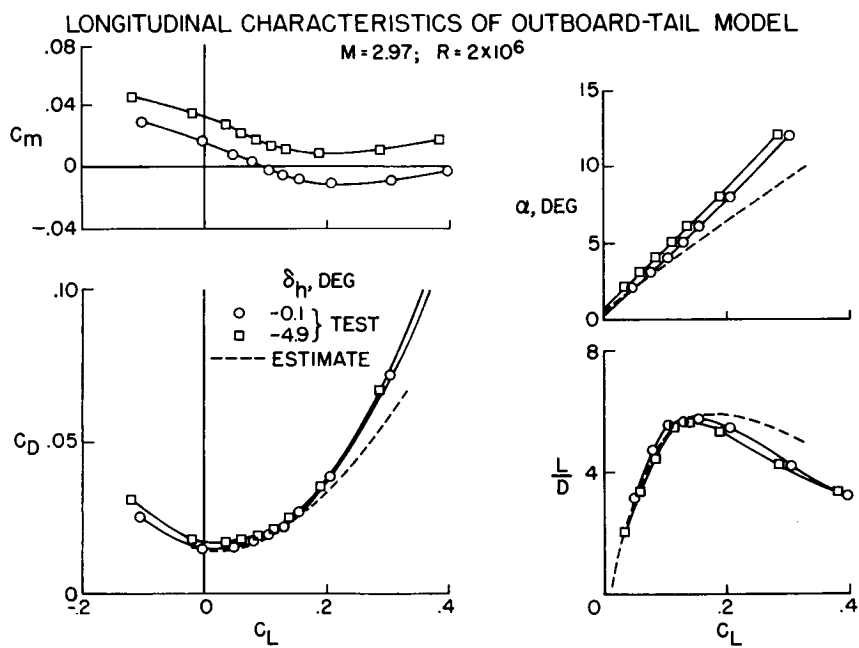$$\Lambda = 62°$$
$$\lambda = 0.437$$
$$\overline{c} = 27 \text{ IN.}$$
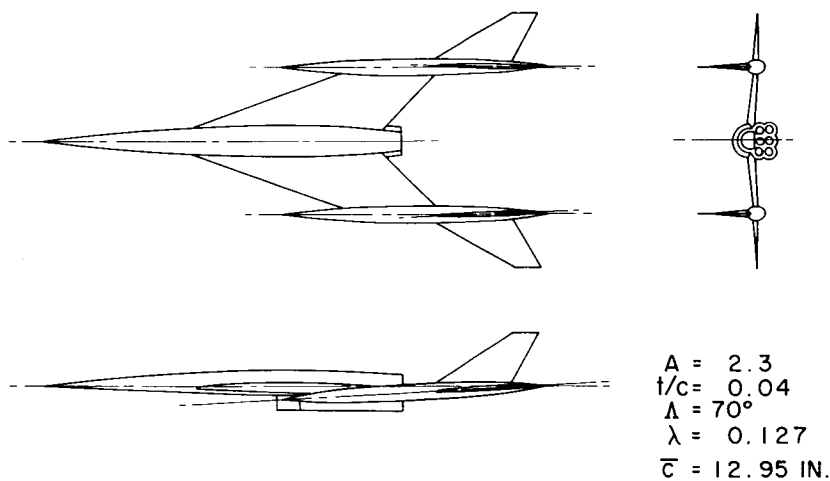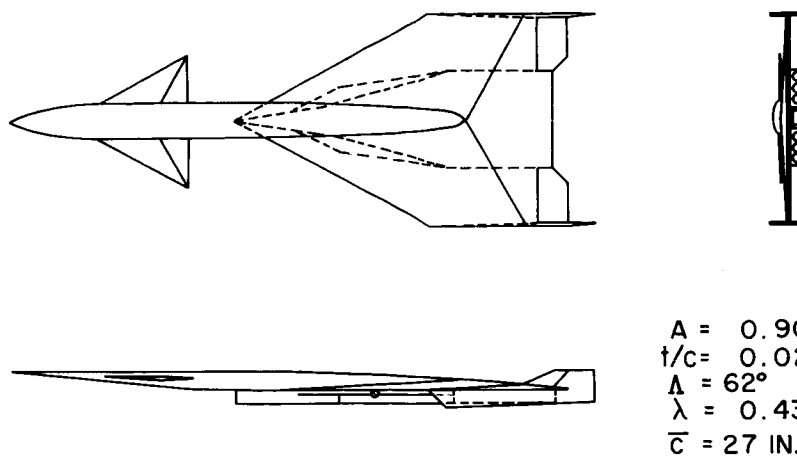
Figure 5

## LONGITUDINAL CHARACTERISTICS OF CANARD MODEL

$$M = 3; \ R = 2.5 \times 10^6$$
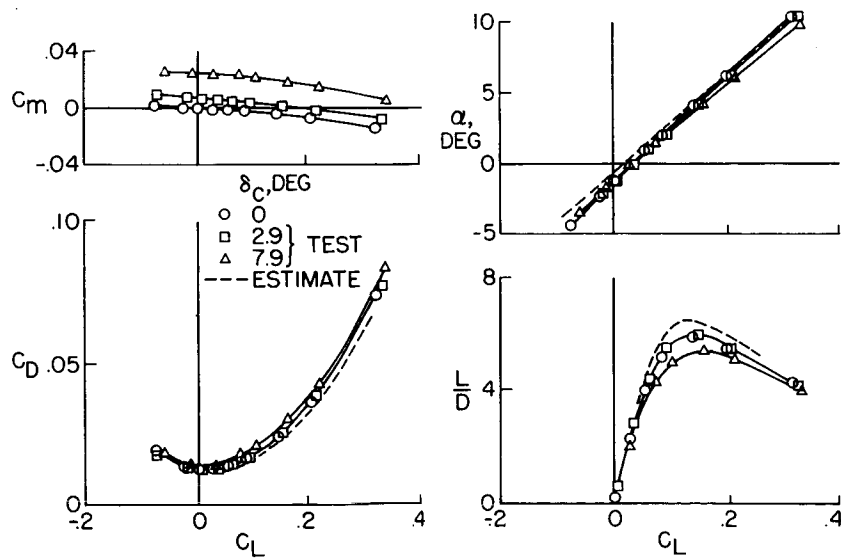


Figure 6

DELTA-WING MODEL



A = 3.00
t/c= 0.02
Λ = 53°
λ = 0
$\bar{c}$ = 3.33 IN.
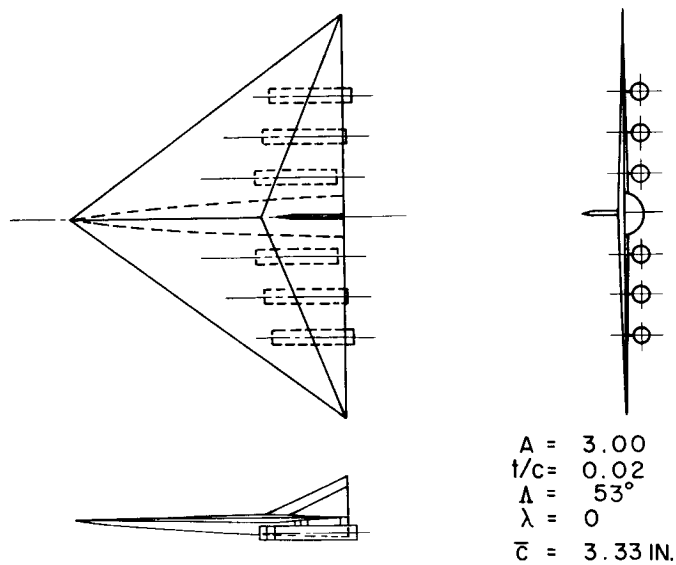
Figure 7

LONGITUDINAL CHARACTERISTICS OF DELTA-WING MODEL
M=2.91; R=1.35x10^6
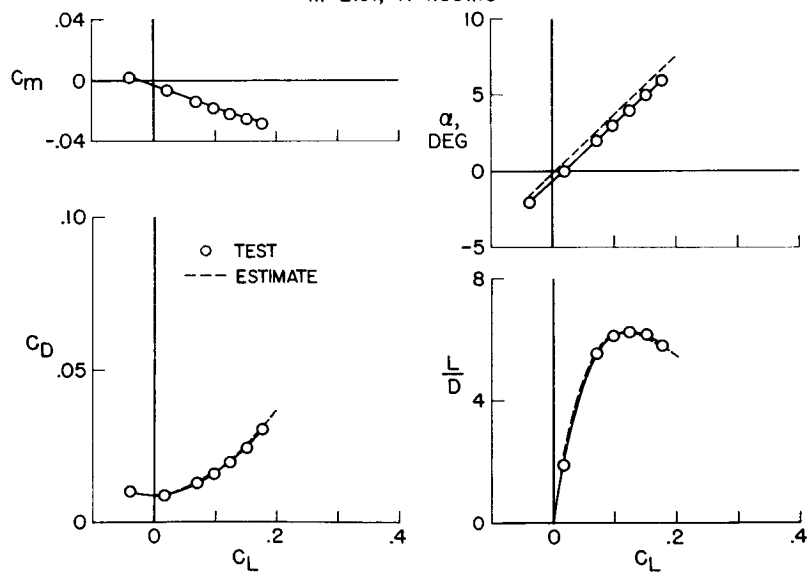


Figure 8

LATERAL CHARACTERISTICS

M ≈ 3.0
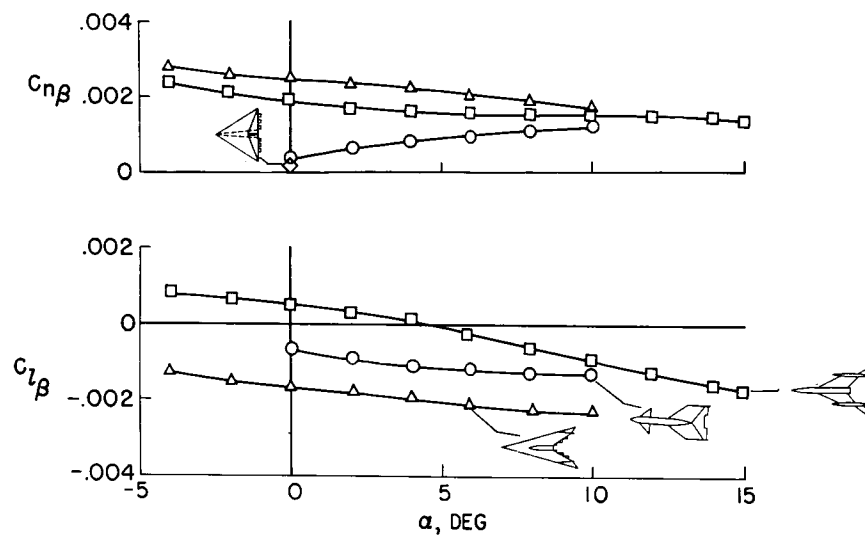


Figure 9

VARIATION OF $\left(\frac{L}{D}\right)_{MAX}$ WITH MACH NUMBER
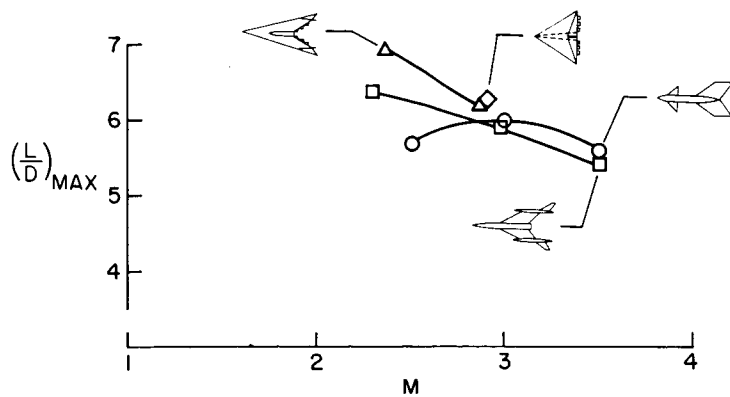


Figure 10

## DRAG POLAR ANALYSIS



$$\left(\frac{L}{D}\right)_{MAX} = \sqrt{\frac{0.5}{c_{D,0}\,\frac{\partial C_D}{\partial C_L^2}}}$$

SLOPE $= \dfrac{\partial C_D}{\partial C_L^2}$

$$C_{L,OPT} = \sqrt{\frac{c_{D,0}}{\frac{\partial C_D}{\partial C_L^2}}}$$
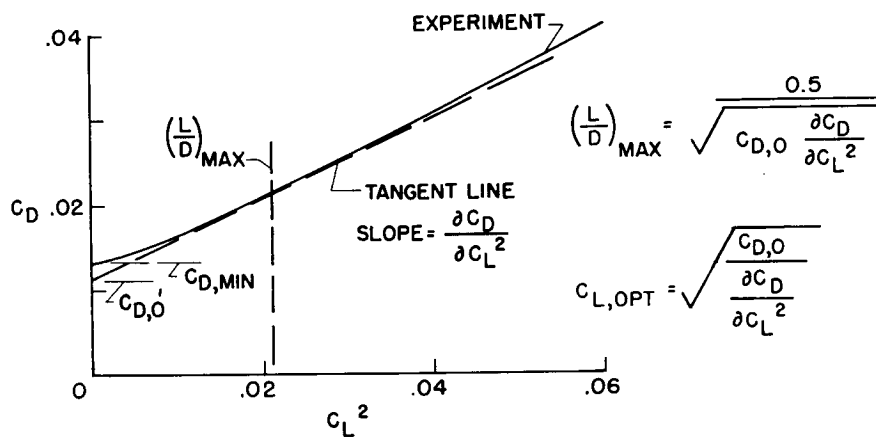
Figure 11

## VARIATIONS OF $C_{D,MIN}$ AND $\dfrac{\partial C_D}{\partial C_L^2}$ WITH MACH NUMBER
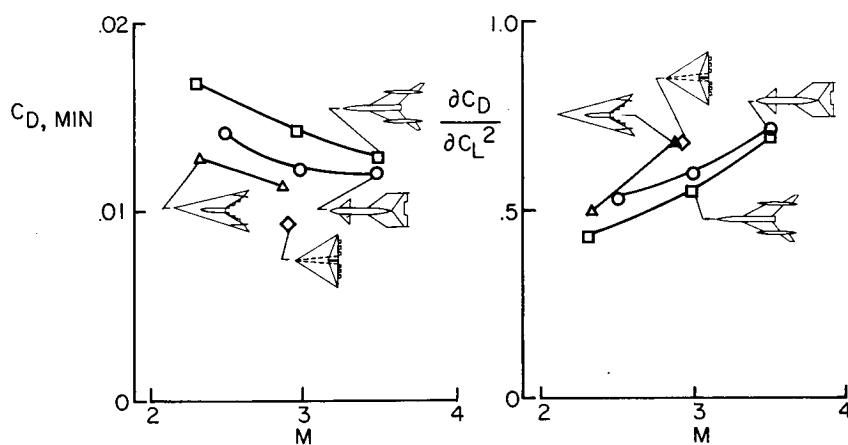


Figure 12

EFFECT OF LONGITUDINAL STABILITY ON $\left(\dfrac{L}{D}\right)_{MAX}$

$M \approx 3.0$



$\left(\dfrac{L}{D}\right)_{MAX}$

VALUE OF $-\dfrac{\partial C_m}{\partial C_L}$ REQUIRED FOR NEUTRAL SUBSONIC STABILITY

STABILITY MARGIN, $-\dfrac{\partial C_m}{\partial C_L}$
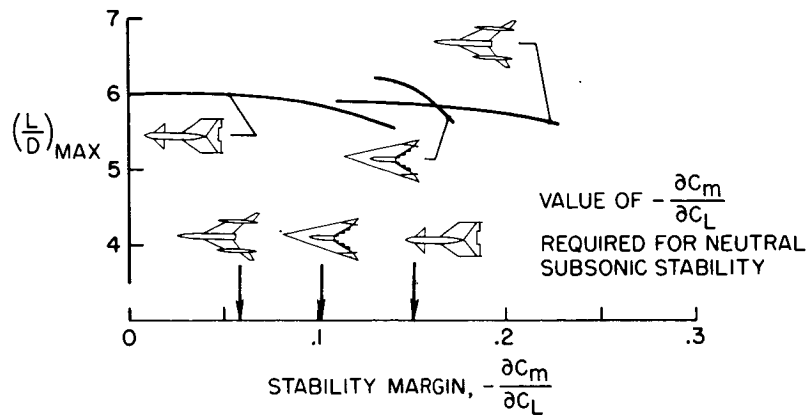
Figure 13

EXTRAPOLATION OF $\left(\dfrac{L}{D}\right)_{MAX}$ TO FULL SCALE

$M = 3.0$



FULL SCALE; 65,000-FT. ALT.

$\left(\dfrac{L}{D}\right)_{MAX}$

$\pm 0.10\ C_f$

THEORETICAL TURBULENT SKIN FRICTION

R

Figure 14

EFFECTS OF CANARDS ON AIRPLANE

PERFORMANCE AND STABILITY

By Charles F. Hall and John W. Boyd

Ames Aeronautical Laboratory

INTRODUCTION

In considering the use of a canard in preference to a trailing-edge flap or tail control, the designer may ask the following questions: (1) What is its effect on lift-drag ratio and maximum trim lift at cruise and high-speed flight? (2) Is the control effective throughout the Mach number range and will it trim the airplane to a sufficiently high lift in the landing and take-off attitude? (3) Will the control affect adversely the longitudinal and lateral stability of the configuration? (4) What effect will the configuration vari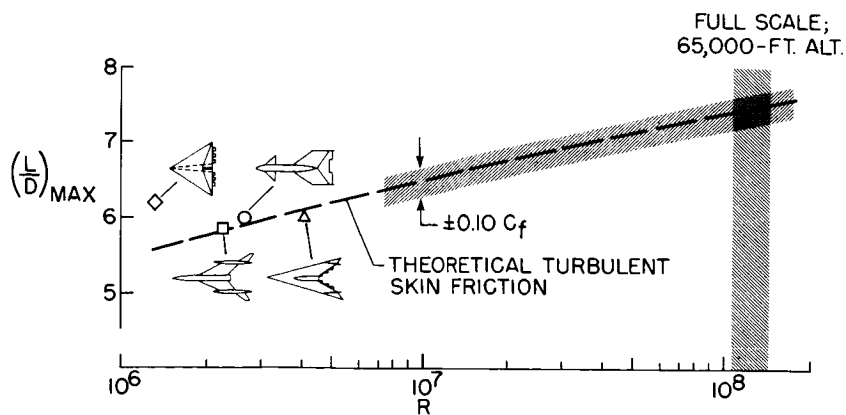ables have on the answers to these questions? To answer these questions an extensive investigation has been conducted at the Ames and Langley laboratories during the past year on canard airplane configurations.

Wide ranges in control plan form, size, and position and in wing plan form have been examined, as shown in figure 1. Also shown in figure 1 are several trailing-edge flap and tail-aft arrangements which have been used for comparison purposes in discussing the various characteristics of the canards. In addition to plan-form effects, experimental investigations of the effects of canard height with respect to the wing and body and of wing height with respect to the body have been made on several of the configurations in figure 1. Various arrangements of vertical tails and ventral fins in combination with canard controls have also been studied experimentally.

It is beyond the scope of this paper to discuss in detail the characteristics of the many configurations shown in figure 1. The purpose of this paper is to give an overall picture of canard characteristics, stressing those characteristics which make the canard either a desirable or an impractical control, and to select data for configurations of figure 1 which are illustrative of these trends. More detailed information on the configuration characteristics can be found in references 1 to 13.

An obvious advantage of canard controls over control-aft arrangements stems from the present-day trends in high-speed aircraft, that is,

an increase in the fineness ratio of the body, a rearward movement of the center of gravity as the engines are brought closer to the fuselage base, and a corresponding rearward movement of the wing with respect to the body. Such trends permit the distance from the control to the center of gravity to be larger in general for the canard than for the aft control arrangement. This geometric advantage permits the control size, force, and hence drag to be less for a canard than for an aft control. Thus, in comparing the trim characteristics of canard and aft control arrangements it should be realized that any advantage of the former over the latter control can result from this geometric advantage. Nevertheless, the comparisons to be made subsequently are considered valid and worthwhile because many of the configurations shown in figure 1 represent actual airplanes presently used by the Air Force or are very similar to proposed airplanes.

## PERFORMANCE

Before discussing the experimental trim-drag characteristics of canard and control-aft arrangements a few simplifying concepts will be considered to determine whether one type of control has certain characteristics which make it superior to the other type and to provide orientation for the experimental data. Figure 2 represents a wing with either a canard or aft control arrangement. The normal forces on these surfaces for trim and stability are indicated as follows: $N$ is the force on the wing, $N_\alpha$ the control force due to angle of attack, $N_\delta$ the control force due to control deflection, and $N_i$ the force on the wing due to canard interference. The center of gravity must be located to assure static stability; that is, it must be ahead of the resultant of $N$ and $N_\alpha$. For the canard the single case is shown in which $\delta/\alpha$ is equal to or greater than 0. For the aft control two cases are important, that in which $\delta/\alpha$ is between 0 and -1 and that in which $\delta/\alpha$ is less than -1; in the first case the control is positively inclined to the free stream and in the second case it is negatively inclined.

Considering first the canard arrangement, figure 2 shows that the canard carries positive lift to balance the wing lift, a beneficial effect. However, the drag component of this lift is greater than that of a comparable lift carried by the wing because of the greater inclination of the force vector to the free stream. When the zero-lift drag of the control is added to the drag due to lift it is seen that the drag of the trimmed wing is higher than that of the untrimmed wing. It is also seen that this difference in drag increases as $\delta/\alpha$ increases because of the greater inclination of the force vector. The diagram shows that the horizontal component of $N_i$ is in the thrust direction.

However, this thrust is always smaller than the drag increase resulting from the increase in wing angle of attack to compensate for the loss in lift due to interference, and thus canard-wing interference results in a net drag increase.

Considering the wing and aft control with $\delta/\alpha$ between 0 and -1 and with the center of gravity behind the wing center of pressure, the diagram shows that the control carries positive lift, which is a beneficial effect. This lift will have a drag component because of its rearward inclination, but the diagram cannot present a clear-cut comparison of this drag increment with that which would occur if the wing were carrying this lift. Nevertheless, when the zero-lift drag of the control is considered it is probable that the drag of the trimmed wing is higher than that of the untrimmed wing. Furthermore, as with the canard arrangement, interference between the wing and aft control increases the trim drag. An increase in downwash from the wing necessitates a clockwise rotation of the control from the position shown in figure 2 to obtain the same normal force, and hence an increase in the horizontal component of the force.

For the second case of a wing having an aft control wherein $\delta/\alpha$ is between 0 and -1, the center of gravity is ahead of the wing center of pressure. The control thus carries a negative lift to balance, which is an adverse effect. Due to a large downwash from the wing the control force is inclined into the free stream so that a thrust exists, which is a favorable effect. The thrust is smaller, however, than the drag increase resulting from the increase in wing angle of attack to compensate for the negative lift on the control. When the zero-lift drag of the control is considered it is seen that the drag of the trimmed wing is greater than that of the untrimmed wing. Nevertheless, it is seen that for $\delta/\alpha$ between zero and -1 the trim drag can be small either because the control is carrying positive lift, as in the first case, or because the negative lift has a horizontal component in the thrust direction, as in the second case.

In the last case, for $\delta/\alpha$ less than -1, the control force is down to balance the wing lift and its horizontal component is in the drag direction. Both effects are adverse, and therefore the trim drag is high. Furthermore, as $\delta/\alpha$ becomes more negative the inclination of the force vector to the free stream increases, and thus causes an increase in trim drag.

It is evident that the simplified force diagrams of figure 2 do not show which is the better control. They show that the trim drag is reduced as $\delta/\alpha$ reduces toward zero for the canard and increases towards -1 for the aft control because of a reduction in the inclination of the force vector, and they serve to aid in the analysis of the data.

Therefore they will be applied to a comparison of the trim drag for canard and aft-control arrangements.

The trim characteristics of an unswept wing having either a canard, an inline tail, or a high tail are compared in figure 3. The center of gravity for each configuration is set so that the minimum static stability occurring in either the subsonic or the supersonic speed range is comparable for all configurations. For the canard and inline-tail arrangements, the results show that the absolute value of $\delta/\alpha$ was greater than 1 in each case so that the forces are as indicated on the left side and right side of figure 2. The results for a Mach number of 1.3 show that the trim drag of the canard was slightly less than that of the tail even though the absolute values of $\delta/\alpha$ were approximately the same. Possibly of greater importance is the effect of Mach number on the characteristics. The wing is the same in each case, but its center of pressure is moved aft and each control lift-curve slope is reduced with Mach number. Both effects tend to increase the absolute value of $\delta/\alpha$ and hence to increase the trim drag. However, the center of lift on the canard and the associated interference lift on the body move forward with increasing Mach number. This movement tends to reduce the required control force and, hence, the deflection, so that $\delta/\alpha$ is essentially constant in the Mach number range of figure 3. In general this forward movement of the center of pressure with increasing Mach number between Mach numbers of 1 and 2 has been characteristic of the canard configurations investigated, and in the case illustrated in figure 3 amounted to 15 percent of the control length. Furthermore, a significant reduction in the interference lift with increasing supersonic Mach number resulted in the increase in the ratio of trim-lift drag to wing-body lift drag. This reduction in interference with Mach number has also been characteristic of the various canards investigated. On the other hand, for the inline-tail configuration no effect existed to compensate for the rearward travel of the wing center of pressure and the decreasing control lift-curve slope with decreasing Mach number, and therefore the control force and negative deflection increased. Furthermore, the wing downwash decreased with Mach number so that the negative deflection of the control was increased to maintain an equal force. From the force diagram on the right of figure 2 it is evident that increasing the download and negative deflection results in an increase in the drag component of the control force and hence an increase in trim drag.

It should be mentioned that in both cases the trim drag could be reduced if at subsonic speeds artificial stability devices were used, or if the canard were permitted to free-float so that the center of gravity could be moved closer to the wing center of pressure and the value of $\delta/\alpha$ for trim could be reduced. Nevertheless, the relative effects of increasing supersonic Mach number would be the same.

The adverse effects of Mach number for the inline tail are not necessarily characteristic of an aft control arrangement, as indicated by the results for the high tail. The data show that for the high-tail arrangement $\delta/\alpha$ was between 0 and -1, and therefore the control forces are as indicated by the lower center diagram of figure 2. The low value of $\delta/\alpha$ resulted from two factors. First, the control drag produced a positive trimming moment and thus reduced the normal force required for trim. This effect would also reduce the canard trim drag if the canard were moved above the center of gravity by negatively cambering the body, as has been done on several of the configurations shown in figure 1. Second, interference between the vertical and horizontal tails induced a download on the tail with no corresponding increase in negative deflection. The results show that the effect of Mach number was favorable for the high-tail arrangement. This favorable effect resulted from the fact that the downwash from the wing in the vicinity of the tail increased between Mach numbers of 1.3 and 2. Thus the inclination of the tail to the free stream was increased to maintain an equal load and the result was a greater thrust component of the control force and, hence, less trim drag. This favorable effect of Mach number on the high-tail characteristics is determined by the location of the tail with respect to the shock waves from the leading and trailing edges of the wing. When the horizontal tail is outside of the region bounded by these two shock waves the downwash from the wing is small and therefore $\delta/\alpha$ is more negative and the trim drag is greater than shown in figure 3 for a Mach number of 2. Thus, these favorable effects of Mach number will disappear at some higher Mach number where the shock wave from the wing leading edge is depressed below the horizontal tail. Also, raising the horizontal tail or moving it forward will lower the range of Mach numbers in which this favorable effect is present. Although the characteristics of the high-tail arrangement shown in figure 3 are very desirable it should be mentioned that these benefits of a high tail may be outweighed by longitudinal-stability and structural problems associated with the arrangement.

Another comparison of the trim-drag characteristics of canard and aft control arrangements is made in figure 4, in which results for a canard and a trailing-edge flap in combination with a triangular wing (configurations 1 and 15) are shown. At low supersonic Mach numbers the absolute value of $\delta/\alpha$ was greater for the canard than for the trailing-edge flap as a result of lower control effectiveness for the canard configuration; the trim drag of the canard configuration was therefore higher. With increasing Mach number the canard became considerably superior to the trailing-edge flap, partly because of the beneficial characteristics mentioned in conjunction with the unswept wing and canard arrangement of figure 3, that is, a forward movement of the center of pressure due to canard lift and its associated interference lift on the body and a reduction in canard-wing lift interference.

In addition to the aforementioned favorable effects of Mach number on the trim-drag characteristics of canard configurations with either unswept or triangular wings, another favorable characteristic was present in the case of the triangular wing which was primarily responsible for its more impressive beneficial effects with increasing Mach number. This additional beneficial effect was the large forward movement of the wing and body center of pressure with increasing Mach number, as indicated in figure 5. The position of the center of pressure is expressed as a percentage of the mean aerodynamic chord of the respective wing, and thus the large differences in the characteristics of the triangular and the unswept wing are due in part to the fact that the mean aerodynamic chord of the former wing is approximately $1\frac{1}{2}$ times that of the latter wing for the same area. Nevertheless, even accounting for these differences, the results of figure 5 indicate that the maximum rearward travel of the center of pressure between subsonic and supersonic speeds was less and the forward movement of the center of pressure with increasing supersonic Mach number was faster for the triangular wing than for the unswept wing. The forward movement of the center of pressure of the triangular wing and body, coupled with the aforementioned forward shift of the center of pressure of lift due to the canard as supersonic Mach number increased, caused the center of pressure of the triangular wing with canard to be the same at a Mach number of 3.4 as at a Mach number of 0.7. The data thus raise the interesting possibility that the position of the center of gravity for a triangular wing and canard arrangement similar to this may be dictated by characteristics at Mach numbers above approximately 3.5 rather than at subsonic speeds.

Returning to trim-drag characteristics of canard and aft control arrangements, figure 6 presents the results for many of the configurations of figure 1 in order to show general trends. The two diagonal lines are symmetrical about a value of $\delta/\alpha$ of zero and are drawn to aid in the comparison of the general trends of canard and aft control configurations. In general the data for the aft control arrangements lie near the diagonal line, whereas those for the canard arrangements are above the line, indicating that for the same absolute value of $\delta/\alpha$ the canard trim drag will in general be less. As before, the results show that the trim drag of inline-tail arrangements increased with Mach number (configurations 15, 16, and 18) whereas the trim drag decreased with increasing Mach number for high-tail arrangements (configurations 19 and 20). Also (as for configuration 1 in fig. 4) the trim drag of configuration 2 (a triangular wing and canard) decreased considerably with increasing Mach number between Mach numbers of 1.3 and 2. Configurations 1 and 2 are the same except that the distance from the control to the wing is larger in the latter case and the control effectiveness is therefore larger. Comparison of the data for these configurations in

figure 6 shows that increasing the distance between control and wing is an effective way of reducing $\delta/\alpha$ and, hence, trim drag. Within limits, another effective way of increasing the control effectiveness and thereby reducing $\delta/\alpha$ and the trim drag is to increase the control area, as indicated by the results for configurations 7, 8, and 9, in which the exposed area of the control was increased from 5.1 percent to 7.6 percent of the wing area.

Beneficial effects of the canard on maximum trim lift-drag ratio also extended to higher lifts, as shown in figure 7. The configurations compared are the same as those in figures 3 and 4. It will be noted that the lift-drag ratios for these configurations are lower than those for the configurations discussed in previous papers by Elliott D. Katzen and by Donald D. Baals, Thomas A. Toll, and Owen G. Morris. These higher ratios are due in part to the fact that in the present case the body volume is considerably larger relative to the wing than in those previous cases. The body size should not affect significantly the comparisons shown herein. More impressive than the drag characteristics is the large increase in maximum trim lift, which was as much as 60 percent greater for the canard than for the aft control arrangement, even though the maximum control deflection was the same in both cases. More than half of this beneficial effect of the canard was due to the fact that the canard had a large positive lift and the canard-wing interference lift was small, whereas a negative lift existed on the aft control.

## STABILITY AND CONTROL

In view of the beneficial effects of canard arrangements on lift-drag characteristics, it is advisable to investigate other aspects of canards, such as their control effectiveness and their effect on longitudinal and lateral stability. Figure 8 presents the lift-curve slope with respect to angle of attack and control deflection for various plan forms as obtained experimentally and theoretically. The theoretical methods were those discussed in reference 14. The experimental results from which the derivatives were obtained were essentially linear in the angle-of-attack and control-deflection ranges up to 10°. The comparison indicates that the theory is adequate for predicting the effects of plan form on lift, such as reduced lift with increasing supersonic Mach number, increasing leading-edge sweep, and decreasing aspect ratio. These data were obtained from the differences between canard-body data and body-alone data in order to eliminate canard-wing interference. They contain the mutual interference between canard and body, however, which in this angle-of-attack and deflection range was favorable, as predicted by theory. At higher angles of attack the effect of interference between the canard and body was such as to suppress the body

lift resulting from viscous cross flow (ref. 15) and, to a smaller extent, the potential lift. Thus at angles of attack near $16^O$ the interference lift on the body was negative, as indicated by a comparison of values for body lift with and without the canard and the measured lift on the canard in the presence of the body. That is, at high angle of attack the canard reduced the lift on the body.

At subsonic speeds an important characteristic of canard arrangements is the maximum lift effectiveness in the presence of a ground plane, and this characteristic is shown in figure 9. The curves labeled "required" are the pitching moment necessary to trim the triangular wing and body combination at various heights above the ground plane. The results indicate a considerable increase in pitching moment and lift at a constant angle of attack; that is, the ground induced a lift on the aft portions of the wing as the wing and body approached the ground. The maximum available trimming moment of the canard, as shown in figure 9, was obtained from an envelope of data for various angles of attack and control deflections. As might be expected, the ground plane did not affect the maximum available trimming moment since the height of the canard above the ground, expressed in terms of its own chord, was considerably greater than that of the wing. Thus, as a result of the large influence of the ground on the wing-body characteristics and the lack of a corresponding influence on the canard, the maximum trimmed lift coefficient for this configuration was reduced approximately 0.2, or 18 percent, as it reached a distance of 0.6 of the wing mean aerodynamic chord above the ground.

Since the ground plane had no effect on the canard characteristics, the effects of canard plan form on the maximum available pitching moment required for trim can be obtained in the absence of a ground plane. Such data have been obtained for canards of various aspect ratio, taper ratio, and sweep, and are shown in figure 10. For these data the exposed canard area and the distance from the control to the center of gravity of the wing are the same in each case. In general the results indicate an increase in maximum pitching moment available for trim with increasing leading-edge sweep or decreasing aspect ratio, or combinations thereof. This is just opposite to the effect of these parameters on the lift effectiveness. For canards, an increase in lift effectiveness produces a destabilizing contribution at low angles of attack. Thus, if it were desired to use one of these canards of higher aspect ratio and lower sweep in combination with the wing-body configuration of figure 9, it would be necessary to increase the stability of the wing-body combination by forward movement of the center of gravity to offset the increased destabilizing moment of the canard. Thus, increasing the aspect ratio or reducing the sweep of the canard has the double deleterious effect on maximum trim-lift coefficient of reducing the available moment and increasing the required moment. In fact, for the triangular wing and

body of figure 9 in combination with either a triangular or an unswept canard, both configurations having the same static margin, the maximum trim lift of the unswept canard arrangement was only about 1/2 of that for the triangular canard configuration.

Interference effects between the canard and the wing or vertical tail may be sufficiently large to prohibit the use of a canard arrangement, and therefore it is necessary to examine these effects. The lift interference between the canard and wing affects primarily the lift-drag characteristics and is shown in figure 11. The experimental data were obtained from the difference in the incremental lifts due to addition of canard to the body in the presence of the wing and in the absence of the wing. The theoretical results are based on the assumption that a vortex originates at the trailing edge of each canard panel and these vortices stream rearward over the wing, altering the flow in the vicinity of the wing and hence the lift on the wing. The spanwise origin of these vortices is determined in the manner presented in reference 14. In this method the spanwise loading on the exposed canard panel must be known. In the present calculations the assumption was made that at zero angle of attack the spanwise loading was elliptical, and that it changed with increasing angle of attack until, at an angle of attack of $30^\circ$, it had the same shape as the wing plan form. Thus for the triangular canard the vortex is located at $\pi/4$ of the exposed span at $0^\circ$ angle of attack and 1/2 of the exposed span at $30^\circ$ angle of attack. It is next assumed that the vortex flows in the free-stream direction from the canard trailing edge to the wing shock wave, where it is deflected downward by the wing downwash field. The downwash field above the wing was determined by the methods of reference 16. The strength of the vortex is determined from the theoretical lift on the exposed canard panel, which includes interference from the body, and the spanwise distance from the body to the vortex at the canard trailing edge. The strength and position of the vortex in the vicinity of the wing are used to determine its influence on the wing lift by means of strip theory. In this method the lift induced by the vortex at any wing section is the product of the angle of attack induced by a two-dimensional vortex and the section lift-curve slope (assumed to be equal to the two-dimensional value $4/\beta$). The results of figure 11 show that the trends of the canard-wing lift interference with increasing Mach number are predictable. The agreement is not entirely satisfactory, however, and studies are continuing to determine the cause of the discrepancies.

The pitching-moment interference between the canard and wing shown in figure 12 can be serious in that the stability of the configuration may be changed. Two sets of experimental data are shown in figure 12. The symbols represent data measured for the complete configuration and the dashed curves represent the condition of no wing-canard interference

as determined from tests of the separate components of the configurations. The centers of gravity were selected to provide the same static margin for all configurations at subsonic speeds, and the Mach number at which the largest interference effects occurred was used for each configuration. The theoretical results were obtained by the methods discussed for the wing-canard lift interference. The experimental and theoretical results show that for wings in which the stabilizing moment of the tip upload resulting from the upwash field of the canard is small, either because of a small tip chord in the case of triangular wings or because the tip is in line with the root chord as for the unswept wing, the interference effects are small. In the cases shown the interference effects are slightly favorable and are unaffected by angle of attack. However, for wings having a sizable tip chord swept considerably behind the center of gravity, the interference effects can be large, particularly at high control deflection and small angle of attack, and as shown in figure 12 can affect adversely the stability of the configuration. As shown, the stabilizing contribution of the upload at the tip of the sweptback wing can become significant at small angles of attack and a control deflection of $20^\circ$. However, with increasing angle of attack the tip moves below the canard-vortex field faster than the root section of the wing. This condition reduces the influence of the tip with respect to that of the root section and thus significantly reduces the stability of the configuration. At higher angles of attack, where the tip effect is small, the interference becomes favorable; that is, for the conditions shown the interference effect has increased the trim angle of attack. However, for small control deflections trim would occur in those regions of reduced stability which might be sufficiently pronounced, for highly swept wings with a sizable tip chord, to determine the center of gravity of the configuration.

Because the directional stability of high-speed aircraft may become marginal at high angles of attack at moderate supersonic Mach numbers, it is necessary to examine the interference effect of the canard on this characteristic. In order to show the relative importance of the canard interference on directional stability, in figure 13 the directional stability of the complete configuration BWVC is subdivided into the stability contributions of the vertical tail, $V$, the body-wing, $BW$, the body-wing interference on the vertical tail, $V_{BW}$, the canard interference on the vertical tail and body at zero deflection, $V_C$, and the canard interference on the body and vertical tail due to canard deflection, $B_\delta$ and $V_\delta$. The results show that the largest interference effect was that of the body-wing on the vertical tail, $V_{BW}$. This effect is due to an increase in the high-velocity field and a reduction in dynamic pressure in the vicinity of the vertical

tail resulting from the wing and body effects which reduced the lift-curve slope of the vertical tail (ref. 17). Calculations have shown that approximately 80 percent of $V_{BW}$ could be attributed to these causes.

The interference of the canard on the body, $B_C$, was stabilizing at high angles of attack. This effect can be traced to the aforementioned reduction in body forces near the canard due to canard interference at high angles of attack.

The interference of the canard on the vertical tail, $V_C$, was destabilizing throughout the angle-of-attack range for the single vertical-tail arrangement shown in figure 13. This destabilizing effect of the canard on the vertical tail results from the interference between the canard-vortex field and the vertical tail. For a configuration in sideslip the interference is such that the flow below the core of the windward-side vortex is in a destabilizing direction, whereas that for the lee side is in a stabilizing direction. Therefore, with increasing sideslip angle the vertical tail moves toward the destabilizing flow field and away from the stabilizing flow field. With increasing angle of attack the vertical tail moves down with respect to these vortex cores and the vortex strength increases. Thus more of the vertical tail is affected by a stronger flow field beneath the core and the adverse interference effect increases. It can be seen that if the vortex cores are lowered with respect to the vertical tail the destabilizing influence of the canard on the vertical tail will be reduced. At high angles of attack $V_\delta$ is stabilizing since in this case the vortex core is moved downward as a result of control deflection.

The interference of the canard on the vertical tail, $V_C$, depends to a large extent on the vertical-tail arrangement, as shown in figure 14. The results show that, as in figure 13, the effect of the canard is destabilizing for a single-tail arrangement. However, for the twin-tail arrangement the interference of the canard on the vertical tail is stabilizing. In contrast to the single vertical tail, the twin vertical tail moved away from the destabilizing flow field beneath the windward vortex and toward the stabilizing flow field of the leeward vortex. Tests of another configuration having twin tails closer together than those of the configuration in figure 14 have indicated that the tail space should be at least equal to the canard span to obtain favorable interference between the canard and vertical tails.

The effects of Mach number on the directional stability of a canard configuration are presented in figure 15 in a manner similar to that of figure 13. The results show that the destabilizing influence of the canard on the vertical tail became essentially zero above a Mach number

of 2.2, whereas the stabilizing contribution due to canard interference on the body extended up to a Mach number of 3.5, the limit of the tests. In fact, it apparently was the favorable body-canard interference that maintained positive directional stability at Mach numbers above 2.5.

For all configurations investigated, canard interference made $C_{l_\beta}$ (rolling moment due to sideslip) more negative; that is, it increased the dihedral effect. Since this interference results from a leeward shift of the center of the canard interference lift on the wing with increasing sideslip, the effects of Mach number and angle of attack on the interference $C_{l_\beta}$ are similar to those on interference lift; that is, $C_{l_\beta}$ reduces with increasing supersonic Mach number and increases with angle of attack.
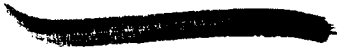
## CONCLUDING REMARKS

The data have indicated factors which cause the trim-drag characteristics of canard configurations to be superior to those of trailing-edge-flap and tail arrangements. The effect of plan form and control lift at low angles is predictable by theory and is opposite to the plan-form effect on the maximum available pitching moment. Interference effects between the canard and other configuration components were not serious, except possibly those which affect the directional stability, and these latter effects can be reduced by rearrangement of the vertical tail.

# REFERENCES

1. Boyd, John W., and Peterson, Victor L.: Static Stability and Control of Canard Configurations at Mach Numbers From 0.70 to 2.22 - Longitudinal Characteristics of a Triangular Wing and Canard. NACA RM A57J15, 1958.

2. Peterson, Victor L., and Menees, Gene P.: Static Stability and Control of Canard Configurations at Mach Numbers From 0.70 to 2.22 - Lateral-Directional Characteristics of a Triangular Wing and Canard. NACA RM A57L18, 1958.

3. Boyd, John W., and Peterson, Victor L.: Static Stability and Control of Canard Configurations at Mach Numbers From 0.70 to 2.22 - Triangular Wing and Canard on an Extended Body. NACA RM A57K14, 1958.

4. Peterson, Victor L., and Menees, Gene P.: Static Stability and Control of Canard Configurations at Mach Numbers From 0.70 to 2.22 - Longitudinal Characteristics of a Triangular Wing and Unswept Canard. NACA RM A57K26, 1958.

5. Peterson, Victor L., and Boyd, John W.: Static Stability and Control of Canard Configurations at Mach Numbers From 0.70 to 2.22 - Longitudinal Characteristics of an Unswept Wing and Canard. NACA RM A57K27, 1958.

6. Hedstrom, C. Ernest, Blackaby, James R., and Peterson, Victor L.: Static Stability and Control Characteristics of a Triangular Wing and Canard Configuration at Mach Numbers From 2.58 to 3.53. NACA RM A58C05. (Prospective NACA paper.)

7. Spearman, M. Leroy, and Driver, Cornelius: Effects of Canard Surface Size on Stability and Control Characteristics of Two Canard Airplane Configurations at Mach Numbers of 1.41 and 2.01. NACA RM L57L17a, 1958.

8. Spearman, M. Leroy, and Driver, Cornelius: Some Factors Affecting the Stability and Performance Characteristics of Canard Aircraft Configurations. NACA RM L58D16. (Prospective NACA paper.)

9. Driver, Cornelius: Longitudinal and Lateral Stability and Control Characteristics of Two Canard Airplane Configurations at Mach Numbers of 1.41 and 2.01. NACA RM L56L19, 1957.

10. Driver, Cornelius: Longitudinal and Lateral Stability and Control Characteristics of Various Combinations of the Component Parts of Two Canard Airplane Configurations at Mach Numbers of 1.41 and 2.01. (Prospective NACA paper.)

11. Sleeman, William C., Jr.: Investigation at High Subsonic Speeds of the Static Longitudinal and Lateral Stability Characteristics of Two Canard Airplane Configurations. NACA RM L57J08, 1957.

12. Spearman, M. Leroy, and Driver, Cornelius: Longitudinal and Lateral Stability and Control Characteristics at Mach Number 2.01 of a 60° Delta-Wing Airplane Configuration Equipped With a Canard Control and With Wing Trailing-Edge Flap Controls. NACA RM L58A20, 1958.

13. Spearman, M. Leroy: Some Factors Affecting the Static Longitudinal and Directional Stability Characteristics of Supersonic Aircraft Configurations. NACA RM L57E24a, 1957.

14. Pitts, William C., Nielsen, Jack N., and Kaattari, George E.: Lift and Center of Pressure of Wing-Body-Tail Combinations at Subsonic, Transonic, and Supersonic Speeds. NACA Rep. 1307, 1957.

15. Allen, H. Julian, and Perkins, Edward W.: A Study of Effects of Viscosity on Flow Over Slender Inclined Bodies of Revolution. NACA Rep. 1048, 1951. (Supersedes NACA TN 2044.)

16. Nielsen, Jack N., and Perkins, Edward W.: Charts for the Conical Part of the Downwash Field of Swept Wings at Supersonic Speeds. NACA TN 1780, 1948.

17. Nielsen, Jack N., and Kaattari, George E.: The Effect of Vortex and Shock-Expansion Fields on Pitch and Yaw Instabilities of Supersonic Airplanes. Preprint No. 743, S.M.F. Fund Preprint, Inst. Aero. Sci., June 1957.
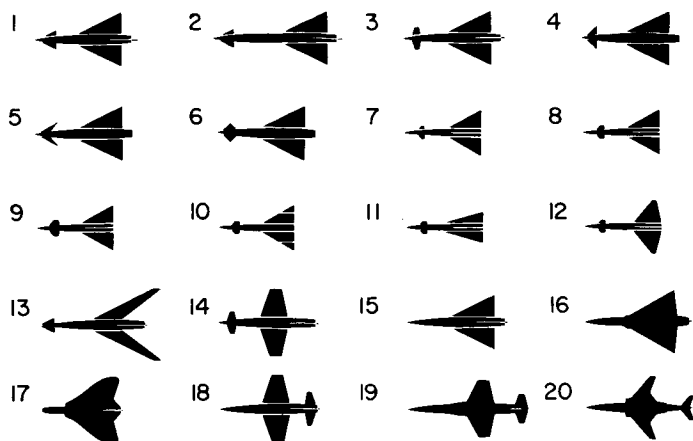
## CONFIGURATIONS INVESTIGATED



Figure 1

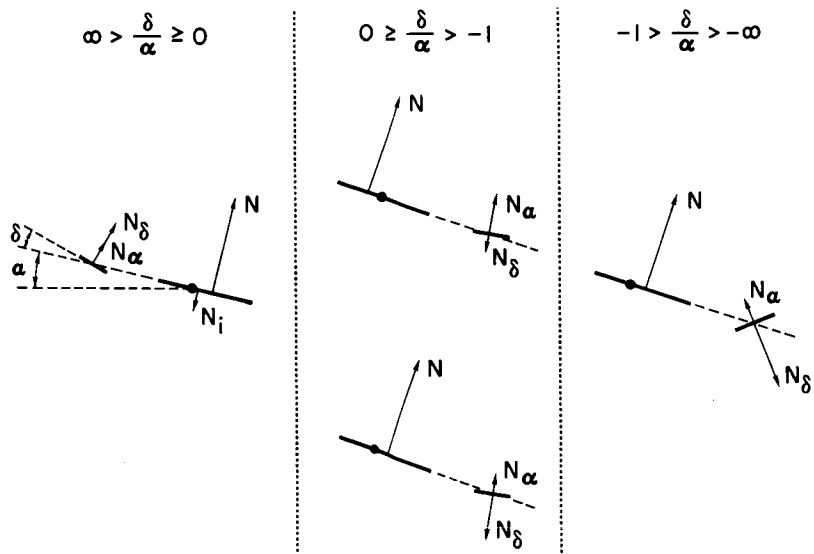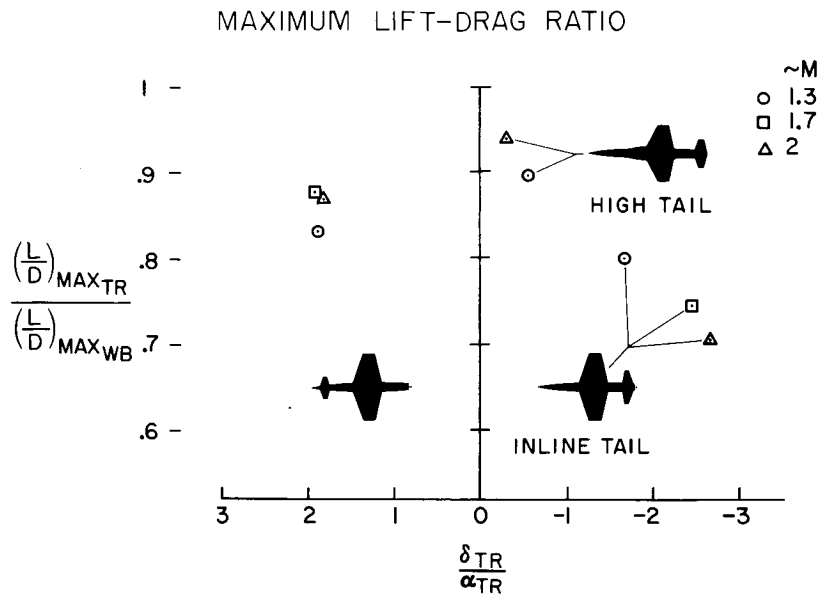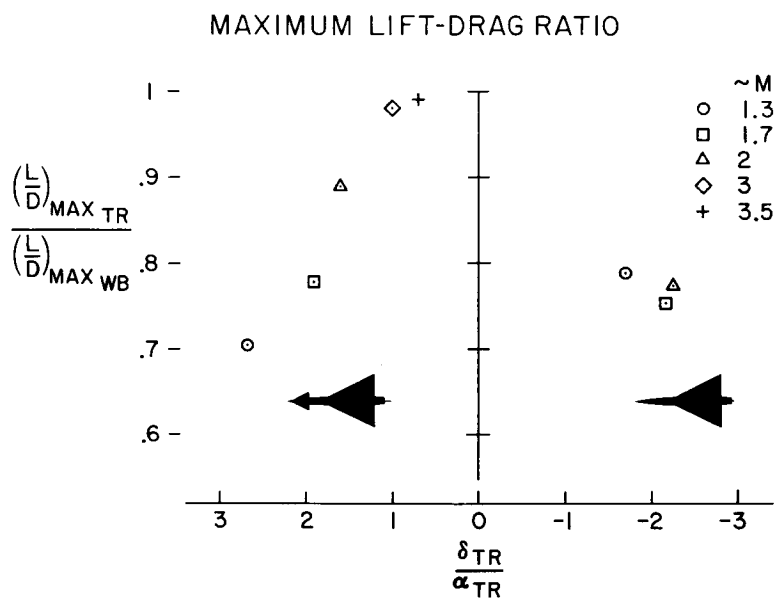## CANARD AND TAIL-AFT CONTROL FORCES FOR TRIM

$$\infty > \frac{\delta}{\alpha} \geq 0 \qquad 0 \geq \frac{\delta}{\alpha} > -1 \qquad -1 > \frac{\delta}{\alpha} > -\infty$$



Figure 2

## MAXIMUM LIFT-DRAG RATIO



Figure 3

## MAXIMUM LIFT-DRAG RATIO



Figure 4

EFFECT OF MACH NO. ON CENTER OF PRESSURE

CANARD ON
CANARD OFF
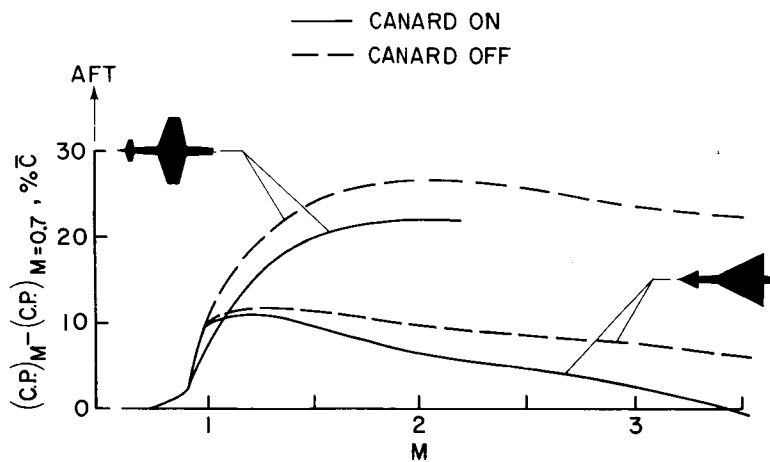
Figure 5

MAXIMUM LIFT-DRAG RATIO

CANARD ← → AFT CONTROL

~ M
○ 1.3
□ 1.7
△ 2.0
◇ 3.0
+ 3.5

$\dfrac{\left(\frac{L}{D}\right)_{MAX\,TR}}{\left(\frac{L}{D}\right)_{MAX\,WB}}$

$\dfrac{\delta_{TR}}{\alpha_{TR}}$

Figure 6

TRIM LIFT-DRAG RATIO

M=2.2



Figure 7

CANARD LIFT EFFECTIVENESS



Figure 8

## GROUND EFFECT
### M=.25



$C_L = 1$

.75

.5

$h/\bar{c}$
- o  ∞
- △  .6
- □  .3

MAX AVAIL

REQUIRED

α

0        .1        .2

$\Delta C_m$ FOR TRIM

Figure 9

## PLANFORM EFFECT
### M=.25



α

0        .1        .2

MAX AVAILABLE $\Delta C_m$
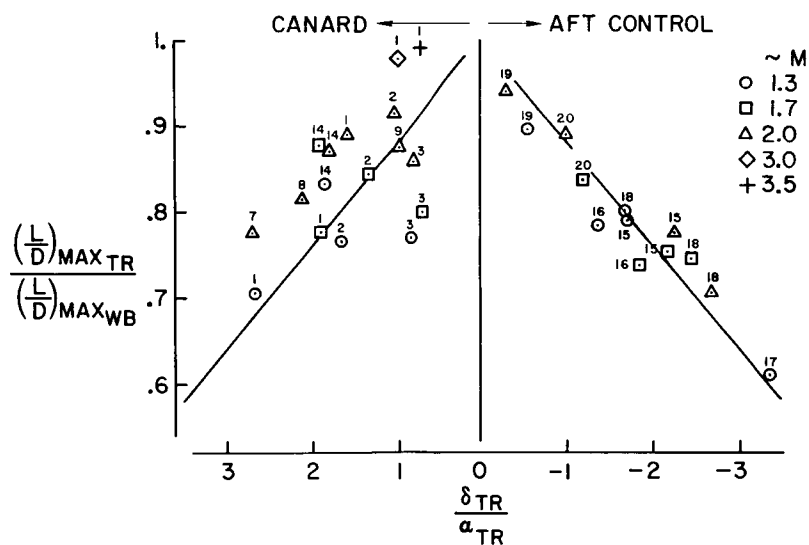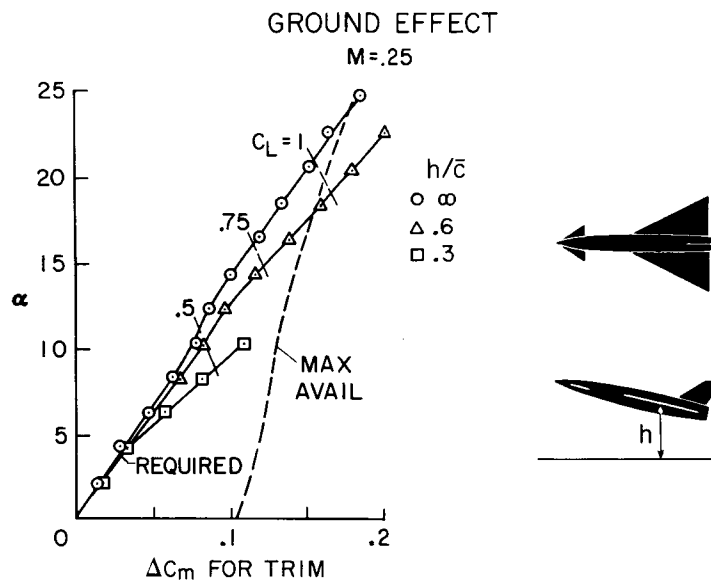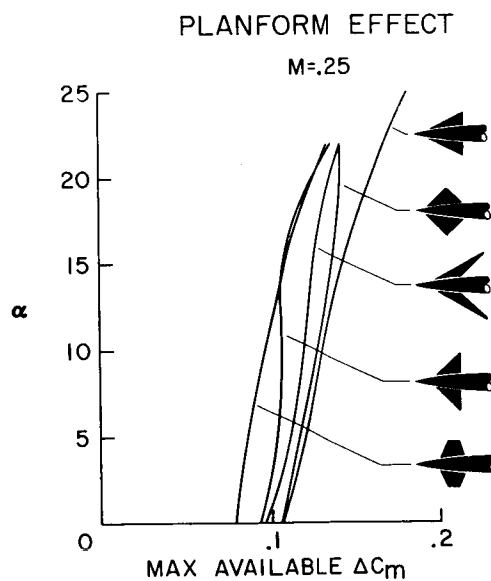
Figure 10

## CANARD-WING INTERFERENCE LIFT
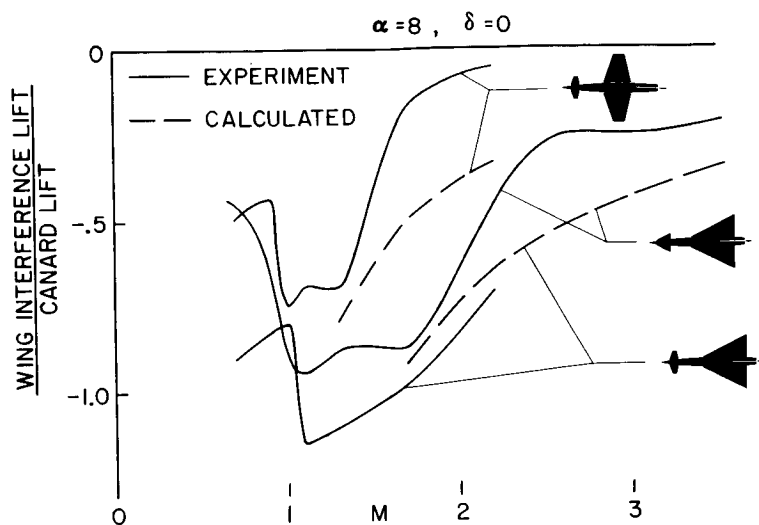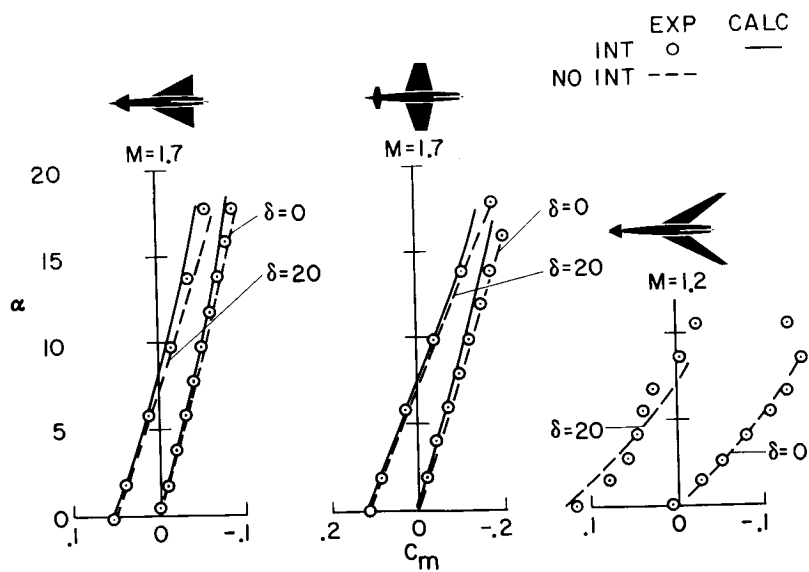


Figure 11

## PITCHING-MOMENT INTERFERENCE
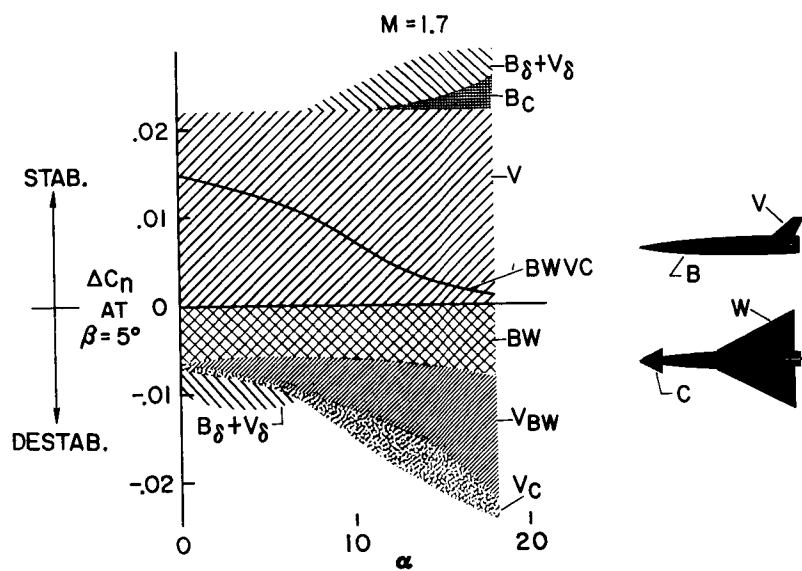


Figure 12

## DIRECTIONAL STABILITY
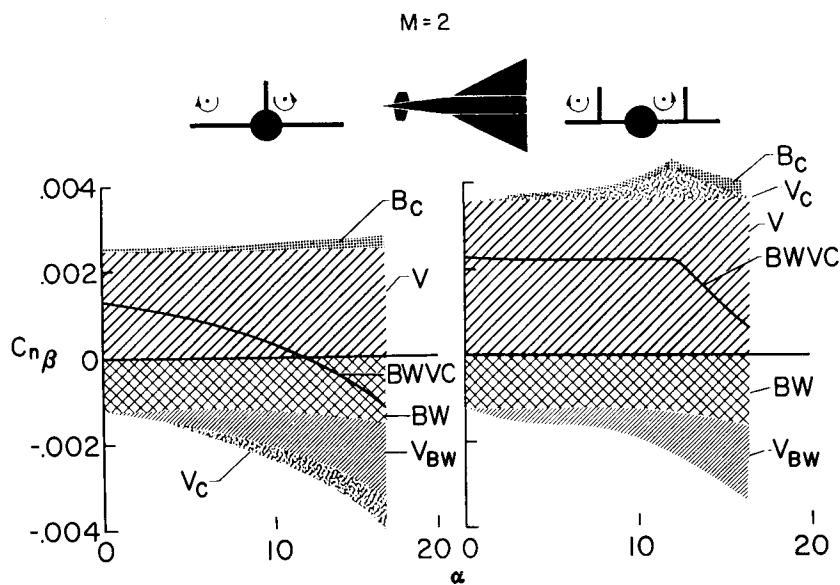
### M = 1.7



Figure 13

## EFFECT OF TAIL LOCATION

### M = 2



Figure 14
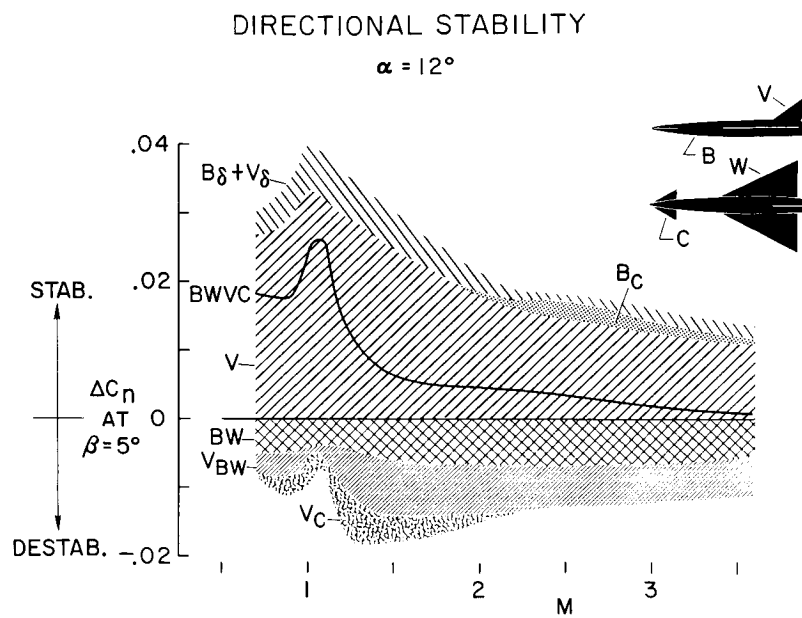
Figure 15

ESTIMATION OF DIRECTIONAL-STABILITY CONTRIBUTIONS

OF AIRPLANE COMPONENTS

By George E. Kaattari

Ames Aeronautical Laboratory

## SUMMARY

Available theories accounting for interference effects between components on airplane stability have been demonstrated to have experimental verification over moderate angle-of-attack ranges. This verification establishes design principles useful in increasing directional stability of supersonic airplanes.

## INTRODUCTION

The flight of airplanes at supersonic speeds has introduced a number of problems in pitch and yaw stability. The underlying causes of instability are pointed out in reference 1. It is the purpose of the present paper to examine in detail one phase of the stability problem; namely, the decay of the directional coefficient $C_{n_\beta}$ with increasing

angle of attack and Mach number. Theoretical methods are presented for calculating the stability contribution of lifting and stabilizing surfaces. These methods reveal means by which $C_{n_\beta}$ for supersonic aircraft

may be improved. In this regard, particular attention will be given to the stabilizing effects of body shape, of wing plan form and location, and of stabilizer plan form and location. Extensive data from wind tunnels at the Ames and Langley Aeronautical Laboratories were compared with theory (e.g., ref. 2).

## DISCUSSION

### Small-Angle Considerations

Determining the directional coefficients of a complete airplane at low angles of inclination is a linear problem. Consider the fighter-type

configuration shown in figure 1. In most cases the direct contribution of horizontal surfaces to stability is negligible. As far as $C_{n_\beta}$ is concerned, add together $C_{n_\beta}$ of the body alone, the change in $C_{n_\beta}$ of the body resulting from the addition of the wing, and the $C_{n_\beta}$ contribution of the tail in the presence of the body-wing combination. These incremental values of $C_{n_\beta}$ associated with the addition of each component are determined by suitable interference constants $K$ times the $C_{n_\beta}$ capability of the isolated component in question. The significance of $K$, as for example pertaining to the tail, is then that it is the ratio of $C_{n_\beta}$ of the tail in the presence of the body-wing combination to $C_{n_\beta}$ of the tail if mounted on a perfect reflection plane. The constant $K$ is a function of the ratio of component span to body radius and can be determined by slender-body theory. Values of $K$ have been evaluated for determining interference effects for a wide variety of component arrangements. These values were determined with the aid of slender-body solutions of reference 3.

The question arises as to the validity of slender-body theory in application to nonslender configurations at supersonic speeds. This question is resolved by experimental verification. In figure 2 are presented increments of $C_{n_\beta}$ contributed by components of a large number of configurations at both subsonic and supersonic Mach numbers. Experimental increments of $C_{n_\beta}$ are plotted against corresponding theoretical values. Test points denote the contribution to $C_{n_\beta}$ of the surfaces designated by the dashed line in each of the sketches. Good correlation exists both at subsonic and at supersonic Mach numbers. Body protuberances, such as duct intakes and canopies, wing nacelles, and jet exhausts, can contribute additional interference effects. A discussion of these effects, however, is not pursued in this brief dissertation.

## Large-Angle Considerations

The foregoing discussion dealt with linear or small-angle theory. In the remainder of the paper the effects of large angles of inclination and Mach number on $C_{n_\beta}$ are considered. Body-alone characteristics are an important source of airplane instability at large angles of inclination. Two bodies of equal volume and length are shown in figure 3. Both have identical circular noses. The top body has a circular cross section along its entire length. The lower body has an afterbody of deep, nearly rectangular cross section. The experimental $C_{n_\beta}$ of the

bodies is plotted as a function of angle of attack. Both have about the same $C_{n_\beta}$ at low angles of attack. When angle of attack is increased, the loading on both bodies shifts rearward because of the development of viscous cross-flow forces on the afterbody. These forces are larger on the rectangular cross-sectional body (hereinafter referred to as rectangular body) than on the circular cross-sectional body (hereinafter referred to as circular body). The rectangular body then has the greater weathercock stability with increasing angle of attack. Identical tails are added to each body. The resulting $C_{n_\beta}$ variations with angle of attack are compared. The stability of the circular-body—tail combination is greater than that of the rectangular-body—tail combination over the greater portion of the angle-of-attack range. This unexpected result can be traced to the greater adverse sidewash due to body vorticity that is associated with the strong viscous cross-flow field about the rectangular body. Smaller vorticity effects characterize flow about the circular body. Thus, smaller losses in tail effectiveness result.

It is evident that the simple superposition of body and component characteristics permissive in linear theory is not valid at large angles of inclination. Additional methods for estimating the nonlinear effects attending large angles are required. Development of such methods is undertaken by first determining the effect of angle of attack and Mach number on side-force interference between body and wing. There are two effects of the wing on body side force. The first effect is shown in figure 4. Viscous cross-flow forces about a body and a body-wing combination are compared at combined sideslip and angle of attack. The body alone senses the side-force component $Y_B$ of the large total force R associated with combined $\alpha$ and $\beta$. The body in the presence of the wing senses only the viscous effects due to pure sideslip since the wing has intercepted the $\alpha$ component of total inclination. The amount of viscous side force developed is thus reduced. The reduction may be estimated by the method of reference 4. This interference effect of the wing on the body depends on the extent of wing root chord along which $\alpha$ suppression takes place. Wings with long root chords or with strakes are effective in linearizing body-wing directional characteristics. The second effect of the wing on the body is shown in figure 5. A rear view of a wing mounted on a body in a high tangent location is represented. Because of the effect of yaw-induced side flow around the body, opposite wing panels encounter differential angles of attack, that is, $+\Delta\alpha$ due to upwash on the windward side and $-\Delta\alpha$ due to downwash on the leeward side. A differential pressure field then exists between the wing panels and reacts on the interposed body. This mechanism accounts for the body reaction which is taken into account in pure sideslip by the linear-theory interference constant $K_{B(W)}$. If the wings are lifting at high angles of attack, the wing-body interference zone

indicated by the shaded area is in an environment of increased pressures and reduced Mach number in respect to free-stream conditions. The combined effect of local pressure and Mach number increases the body reaction nonlinearly with angle of attack and flight Mach number. These effects may be calculated with shock-expansion theory. The total effect of the wing on the body is then the sum of viscous effects and pressure effects. Estimates of this total effect can be computed and compared with experiment. A typical correlation of theory and experiment is shown in figure 6 for three body-wing combinations. Side-force increments due to adding a wing to a body are plotted as a function of angle of attack. Wings in high, low, and midbody position are considered. In each case, experiment and theory are in accord over the angle range shown. It is pointed out that this interference force on the body arises from any horizontal surface such as canards and conventional pitch stabilizers. These interference forces may be exploited for increased directional stability. Midbody surfaces give negative interference forces. Such surfaces should be attached to the body forward of the airplane center of gravity for positive directional stability. Canards and wings of highly sweptback plan form meet this requirement of position in respect to airplane center of gravity. High-body surfaces give positive interference forces. Such surfaces should be attached to the body rearward of the airplane center of gravity. Conventional pitch stabilizers and unswept or sweptforward wings meet this requirement of position in respect to airplane center of gravity.

The next consideration is to determine the $C_{n_\beta}$ increment due to the addition of a tail to a body-wing combination. For this purpose divide the airplanes into two classes: (1) airplanes which have large bodies and small wings and (2) airplanes which have large wings and small bodies. The stability characteristics of the first class are dominated by body-tail interference and those of the second class by wing-tail interference. The upper sketch in figure 7 depicts the mechanism of body-tail interference. At high angles of attack, separated flow about the body forms into two vortices that pass near the empennage shown in the cross section. Their influence on the tail can be calculated (ref. 1). It is a destabilizing effect which increases approximately as the square of the angle of attack. The lower sketch shows the tail in combination with a body-wing combination. The wing has the several indicated effects. Because of the viscous cross-flow suppressing effect of the wing, body vorticity is prevented from developing in strength along the wing root chord. An indirectly favorable effect of the wing results in this respect; however, the vorticity remains a destabilizing influence. In the zone above the wing and between the wing shock lines originating at the leading and trailing edges, the dynamic pressure is reduced and the Mach number is increased in respect to free-stream conditions. The effectiveness of $C_{n_\beta}$ of a stabilizer in

this zone is reduced; however, highly sweptback tail plan forms can, to some extent, avoid this unfavorable region. The opposite effect takes place below the wing in regions where a ventral fin may be located. The effectiveness of a ventral fin, then, increases with angle of attack. Wing vortices are usually a minor consideration in closely coupled wing-tail cases such as considered here. A typical correlation of experiment and theory for $\Delta C_n$ contributed by a tail to a body and to a body-wing combination is presented in figure 8. The $\Delta C_n$ of a tail in presence of a body at $\beta = 5^\circ$ is plotted as a function of angle of attack on the left-hand side of the figure. Experimental values are denoted by the small circles. The dashed curve gives theoretical values resulting when the effect of body vortices is taken into account. The agreement between theory and experiment is satisfactory over the angle-of-attack range considered. The $\Delta C_n$ of a tail in the presence of a body-wing is plotted as a function of angle of attack on the right side of the figure. Two locations of wing on body are considered with a conventionally positioned stabilizer. The top curve of these two cases pertains to the low wing and the lower curve, to the high wing. Theory and experiment are again generally in good accord. A significant point demonstrated here is that while the stability of the high-wing model is less than that of the low-wing model, its stability is less sensitive to angle of attack. At higher Mach numbers than considered here, it is possible for a high-wing airplane to have the greater stability in a high angle-of-attack range. The other curve pertains to a ventral-tail contribution in presence of a high-wing—body combination. Experiment and theory are in fair accord. The effect of the wing compressive field on the ventral-tail contribution is evident by the increasing value of $\Delta C_n$ with angle of attack. The degree of correlation between experiment and theory, as shown in figure 8, extends over a wide range of component plan form and supersonic Mach number.

## CONCLUSIONS

On the basis of experimental and theoretical studies of the contribution of components to airplane directional stability, it is concluded that the following items are of particular importance in increasing the directional stability of airplanes at supersonic Mach number:

1. The destabilizing effect of body vorticity may be reduced through use of wings with long root chords and by selection of suitable afterbody cross sections.

CONFIDENTIAL

2. Lifting and pitch-control surfaces can be made to contribute directional stability through plan-form effects and location on the body.

3. Ventral fins are highly effective at large angles of attack.

# REFERENCES

1. Nielsen, Jack N., and Kaattari, George E.: The Effect of Vortex and Shock-Expansion Fields on Pitch and Yaw Instabilities of Supersonic Airplanes. Preprint No. 743, S.M.F. Fund Preprint, Inst. Aero. Sci., June 1957.

2. Jaquet, Byron M., and Fournier, Roger H.: Experimental Effects at Mach Numbers From 2.29 to 4.65 of Changes in Wing Sweep, Horizontal Tail Configuration, and a Ventral Fin on Static-Stability Characteristics of a Model With a Wing of Aspect Ratio 3. (Prospective NACA paper.)

3. Bryson, Arthur E., Jr.: Evaluation of the Inertia Coefficients of the Cross Section of a Slender Body. Jour. Aero. Sci. (Readers' Forum), vol. 21, no. 6, June 1954, pp. 424-427.

4. Polhamus, Edward C.: Effect of Flow Incidence and Reynolds Number on Low-Speed Aerodynamic Characteristics of Several Noncircular Cylinders With Applications to Directional Stability and Spinning. NACA TN 4176, 1958.
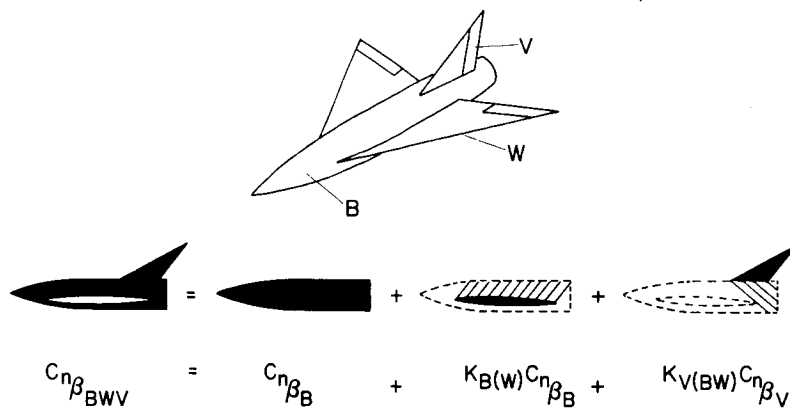
ORIGIN OF CONTRIBUTIONS TO $C_{n_\beta}$

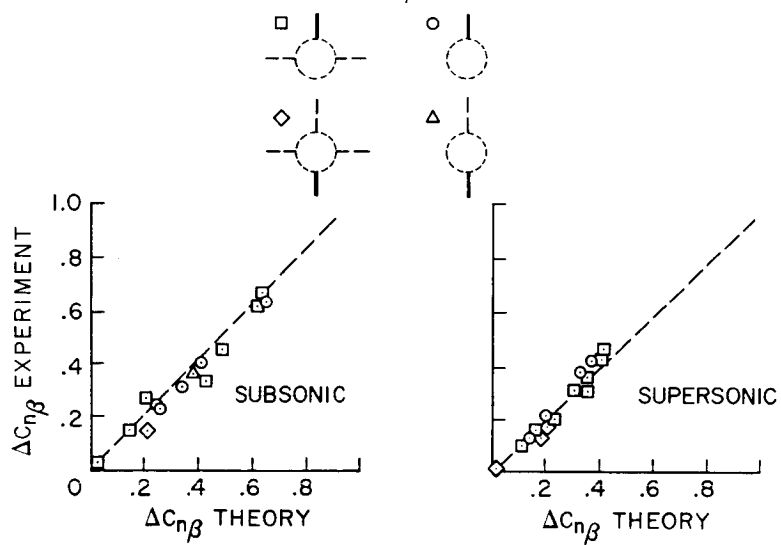$$C_{n_{\beta_{BWV}}} = C_{n_{\beta_B}} + K_{B(W)}C_{n_{\beta_B}} + K_{V(BW)}C_{n_{\beta_V}}$$

Figure 1

CORRELATION OF $\Delta C_{n_\beta}$ AT SMALL $\beta$ AND $\alpha$

Figure 2

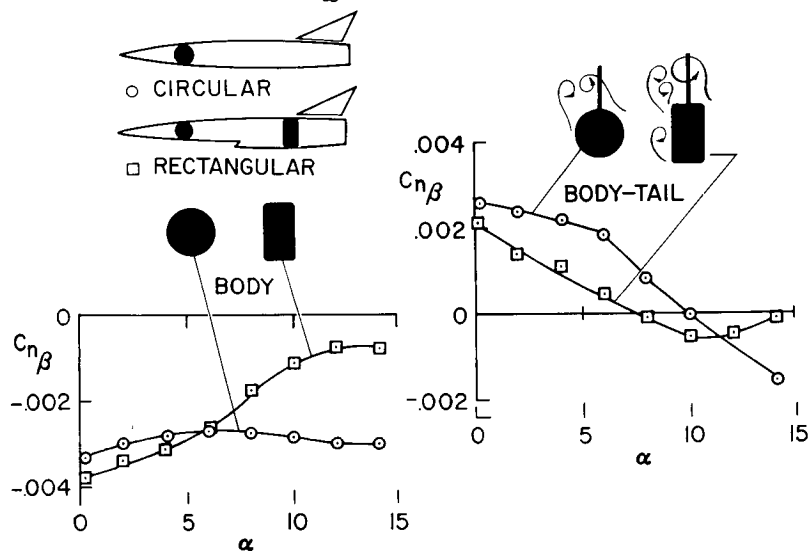EFFECT OF BODY SHAPE ON $C_{n\beta}$ AT LARGE $\alpha$

$M_\infty = 2.94$ $\beta = 5°$
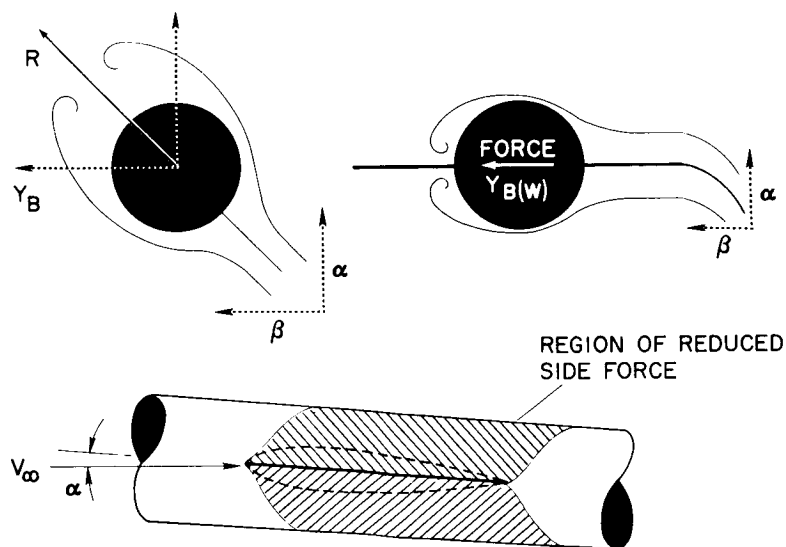


Figure 3

REDUCTION OF BODY VISCOUS FORCES BY WING
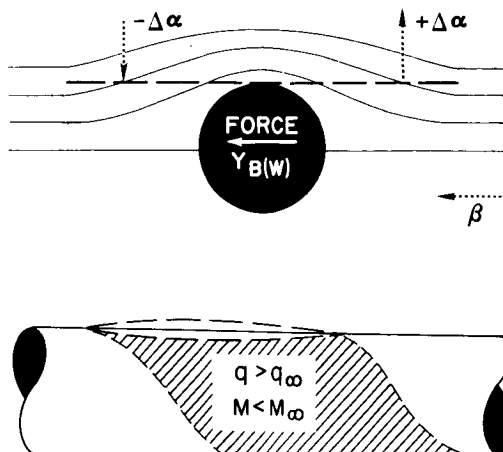


Figure 4

INCREASE OF BODY PRESSURE FORCES BY WING



Figure 5

EFFECT OF WING POSITION AND $\alpha$ ON $C_{Y_{B(W)}}$

M = 2.94     $\beta$ = 5°



Figure 6

# FLOW FIELD ABOUT TAIL AT LARGE $\alpha$



BODY-TAIL

$-\Gamma_B$    $+\Gamma_B$

$\alpha$

$\beta$



$\left.\begin{array}{l} q < q_\infty \\ M > M_\infty \end{array}\right\}$ DESTABILIZING

$-+\Gamma_B$ DESTABILIZING

$\left.\begin{array}{l} q > q_\infty \\ M < M_\infty \end{array}\right\}$ STABILIZING

BODY-WING-TAIL

Figure 7

## $Cn_\beta$ CONTRIBUTION OF VERTICAL TAIL
### $M_\infty = 2.94$, $\beta = 5°$



— — THEORY
o EXPERIMENT

BODY-TAIL

— — THEORY
□ o ● EXPERIMENT

BODY-WING-TAIL
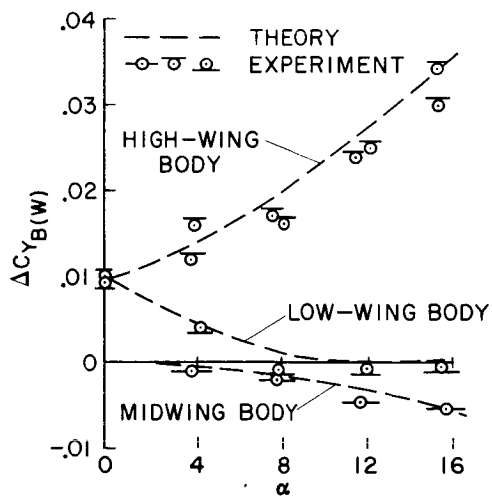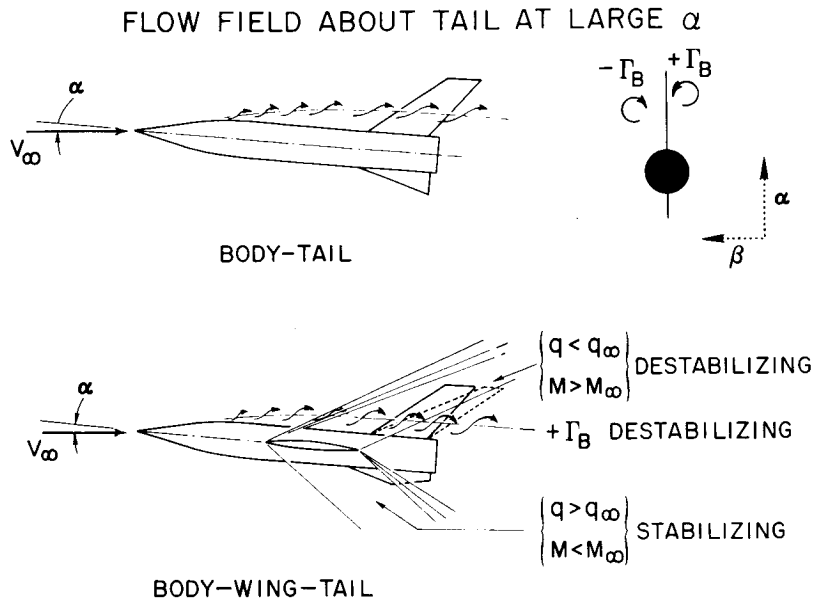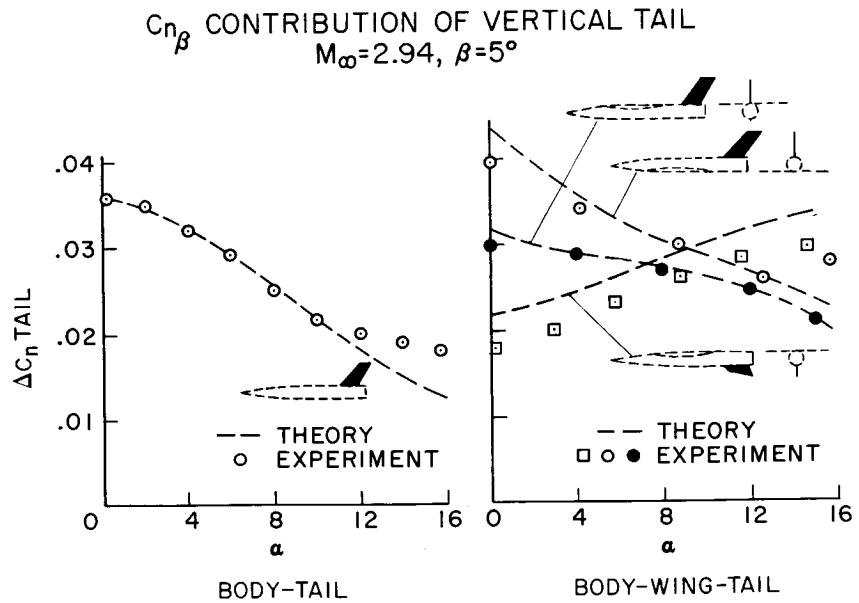
Figure 8

# VISCOUS FLOWS IN INLETS

By Richard Scherrer, John H. Lundell,
and Lewis A. Anderson

Ames Aeronautical Laboratory

## INTRODUCTION

It is well known that total-pressure ratios approaching 0.9 at Mach numbers of about 4 are desirable but have not been attained because of a group of problems termed "viscous effects." The purpose of this paper is to demonstrate how viscous effects can be minimized. Results of the basic research are first presented; these results are then applied to the design of an idealized inlet and the performance of this inlet is described.

The primary effect of viscosity at increasing free-stream Mach numbers is to increase the total pressure losses due to friction. This effect, coupled with the increasing positive pressure gradients in inlets, results in difficulty in preventing separation. It may not be possible to do much about this primary viscous effect other than to remove the low energy flow; however, there are a group of secondary viscous effects that can be eliminated at their sources. Some of these occur in the inlet shown in figure 1. This inlet is rectangular and has partial internal contraction. The effects of corners and of the oblique pressure fields on the side walls are typical secondary viscous effects. These effects result in local regions of thickened boundary layer, and the first separations, in strong positive pressure gradients, would occur in these regions. When the positive pressure gradient is continued downstream, the regions of separation grow into wakelike flows having strong large-scale low-frequency mixing. The transonic region in inlets is particularly sensitive to the development of wakelike flows because of the effect of fluctuations in effective throat area on the throat Mach number and thus on the total pressure losses at the terminal shock and in the subsonic diffuser. It appears that care must be exercised in inlet design to maintain uniform steady boundary-layer and core flows in the throat. The initial reaction to such an idealized requirement is that it is unnecessarily restrictive, but that this is not the case will be demonstrated.

SYMBOLS

M            Mach number

$p_t$          total pressure

$p_{t_\infty}$        ambient total pressure

$\left(\Delta p_t\right)_{max}$     peak-to-peak fluctuation in total pressure

r            distance from surface

R            local duct radius

$S/A_t$        ratio of wetted area of supersonic diffuser to throat
             cross-sectional area

## BASIC RESEARCH RESULTS

The basic research has been directed toward providing sufficient understanding of unsteady transonic diffusing flows to allow the design of a Mach number 4.0 inlet with a weak terminal shock and steady transonic flow. The most important result of this research is demonstrated with motion pictures. These pictures have been taken by use of an instrumentation system which provides a continuous display and record of transient-total-pressure profiles in boundary layers. The test apparatus is shown in figure 2. A four-tube total-pressure rake with transient-pressure transducers and a similar wall-static-pressure transducer are located at the exit of an $8^\circ$ conic diffuser in which supersonic flow exists to a Mach number of about 1.1 just downstream of the throat. The outputs of the transducers are displayed on an oscilloscope, as shown in figure 3, with total-pressure ratio as the abscissa and radial position in the duct as the ordinate. Fluctuations in local total pressure appear as horizontal motions of the spot at each tube position. The local static pressure is plotted at the wall to provide an indication of separation.

The first flow that is shown is called unsteady; that is, large-scale, low-frequency total pressure losses occur with separation at the wall and simultaneous large losses in pressure at the tube farthest from the wall. Selected frames from the first motion picture are reproduced in figures 4(a) and 4(b). The time between frames is 0.125 second.

The second flow is relatively steady in that the largest and lowest frequency disturbances have been eliminated. The total pressure farthest from the wall is almost constant and the flow at the wall is not quite separated. Selected frames from the second motion picture are reproduced in figure 5. The time between frames is 0.125 second. The difference between the two flows is due to an improvement in initial flow uniformity of less than 1 percent in total pressure. This is so small that the critical disturbances may not be total-pressure fluctuations, but rather small fluctuations in local stream angles or vorticity. In either case, the conclusion is that the initial flow should be uniform and steady in order to attain steady exit flows in diffusers.

The sensitivity of diffusing flows to small initial disturbances was unexpected and it was believed that some rational explanation was essential if the result was to be employed with confidence. The general question is: How does large-scale turbulence grow from some initial shear? This is one of the most basic fluid-mechanics problems and one possible explanation of the phenomenon is shown in figure 6.

It is assumed that some initial shear exists in a field of random three-dimensional disturbances. When angular momentum is conserved, some spectrum of random streamwise vortices is produced, each of which is a conventional secondary-flow vortex. (See ref. 1.) Any vortex has a low-energy core which grows in diameter with distance downstream, and because of this growth a positive static-pressure gradient must exist along the axis. Now, assume the existence of a single disturbance sufficiently strong to slow the core appreciably. The core must expand rapidly in response to this pulse and may be forced to continue to expand because of the abrupt increases in positive pressure gradient demanded by the growing diameter and because of the deflection of the ambient flow about the rapidly growing core. Thus, some of the vortices in the shear layer can be unstable and explode, as indicated. This concept is consistent with the requirement of self-preservation of turbulent flows because each explosion results in the two features required for more explosions, namely, new vortices and a pressure wave. In such a flow it would be expected that each generation of vortices and explosions would become larger in size.

When this hypothesis is applied to the flow in a choked diffuser, it is apparent that the effect of the additional positive pressure gradient, the confining effect of the duct walls on the pressure pulses, and the effect of the terminal shock are to accentuate the growth of initial shear into large-scale turbulence. The effect observed in the motion pictures appears to be consistent with this simple physical reasoning and the physical reasoning is consistent with many diverse features of turbulence. (See ref. 2.) Thus, both the unsteadiness observations and the hypothesis can be used with some confidence.

## SUPERSONIC-INLET DESIGN AND TEST RESULTS

The need for maintaining uniform and steady throat flows has been emphasized. This result will now be applied to the design of an inlet for a Mach number of about 4. The inlet shown in figure 7 is one of several possible designs that can satisfy the need for uniform throat flow. All the features of this inlet - axial symmetry, internal contraction, isentropic compression, scoop location, terminal-shock compensation, and the $4^\circ$ diffuser - were selected to allow attainment of steady, uniform throat flow.

Two features of this axisymmetric isentropic inlet are unusual; namely, the location of the boundary-layer scoop just ahead of the inflection point and the abrupt growth in cross-sectional area in the terminal-shock region. The scoop location provides a thin boundary layer in the region of maximum pressure gradient, which should prevent separation and thus provide steady flow in the throat. Terminal-shock compensation has been used for several reasons and the most interesting reason can be demonstrated by use of the shear-to-turbulence hypothesis presented earlier. It is well known that turbulent boundary layers have two basic components: eddies, or small finite-length streamwise vortices, and "balls" of turbulence. If it is assumed that the terminal shock will increase the local production of turbulent balls from the eddies, the local flow cross section must be expanded to allow for the local total pressure loss in the turbulence. Thus, the use of terminal-shock compensation allows for departure from the assumed uniform throat flow. It should be noted that the mixing due to production of new eddies at the terminal shock is probably of some significance in separation or reattachment just downstream of the shock.

It is somewhat incidental to the main subject of this paper, but the question of flow-starting with internal-contraction inlets always occurs. In the inlet shown in figure 7, the top half of the supersonic flow region was arranged to move upward and forward on links to allow the excess air to be bypassed around the throat during starting.

Tests have been conducted with components of the idealized inlet at Mach numbers from 3.6 to 3.94, and tests of the complete inlet were conducted at Mach numbers of 3.70 to 3.83 for several configurations. The test Reynolds numbers were from $1.3 \times 10^6$ to $2.6 \times 10^6$, based on inlet diameter. The component tests were conducted to allow boundary-layer surveys at the inflection point and at the minimum-area station. Further flow profiles were measured just downstream of the terminal shock and at the duct exit with the complete configurations. Typical profiles obtained at these stations are presented in figures 8 and 9 in

terms of the mean total-pressure ratio and the peak-to-peak total-pressure-fluctuation ratio. It should be noted that there is no exit-fluctuation profile because the mean profile was obtained with a liquid manometer.

At the inflection point (fig. 8), the mean total-pressure profile shows the concavity that is due to the friction total pressure loss. The fluctuation profile (fig. 9) indicates large fluctuations to occur well off of the surface, and this result is an indication of separation ahead of the inflection point. Unfortunately, in this investigation it was not possible to move the scoop forward; therefore, the next best thing was to remove all the separated flow. As a result, the shock waves due to the separation remain in the core flow and prevent attainment of isentropic compression. At the minimum-area station, the mean input to the terminal shock is not unusual and the fluctuation profile has a low-amplitude peak near the surface. The output from the terminal shock in terms of the mean profile appears favorable; however, the fluctuation profile, as well as the examination of the oscillograph records, suggests occasional separation. The last mean profile is at the duct exit and the distortions, both radial and circumferential, are small - less than 3 percent. This, in view of the occasional separation at the diffuser entry, indicates that the choice of a $4^{\circ}$ divergence in the subsonic diffuser was judicious.

The overall performance of the idealized inlet is shown in figure 10 as the variation of total-pressure ratio with Mach number. Test data for the present inlet are for a Reynolds number of $2 \times 10^6$ because no improvement in recovery occurred with further increase in Reynolds number. The best available results from several other inlet investigations at Mach numbers above 3 are shown for comparison. (Some of these data are presented in refs. 3, 4, and 5.) Values of the ratio of supersonic wetted area $S$ to throat cross-sectional area $A_t$ are listed in figure 10 to indicate roughly the relative size per unit mass flow of the various inlets. The inlet of the present investigation is relatively short, but it can be seen that it has the highest pressure recovery. A pressure recovery of 85 percent was obtained at a Mach number of 3.70 and of 82 percent was obtained at a Mach number of 3.83. Since the boundary-layer-bleed flow rates are roughly from 20 to 25 percent of the total flow in all the inlets presented, the comparison in figure 10 is sufficient to indicate relative merit. Although the level of pressure recovery that has been achieved is unusual, it is evident that the goal of 90-percent pressure recovery has not been achieved. However, by using the total-pressure profiles, the component losses in the duct can be evaluated to find out why the goal was not achieved.

A summary of the component losses in the idealized inlet is as follows:

Subsonic diffuser, percent $p_{t_\infty}$ . . . . . . . . . . . . . . . . . . . . . . 2

Terminal shock, percent $p_{t_\infty}$ . . . . . . . . . . . . . . . . . . . . . 1

Scoop-to-throat friction, percent $p_{t_\infty}$ . . . . . . . . . . . . . . . 6

Supersonic core flow, percent $p_{t_\infty}$ . . . . . . . . . . . . . . . . 9

Total loss, percent $p_{t_\infty}$ . . . . . . . . . . . . . . . . . . . . . . 18

The data shown are temporal mean values and were obtained at $M = 3.83$ from total-pressure profiles with the assumption that the flow is actually axisymmetric. It should be noted that the possible error in each of the component losses is about $\pm 0.01p_{t_\infty}$ and the possible error in the total loss is $\pm 0.005p_{t_\infty}$. The total pressure loss in the subsonic diffuser is small, which was also indicated qualitatively by the fact that the exit distortions were small. The Mach number ahead of the terminal shock is about 1.1 and the total pressure loss at the terminal shock is less than 1 percent. The fact that a Mach number as low as 1.1 was measured is evidence that the flow must have been steady and relatively uniform in the throat. The friction loss from the boundary-layer scoop to the throat is about 6 percent and the remainder of the total pressure loss is in the supersonic core flow and is roughly 9 percent. In theory, there should be no supersonic core-flow loss, but the separation ahead of the boundary-layer scoop has prevented attainment of the theoretical flow. It would be expected that elimination of the separation, by moving the scoop forward or decreasing the local pressure gradient, would reduce the core-flow loss substantially. This should result in a pressure recovery near 90 percent at a Mach number of 3.83, and thus the initial goal is not unrealistic.

## CONCLUDING REMARKS

It has been shown that the favorable end result of the present investigation has been obtained because of a basic research program directed toward understanding unsteady flows. A new experimental technique, the continuous display of transient-total-pressure profiles, has been used to demonstrate one origin of unsteady internal flows, and a qualitative understanding of such flows has been achieved. This has resulted in a useful hypothesis regarding one possible origin of turbulence and has indicated that uniform and steady throat flows are required for efficient inlets. Rigid application of this design requirement has produced an efficient inlet and thus it has been shown that, for the Mach numbers of this investigation, adverse viscous effects can be minimized.

REFERENCES

1. Preston, J. H.:  A Simple Approach to the Theory of Secondary Flows. Aero. Quarterly, vol. V, pt. 3, Sept. 1954, pp. 218-234.

2. Townsend, A. A.:  The Structure of Turbulent Shear Flow.  Cambridge Univ. Press, 1956.

3. Gunther, Fred C., and Carr, John H.:  Development of an Adjustable Supersonic Inlet Utilizing Complete Boundary-Layer Removal at the Throat.  Progress Rep. No. 20-231 (Contract No. DA-04-495-Ord 18), Jet Propulsion Lab., C.I.T., June 14, 1957.

4. Anon.:  Combined Bimonthly Summary No. 60.  Jet Propulsion Lab., C.I.T., Aug. 15, 1957, pp. 28-32.

5. Flaherty, Richard J., and Luidens, Roger W.:  Use of Shock-Trap Bleed To Improve Pressure Recovery of a Fixed and a Variable-Capture-Area Internal-Contraction Inlet at Mach Numbers From 2.0 to 3.5.  (Prospective NACA paper.)

RECTANGULAR INLET
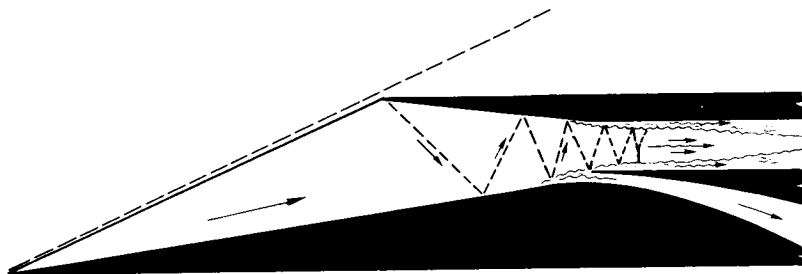


Figure 1

DIFFUSER TEST APPARATUS

MEAN $M_{MAX}$ = 1.1



Figure 2
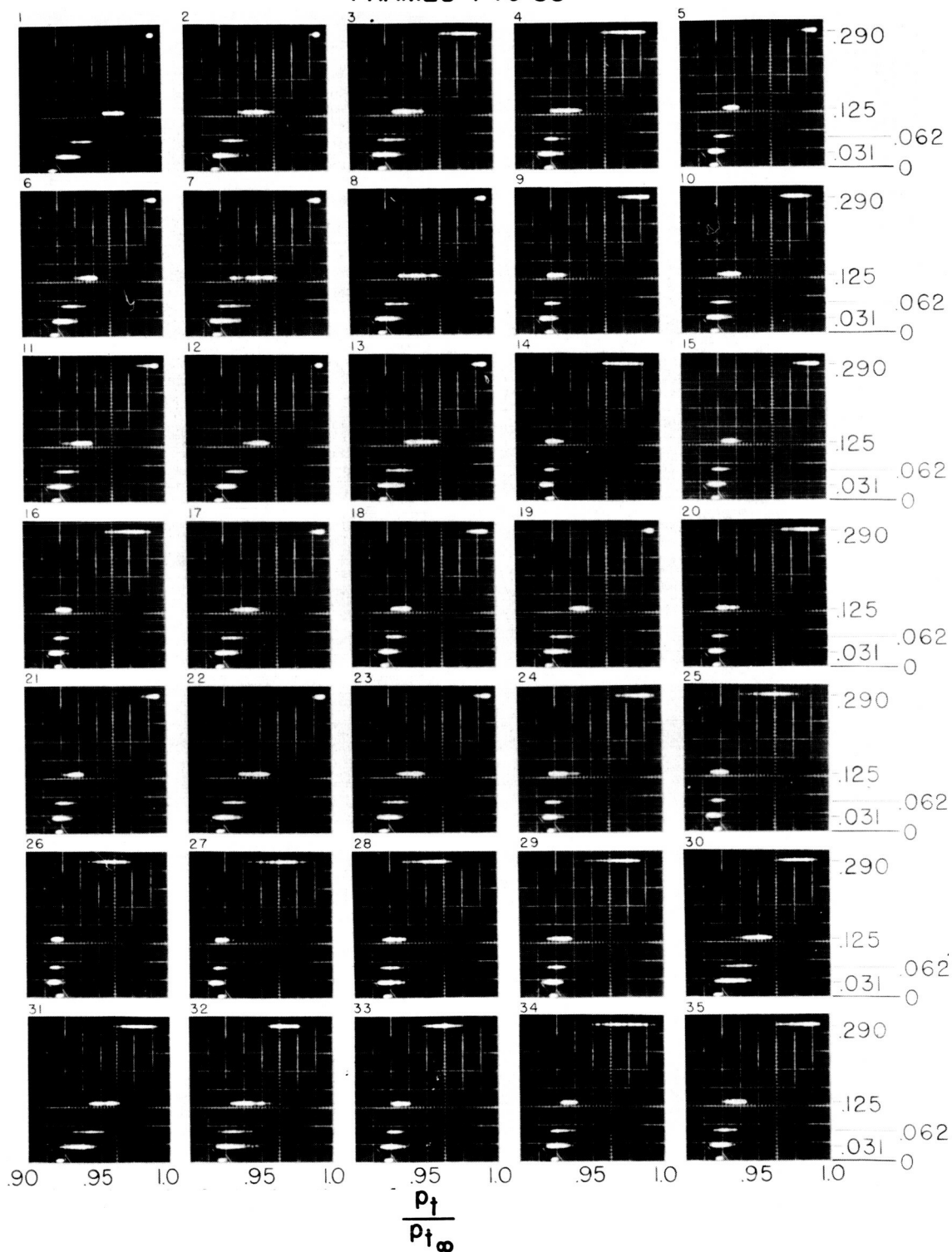
TRANSIENT-TOTAL-PRESSURE PROFILE
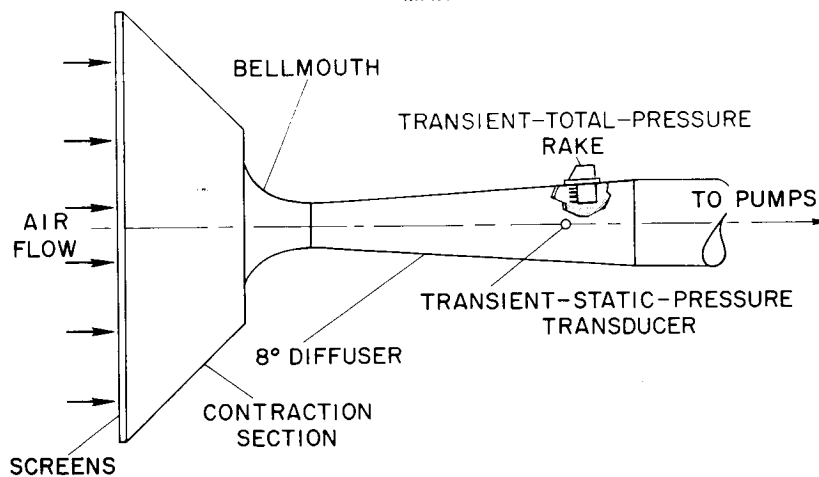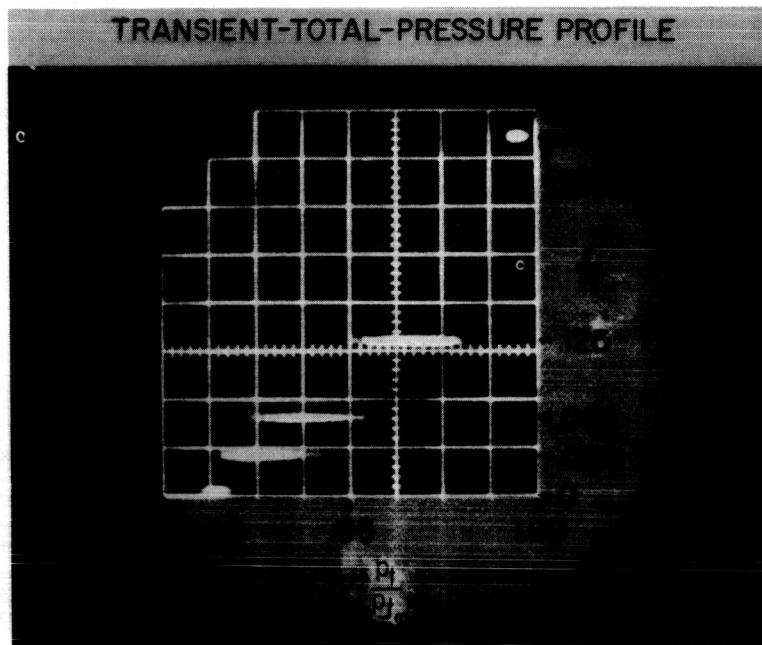
Figure 3

# SELECTED FRAMES FROM MOTION PICTURE OF UNSTEADY FLOW
## FRAMES I TO 35



$$\frac{p_t}{p_{t_\infty}}$$

Figure 4(a)

# SELECTED FRAMES FROM MOTION PICTURE OF UNSTEADY FLOW
## FRAMES 36 TO 70



$$\frac{r}{R}$$

$$\frac{p_t}{p_{t_\infty}}$$
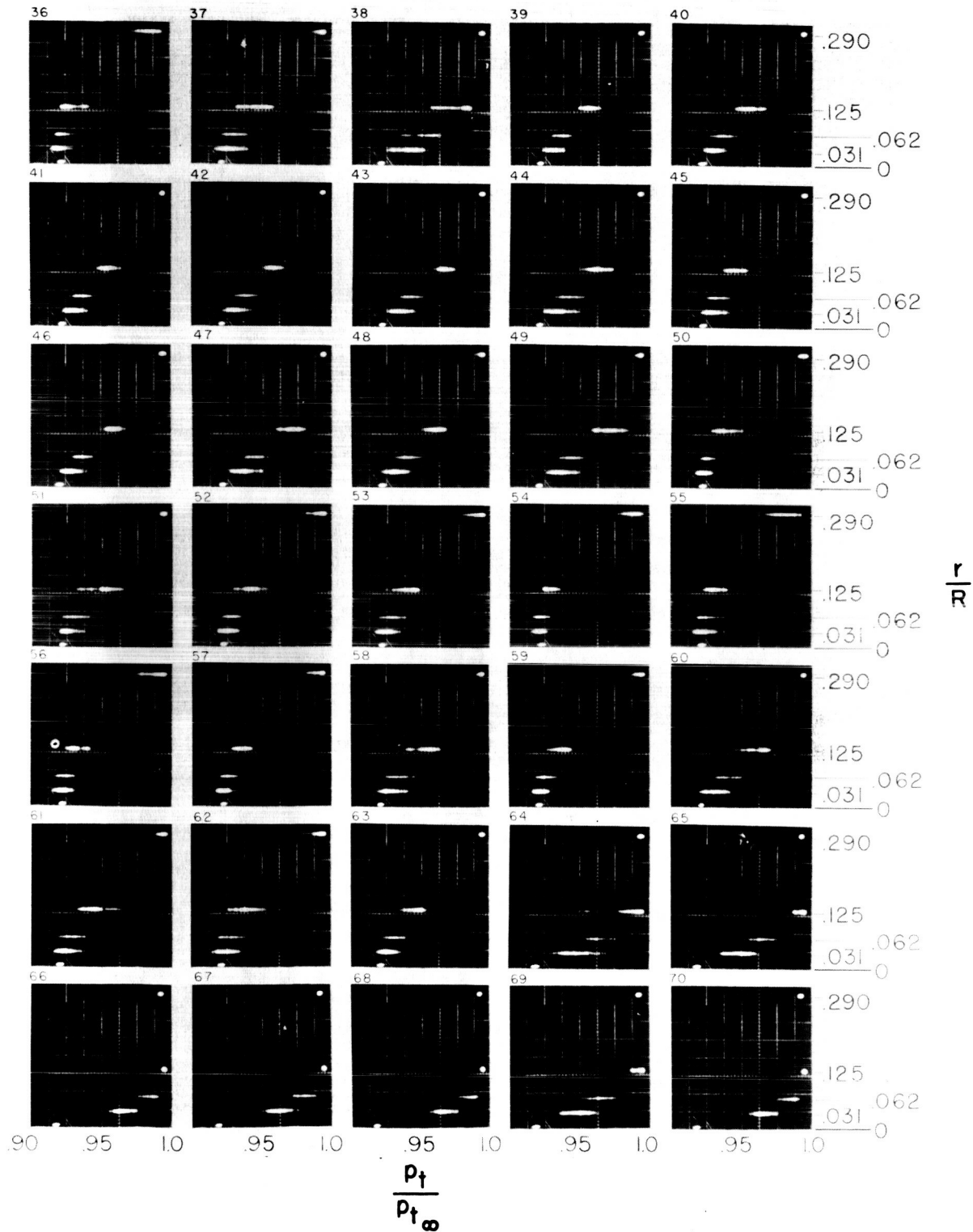
Figure 4(b)

# SELECTED FRAMES FROM MOTION PICTURE OF STEADY FLOW
## FRAMES 1 TO 35
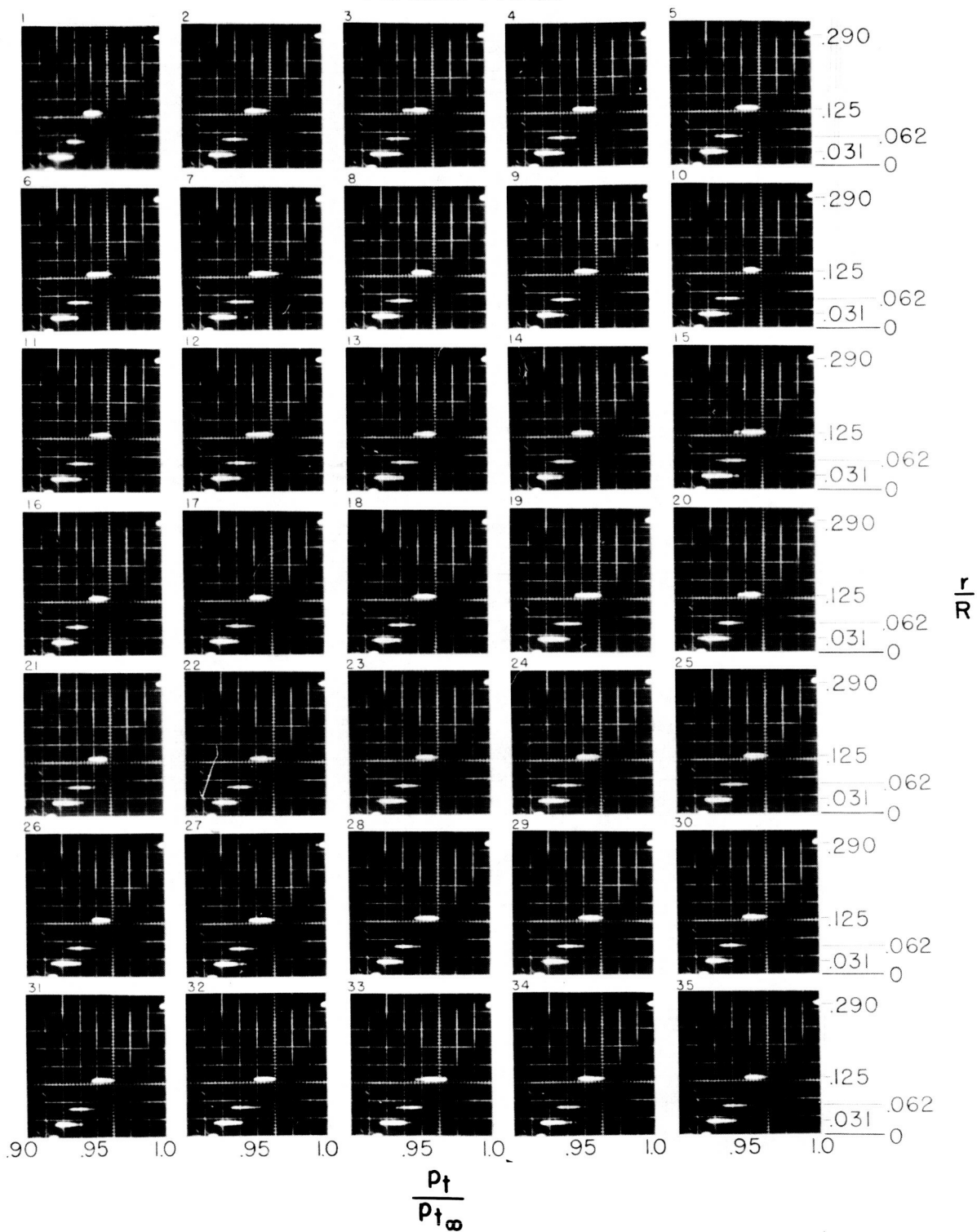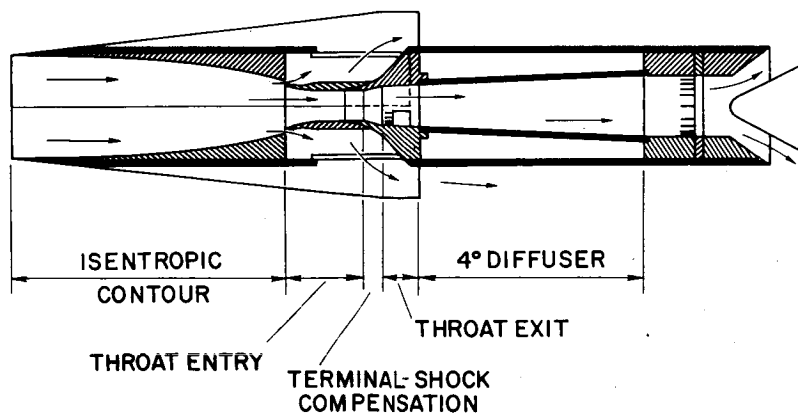


Figure 5

## SHEAR-TO-TURBULENCE HYPOTHESIS
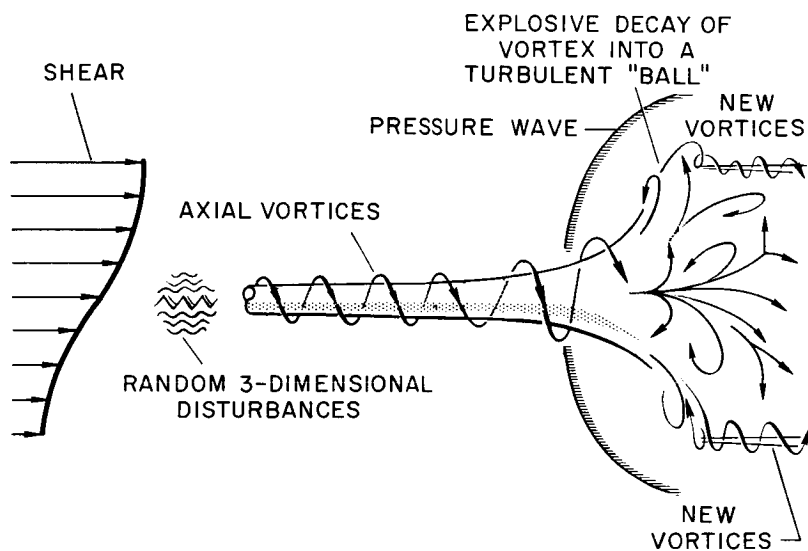


Figure 6

## AXIALLY SYMMETRIC, ISENTROPIC, INTERNAL-CONTRACTION INLET
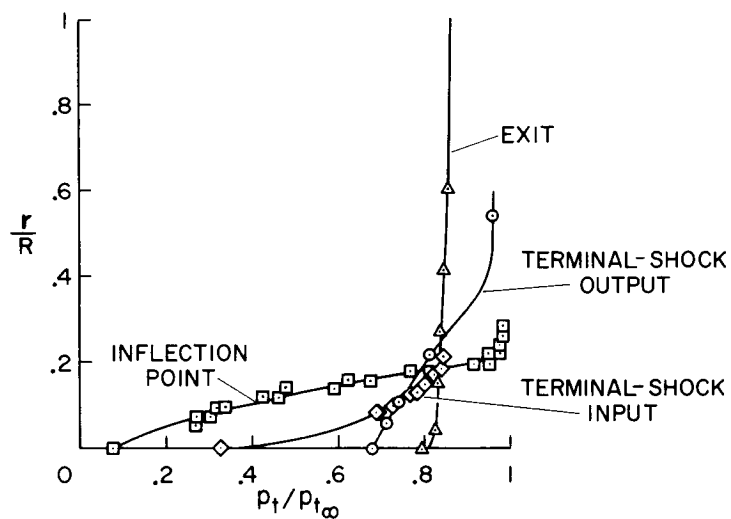


Figure 7

## TYPICAL PRESSURE PROFILES
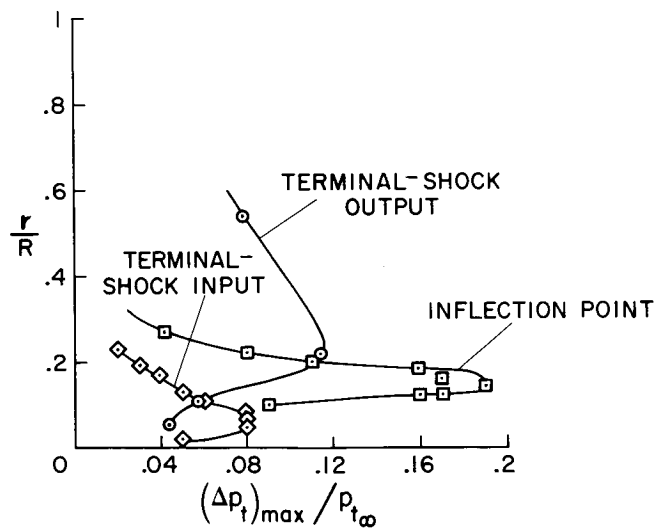


Figure 8

## TYPICAL PRESSURE-FLUCTUATION PROFILES



Figure 9

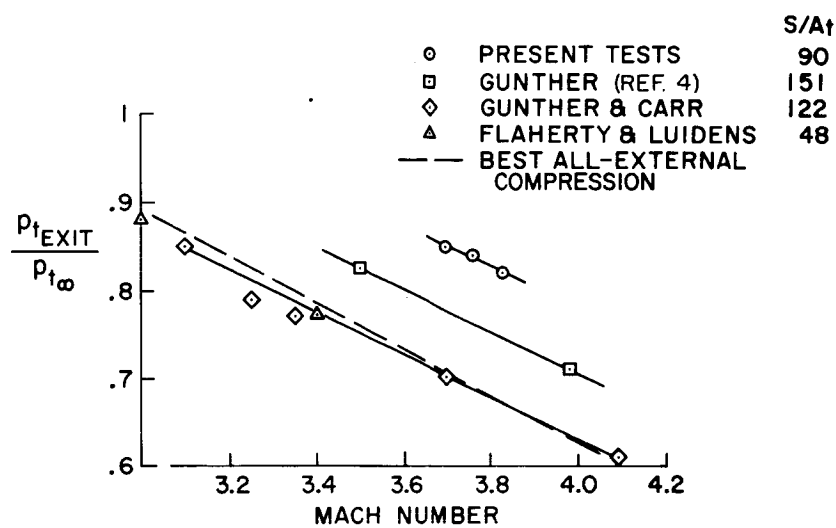PRESSURE - RECOVERY COMPARISON



Figure 10

## SOME CONSIDERATIONS INFLUENCING INLET SELECTION

By Leonard J. Obery

Lewis Flight Propulsion Laboratory

## INTRODUCTION

The designer of high Mach number airplanes finds, as he has in the past, that the overall performance of the aircraft is critically dependent on the powerplant performance and that in the high Mach number range, a large amount of the potential performance of the engine can be lost through the air-inlet system. It is the purpose of this paper to explore the state of the art in air-inlet development and to examine some of the characteristics or peculiarities of the various types of inlets that would be considered in the selection of an inlet by a powerplant designer. Furthermore, this paper will deal only with the on-design performance of the inlets, and none of the characteristics at off-design conditions, either angle of attack or Mach number, will be included in the comparisons made in this paper.

Neglecting, for the moment, the geometry or the particular type of installation on the aircraft, the two factors which primarily affect the engine performance are the inlet pressure recovery and the drag produced by the inlet. Other factors, of course, enter into the inlet selection: whether it should be two-dimensional or three-dimensional in geometry; the length, complexity, and starting requirements if it has high internal contraction; and the control problems, among others. The two primary factors, the inlet recovery and the associated drag, will be examined first.

Many of the data to be presented herein are as yet unpublished. A short bibliography of available published data is included.

## TOTAL PRESSURE RECOVERY

### External-Compression Inlets

Figure 1(a) shows total pressure recoveries that have been measured recently from all-external supersonic-compression inlets at

free-stream Mach numbers up to 5.0, and in figure l(b) are sketches of
the inlets used in the various investigations. As the sketches show,
all the supersonic compression is accomplished ahead of the cowl lips,
and for best performance the terminal shock would stand at the cowl lip
as shown. The isentropic spike inlet has a compression surface which
compresses the supersonic flow as much as possible. The limiting com-
pression at any design Mach number occurs when the focused waves at the
point of coalescence develop a pressure rise equivalent to the normal-
shock value as explained in reference 1. This maximum turning limits
the pressure recovery that can be attained with this inlet type, and
the isentropic inlets presented in this paper have all been designed
for that limit. Most of the inlets presented also have a flush slot
bleed at the throat for compression-surface boundary-layer control.
The total pressure recoveries of these inlets (fig. l(a)) are believed
to be about the highest that have been measured to date with this inlet
type and lie at a kinetic-efficiency level of about 97 percent at the
lower Mach numbers and of about 95 percent at a Mach number of 5.00.
This dropoff in recovery directly reflects the limiting compression that
can be designed into the all-external-compression inlets, and as shown
by a comparison with the theoretical limiting curve, not a great deal
of improvement in the recovery levels of all-external-compression inlets
can be expected.

## Internal-Compression Inlets

The obvious way to hurdle the external-compression limit is, of
course, to incorporate internal compression into the inlet designs.
This course was pursued several years ago at the Ames Laboratory with
the axisymmetric center-body type of inlets shown in the top sketch of
figure 2(a). These inlets had low-angle center bodies which translated
forward along their axis to vary the throat area and to provide the
reduced contraction to allow the supersonic flow to "start" in the
inlet. The low-angle compression in this case was required to keep the
compression-surface boundary layer from excessive thickening or sepa-
rating, and it results in a characteristic long supersonic diffuser
passage. The inlet shown in the middle sketch represents a design
tested recently at the Lewis Laboratory. The supersonic compression is
formed by the inside of a frustum of a cone, and the boundary layer
generated along the walls of the supersonic diffuser is bled away from
the inlet ahead of the entrance to the subsonic diffuser. Starting of
this device was accomplished by opening most of the top half of the
supersonic diffuser until the internal compression was sufficiently
reduced to establish the supersonic flow. The third inlet shown in fig-
ure 2(a) is two-dimensional, each jaw pivoting to reduce the capture
area and increase the throat area until supersonic flow can be attained.
Again the boundary layer is diverted away from the subsonic diffuser by

a bleed system at the throat. In contrast to the all-external-compression inlets, no theoretical limits exist to the amount of supersonic compression that may be built into these inlets. Practical considerations, possibly attendant with fluctuations in the internal boundary layer, however, usually limit the minimum supersonic Mach number just ahead of the inlet throat to about 1.2 at free-stream Mach numbers below 3.0 and, in the case of the investigation at a Mach number of 5.0, to about 1.7 at the end of supersonic compression.

The recovery obtained with the internal-compression inlets (fig. 2(b)) is the highest measured to date over the whole Mach number range. The data shown represent essentially the peak pressure recoveries of various inlets near their design Mach number. No single inlet is shown over the entire Mach number range.

Near the design Mach numbers, kinetic-energy efficiencies of 97 percent have been obtained by internal-compression inlets at Mach numbers up to 5. As shown by the reference points, the recoveries of the all-external- and all-internal-compression inlets are comparable at Mach numbers below about 3.0, but above 3.0 the restrictions of limited compression begin to drop the pressure recovery of the all-external inlet well below that obtained with all-internal compression. The high values of recovery shown for the all-internal-compression inlets were obtained, however, with large amounts of boundary-layer bleed. In most cases, bleed of the order of 20 to 30 percent of the air entering the inlet was required to maintain the high recoveries. When this bleed was reduced, the recovery level was also reduced as shown by the data for a Mach number of 5.0. Reducing the bleed by enlarging the subsonic-diffuser entrance caused the recovery to drop to 60 percent with 18 percent bleed and to 41 percent with 6 percent bleed. Here with comparable bleed, about the same recoveries were measured with all-internal- or all-external-compression inlets.

These all-internal-compression inlets apparently will require a large amount of bleed and as shown in the sketches of figure 2(a) have long supersonic passages which require large geometry variations for starting. In an effort to cut down on the amount of boundary-layer removal required and to shorten the internal supersonic passage, a third type of inlet has been designed and investigated recently. As shown in figure 3(a), this type of inlet combined external compression with high-pressure-gradient internal compression.

External-Internal-Compression Inlets

The high pressure gradients of the external-internal compression inlets result in a very short internal contraction passage; however,

inasmuch as the pressure rise across the focal point of the internal shocks is more than enough to separate a boundary layer, the boundary layer developed by the external-compression surface had to be removed ahead of the point of impingement of the high-strength internal shocks. Without this bleed the inlets could not be brought to their design conditions.

The pressure recoveries obtained with this inlet type are shown in figure 3(b). Reference values of the all-external inlets presented previously are shown for comparison. To date, recoveries nearing a kinetic-efficiency level of 97 percent have been measured at Mach numbers of 3 and below. At a Mach number of 5.0 a two-dimensional combined-compression inlet again gave a pressure recovery comparable to the best value measured with an all-external-compression inlet to date. This inlet type has no apparent limitation on potential recovery and should be capable of recoveries at least as high as the all-internal-compression inlets. It is expected that recoveries comparable to the best measured to date can be attained with more refined compression surfaces or with a boundary-layer-control system in the region of the terminal shocks. For, as with any other inlet, the interaction between the inlet terminal shock and the boundary layer formed along the diffuser walls can cause very large losses in pressure recovery, and the attainment of high pressure recovery will probably depend largely on the degree to which the internal boundary-layer separation can be controlled.

## INLET DRAG

The other factor that has a primary influence on powerplant performance is the drag produced by or directly chargeable to the inlet. This drag may be produced by projecting surfaces, such as the cowl lip or the side fairings of an inlet, or may result from the spilling or diverting of air by the inlet such as that which occurs, for example, with boundary-layer bleed air. In any case, the drag directly reduces the net propulsive thrust available to power the aircraft.

The general levels of the drag produced by the three types of inlets are shown in figure 4. The drag is presented over the Mach number range as a percent of the engine propulsion thrust; that is, the thrust that the engine could actually deliver at the pressure recovery being produced by the respective inlets. In computing the thrust, the assumptions have been made that at Mach numbers less than 3.0 the afterburner temperature will be 3,500° R and at Mach numbers above 3.0, 4,000° R. It was further assumed that the pressure ratio across the engine, or the ramjet combustor, as the case might be, was equal to 1. This appears to be a reasonable assumption for high Mach number turbojet

engines, or for ramjet engines it requires the assumption that the loss across the combustor be neglected. The bleed drags for all the inlets were computed by assuming axial discharge through a sonic nozzle with 100 percent velocity coefficient at either a measured recovery in the bleed duct or at 70 percent of diffuser-exit total pressure recovery. The 70-percent value would essentially correspond to the static pressure behind the inlet terminal shock, and it requires the assumption that the bleed system could recover all the static pressure at the beginning of subsonic diffusion. If the bleed air could be used elsewhere, the drag charged to the inlet could be reduced; however, since the purpose of the present paper is a comparison of inlet types, external mitigating factors are beyond its scope.

The external-compression inlets generally yielded the highest drag values, primarily because of the cowl drag. Even with low cowl projected areas, on the order of only 20 percent of the projected area, the drag at a Mach number of 3.0 accounted for about 13 percent of the thrust that could be produced by the engine. The difference in the drag levels of the external compression inlets at a Mach number of 3.0 resulted from subcritical spillage. The point shown at about 19 percent is the drag of the highest total-pressure-recovery point presented in figure 1(a) at a Mach number of 3.0.

The drag of the internal-compression inlets resulted entirely from the momentum change in the boundary-layer air spilled from the inlets. These drag values generally fell on a single line and indicate the thrust penalty that can result from the high spillage rates.

The low values of drag shown for the external-internal-compression inlets resulted from the low cowl projected areas and the small amounts of spillage necessary for their satisfactory operation. For the cases shown, only about 2 percent spillage was required at a Mach number of 3.0 and less than 5 percent at a Mach number of 5.0.

INLET EVALUATION

The combined effects of drag and pressure recovery largely determine the overall performance of the engine package. In order to compare the relative worths of the various inlets, they must be applied to some particular type of operational requirement. For comparison, therefore, these inlets will be used on two distinct, diametrically opposed types of aircraft configurations. First, consider a missile that would be required to accelerate rapidly up to its design speed and altitude and make sharp maneuvers. For this configuration the primary interest is in obtaining the maximum thrust minus inlet drag from the engine.

Figure 5 shows the net propulsion thrust which the inlet-engine combination could deliver to the aircraft as a percent of the ideal (or 100-percent recovery - no drag) thrust. Here the net thrust produced by the all-internal-compression inlets is shown to be highest over the whole Mach number range. This, of course, results from the high recovery of these inlets in spite of their relatively high drag. It is interesting to note that over most of the Mach number range the drag of the all-internal-compression inlets was 3 to 4 times the drag of the combined-compression inlets, but because of their higher recovery their net thrust was higher by 10 to 20 percent.

Of course, it might be expected that the internal-compression inlets will be heavy and will weigh considerably more than the other types. The question naturally arises of how much the engine weight can be increased and take advantage of the higher recoveries. Calculations of allowable weight increases were made for a hypothetical missile with a total weight of 10,000 pounds. An engine weight of 25 percent of the missile gross weight was assumed to make changes in the engine weight as significant as possible. The calculations showed that, if a change were made from the highest thrust external-compression inlet to the high thrust internal-compression inlet at a Mach number of 3.0, the engine weight could be increased by 62 percent, or some 1,500 pounds could be added to the original 10,000-pound missile without a reduction in acceleration potential. Any increase in weight less than that amount would, of course, give a higher acceleration to the internal-compression inlet. It appears then that a considerable amount of weight can be a added to an acceleration-type aircraft to obtain better performance. The conclusion appears inescapable: for the acceleration vehicle the pressure recovery obtained by the inlet has a very great effect on the overall performance, and it will not be possible to sacrifice pressure recovery to any great extent in the interest of obtaining lower drag.

Consider now an inlet-engine installation on a second type of aircraft for which range is of paramount importance and the highest impulse will be needed from the powerplant. Figure 6 presents impulse ratios computed from the previous inlet-engine characteristics. The impulse ratio is defined as the impulse that the engine package would deliver (that is, the pounds of net propulsive thrust per pound of fuel burned) divided by the impulse that would be obtained from a powerplant which operated at 100-percent recovery and zero drag. Again the propulsion figure of merit (here the impulse) must be balanced against an engine weight increase. Consider a heavy bomber-type configuration. For this case the engine weight is only about 6 percent of the total weight and intuitively it probably could be expected that large increases in engine weight could be made with only minor effects on the airplane range. Calculations indicated that such indeed is the case and that, at least

to a first order, the aircraft ranges can be compared directly from their impulse ratios.

Now the inlets which had the lowest drag gave the highest impulse or would give the longest range and conversely the high-drag inlets gave the poorest impulse and hence the shortest range. Here, in contrast to the previous curves of net thrust ratio (fig. 5), the pressure recovery developed by the respective inlets had considerably less effect on the impulse ratio and, hence, would have a smaller effect on the aircraft range. Even at the highest Mach number, where the recovery of the internal-compression inlet was nearly 20 percent of the total pressure higher than the combined-compression inlet, this higher recovery did not offset the drag penalty.

From the two analyses presented, several conclusions can be reached. First, it appears from the calculations that for either of the two types of applications relatively large increases in inlet weight will be permissible for reasonable increases in performance; therefore, at least to a first order, the overall performance will depend primarily on the total pressure recovery and the drag. Of these two factors, the inlet total pressure recovery will be the dominant factor for the acceleration vehicle while the inlet drag will predominate for the long-range aircraft. In either case, however, for the airplane or the missile, the best inlet would be the one that produces high pressure recovery and low drag simultaneously. The desirable high pressure recovery will come from designing the supersonic-compression surfaces for maximum recovery but particularly from an ability to control the shock—boundary-layer interaction inside the inlets. It seems that the external-compression inlets will not be able to achieve low drag and that the maximum total pressure recoveries, both expected theoretically and measured experimentally, show that the all-external-compression inlets will not be able to give the high pressure recoveries needed at the higher Mach numbers and that some degree of internal contraction will be required.

## ADDITIONAL CONSIDERATIONS

With the use of internally contracted passages come additional factors that must be considered by the inlet designer. Internal contraction greater than the Kantrowitz value will require variable geometry to "start" the supersonic flow in the inlet, and, of course, variable geometry of this type will add considerable complexity, structural problems, and weight to the inlet designs.

Figure 7 shows examples of the geometry variations required to eliminate the internal contraction from the inlet passages to enable starting at the lower Mach numbers. The lengths of the surfaces required to move for elimination of the internal contraction are shown for two-dimensional inlets in figure 7(a) as a function of inlet height for the design Mach number. The top sketch shows a current external-internal-compression inlet with a starting door of only $62\frac{1}{2}$ percent of the inlet height. This inlet was designed for a Mach number of 3.0, and opening the door to the position indicated by the dashed line allowed the inlet to start. The door was then, of course, returned to its design position for normal operation. The other two-dimensional inlet (shown in the bottom sketch) varies the inlet capture area to eliminate internal compression and start the inlet flow. In this case it is necessary to rotate the whole length of the supersonic compression ramps. This length for a Mach 3.0 design is equal to almost 3 inlet heights.

For the three-dimensional inlets (fig. 7(b)) the most common method of reducing the internal contraction is to translate the center body. For the two cases shown in this figure, a combined-compression and an all-internal-contraction inlet, the respective translational require-ments are 1/4 and $2\frac{1}{2}$ inlet diameters. In both the three-dimensional and the two-dimensional cases shown here (and from other inlets as well), it appears that considerable savings in the amount of variation required for the internal-contraction inlets can be made by using par-tial external compression and short internal supersonic passages having relatively high pressure gradient shocks.

The control problem of positioning both the spike or ramp and the internal terminal shock is similar for the two types of inlets. In general, however, it probably would be easier to position the spike or the ramp of the combined-compression inlets because of the distinct and relatively high-strength shock waves set up by the cowl. The spike or ramp of the all-internal-contraction inlets would probably have to be scheduled as a function of Mach number and Reynolds number according to the few preliminary control investigations that have been conducted to date. While this type of control system is reasonable, it is undoubt-edly more complex than the relatively simple shock-positioning system possible for the combined-compression inlets.

## CONCLUDING REMARKS

In conclusion, it appears that high pressure recovery can be obtained from all three types of inlets considered and that the current

level of peak recovery is about 97-percent kinetic-energy efficiency. In order to attain high pressure recovery, particularly with low drag, some degree of internal contraction will be needed, especially at the higher Mach numbers. While the supersonic-compression surfaces must be designed to produce their maximum potential, the most important and probably the most difficult development work will be to control the terminal-shock—internal-boundary-layer interaction.

With the low-angle all-internal-compression inlets come the attendant long supersonic passages and the large translational or rotational distances, probably with complex control systems. It appears that the combined-compression inlets will probably offer important advantages from the small geometry variations possible with this type of inlet. But whatever the advantages, disadvantages, or characteristics peculiar to each inlet type, the selection of the propulsion-system inlet will be dictated by the aircraft requirements and, to be successful, it must be compatible with the aircraft mission.

REFERENCE

1. Conners, James F., and Meyer, Rudolph C.: Design Criteria for Axisymmetric and Two-Dimensional Supersonic Inlets and Exits. NACA TN 3589, 1956.

CONFIDENTIAL

# BIBLIOGRAPHY

Conners, James F., Lovell, J. Calvin, and Wise, George A.: Effects of Internal-Area Distribution, Spike Translation, and Throat Boundary-Layer Control on Performance of Double-Cone Axisymmetric Inlet at Mach Numbers From 3.0 to 2.0. NACA RM E57F03, 1957.

Vargo, Donald J., Parks, Philip W., and Davis, Owen H.: Investigation of a High-Performance Top Inlet to Mach Number of 2.0 and at Angles of Attack to 20°. NACA RM E57A21, 1957.

Obery, Leonard J., and Stitt, Leonard E.: Performance of External-Internal Compression Inlet With Abrupt Internal Turning at Mach Numbers 3.0 to 2.0. NACA RM E57H07a, 1957.

Gertsma, L. W., and Beheim, M. A.: Performance at Mach Numbers 3.07, 1.89, and 0 of Inlets Designed for Inlet Engine Matching up to Mach 3. NACA RM E58B13, 1958. (Prospective NACA paper.)

Anon: Combined Bimonthly Summary No. 56. Jet Propulsion Lab., C.I.T., Dec. 15, 1956, pp. 31-33.

RECOVERY
ALL-EXTERNAL-COMPRESSION INLETS

GEOMETRICAL TYPE
O     3-DIM
□     2-DIM

THEORETICAL LIMIT

$\eta_{KE}$

.97

.95

TOTAL
PRESSURE
RECOVERY

1.00

.80

.60

.40

.20

FREE-STREAM MACH NO.
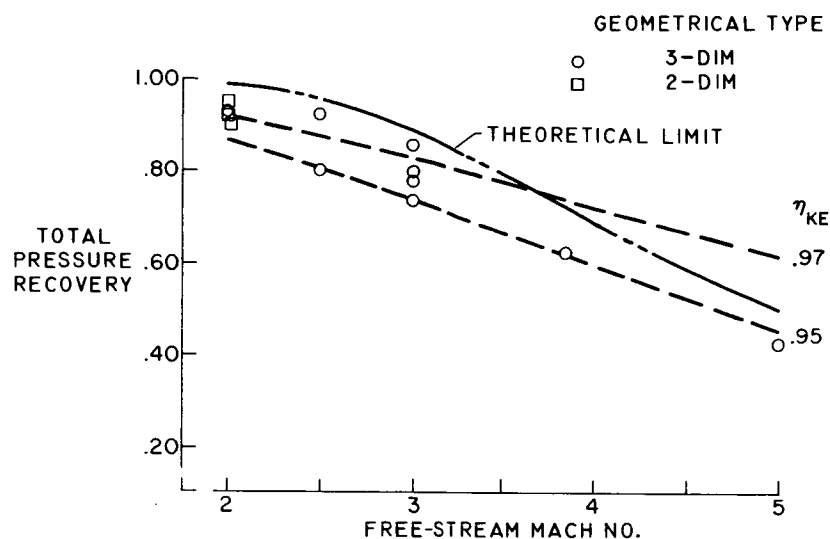
Figure 1(a)

ALL-EXTERNAL-COMPRESSION INLETS

3-DIMENSIONAL ISENTROPIC SPIKE

2-DIMENSIONAL DOUBLE-RAMP
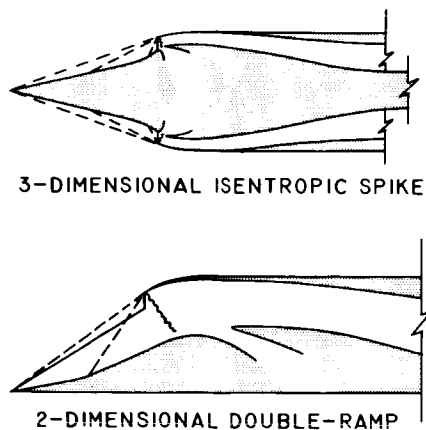
Figure 1(b)

## ALL-INTERNAL-COMPRESSION INLETS



3-DIMENSIONAL, TRANSLATING CENTERBODY

3-DIMENSIONAL, CONICAL COMPRESSION

2-DIMENSIONAL, VARIABLE CAPTURE AREA
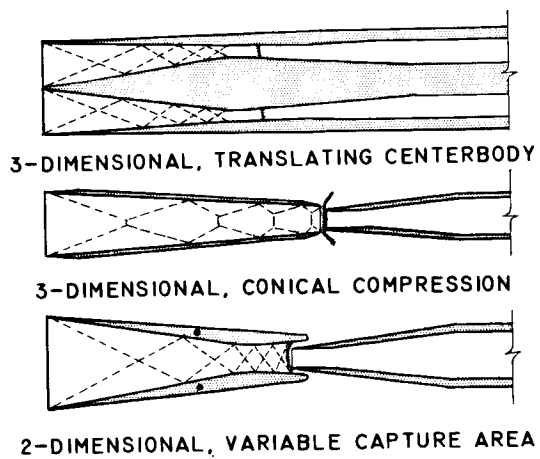
Figure 2(a)

## RECOVERY
## ALL-INTERNAL-COMPRESSION INLETS



GEOMETRICAL
TYPE

□   2-DIM
○   3-DIM
ALL-EXT REF

$\eta_{KE}$

.97

.95

TOTAL
PRESSURE
RECOVERY

FREE-STREAM MACH NO.
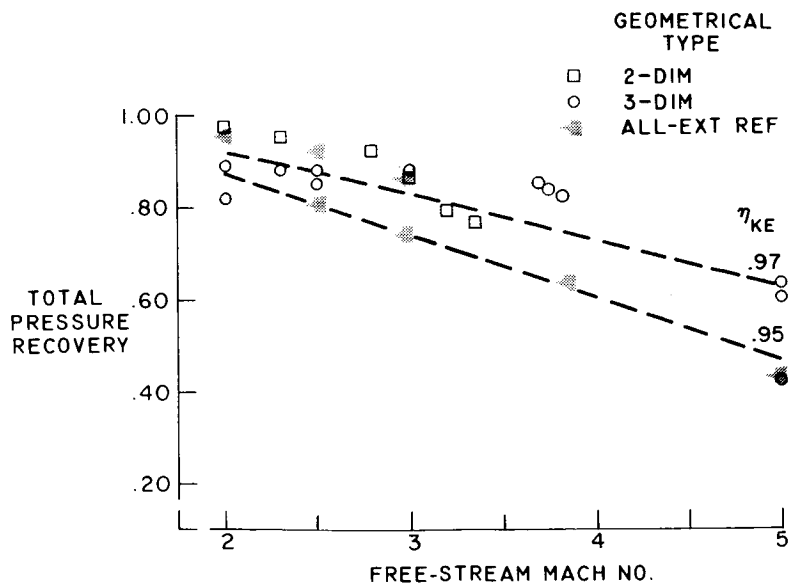
Figure 2(b)

# EXTERNAL-INTERNAL-COMPRESSION INLETS



3-DIMENSIONAL, TRANSLATING SPIKE

2-DIMENSIONAL, BYPASS DOOR
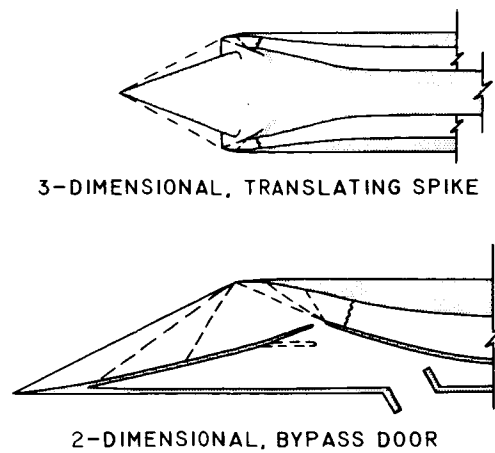
Figure 3(a)

# RECOVERY
# EXTERNAL-INTERNAL-COMPRESSION INLETS
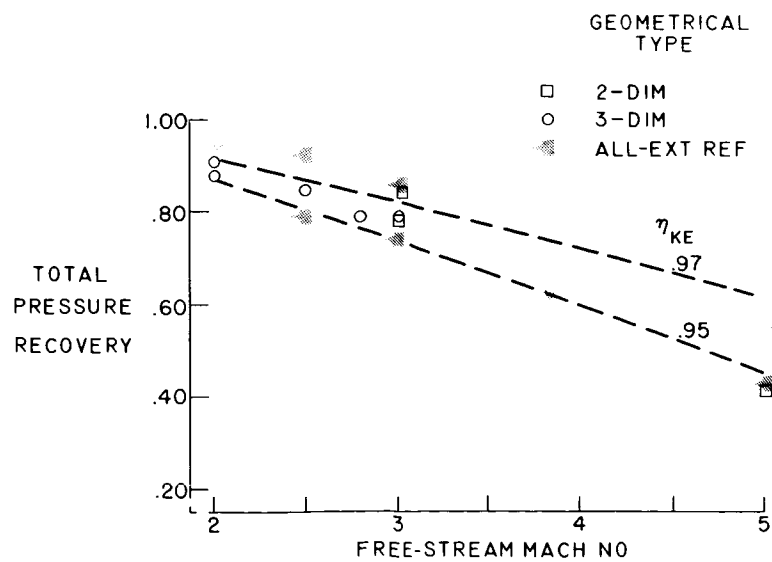


Figure 3(b)

# INLET DRAG
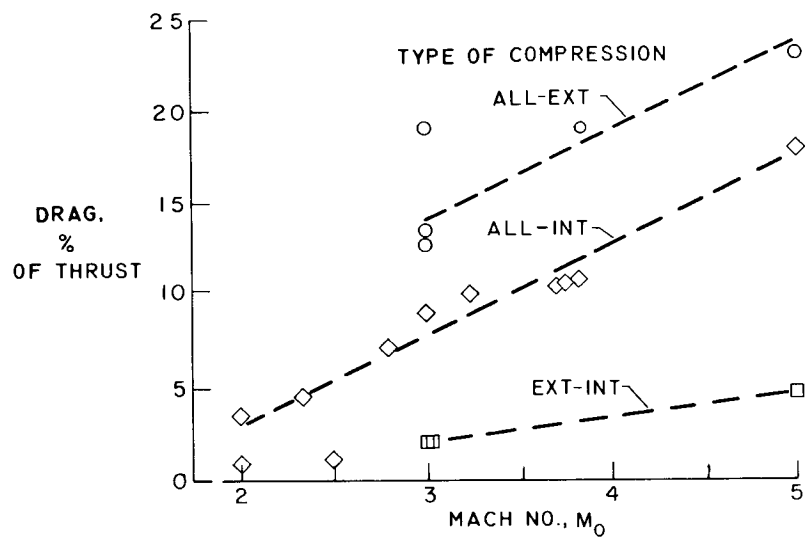


Figure 4

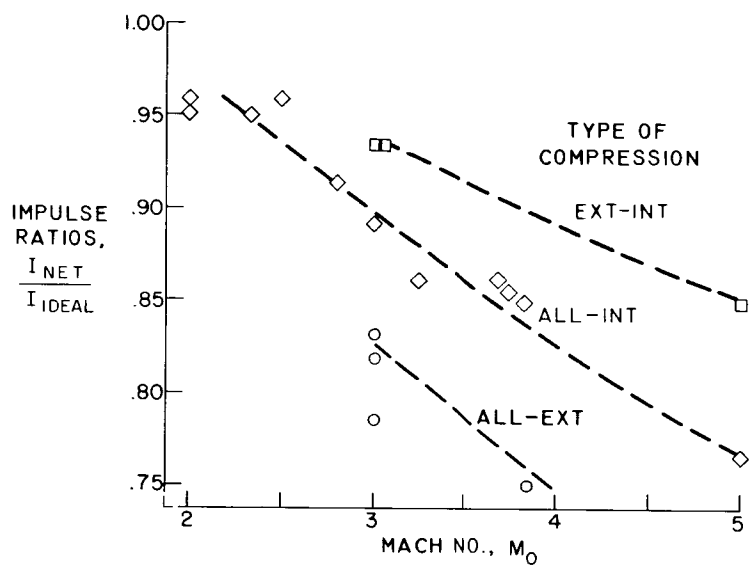# NET THRUST COMPARISON
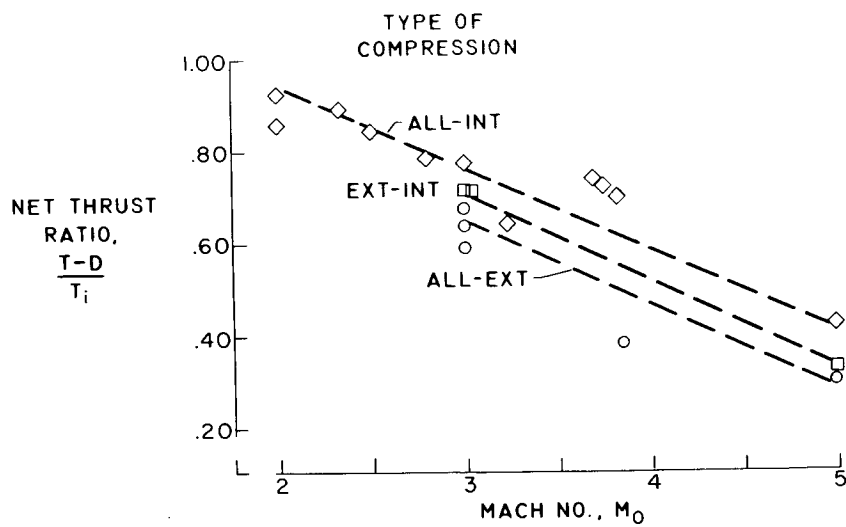


Figure 5

## RELATIVE RANGE COMPARISON



Figure 6
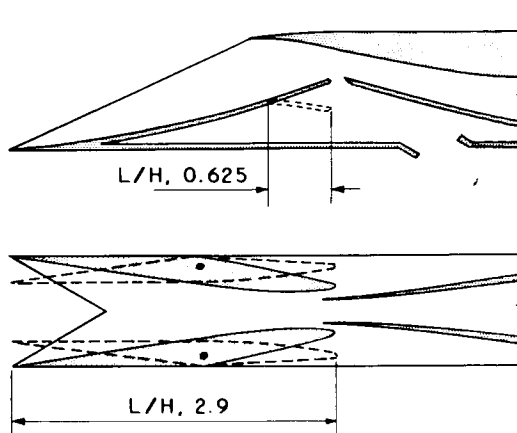
## REQUIRED GEOMETRY VARIATION

### TWO-DIMENSIONAL INLETS

L/H, 0.625

L/H, 2.9

Figure 7(a)

## REQUIRED GEOMETRY VARIATION
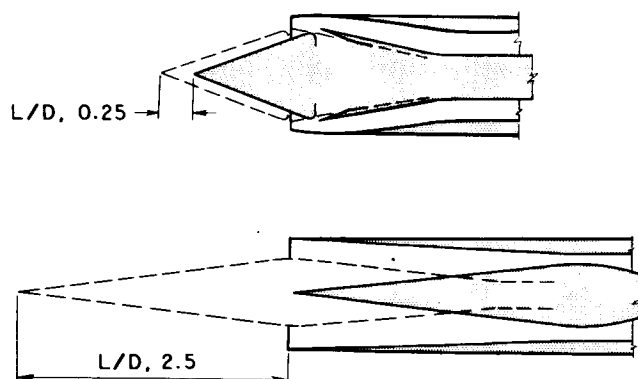
### THREE-DIMENSIONAL INLETS

L/D, 0.25

L/D, 2.5

Figure 7(b)

# THE OFF-DESIGN PERFORMANCE CHARACTERISTICS OF INLETS

By Leonard E. Stitt

Lewis Flight Propulsion Laboratory

## INTRODUCTION

The factors influencing the selection of inlet systems from design-point considerations were discussed in the preceding paper by Leonard J. Obery. The selection of an inlet for a particular engine, however, requires peak performance not only at the design speed but at off-design Mach numbers as well. It appears that, as the design Mach number of turbojet-powered aircraft increases, the off-design matching problem of the inlet to the engine becomes intensified. It is conceivable that an inlet, although it possesses high performance at the design Mach number, could impose excessive performance penalties at some lower speed by inadequate matching.

It is the purpose of this paper, then, to discuss the off-design performance characteristics of various types of inlets and the thrust penalties that occur when these inlets are matched to an engine. This will be done in the following three steps: First, a series of basic inlet types that appear to be attractive, strictly from design-point considerations, will be selected. Second, off-design air-flow characteristics of these inlets will be presented and compared with the air-flow schedule of a particular engine. Finally, the thrust penalties that occur when these inlets are matched to this engine will be indicated at the design speed and an off-design Mach number.

## INLET CONFIGURATIONS

Consider the four inlet configurations that are shown schematically in figure 1. Based on the results obtained by Obery, the selection is being limited to either external-internal-compression or all-internal-compression inlets. (The all-external-compression inlet is not considered herein for high Mach number turbojet application.) The first two inlets shown in figure 1 have a combination of external and internal compression with fixed capture areas, while the second two have all internal compression and incorporate, to some extent, variations in the capture area.

The first configuration, which will be called the translating-center-body inlet, is a three-dimensional external-internal-compression inlet that has been tested experimentally in the Lewis 10- by 10-foot supersonic tunnel (ref. 1). The external compression resulted from a low-angle cone, while the internal compression resulted from turning the supersonic flow with the cowl surface. The resulting oblique shocks were focused on the center body at a common station.

The second inlet, which will be called the variable-throat inlet, has a combination of isentropic external plus internal compression; however, the throat Mach number at design was approximately the same as in the translating-center-body inlet. This inlet is two-dimensional, and large variations in throat area result at off-design speeds as the ramps are lowered for optimum compression. An inlet of this type is under development in the small supersonic wind tunnels at the Lewis Laboratory at Mach numbers of 3.0 and 5.0.

A principal difference between the first two inlets is the amount of supersonic spillage that occurs at off-design Mach numbers. The translating-center-body inlet spills about 60 percent of the capture mass flow ahead of the inlet lip at transonic speeds, while the two-dimensional inlet spills from 10 to 20 percent. It is evident that, with the external-internal-compression technique, the projected cowl area and initial cowl lip angle can be kept low, of the order of 10 percent of maximum cross-sectional area and $10^\circ$, respectively.

The other two inlets, best represented as two-dimensional, are all-internal-compression inlets without center bodies and include some variation in capture area. The first inlet varies capture area only and has no change in throat size. A maximum contraction ratio between the inlet and throat, coincident with peak recovery, is determined at each free-stream Mach number by varying the capture area. An inlet of this type has been tested experimentally in the small supersonic wind tunnels at the Lewis Laboratory.

The last inlet varies both the capture and throat areas simultaneously by locating the pivot point between these two stations. Again, a maximum contraction ratio is set at each Mach number by the variable-geometry feature. An inlet of this type is currently under investigation (ref. 2).

## AIR-FLOW SCHEDULES

Inlet-engine matching is primarily a function of the particular engine air-flow schedule that is assumed. This example is limited to

the Mach 3.0 family of aircraft, either bomber or interceptor. The turbojet engine receiving the most consideration for this flight regime at this time has the air-flow characteristics shown in figure 2. The corrected air flow of this engine, which is referenced to a Mach number of 1.0, decreases about 50 percent over the Mach number range from 1.0 to 3.0.

The theoretical corrected air-flow schedule of each of the four inlets is also shown in figure 2. The figure includes the available experimental datum points, which verify the predicted air-flow trends for these inlets. Estimates of mass flow ratio and overall recovery were necessary to obtain the theoretical curves. The mass flow ratio was estimated by using the equation of continuity between the free stream and the initial diffuser flow area at the inlet lip station. Very close agreement between theoretical and measured mass flow ratios has been obtained with this technique. The overall total pressure recovery, which depends largely on the amount and type of internal bleed, is fairly hard to predict theoretically; therefore, measured levels of overall recovery for the various inlet types, such as those presented by Obery, are relied on.

The translating-center-body inlet has a relatively small variation in corrected air flow at Mach numbers from 1.0 to 3.0. This schedule is characteristic of all spike-type inlets, even with translation, and results primarily from the small change in throat area. It is obvious that this inlet, if it were matched to the engine at a Mach number of 3.0, would operate supercritically in the transonic region. Therefore, the inlet is designed to match the engine at a Mach number of 1.0, and this requires excess air to be spilled ahead of the engine at the higher Mach numbers.

The variable-throat inlet, on the other hand, has large variations in air flow over the Mach number range. This particular inlet has some supercritical spillage at transonic speeds. An all-internal-compression inlet of this type would have an even greater amount of air-flow variation than that shown. Matching this inlet with the engine at a Mach number of 3.0 requires spillage of air at the lower Mach numbers to match the engine.

The variable-capture-area inlet, which has no throat variation, gives even less air-flow regulation than the translating-center-body inlet. Again, this inlet has been designed to match the engine at a Mach number of 1.0 and spills air at the higher Mach numbers to match the engine. This spillage might not be too bad, however, since relatively large amounts of bleed are required with this inlet type to obtain the high values of total pressure recovery that have been reported.

The most versatile of all the inlets appears to be the one with variations in both capture and throat area. In fact, by a judicious selection of the pivot point, the engine air-flow requirements can be matched with this inlet.

## BREAKDOWN OF LOSSES

The corrected air-flow schedules of the four inlets have been shown and compared with the schedule for a particular engine. The next step will be to indicate the penalties that occur at Mach numbers of 3.0 and 1.5 when the comparative air-flow schedules shown in figure 2 are used with this engine. These losses, presented in figure 3 as percent of ideal engine thrust, are made up of the following items: (1) total pressure recovery, (2) cowl pressure drag, (3) additive drag, and (4) bypass or bleed drag. Experimental values, which represent "state of the art" for these inlet types, were used wherever available. Since internal compression was assumed, the inlet will be matched to the engine, where necessary, by bypassing air ahead of the engine. The following paper by Milton A. Beheim and John L. Klann will consider using any excess air that might be available in the transonic region for the ejector. Bypass drags were computed with the assumption of a fully expanded nozzle and a thrust coefficient of 0.9. Bypass recovery was assumed to be equal to the diffuser-exit total pressure recovery, while the bleed recovery was assumed to be 70 percent of that value.

The translating-center-body inlet has a 28 percent loss in ideal thrust due to total pressure recovery. To date, a total pressure recovery of 79 percent has been measured with this inlet at a Mach number of 3.0. At the present time, more refined compression surfaces are being proposed to increase the recovery of this inlet. The low cowl drag resulted from the use of a 10 percent projected cowl area and an initial external lip angle of about $7^\circ$. Bypassing 30 percent of the flow at a Mach number of 3.0 to match the engine costs about 5 percent in ideal thrust. In the transonic range, a large part of the total loss is from additive drag. This inlet spills about 60 percent of its air flow ahead of the lip at the lower Mach numbers, and even though the spillage is behind a low-angle cone, the penalty is about $12\frac{1}{2}$ percent of the ideal thrust. Although more refined surfaces would improve the recovery at a Mach number of 3.0, they would not reduce the additive drag at a Mach number of 1.5. In fact, the additive drag would probably increase.

A total pressure recovery of 79 percent has also been measured with the variable-throat inlet. Since this inlet already has

isentropic surfaces, a more refined internal-bleed system is being proposed to improve its recovery. At a Mach number of 1.5 the 30 percent bypass required to match the engine costs about 3 percent of the ideal thrust. This loss, as far as the inlet is concerned, could be eliminated by supplying the excess air to the ejector.

The variable-capture-area inlet utilizes the 35 percent spillage required to match the engine as boundary-layer bleed in order to obtain the high values of recovery that have been reported with this inlet type. With the assumption of an overall recovery of 88 percent, a 13-percent thrust gain over the previous two inlets results from the higher recovery at a cost of 6-percent thrust loss from the bleed. At a Mach number of 1.5 the reduction in capture area exposed a large projected cowl area which costs about $9\frac{1}{2}$ percent in ideal thrust.

In figure 2 it was shown that by varying both the inlet capture and throat areas simultaneously, the engine characteristics could be matched. However, in order to obtain the high total-pressure-recovery values reported with this inlet type, it has been necessary to bleed 30 percent of the mass flow at the throat. This bleed drag costs about 5 percent of the ideal thrust at a Mach number of 3.0 and about 2 percent at 1.5. However, the cowl drag at a Mach number of 1.5 has been reduced, compared with that of the previous inlet, by decreasing both the external cowl angle and the projected area.

## CONCLUDING REMARKS

It has been shown that large differences in the off-design inlet air-flow characteristics can occur, depending on the type of inlet selected and the amount of variable geometry that is included. For example, the center-body types of inlet have little air-flow variation and also have large values of additive drag transonically. The variable-throat inlet has large variations of air flow and will probably require bypassing in the transonic range. This feature may not be too bad if this excess flow can be used for the ejector or nozzle base region. The variable-capture-area inlet with fixed throat has relatively small air-flow variation and, to date, has required high bleed for obtaining high recovery. This inlet also has large values of cowl drag in the transonic region. Finally, the most versatile inlet appears to be the one with variations in both capture and throat areas. However, this inlet type also has required high bleed flows to obtain high recoveries.

## REFERENCES

1. Obery, Leonard J., and Stitt, Leonard E.:  Performance of External-Internal Compression Inlet With Abrupt Internal Turning at Mach Numbers 3.0 to 2.0.  NACA RM E57H07a, 1957.

2. Gunther, Fred C., and Carr, John H.:  Development of an Adjustable Supersonic Inlet Utilizing Complete Boundary-Layer Removal at the Throat.  Progress Rep. No. 20-321 (Contract No. DA-04-495-Ord 18), Jet Propulsion Lab., C.I.T., June 14, 1957.
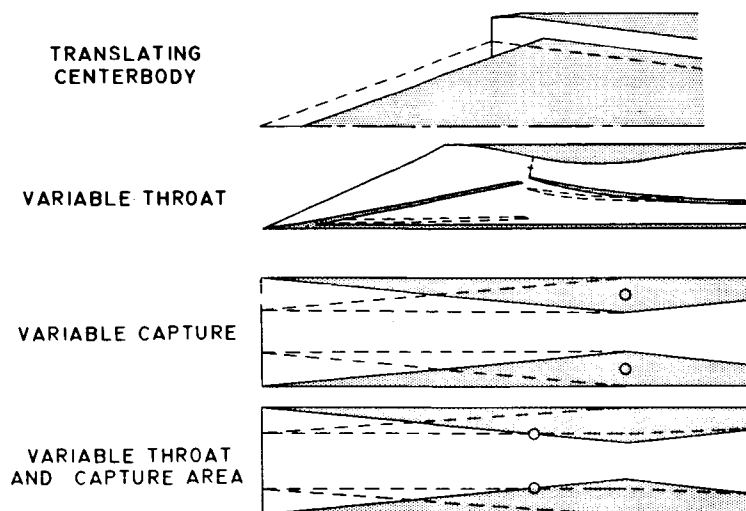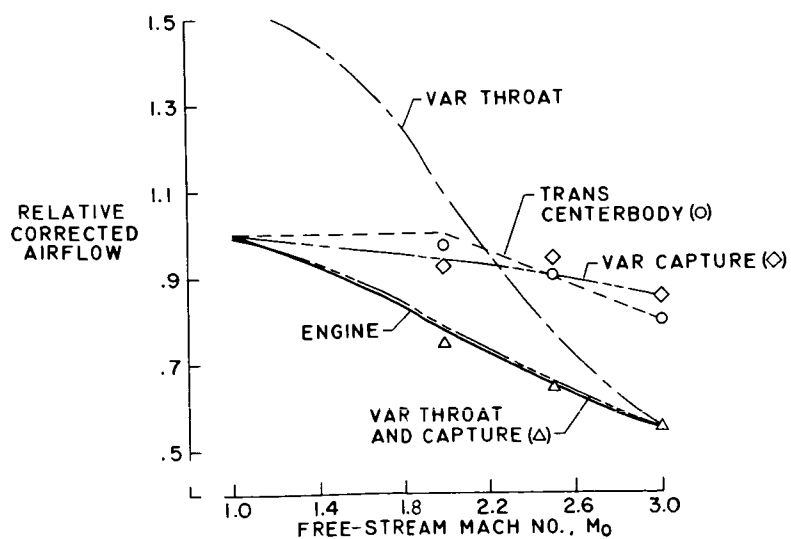
# INLET CONFIGURATIONS

TRANSLATING
CENTERBODY

VARIABLE THROAT

VARIABLE CAPTURE

VARIABLE THROAT
AND CAPTURE AREA

Figure 1

# AIRFLOW SCHEDULES

RELATIVE
CORRECTED
AIRFLOW

VAR THROAT

TRANS
CENTERBODY (O)

VAR CAPTURE (◇)

ENGINE

VAR THROAT
AND CAPTURE (△)

FREE-STREAM MACH NO., $M_0$

Figure 2

## BREAKDOWN OF LOSSES
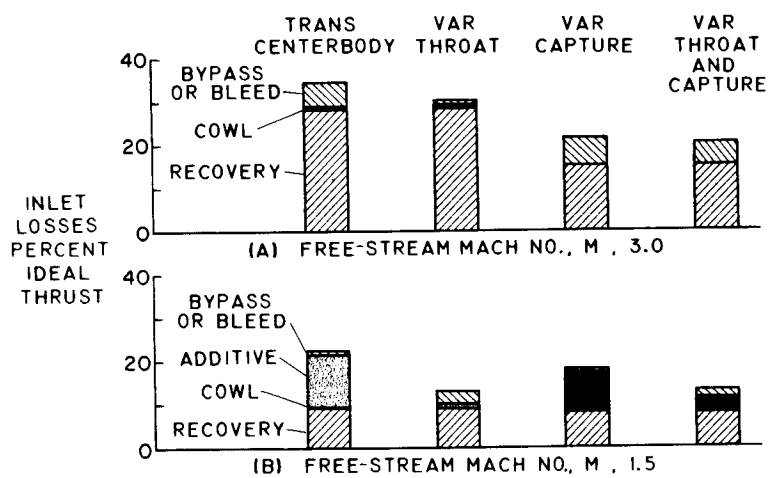


Figure 3

# OFF-DESIGN EJECTOR PERFORMANCE

By Milton A. Beheim and John L. Klann

Lewis Flight Propulsion Laboratory

## INTRODUCTION

The problems of designing an efficient jet-aircraft exit have become more complex as higher flight Mach numbers have been reached. Fixed-ejector configurations, designed for particular cruise conditions, are known to incur thrust losses at off-design conditions. These losses can be too large to be compensated for by high-thrust engines. Variable-geometry ejectors, on the other hand, can be constructed to perform efficiently over a wider Mach number range. This solution, however, adds weight and complexity to the aircraft.

In order to answer some of these design problems, several Mach number 3 design ejectors were investigated in the Lewis 8- by 6-foot wind tunnel in the Mach number range of 0.8 to 2.0.

## DISCUSSION

For the purpose of comparing ejector performances, several assumptions have been made and applied to each ejector. Figure 1 shows the assumed variation of primary-nozzle pressure ratio and also the accompanying variation in ideal-nozzle expansion ratio with free-stream Mach number. In addition to the exit area variation of the ideal nozzle required by the changing nozzle pressure ratio, variation of the exit area is needed as a result of the changes in primary throat area, which depend upon the degree of afterburning. Arbitrarily, afterburning was assumed to be "full on" above a Mach number of 1.35 and "full off" below that Mach number. It is felt that this assumption will have no effect on the generality of the analysis to follow. The ratio of primary-nozzle diameter without afterburning to that with afterburning was 0.75.

Figure 2 shows the performance of a fixed Mach number 3 design ejector, which has a low divergence angle of 11° and the ideal expansion ratio 1.8, for a Mach number of 3. The estimated on-design performance of this ejector, in terms of an effective gross-jet-thrust parameter, was good; however, it can be seen that off-design performance fell off rapidly, as was expected. The abscissa of figure 2 is the flight Mach

number, whereas the ordinate is a ratio of gross ejector jet thrust minus secondary free-stream momentum minus base and boattail drags and the ideal gross thrust attainable from the primary flow.

For all data in figure 2, the secondary weight-flow ratio was held constant at 2 percent. This is about the amount of secondary flow that has been used in the past for engine-cooling requirements.

The off-design thrust losses of the fixed Mach number 3 configuration result mainly from overexpansion of the flow in the divergent portion of the ejector. One way of reducing this loss is to increase the divergence angle and improve the lower Mach number separation characteristics. The performance at a Mach number of 3 of an ejector with a divergence angle of $25°$ and the same expansion ratio (fig. 2) is estimated to decrease slightly. The performance at low Mach numbers did improve as expected.

Another possible design compromise would be reducing the expansion ratio by effectively designing the ejector for a lower Mach number and splitting off-design losses between underexpansion and overexpansion. As seen in figure 2, about $4\frac{1}{2}$ counts in the effective thrust parameter would be lost because of underexpansion at a Mach number of 3 for a 1.45-diameter-ratio ejector. However, the performance at the lower speeds has been improved.

Still another method for handling the off-design problem at the low Mach numbers is to use large amounts of secondary air to fill a portion of the exit area and thus prevent overexpansion of the primary flow. This method seems to be suited to the off-design inlet problem discussed in the paper by Leonard E. Stitt in which large amounts of air were available at the lower Mach numbers with certain inlet types. In order to determine the effects of larger amounts of secondary flows, an inlet-engine combination has been assumed. The inlet has a variable throat and may capture a full stream tube over the flight range. The inlet air minus the engine requirements yields the typical bypass mass-flow schedule shown in figure 3. If all this bypass air were used as secondary flow in the ejector, and with the assumptions that the temperature with the primary afterburner on was $3,500°$ R, whereas the temperature with the afterburner off was $1,600°$ R, an upper limit of corrected secondary weight-flow ratio can be computed and is shown in figure 3. With an assumed inlet pressure recovery and the assumption of additional total-pressure losses in ducting the bypass air around the engine and back to the ejector, an upper limit of secondary total-pressure ratio can be computed and is also shown in figure 3. These two limits on the bypass air available at the ejector will be referred

to as bypass-air limitations. The mechanical difficulties that might be involved in ducting this bypass air back to the ejector have not been considered.

Figure 4 shows the effect of such high secondary flow on the performance of the 1.45-diameter-ratio ejector of figure 2. Using all the flow that the inlet can supply produced large thrust gains. The 50-percent values of corrected secondary flow are considerably larger than those generally considered in the past.

With respect to these large flows, it should be remembered that in the effective thrust parameter the ejector has been penalized with the full free-stream momentum of all secondary air. Therefore, if large amounts of secondary air cannot be obtained from the main inlet bypass, it may be desirable to have auxiliary inlets for this purpose. However, the problems of installing large auxiliary inlets are not considered herein.

In turning now to the other design philosophy, that is, variable-geometry ejectors, the upper ejector of figure 5 can be seen to be an extreme design. It is mechanically complex. This ejector has very long leaves in order that boattail drag be negligible and also has multiple pivot points to vary the secondary throat, the exit area, and the boattail angle. If this idealized configuration had been investigated, it is felt that it could produce a thrust parameter of 0.97 over the entire flight range. Somewhat simpler geometries have been investigated. The first of these designs, shown in figure 5, had a variable boattail and exit with a single compromised pivot point. The secondary diameter was fixed. The simpler ejector in this figure was supplied with 2-percent cooling air. Performance with the afterburner off dropped at Mach numbers of 1.35 and 1.00 because of afterbody drags and the inability of this ejector to handle secondary area variations required for operation with the afterburner off.

To explain this problem with a fixed secondary diameter further, figure 6 presents a comparison of the ideal expansion ratio and the actual test value of expansion ratio for the variable boattail ejector. With the ideal expansion ratio at some Mach number (for example, a Mach number of 1), the ejector shroud leaves formed a convergent flow passage, which resulted in poor internal performance. An alternative would have been to avoid such a convergent passage and permit overexpansion of the primary flow by setting larger values of exit- to primary-nozzle-diameter ratio than the ideal, as was done at a Mach number of 1.35 with no afterburning. In either case, performance would be less than ideal as a result of the mechanical simplification of permitting the secondary diameter to remain constant.

A different approach to the problem of simplifing the complex idealized nozzle is considered in figure 7. Here the boattail was fixed, whereas inner leaves varied the expansion ratio. Again, secondary diameter was fixed. As the exit area decreased, the base area increased. This configuration was investigated with and without flow into the base. For the case with base flow, bypass air was used according to the schedule of the lower curve in figure 7. The bypass-air limitations were applied to these data. When secondary air and no base bleed were used, the tertiary passage being blocked off, performance dropped off. This result was partly due to the added base drag of the configuration and partly due to primary flow overexpansion.

Figure 8 compares the schedule of expansion ratios for this ejector with the ideal expansion ratios. It can be noted that the Mach number 3 design has been slightly compromised and that, for performance with the afterburner off, the ejector shroud became cylindrical in shape. As a result, the expansion ratio was greater than ideal. This modification was made in order to avoid the performance penalty resulting from a convergent shroud, as discussed for the ejector of figure 5.

Still another variable-geometry type that was considered is the fixed boattail and exit with a variable secondary diameter as shown in figure 9. Engine bypass air was employed according to the lower curve and, as in figure 7, the bypass-air limitations were applied. Performance was very good at all Mach numbers.

A summary of the best configurations is shown in figure 10 where the variable boattail with cooling air, the variable secondary throat diameter with bypass air, and the fixed lower Mach number design compromise with bypass air are compared. It appears that a variable-geometry exit considerably simpler than an ideal exit and with only sufficient secondary air to cool the engine can provide reasonably good performance at all Mach numbers. If large amounts of high-pressure secondary air can be obtained, the performance of a fixed-geometry ejector, with suitable values of secondary diameter, can be maintained at a high level at all Mach numbers. If a variable secondary diameter is employed with these large amounts of secondary air, even better thrust performance can be obtained.
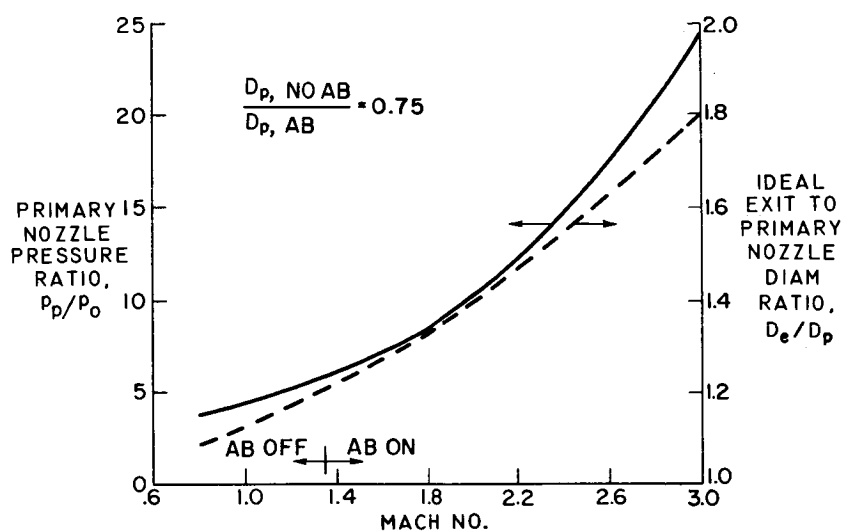
## PRIMARY NOZZLE SCHEDULE



$$\frac{D_p, \text{NO AB}}{D_p, \text{AB}} = 0.75$$

Figure 1

## DESIGN COMPROMISES FOR FIXED EJECTORS
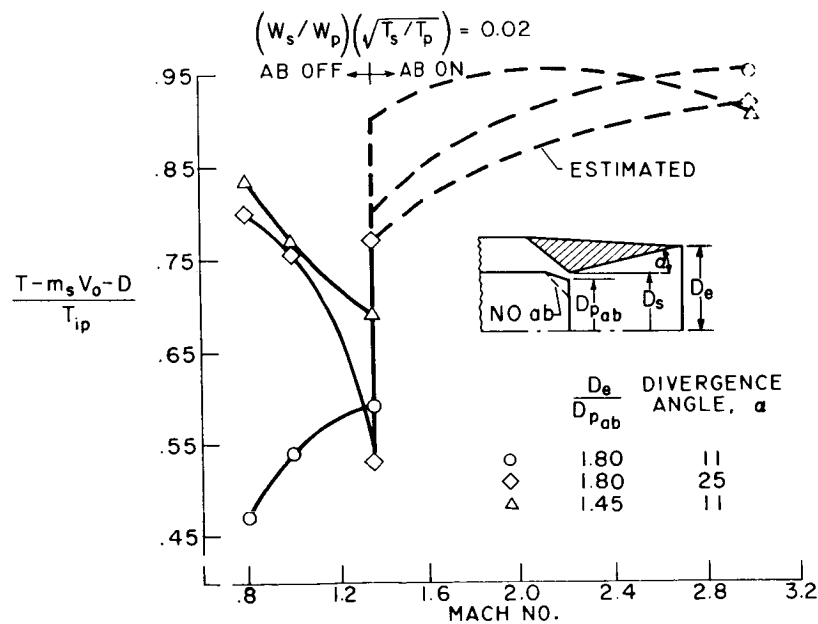
$$\left(W_s/W_p\right)\left(\sqrt{T_s/T_p}\right) = 0.02$$



Figure 2

## SCHEDULE OF INLET BYPASS AIR AVAILABLE FOR EJECTOR

$T_{p, AB} = 3500° R$

$T_{p, NO AB} = 1600° R$

BYPASS MASS FLOW RATIO, $m_b/m_o$

MAX CORRECTED WEIGHT FLOW RATIO, $\dfrac{W_s}{W_p}\sqrt{\dfrac{T_s}{T_p}}$

MAX SECONDARY TO PRIMARY TOTAL PRESSURE RATIO, $P_s/P_p$

$\dfrac{W_s}{W_p}\sqrt{\dfrac{T_s}{T_p}}$

$P_s/P_p$

$m_b/m_o$

$m_o$ $m_b$ ENGINE

MACH NO.

Figure 3

## EFFECT OF SECONDARY FLOW

FIXED EJECTOR, $D_e/D_{p_{ab}} = 1.45$, $D_s/D_{p_{ab}} = 1.21$

AB OFF | AB ON

$\dfrac{T - m_s V_o - D}{T_{ip}}$

ESTIMATED

HIGH SECONDARY FLOW

LOW SECONDARY FLOW

CORRECTED WEIGHT FLOW RATIO, $\dfrac{W_s}{W_p}\sqrt{\dfrac{T_s}{T_p}}$

PRESSURE LIMITED

MACH NO.

Figure 4

## VARIABLE SHROUD AND BOATTAIL

$$\frac{W_S}{W_P}\sqrt{\frac{T_S}{T_P}} = 0.02$$
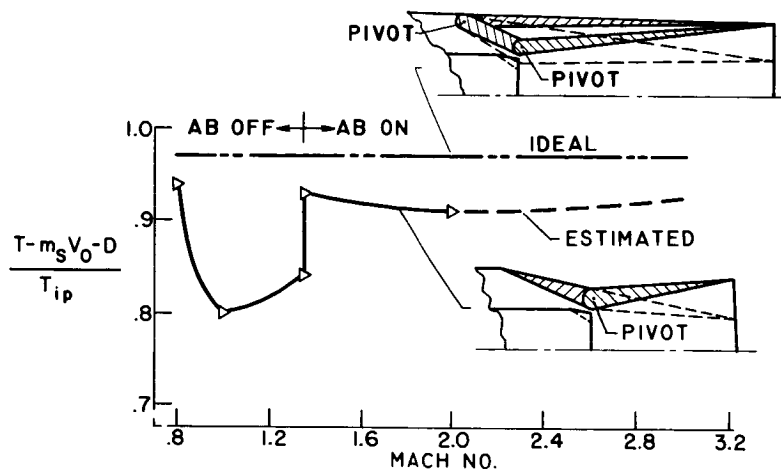


Figure 5

## EXPANSION RATIO SCHEDULE

### VARIABLE EXIT AREA AND BOATTAIL
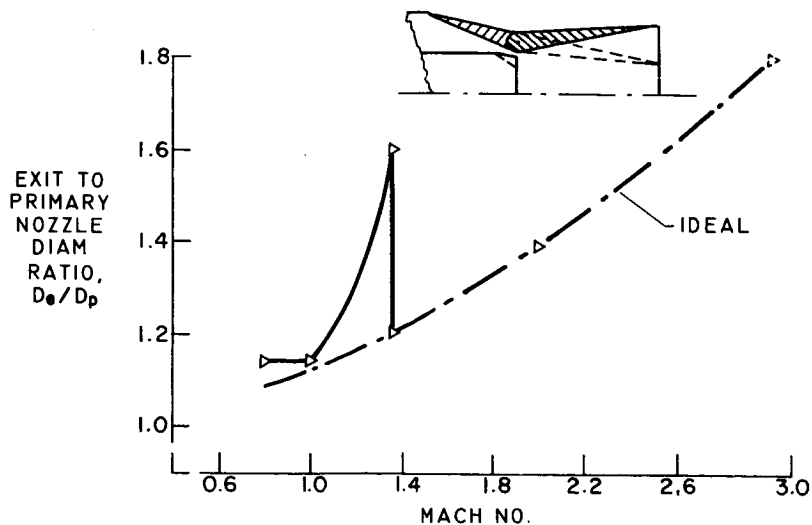


Figure 6

## VARIABLE EXIT WITH FIXED BOATTAIL

AB OFF ◄———— | ————► AB ON

IDEAL

ESTIMATED

$$\frac{T - m_s V_o - D}{T_{ip}}$$

BASE FLOW

NO BASE FLOW

CORRECTED WEIGHT FLOW RATIO,

$$\frac{W_s}{W_p}\sqrt{\frac{T_s}{T_p}}$$

AIR BASE PIVOT

MACH NO.
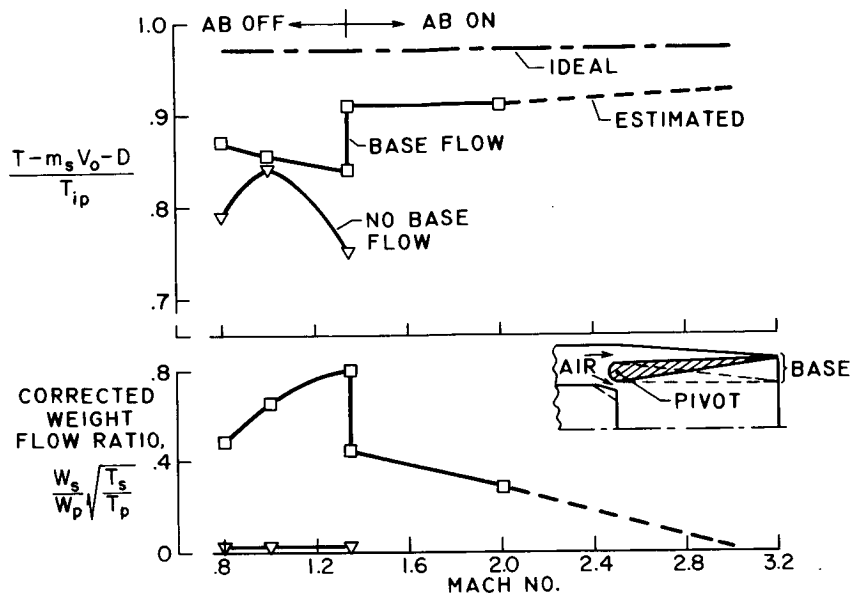
Figure 7

## EXPANSION RATIO SCHEDULE

### VARIABLE EXIT AREA WITH FIXED BOATTAIL

IDEAL

EXIT TO PRIMARY NOZZLE DIAM RATIO, $D_e/D_p$

AB OFF ◄——+——► AB ON

MACH NO.
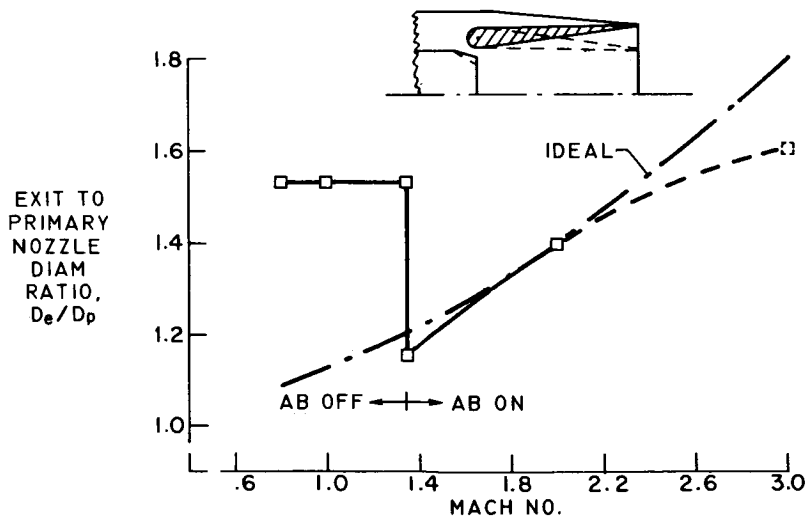
Figure 8

## FIXED EXIT WITH VARIABLE SECONDARY THROAT DIAMETER
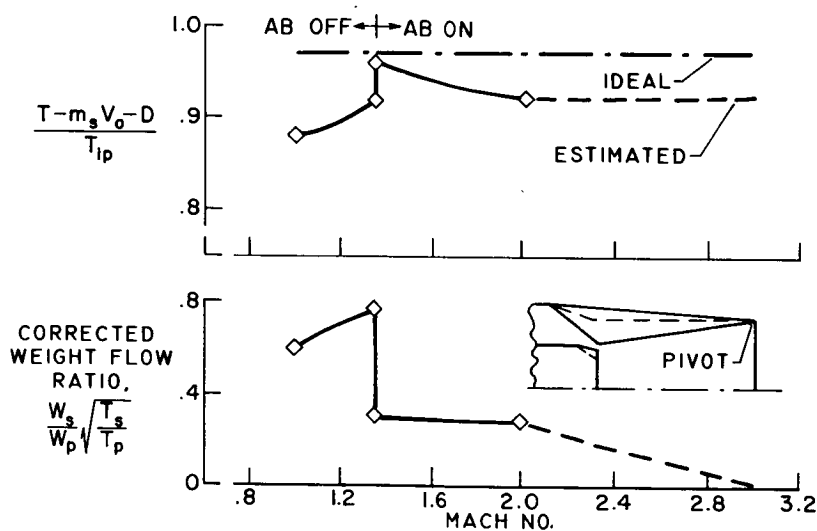


Figure 9

## COMPARISON OF BEST TYPES
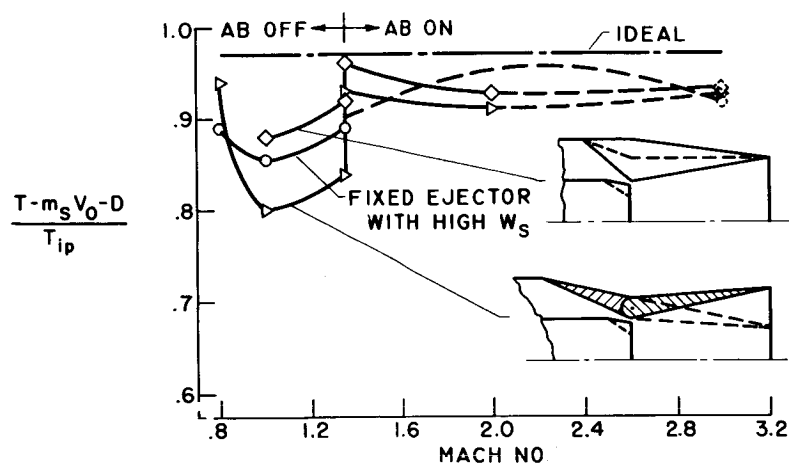


Figure 10

# PERFORMANCE OF MULTIPLE JET-EXIT INSTALLATIONS

By John M. Swihart and William J. Nelson

Langley Aeronautical Laboratory

## SUMMARY

This paper presents the results of recent exploratory investigations of the performance of clustered jet-exit installations at Mach numbers from 0.60 to 3.05. Data presented herein were obtained with tunnel-wall-mounted models with cold-air-jet exhaust. The results indicate that large base-pressure drag coefficients may be encountered in the transonic and low supersonic speed range and that the best configuration investigated was boattailed between the nacelles, had a cylindrical nacelle afterbody, and a divergent nozzle with a design pressure ratio of 15. It was also indicated that afterbody terminal fairings or base bleed might be used to eliminate the performance losses of overexpanded nozzles. If the terminal fairings or base bleed were applied to fixed ejector geometry, an important saving in weight and complexity would result.

## INTRODUCTION

Recent supersonic airplane designs, where the engines are clustered along the trailing edge of the wing in a side-by-side arrangement, have raised many questions relative to internacelle and interjet interferences on the base and afterbody drag. The purpose of this paper is to discuss the results of some recent investigations of clustered exit installations. Tests were conducted at Mach numbers from 0.60 to 3.05 with jet total-pressure ratios up to 40.

## SYMBOLS

$C_D$        drag coefficient, $\dfrac{D}{qS}$

$C_{D,b}$        base-pressure drag coefficient

46

$C_F$     thrust coefficient, $\dfrac{F}{qS}$

$C_{p,b}$     base pressure coefficient, $\dfrac{p_b - p_\infty}{q}$

$D$     drag

$F$     thrust

$M$     Mach number

$p_b$     base pressure

$\dfrac{p_{t,j}}{p_\infty}$     ratio of jet total pressure to free-stream static pressure

$p_\infty$     free-stream static pressure

$q$     dynamic pressure

$S$     assumed model wing area, 0.37 sq ft

$\Delta\left(C_F - C_D\right)$     incremental thrust-minus-drag coefficient

$\theta$     nozzle divergence angle

$\beta$     boattail angle

## APPARATUS

An exploratory investigation has been conducted in the Langley 9- by 12-inch blowdown tunnel and in the Langley internal aerodynamics laboratory by using wall-mounted models which approximately duplicated half of the configuration shown in figure 1. Interchangeable exit configurations with different amounts of boattailing, nozzle-divergence angles, and afterbody terminal fairings are presented subsequently. The jet exhaust was simulated with cold air; numerous test data have shown that this simulation is adequate for an exploratory investigation of this type. (See refs. 1 and 2.) Base pressures, surface pressures between the nacelles, drag, and thrust-minus-drag were measured, and flow-visualization studies have been made over the Mach number range.

# RESULTS AND DISCUSSION

## Base Pressures

Effect of pressure ratio at transonic speeds.- Figure 2 shows the base-pressure coefficients of side-by-side arrangements at transonic speeds. The average base-pressure coefficient obtained by averaging the pressures over the base is plotted against the ratio of jet total pressure to free-stream static pressure at Mach numbers of 0.90 and 1.25. Data are for a three-engine configuration with a jet-to-base diameter ratio of 0.5 and sonic exits. This configuration is a basic model with slight boattailing and a flat base and is not intended as a practical configuration; however, configurations with similar lines have been proposed where large amounts of secondary flow are available for base bleed. Single-engine nacelle data are shown for comparison, inasmuch as wide ranges of shape variables have been investigated on single-engine nacelles at transonic and supersonic speeds. The data for the single-engine configuration are for a cylindrical nacelle with a sonic jet exit and the same base-to-diameter ratio as the three-engine clustered configuration. The data indicate that the trends of the single-engine and the three-engine configurations are very similar; thus, the single-engine nacelle data could probably be applied qualitatively to the clustered exit design. The important thing in figure 2, however, is the magnitude of the base-pressure coefficient, inasmuch as the peak negative values occur near the operating pressure ratios for supersonic engines for each Mach number. In fact, at a Mach number of 1.25 for a six-engine airplane with 5-foot-diameter nacelles and 6,000 square feet of wing area, the base-pressure drag coefficient would be 0.0066. This value of $C_{D,b}$ indicates that, in a region where the thrust margin of the supersonic engine may be a minimum, the base-pressure drag may be a maximum; consequently, there would be an increase in acceleration time and a loss in airplane range.

Effect of Mach number.- Figure 3 shows the effect of Mach number on base-pressure coefficient. The average base-pressure coefficient is plotted against Mach number at pressure ratios corresponding to this schedule of engine-pressure-ratio variation with Mach number also shown in this figure. This pressure-ratio schedule is considered to be typical for the supersonic engine. The data shown in the transonic speed range are for the three-engine configuration shown in figure 2 with sonic jet exits. The data shown at Mach numbers of 1.62 and above are for a similar flat-base configuration with convergent-divergent nozzles with design pressure ratios of 8. The nozzles are underexpanded for all Mach numbers above 1.62; however, this is the design condition for some supersonic engine configurations. Expansion ratios greater than this value would make $C_{p,b}$ more negative. The data indicate

that the base-pressure coefficient reaches a peak negative value between
Mach numbers of 1 and 1.5 and then falls rapidly with an increase in
Mach number. The value looks small at a Mach number of 3.05; however,
if it were applied to the six-engine airplane with a wing area of
6,000 square feet mentioned previously, the base-pressure drag coeffi-
cient would be about 0.0010 or approximately 7 percent of the expected
total drag of such a configuration.

## Effect of Boattailing

The question arises - how much should the clustered exit configu-
ration be boattailed? Shown in figure 4 are three configurations with
various amounts of boattailing. All three of these configurations have
the same internal nozzle contour, namely, convergent-divergent nozzles
with design pressure ratios of about 8. Configuration 1 is an idealized
configuration with zero base area and 6° of boattailing on the individual
nacelle. It is also boattailed between the individual nacelles. Con-
figuration 2 has cylindrical nacelles, a base annulus, and boattailing
between the nacelles. Configuration 3 has no boattailing whatsoever.
As was stated previously, consideration has been given to configurations
with flat bases similar to configuration 3.

Figure 5 shows the effect of boattailing on incremental thrust
minus drag coefficient. The incremental thrust drag is obtained by
subtracting the measured thrust minus drag of the configuration from
that of configuration 1 at pressure ratios corresponding to the schedule
with Mach number also shown in the figure. Configuration 1 will be used
as the reference configuration in all subsequent plots of $\Delta\left(C_F - C_D\right)$
in this paper. The data indicate that progressive boattailing from
configuration 3 to configuration 1 results in a reduction of drag in
that same order. It appears that the overall boattailing of the configu-
ration may be more important than that of the individual nacelle, since
configuration 2 has reduced the drag so that it approaches that of con-
figuration 1. Base pressures measured on configurations 2 and 3 at a
Mach number of 3.05 indicate that the jet interference due to the under-
expanded jet has a more marked beneficial effect on configuration 2
than on configuration 3, as is shown in figure 6. The improvement to
configuration 3 that would be obtained by the addition of base bleed is
unknown, but it is expected that base bleed would provide a small improve-
ment in base-pressure drag coefficient.

## Effect of Afterbody-Nozzle Geometry

In figure 5 the effect of boattailing with fixed nozzle geometry
was shown. Figure 7 shows three configurations which represent a schedule

of afterbody-nozzle geometry over the Mach number range where each setting is designed to produce optimum thrust at a particular Mach number. Configuration 1 is repeated from the previous figures and configuration 4 represents a maximum afterburner setting with a cylindrical nacelle and a convergent-divergent nozzle with a design pressure ratio of 15 at a Mach number of 2.4. Configuration 5 represents an intermediate setting with a design pressure ratio of 11 and design Mach number of 1.9. The variation of incremental thrust-minus-drag coefficient with Mach number for these three configurations is shown in figure 8. The data are presented for the pressure-ratio schedule also shown in figure 8. It is indicated that configuration 4 is better than the other two configurations over the entire Mach number range. It would be expected that configuration 4 would be the best above a Mach number of 2.4, since it has a zero pressure drag nacelle and the nozzle is at or above its design pressure ratio. In other words, it is developing more divergent nozzle thrust above this Mach number. The low value of $\Delta\left(C_F - C_D\right)$ of configuration 4 suggests the possibility of even better performance near $M = 3.0$ with a larger nacelle and a nozzle having a higher design pressure ratio. It is surprising that configuration 4 does not exhibit more of the expected large overexpansion losses at speeds below design. It is noted that some delay in experiencing these losses has already occurred, probably because of external stream and separation effects in the nozzle. It may also be caused by the low Reynolds number of the internal flow. If the good performance of configuration 4 can be maintained into the transonic speed range by eliminating the overexpansion losses, it might be possible to operate the clustered exit over the Mach number range of this investigation with fixed ejector geometry and thereby make a large saving in weight and complexity.

<center>Terminal Fairings</center>

Figure 9 shows photographs of two special devices which were investigated at transonic speeds in an attempt to reduce the overexpansion losses of fixed ejector geometry and to improve the configuration performance. To the first device, shown in the upper left of the figure, six bodies have been applied to a combination of a low-design-pressure-ratio convergent-divergent nozzle and a curved-afterbody, and these fairings are very carefully designed to increase the effective fineness ratio of the afterbody and to provide surfaces for the underexpanded jet to act upon. The slotted afterbody shown in the lower right of the figure is a variation of the terminal fairing idea which looks a little more conventional. It consists of a basic curved afterbody with a fixed-divergent ejector designed for a pressure ratio of 10 with longitudinal slots cut into the ejector throat to ventilate the surface at sonic

speeds. Both of these terminal fairing models showed significant improvement in thrust minus drag over their basic configurations throughout most of the transonic speed range.

Since some success had been attained at transonic speeds, terminal fairings were applied to the flat-base configuration (configuration 3), and figure 10 shows the complete model used for the supersonic investigation with the terminal fairings installed. The internal contour of the nozzles is the same as that of the flat-base configuration and the boattailed configuration (configuration 1) that was shown earlier. The results shown in figure 11, where $\Delta\left(C_F - C_D\right)$ is plotted against Mach number for the pressure-ratio schedule shown in the figure, indicate that the fairings provide a significant improvement over the flat-base configuration. In fact, they reduce the drag about one-half the way toward configuration 4, which was the best studied. The drag of the fairing model was about the same as the best of the boattail series shown here as the reference. Obviously, the fairings could have been applied to a boattailed design and, of course, the fairing design has not been optimumized in the supersonic speed range. The success gained to date with these terminal fairings indicates the need for further research on this type of design.

CONCLUSIONS

Recent exploratory investigations of the performance of clustered jet-exit installations at Mach numbers from 0.60 to 3.05 indicated the following conclusions:

1. There is a large amount of single-engine data available that would apply qualitatively to the clustered-exit design.

2. The clustered-exit installations may encounter very large base pressure drags in the transonic and low supersonic speed range where the exit nozzle is closed down to provide maximum internal performance.

3. Significant effects of configuration geometry were shown with the indication, at least, that overall boattailing may be more powerful than that of the individual nacelle.

4. The best configuration investigated was a cylindrical nacelle with boattailing between the nacelles and a convergent-divergent exhaust nozzle with a design pressure ratio of 15. This configuration was superior well into the region where the nozzle was overexpanded. It appears that, if some method of delaying these adverse overexpansion effects can be found, important savings in weight and complexity can be

gained by fixed ejector geometry. One possible method of accomplishing this is by the use of terminal fairings and another method may be by the use of base bleed.

## REFERENCES

1. Love, Eugene S., and Grigsby, Carl E.: Some Studies of Axisymmetric Free Jets Exhausting From Sonic and Supersonic Nozzles Into Still Air and Into Supersonic Streams. NACA RM L54L31, 1955.

2. Baughman, L. Eugene, and Kochendorfer, Fred D.: Jet Effects on Base Pressures of Conical Afterbodies at Mach 1.91 and 3.12. NACA RM E57E06, 1957.

## CLUSTERED ENGINE ARRANGEMENT
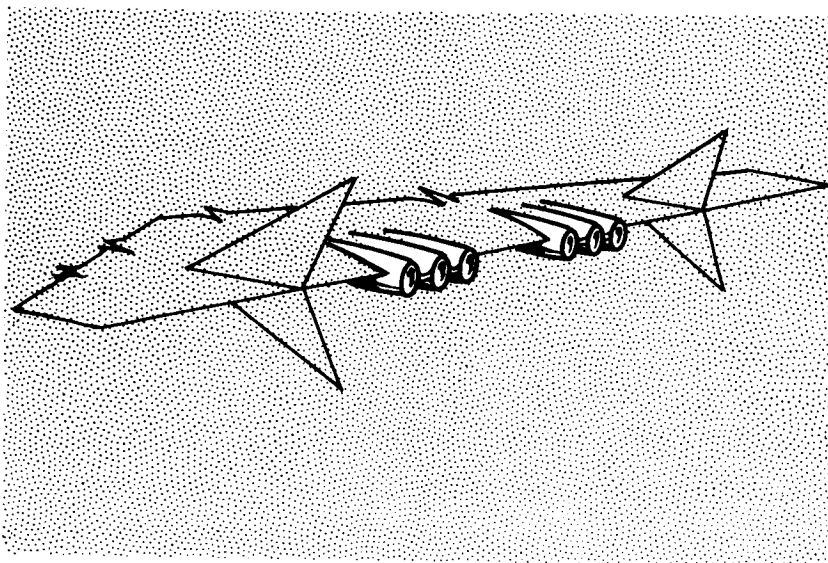


Figure 1

## TRANSONIC BASE PRESSURE
### JET EFFECT OF SIDE-BY-SIDE NACELLES
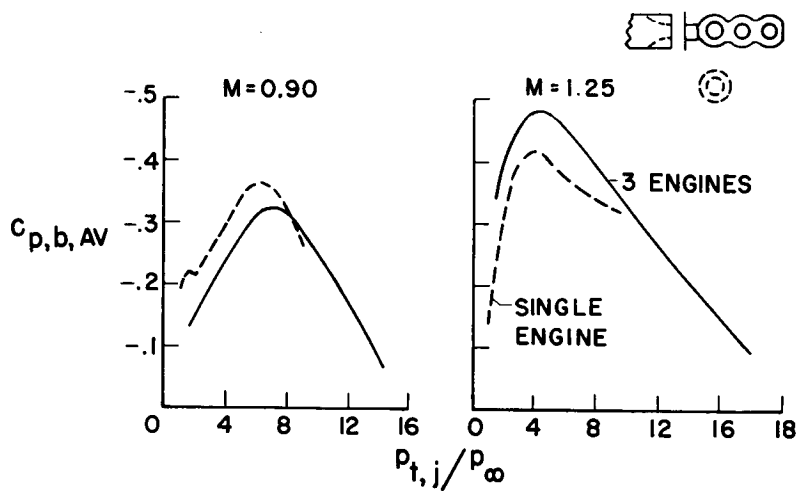


Figure 2

EFFECT OF MACH NUMBER ON BASE PRESSURE COEFFICIENT
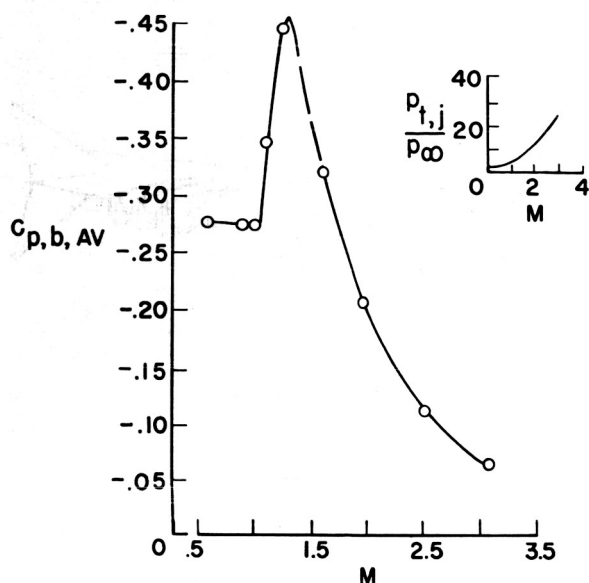


Figure 3

AFTERBODY GEOMETRY



CONFIGURATION I
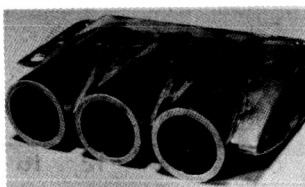


CONFIGURATION 2



CONFIGURATION 3

Figure 4

## INCREMENTAL THRUST-DRAG
### EFFECT OF BOATTAILING
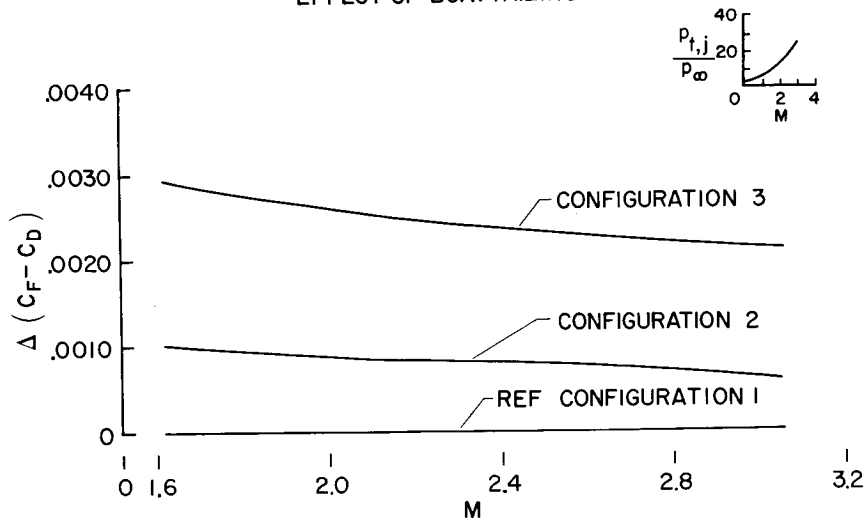


Figure 5

## BASE PRESSURE COEFFICIENTS
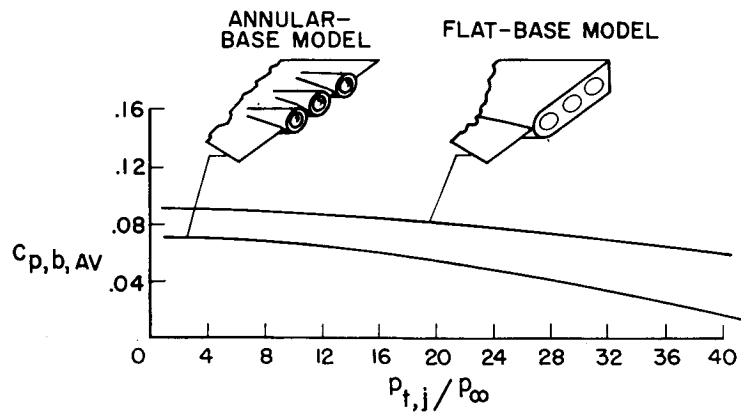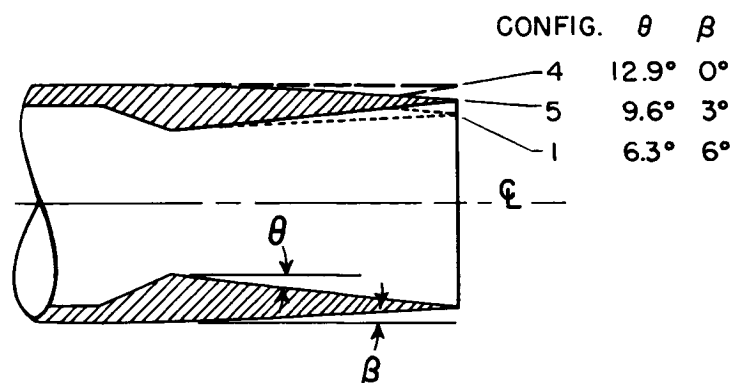### M = 3.05



Figure 6

# BOATTAIL AND NOZZLE GEOMETRY

| CONFIG. | $\theta$ | $\beta$ |
|---------|----------|---------|
| 4 | 12.9° | 0° |
| 5 | 9.6° | 3° |
| 1 | 6.3° | 6° |

Figure 7

## INCREMENTAL THRUST—DRAG
### BOATTAIL AND NOZZLE VARIED SIMULTANEOUSLY

REF CONFIGURATION 1

CONFIGURATION 5

CONFIGURATION 4

$\dfrac{p_{t,j}}{p_\infty}$
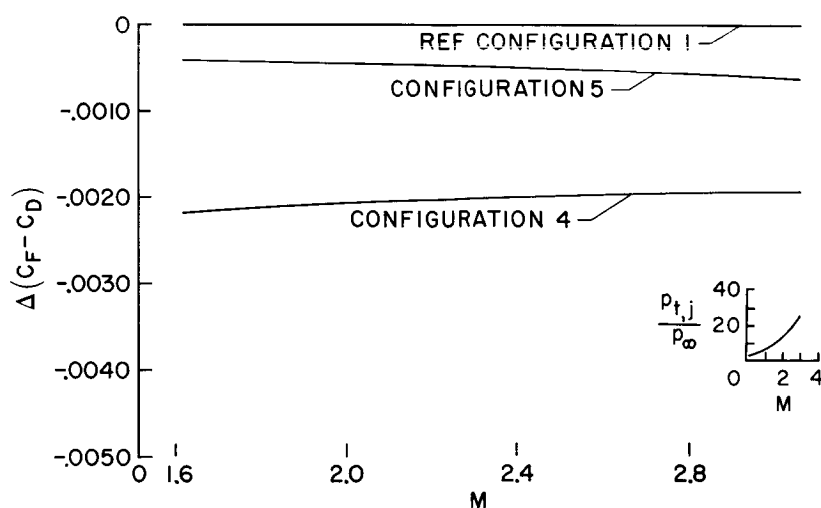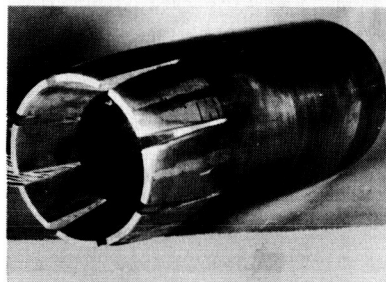
Figure 8
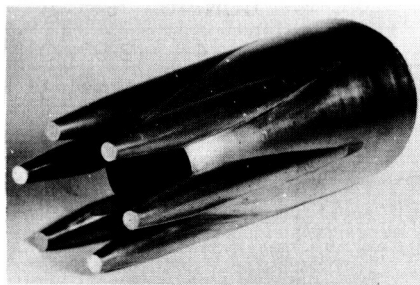
TERMINAL FAIRINGS



SIX FAIRINGS

SLOTTED AFTERBODY

Figure 9

TERMINAL FAIRINGS APPLIED TO CLUSTERED EXIT ARRANGEMENT



Figure 10

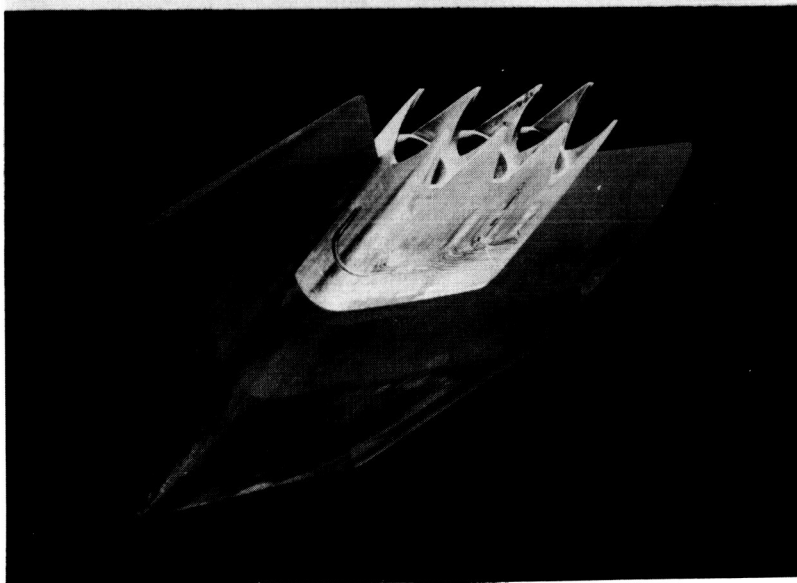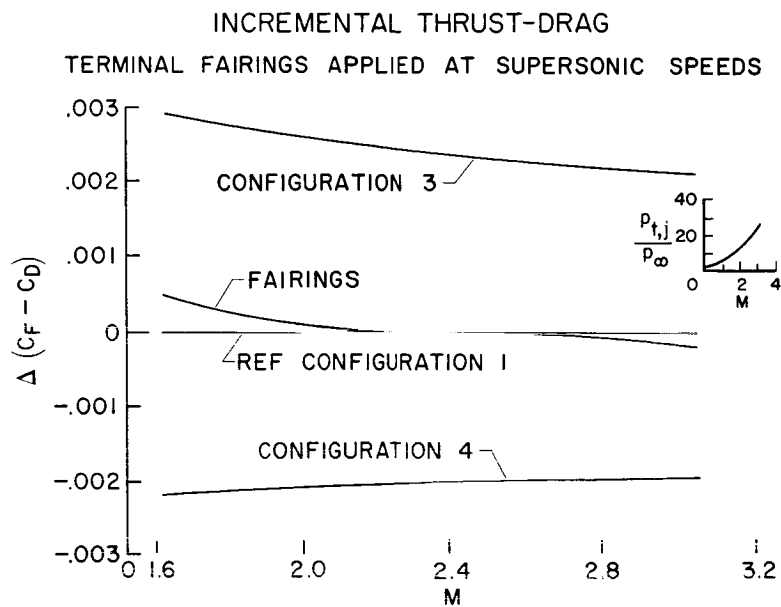INCREMENTAL THRUST–DRAG

TERMINAL FAIRINGS APPLIED AT SUPERSONIC SPEEDS



Figure 11